CIRCULATING FLUIDISED BED FLUID AND PARTICLE MECHANICS: MODELLING AND EXPERIMENTAL STUDIES WITH APPLICATION TO COMBUSTION

by

Richard C. Senior

B. E. (Hons.) Monash University, Clayton, Australia, 1983

A THESIS SUBMITTED IN PARTIAL FULFILLMENT OF

THE REQUIREMENTS FOR THE DEGREE OF

DOCTOR OF PHILOSOPHY

in

THE FACULTY OF GRADUATE STUDIES

DEPARTMENT OF CHEMICAL ENGINEERING

We accept this thesis as conforming

to the required standard

THE UNIVERSITY OF BRITISH COLUMBIA

April 1992

Department of Chemical Engineering
The University of British Columbia
2216 Main Mall
Vancouver, BC, Canada
V6T 1W5

Date: JUNE 5, 1992

ABSTRACT

The fluid and particle mechanics of circulating fluidised beds (CFBs) was studied in a series of theoretical and experimental investigations, leading to the development of two riser models. Though the study focussed primarily on CFB combustors, most of the results apply to all CFB applications.

Experimental tests were performed in a 9.3 m high, 152 mm ID transparent cold model riser. The effects of varying the riser base section geometry, riser exit geometry, secondary air injection, particle size distribution (PSD) and particle density were investigated. Local solids concentrations within the riser were measured by a needle capacitance probe, and axial suspension density profiles were estimated from measured differential pressures along the riser length. All parameters investigated influenced the solids flow and distribution in the riser. In particular, changing the base section of the riser from a cylindrical to conical geometry significantly influenced suspension densities in the lower part of the riser. PSD affected solids hold-up within the riser when there was downflow of particle sheets or "streamers" at the wall. Radial particle size segregation was detected in tests with wide PSD particles.

Experimental results were also obtained from a 7.3 m high, 152 mm $\times$ 152 mm square pilot-scale CFB combustor. Axial suspension density profiles were recorded for typical CFB combustor operating conditions. Wear patterns on erosion probes and results from high temperature capacitance probe traverses indicated a core-annulus solids distribution, similar to that observed in cold unit risers.

Detailed analyses of likely gas-particle and particle-particle interactions within the riser were performed. An extension to existing methods for estimation of the response of discrete particles to gas turbulence was derived that allowed for particle inertia and "crossing trajectory" effects. Based on these analyses, a comprehensive model for dilute gas-particle suspension flow

was developed. Both particle collisions and particle-turbulence interactions were considered. The turbulence was represented by energetic eddies of characteristic size and decay time. The particle phase was discretised into multiple size/density fractions, and ensemble average r.m.s. fluctuating and mean velocity components were assigned to each fraction. Particle fraction mass, momentum and fluctuating kinetic energy balances were derived. An additional energy balance for the modulation of the gas turbulence intensity by particles was included. A fully-developed flow version of the model was coded, and simulations of riser flows were performed.

Model simulations predicted particle fluctuating velocities that were similar in magnitude to reported values measured in pilot-scale tests. Trends were consistent with those observed in the cold unit PSD tests. In simulations with small FCC catalyst particles, gas turbulence was predicted to significantly influence the particle motion. In contrast, turbulence was of secondary importance in simulations with larger particles used in CFB combustors. Greater reductions in gas turbulence intensity, due to modulation by the particles, were predicted in larger diameter and elevated temperature risers, than in cold unit pilot-scale units.

A semi-empirical predictive model was also developed, based on a core-annulus two-zone approach. A mechanistic equation for entrainment of particles from wall streamers into the riser core flow was proposed. "Exit effects" observed in the cold unit tests, due to the riser exit geometry, were characterised by an exit "reflection coefficient." Constants needed for the model were obtained by fitting to results from the pilot-scale combustor. Good agreement between model predictions and data from a larger prototype CFB combustor was achieved using these constants, except that a different "reflection coefficient"was used, which was consistent with the prototype unit exit geometry.

A mechanism for the formation of wall streamers was proposed, supported by calculations of discrete particle trajectories in the region of steep gas velocity gradient near the riser wall. The estimated shear-flow-induced lift force on the particles in this region can be significant. This investigation suggested that "non-continuum effects" in the particle phase may exist in these layers. These effects are not allowed for in two-fluid model formulations.

TABLE OF CONTENTS

LIST OF TABLES

LIST OF FIGURES

ACKNOWLEDGEMENT

I would like to express my sincere appreciation to a number of people whose efforts have contributed greatly to the success of this thesis.

To Dr. John R. Grace, whose integrity, guidance and encouragement have been a source of inspiration over the course of this project, I am more grateful than I can adequately express. I am also indebted to my co-supervisors, Dr. Clive Brereton and Dr. C. Jim Lim, for the ideas, discussion and support they provided.

The efforts of those involved with operation of the CFB combustor, Hugh Ackroyd, Dr. Richard Wu, James Muir, Jiansheng Zhao and Dr. Adam Luckos, are greatly appreciated. In particular, I want to thank Dr. Robert Legros. Our collaborative combustor experiments are described in this thesis. I also thank Dr. William Goldblatt for his assistance with the cold model CFB, and Irene Hwang for her efforts in analysis of numerous particle samples.

Financial support from the Killam Memorial Fund for Advanced Studies, the U.B.C. Graduate Fellowship Fund, ABB Combustion Engineering of Connecticut, U.S.A., Studsvik Energiteknik of Sweden, and Energy, Mines and Resources Canada is also gratefully acknowledged.

For her love, support and understanding, I thank my wife Kate. Her encouragement and unwavering confidence in me have been essential to the success of this thesis.

Chapter 1

INTRODUCTION

Circulating fluidised bed (CFB) technology originated in the 1940's with the development of fluidised catalytic cracking of heavy oils. The technology remained largely in the domain of this industry until the late 1970's, when advantages of CFB combustors over conventional bubbling fluidised bed boilers began to be realised. Since then there has been a marked increase in CFB research. CFB reactors are now recognised as an excellent gas-solid contacting scheme for a broad range of commercial processes, including combustion of low grade and high sulphur fuels (Engstrom and Lee, 1991) and calcination of aluminum ores and phosphates (Reh, 1986).

The principal component of a circulating fluidised bed facility is the *riser* or reactor section, a tall column with a large height-to-width ratio. Riser heights typically vary between 10 and 35 m. Fluidising gas enters the base of the riser, and contacts particles in suspension. Gas velocities in the riser are substantially higher than in conventional bubbling beds, and there is a considerable carryover of particles from the top of the riser. Entrained particles are separated from the riser exit gas stream by solids separators, such as cyclones, and returned continuously near the base of the riser. The high gas velocities in the riser result in vigorous solids mixing, intimate gas-solid contacting, and relatively uniform riser suspension temperatures under normal operating conditions. In many CFB applications, the mass of solids in suspension within the riser is controlled by adjusting the external solids recirculation rate.

The theoretical work presented in this thesis applies generally to all CFB applications. However, the primary focus here is the fluid and particle mechanics of CFB combustors. The theoretical discussions and model simulations generally assume a range of particle properties

and operating conditions typical of these units. The theoretical studies are supported by hydrodynamic testwork performed in the University of British Columbia (UBC) pilot-scale CFB combustor, and tests in a pilot-scale CFB cold unit. CFB combustors utilise relatively larger and denser particles, than in other CFB applications. Differences between the behaviour of suspensions of small, low density particles, as in fluid catalytic cracking (FCC) risers, and CFB combustor particle suspensions, are explored in Chapter 8.

Although all CFB operations are similar in principle, riser designs vary significantly, even for the same application. Figure 1.1 shows a schematic of a typical CFB combustor. Staged air injection in these units is used to reduce NO_X formation. Secondary-to-primary air ratios generally range between 1:3 and 3:1, and typical superficial gas velocities above the secondary air ports are between 5 and 10 m/s. Tertiary air injection is also sometimes employed. The particle mixture is comprised mainly of sorbent limestone (for in-situ capture of SO_X), residual ash from the fuel, and sand. Particle diameters typically range between 20 and 500 μm, and mean particle densities are of the order 2000 – 3000 kg/m^3. Solid fuel particles constitute a small fraction of the total bed inventory ($<$ 5 wt%), and range in size from 20 to 3000 μm. Removal of heat from within the riser occurs via exposed vertical membrane waterwall surfaces. Solids return to CFB combustors may be controlled by a number of devices, e.g. by an L-valve as in the experiments carried out in this study. The base of a CFB combustor riser may taper inwards, have constant cross-section, or flare outwards, depending on the manufacturer. Similarly the exit geometry may vary. The significant influence of these designs on the gas-solid flow patterns within the riser is investigated.

Research in the past decade has dispelled an earlier misconception that gas and particles travel up the riser in plug flow. It is now known that there are substantial variations in lateral and axial solids concentration and velocity within the riser. Despite high riser gas velocities, which are generally at least an order of magnitude greater than particle terminal settling velocities, significant downflows of solids are often detected, predominantly along the riser walls. The riser diameter, D, exit and base section geometry, superficial gas velocity, U_g,

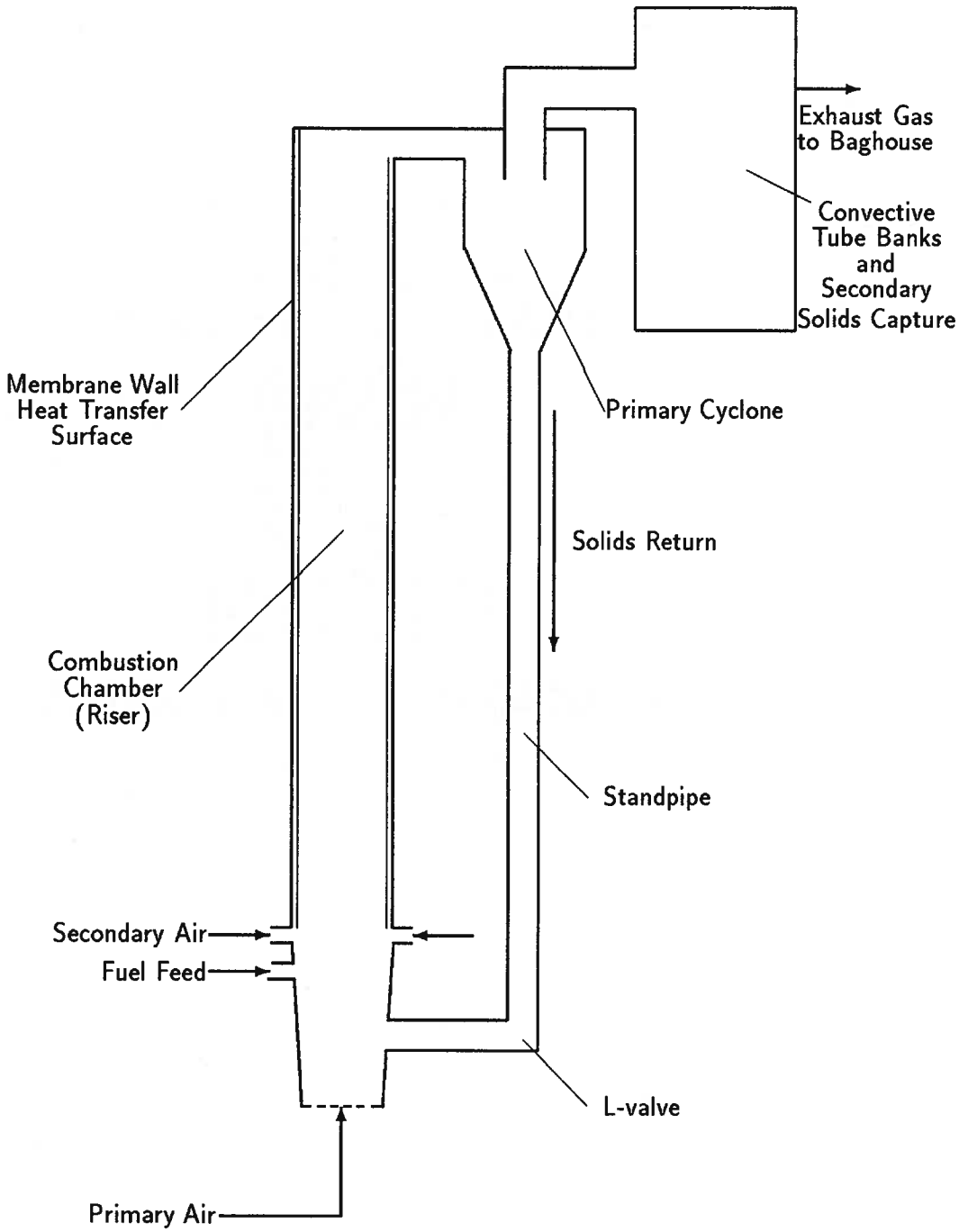

Figure 1.1: Simplified schematic diagram of a circulating fluidised bed combustor.

solids recirculation rate, G_s, temperature, T, and particle properties (diameter, d_p, density, ρ_p, shape, impact behaviour, etc.) *all* significantly influence the operational characteristics of the unit. All vary substantially between different CFB applications, and even between units with similar applications. In view of this large parameter space and the non-uniformities in riser solids concentration, it is not surprising that empirical correlations have had little success in predicting key riser phenomena.

Understanding of the fundamental dynamics in the riser is far from complete. It is not uncommon to see apparently contradictory general statements or modelling assumptions. For example, there are two explanations for the lateral motion of particles across the riser, and subsequent particle deposition at the riser walls. Some investigators contend that it is due to the effects of gas turbulence on the particles, whilst others assert that it arises because of oblique particle collisions. Different model predictions, based on one or other of these assumptions, have even been compared to the same experimental data. From a theoretical perspective, it is clearly desirable to resolve such uncertainties. The practical benefits of a better understanding of fundamental riser dynamics are obvious: improved design and operating strategies, reduced pilot-scale test costs for new applications, and reduced risk of scale-up problems.

The general objective of this study was to improve our understanding of CFB riser mechanics by a series of inter-related experimental investigations and theoretical and semi-empirical modelling studies. Dynamics of the standpipe and cyclones were not considered. A more specific objective was to establish a sound framework for future development of comprehensive CFB models. The merits of various modelling methods are discussed, and the limits of common assumptions are evaluated, based on both the experimental and theoretical investigations described.

The results of a number of prior hydrodynamic investigations are summarised in Chapter 2, and the gas and solids flow patterns commonly inferred from these measurements are discussed. Methods for characterising the fundamental dynamics of a discrete particle in gas

flow are next considered in Chapter 3. In particular, the interaction of gas turbulence and particles in suspension are investigated. A new, relatively simple approach for predicting particle response to turbulence, and simultaneous modulation of turbulence intensity, is proposed. The concepts of particle collision dynamics are also introduced. In Chapter 4, general criteria for a riser model are established. The continuum "two-fluid" equations of motion for gas-particle suspension flow are presented, and difficulties with their application to CFB riser modelling are pinpointed. The merits and advantages of various riser modelling approaches, including simple correlations, multi-zone methods, and complex multi-dimensional models, are discussed in Chapter 5. The cold unit and combustor experimental results are then presented in Chapters 6 and 7, respectively. The theoretical material presented in prior chapters is used to interpret the data.

In Chapter 8, a novel "integrated particle collision and turbulent diffusion" model for dilute gas-particle suspension flows is developed, using concepts and results from Chapter 3. This model allows for effects of particle size distribution, particle collisions and gas turbulence. It overcomes several objections to existing multi-dimensional models raised in Chapters 4 and 5. It is incorporated in a riser model for fully-developed flow. Subsequent model simulations provide answers to a number of important modelling questions. Riser wall dynamics, and riser "exit" and "entry" effects are discussed from a theoretical viewpoint in Chapter 9, drawing on the experimental results of Chapters 6 and 7. Finally, a semi-empirical predictive "engineering" model for solids flow and distribution in the riser is presented in Chapter 10 that is fitted to the Chapter 7 data.

Chapter 2

SYNOPSIS OF CIRCULATING FLUIDISED BED HYDRODYNAMICS

A qualitative description of the gas and solid flow patterns within risers is presented in this Chapter. The discussion is brief, as many of the described phenomena, and their underlying causes, are examined in greater detail in the following Chapters. Most detailed hydrodynamic tests performed by previous investigators have been at ambient temperature in bench-scale or pilot-scale units. The discussion therefore focuses primarily on a number of the more significant results from these studies. The results of several preliminary studies at elevated temperature, including CFB combustor hydrodynamic tests presented in Chapter 7, suggest that similar flow patterns exist in CFB risers at high temperature. The accuracy of riser hydrodynamic data is typically $O(\pm\ 20\%)$. Definitions for this study of "turbulent" and "fast" fluidisation regimes are also given. It is assumed that the terms "riser," "CFB reactor," "fast bed," "reactor column," and "riser reactor" are synonymous. Furthermore, the term "circulating fluidised bed" ("CFB") is assumed to refer to the CFB riser, rather than the full CFB facility, unless otherwise stated.

2.1 Axial Solids Distribution and "Apparent" Suspension Density Profiles

The most commonly reported experimental variable from CFB riser investigations is an estimate of the suspension density from the measured axial gas pressure gradient:

$$\rho_{sa} = -\ \frac{1}{g}\frac{dp_g}{dz}\ , \tag{2.1}$$

where dp_g/dz is estimated from measurements of pressure drop, Δp_g, over a given height increment, Δz. Pressure is normally measured at the riser wall using small ports flush with the wall. Equation (2.1) is based on the assumptions that the flow is steady and fully-developed, and effects of gas-wall friction and particle-wall friction are neglected.

The estimated suspension density is a cross-sectional average. In this study it is termed the "apparent suspension density," ρ_{sa}. The derivation of eq. (2.1) is given in Chapter 4, and limits of its applicability are investigated in Chapters 4 and 6. Pre-empting those results, it should be noted that ρ_{sa} is a reasonable estimate (O $\pm 20\%$) of the true cross-sectionally averaged suspension density at typical CFB operating conditions, except within about 1–3 m of the base of the riser and 1–2 m from the riser exit. Some investigators overlook these limits and assume ρ_{sa} to be equal to the true average suspension density.

The variety of shapes of apparent suspension density profiles reported in the CFB literature are illustrated in Figure 2.1. Trends, common to all profiles, are relatively high suspension densities near the base of the riser that decay to lower levels in the middle heights of the riser. The higher *apparent* suspension densities in the bottom of the riser are due to both high solids acceleration in this region and relatively high true suspension densities. Solids volume fractions in the base section are typically in the range 0.05–0.3, and decay to values generally less 0.03 further up the riser. Note that the denser regions are significantly more dilute than a packed bed.

The "S-shaped" or "sigmoidal" profile, curve (i) in Figure 2.1, has gained some pre-eminence in the literature, due to the pioneering work of Li and Kwauk (1980), who measured profiles for a range of particle types (d_p from 50 to 105 μm, ρ_p from 1800 to 4500 kg/m^3) in a 90 mm diameter cold unit. They fitted sigmoidal curves to their data and proposed correlations to predict these profiles. The almost constant apparent suspension density profile in the lower part of the riser is often assumed to indicate the formation of a relatively dense "turbulent" fluidised bed, a region of refluxing strands and packets of particles intermixed with rapid dilute suspension upflow, discussed below. Following the example of Li and Kwauk, a number of investigators have fitted sigmoidal profiles to their apparent suspension density data (e.g. Horio *et al.*, 1988; Hartge *et al.*, 1986; Arena *et al.*, 1988). A survey of the cold unit test data shows that a *full* sigmoidal profile is generally only observed at low gas velocities (e.g. $U_g < 4.0$ m/s for typical particles used in CFB combustors, and $U_g < 2.0$ m/s for lighter FCC catalyst), or very high

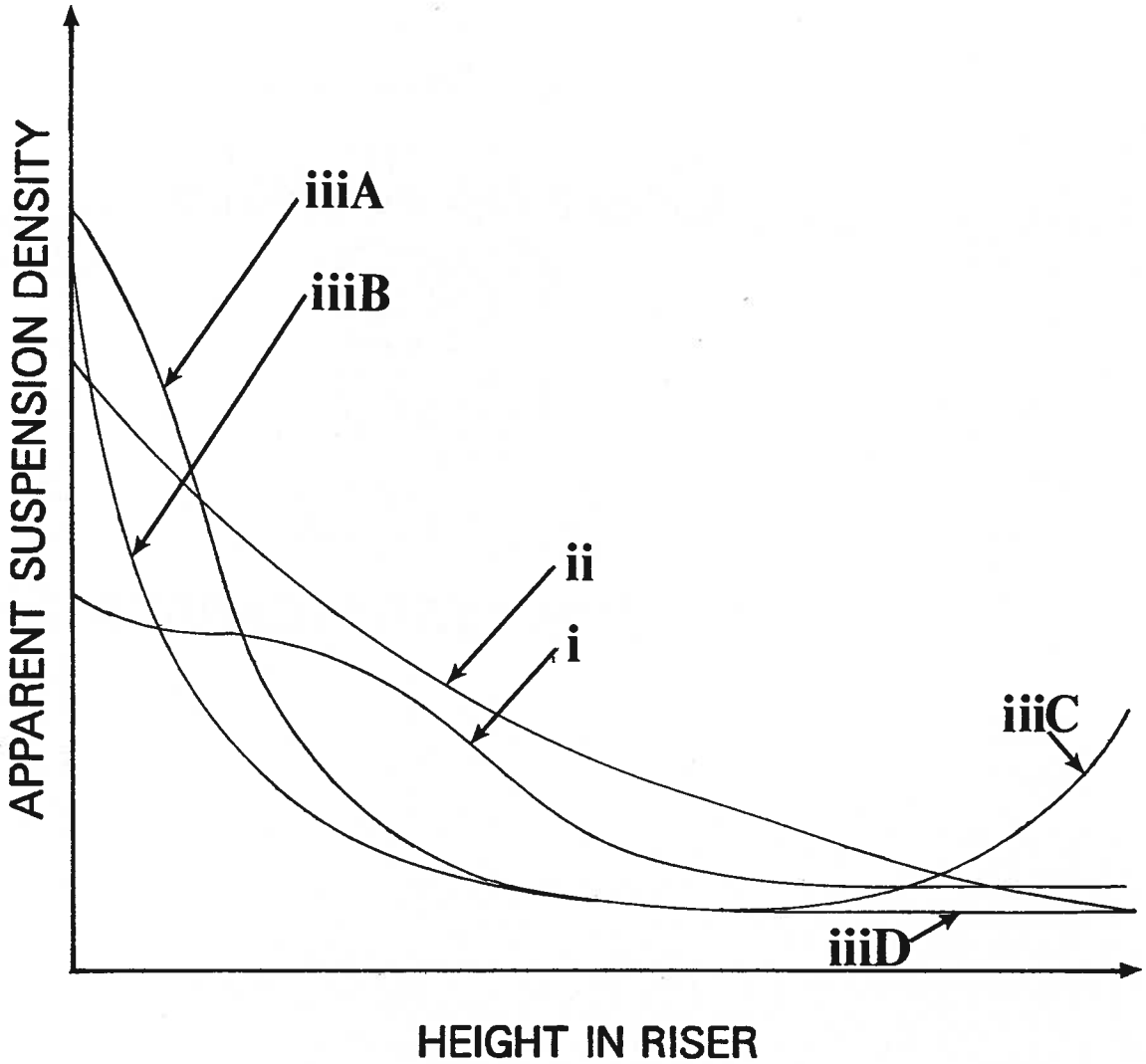

Figure 2.1: Variation in shapes of apparent suspension density profiles reported in CFB literature: (i) Li and Kwauk (1980); (ii) Weinstein *et al.* (1981); (iii)A–D this study (see Chapters 6 and 7).

solids circulation rates, G_s. Furthermore, the sigmoidal profile is not a unique feature of CFBs. For example, Weinstein *et al.* (1981) measured two profile shapes, similar to curves (i) and (ii) in Figure 2.1, using two different particle types in the same riser. In both cases, a relatively dense "turbulent bed" formed in the bottom of the riser. Thus the shape of the density profile can be influenced by the particle properties.

In commercial units, and at higher velocities in pilot-scale units, profiles similar to the variations of curve (iii) are typically observed (Weinstein *et al.*, 1981; Hartge *et al.*, 1986; Brereton, 1987; Schaub *et al.*, 1989; Leckner, 1991). Both the geometry of the bottom and exit regions of the riser may also influence the apparent suspension density profile (Bierl *et al.*, 1980; Brereton, 1987; Bader *et al*, 1988; Grace *et al.*, 1989a). Typical effects are shown as curves (iiiA)–(iiiD) in Figure 2.1. Sharp or "abrupt" riser exits may result in an upturn in the profile towards the exit, illustrated by profile (iiiC). Entry and exit effects are investigated in Chapters 6 and 9. The absence of a "universal" apparent suspension density profile shape greatly complicates the task of empirically predicting density profiles.

When a turbulent fluidised bed is established in the bottom part of a pilot-scale riser, at relatively low U_g, very small changes in U_g and/or G_s may result in quite large changes in the turbulent bed height and overall solids hold-up (Brereton, 1987; Rhodes, 1989). This phenomenon, also observed during cold unit tests in this study, is likely due to the low rate at which entrained solids leave the riser exit at low U_g, as proposed by Rhodes (1989). Weinstein (1983) reported that the "imposed pressure drop" across the riser, due to the inventory of solids in the return loop, influences the hold-up of solids in the riser. Although a number of investigators have cited this result, it does not appear to have been corroborated by other investigations. It is possible that Weinstein's riser was operating in the range of U_g where solids hold-up is very sensitive to minor changes, as suggested by Brereton (1987).

2.2 Radial Variations and Local Heterogeneity in Solids Distribution

A major limitation of the apparent suspension density is that it gives no information about the radial variation in concentration and axial mass flux of the solids. Investigators have utilised a number of experimental techniques over the last decade to determine local solids distribution in risers. These include mass and momentum flux probes to measure axial solids flow (Bierl *et al.*, 1980; Monceaux *et al.*, 1986; Bader *et al.*, 1988; Rhodes *et al.*, 1989; Couturier *et al.*, 1989, 1991), capacitance probes for instantaneous solids concentrations (Brereton, 1987; Herb *et al.*, 1989; Louge *et al.*, 1990), optical fibre probes for local solids concentration and velocity (Hartge *et al.*, 1986; Hartge *et al.*, 1988; Horio *et al.*, 1988; Rhodes *et al.*, 1991), and X-ray attenuation to obtain local solids concentrations (Weinstein *et al.*, 1986).

From studies of local solids concentration and flux, we now have a good qualitative knowledge of typical solids flow patterns. In the middle and upper heights of the riser, solids concentrations are significantly higher near the riser wall than in the central core, and there is generally a relatively abrupt transition between these two regions. Typical (time-averaged) radial voidage profiles, reported by Bader *et al.* (1988) from investigations in a 305 mm diameter riser, are shown in Figure 2.2. Note that at the higher height (9.1 m) the core voidage is almost constant. The average solids fraction at the lower height (4.0 m) is higher, and the wall-core transition in solids concentration is not as abrupt. The wall solids concentration is much greater than the core concentrations. The radial variation of axial solids mass flux (kg/m^2s), measured by Rhodes *et al.* (1989) in a 152 mm diameter column, appears in Figure 2.3. The mass flowrate of solids moving downwards near the wall is similar in magnitude to the external solids recirculation rate. Although the "wall region" thickness varies with apparent suspension density, it is typically a small fraction of the riser radius. In both Figures 2.2 and 2.3 this thickness is roughly 15% of the riser radius, i.e. the wall region occupies about 30% of the riser cross-sectional area. This solids flow structure is commonly referred to "core-annulus" flow in the CFB literature.

In the "core" of the riser, at the heights under consideration, the dilute suspension is

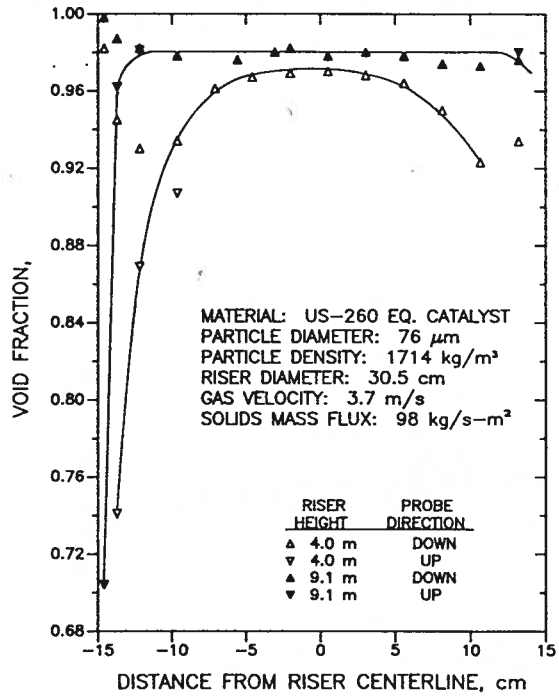

Figure 2.2: Radial variation in riser voidage operating at 24 °C (Bader *et al.*, 1988).

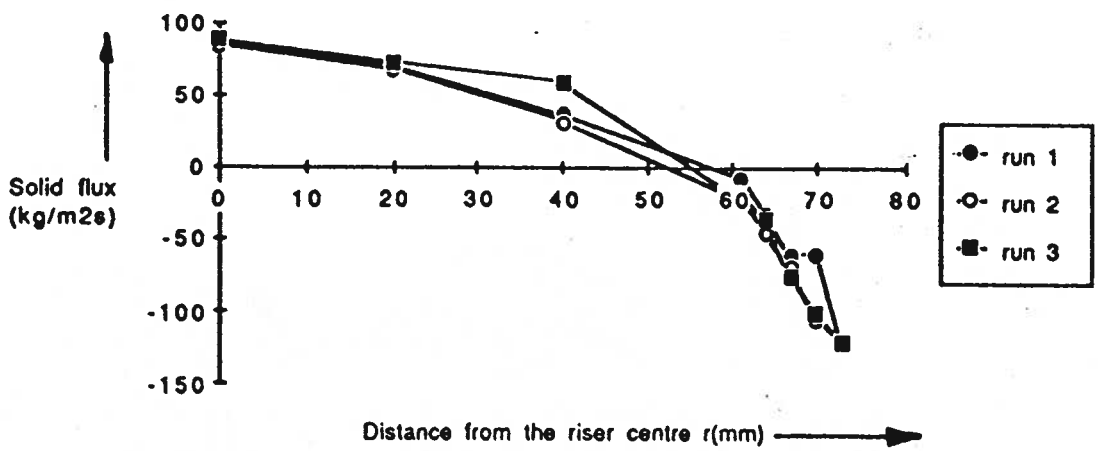

Figure 2.3: Radial variation of axial solids mass flux in the riser (Rhodes *et al.* (1989): $D = 152$ mm, $U_g = 3$ m/s, $G_s = 30$ kg/m^{2}s, $T = 25$ °C, alumina powder, $d_p = 70$ μm, $\rho_p = 2420$ kg/m^3, measurement at height, $z = 1.35$ m).

relatively uniform and travels rapidly upward at velocities that are similar in magnitude to the gas superficial velocity. In contrast, the local distribution of solids in the wall region is highly non-uniform. Alternating regions of dilute suspension upflow and dense suspension downflow are generally detected. The dense suspension regions correspond to falling sheets of particles at the wall that intermittently form and break up. In this study these particle sheets are termed "wall streamers," or simply "streamers." Others investigators have called them "streaks" (Arena *et al.*, 1989), "swarms" (Rhodes *et al.*, 1991), or "wall clusters" (Horio *et al.*, 1988). A more rigid definition of a "cluster," used in this study, is defined below. Although there is some solids upflow in the wall region, the net solids flux is generally downward in this region, as in the example in Figure 2.3.

From a modeller's perspective, it is important to note that there is significant heterogeneity in the wall region solids concentration, and that wall streamers are transient structures. Instantaneous capacitance probe and optical fibre results (Brereton, 1987; Hartge *et al.*, 1988; Herb *et al.*, 1989; Louge *et al.*, 1990) show fluctuation frequencies in the wall region in the range 1–20 Hz, while instantaneous "interfaces" between the denser suspension regions and dilute suspension are more abrupt (i.e. $O(10\ d_p)$ in cold units) than can generally be inferred from the time-averaged profiles. The fraction of the wall covered at any instant by wall streamers and the wall streamer voidage vary over the riser height and are affected by riser operating conditions (Wu, 1989; Louge *et al.*, 1990). Although wall streamer solids concentrations are typically an order of magnitude greater than the core suspension concentration, they rarely approach packed bed concentrations. Measured downward velocities of wall streamers vary over the range from 0 to about 3.5 m/s. Average values have been reported in the range of approximately 0.5 to 2.0 m/s (Bader *et al.*, 1988; Hartge *et al.*, 1988; Horio *et al.*, 1988; Wu, 1989). This range is much smaller than the corresponding range of core suspension velocities (2–15 m/s) in these experiments. Wu (1989) found that the average streamer velocity was independent of apparent suspension density in his studies. Wall streamer dynamics are investigated in Chapter 9.

For this study, a "fast fluidised bed" is assumed to refer to a core-annular solids flow

structure. A riser operating in the fast fluidisation regime thus exhibits a core-annulus structure over most of its length. If the riser is operated with very high gas velocities and/or low solids recirculation rates causing the riser walls to be devoid of wall streamers, the riser is assumed to be operating in a "dilute pneumatic conveying" mode. At the bottom of the riser, a region of higher suspension density, or "turbulent" bed, is often established. Here the core-annulus divisions are not as well defined, and there is substantial heterogeneity in solids concentration in the core. Nevertheless, the time-averaged solids concentration near the wall is still significantly higher than in the core (Abed, 1983; Louge *et al.*, 1990; Chapter 6), and the extent of local heterogeneity in the core solids concentration is less than at the wall. The solids concentrations in the transient denser solids structures in the core also vary substantially in a transition region between the turbulent bed at the bottom of the riser and a well-defined core-annulus flow structure further up the riser (Hartge *et al.*, 1988). The denser solids structures in the core generally move downward or at much lower upward velocities than the dilute suspension. As mentioned, these regions have been described as refluxing strands and packets of particles (Brereton, 1987; Horio *et al.*, 1988; Wirth, 1991). In this study, higher suspension density "clumps" of particles, of roughly spherical shape, are termed "clusters." If the vertical length of the denser particle regions is at least an order of magnitude greater than their smallest lateral dimension, they are then referred to as "free streamers" or "strands." There is evidence that significantly higher solids recirculation rates are required before a turbulent bed region forms in the lower part of a larger diameter riser (Arena *et al.*, 1991). Model simulation results in Chapter 8 concur with this result.

Several investigators have reported solids concentration and mass flux radial profiles of similar parabolic shape for various values of G_s. These profiles fall roughly on the same curve when non-dimensionalised by the corresponding cross-sectionally averaged value (Monceaux, 1986; Herb *et al.*, 1989). However, this only appears to occur in the "fully-developed flow" upper regions of the riser, and at moderate or low solids circulation ($G_s < 50$ kg/m^{2}s). A theoretical analysis by Molodstof and Muzyka (1991) indicates that these profiles, measured at

different G_s in the fully-developed flow regions of the riser, should be similar providing that all other operating parameters (D, U_g, d_p, etc.) are invariant. There are no simple methods to predict changes in the profiles with these other parameters. Furthermore, not all reported radial profiles exhibit the "parabolic" shape ascribed to the similar profiles, e.g. Figure 2.2.

2.3 Lateral Solids Motion

From direct solids tracer measurements, consideration of the momentum transfer required between the core and annular regions to maintain similar axial gas pressure gradients, and trends in local solids flux and apparent suspension densities with height in the riser, it is known that solids are exchanged laterally between the core and the annular wall regions (Bierl *et al.*, 1980; Dry, 1987; Bader *et al.*, 1988; Senior and Brereton, 1990). Two mechanisms have been proposed to explain the deposition of particles on riser walls, (i) turbulent diffusion of particles due to gas turbulence (e.g. Berker and Tulig, 1986; Bolton and Davidson, 1988) and (ii) oblique inter-particle collisions (e.g. Sinclair and Jackson, 1989; Tsuo and Gidaspow, 1990). Particle exchange mechanisms are investigated and modelled in later Chapters. However, it is instructive to consider the likely order of magnitude of the lateral particle motion. Bierl *et al.* (1980) injected tracer particles vertically upwards in the centre of a 305 mm diameter riser containing FCC catalyst. The particles were injected with the same average velocity as the core particles in suspension. The average lateral particle migration was found to be about 25 mm over a vertical distance of 0.5 m. Using their estimate of 10.7 m/s for the core suspension particle velocities gives a mean lateral velocity of about 0.5 m/s. Similar lateral "fluctuating" particle velocities have been measured directly by laser Doppler velocimetry (LDV) in bench-scale risers at low G_s (Tsuji *et al.*, 1984; Lee and Durst, 1982).

2.4 Elevated Temperature Flow Patterns

Preliminary hydrodynamic measurements in pilot-scale and commercial size CFB combustors (Schaub *et al.*, 1989; Grace *et al.*, 1989a, 1989b; Couturier *et al.*, 1989, 1991; Leckner, 1991;

Chapter 7) indicate that solids flow patterns are qualitatively similar to those observed in cold unit risers. Due to the lower gas velocities below the secondary air ports in CFB combustors, the "primary zone" region generally operates as a turbulent bed. Above the secondary air ports a fast fluidised bed core-annulus solids distribution has been observed. The influence of secondary air jets on the solids distribution in the riser is discussed in Chapter 6. Due to the high heat capacity of the solids, compared with the gas, and the excellent gas-solid contacting in the riser, temperatures are relatively uniform throughout the riser under normal operating conditions (Grace, 1986a). Reported radial and axial temperature variations in CFB combustors operating at normal load are typically $O(\pm\ 50\ ^{\circ}\mathrm{C})$ (Grace *et al.*, 1989a; Wu, 1989; Schaub *et al.*, 1989), although Leckner (1991) reported larger variations than this over a thin thermal boundary layer at the wall. Additional commercial unit data are required to enable quantitative comparison of hydrodynamic properties in commercial and pilot-scale cold units.

2.5 Gas Flow and Mixing

Gas tracer tests have been performed at ambient temperature in several cold unit risers (e.g. Bierl *et al.*, 1980; Brereton, 1987; Bader *et al.*, 1988; Adams, 1988; Werther *et al.*, 1991). It is generally found that axial backmixing in the core of the riser is small relative to the bulk convective flow. In the wall region, axial backmixing may occur due to streamers dragging gas downward. The bulk of the gas flows up through the riser core region. Werther *et al.* (1991) modelled the radial gas mixing in the core by treating it as a single phase turbulent gas flow. Although gas mixing is not specifically examined in this study, gas turbulence in the core region is modelled.

Chapter 3

DYNAMICS OF GAS-PARTICLE SUSPENSION FLOWS

There is a great variety of dynamical interactions that may occur within a flowing gas-particle suspension. In this Chapter the interactions which are important in suspension flows in typical circulating fluidised bed riser operations are identified, and a coherent approach to characterising these interactions is provided. Two key interactions that are of particular interest are the response of the particles to the gas turbulence and the effect of collisions amongst particles. As mentioned, both have been proposed as likely mechanisms by which particles gain fluctuating lateral components of velocity, resulting in particle deposition on riser walls. Generally modellers of suspension flows are polarised, either assuming that one or other mechanism is dominant. Despite this, there does not appear to have been a comprehensive study to establish under what conditions each mechanism is important. A study of the interaction of the particles and turbulence is presented here to establish a framework for answering this question. Although a primary objective of this Chapter is to develop concepts for the comprehensive gas-particle suspension flow model presented in Chapter 8, several intriguing results arise from the analysis that have important implications for particle selection, riser scale-up and interpretation of experimental data.

3.1 Characterisation of Particle Size and Shape

For a particle of non-spherical shape there are several ways to characterise its size. The four most common particle diameter definitions for particles in fluidised beds are:

d_p= *sieve size*, the width of the minimum square sieve aperture through which the particle will pass;

Table 3.1: Typical particle sphericities for some common materials (Geldart, 1986).

Material	Sphericity
Crushed coal	0.75
Round sand	0.92 – 0.98
Crushed sandstone	0.8 – 0.9

d_v= *volume-equivalent diameter*, the diameter of a sphere having the same volume as the particle;

d_{sv}= *surface/volume diameter*, the diameter of a sphere having the same external surface area/volume ratio as the particle;

d_s= *surface diameter*, the diameter of a sphere having the same surface area as the particle.

Correlations for flow in fluidised beds generally use either d_{sv} or d_v.

The most common measure of particle shape is its sphericity ψ, defined as the ratio of the surface area of an equivalent-volume sphere to the surface area of the particle. The surface area of the particle a_p, the volume φ and the sphericity ψ may be expressed in terms of the particle diameters to give the identities:

$$\begin{aligned} \varphi &= \frac{\pi}{6} d_v^3 \,, \\ a_p &= \pi d_s^2 \,, \\ \frac{a_p}{\varphi} &= \frac{\pi d_{sv}^2}{\frac{\pi}{6} d_{sv}^3} = \frac{6}{d_{sv}} \,, \\ \text{and } \psi &= \frac{\pi d_v^2}{a_p} \,. \end{aligned} \tag{3.1}$$

By re-arranging these expressions, one obtains the useful relations $\psi = d_{sv}/d_v$ and $\psi = (d_v/d_s)^2$. Examples of particle sphericity reported by Geldart (1986) are given in Table 3.1. The upper limit on ψ is 1.0, corresponding to a perfect sphere. For spherical or near-spherical particles,

$$d_v \approx d_{sv} \approx d_p \,. \tag{3.2}$$

For a mixture of particles of invariant particle density, the mean surface/volume diameter may be defined by dividing the mixture into a series of composite sizes, d_{p1}, d_{p2}, and so on, of weight fractions x_1, x_2, ... The corresponding number of particles in each fraction in the mixture is proportional to x_i/φ_i. If the particles are nearly spherical then, from eq. (3.1),

$$\begin{aligned} \frac{\pi d_{sv}^2}{\frac{\pi}{6} d_{sv}^3} &= \frac{\text{surface area of the mixture}}{\text{volume of the mixture}} \\ &= \frac{\sum (x_i/\varphi_i)\pi d_{pi}^2}{\sum (x_i/\varphi_i)\frac{\pi}{6} d_{pi}^3}, \end{aligned} \tag{3.3}$$

where the summation is over all particle sizes. As $\varphi_i = \pi d_{pi}^3/6$, eq. (3.3) simplifies to

$$d_{sv} = \frac{1}{\sum x_i/d_{pi}} . \tag{3.4}$$

For particle size ranges typical of CFB operations, sieving is generally used to determine the particle size distribution. For sieve results, it is normal to assume that the d_{pi} values in eq. (3.4) correspond to the averages of adjacent sieve apertures. The surface/volume mean diameter given by eq. (3.4) is often referred to as the "Sauter" mean diameter. It is possible for mixtures of particles to have the same Sauter mean diameter but significantly different size distributions. As size distributions may influence the behaviour of the mixture in a flowing suspension, further characterisation of the particle mixture is sometimes required.

If the particles are non-spherical, then a more general sieve diameter d_p should replace d_{sv} in eq. (3.4). For non-spherical particles there is no direct relationship between d_p determined by sieve results and d_{sv} or d_v. Abrahamsen and Geldart (1980) estimate that for many materials with $\psi \approx 0.8$, $d_v \approx 1.13 d_p$. Generally it is either assumed that $d_{sv} \approx d_p$ for nearly-spherical particles, or that $d_v \approx d_p$ for particles of lower sphericity. Henceforth, it will be assumed that the particles are nearly spherical and that $d_p \approx d_{sv}$ unless otherwise stated. For smaller particles, the particle size distribution may also be determined by a Coulter counter which gives the volume mean diameter d_v of the mixture.

3.2 Interparticle Forces and Particle Classification

Geldart (1973) proposed a particle classification scheme based on observations of particle behaviour in low velocity gas fluidised beds at atmospheric pressure and temperature. Although a mixture of all four particle categories may exist in a high velocity fluidised bed, the particles usually consist predominantly of Group A and/or B particles. Grace (1986) gives the following general properties and low velocity fluidised bed behaviour of particles in each Geldart grouping:

C: Fine cohesive materials (e.g. fly ash, flour) which channel rather than fluidise when air is made to flow through them. Typically d_p is less than about 20 μm.

A: Quite fine aeratable solids (e.g. cracking catalyst) which fluidise nicely and show an appreciable range between minimum fluidisation velocity and the velocity at which bubbling first occurs. For most cases, d_p is from 30 to 100 μm.

B: Intermediate size particles (e.g. sand) which bubble as soon as the bed is fluidised and collapse immediately when the fluidising air is turned off. For most cases d_p is from 100 to 800 μm.

D: Coarse particles which fluidise rather poorly (e.g. coarse crushed coal). For most cases, d_p is greater than 1 mm.

The different behaviour of particles in groups C, A and B in low velocity beds is attributed to the relative effects of close-range interparticle forces, including van der Waals forces, capillary forces, magnetic forces and electrostatic forces (Clift, 1985; Grace, 1986). Van der Waals forces arise from the attraction between atomic or molecular dipoles. Electrostatic forces result from the electrical charge that may be acquired by particles when they slide over surfaces of a dissimilar material such as the wall of a CFB. Electric charge accumulations can be reduced by several methods, including humidifying the fluidising gas and electrically grounding the fluidised bed apparatus. Capillary forces arise in gas fluidised beds when a small amount of liquid is

introduced into the bed, and can be up to an order of magnitude greater than electrostatic or van der Waals forces in low velocity fluidised beds (Clift, 1985).

Although the effects of interparticle forces on low velocity fluidised bed behaviour have been observed, it is not clear to what extent such forces influence the behaviour of fast fluidised beds. Certainly substantial charge accumulation occurs in some lower temperature units if preventative measures are not taken. It is possible that the opposite charges on the wall of a riser column and a layer of particles in contact with the wall stabilise the particle layer against disruption by the high velocity gas in the core of the riser. The high gas velocities and large wall shear and core drag forces typical of fast beds relative to bubbling beds suggest that van der Waals forces are unlikely to significantly influence fast bed behaviour. However, some aggregation of the small mass fraction of very fine particles is possible. In this study it is assumed that close-range interparticle forces have negligible influence on the behaviour of fast fluidised bed hydrodynamics (except for clean-up of the dusty exit gas). This assumption may need review as future studies explore the effects of interparticle forces in CFB's. It is also assumed that charge accumulations due to frictional effects are minimised in units predisposed to such effects. Consequently, it is assumed that all forces due to magnetic fields and electrical charging of particles may be neglected. The following theoretical and modelling studies apply to two-phase gas-solid suspension flow; capillary forces due to the wetting of solid particles are not considered.

3.3 Motion of a Single Particle in Steady Gas Flow

In this section the forces that influence the motion of a single particle suspended in a gas stream are discussed, and equations of motion for a single particle are presented. The importance of particle and gas physical properties on the particle drag force is investigated. From consideration of the relative magnitudes of forces acting on the particle, simplified particle equations of motion are given that are applicable over the range of conditions typical of CFB units.

3.3.1 Steady Drag and Particle Motion in Uniform Vertical Gas Flow

Consider a single spherical particle suspended in an upwardly flowing gas stream. Assume that the gas flow is steady and that the effect on the particle of any horizontal gas velocity gradient is negligible. Furthermore, assume that the particle is travelling at a steady vertical velocity without rotation and that its motion is not influenced by gas turbulence. Under these conditions only gravitational, buoyancy and gas drag forces need be considered.

For this assumed particle motion, the relative velocity between the gas and the particle, termed the slip velocity, $\mathbf{v}_s$, is constant and equal to the terminal velocity of the particle, $\mathbf{v}_t$. The particle equation of motion simplifies to a balance of the three forces,

$$0 = -\rho_p \varphi g + \mathbf{f}_D + \rho_g \varphi g \ , \tag{3.5}$$

where subscripts p and g refer to the particle and gas respectively. The force, $\mathbf{f}_D$, is the drag force due to the difference in rectilinear motion of the particle and the gas. For solid particles in gases, $\rho_g \ll \rho_p$ and the buoyancy force is thus negligible compared to the gravitational force. The buoyancy force is therefore omitted from here on.

The drag force on a particle can be written in terms of a drag coefficient, C_D, as

$$\mathbf{f}_D = C_D \left(\frac{1}{2} \rho_g \left| \mathbf{U} - \mathbf{V} \right| (\mathbf{U} - \mathbf{V}) \right) a_P \ . \tag{3.6}$$

$\mathbf{V}$ and $\mathbf{U}$ are the instantaneous velocity vectors of the particle and the surrounding gas, respectively, and a_P is the projected particle area perpendicular to the relative direction of motion, $(\mathbf{U}-\mathbf{V})$. The particle Reynolds number, Re_p, is defined as $\rho_g|\mathbf{U}-\mathbf{V}|d_p/\mu_g$. For nearly-spherical particles $a_P \approx \pi d_p^2/4$. Substituting this relation and Re_p into eq. (3.6) gives

$$\mathbf{f}_D = \frac{\pi}{8} \mu_g d_p C_D Re_p (\mathbf{U} - \mathbf{V}) \ . \tag{3.7}$$

The drag coefficient has been correlated with Re_p for particles of various shapes. The conventional correlation of drag for a spherical particle in steady motion is presented as a graph called the "standard drag curve". Many empirical or semi-empirical equations have been

proposed to approximate this curve. Clift *et al.* (1978) compare standard drag curve data and some of these correlations. In the limit as $Re_p \rightarrow 0$, the steady flow around the particle may be approximated as creeping or "Stokes" flow, and an analytical solution gives $C_D = 24/Re_p$, which is accurate for $Re_p < 0.2$. In this case the particle motion is described as motion in the "Stokes regime." Substitution of this relation into eq. (3.7) gives the drag force on a single particle in the Stokes regime,

$$\mathbf{f}_D = 3\pi\mu_g d_p(\mathbf{U} - \mathbf{V}) \,. \tag{3.8}$$

Thus, in the Stokes regime, the drag force on the particle is a linear function of the relative velocity between the gas and particle.

For particle motion outside the Stokes regime, the steady drag coefficient can be calculated by an empirical relationship such as that proposed by Clift and Gauvin (1971),

$$C_D = \frac{24}{Re_p}\left(1 + 0.15 Re_p^{0.687}\right) + \frac{0.42}{1 + 4.25 \times 10^4 Re_p^{-1.16}} \,. \tag{3.9}$$

Clift *et al.* (1978) estimate the limits of accuracy of this correlation to be +6% to −4% for $Re_p < 3 \times 10^5$.

For steady motion of a spherical particle the instantaneous gas and particle velocities in eq. (3.7) are constant and co-linear, and $(\mathbf{U} - \mathbf{V}) = \mathbf{v}_s = \mathbf{v}_t$. Substitution of eq. (3.7) and $\varphi = \pi d_p^3/6$ into eq. (3.5) gives an expression for particle terminal velocity,

$$\mathbf{v}_t = \frac{4\,\rho_p\,g\,d_p^2}{3\,\mu_g\,Re_t\,C_D} \,. \tag{3.10}$$

Here Re_t is the value of Re_p when the slip velocity equals the terminal velocity of the particle. As the product $Re_t C_D$ is only constant in the Stokes regime, the solution of eq. (3.10) is generally iterative. As an alternative to iterative solution for determining $\mathbf{v}_t$, the variables in Re_t and C_D are normally combined into two dimensionless groups, one containing $\mathbf{v}_t$ and one independent of $\mathbf{v}_t$. These two groups are then empirically correlated using standard drag curve data. In this study the dimensionless particle diameter, $d_p^\star$, and dimensionless velocity, $\mathbf{v}_s^\star$, were chosen and the correlations given by Grace (1986) for the dimensionless terminal velocity (i.e.

Table 3.2: Terminal velocity correlations for spheres from Grace (1986).

$d_p^\star$ Range	$\mathbf{v}_t^\star$ Range	Equation
≤ 3.8	≤ 0.624	$\mathbf{v}_t^\star = (d_p^\star)^2/18 - 3.1234 \times 10^{-4}(d_p^\star)^5 + 1.6415 \times 10^{-6}(d_p^\star)^8$ $-7.278 \times 10^{-10}(d_p^\star)^{11}$
3.8 to 7.58	0.624 to 1.63	$\log_{10} \mathbf{v}_t^\star = -1.5466 + 2.9162w - 1.0432w^2$
7.58 to 227	1.63 to 28	$\log_{10} \mathbf{v}_t^\star = -1.64758 + 2.94786w - 1.09703w^2 + 0.17129w^3$
227 to 3350	28 to 91.7	$\log_{10} \mathbf{v}_t^\star = 5.1837 - 4.51034w + 1.687w^2 - 0.189135w^3$
Definitions:	$d_p^\star = d_p[\rho_g g \Delta\rho/\mu_g^2]^{1/3}$	
	$w = \log_{10} d_p^\star$	
	$\mathbf{v}_t^\star = \mathbf{v}_t[\rho_g^2/\mu_g g \Delta\rho]^{1/3}$	

$\mathbf{v}_t^\star = \mathbf{v}_s^\star$) were used. These correlations are presented in Table 3.2. Note that $(d_p^\star)^3 = Ar$, where Ar is the Archimedes number, and $\Delta\rho \approx \rho_p$ for gas fluidisation.

Table 3.3 gives values of Re_p, C_D and $\mathbf{v}_t$ for particle densities, gas temperatures and particle diameters typical of CFB's. The particle densities of 2700 kg/m^3 and 1400 kg/m^3 are indicative of sand (or combustor ash) and coal, respectively. The two temperatures considered are typical of ambient temperature conditions and CFB combustor temperatures. If an additional constant vertical force is added to eq. (3.5), then the particle travels at a constant slip velocity different from its terminal velocity. Table 3.3 also gives values for Re_p and C_D for each of the particles assuming they have the same slip velocity. Slip velocities of 3.0 m/s and 7.5 m/s are considered.

Several important trends appear in Table 3.3. Firstly, the changes in the terminal velocity of the particles with temperature should be noted. The 40 μm and 230 μm sand particles ($\rho_p = 2700$ kg/m^3) and 400 μm coal particle ($\rho_p = 1400$ kg/m^3) have lower terminal velocities at the higher gas temperature, the difference being significant for the 40 μm particle. In contrast, the terminal velocity of the 1.5 mm coal particle increases and there is little change for the 500 μm sand particle. These trends may be explained by noting that an increase in gas temperature results in an increase in the gas kinematic viscosity (μ_g/ρ_g) and a consequent decrease in particle Reynolds number. This, in turn, results in an increase in the drag coefficient. The expression for particle terminal velocity given in eq. (3.10) may be rewritten,

$$\mathbf{v}_t^2 = \frac{4\,\rho_p\,g\,d_p}{3\,\rho_g\,C_D}\ . \tag{3.11}$$

Table 3.3: Particle Reynolds numbers (Re_p) and steady drag coefficients (C_D) for particle diameters (d_p), particle densities (ρ_p) and slip velocities ($\mathbf{v}_s$) typical of those for CFB units. ($\mathbf{v}_t$ = particle terminal velocity, spherical particles assumed.)

		$\mathbf{v}_s = \mathbf{v}_t$			$\mathbf{v}_s$ = 3.0 m/s		$\mathbf{v}_s$ = 7.5 m/s	
d_p μm	ρ_p kg/m^3	$\mathbf{v}_t$ m/s	Re_p	C_D	Re_p	C_D	Re_p	C_D
Air at 25 °C and 101 kPa pressure								
40	2700	0.13	0.33	78	7.8	5.0	20	2.6
230	2700	1.8	26	2.2	45.	1.6	113	1.0
500	2700	4.0	132	1.0	98.	1.1	245	0.8
400	1400	2.1	55	1.5	78.	1.2	196	0.8
1500	1400	6.5	636	0.5	294.	0.7	735	0.5
Gas with properties of air at 870 °C and 101 kPa pressure								
40	2700	0.05	0.01	1700	0.8	33	2.0	15
230	2700	1.4	2.1	14	4.7	7.3	12	3.7
500	2700	4.0	14	3.3	10	4.1	26	2.2
400	1400	1.8	5.1	6.9	8	4.8	21	2.6
1500	1400	9.1	93	1.1	31	2.0	77	1.2

A change in gas temperature only appreciably alters the product $\rho_g C_D$ in the denominator of this equation. For particle Reynolds numbers les than $O(100)$, this product increases with an increase in temperature, the reverse being true for Re_p greater than $O(100)$.

The behaviour of these different particles with changes in gas temperature highlights one of the possible pitfalls involved in characterising a mixture of particles of different densities and sizes by a single mean diameter and density. Investigators involved in experimental and theoretical scaling of CFB units should consider including more than one (dimensionless) particle type in their models if they are interested in the behaviour of significantly different particles. For example, when scaling CFB combustors, knowledge of the motion of the bulk of the solids (predominantly sand or ash) is desired for determining bed-to-wall heat transfer coefficients. Knowledge of the motion of small and large fuel particles aids in predicting heat release patterns and combustion efficiencies.

It is also shown in Table 3.3 that large coal particles (or carbon-based fuel particles in general) have terminal velocities comparable to superficial gas velocities of CFB combustor

units. These particles are likely to move slowly, thereby interfering with the rapid upflow of the smaller inert bed particles. This suggests that to dynamically model the motion of particles in a CFB, direct interaction by contact (collision) of particles may have to be considered. The concepts of collision modelling are introduced later in this chapter and developed in detail in Chapter 8.

The values of Re_p and C_D given in Table 3.3 for slip velocities of 3.0 m/s and 7.5 m/s are included to give an estimate of the order of magnitude these variables may take when the particle slip velocity is comparable to typical gas velocities in CFB units. 7.5 m/s corresponds approximately to the maximum gas-particle slip velocity to be expected in a CFB. Therefore, considering all the particles listed in the table, the maximum particle Reynolds numbers expected in a CFB are $O(10^2)$ at high temperature and $O(10^3)$ at ambient temperature. Considering only sand or ash particles, these numbers are $O(30)$ and $O(300)$ respectively. These limits are used below.

Thus far the steady drag force has been calculated assuming particles to be of spherical shape. This is not the case for many particles in CFB's. For isometric particles (particles with half-body symmetry independent of the cutting plane orientation), Haider and Levenspiel (1989) claim that sphericity is "most likely" the best particle shape parameter with which to correlate drag. These authors propose a correlation for drag on non-spherical isometric particles,

$$C_D = \frac{24}{Re_v}\left[1 + 8.1716\exp(-4.0655\psi) \times Re_v^{(0.0964+0.5565\psi)}\right] + \frac{73.69 Re_v \exp(-5.0748\psi)}{Re_v + 5.378\exp(6.2122\psi)} . \tag{3.12}$$

For explicit calculation of non-spherical particle terminal velocities, they propose

$$\mathbf{v}_t^\star = \left[\frac{18}{(d_v^\star)^2} + \frac{(2.3348 - 1.7439\psi)}{(d_v^\star)^{0.5}}\right]^{-1} . \tag{3.13}$$

The Haider and Levenspiel (1989) correlations are based on the particle volume diameter, d_v. Thus the particle Reynolds number and dimensionless particle diameter, denoted in eqs. (3.12) and (3.13) as Re_v and $d_v^\star$, must also be based on d_v. Haider and Levenspiel (1989) report an accuracy of fit of eq. (3.12) of about $\pm$ 5% to their correlation data for isometric particles ($\psi \geq$

Table 3.4: Comparison of steady drag coefficients C_D and particle terminal velocities $\mathbf{v}_t$ calculated with allowance for particle shape ($\psi \neq 1.0$, Haider and Levenspiel (1989) correlations), and calculated assuming spherical particles ($\psi = 1.0$, Clift and Gauvin (1971) and Grace (1986) correlations).

d_v (μm)	ψ	ρ_p (kg/m^3)	$\mathbf{v}_t$ (m/s)			C_D (@ $\mathbf{v}_s$ = 7.5 m/s)		
			$\psi = 1.0$	$\psi \neq 1.0$	%[a]	$\psi = 1.0$	$\psi \neq 1.0$	%[b]
Gas temperature 25° C.								
40	0.95	2700	0.125	0.119	+6	2.6	2.8	−7
230	0.95	2700	1.8	1.9	−5	1.0	1.1	−9
500	0.95	2700	4.0	4.0	0	0.8	0.8	0
400	0.75	1400	2.1	1.6	+31	0.8	1.4	−43
1500	0.75	1400	6.5	3.9	+67	0.5	1.5	−67
Gas temperature 870° C.								
40	0.95	2700	0.052	0.051	+2	15.	15.	0.
230	0.95	2700	1.4	1.4	0	3.7	4.0	−7
500	0.95	2700	4.0	4.4	−9	2.2	2.4	−8
400	0.75	1400	1.8	1.6	+13	2.6	3.0	−13
1500	0.75	1400	9.1	6.6	+38	1.2	1.6	−25

[a]% = % difference in $\mathbf{v}_t$ assuming a correct value for $\psi \neq 1.0$
[b]% = % difference in C_D assuming a correct value for $\psi \neq 1.0$

0.67) and $Re_v < O(10^4)$. Similarly, eq. (3.13) predicted the isometric particle correlation data within about $\pm$ 4% for $d_v^\star < 10^3$. For particles of constant d_v, the drag coefficient correlation for non-spherical particles predicts little effect of sphericity on C_D for $Re_v < 10$, and an increase in C_D with decreasing sphericity for $Re_v > 10$. It is likely that these correlations are also reasonable for all spherically isotropic particles when $\psi > 0.67$. However, for particles of very irregular shape and $\psi < 0.67$, Clift *et al.* (1978) suggest that particle sphericity is not a good correlation parameter for drag.

Table 3.4 compares terminal velocities and drag coefficients calculated for non-spherical particles with and without allowance for particle shape. Suitable values of ψ for sand ($\rho_p = 2700$ kg/m^3) and coal ($\rho_p = 1400$ kg/m^3) are assumed. Providing that the particle diameter is defined as $d_p = d_v$, the errors involved in using spherical particle drag correlations for the particles of sphericity 0.95 are of similar magnitude to the accuracy of the particle drag correlations.

However, for the particles with sphericity of 0.75 there are significant differences in calculated drag, and a particle drag correlation should be used that accounts for the particle shape. It is important to note that considerable erosion of particle surface asperities probably occurs within a CFB. Thus, for example, the sphericity of crushed coal may differ from that of the same coal sampled from a CFB combustor.

3.3.2 Accelerated Rectilinear Particle Motion in Risers

The discussion of particle motion is now extended to the general case of accelerated rectilinear particle motion of a discrete solid particle in steady gas flow. Both Clift *et al.* (1978) and Hinze (1972) provide good reviews of the relevant equations and forces involved with accelerated rectilinear motion of single particles in a fluid. For the motion of a solid particle accelerated by a gas (i.e. $\rho_p/\rho_g \approx 10^3$), several terms in the general particle equation of motion may be neglected, namely the "added" or "virtual" mass term, the "Basset history integral" term, and the buoyancy term discussed earlier. The (Lagrangian) equation of motion for a solid particle in a gas is then

$$\rho_p \varphi \frac{d\mathbf{V}}{dt} = -\rho_p \varphi g + \mathbf{f}_D + \mathbf{f}_S \ . \tag{3.14}$$

Neglecting external field forces (e.g. electrical), the force $\mathbf{f}_S$ on the particle includes

(a) a force due to the pressure gradient in the surrounding gas in the direction of the particle motion;

(b) forces due to shear by the gas;

(c) forces due to rotation of the particle.

The pressure gradient force term is normally derived as $-\varphi \nabla p$, where ∇p is the gas pressure gradient (e.g. Anderson and Jackson, 1967; Hinze, 1972). (Note that Clift *et al.* (1978) assume a form for the pressure gradient term which differs from that given here.) If we consider steady gas flow in a CFB riser containing only one discrete particle under study, we may estimate the gas pressure gradient using a correlation for single phase flow pressure drop in a pipe. This

pressure gradient or "drop" is a maximum for small diameter pilot-scale risers operating at ambient temperature. Even for these units and the highest gas velocities encountered in risers, $\nabla p < 5\text{N/m}^3$ (e.g. see Table 3.7). Comparison of the magnitudes of pressure gradient force ($\varphi \nabla p$) and gravitational force ($\rho_p \varphi g$, or $\Delta\rho\varphi g$ if buoyancy is included) shows that the pressure gradient force may be neglected in this case because $\Delta\rho g \gg 5\ \text{N/m}^3$ (i.e. $\rho_p g \gg 5\ \text{N/m}^3$).

Next consider the flow of a uniform dilute suspension in the riser, and assume that there is no interaction of particles. Equation (3.14) is still valid. For steady gas flow the pressure drop may now be approximated from the mass of particles suspended in the gas (this common assumption is discussed in Chapter 4). Thus $\nabla p \approx \partial p/\partial z \approx \rho_s g$, where ρ_s is the suspension density. In this case a comparison of the magnitudes of pressure gradient force $\rho_s \varphi g$ and gravitational force $\rho_p \varphi g$ shows that the pressure gradient force may also be neglected for dilute suspensions, since $\rho_p \gg \rho_s$. For denser suspensions, such as those in a bubbling bed, the suspension density is much greater and the pressure gradient force becomes significant. The pressure gradient force may also be significant in regions where the gas acceleration is substantial (e.g. near the secondary air ports in a CFB combustor).

Particles in gas shear flow also experience a shear flow-induced lift force perpendicular to the gas flow direction. Saffman (1965) calculated this force f_L for a single particle to be

$$\mathbf{f}_L = 6.46 \frac{d_p^2}{4} \sqrt{\rho_g \mu_g \frac{d\mathbf{U}}{dy}}\ (\mathbf{V} - \mathbf{U})\ , \tag{3.15}$$

where y is in a direction perpendicular to $\mathbf{U}$ and $d\mathbf{U}/dy$ is the gas shear rate. This equation is strictly valid only for free shear flow (i.e. no wall effects) and for both Re_p and $\rho_g d_p^2 (d\mathbf{U}/dy)/\mu_g \ll 1.0$. However, it is often applied close to the wall of pipes (or risers) where gas shear is largest and the lift force becomes important. The lift force on particles near the wall of a riser is investigated in Chapter 9. There it is shown that the gas shear rate near the wall is at least $O(10^3)$ times that in the core of the riser. At these high wall shear rates, the lift force is of similar magnitude to the gravitational force. Consequently, it is reasonable to ignore the effects of lift force in the core of a riser.

The effects of particle rotation on the motion of a particle have been studied in some detail for very low and high particle Reynolds numbers. At higher Reynolds numbers than those relevant for CFB particles, (i.e. $> O(10^3)$), the Magnus effect becomes important (Clift *et al.*, 1978). For low particle Reynolds numbers (< 0.1) the effects of particle angular velocity are small compared to the lift force (Hinze, 1972). According to Clift *et al.* (1978), little work has been done on the motion of rotating particles at intermediate Re_p. In view of both the lack of knowledge in this area, and the complexity of modelling phenomena such as particle rotation, effects of particle rotation are not considered in the modelling work presented later in this study.

In the absence of appreciable particle rotation effects, lift forces or pressure gradient forces (i.e. $\mathbf{f}_S \approx 0.$), the equation of accelerated particle motion, eq. (3.14) simplifies to

$$\rho_p \varphi \frac{d\mathbf{V}}{dt} = -\rho_p \varphi g + \mathbf{f}_D \ . \tag{3.16}$$

If it assumed that the particle is nearly-spherical (or defined by some appropriate diameter d_p), then the particle drag force $\mathbf{f}_D$ in eq. (3.7) may also be written as

$$f_D = \varphi \rho_p \left(\frac{3 C_D \rho_g \left| \mathbf{U} - \mathbf{V} \right|}{4 d_p \rho_p} \right) (\mathbf{U} - \mathbf{V}) \ . \tag{3.17}$$

Defining the term τ_p as

$$\tau_p = \frac{4 d_p \rho_p}{3 C_D \rho_g \left| \mathbf{U} - \mathbf{V} \right|} = \frac{4 d_p^2 \rho_p}{3 \mu_g Re_p C_D} \ , \tag{3.18}$$

and substituting τ_p into eq. (3.16), gives a succinct form of the particle equation of motion,

$$\frac{d\mathbf{V}}{dt} = \frac{(\mathbf{U} - \mathbf{V})}{\tau_p} - g \ . \tag{3.19}$$

The term τ_p has the units of time and is the "particle relaxation time" or "particle response time." It is a measure of the time a particle takes to return to steady motion (zero net force condition) from an initial condition where there is an imbalance in the drag and gravitational forces.

The importance of τ_p may be illustrated by considering a particle in the Stokes regime, where $C_D = 24/Re_p$. In this case eq. (3.18) gives $\tau_p = \rho_p d_p^2 / 18 \mu_g$. Thus in the Stokes regime

the particle response time is a constant at a given temperature. This allows the vector eq. (3.19) to be simply integrated to find $\mathbf{V}$ as a function of time t if $\mathbf{U}$ is either constant or a known function of t. Equation (3.19) may be further simplified by separating the relative particle velocity $(\mathbf{U} - \mathbf{V})$ into two components, corresponding to a steady slip velocity and a changing or "fluctuating" component, i.e.

$$(\mathbf{U} - \mathbf{V}) = \mathbf{v}_s + (\mathbf{u}' - \mathbf{v}') \ . \tag{3.20}$$

When only drag and gravitational forces affect the steady slip velocity $\mathbf{v}_s$, this velocity is equal the particle terminal velocity (as discussed previously). Hence, in terms of particle response time, $\mathbf{v}_s = \mathbf{v}_t$ and $\mathbf{v}_t/\tau_p = g$. Thus eq. (3.19) reduces to

$$\frac{d\mathbf{v}'}{dt} = \frac{(\mathbf{u}' - \mathbf{v}')}{\tau_p} \ . \tag{3.21}$$

Now consider a perturbation at initial time $t = 0$ to the steady particle velocity condition due to either a sudden step change in the gas velocity (i.e. $\mathbf{u}' \neq 0$, but constant) or to a sudden change in particle velocity. (These two cases are later assumed to approximate the events of the particle entering a large gas eddy and the particle colliding with another particle). In general, a vector differential equation must first be divided into its relevant component equations, and each of these solved simultaneously. For this specific case, where drag is linearly dependent on relative velocity, eq. (3.21) may be solved directly treating the vectors as if they were scalars. Integration from initial time, $t = 0$, to some arbitrary time, t, or over the full interaction period τ_k gives

$$\begin{aligned} \mathbf{v}'(t) &= \mathbf{u}' - (\mathbf{u}' - \mathbf{v}_1') \exp\left(-t/\tau_p\right) , \\ \mathbf{v}_2' &= \mathbf{u}' - (\mathbf{u}' - \mathbf{v}_1') \exp\left(-\tau_k/\tau_p\right) , \end{aligned} \tag{3.22}$$

where $\mathbf{v}_1'$ is the particle velocity at zero time and $\mathbf{v}_2'$ the velocity at a final time τ_k. Note that when $t = \tau_p$ the initial relative particle velocity $(\mathbf{u}' - \mathbf{v}')$ is reduced by 63% as the particle responds to the imbalance in force caused by the perturbation. Large or dense particles have longer particle response times than do small or light particles. Hence small or light particles

respond rapidly to changes in the gas flow and follow gas flow fluctuations more closely than larger or denser particles.

Several other important quantities may be defined that describe the particle motion under consideration. Firstly, a mean fluctuating particle velocity may be calculated:

$$\begin{aligned}\overline{\mathbf{v}'} &= \frac{1}{\tau_k}\int_0^{\tau_k}\mathbf{v}'dt \\ &= \mathbf{u}' - \frac{\tau_p}{\tau_k}\left(\mathbf{u}' - \mathbf{v}_1'\right)\left(1 - \exp\left(-\tau_k/\tau_p\right)\right) \ . \end{aligned} \tag{3.23}$$

Again, this integration is only correct for linear drag dependence. Substituting the expression for $\mathbf{v}_2'$ given in eq. (3.22) into eq. (3.23) to eliminate $\mathbf{u}'$, and re-arranging give

$$\overline{\mathbf{v}'} = \mathbf{v}_1'\left[\frac{\tau_p(1-\Theta) - \tau_k\Theta}{\tau_k(1-\Theta)}\right] + \mathbf{v}_2'\left[\frac{\tau_k - \tau_p(1-\Theta)}{\tau_k(1-\Theta)}\right] \ , \tag{3.24}$$

where $\Theta = \exp\left(-\tau_k/\tau_p\right)$. Thus the mean velocity can be completely defined in terms of the initial and final velocities, the particle response time and the "interaction time," τ_k. If the first expression in square brackets on the right hand side (r.h.s.) of eq. (3.24) is defined as the "velocity weighting factor," λ, then the second r.h.s. expression in square brackets may be written as $(1-\lambda)$, and

$$\overline{\mathbf{v}'} = \mathbf{v}_1'\lambda + \mathbf{v}_2'\left(1-\lambda\right) \ , \tag{3.25}$$

where

$$\lambda = \left[\frac{\tau_p(1-\Theta) - \tau_k\Theta}{\tau_k(1-\Theta)}\right] \ . \tag{3.26}$$

If the motion under study is repeated periodically (with constant period τ_k), and the period is too short for the particle to reach its steady terminal velocity before the next perturbation, then the particle time-averaged velocity $\overline{\mathbf{v}}$ will not be equal to $\mathbf{v}_t$. Instead, $\overline{\mathbf{v}} = \mathbf{v}_t + \overline{\mathbf{v}'}$. The instantaneous particle velocities immediately following one perturbation and just before the next perturbation are $\mathbf{V}_1 = \mathbf{v}_t + \mathbf{v}_1'$ and $\mathbf{V}_2 = \mathbf{v}_t + \mathbf{v}_2'$. Therefore eq. (3.25) may also be written in terms of the time-averaged particle velocity $\overline{\mathbf{v}}$ and the upper/lower limits of velocity $\mathbf{V}_1$ and $\mathbf{V}_2$ between which the instantaneous particle velocity fluctuates with period τ_k,

$$\overline{\mathbf{v}} = \mathbf{V}_1\lambda + \mathbf{V}_2\left(1-\lambda\right) \ . \tag{3.27}$$

Table 3.5: Equations for evaluating particle velocity weighting factor, λ, for fluctuating particle motion.

Particle Type	λ	Applicable Range	Error Limit
"small"	τ_p/τ_k	$\tau_k/\tau_p > 5.0$	$\pm$ 3.5%
"large"	$\frac{1}{2}$	$\tau_k/\tau_p < 0.2$	$\pm$ 3.5%
all types	$\tau_p/\tau_k - \frac{\Theta}{1-\Theta}$	no limit	exact

τ_p = particle response time
τ_k = interaction period
$\Theta = \exp(-\tau_k/\tau_p)$

It is useful to consider two cases for the described motion, designated as a "small particle" case and "large particle" case. For small particles, the particle response time is very short and $\tau_k \gg \tau_p$. Hence $\Theta \to 0$ and $\lambda \approx \tau_p/\tau_k$. As τ_p/τ_k is very small, the average velocity is close to the limit velocity $\mathbf{V}_2$. This is the expected result for small particles which rapidly respond to perturbations in a time orders of magnitude less than the time between perturbations.

For a large particle $\tau_k \ll \tau_p$. For this case we can accurately approximate Θ by three terms of its Taylor series expansion, i.e.

$$\Theta = \exp(-\tau_k/\tau_p) = 1 - \frac{\tau_k}{\tau_p} + \frac{\tau_k^2}{2\tau_p^2} \,. \tag{3.28}$$

Substitution of this approximation into eq. (3.26) gives for $\tau_k \ll \tau_p$,

$$\lambda = \frac{1 - (\tau_k/2\tau_p)}{2 - (\tau_k/2\tau_p)} \approx \frac{1}{2} \,. \tag{3.29}$$

Thus, for large particles the arithmetic average of the velocities $\mathbf{V}_1$ and $\mathbf{V}_2$ gives an appropriate time-averaged particle velocity. This situation arises when the particle is subject to a high frequency of very small perturbations. The simplified expressions for λ for small and large particles in Table 3.5 may be used to accurately estimate λ ($\pm$ 3.5% for the limits given) in place of the more general expression when rapid calculation is required in numerical simulations.

3.3.3 Extension of the Linear Drag Expression to Higher Reynolds Numbers

When the particle Reynolds number is too high for the Stokes regime range, the particle response time is no longer independent of the relative particle velocity, $(\mathbf{V} - \mathbf{U})$. For the range 400 <

$Re_p < 3 \times 10^5$, the drag coefficient C_D is relatively insensitive to Re_p and may be approximated as a constant. In this case,

$$\frac{d\mathbf{V}}{dt} = K_1 \, |\mathbf{U} - \mathbf{V}| (\mathbf{U} - \mathbf{V}) \ , \tag{3.30}$$

where K_1 is a constant. For cases where $\mathbf{U}$ and $\mathbf{V}$ are co-linear, this equation may be analytically integrated. Otherwise simultaneous integration of the respective component equations requires numerical integration.

Unfortunately, for particle Reynolds numbers typical of CFB operations (see Table 3.3), C_D is neither given by Stokes Law ($C_D = 24/Re_p$) nor is it constant, and analytical development of particle dynamic equations becomes very difficult. Most theoretical treatments circumvent this problem either by assuming that Stokes Law may be extended to higher values of Re_p (say $O(10)$) or by assuming that the drag force on the particle is linearly dependent on the relative particle velocity over a limited particle velocity range. The accuracy of this second assumption is considered here for CFB particles.

From eqs. (3.17) and (3.18) the drag force on a particle may be written as

$$\mathbf{f}_D = \frac{\rho_p \varphi}{\tau_p} (\mathbf{U} - \mathbf{V}) = K_2 (\mathbf{U} - \mathbf{V}) \ , \tag{3.31}$$

with τ_p as defined in eq. (3.18). The linear drag assumption is valid if solution of the particle equation of motion, eq. (3.16), with a constant value for K_2 does not introduce excessive error. When the linear drag assumption is reasonable, all equations in the previous section for the perturbed motion of a particle in the Stokes regime are still applicable.

To investigate the magnitude of this error for particles in suspension flow in a CFB riser, a series of cases for 230 μm and 500 μm diameter particles are considered. As before, the particles are assumed to have a time-averaged velocity and fluctuating component of velocity between perturbations. The magnitude of the velocity fluctuations is assumed to be $\pm$ 0.2 m/s. This is a typical fluctuation magnitude based on modelling results given later and limited available experimental data from bubbling bed freeboards and dilute vertical suspension flow (e.g. Tsuji *et al.*, 1984; Lee and Durst, 1982; Chandok and Pei, 1972; Horio *et al.*, 1980; and

Levy and Lockwood, 1980). The relevance and interpretation of such data are discussed later. For convenience the time-averaged particle velocity is assumed equal to its terminal velocity $\mathbf{v}_t$. The limits of the particle velocity are thus $\mathbf{v}_t \pm 0.2$ m/s. The linear drag force is computed assuming that τ_p (and hence K_2) is constant over this range of velocities, and equal to the exact value at the mean velocity $\mathbf{v}_t$.

Consider first the vertical motion of the gas and solid with the particle velocity fluctuations also in the vertical direction. The exact vertical drag force is also calculated by eq. (3.31), but with allowance for changes in τ_p with velocity. Table 3.6 gives the exact and linear drag forces for this case and the error involved in the linear assumption. For the magnitude of fluctuations considered, the linear drag assumption introduces a maximum error in the drag force of $O(5\%)$, which occurs at the maximum deviation in velocity from the mean. This result is for particles with Reynolds numbers between $O(2)$ and $O(150)$.

The second case considered is the steady vertical (z direction) motion of gas and a 230 μm particle with the particle velocity fluctuations in a horizontal plane (r direction). For the linear assumption, the drag force expression may be simply divided into the two component equations with τ_p assumed constant. To calculate the exact drag, τ_p must be first evaluated for each value of $|\mathbf{V} - \mathbf{U}|$ before the drag force is resolved into components. The error of the linear assumption for this motion, also given in Table 3.6, is less than 1%. The error for horizontal particle fluctuations is an order of magnitude less than for vertical fluctuations because of the smaller changes in $|\mathbf{U} - \mathbf{V}|$, and hence τ_p, for lateral fluctuations.

Although specific particle sizes and mean velocities were chosen to illustrate the magnitude of error involved in the linear drag assumption, the results may be generalised by considering the motion in terms of Re_p at the mean particle slip velocity, and the magnitude of particle velocity fluctuations compared to the mean slip velocity. The accuracy of the linear assumption depends only on these two parameters as they contain all the variables on which τ_p depends (see eq. (3.18)). For particle motion with Re_p an order of magnitude less than that considered in Table 3.6, it may be assumed that Stokes Law applies providing fluctuations are limited to

Table 3.6: Error involved in linear drag force assumption for typical mean and fluctuating CFB particle velocities.

Relative Particle Velocity Vertical $(\mathbf{U}-\mathbf{V})_z$ m/s	Horizontal $(\mathbf{U}-\mathbf{V})_r$ m/s	Re_p –	Exact Results τ_p s	$f_{Dz} \times 10^{-7}$ kg m/s^2	Linear Drag τ_p s	$f_{Dz} \times 10^{-7}$ kg m/s^2	Error in f_{Dz} %
230 μm particle, 870 °C., vertical fluctuations:							
1.36	0.0	2.1	0.141	1.66	0.141	1.66	0
1.56	0.0	2.4	0.139	1.94	0.141	1.90	−2
1.16	0.0	1.8	0.144	1.38	0.141	1.42	+2
230 μm particle, 25 °C., vertical fluctuations:							
1.76	0.0	27	0.18	1.68	0.18	1.68	0.
1.96	0.0	30	0.17	1.95	0.18	1.86	−4
1.56	0.0	24	0.19	1.41	0.18	1.47	+5
500 μm particle, 25 °C., vertical fluctuations:							
4.04	0.0	135	0.39	18.3	0.39	18.3	0.
4.24	0.0	142	0.38	18.7	0.39	19.2	+3
3.84	0.0	128	0.40	17.8	0.39	17.4	−2

Relative Particle Velocity Vertical $(\mathbf{U}-\mathbf{V})_z$ m/s	Horizontal $(\mathbf{U}-\mathbf{V})_r$ m/s	Re_p –	Exact Results τ_p s	$f_{Dr} \times 10^{-7}$ kg m/s^2	Linear Drag τ_p s	$f_{Dr} \times 10^{-7}$ kg m/s^2	Error in f_{Dr} %
230 μm particle, 25 °C., horizontal fluctuations:							
1.76	0.0	27.0	0.18	0.0	0.18	0.0	0.0
1.76	0.2	27.1	0.18	0.190	0.18	0.191	+0.3

Particle density $\rho_p = 2700$ kg/m^3

Gas flow and mean particle flow in a vertical direction

Particle mean relative velocity = particle terminal velocity, $\mathbf{v}_s = \overline{(\mathbf{U}-\mathbf{V})} = \mathbf{v}_t$

$\pm$ 0.2 m/s. For Re_p orders of magnitude greater than $O(150)$, the fluctuations are a negligibly small fraction of the slip velocity, τ_p is nearly constant for the fluctuating velocity considered, and the linear approximation applies.

The errors of the linear drag approximation for the limits considered here are $\leq 5\%$, which is of similar magnitude to the error of the standard drag curve correlations. In the suspension flow model described in Chapter 8 the linear drag assumption is applied for linear velocity fluctuations up to $O(\pm 0.6$ m/s). For such fluctuation magnitudes the error of the vertical drag calculated from by the linear drag assumption is less than 15%, which is of similar magnitude to the expected general accuracy of the model ($\pm$ 20%) due to other simplifications. As shown above, corresponding lateral drag forces, and the resulting lateral particle fluctuating motion, are calculated with much greater accuracy. Therefore, even at the highest levels of particle fluctuating velocity, the inclusion of the linear drag assumption in the model is unlikely to significantly affect the accuracy of predictions.

3.4 Interaction of Gas Turbulence and Particles in Dilute Suspension Flow

Of key importance to the modelling of CFB riser dynamics is an understanding of lateral particle motion which results in the deposition of particles on the riser wall. The two most likely mechanisms which may impart non-vertical motion to particles travelling up the core of a riser are the interaction of the particles with gas turbulence and the scattering of particles due to direct collision with one another. In this section the interaction of particles and gas turbulence is discussed in detail. Equations are developed for estimating the modulating effect of the particles on the turbulence and the resulting fluctuating motion of the particles due to turbulence.

3.4.1 Basic Concepts of Turbulent Gas Flows in Pipes and Risers

To provide a framework for discussion of two-phase turbulent suspension flows in CFB risers, it is first necessary to present some specific concepts and equations for single-phase turbulent flows.

Turbulence is a complex phenomenon that has been studied extensively, both theoretically and experimentally, over the last century. The concepts of turbulent flows are outlined briefly below; the cited literature should be consulted for more detail. There are a number of good general texts on turbulence (e.g. Hinze, 1975; Tennekes and Lumley, 1972).

Turbulent flows arise at high flow Reynolds numbers, defined as $Re_D = \rho_f U_0 D/\mu_f$, where subscript f denotes fluid, D is the hydraulic diameter of the pipe or riser, and U_0 is the velocity averaged over the flow cross-section. Providing the length/diameter (L/D) ratio is not too small, single phase flow in a CFB riser may treated in the same manner as single phase fully-developed flow in a pipe. For pipe flow the transition from laminar to turbulent flow generally occurs at $Re_D \approx 2.1 \times 10^3$. The Reynolds number for gas flow in commercially-sized risers is always well above this transition level, and essentially all pilot-scale units also operate with Re_D in the turbulent regime.

Turbulent motion in a fluid arises from instabilities related to the interaction of viscous terms and non-linear inertia terms in the fluid equation of motion. Hinze (1975) defines turbulence as "an irregular condition in which the various quantities show a random variation with time and space coordinates so that statistically averaged values can be discerned." Flows in CFB risers may generally be assumed to be incompressible so that only velocity and pressure fluctuations need be considered (see Chapter 4). The fluctuations are normally associated with the motion of "clumps" of fluid called eddies. Within a turbulent fluid there is a range of eddy sizes. The largest eddies in turbulent pipe flow result primarily from instabilities in the shear flow in the wall layer. These eddies are normally of size similar to the pipe or riser diameter. It is postulated (e.g. see Tennekes and Lumley, 1972) that the largest eddies can only transfer a significant fraction of their energy to smaller eddies of size within an order of magnitude of their size. Hence a cascade of energy occurs proceeding from the larger eddies via intermediate-sized eddies down to the smallest eddies. There is little dissipation of energy from the intermediate-sized eddies. The energy of the small eddies is dissipated by viscous action. It may be shown (e.g. Tennekes and Lumley, 1972) that most of the energy of the turbulence is associated with

the larger-sized eddies.

The level or intensity of turbulence is often characterised by the root mean square (r.m.s.) fluctuating velocity, u. The fluctuating velocity is measured relative to a frame of reference following the time-mean fluid motion. If the r.m.s. fluctuating velocity in one of three orthogonal planes (e.g. along the z axis) is defined as $u_z = \sqrt{\overline{\mathbf{u}_z'^2}}$, then $u^2 = u_z^2 + u_x^2 + u_y^2$. A linear velocity, characteristic of the turbulence and frequently employed in correlations, is the "turbulence velocity," u_e, defined simply as $u_e^2 = \frac{1}{3}u^2$. It is also useful to consider the turbulence as being composed of energetic larger eddies possessing a characteristic size l_e and decay time τ_e. The kinetic energy per unit mass of such eddies is approximately $u^2/2$. Turbulence theory (Tennekes and Lumley, 1972) predicts that the large eddies lose a significant fraction of their kinetic energy in one "turnover time" l_e/u. Hence we have order of magnitude approximations (denoted $\sim$) for the decay time, τ_e, of the characteristic large eddy and the energy transfer rate (per unit mass), ϵ_t, from large to small eddies:

$$\tau_e \sim l_e/u \,, \tag{3.32}$$

$$\epsilon_t \sim u^3/l_e \,. \tag{3.33}$$

For single phase flow, the energy transfer rate from large eddies to small eddies approximates the rate of viscous energy dissipation from the small eddies.

The scales of motion of the small energy dissipating eddies are termed the Kolmogorov microscales:

$$\text{Length scale } \eta_\kappa = \left(\nu^3/\epsilon_t\right)^{\frac{1}{4}} \,, \tag{3.34}$$

$$\text{Time scale } \tau_\kappa = (\nu/\epsilon_t)^{\frac{1}{2}} \,, \tag{3.35}$$

$$\text{Velocity scale } u_\kappa = (\nu\,\epsilon_t)^{\frac{1}{4}} \,. \tag{3.36}$$

where ϵ_t is the energy supply or dissipation rate per unit mass ($\mathrm{m}^2/\mathrm{s}^3$) and ν is the fluid kinematic viscosity. The small dissipating eddies are essentially independent of the boundary conditions of the flow and are nearly isotropic. The smallest eddies are still very much larger than the molecular mean free path of the fluid.

3.4.2 Correlations for Turbulent Gas Flows in Pipes and Risers

The Navier-Stokes equation becomes difficult to solve for turbulent flows because of the introduction of terms (Reynolds stresses) that arise from the fluctuating components of velocity. In most of the turbulent flow field the Reynolds stresses are orders of magnitude greater than stresses due to molecular diffusion (viscous stress). There is insufficient information to fully define the Reynolds stress terms without the inclusion of empirical relationships in the stress tensor. The problem of defining these relationships is commonly referred to as the closure problem.

For single-phase turbulent flows in pipes, solution of the turbulent Navier-Stokes equation is rarely required as sufficient information on the gas flow properties is often obtained from relatively simple empirical equations and models, providing the flow is fully developed and incompressible. In addition to these assumptions, in the following discussion it shall also be assumed that the mean flow is in the vertical z direction and that no time-averaged flow occurs in the horizontal or "lateral" direction. Two common empirical relationships provide accurate predictions of time-averaged velocity profiles for smooth-pipe fully-developed turbulent flow. The profiles of time-mean velocity in the outer regions of the pipe may be calculated by the "Law of the Wall" relationships,

$$\begin{aligned} \text{Viscous sub-layer } 0 \leq y^+ \leq 5: \quad \mathbf{u}_z/\mathbf{u}_\star &= y^+ \,, \\ \text{Buffer layer } 5 \leq y^+ \leq 30: \quad \mathbf{u}_z/\mathbf{u}_\star &= -3.05 + 5.00 \ln y^+ \,, \\ \text{Inertial sub-layer } y^+ \geq 30: \quad \mathbf{u}_z/\mathbf{u}_\star &= 5.5 + 2.5 \ln y^+ \,. \end{aligned} \tag{3.37}$$

Here $y^+ = y\mathbf{u}_\star/\nu$ is the dimensionless distance from the wall, where y is the distance from the wall. The wall friction velocity $\mathbf{u}_\star$ is an important variable for turbulent pipe flow and is directly related to the intensity of the turbulence. It is related to the average gas velocity in the pipe by

$$\mathbf{u}_\star = U_0 \sqrt{\frac{f_g}{2}} \,, \tag{3.38}$$

where f_g is the Fanning friction factor. The pressure gradient in the pipe ($\Delta p/\Delta z$) equals

Table 3.7: Wall layer thicknesses, wall velocities and friction factors for fully-developed particle-free gas flow in three typical risers — (1) pilot-scale ambient temperature riser; (2) pilot-scale CFB combustor; (3) commercial size CFB combustor.

		Case (1)	Case (2)	Case (3)
Diameter (m)	D	0.15	0.15	4.0
Average gas velocity (m/s)	U_0	6.5	6.5	6.5
Temperature (°C)	T_g	25	870	870
Gas viscosity (kg/m s)	μ_g	1.8×10^{-5}	4.5×10^{-5}	4.5×10^{-5}
Gas density (kg/m^3)	ρ_g	1.2	0.3	0.3
Reynolds number (–)	Re_D	6.57×10^4	6.58×10^3	1.70×10^5
Fanning friction factor (–)	f_g	0.0049	0.0087	0.0039
Wall friction velocity (m/s)	$\mathbf{u}_\star$	0.322	0.430	0.287
Turbulence velocity (m/s)	u_e	0.26	0.34	0.23
Viscous layer thickness (mm)	$y@y^+ = 5$	0.23	1.7	2.6
Velocity at edge of the viscous sub-layer (m/s)	$\mathbf{u}_z@y^+ = 5$	1.6	2.15	1.44
Thickness of viscous sub-layer and buffer layer (mm)	$y@y^+ = 30$	1.4	10.2	15.6
Velocity at buffer layer-inertial layer interface (m/s)	$\mathbf{u}_z@y^+ = 30$	4.3	5.8	3.9
Pressure gradient (N/m^3)	$\Delta p/\Delta z$	3.3	1.5	0.025

$4\rho_g \mathbf{u}_\star^2/D$. In the viscous sub-layer, although there are still fluctuations in the flow, viscous stresses dominate Reynolds stresses, whilst in the inertial sub-layer the reverse is true. The Law of the Wall gives reasonable estimates of the velocity profile up to $y/R \approx 1/4$, where R is the pipe radius. The Law of the Wall must be modified when roughness elements protrude beyond the viscous sub-layer.

The thickness of the viscous and inertial sub-layers and the mean gas velocities at these distances from the wall are given for three typical CFB risers in Table 3.7 assuming particle-free fully-developed gas flow in a smooth-walled riser. The viscous sub-layer thickness is of similar magnitude to a typical CFB particle diameter for the cold unit (case 1), and an order of magnitude greater for high temperatures (cases 2, 3). The magnitude of the velocities at the buffer layer/inertial sub-layer interface demonstrate the very steep wall velocity gradients

typical of turbulent flows. Although the commercially-sized riser has a diameter about 25 times larger than that of the pilot-scale combustor, the gas wall layers in the two cases are similar in thickness.

The purpose of Table 3.7 is only to demonstrate the typical magnitude of the gas wall layers. The assumptions upon which it is based are not strictly applicable for all risers. For example, the walls of a CFB combustor consist of both rough refractory and exposed membrane-wall heat transfer surfaces. Furthermore, single phase gas flow in a commercial size riser is unlikely to be fully-developed. The effect of wall roughness for two-phase flows is discussed in Chapter 9. The concepts of entry length and fully-developed flow for two-phase flows are discussed later in this Chapter.

For flow in the core of the pipe the velocity distribution may be estimated by the well-known ($\frac{1}{7}$)-power law,

$$\frac{\mathbf{u}_z}{\mathbf{u}_\star} = 8.56 \left(\frac{y\mathbf{u}_\star}{\nu} \right)^{\frac{1}{7}} . \tag{3.39}$$

This equation predicts a relatively flat profile in the core of the pipe or riser compared to a laminar velocity profile.

For flow in the core of pipes ($|r/R| \leq 0.8$) Tennekes and Lumley (1972) report that the larger scale turbulence is nearly isotropic and therefore the r.m.s. velocity fluctuations in each direction are similar in magnitude. Tennekes and Lumley estimate this magnitude to be

$$u_e = u_x = u_y = u_z = 0.8\mathbf{u}_\star . \tag{3.40}$$

The characteristic size, l_e, of the energetic eddies is often approximated by the Eulerian transverse integral length scale, L_E (Hinze, 1972; Hetsroni, 1989; Gore and Crowe, 1989; and Rizk and Elghobashi, 1989). The length scale, L_E, and the "Eulerian"[1] integral timescale, $\mathcal{T}_{Eg}$, are related by the expression $L_E = u_e \mathcal{T}_{Eg}$ (Williams and Crane, 1983) providing that the turbulence can be approximated as homogeneous and isotropic. Comparison of this expression and eq. (3.32) suggests that τ_e may be approximated by $\mathcal{T}_{Eg}$. However, a small particle following

[1]This is the "Eulerian moving with the mean flow" frame of reference (Abrahamson, 1975; Williams and Crane, 1983). In contrast, the Lagrangian frame follows the fluctuating motion of individual elements of fluid.

the fluid in an eddy is in a Lagrangian frame of reference, and a superior estimate of τ_e is the Lagrangian integral timescale, $\mathcal{T}_{Lg}$. The Lagrangian and "Eulerian" timescales are generally related via a constant Φ of order unity (Hutchinson *et al.* (1971): $\Phi = \mathcal{T}_{Lg}/\mathcal{T}_{Eg} = 1.6$; Abrahamson (1975): $\Phi = 1.5$; Williams and Crane (1983): $\Phi = 1.0$). Therefore, the eddy decay time τ_e is

$$\tau_e = \Phi\, \mathcal{T}_{Eg} = \Phi \frac{l_e}{u_e} \,. \tag{3.41}$$

Hutchinson *et al.* (1971) show that the energetic eddy size is relatively insensitive to Re_D considering data at $Re_D = 5 \times 10^4$ and $Re_D = 5 \times 10^5$, and it is common to assume that l_e is only dependent on D (e.g. Hetsroni, 1989; Rizk and Elghobashi, 1989). Hutchinson *et al.* (1971) provide estimates of the energetic eddy size l_e for pipe core flow which are used in this study:

$$l_e = 0.11\, D \,. \tag{3.42}$$

In Table 3.7 the turbulence velocity is given for an ambient temperature pilot-scale unit, a pilot-scale combustor and a commercial-size combustor. Although the turbulence velocity is of similar magnitude in each case, this parameter alone is not sufficient to characterise the turbulence. Equation (3.42) predicts that the eddy size is far greater for the commercial riser.

3.4.3 Response of a Discrete Particle to Turbulent Riser Gas Flow

The following discussion is limited to the response of a discrete particle to turbulence in riser gas flow. It is generally accepted that a discrete particle only responds to turbulent eddies larger than the particle diameter (e.g. Hinze, 1972). However, although the randomly directed forces of small eddies acting on the surface of the particle may be expected to cancel, this scale of turbulence may influence the steady drag of the mean fluid flow on the particle (Clift *et al.*, 1978; Hinze, 1972). It is also reasonable to expect that the most energetic eddies have the greatest influence on particle motion. It is common in models that represent the spectrum of eddy sizes and energies by a single characteristic or average energetic eddy size and decay time to assume that the interaction of a particle and the turbulence may be modelled as a series of

interactions with these average eddies (e.g. Owen, 1969; Hutchinson *et al.*, 1971; Govan, 1989; Govan *et al.*, 1989; Binder and Hanratty, 1991). This approach is also adopted in this study.

Consider the response of a particle to an energetic turbulent eddy of characteristic size l_e, decay time τ_e and lateral velocity u_e. If the particle is very "small" based on its response time τ_p, then the particle will rapidly gain a lateral velocity u_e and closely follow the gas flow in the eddy for almost the full duration of the eddy lifetime. This particle behaves like an element of fluid in the flow, and over a longer period of time the particle will have a fluctuating motion similar to that of the gas. If the gas turbulence velocity increases, the small particle fluctuating velocity correspondingly increases. However, if τ_p is comparable to τ_e there will be insufficient time for the particle to attain velocity u_e. The latter particle will tend to lag behind the gas velocity fluctuations and the magnitude of the particle fluctuations will be less. If the particle is large and has a significant slip velocity, $\mathbf{v}_s$, it may fall through the eddy in a time τ_d that is less than τ_e, reducing the time available for the particle to respond to each eddy, and hence diminishing the fluctuating velocity of this particle over a longer period. This effect is known as the crossing trajectory effect (Wells and Stock, 1983). The time to travel through a characteristic eddy τ_d is defined in this study as the "drift time" and estimated as

$$\tau_d = l_e / \mathbf{v}_s \, . \tag{3.43}$$

It is also convenient to define a "particle interaction time" τ_r, which is the lesser of τ_e and τ_d, and corresponds to the time available for a particle to respond to each individual energetic eddy, i.e.

$$\tau_r = \mathrm{MIN}\left[\tau_e \, ; \, \tau_d\right] \, , \tag{3.44}$$

where function "MIN" returns the minimum value of the terms inside the square brackets. Hence the magnitude of the fluctuating particle motion in turbulent flows is influenced by:

(a) intensity of the turbulence,

(b) particle inertia,

(c) crossing trajectory effect.

Table 3.8 gives values for the various time constants τ_p, τ_e and τ_d for a matrix of the three sand/ash (ρ_p = 2700 km/m^3) particle sizes considered in Table 3.3 and the three CFB riser cases considered in Table 3.7. The slip velocity of the particles is assumed equal to the particle terminal settling velocity in the corresponding gas. For 40 μm particles in all riser diameters, the response time τ_p is an order of magnitude or more smaller than the eddy decay time. The drift time is greater than the eddy decay time and the crossing effect is small for case 1 and may be assumed insignificant for cases 2 and 3. Consequently, particles of this size are expected to respond significantly to gas turbulence in all cases. In the small diameter risers (cases 1, 2) both 230 μm and 500 μm particles have drift times an order of magnitude less than the eddy decay time, and the crossing effect is expected to be important. The interaction time τ_r, equal to the drift time in this instance, is an order of magnitude less than the particle response time, and the particles are not expected to respond significantly to the turbulence. Although significant drift occurs in the commercial size riser, the interaction time is still comparable to the particle response time for the 230 μm particles, and particles of this size may be expected to respond at least partially to the gas turbulence.

The turbulence parameters in Table 3.8 are based on the assumption that the turbulence is not modified by the presence of the particles. It is shown later that this assumption is only reasonable at very low suspension densities (or in the redundant case for large particles, where gas turbulence-particle interactions are insignificant and thus not relevant). However, it is a reasonable approximation for the dilute freeboard of a bubbling bed. Table 3.8 data suggest that motion of particles in pilot-scale bubbling bed freeboards may be very different from that in full-scale units if similar particles are used.

Before considering the effect of many particles on the turbulence, relations to estimate the average response of a particle in a gas flow of known turbulence intensity are first developed. Taylor (1921) described the turbulent diffusion of fluid elements or fluid "particles" originating from a point source in a field of homogeneous turbulence. For an isotropic turbulence field,

Table 3.8: Relevant time constants that determine the response of discrete particles to turbulent gas flow for a range of particle sizes, gas temperatures and riser diameters. Riser turbulence estimates are based on particle-free flow. (See Tables 3.3 and 3.7 for further details).

Riser		Particle			Turbulence		Time Constants			
D (m)	T_g (°C)	d_p (μm)	Re_p (-)	$\mathbf{v}_t$ (m/s)	u_e (m/s)	l_e (mm)	τ_e (s)	τ_p (s)	τ_d (s)	$\tau_p\tau_d/\tau_e^2$ (-)
0.15	25	40	0.33	0.13	0.26	17	0.1	0.012	0.13	0.16
0.15	25	230	26	1.8	0.26	17	0.1	0.2	0.01	0.20
0.15	25	500	132	4.0	0.26	17	0.1	0.4	0.004	0.16
0.15	870	40	0.01	0.05	0.34	17	0.08	0.005	0.32	0.25
0.15	870	230	2.1	1.4	0.34	17	0.08	0.15	0.01	0.23
0.15	870	500	14	4.0	0.34	17	0.08	0.4	0.004	0.25
4.0	870	40	0.01	0.05	0.23	440	2.0	0.005	8.5	0.011
4.0	870	230	2.1	1.4	0.23	440	2.0	0.15	0.32	0.012
4.0	870	500	14	4.0	0.23	440	2.0	0.4	0.1	0.062

Gas velocity 6.5 m/s
Particle density 2700 kg/m^3
Slip velocity = Terminal velocity

τ_e = eddy decay time
τ_p = particle response time
τ_d = particle drift time

Taylor's analysis gives the long-time fluid element diffusion coefficient $\mathcal{D}_e$ as

$$\mathcal{D}_e = \frac{1}{2}\frac{d}{dt}\overline{X_e^2(t)} = u_e^2\,\mathcal{T}_{Lg}\,, \tag{3.45}$$

where $X_e(t)$ is the total displacement of the fluid element from a point travelling at the mean fluid velocity, and the overbar denotes an ensemble average over all possible outcomes at time t. The Lagrangian integral timescale $\mathcal{T}_{Lg}$ ($= \tau_e$ in this study) for the fluid element motion is

$$\mathcal{T}_{Lg} = \int_0^\infty R_{Lg}(\theta)\,d\theta\,, \tag{3.46}$$

where θ is the lag time. For isotropic turbulence, the fluid element (Lagrangian) autocorrelation R_{Lg} is independent of direction. For example, considering the z (vertical) direction, it is

$$R_{Lg}(\theta) = \frac{\overline{\mathbf{u}_z'(t)\mathbf{u}_z'(t+\theta)}}{\overline{\mathbf{u}_z'^{\,2}}}\,, \tag{3.47}$$

where $\overline{\mathbf{u}_z'^{\,2}} = u_e^2$. Though experimental measurement of $\mathcal{T}_{Lg}$ is not practical, $\mathcal{T}_{Eg}$ may be estimated from experimental measurement and the relation $\Phi = \mathcal{T}_{Lg}/\mathcal{T}_{Eg}$ (eq. (3.41)) used to estimate $\mathcal{T}_{Lg}$.

Taylor's theory also applies to the fluctuating motion of particles and is frequently used in the theoretical and experimental analysis of particle diffusion (e.g. Csanady, 1963; Reeks, 1977; Wells and Stock, 1983; Govan, 1989; Binder and Hanratty, 1991). The equation corresponding to eq. (3.45) for particle diffusion in terms of the particle linear r.m.s. fluctuating velocity, v_e, and particle Lagrangian timescale, $\mathcal{T}_{Lp}$, is

$$\mathcal{D}_p = \frac{1}{2}\frac{d}{dt}\overline{X_p^2(t)} = v_e^2\,\mathcal{T}_{Lp}\,. \tag{3.48}$$

The Lagrangian particle timescale represents the average period with which the particle motion fluctuates under the influence of the gas turbulence. It is similar to τ_e only when the particle is very small and closely follows the gas fluctuations.

The vast majority of models that predict the response of particles to gas turbulence have been developed using a linear drag law. In the following discussions a linear drag approximation is assumed reasonable for CFB particles small enough to be affected by turbulence. This assumption is validated later in view of expected turbulence levels in risers and the criteria established previously for the linear drag assumption. Three types of particle motion in a turbulent gas flow may be broadly defined as:

(1) particles that respond to individual eddies and are not affected by crossing trajectories (typical of small or low density particles);

(2) particles that respond to individual eddies but which do exhibit some effects of crossing trajectories;

(3) particles that are dominated by the crossing trajectory effect so that there is little response of particles to individual eddies (typical of large or dense particles).

Most models only consider type 1 particles and thus assume that the crossing effect may be neglected (i.e. $\tau_r = \tau_e$) (Govan, 1989). Both the theoretical work of Reeks (1977) and experimental results discussed by Binder and Hanratty (1991) indicate that for type 1 particles the gas diffusivity, $\mathcal{D}_g$, and particle diffusivity, $\mathcal{D}_p$, are approximately equal. (However, Reeks

(1977) predicts that for turbulence intensities of $O(100)$ times those expected in risers, $\mathcal{D}_p$ may be greater than $\mathcal{D}_g$). The general form of the correlation between v_e and the gas turbulence velocity u_e from these studies is

$$\left(\frac{v_e}{u_e}\right)^2 = \frac{1}{1 + c_2\tau_p/\tau_e} \,. \tag{3.49}$$

The constant c_2 is of O (1) (e.g. Binder and Hanratty (1991): $c_2 = 0.7$; Abrahamson (1975): $c_2 = 1.0$; Williams and Crane (1983): $c_2 = 1.0$). Based on the work of Reeks (1977), Binder and Hanratty (1991) estimate that the crossing effect may be neglected if $\mathbf{v}_s/u_e < 0.5$. Combining eqs. (3.45), (3.48) and (3.49) and assuming equal diffusivities for the gas and type 1 particles, we obtain an expression for the particle timescale $\mathcal{T}_{Lp}$ for type 1 motion,

$$\mathcal{T}_{Lp} = \tau_e \frac{u_e^2}{v_e^2} = \tau_e + \tau_p \,. \tag{3.50}$$

In the limit as $\tau_p \to 0$, i.e. for very small particles that respond rapidly to the gas velocity fluctuations, eq. (3.50) correctly predicts that $\mathcal{T}_{Lp} \to \tau_e$.

Csanady (1963) considered the influence of crossing trajectories on the particle diffusion coefficient. Csanady assumed a particle sufficiently heavy to have a significant slip velocity, but which also had a small inertia and thus closely followed the eddy velocity fluctuations whilst in an eddy. Csanady's equation relating long-time diffusion coefficients may be written in terms of the eddy decay time τ_e and the drift time τ_d as

$$\frac{\mathcal{D}_p}{\mathcal{D}_g} = \frac{1}{\left(1 + c_p^2\tau_e^2/\tau_d^2\right)^{\frac{1}{2}}} \,. \tag{3.51}$$

The factor c_p is equal to 1.0 for diffusion in the vertical (z) flow direction and 2.0 in the lateral (x or y) directions. The difference in diffusion in the vertical and lateral directions arises from "continuity effects" related to the difference in spatial correlation functions for parallel and normal velocities. Csanady interprets this effect as the physical process of "particles falling out of an eddy and into its back-flow."

The motion of a type 3 particle is characterised by large τ_p (e.g. $\tau_p/\tau_e > 5$) and high slip velocity ($\tau_d \ll \tau_e$). Crossing effect dominates and eq. (3.51) predicts that $\mathcal{D}_p/\mathcal{D}_g = \tau_d/c_p\tau_e$.

An important result of the continuity effect is that when the particle slip velocity and the crossing effect are large, the r.m.s. fluctuating velocities in the lateral and vertical directions are not equal; instead $v_{ez}^2 = 2v_{ex}^2 = 2v_{ey}^2$. This result, based on Csanady's assumption of zero inertia, is still valid when inertia is included providing crossing dominates the particle motion (Reeks, 1977). Anisotropies in fluctuating velocities have been reported by Chandok and Pei (1972). Using a photographic technique, these authors measured significantly higher axial than lateral fluctuating particle velocities in vertical dilute pneumatic conveying experiments with relatively large particles ($175 - 425\ \mu$m). Govan (1989) considered the motion of type 3 particles as a large number of small lateral perturbations as the particle fell through average energetic eddies of lateral velocity u_e. From ensemble averaging of the possible outcomes he obtained $\mathcal{D}_p/\mathcal{D}_g = \tau_d/2\tau_e$, identical to the Csanady result for lateral motion of type 3 particles.

For type 2 particles both the crossing effect and particle inertia are important in determining the response of the particle. Although these two effects are actually coupled, as crossing is an indirect effect of particle inertia when gravity is the only force field, their influence on particle motion is best understood by considering each individually. Firstly consider particle motion where there is no crossing. If the particle inertia (measured by τ_p) is very small, the particle fluctuates with the gas and $\mathcal{T}_{Lp} = \tau_e$ as discussed. As the inertia of the particle is increased, the particle lags behind the fluid and it "remembers" its history more. Consequently, its characteristic period of motion (i.e. timescale $\mathcal{T}_{Lp}$ derived from ensemble averaging of the motion over many repetitions) increases monotonically with inertia, and its r.m.s. velocity fluctuation decreases. In the upper limit, $\tau_p \gg \tau_e$, the particle becomes insensitive to the gas velocity fluctuations and the particle timescale of motion $\mathcal{T}_{Lp}$ approaches the particle response time τ_p in steady gas flow (Govan, 1989; Reeks, 1977).

The motion of a type 2 particle that responds perfectly to the gas fluctuations but has a large slip velocity corresponds to the particle motion assumed by Csanady (1963). This particle falls from one eddy to another at a rate faster than the average decay rate. In this case $\mathcal{T}_{Lp}$ is expected to decrease monotonously with τ_d, providing that $\tau_d < \tau_e$. Combining the effects

of inertia and crossing, we note that the particle timescale $\mathcal{T}_{Lp}$ may be greater or less than τ_e depending on the relative influences of these two effects. It is expected that crossing will exceed inertia effects when the particle motion is in a "window" of timescales where $\tau_p < \tau_d < \tau_e$ (i.e. a "Csanady" particle), and inertia will overshadow crossing when $\tau_d < \tau_e < \tau_p$. For the situation where $\tau_d < \tau_p < \tau_e$ both effects are expected to be comparable.

Reeks (1977) developed a comprehensive theoretical model for prediction of particle diffusion, velocity fluctuations and integral timescales considering both inertia and the crossing effect and assuming homogeneous isotropic turbulence and linear drag. The qualitative variation of particle timescale $\mathcal{T}_{Lp}$ with particle response time τ_p expected from the discussion on type 2 particles agrees with Reeks predictions. Figure 3.1 gives Reeks results for the particle integral timescale $\mathcal{T}_{Lp}$ in terms of the characteristic times used here. The regions corresponding to each of the three particle motions are also shown. For these results Reeks approach was equivalent to assuming that $\tau_e \approx l_e/u_e$. The curves shown represent loci of constant $u_e/\tau_e g = \tau_p\tau_d/\tau_e^2$. It is seen that as the turbulence intensity decreases or the eddy decay time increases, crossing increasingly dominates inertia effects for type 2 motion and $\mathcal{T}_{Lp} < \tau_e$. For type 2 motion there is a difference between $\mathcal{T}_{Lpz}$ and $\mathcal{T}_{Lpx}$ that increases with crossing. This is a result of the difference in the fluctuating vertical and lateral velocities of the particle due to crossing (accounted for by Csanady's analysis) and the imperfect response of the particle to the gas fluctuations due to a finite particle inertia (not accounted for by Csanady). Typical values of $\tau_p\tau_d/\tau_e^2$ for CFB particles and risers are given in Table 3.8. The motion of the CFB particles falls into all categories, depending on the relative magnitudes of the characteristic times.

A simple empirical equation that approximates the far more complicated expressions given by Reeks (1977) for particle integral timescale $\mathcal{T}_{Lp}$ is

$$\mathcal{T}_{Lp} = \tau_r + \tau_p \ , \tag{3.52}$$

To match Reek's results and account for possible anisotropy in the particle motion τ_r is redefined (see eq. (3.44)) as $\tau_r = \mathrm{MIN}[\tau_e\,;\,2\tau_d/c_p]$. The predictions of this expression are also plotted in Figure 3.1. This simple relation correctly approaches the limits $\mathcal{T}_{Lp} = \tau_e + \tau_p$ for small

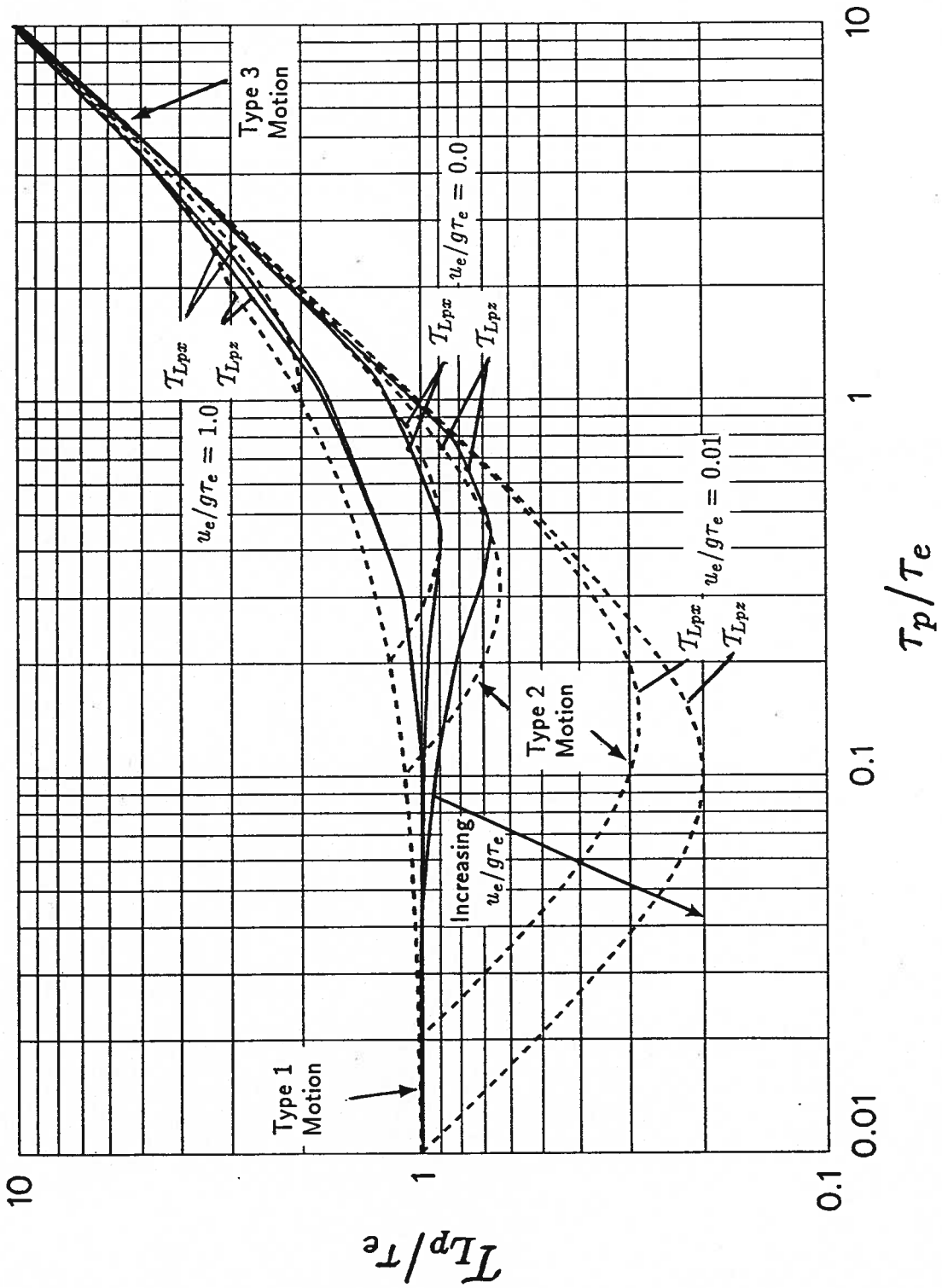

Figure 3.1: Comparison of the particle integral timescale $\mathcal{T}_{Lp}$ given by Reeks (1977) (solid lines) and eq. (3.52) (dashed lines).

type 1 particles (eq. (3.49)) and $\mathcal{T}_{Lp} = \tau_p$ for large type 3 particles. It also gives reasonable approximations for type 2 particles.

There is strong evidence that the particle diffusion coefficient is predominantly dependent on the crossing effect and that inertia effects have relatively little influence on this parameter. Wells and Stock (1983) performed an ingenious series of experiments on the crossing effect where they were able to separate inertia and crossing by controlling the particle slip velocity with an electric field. They found little effect of particle inertia on particle diffusion, and their experimental particle diffusion coefficients were reasonably predicted by Csanady's equation (eq. (3.51)). The diffusion coefficients given by the theoretical results of Reeks (1977) were also reasonably predicted by Csanady's equation. Therefore, it is assumed that we may use Csanady's equation to approximate the particle diffusion coefficient for particles of finite inertia. The gas and particle r.m.s. velocities and timescales may be related to the diffusion coefficients by combining Taylor's expressions for particles and gas (eqs. (3.45) and (3.48)), i.e.

$$\frac{\mathcal{D}_p}{\mathcal{D}_g} = \frac{\mathcal{T}_{Lp}\, v_e^2}{\tau_e\, u_e^2} \,. \tag{3.53}$$

Substituting this expression for $\mathcal{D}_p/\mathcal{D}_g$ and eq. (3.52) into eq. (3.51) leads to an expression for prediction of the fluctuating r.m.s. particle velocity,

$$\frac{v_e^2}{u_e^2} = \frac{\tau_e}{(\tau_r + \tau_p)\left(1 + c_p^2\tau_e^2/\tau_d^2\right)^{\frac{1}{2}}} \,. \tag{3.54}$$

Note that, although lateral velocities $v_{ex} = v_{ey}$ for all cases, generally $v_{ez} \neq v_{ex}$ and $v_{ez} \neq v_{ey}$ when the crossing effect is important. In the limit of type 1 or 3 motion, this expression simplifies to forms in agreement other proposed expressions for these limiting cases (e.g. Binder and Hanratty, 1991; Abrahamson, 1975; Williams and Crane, 1983; Govan, 1989). Govan's (1989) expression for type 3 motion particles may be generalised to allow also for vertical particle velocity fluctuations also, i.e.

$$\frac{v_e^2}{u_e^2} = \frac{\tau_d}{c_p\tau_p} \,. \tag{3.55}$$

Table 3.9 gives the values for $(v_{ez}/u_e)^2$ and $(v_{ex}/u_e)^2$ predicted by eq. (3.54) and eq. (3.49) for type 1 motion particles and the modified Govan (1989) expression (eq. (3.55)) for type 3

Table 3.9: Fluctuating r.m.s. particle velocities given by eq. (3.54) and the models of Binder and Hanratty (1991) and Govan (1989). Particle and riser conditions as in Tables 3.3, 3.7 and 3.8.

Riser[a]		Particle	Time Constants & Motion Type				Particle r.m.s. Velocities			
							This Theory		"Binder/Govan"[b]	
Case	D	d_p	τ_e	τ_p	τ_d	type	$\left(\frac{v_{ez}}{u_e}\right)^2$	$\left(\frac{v_{ex}}{u_e}\right)^2$	$\left(\frac{v_{ez}}{u_e}\right)^2$	$\left(\frac{v_{ex}}{u_e}\right)^2$
	(m)	(μm)	(s)	(s)	(s)	(–)	(–)	(–)	(–)	(–)
1	0.15	40	0.1	0.012	0.13	1–2	0.71	0.49	0.89	0.89
1	0.15	230	0.1	0.2	0.01	3	0.045	0.024	0.05	0.025
1	0.15	500	0.1	0.4	0.004	3	0.01	0.005	0.01	0.005
2	0.15	40	0.08	0.005	0.32	1	0.91	0.84	0.94	0.94
2	0.15	230	0.08	0.15	0.01	3	0.06	0.03	0.07	0.035
2	0.15	500	0.08	0.4	0.004	3	0.01	0.005	0.01	0.005
3	4.0	40	2.0	0.005	8.5	1	0.97	0.90	0.998	0.998
3	4.0	230	2.0	0.15	0.32	2	0.40	0.34	–	–
3	4.0	500	2.0	0.4	0.1	2–3	0.17	0.10	0.25	0.125

[a]Case 1, $T_g = 25$ °C.; Cases 2 and 3, $T_g = 870$ °C.
[b]eq. (3.49) for type 1 particles; eq. (3.55) for type 3 particles.

motion particles. For types 1 and 3 motion there is good agreement (within ± 10%) between the proposed general correlation and existing limit correlations as expected. The proposed correlation predicts partial but significant response of the type 2 particles to the turbulence. Interestingly, due to the relative trends in $\mathcal{T}_{Lpz}$ and $\mathcal{T}_{Lpx}$, it is predicted that lateral and axial r.m.s. particle velocities may be similar in magnitude for some type 2 motions, although substantial crossing occurs (e.g. case 3, 230 μm particles). In Table 3.9 two of the particle motions are intermediate between motion types and thus do not satisfy criteria of the limit correlations for types 1 or 3 motion. Although in case 1 the results of the "Binder" limit correlation are given for 40 μm particles, they cannot be considered accurate. For case 3, 230 μm particle motion, the "Govan" limit correlation predicts a result which is not physically feasible and therefore is not listed in the table. This highlights the usefulness of the proposed general correlation, eq. (3.54).

The proposed general expression for prediction of the fluctuating particle velocity, eq. (3.54), has been developed from the results of other studies that have considered both theoretical and

experimental particle r.m.s. velocities for types 1 and 3 motion, and long-time particle diffusion coefficients for all types of motion. For smaller diameter CFB risers, where particles may pass through many eddies as they move up the riser core, it is likely to give reasonable quantitative results for types 1 and 3 motion, and at least good order of magnitude estimates (say $\pm$ 50%) for type 2 motion. However, for larger commercial units, particles are expected to encounter only a relatively small number of the very large energetic eddies as they travel up the core and the particle motion may no longer be considered a diffusive process. Despite this, similar trends to those observed in small CFBs are expected and, as experimental measurements of the turbulence levels in commercial CFB units are not yet available, it is assumed that the proposed equation provides reasonable estimates for large CFB risers.

In addition to the approximations made in developing theoretical predictions for the response of particles to turbulence, there are many difficulties involved with experimentally measuring and interpreting signals representative of gas and particle instantaneous velocities in two-phase turbulent flows. Few comprehensive experimental studies relating to pipe or riser flows are considered reasonably accurate (Homsy *et al.*, 1991) and often complicating factors such as particle collisions make interpretation of results difficult. As good pipe and riser flow data become available, further refinement of the proposed equation will probably be required. Nevertheless, it currently predicts all observed experimental trends (Reeks, 1977), and its accuracy is adequate for the order of magnitude estimates of particle modulation of gas turbulence developed next.

3.4.4 Modulation of Gas Turbulence by Particles

When there are many particles present in a turbulent gas stream, the particles may modulate the turbulence in a number of ways. Increases in turbulence intensity in the presence of large particles have been observed experimentally. This is generally attributed to the shedding of vortices from individual large particles at high Re_p (Hinze, 1972; Hetsroni, 1989). On the other hand, energy transferred from the turbulent eddies to the smaller particles, which respond to the turbulent fluctuations, results in a decrease in the turbulence intensity (Owen, 1969; Hinze,

1972). In addition to the effects of individual particles, it may be reasonably expected that particle structures, such as wall streamers, increase the shear in the gas flow, thereby increasing the turbulence intensity. Collisions amongst particles may also result in the indirect transfer of energy from the gas turbulence via small responsive particles to larger, less responsive particles.

Considering the enhancement of turbulence due to large particles, Hetsroni (1989) cites a lower limit of $Re_p = 400$ for the onset of vortex shedding from spheres. Based on the analysis of fifteen sets of experimental data, Gore and Crowe (1989) propose an alternative lower limit for this enhancement as $d_p/l_e = 0.1$. For Re_p values for particles typical of CFBs (see Table 3.3), all values are below the Hetsroni limit, except for the largest coal particle in ambient temperature gas flow. Such large coal particles are generally present only in small proportions in hot CFB combustors. A comparison of d_p and l_e in Table 3.8 shows that all these particles have $d_p/l_e < 0.1$ for typical CFB riser gas velocities. Therefore, based on both the Hetsroni and Gore and Crowe limits, it can be assumed that there is negligible enhancement of turbulence intensity due to vortex shedding from individual particles in CFB's.

A reduction of turbulence intensity due to the presence of particles is also frequently observed (e.g. Tsuji *et al.*, 1984). In single phase gas flow the turbulent energy cascades down from the larger energetic eddies to be dissipated by viscous action in the small eddies of size comparable to the Kolmogorov sized eddies. When particles which respond to the gas velocity fluctuations are introduced into the gas flow, a portion of the energy of the larger eddies is also transferred to the particles to maintain their fluctuating motion. As the particles encounter each new eddy they not only gain kinetic energy and a component of velocity in the direction of the eddy velocity, but they also lose some kinetic energy by viscous dissipation because of the component of their velocity that is uncorrelated with the new eddy velocity. Hence, the presence of the particles provides an additional parallel pathway by which turbulent energy is dissipated.

The method used here to estimate the reduction in turbulence intensity due to the particles' presence is similar to that given by Owen (1969). It is expected to provide estimates of the turbulence energy reduction that are at least of the correct order of magnitude (Hetsroni, 1989).

It is assumed that (i) the turbulence energy production and dissipation proceed at comparable rates, and that (ii) the scale, l_e, of the energetic eddies is unaffected by the presence of particles. Both assumptions are common in the modelling of single and two-phase turbulent flows (e.g. Tennekes and Lumley, 1972; Rizk and Elghobashi, 1989). Assumption (i) for riser flow is discussed in more detail later in this chapter.

Owen (1969) interpreted the turbulent integral scale, l_e, as both an approximation of the energetic eddy size (as assumed in this study) and as a mixing length. For vertical pipe or riser gas flow and with l_e equal to the mixing length, the vertical shear stress due to eddy diffusion in a lateral (say x) direction is (Tennekes and Lumley, 1972):

$$\tau_{xz} = \rho_g \, u_x \, l_e \frac{\partial \mathbf{u}}{\partial x} \, , \tag{3.56}$$

where $\partial \mathbf{u}/\partial x$ is the x direction gradient of the mean gas velocity. The work performed by the shear stress, τ_{xz} , per unit volume and time on a small element of volume $\Delta x \Delta y \Delta z$ is

$$\begin{aligned} P_{gtx} &\approx \frac{(\tau_{xz} \, \Delta z \Delta y) \, \Delta \mathbf{u}}{\Delta x \Delta y \Delta z} \\ &= \rho_g \, u_x \, l_e \left(\frac{\partial \mathbf{u}}{\partial x} \right)^2 . \end{aligned} \tag{3.57}$$

For an axisymmetric gas velocity profile, $\left(\frac{\partial \mathbf{u}}{\partial x}\right)^2 + \left(\frac{\partial \mathbf{u}}{\partial y}\right)^2 = \left(\frac{\partial \mathbf{u}}{\partial r}\right)^2$. Assuming the turbulence is nearly isotropic gives $u_x \approx u_y \approx u_e$. Thus the total production of turbulent energy due to shear in the mean flow is

$$P_{gt} \approx \rho_g u_e l_e \left(\frac{\partial \mathbf{u}}{\partial r} \right)^2 , \tag{3.58}$$

where $\partial \mathbf{u}/\partial r$ is an "average" gradient representative of the shear that produces the eddies.

Consider first the case of single phase gas flow (denoted by subscript "0") in the riser. The kinetic energy per unit volume of the energetic turbulent eddies is approximately $\frac{3}{2}\rho_g u_{e0}^2$. As discussed earlier, this quantity of energy is transferred to smaller eddies in a time approximated by the energetic eddy decay time, τ_e. Assuming that the production rate P_{gt} is comparable to the dissipation rate, D_{gt}, gives for single phase flow,

$$\rho_g u_{e0} l_e \left(\frac{\partial \mathbf{u}}{\partial r} \right)^2 \approx \frac{3}{2} \frac{\rho_g u_{e0}^2}{\tau_{e0}} . \tag{3.59}$$

Now consider the case when particles are present. If the particle r.m.s. fluctuating velocity is $\overline{v_e}$, where $(\overline{v_e})^2 = \frac{1}{3}(v_{ex}^2 + v_{ey}^2 + v_{ez}^2)$, then the "fluctuating" kinetic energy of a single particle is $\frac{3}{2}\, m_p \overline{v_e}^2$. Small particles that respond rapidly to each eddy will lose/gain this amount of energy with each eddy interaction. However, larger particles only lose/gain a fraction of their energy with each interaction, and the interaction time may be substantially less than the eddy decay time due to the crossing effect[2]. The characteristic or average period with which particles fluctuate (i.e. period of time t after which their velocity is no longer correlated with their velocity at zero time) is the particle Lagrangian integral timescale, $\mathcal{T}_{Lp}$. Thus an amount of energy equivalent to the instantaneous kinetic energy of the particles will be transferred from the energetic eddies to the particles over an average time of approximately $\overline{\mathcal{T}_{Lp}}$. Both $\overline{v_e}^2/u_e^2$ and $\overline{\mathcal{T}_{Lp}}$ are written as averages because of the possible anisotropy in particle fluctuating velocities. They may be determined from eqs. (3.52) and (3.54) if the turbulence velocity u_e is known. For convenience the overbars on $\overline{v_e}$ and $\overline{\mathcal{T}_{Lp}}$ are omitted in the following discussion. The energy transfer rate per unit riser volume is therefore $\frac{3}{2}\rho_s v_e^2/\mathcal{T}_{Lp}$, where ρ_s is the suspension density.

When particles are present, a balance equivalent to eq. (3.59) for energy production and loss for the energetic eddies is,

$$\rho_g u_{e1} l_e \left(\frac{\partial \mathbf{u}}{\partial r}\right)^2 \approx \frac{3}{2}\frac{\rho_g u_{e1}^2}{\tau_{e1}} + \frac{3}{2}\frac{\rho_s v_e^2}{\mathcal{T}_{Lp}}\,, \tag{3.60}$$

where subscript "1" denotes the condition with particles present. If it is assumed that the eddy producing gas shear $(\partial \mathbf{u}/\partial r)$ does not change appreciably with the introduction of particles, then an expression for the reduction in gas turbulent energy due to the particles may be obtained by combining eqs. (3.41), (3.59) and (3.60):

$$u_{e0}^2 = u_{e1}^2 + \frac{\rho_s v_e^2 \tau_{e1}}{\rho_g \mathcal{T}_{Lp}}\,. \tag{3.61}$$

This general equation for prediction of reduction in turbulence intensity due to the presence of particles may be simplified for types 1 and 3 particle motion. For type 1 particle motion,

[2]Here the analysis deviates from that of Owen (1969). Owen appears to incorrectly assume that particles gain/lose all their kinetic energy with each eddy interaction. Owen also does not consider the crossing effect.

the particle velocity fluctuations are isotropic and $\mathcal{T}_{Lp} = \tau_{e1} + \tau_p \approx \tau_{e1}$. Equation (3.54) then simplifies to $v_e^2/u_{e1}^2 \approx 1$ which, when substituted into eq. (3.61), gives

$$\frac{u_{e1}^2}{u_{e0}^2} = \left(1 + \frac{\rho_s}{\rho_g}\right)^{-1} . \tag{3.62}$$

This is the same as Owen's (1969) result for small particles. For type 3 particle motion, $\tau_d \ll \tau_e$, and $\mathcal{T}_{Lp} \approx \tau_p$. In this case, considering an average that allows for both vertical and lateral fluctuations, $v_e^2/u_{e1}^2 \approx \frac{2}{3}\tau_d/\tau_p$. Thus for type 3 particle motion,

$$\frac{u_{e1}^2}{u_{e0}^2} = \left(1 + \frac{2\rho_s\tau_{e1}\tau_d}{3\rho_g\tau_p^2}\right)^{-1} . \tag{3.63}$$

This result differs from Owen's (1969) result for "more massive" particles. Although no derivation of the massive particle result was given by Owen, it is clear that the crossing effect was not considered. For type 3 particles, $\tau_p > \tau_d > \tau_e$, and modulation of the turbulence is generally small.

Except for type 1 particle motion, solution of the equations for reduction in turbulence intensity are generally iterative, since τ_{e1} on the r.h.s. of eq. (3.61) is a function of u_{e1}. Some important trends predicted by the turbulence reduction equations may be illustrated by considering effects of the 40 μm and 230 μm particles in the 4.0 m commercial size combustor. The time constants and velocity responses for these two sizes of particles are given in Table 3.9. For the 40 μm particles (type 1 motion) the turbulence reduction is

$$\frac{u_{e1}^2}{u_{e0}^2} \approx \left(1 + \frac{0.9\rho_s}{\rho_g}\right)^{-1} . \tag{3.64}$$

Therefore only a very small concentration of responsive particles ($\rho_s = 1$ kg/m^3, say) is required before the reduction in the turbulence energy level of the gas becomes significant. For the 230 μm particles (type 2 motion), assuming $\tau_{e1} \approx \tau_{e0}$ (i.e. dilute particle concentrations), the turbulence reduction expression is

$$\frac{u_{e1}^2}{u_{e0}^2} \approx \left(1 + \frac{1.3\rho_s}{\rho_g}\right)^{-1} . \tag{3.65}$$

Thus the reduction in turbulence energy is predicted to be greater at equivalent suspension densities when the larger, less responsive 230 μm particles are used rather than the small 40 μm particles. This important result is due to the crossing effect. The 40 μm particles have an interaction time of $\tau_r \approx \tau_e = 2.0$ s, whilst the 230 μm particles have an interaction time of $\tau_r \approx 0.5$ s. Although the 230 μm particles do not respond as much to each eddy they encounter, due to their much greater slip velocities they interact with more eddies per unit time than the smaller particles. This effect is important for scale-up of CFBs. Particles that exhibit type 3 motion in small diameter risers may exhibit type 2 motion in larger diameter risers with larger energetic eddies. Although type 3 motion particles have high slip velocities, their response to the gas turbulence is so small that little modulation of the turbulence is observed. Therefore, turbulence levels may be significantly higher in pilot-scale units than larger units. This has important implications for gas reactions dependent on micro-mixing.

Many of the modelling studies on vertical dilute suspension flows have used the experimental data of Tsuji *et al.* (1984) to either establish empirical constants for their models or to interpret and support trends given by their models. The results of Tsuji *et al.* are discussed in some detail here and in Appendix A to highlight the complex interactions that can occur in turbulent two-phase flows and to demonstrate the usefulness of the proposed "order of magnitude" turbulence reduction correlations for interpreting experimental data.

Tsuji *et al.* (1984) measured mean and fluctuating axial gas and particle velocities in vertical dilute suspension upflow using a laser-Doppler velocimeter (LDV). The experiments were performed with air at ambient temperature in a column of 30 mm diameter. Several sizes of plastic particles of density $\rho_p = 1020$ kg/m^3 and diameters from 200 μm to 3 mm were investigated. Tsuji *et al.* reported solids loading in terms of a loading ratio m_s, equal to the particle-to-air mass flowrate ratio. The loading ratio is related to the solids circulation by $G_s = \rho_g U_0 m_s$. Although Tsuji *et al.* found an increase in turbulence intensity for the large particles, this is probably not an important phenomenon in CFB units, as discussed earlier.

Some of the results of Tsuji *et al.* for 200 μm particles are shown in Figures 3.2 and 3.3.

For these 200 μm particle tests, the gas velocities were in the range of 10 to 15 m/s. At these relatively high gas velocities and low solids loadings, Tsuji *et al.* only detected upward solids velocities near the wall (no wall streamers). Re_p for these particles was always less than 50, and thus enhancement of turbulence due to vortex shedding was unlikely to have occurred. The terminal velocity of these 200 μm particles was 0.7 m/s.

Some interesting trends shown in Figure 3.2 are a significant flattening of both the mean gas velocity profile and the turbulence intensity profile with an increase in solids loading m_s. It should be noted that the turbulence intensity in the figure is defined as the r.m.s. gas fluctuating velocity divided by the mean axial centreline velocity, $\mathbf{u}_c$. Both the r.m.s. velocities and centreline velocity change with solids loading for a constant mean gas velocity U_0 (i.e. constant Re_D). Therefore, although the turbulence intensity at the centre of the riser first decreases and then begins to increase with solids loading, the magnitude of the absolute r.m.s. velocity fluctuations at the riser centre only declines slightly ($O(20\%)$) with an increase in solids loading. For the same reason, the decreases with m_s of the r.m.s. gas velocities in regions between the wall and the centreline are even greater than the equivalent reductions in turbulence intensities shown in the figure. The greatest reduction in turbulence occurs at $r/R \approx 0.7$, which is mid-way between the centreline and wall in terms of cross-sectional area. The changes very close to the wall are similar in magnitude to those at the centreline.

From Figure 3.2 it is apparent that the particles have a far greater effect in reducing turbulence energy levels in the region $0.4 < r/R < 0.9$ than in the centre of the riser. Based on prior discussions, it may be postulated that this is due to higher slip velocities in the core than nearer the wall, and hence a reduction in particle response in the core due to the crossing effect. Figure 3.3 data (although not taken at the same Re_D as the Figure 3.2 data) qualitatively support this assumption. Figure 3.3 shows that in the core of the riser the particles lag behind the gas flow, whilst at the wall they may lead the gas flow, with a crossover in velocities occurring close to the wall. This crossover is possible because particles may slide at the wall, which likely occurs when faster moving particles further from the wall (e.g. at $r/R \approx 0.75$) are sufficiently

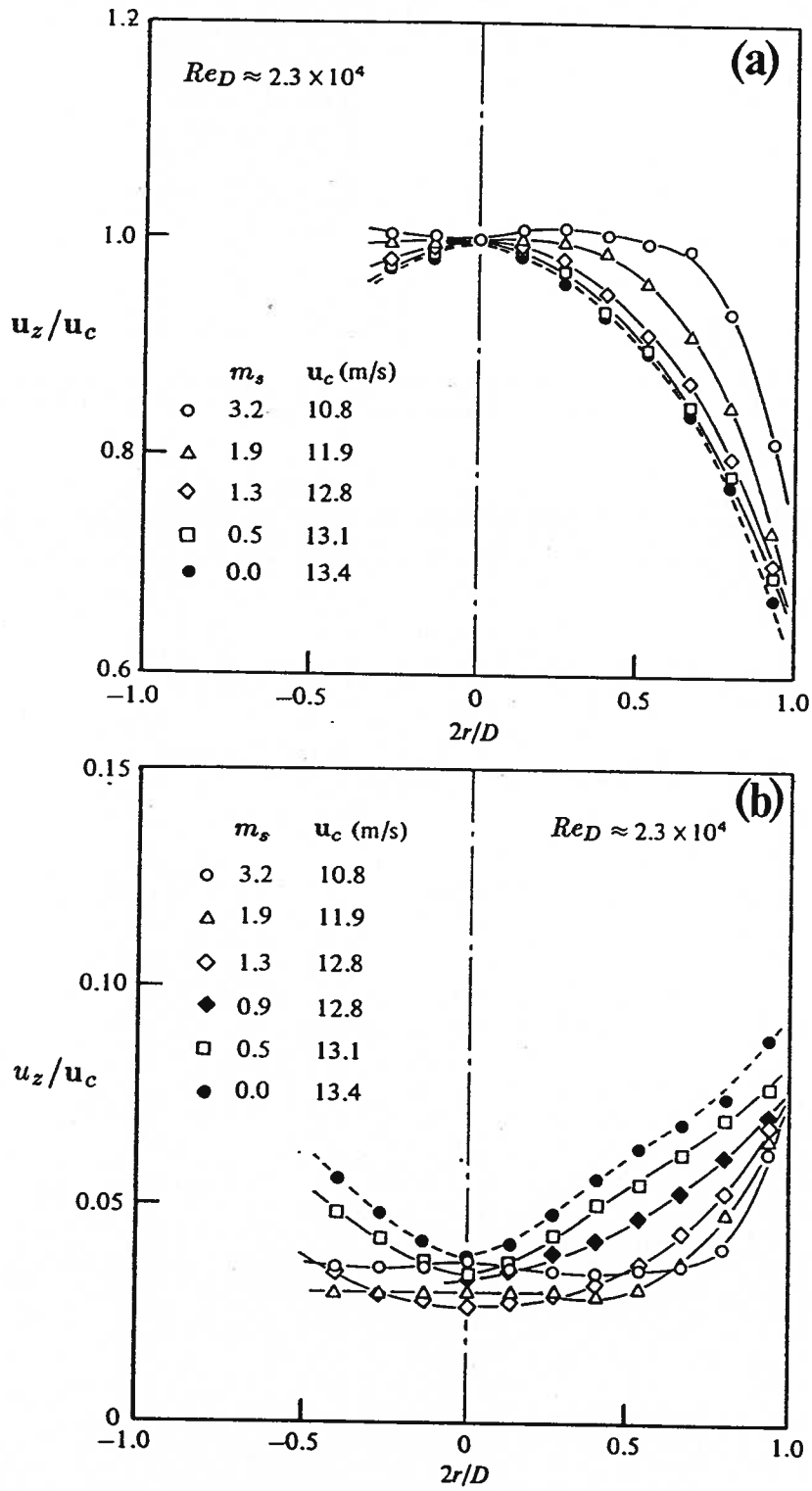

Figure 3.2: Experimental results of Tsuji *et al.* (1984) for 200 μm diameter plastic particles at $Re_D = 2.3 \times 10^4$; (a) mean air velocity distribution (u_z/u_c), and (b) axial turbulence intensity of air (u_z/u_c).

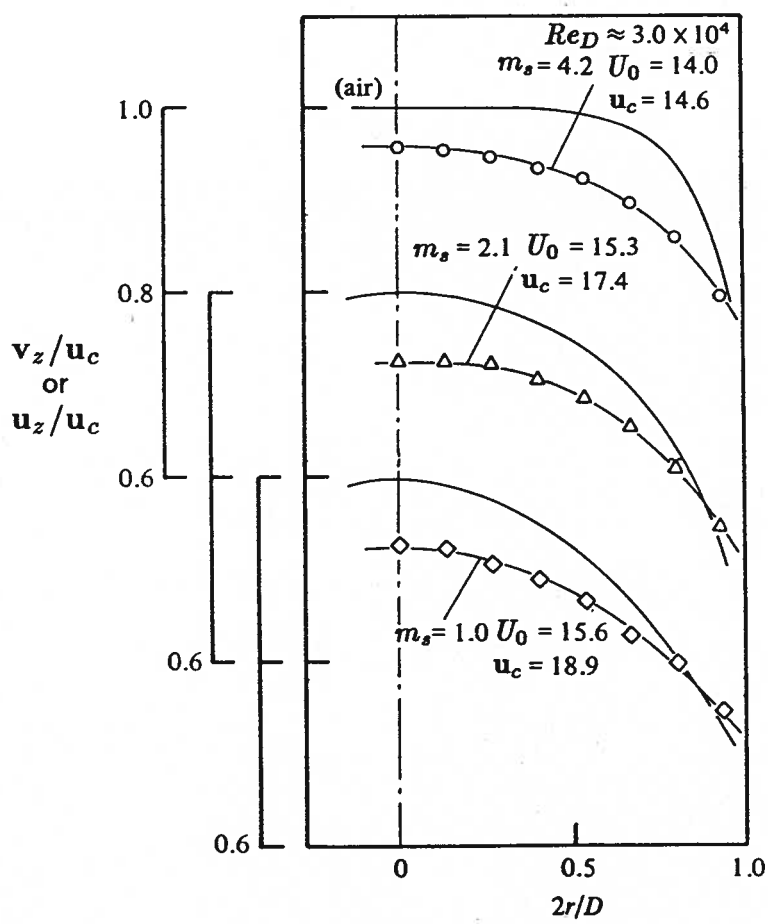

Figure 3.3: Mean gas and particle velocity profiles measured by Tsuji *et al.* (1984) for 200 μm particles at $Re_D = 3.0 \times 10^4$. Solid lines: gas profile, $\mathbf{u}_z/\mathbf{u}_c$. Lines with symbols: particle profile, $\mathbf{v}_z/\mathbf{u}_c$.

influenced by either collisions or turbulence to move laterally towards the wall and vertically accelerate the wall particles.

Rizk and Elghobashi (1989) propose that the flattening of the gas velocity profile in the core of the riser and its steepening nearer the wall are due to the drag interaction of the gas and particles. They suggest that the slower core particles retard the core gas flow, whilst particles nearer the wall, which lead the gas flow due to finite particle slip at the wall, increase gas velocities in the wall region. Close inspection of Figure 3.3 shows that the gas velocity profile becomes even flatter than the particle profile at the higher solids loadings. Tsuji *et al.* (1984) even measured profiles that were concave in the riser core, with the highest gas velocities at $r/R \approx 0.5$. Clearly this effect cannot be caused by particle drag effects alone. It can be explained by the significantly greater reduction in gas turbulence that occurs close to the wall in comparison to the core. As a consequence of this reduction, the local shear force resistance to gas flow decreases more in an intermediate region between wall and core than in the core (i.e. a more significant decrease in "eddy diffusivity" or Reynolds stresses occurs.)

Thus far the trends measured by Tsuji *et al.* have all been explained by qualitative consideration of mean gas-particle drag, radial differences in particle slip velocity and the crossing trajectory effect. However, implicit in this discussion has been the assumption that the 200 μm particles respond to the turbulent gas flow, at least near the riser wall. To test this assumption, consider the case where the particle is most likely to respond to the turbulence. This occurs when there is negligible crossing, i.e. for $Re_p < 0.1$. At this low slip velocity the standard drag curve simplifies to Stokes Law, giving $\tau_p = d_p^2 \rho_p / 18\mu_g = 0.1$ s. For air flow of $Re_D = 2.3 \times 10^4$ in the 30 mm column of Tsuji *et al.*, relations presented earlier give a predicted wall friction velocity of $\mathbf{u}_\star = 0.62$ m/s, turbulence velocity in the core of $u_e \approx 0.5$ m/s, energetic eddy size $l_e \approx 3.3$ mm and an energetic eddy decay time of $\tau_e \approx 0.01$ s. In excellent agreement with these results is the measured value of the core turbulence velocity, also equal to 0.5 m/s for gas flow only. When there is no crossing effect influencing the particle motion, eq. (3.49) may be used to predict v_e^2/u_e^2. Using a value of $c_2 = 1.0$ in this equation for the 200 μm particle case of Tsuji *et*

al. gives $v_e^2/u_e^2 = 0.09$. Contrary to clear experimental evidence, this prediction suggests that there should have been little response of the 200 μm particles to the turbulence, regardless of radial location.

The likely explanation for this apparent inconsistency is rather subtle, and does not appear to have been recognised by the majority of modellers who have used the Tsuji *et al.* data. The particles probably responded because of drag enhancement caused by eddies of a scale smaller than the particles. Using the relation given by Tsuji *et al.* for estimating the viscous dissipation of energy in single phase flow in the core of a pipe or riser,

$$\epsilon_t = \frac{2.2}{R}\mathbf{u}_\star^3 , \tag{3.66}$$

gives an estimate of the energy dissipation rate ϵ_t of 55 m^2/s^3 in the riser core for the 200 μm particle experiment of Figure 3.2. The corresponding Kolmogorov core eddy size η_κ for this case is 88 μm (eq. (3.34)). As this is significantly smaller than the particle size, the drag of the mean gas flow on the particle may have been modified due to local eddy flow variations around the particle surface (Hinze, 1972). Near the wall even smaller eddies typically exist due to the greater shear and higher energy production and dissipation rates. In Appendix A it is shown that the response of the 200 μm particles may be reasonably predicted if correlations including drag enhancement are used.

The enhancement of drag due to small scale eddies adds a level of complexity to prediction of the behaviour of two-phase flowing suspensions. Although it can be a dominant influence, as apparently in the Tsuji *et al.* work, relatively little research has been performed on this topic. However, for most CFB units of interest here it is not likely to be significant. Table 3.10 gives the Kolmogorov eddy sizes for the three CFB cases considered earlier. These eddies correspond to the smallest eddy sizes likely to be encountered by the particles. The 150 mm diameter cold unit (case 1), operating with a typical riser gas velocity of 6.5 m/s, has Kolmogorov eddies of comparable size to the 230 μm particles. The Kolmogorov eddies are significantly larger at elevated temperatures (cases 2, 3). Based on the postulate that only eddies significantly smaller than the particles influence gas-particle drag, it may be assumed that CFB particles in

Table 3.10: Core turbulent energy dissipation rates ϵ_t and Kolmogorov eddy sizes η_κ for the riser conditions as in Tables 3.3, 3.7 and 3.8.

Case (–)	T_g (°C.)	D (m)	ϵ_t (m^2/s^3)	η_κ (μm)
1	25	0.15	0.97	240
2	870	0.15	2.3	1100
3	870	4.0	0.03	3400

CFB pilot-scale units of 150 mm diameter or greater are unlikely to be affected by small scale eddies. In contrast, suspension dynamics in very small diameter bench-scale CFBs operating at ambient temperature may differ profoundly from those in larger units, if similar particles are used. Unfortunately, practically all the detailed turbulence measurements in "dilute" CFBs (vertical pneumatic conveyors) have been performed in cold units of 100 mm diameter or less (e.g. Tsuji *et al.*, 1984; Lee and Durst, 1982; Chandok and Pei, 1972; Min, 1966).

Two important additional observations may be made from the Tsuji *et al.* data in Figure 3.1 which support earlier postulates. Firstly, although the gradient in the gas velocity profile near the wall ($r/R > 0.8$) steepens with particle loading in Figures 3.1 and 3.3, this is misleading as the gas velocity is plotted as a fraction of the centreline velocity, which also changes. In fact, crude estimates of $\partial \mathbf{u}/\partial r$ from these figures indicate relatively little change in the gradient $\partial \mathbf{u}/\partial r$ in this region. As most of the turbulence arises from this high shear region, the assumption of a constant "eddy producing" shear in eq. (3.60) does not appear unreasonable, at least for low suspension densities such as those in the Tsuji *et al.* tests (i.e. $\rho_s < 5$ kg/m^3). The second important result given by Tsuji *et al.* is the change in the frequency power spectrum with particle loading for the 200 μm particle tests. Increasing particle loading reduced the power of the larger eddies in comparison to the mid-sized and smaller eddies. This is in agreement with the postulate that the particles are predominantly influenced by the larger energetic eddies.

Thus far it has been assumed that there is not a significant change in turbulence producing shear in dilute suspension flows. This assumption is unlikely to be true for many CFB operations, where disrupted particle streamers often form at the riser wall and turbulent fluidised

beds are generally present at the base of the riser. The presence of streamers at the wall is similar to the effect of roughening the riser wall. Both gas friction velocity and turbulence energy production are likely to increase. The friction factor for the core flow in gas-liquid annular flow has been estimated to be as high as 10 times that of a smooth pipe due to a disrupted annular liquid film (Wallis, 1970; Asali and Hanratty, 1985). Wall streamer thicknesses as great as 10% of the riser diameter were measured in this study (Chapter 7). If this corresponded to a relative pipe roughness "k/D" of 0.1, there would be an order of magnitude increase in friction factor compared to the friction factor for a smooth pipe. As the turbulence energy level predicted by pipe flow correlations is proportional to the friction velocity, there would be approximately a threefold increase in turbulence energy. Such wall streamer thicknesses typically corresponded to densities of the upflowing dilute suspension of magnitude greater than 10 kg/m^3 in the tests performed in this study.

For a conservative estimate of the net change in gas turbulence levels due to wall friction and particle modulation effects, the case of $\rho_s = 10$ kg/m^3 and $u'^2_{e0} = 3u^2_{e0}$ is considered. Here u'_{e0} is the r.m.s. turbulence velocity in an equivalent "roughened wall" riser without particles. This case corresponds to the minimum expected suspension density that may be present when an order of magnitude increase in wall friction occurs. The turbulence reduction may be calculated for the typical CFB particles given in Table 3.9 using eqs. (3.54) and (3.61) and assuming isotropy in the gas turbulence. The results with allowance for anisotropy in particle fluctuations are given in Table 3.11. The turbulence energy change is given relative to the turbulence energy level, u^2_{e0}, in a smooth particle-free riser.

In Table 3.11 the turbulence reduction due to the particles is greater than turbulence enhancement due to wall friction for the responsive type 1 and 2 particles. As these values were computed at conditions corresponding roughly to the expected minimum reduction by particles and maximum enhancement by wall roughness, the results suggest that turbulence levels are generally much lower in a CFB riser when *responsive* particles are added than for the equivalent particle-free gas flows. In Table 3.11 the reduction due to 40 μm particles is not as great in the

Table 3.11: Relative gas turbulence energy (u_{e1}^2/u_{e0}^2) and lateral r.m.s. particle fluctuating velocity v_{ex1} at suspension density $\rho_s = 10$ kg/m^3. Riser case conditions, relative particle time constants and individual particle responses are given in Tables 3.3, 3.7, 3.8 and 3.9.

Case (–)	D (m)	d_p (μm)	Motion Type (–)	τ_{e0} (s)	τ_{e1} (s)	u_{e0}^2 (m^2/s^2)	u_{e1}^2/u_{e0}^2 (–)	u_{e1} (m/s)	v_{ex1} (m/s)
1	0.15	40	1–2	0.10	0.13	0.068	0.60	0.20	0.13
1	0.15	230	3	0.10	0.06	0.068	2.80	0.44	0.06
1	0.15	500	3	0.10	0.06	0.068	2.98	0.45	0.03
2	0.15	40	1	0.08	0.20	0.116	0.10	0.11	0.08
2	0.15	230	3	0.08	0.06	0.116	2.00	0.48	0.08
2	0.15	500	3	0.08	0.05	0.116	2.92	0.58	0.04
3	4.0	40	1	2.0	5.6	0.053	0.13	0.08	0.06
3	4.0	230	2	2.0	29.0	0.053	0.004	0.01	0.008
3	4.0	500	2–3	2.0	10.0	0.053	0.04	0.05	0.015

condition 0, gas flow only: 1 gas-particle suspension flow
u_{e0} = smooth pipe r.m.s. gas fluctuating velocity
u'_{e0} = "rough" pipe r.m.s. gas fluctuating velocity
u_{e1}^2 includes enhancement effects of roughened riser wall ($u_{e0}'^2 = 3u_{e0}^2$)

cold unit (case 1) as in the hot units (cases 2 and 3) because of the greater kinetic energy per unit volume of the denser cold gas. The 230 μm particles in the hot commercial unit (case 3) fully dampen the turbulence and 500 μm particles substantially dampen the turbulence. The larger particles in the hot unit (case 3) have a greater influence on the turbulence than the 40 μm particles because of the crossing effect discussed earlier. The new eddy decay times, also shown, increase with reduction in the gas turbulence energy for types 1 and 2 particles. The long "eddy decay" times for the 230 μm and 500 μm particles in the hot commercial unit (case 3) probably have no physical significance as the turbulence has been almost fully suppressed in these cases. The presence of the unresponsive type 3 particles only causes a minor reduction in the turbulence energy.

Also given in Table 3.11 are the predicted lateral r.m.s. particle fluctuating velocities v_{ex1} computed at the particle-laden turbulence levels. Although the type 3 particles respond little to the turbulence, the greater turbulence intensities experienced by these particles result in fluctuations (v_{ex}) of magnitude similar to that predicted for type 1 particles, and greater than

that predicted for type 2 particles. If gas turbulence alone were responsible for lateral motion of particles, then the results of Table 3.11 suggest that the particle lateral velocities are always less than the level of 0.2 m/s assumed in the earlier linear drag analysis. If one postulates that particle r.m.s. fluctuating velocities of $O(0.1$ m/s) are typical of CFB operations with particle diameters between 200 and 800 μm, then Table 3.11 suggests that gas turbulence cannot fully account for the particle fluctuating motion. Furthermore, the substantial reduction in gas turbulence intensity due to low concentrations of responsive particles suggests that at higher concentrations the influence of gas turbulence on particle fluctuating motion may be negligible.

The large spatial and temporal variations observed in solids concentration in turbulent fluidised beds and the resulting tortuous paths the gas traverses at high velocity through the transient higher voidage regions suggests that gas turbulence energy production may be very high in the base of CFB risers. Correspondingly, particle concentrations and turbulent energy dissipation rates are also likely to be very high. Gas mixing in a turbulent bed is likely to be rapid given the fluctuations in particle motion and concentration, and homogeneous gas-phase reactions are likely to be controlled kinetically. Also, irrespective of particle response or gas turbulence, particles managing to escape from denser clumps, strands or sheets into regions of rapid dilute suspension upflow are likely to be quickly captured in denser particle regions above as the gas follows its upwards tortuous path. In this case, the upward motion of such particles is largely governed by the dynamics of the dense and dilute structures of the turbulent bed, irrespective of discrete particle response to gas turbulence or individual particle collisions in the dilute regions. Thus estimation of gas turbulence intensity in the turbulent bed region may only be important if motion of the denser particle "structures" is significantly influenced by turbulence. From measurements in a 197 mm diameter riser, Louge *et al.* (1990) suggest that this is not the case. They observed little effect of superficial gas velocity on the frequencies of solids concentration fluctuations, both in the wall region (i.e. due to wall streamers) and in the lower turbulent bed region.

Unlike a bubbling bed and its freeboard, there is no distinct interface between a turbulent

bed in the base of a CFB riser and the more dilute regions above it. The transition from a denser turbulent bed to a far more dilute core-annular radial solids distribution may occur over a height of 1 – 5 m. Consequently, it is not advisable to divide the CFB riser into a dense bed and dilute freeboard, and assume high turbulence levels just above the bed "surface" due to phenomena analogous to the eruption of bubbles at the surface of a bubbling bed. If such a hypothetical interface were drawn (e.g. at a height where $\overline{\epsilon_p} = 0.05$), then the particle concentration above this level would be several orders of magnitude greater than freeboard concentrations, and it is likely that turbulence arising from the "bed surface" would be quickly dissipated by the particles (assuming responsive particles were present).

In the discussion in this Chapter and in the model for dilute suspension dynamics in Chapter 8 it is assumed that gas turbulence energy production and dissipation occur at similar rates at all heights. This is equivalent to assuming that the net convection of turbulent energy into any region of incremental riser height is a small fraction of the production and dissipation rates. The validity of this assumption for particle-free riser flow may be tested by calculating the distance travelled by the turbulent energetic eddies before they decay. For the 150 mm diameter risers (cases 1, 2), $\tau_{\epsilon 0} \approx 0.1$s (Table 3.8) for a gas flow of 6.5 m/s and the eddies travel approximately 0.7 m. Thus if the energy production rate were suddenly halved due to changes in the wall roughness, the resulting imbalance in turbulence production and dissipation would approach zero within 0.7 m above the wall transition. For the larger 4.0 m diameter unit (case 3), this distance is 13.0 m. Therefore, although the assumption of equality of production and dissipation in the absence of particles is possibly valid for small diameter risers, it is clearly not valid for the large unit.

When responsive particles are present, the turbulence levels are generally expected to be significantly less than those for particle-free risers. Equation (3.58) predicts that turbulence production will decrease proportionally with u_e. Consider the data given in Table 3.11, corresponding to expected minimum reductions in turbulence due to the particles. In this case production has been assumed to not only change with u_e, but to increase threefold due to wall

effects (i.e. changes in $(\partial \mathbf{u}/\partial r)^2$). Therefore, for the 230 μm particles in the 4.0 m diameter riser (case 3) in Table 3.11, the fractional change in production rate over that in a smooth particle-free riser is $3 \times u_{e1}/u_{e0} = 0.18$. Thus the distance travelled before eddies decay becomes approximately 0.18×13.0 m $= 2.3$ m. For commercial risers of typical heights 30 – 40 m this is now a small fraction of the total riser height and the assumption of balanced production and dissipation rates involves far less error than for the particle-free case. A similar analysis for the large diameter riser and 40 μm particles gives decay distances of order 13.0 m, which suggests that for modelling large risers, operating with relatively low concentrations of fine particles, a differential balance for gas turbulent energy may be required. For large diameter riser operations with bigger, less responsive particles (e.g. > 800 μm), the turbulence may not be significantly suppressed. However, in this case, a good estimate of gas turbulence is not of such importance, as the particle dynamics are essentially independent of the turbulence.

A feature of particle-free riser flow which has no exact equivalent in suspension flows in CFBs is the concept of entry length. For particle-free gas flow in a pipe or riser there exists an initial finite length before fully-developed wall boundary layers and velocity profiles are established. However, upon entering the base of an operating CFB, the gas immediately encounters a very high concentration of particles. In this region, the gas-particle drag force in the gas equation of motion is very large and "entry effects" that may occur are very different from flow an empty riser. If a turbulent bed is present, the gas flow may be considered to enter at high velocity through a series of smaller diameter low voidage "channels," with the characteristic single-phase entry length of each channel being orders of magnitude less than entry lengths calculated for particle-free flow in the riser at the same superficial gas velocity. However, the gas-particle suspension flow does develop with height, and the two-phase developing flow length or "entry length" is typically a significant fraction of the total riser height. It is assumed in this study that the dynamics of two-phase developing flow are dominated by gas-particle interaction forces, and that the gas turbulence properties may be reasonably predicted from fully-developed single-phase flow correlations, appropriately modified to account for the presence of the particles.

3.5 Particle Collisions in Suspension Flows

3.5.1 Causative Factors in Particle Collisions

Particle collisions in gas-particle suspension flows result from:

(1) the relative velocity between particles of different sizes or densities due to different responses to the mean gas flow;

(2) the radial gradient in particle vertical velocity due to wall effects and radial gradients in gas velocity;

(3) relative velocities arising from different particle responses to gas velocity fluctuations (motion within a turbulent eddy);

(4) the projection of particles towards one another from regions of gas flow with uncorrelated velocity fluctuations (motion between gas eddies).

The effects of relative mean particle velocity may be illustrated by considering the upward flow of a mixture of small and large particles. The slower moving larger particles are "peppered" from below by the smaller particles. This accelerates the larger particles and decelerates the smaller particles, shifting both sizes from their steady slip velocity in the absence of collisions. Between collisions the smaller particles generally accelerate upwards and the larger particles decelerate due to the imbalance in gravitational and drag forces caused by the perturbation of collision. As the concentration of particles increases, the collision frequency also increases and the particles have less time to respond between collisions. Thus at higher concentrations the particles travel closer to a mean velocity intermediate between the steady collision-free velocities of the two separate sizes. One can then consider a pseudo "collision force" that maintains the particle velocities at levels differing from their collision-free terminal velocities.

Few collisions between the particles are head-on. Consequently the particles also scatter in any lateral direction in a plane perpendicular to the mean suspension flow. Further collisions result as scattered particles approach from different oblique collisions. Eventually the small and

large particles achieve steady velocity distributions with fluctuating components of velocity in all directions (axial and lateral) as well as mean axial velocities. Collisions due to differences in mean slip velocity depend on the particle size distribution.

The most obvious example of collisions resulting from radial particle velocity gradients is the re-entrainment of particles from downflowing wall streamers into rapid suspension upflow in a CFB. Clearly the very high relative velocities between particles leaving the wall and dilute suspension particles result in very energetic collisions and substantial scattering. Both particle collisions due to mean velocity differences and velocity gradients are independent of gas turbulence and result from wall effects and the mean gas flow.

The collision of particles within eddies results from different responses of particles to transient gas flow. Small particles tend to rapidly attain the eddy velocity, whereas large particles may be unaffected by the eddy fluctuating velocity. Consequently particles within an eddy have different velocities and this causes collisions. As with collisions due to differences in steady velocity, collisions within eddies are a function of particle size distribution. As particles of the same size and density respond similarly to the gas flow, their relative velocities within an eddy will be negligible if they entered the eddy at the same time with similar velocities. Particles that partially respond to an eddy and have significant inertia may also be thrown together from different eddies.

There are obviously many factors that influence the four collision mechanisms outlined above, including particle size, particle size distribution, particle elasticity, riser wall effects and particle concentration. To estimate the influences of particle collisions on the magnitude of fluctuating particle motion and wall deposition is not a simple task. Based on the analysis of the interaction of particles and gas turbulence in this chapter and the expected level of particle velocity fluctuations, it appears that turbulence can, at most, only partially account for particle fluctuations at typical riser suspension densities. However, to provide strong evidence in support of this assertion, it is necessary to model the flow of riser suspensions, allowing for all the important particle-particle and gas-particle interactions discussed thus far. The major

limitation of the approach taken in this chapter to estimating the response of the particles of a single size is that the effect of particle-particle collisions have been ignored. Thus this analysis is strictly limited to very dilute suspensions. In a typical riser flow, collisions between particles due to eddy gas fluctuations are likely to indirectly increase the response of the larger particles to the turbulence, thereby suppressing the turbulence intensity further. An approach that accounts for all these effects is presented in Chapter 8, where a model for suspension flow is presented. To gain some perspective of the relative importance of collisions compared to turbulent fluctuations, we pre-empt the model development by using some model equations here.

Consider suspensions of single-size particles consisting, respectively, of 40 μm, 230 μm and 500 μm particles ($\rho_p = 2700$ kg/m^3). The numbers of these particles per cubic metre, $\mathbf{n}$, in a suspension of concentration 10 kg/m^3 are 1.1×10^{11}, 5.8×10^8 and 5.6×10^7. Now for cases 1 and 2 the energetic eddies are of characteristic size $l_e = 17$ mm (Table 3.8). If one assumes these eddies are approximately spherical, then their volume is 2.6×10^{-6} m^3. The corresponding numbers of 40 μm, 230 μm and 500 μm particles is this volume are, respectively, 2.9×10^5, 1500 and 150. As a suspension density of 10 kg/m^3 is relatively low for riser flow and eddies of size $l_e \approx 17$ mm correspond to the smallest size of energetic eddies considered in this study, it may be assumed that energetic eddies generally contain many particles ($> O(10^2)$). For the eddies in the 4.0 m diameter commercial size unit (case 3, $l_e = 440$ mm) the corresponding number of particles in the eddies increases by a factor of 10^4.

In Chapter 8 an expression for the collision frequency amongst similar sized particles due to their fluctuating velocity is developed (eq. (8.37)). If we assume that the particles in the 10 kg/m^3 suspensions have r.m.s. fluctuating velocities of magnitude 0.2 m/s, then the period between collisions, τ_k, for the 40 μm, 230 μm and 500 μm suspension are, respectively, 0.07 s, 0.39 s and 0.86 s. For the 40 μm particles this is less than the estimated eddy interaction times for these particles (see Table 3.11), and these particles may be expected to make at least several collisions during their time in an energetic eddy. However, for the 230 μm and 500

μm particles in the 0.15 m diameter riser, $\tau_k \geq \tau_r$, and not all these particles are expected to collide during each eddy interaction. Of course, these estimates of collision period overlook the other collision mechanisms which will further decrease τ_k. Also they do not consider the energy transfer of the collisions which may differ significantly from the energy transferred to a particle by the eddy. Nevertheless, it appears that in the most dilute suspensions typical of risers, both collisions and turbulence interactions may be important in determining the fluctuating motion of the particles. At higher suspension densities the effect of collisions will become increasingly important. Henceforth, a "very dilute suspension" is defined as a suspension in which the eddy interaction frequency is greater than the collision frequency for all discrete particles in the suspension. The definition of a "dilute suspension" is given in Chapter 8.

Consider next a mixture of 25 wt% 40 μm particles and 75 wt% 230 μm particles. If the particles are assumed to travel with mean slip velocities equal to their respective terminal velocities, and the suspension density is assumed to be 10 kg/m^3, then the collision frequency between these particles may again be evaluated using Chapter 8 relations (see eq. (8.31)). For this case the period between collisions involving a 40 μm and 230 μm particle is 0.02 s for the 40 μm particle and 0.0004 s for the 230 μm particle. Although it is likely that the difference between mean velocities will be smaller than assumed here due to collisional forces discussed earlier, it is possible that mixtures of particles with wide size distributions will behave differently from those with narrow distributions due to collisional forces. This possibility is investigated later in Chapters 6 and 8.

3.6 Summary and Conclusions

The interactions in the flow of gas-particle suspensions in circulating fluidised beds have been identified, and the importance of considering particle shape and particle size distribution emphasised. An approach was postulated to characterise and estimate the interaction of gas turbulence and particles, thereby establishing a framework for evaluating existing experimental

data for turbulent two-phase flows. A discussion of the combined effects of particle-gas turbulence interactions and particle-particle collisions laid the foundation for dynamic suspension flow modelling.

The important findings and conclusions pertaining to circulating fluidised beds are:

(1) The effect of gas turbulence on fluctuating particle motion cannot be assumed negligible in all instances. At the low suspension densities found within CFB risers, it appears that turbulence can account for a portion of the expected particle fluctuating motion.

(2) At higher suspension densities, substantial suppression of the turbulence should occur, providing the particles are responsive to gas fluctuations.

(3) There is evidence that the particles that respond to gas turbulence are predominantly influenced by the larger energetic eddies.

(4) Denser or larger particles respond more to the turbulence in large diameter commercial risers than in small pilot-scale or bench-scale units. Consequently, greater suppression of turbulence is expected in commercial size risers.

(5) In small diameter bench-scale units drag enhancement may occur. This complication to interpreting two-phase turbulent flow data does not appear to have been generally recognised.

(6) The very different response of particles of greatly differing density or size to steady gas motion, fluctuating gas motion, and gas temperature variations suggests that it is inadequate to model the motion of a particle mixture of wide size or density distribution with a single mean particle diameter and density.

(7) The accuracy of the proposed equations for estimating the fluctuating particle motion due to gas turbulence is expected to diminish at higher suspension densities as particle-particle collisions begin to dominate. In this case, one must resort to more detailed modelling.

Chapter 4

EQUATIONS OF MOTION FOR TWO-PHASE DISPERSED FLOW

Methods that may be suitable for predicting the behaviour of gas and particle flows in CFB risers are presented in this chapter. It is impractical to model such flows by considering the individual motion of the large number of discrete particles present. The majority of approaches involve some form of statistical averaging of properties of the particle assemblage. Nevertheless, the macroscopic motion of a cloud of particles in a gas stream results from the combined effects of individual discrete particle-particle and gas-particle interactions, and factors such as drag that significantly influence the motion of *discrete* particles in a gas stream must be accounted for in equations describing the motion of a cloud of particles. The important effects for discrete particle motion in riser suspension flows were discussed in Chapter 3. The ability of the modelling methods to reasonably represent these effects is discussed. In addition, the theoretical bases of the more common methods are examined.

Known and postulated instabilities in gas-solid suspension flows are also discussed. A number of instability studies based on two-phase models have focussed on predicting instabilities at high suspension densities, i.e bubbles. Although there is still considerable disagreement over the "correct" form of two-phase equations of motion, a review of these studies provides additional insight into the terms that probably should be included in these equations. It also lays a sound foundation for discussion of "cluster" formation in unbounded dilute suspension flows.

Another method that is gaining favour for the modelling of bubbling beds and CFBs incorporates "granular flow" theory, whereby a "fluctuating" kinetic energy or "granular temperature" equation for the particle phase is included in the model. This kinetic energy corresponds to the fluctuating component of velocity of the constituent particles in the suspension. The method

is based on an analogy with the kinetic theory for dense gases. The application of this theory to dilute suspension flow modelling is discussed, and the difficulties involved pinpointed.

Discussion in this chapter is limited to general methods and theory for modelling the local behaviour of a suspension. In a local region, approaches based on some form of statistical averaging assume that macroscopic suspension variables, such as mean particle velocity, are constant. Limits to this assumption are discussed. Also introduced are the basic equations of motion and several concepts used in Chapter 8. Simplifications to the detailed equations of motion, and discussion of the necessary approximations involved, provide the background theory required for the evaluations of specific CFB riser models in Chapter 5. In particular, the assumptions underlying the estimation of suspension density from pressure gradient are explained.

Although there is clearly a dispersed two-phase suspension at any specific location in the riser, the near discontinuity in voidage between wall streamers and dilute suspension core flow, discussed in Chapter 2, is characteristic of a separated flow such as gas-liquid annular flow. The possible limitations of statistically averaged continuum methods for modelling this abrupt change are outlined, prior to further analysis in Chapters 5 and 9.

4.1 General Criteria for a Riser Flow Model

The degree of complexity of a model depends on the phenomena which the modeller wishes to predict, and the desired accuracy of those predictions. Thus establishing *general* objective criteria for a unit operation is a somewhat nebulous process. Here it is assumed that we are only concerned with modelling local suspension flow, and the important gas-particle interactions on that scale. As mentioned, a more general discussion of riser modelling, including boundary conditions and the need for multi-dimensional or multi-zone representations of the entire riser, is given in Chapter 5.

For the prediction of gas and particle flow patterns, the riser is assumed to be isothermal, and the gas and particulate phases incompressible. Gas incompressibility is assumed, based

on typical gas density changes in riser flow and the magnitude of gas flow Mach numbers (see Schlichting (1979), pp. 9–10). At elevated temperatures, the variations in gas transport properties affecting the riser suspension flow, due to typical riser temperature variation, are relatively small, as discussed in Chapter 2. Therefore, for riser reaction modelling, it is probably a better approach to assume riser isothermality (or a simple temperature profile), and to iteratively find the mean riser temperature from repeated solution of separate hydrodynamic and enthalpy/chemical reaction models, rather than further complicate the hydrodynamic model by adding enthalpy balances. Although isothermality is generally a reasonable approximation for elevated temperature CFB units, possible correction in a thermal boundary layer at the wall may also be useful for improved model prediction, as discussed in Chapter 9.

Investigations presented in Chapter 9 indicate that lift forces on particles near the riser wall are significant, and cannot be ignored in models designed to predict particle phase motion throughout the entire riser. Based on the analysis of Chapter 3, and pre-empting such additional results presented later, it is proposed that a *general* CFB riser model should account for the following interactions:

(1) particle-particle collisions

(2) the influence of gas turbulence on particle motion

(3) the modulation of gas turbulence intensity due to particles

(4) drag

(5) gravitational force

(6) shear-induced lift force on the particles.

Many CFBs operate with wide particle size distributions (PSDs), and the relative importance of the above interactions is likely to differ greatly between smaller and larger particles. To ensure generality of the model, PSD effects should be accounted for. This is usually achieved by discretizing the PSD into a number of particle fractions, with a mean particle size assumed

for each fraction. In some instances, where the motion of different particle types is important, e.g. for coal and inert particles in a CFB combustor, the requirement for a further division by particle type is indicated. Note that for gas-fluidised systems, virtual mass and history effects may be assumed negligible, as discussed in Chapter 3.

For more specific model development, not all these criteria must be met. If all particles are large or the suspension densities high, and microscale gas properties are not of interest, then it is reasonable to ignore the details of gas turbulence and gas turbulence-particle interactions. Particles with a narrow PSD may be reasonably modelled with a single particulate phase.

4.2 Continuum-Mechanical Theories: An Overview of Mixture and Two-Fluid Models

The basic concept behind both mixture and two-fluid models is that the particulate phase may be assumed to have properties of a continuum. In the two-fluid model both the continuous gas phase and dispersed particle phase are treated as separate continua that occupy the same region and interact with one another. Equations of motion are written for each individual phase that include the standard single-phase continuum mechanical terms, and a term for the interaction between phases. In mixture models the gas-particle suspension is treated as a uniform continuum, with only a single equation of motion describing its flow.

Mixture models require constitutive relations to describe the velocities of gas and particles relative to that of the mixture. In dilute suspension flows of very fine particles this does not pose a problem because the particles closely follow the gas flow. However, in virtually all gas-solid fluidisation regimes the much greater inertia of the particles in comparison to the gas results in significant differences in the magnitude and direction of the gas and particulate phase velocities and accelerations. Mixture models do not allow for substantial differences in gas and particulate phase accelerations. There are also substantial non-uniformities in solids velocity and distribution in the two-phase developing flow in a riser. It seems unlikely that constitutive relations could be developed that could reasonably predict relative phase velocities

in this case. A mixture model approach also appears poorly suited for incorporation of riser boundary conditions such as abrupt exit effects.

Although mixture models have some advantages, the majority of two-phase continuum models that have been applied to bubbling fluidised bed behaviour, and the few multi-dimensional CFB riser models under development, are two-fluid formulations. In this study a two-fluid formulation is used for modelling suspension flow in the riser core. The discussion on two-fluid models henceforth focuses on the generally accepted form of two-fluid models, both from a theoretical and applied viewpoint. The analysis is not intended to be a comprehensive review of all two-fluid models that have appeared in the literature. For further information on mixture and two-fluid models, see Ishii (1975), Drew (1983), Bedford and Drumheller (1983), Ishii and Kocamustafaogullari (1983), Hyppanen (1989), Davidson (1990) and Krzywanski (1992).

4.3 Two-Fluid Models

4.3.1 Model Formulations

The development of two fluid models begins with the assumption that the motion at a single point within each phase may be described by the standard single phase continuum equations. For a phase k (either gas or particle fraction) the continuity equation (mass balance) is

$$\frac{\partial \rho_k}{\partial t} + \nabla\cdot\ (\rho_k \mathbf{v}_k) = 0\ , \tag{4.1}$$

and the equation of motion (momentum balance) is

$$\frac{\partial \rho_k \mathbf{v}_k}{\partial t} + \nabla\cdot\ (\rho_k \mathbf{v}_k \mathbf{v}_k) = -\ \nabla p_k + \nabla\cdot\ \mathbf{T}_k + \rho_k \mathbf{g}\ . \tag{4.2}$$

where $\mathbf{T}_k$ is the usual deviatoric part of the stress tensor.

These equations are written in terms of "point mechanical variables," such as instantaneous gas and particle velocity, and apply only *within* each phase. At a given position within a riser, these variables vary rapidly with time, as particles and gas alternately pass this point with complicated paths resulting from individual particle-particle and gas-particle interactions. We

are more interested in predicting some form of local mean particle and gas mechanical variables that are smoothed versions of these point variables, and the logical progression is therefore to develop equations similar to eqs. (4.1) and (4.2) for the smoothed variables. As these smooth variable equations no longer represent the behaviour within a phase at a specific point and time, but rather some "average" phase behaviour, the smooth variable "two-fluid" equations should include terms for mass and momentum transfer between the phases.

Although the originally proposed two-fluid model equations were largely postulated (e.g. Van Deemter and Van der Laan, 1960), currently accepted models are based on mathematical methods of averaging involving integral operators. Ishii and Kocamustafaogullari (1983) divide the methods of averaging into the categories of Eulerian, Lagrangian, and Boltzmann statistical averaging. Whilst Lagrangian and Boltzmann statistical averaging have some conceptual advantages over Eulerian averaging, the most useful and widely applied two-phase equation formulations are based on Eulerian averaging methods (Ishii and Kocamustafaogullari, 1983; Krzywanski, 1992). Most two-fluid fluidised bed models are based on Eulerian formulations, although Murray (1965) used a Boltzmann average for the particulate phase in a fluidised bed stability study.

Eulerian averaging methods may be further sub-divided into methods of time averaging, spatial averaging, ensemble averaging, and variations and combinations of these. The degree of mathematical rigour in the averaging process may be broadly divided into earlier models based only on averages of the balance equations (mass and momentum), and more recent models that also include conditions at the interfaces between the phases in the averaging by use of jump conditions at the interfaces. An example of the earlier formulation is that of Anderson and Jackson (1967), who employed a weighted spatial averaging technique. In contrast, Ishii (1975) and Drew (1983) used more rigorous averaging techniques to obtain formulations that appear to be now generally accepted as theoretical improvements on the earlier formulations (Bedford and Drumheller, 1983). Nevertheless, several of the bubbling bed models that have had some success in predicting phenomena similar to bubbling have been based on the Anderson and

Jackson approach (Gidaspow, 1986).

Irrespective of the averaging method, there is general agreement on the form of the two-fluid continuity equation (Drew, 1983), which, after averaging, becomes,

$$\frac{\partial \epsilon_k \rho_k}{\partial t} + \nabla\cdot\ (\epsilon_k \rho_k \mathbf{v}_k) = \dot{m}_k\ , \tag{4.3}$$

where ϵ_k is the kth phase volume fraction, $\dot{m}_k$ is the net rate of phase k mass formation per unit volume, and the phase dependent variables, such as $\mathbf{v}_k$, are now smoothed or averaged variables. In the discussion from here on, interfacial mass transfer, $\dot{m}_k$, and the associated production of momentum, $\dot{m}_k \mathbf{v}'_k$, are assumed to be zero. This is a common assumption in riser flow modelling. In CFB combustion units, where $\dot{m}_k$ is not zero, the production of gas mass from heterogeneous reactions can be shown to be typically only a small fraction of the total gas flow.

The Anderson and Jackson (1967) formulation for the momentum balance equations, which we will denote as "Model A", is

$$\frac{\partial \epsilon_k \rho_k \mathbf{v}_k}{\partial t} + \nabla\cdot\ (\epsilon_k \rho_k \mathbf{v}_k \mathbf{v}_k) = -\nabla p_k + \nabla\cdot\ \mathbf{T}_k + \epsilon_k \rho_k \mathbf{g} + \mathbf{M}_k\ , \tag{4.4}$$

where $\mathbf{M}_k$ is the interfacial momentum source term due to phase interactions. Note that $\mathbf{M}_g$ must equal $-\mathbf{M}_p$ (from Newton's third law). The "Model B" formulation, typical of forms obtained by methods that also average interfacial terms, is (Ishii, 1975; Drew, 1983):

$$\frac{\partial \epsilon_k \rho_k \mathbf{v}_k}{\partial t} + \nabla\cdot\ (\epsilon_k \rho_k \mathbf{v}_k \mathbf{v}_k) = -\nabla(\epsilon_k p_k) + \nabla\cdot\ (\epsilon_k \mathbf{T}_k) + \epsilon_k \rho_k \mathbf{g} + \mathbf{M}_k\ . \tag{4.5}$$

The l.h.s. of the equation of motion is frequently expressed in an alternative form by eliminating the terms corresponding to those in the continuity equation that sum to zero when $\dot{m}_k = 0$, i.e.

$$\frac{\partial \epsilon_k \rho_k \mathbf{v}_k}{\partial t} + \nabla\cdot\ (\epsilon_k \rho_k \mathbf{v}_k \mathbf{v}_k) = \epsilon_k \rho_k \frac{\partial \mathbf{v}_k}{\partial t} + \epsilon_k \rho_k \mathbf{v}_k\cdot\ \nabla \mathbf{v}_k\ . \tag{4.6}$$

Several variations of these stress tensor formulations have also been used. The total stress terms $\nabla\cdot\ \boldsymbol{\Pi}_k = -\nabla(\epsilon_k p_k) + \nabla\cdot\ \mathbf{T}_k$ and $\nabla\cdot\ \boldsymbol{\Pi}_k = -\nabla p_k + \nabla\cdot\ (\epsilon_k \mathbf{T}_k)$ have been proposed (e.g. Garg and Pritchett, 1975; Fanucci *et al.*, 1979; Gidaspow *et al.*, 1989a; Gidaspow *et al.*, 1989b).

Also models have appeared with a solid phase total stress tensor in Model A form, and the equivalent gas phase stress tensor in Model B form (e.g. Pritchett *et al.*, 1978). Theoretical objections to all these variations of Model A or B forms may be raised, as they can only be derived if the averaging methods applied to the solids and gas phases differ (Anderson and Jackson, 1967). However, in many cases, such objections are of little practical relevance, as there is considerable disagreement on the form of constitutive relations for $\mathbf{M}_k$. By inclusion or omission of various terms in $\mathbf{M}_k$, and simplification of the deviatoric stress tensor, models that differ when written with all interaction terms lumped in $\mathbf{M}_k$, become the same formulation when chosen terms for $\mathbf{M}_k$ are included.

The disagreement over the terms that should be included in $\mathbf{M}_k$ is a disadvantage of the two-fluid approach. Ishii (1975) pointed out that the different more rigorous methods of averaging do not result in any difference in the general momentum balance formulation, but rather in the interpretation of the variables. For example, using a combined temporal-spatial method of averaging, Drew (1983) obtained

$$\mathbf{M}_k = \overline{\left[\rho_k \mathbf{v}_k \left(\mathbf{v}_k - \mathbf{v}_k'\right) - \boldsymbol{\Pi}_k\right] \cdot \nabla X_k} \,, \tag{4.7}$$

where $\boldsymbol{\Pi}_k$ is the total stress tensor, ∇X_k is an operator equal to zero except at the phase interface[1], $\mathbf{v}_k'$ is an "average interfacial velocity" on the phase k side of the interface, and the overbar denotes averaging according to Drew's method. Interpretation of this expression in terms of more familiar phase interactions, such as drag or buoyancy, is not clear. On Drew's formulation, Batchelor (1988) stated that "...his procedure achieves rigour at the cost of introducing the intractable problem of closure of averages of a complicated kind." Understandably, there is some disagreement over the forms of the constitutive relations that replace expressions such as that on the r.h.s. of eq. (4.7).

A second point of disagreement in two-fluid models is the interpretation of the solids phase "pressure," arising from differences in treating the solids phase as a continuum. To examine this in more detail, consider a single particle in a gas-solid suspension. For much of the time

[1] $\overline{\nabla X_k} = \nabla \epsilon_k$

the particle is in contact only with gas. The component of particle pressure due to gas pressure is a smoothed variable that should not include the rapid fluctuations in gas pressure over the particle surface. It is generally assumed that the smoothed component of gas pressure acting on the particle surface is equal to the local mean gas pressure. The effects of the *difference* between gas interfacial pressure distribution and the bulk gas pressure on the particle are either assumed negligible (e.g. Drew, 1983; Krzywanski, 1992), or to be a component of drag, and thus accounted for by the constitutive drag relation (e.g. Stuhmiller, 1977; Prosperetti and Jones, 1984). With either assumption, the particle pressure and drag expressions are the same.

In addition to the almost continual contact with gas, a particle occasionally comes in contact with another particle for a brief period. This contact raises the stress within the particle above that due solely to the surrounding gas. The point of contact for the collision may be on any part of the particle surface. Over many collisions, there will an *average* stress within the particle due to collisions, in addition to the stress due to mean gas pressure. Furthermore, this stress may be resolved into a normal component and deviatoric component. The stresses arising from single collisions cause a fluctuating motion of the particle. By analogy with a kinetic theory gas consisting of hard spheres, the kinetic energy associated with the fluctuating motion of the particles may be interpreted as a "particle temperature." A collisional pressure, deviatoric stress, and other transport properties of the particle assemblage due to collisions may be deduced. This is the general concept behind the use of "solids viscosities" in two-fluid models, and the "granular kinetic" theory discussed below.

A final component of mean pressure on the particles that has sometimes been included as a separate term is due to the disturbance of the fluid flow field by the particles. However, for gas-solid flow it may be assumed negligible compared to the magnitude of gas pressure. (Givler, 1987; Krzywanski, 1992). From the preceding discussion, a general expression for the total solids phase stress tensor in gas-solid dispersed flow becomes:

$$\begin{aligned} \boldsymbol{\Pi}_p &= \boldsymbol{\Pi}_g + \boldsymbol{\Pi}_c \\ &= (-p_g\mathbf{I} + \mathbf{T}_g) + (-p_c\mathbf{I} + \mathbf{T}_c) \ , \end{aligned} \tag{4.8}$$

where the subscripts p, g and c denote the solids phase, the gas phase, and the contribution due to particle collisions, respectively.

From granular theory, the magnitude of the particle pressure due to collisions may be estimated to be typically less than $O(10^{-4})$ that of the gas pressure. Consequently, some modellers have omitted p_c from their equations of motion (e.g. Anderson and Jackson, 1967). This overlooks the fact that it is the gradient of particle pressure that appears in the solid phase equation of motion. It is possible that this gradient is large across bubble-dense region interfaces or cluster-dilute region interfaces. For unsteady state models, used to predict the growth of instabilities, such as bubbles or "clusters," it would appear important to retain the collisional pressure gradient term in eq. (4.8). Its significance is discussed further below in the section on flow instabilities.

4.3.2 Constitutive Relations

In "engineering" type B models, the interaction term is often separated into three components (Drew, 1983; Prosperetti and Jones, 1984):

$$\mathbf{M}_k = \dot{m}_k \mathbf{v}'_k + p_k \nabla \epsilon_k + \mathbf{M}^d_k \,, \tag{4.9}$$

where $\mathbf{M}^d_k$ represents the "total interfacial drag," including virtual mass and history effects (assumed negligible here), drag and shear-induced lift forces. As mentioned above, it is assumed here that interfacial mass transfer, $\dot{m}_k$, and the associated production of momentum, $\dot{m}_k \mathbf{v}'_k$, are zero.

There is some disagreement as to whether the term $p_k \nabla \epsilon_k$ should be included in eq. (4.9) (Sha and Soo, 1979; Bedford and Drumheller, 1983; Prosperetti and Jones, 1984). Garg and Pritchett (1975) state that it arises due to porosity gradients, whilst Drew[2] (1983) calls it a buoyancy term. The motivation behind this term appears to be to ensure the consistency of the Model B momentum balance equations when the gas pressure gradient approaches zero.

[2]Drew (1983) initially introduces a buoyancy term $p'_k \nabla \epsilon_k$, where p'_k is an average interfacial pressure, and then assumes $p'_k = p_k$.

Without this term, Garg and Pritchett point out that fluid motion may occur in the absence of gas pressure gradient. In addition to this physical motivation, Prosperetti and Jones (1984) provide greater insight into the theoretical basis for its inclusion. From a momentum balance over a macroscopic control volume containing a gas-solids suspension, they obtain the following expression, $\boldsymbol{\Gamma}_k$, that contains all terms involving phase pressure in their balance:

$$\boldsymbol{\Gamma}_k = -\epsilon_k \nabla p_k - p_k \nabla \epsilon_k - \frac{1}{V_c} \int_s p_k'' \, \mathbf{k} \, ds \tag{4.10}$$

$$= -\epsilon_k \nabla p_k - \frac{1}{V_c} \int_s (p_k'' - p_k) \, \mathbf{k} \, ds \, , \tag{4.11}$$

where V_c is the volume of the control region, s the total gas-particle interface in this volume, p_k'' the phase pressure at point ds on the interface (*not* the average interfacial pressure, p_k'), and $\mathbf{k}$ the unit normal vector directed outward from phase k at ds. Note that the identity $\nabla \epsilon_k = -(1/V_c) \int_s \mathbf{k} \, ds$ is employed. Prosperetti and Jones point out that confusion over the form of $\boldsymbol{\Gamma}_k$ in engineering models is that the last term in eq. (4.10), i.e. the integral of the phase pressure over the interface, is often interpreted as $\mathbf{M}_k^d$. They indicate that $\mathbf{M}_k^d$ is probably a better *approximation* to the last term in eq. (4.11), i.e. the integral of the *excess* pressure over the interfaces.

From eqs. (4.5) and (4.9), the expression containing all pressure terms for the Model B formulation is

$$\boldsymbol{\Gamma}_k = -\epsilon_k \nabla p_k + \mathbf{M}_k^d \, . \tag{4.12}$$

Thus $\mathbf{M}_k^d$ in eq. (4.12) may be equated with the integral of excess pressure in eq. (4.11). The debate over the $p_k \nabla \epsilon_k$ term highlights a disadvantage of rigorous averaging methods which include interfacial terms. Care must be taken not to include the same effects twice: once via the averaged terms, and again in constitutive relations. Assuming $\dot{m}_k = 0$, and substituting the non-zero terms of eq. (4.9) into eq. (4.5), gives a general Model B form with constitutive relations:

$$\frac{\partial \epsilon_k \rho_k \mathbf{v}_k}{\partial t} + \nabla \cdot \left(\epsilon_k \rho_k \mathbf{v}_k \mathbf{v}_k \right) = -\epsilon_k \nabla p_k + \nabla \cdot \left(\epsilon_k \mathbf{T}_k \right) + \epsilon_k \rho_k \mathbf{g} + \mathbf{M}_k^d \, . \tag{4.13}$$

For Model A formulations a common general form of the constitutive relation is (Jackson, 1971),

$$\mathbf{M}_k = \dot{m}_k \mathbf{v}_k' \pm \epsilon_p \left(-\nabla p_g + \nabla\cdot \mathbf{T}_g\right) + \mathbf{M}_k^d \,, \tag{4.14}$$

where the term following the $\pm$ sign is taken as positive for the solids phase and negative for the gas. The term $-\epsilon_p \nabla p_g$ is the common form of the pressure gradient term, which equals the buoyancy force on the particles when the particles and fluid are at rest (Anderson and Jackson, 1967). Jackson (1971) assumes that the particle stress is due solely to particle interactions, i.e. $\nabla\cdot \boldsymbol{\Pi}_p = (-\nabla p_c + \nabla\cdot \mathbf{T}_c)$. Substituting this expression and eq. (4.14) into eq. (4.4) gives a typical Model A form with constitutive relations for the gas and solids phase, respectively,

$$\frac{\partial \epsilon_g \rho_g \mathbf{v}_g}{\partial t} + \nabla\cdot \left(\epsilon_g \rho_g \mathbf{v}_g \mathbf{v}_g\right) = \epsilon_g \left(-\nabla p_g + \nabla\cdot \mathbf{T}_g\right) + \epsilon_g \rho_g \mathbf{g} + \mathbf{M}_g^d \,, \tag{4.15}$$

and,

$$\frac{\partial \epsilon_p \rho_p \mathbf{v}_p}{\partial t} + \nabla\cdot \left(\epsilon_p \rho_p \mathbf{v}_p \mathbf{v}_p\right) = \epsilon_p \left(-\nabla p_g + \nabla\cdot \mathbf{T}_g\right) + \left(-\nabla p_c + \nabla\cdot \mathbf{T}_c\right) + \epsilon_p \rho_p \mathbf{g} + \mathbf{M}_p^d \,. \tag{4.16}$$

Hence, after substitution of common forms of the constitutive relations, we observe differences between the A and B formulations in both the pressure gradient and deviatoric stress tensor terms. Models using both forms can be found in the literature, and the significance of this difference to model predictions does not appear to have been reported. It should be remembered that, although these forms of the two-fluid model are often used and are perhaps the best justified forms from a theoretical perspective, other versions do exist in working models. For example, several models do not include a gas pressure gradient term in the solids phase equation of motion. This omission is typically to overcome numerical instability problems.

Although the two-fluid equations have been presented with the implicit assumption that there are only two phases, extension of the general form of the equations to multiple solids phases is relatively straightforward. For example, from eq. (4.13), the Model B momentum balance for the ith particle fraction is

$$\frac{\partial \epsilon_{pi} \rho_{pi} \mathbf{v}_i}{\partial t} + \nabla\cdot \left(\epsilon_{pi} \rho_{pi} \mathbf{v}_i \mathbf{v}_i\right) = -\,\epsilon_{pi} \nabla p_{pi} + \nabla\cdot \left(\epsilon_{pi} \mathbf{T}_{pi}\right) + \epsilon_{pi} \rho_{pi} \mathbf{g} + \mathbf{M}_{pi}^d \,, \tag{4.17}$$

where the ith fraction particle density and volume fraction are, respectively, ρ_{pi} and ϵ_{pi}. For multiple particle fractions or "phases," an additional solid-solid phase interaction force must be included in $\mathbf{M}_{pi}^{d}$, due to collisions with particles from other particle fractions. Such collisions may also be expected to alter the distribution of fluctuating velocities within fraction i, thereby influencing the collisional component of total stress, $\boldsymbol{\Pi}_{ci}$. Models with multiple particle fractions based on two-fluid equations are also usually still referred to as "two-fluid" models.

Summarising the analysis thus far, we observe that, even in very general form, there is disagreement over the formulation of the two-fluid equations. Although many formulations may be rejected based on theoretical or physical arguments, there is no unique, fully-justified formulation. Nevertheless, the two-fluid method is intuitively attractive given the predictive successes of single phase continuum mechanics.

The terms in eqs. (4.13), (4.15), and (4.16) are sufficiently general that all the CFB riser model criteria given earlier may, in some way, be incorporated. For some effects, this incorporation is straightforward. Gravitational force is already included in the appropriate form. Expressions for drag and lift forces, such as those introduced in Chapter 3 and presented later in Chapter 8, are components of $\mathbf{M}_{k}^{d}$. Thereafter, however, the process becomes more difficult. Gas turbulence, particle-particle collisions and particle-gas turbulence interactions result in phase stresses, indicating that the first step is to make an assumption about the dependence of stress on strain rate. Secondly, it must be decided which stresses may be neglected, and whether the phase pressure and transport properties pertaining to the important stresses are to be assumed constant, empirically predicted, or determined by supplemental theories, such as granular theory for particle motion or "k-ϵ" models for gas turbulence. If multiple particle phases are included in the model, as required by the criteria established here, then a supplemental theory must be included to account for interactions of the solids phases.

This section closes with a discussion of the simpler assumptions for phase stress. Pritchett *et al.* (1978) expressed the particle pressure gradient due to particle collisions in terms of the

particle assemblage bulk modulus, $G(\epsilon_p)$:

$$\begin{aligned} \nabla p_c &= \frac{dp_c}{d\epsilon_p} \nabla \epsilon_p \\ &= G(\epsilon_p) \nabla \epsilon_p \, . \end{aligned} \tag{4.18}$$

The importance of $G(\epsilon_p)$ for flow instabilities is discussed below.

In most applied models the gas phase and collisional solids phase deviatoric stress tensors are assumed to be Newtonian, i.e.

$$\mathbf{T}_k = \mu_k \left[\nabla \mathbf{v}_k + (\nabla \mathbf{v}_k)^{\mathbf{T}} \right] - \left(\frac{2}{3} \mu_k - \kappa_k \right) (\nabla \cdot \mathbf{v}_k) \mathbf{I} \, , \tag{4.19}$$

where the phase shear viscosity, μ_k, and bulk viscosity, κ_k, are assumed independent of the rate of strain. The majority of bubbling fluidised bed models assume that the gas is inviscid (e.g. Garg and Pritchett, 1975; Pritchett *et al.*, 1978; Gidaspow, 1986; Bouillard, 1989). This is probably reasonable given the dominant effect of drag on the gas motion. Although the gas deviatoric stress tensor is sometimes split into viscous and turbulent components in theoretical analyses, applied models generally retain a single gas stress tensor, with an "effective" viscosity coefficient, μ_{ge}, incorporating shear and turbulent effects on the gas motion. Most existing two-fluid riser models retain an effective gas viscosity in the formulation (e.g. Sinclair and Jackson, 1989; Gidaspow *et al.*, 1990). Measured solids viscosity magnitudes are $>10^4$ times those of typical gas viscosities, and solids phase "viscous shear" forces can be significant.

For bubbling fluidised bed models, several different assumptions have been made for the solids phase shear viscosity, μ_c, due to collisions. Gidaspow *et al.* (1986) assumed an inviscid solids phase, while Bouillard *et al.* (1989) used a constant solids shear viscosity of 0.1 Pa s. Pritchett *et al.* (1978) used a simple empirical relation for μ_c, dependent only on solids volume fraction, ϵ_p. All these formulations assumed the solids bulk viscosity, κ_c, to be zero, though Murray (1965) suggested that κ_c may be significant in a bubbling bed. These shear viscosity assumptions were based primarily on experimental measurements. Several CFB riser models have recently appeared that predict μ_c and κ_c from more fundamental approaches (e.g. Sinclair

and Jackson, 1989; Gidaspow *et al.* 1990; Pita and Sundaresan, 1991), based on granular kinetic theory described below.

4.3.3 Two-Fluid Equation Simplifications

Two-dimensional Unsteady-State Models

The general two-fluid Model A and B eqs. (4.13), (4.15), and (4.16) are written for unsteady flow in three dimensions. The calculation of the full suspension flow field in three dimensions for a riser or bubbling bed model is likely to be an expensive and time-consuming task requiring massive computation, even for a single particle fraction. Unsteady-flow bubbling bed and riser models calculations have been reported for two-dimensional versions of the two-fluid equations (Pritchett *et al.*, 1978; Gidaspow, 1986; Bouillard *et al.*, 1989; Tsuo and Gidaspow, 1990). These models use planar Cartesian (x-z) coordinates. Alternatively, for riser flows, axial symmetry may be assumed, and the equations written in cylindrical coordinates (e.g. Sinclair and Jackson, 1989). The Cartesian coordinate two-dimensional riser model is better suited to modelling time-averaged maldistribution of solids around the riser circumference. Solids concentrations may be significantly greater on one side of the riser in comparison to the other, due to the orientation and design of the riser entry and exit sections. If asymmetry of solids distribution about the riser axis is negligible, then the cylindrical coordinate formulation is arguably superior, as it correctly accounts for wall effects by including all the wall surface in the calculation. Even two-dimensional unsteady-state models are computationally intensive (Gidaspow *et al.*, 1986), and this currently limits their usefulness.

Steady-State and Fully-Developed Flow Models

Frequently, we are interested primarily in the steady-state behaviour of a fluidised bed. For the majority of gas-particle flows, steady-state behaviour is influenced by transient phenomena, such as bubble formation and motion in bubbling beds, and "cluster," "wall streamer" and "strand" motion in CFB risers.

If an alternative method exists to account for the influence of the transients on the steady flow behaviour, it is not necessary to solve the unsteady flow model. For example, correlations for the prediction of bubble characteristics in a bubbling bed are often used. The two-fluid steady-state equations are obtained by setting the time derivative to zero. For Model B this gives

$$\nabla\cdot\ (\epsilon_k\rho_k\mathbf{v}_k\mathbf{v}_k) = -\ \epsilon_k\nabla p_k + \nabla\cdot\ (\epsilon_k\mathbf{T}_k) + \epsilon_k\rho_k\mathbf{g} + \mathbf{M}_k^d\ . \tag{4.20}$$

Similarly, from eq. (4.3), the two-fluid steady flow continuity equation is

$$\nabla\cdot\ (\epsilon_k\rho_k\mathbf{v}_k) = \dot{m}_k\ . \tag{4.21}$$

In addition, for vertical suspension flows, when the flow is fully-developed, all volume fraction and velocity spatial derivatives in the vertical direction are zero (i.e. $\partial\epsilon_k/\partial z = 0$ and $\partial\mathbf{v}_k/\partial z = 0$).

The most common assumption for riser models that use steady two-fluid equations is that the suspension is locally uniform, and that the effects of transient non-uniformities, if they exist, are unimportant. Sinclair and Jackson (1989) and Pita and Sundaresan (1991) adopt this approach. They solve a form of the two-fluid two-dimensional fully-developed equations to obtain radial profiles of concentration, pressure, and velocity.

One-dimensional Two-Fluid Equations for Multi-Zone Models

An alternative to using one set of multi-dimensional equations to describe the suspension flow throughout the entire flow space is to divide the space into different zones, and make various simplifying assumptions about each zone that are consistent with experimental observations and/or multi-dimensional modelling results. For example, in this study, it is assumed that *mean* gas and particle flows only occur in the vertical z direction, and that phase concentrations and pressures are *radially* uniform in the riser core. Thus only vertical (z) derivatives are non-zero in the two-fluid equations and the model becomes one-dimensional[3].

[3] For a single-fluid steady flow, continuity gives ($\nabla\cdot\mathbf{v} = 0$), and the vertical spatial velocity derivative $\partial\mathbf{v}/\partial z$ must also equal zero when there is no radial flow. For two-fluid steady flow with negligible mass creation, only the combination ($\nabla\cdot[\epsilon_k\mathbf{v}_k]$) is zero, and this restriction does not apply.

Using the restrictions $\partial/\partial x = 0$ and $\partial/\partial y = 0$, and a Newtonian form for the deviatoric stress tensor, the term $\nabla\cdot\,(\epsilon_k \mathbf{T}_k)$ in Model B eq. (4.13) simplifies (see Bird *et al.*, 1960) to:

$$\nabla\cdot\,(\epsilon_k \mathbf{T}_k) \;=\; \left(\frac{4}{3}\mu_k + \kappa_k\right)\left(\epsilon_k \frac{d^2\mathbf{v}_{zk}}{dz^2} + \frac{d\epsilon_k}{dz}\frac{d\mathbf{v}_{zk}}{dz}\right) . \tag{4.22}$$

Substituting eq. (4.22) into eq. (4.20) gives the one-dimensional steady-state two-fluid equation of motion in Model B form for vertical suspension flow:

$$\epsilon_k \rho_k \mathbf{v}_{zk}\frac{d|\mathbf{v}_{zk}|}{dz} = -\,\epsilon_k \frac{dp_k}{dz}\,\boldsymbol{\delta}_z + \left(\frac{4}{3}\mu_k + \kappa_k\right)\left(\epsilon_k \frac{d^2\mathbf{v}_{zk}}{dz^2} + \frac{d\epsilon_k}{dz}\frac{d\mathbf{v}_{zk}}{dz}\right) + \epsilon_k \rho_k \mathbf{g} + \mathbf{M}^d_{zk} \,, \tag{4.23}$$

By the same process, the one-dimensional steady-state Model A forms for the gas and solids phase become, respectively,

$$\epsilon_g \rho_g \mathbf{v}_{zg}\frac{d|\mathbf{v}_{zg}|}{dz} = -\,\epsilon_g \frac{dp_g}{dz}\,\boldsymbol{\delta}_z + \left(\frac{4}{3}\mu_g + \kappa_g\right)\left(\epsilon_g \frac{d^2\mathbf{v}_{zg}}{dz^2}\right) + \epsilon_g \rho_g \mathbf{g} + \mathbf{M}^d_{zg} \,, \tag{4.24}$$

$$\epsilon_p \rho_p \mathbf{v}_{zp}\frac{d|\mathbf{v}_{zp}|}{dz} = -\left(\epsilon_p \frac{dp_g}{dz} + \frac{dp_c}{dz}\right)\boldsymbol{\delta}_z + \left(\frac{4}{3}\left[\epsilon_g \mu_g + \mu_c\right] + \left[\epsilon_g \kappa_g + \kappa_c\right]\right)\frac{d^2\mathbf{v}_{zp}}{dz^2} + \epsilon_p \rho_p \mathbf{g} + \mathbf{M}^d_{zp} \,. \tag{4.25}$$

These one-dimensional equations of motion for steady developing flow are used in the development of a model presented in Chapter 8.

Clearly, the one-dimensional equations are great simplifications of the multi-dimensional two-fluid models. However, their application introduces additional model requirements not relevant in multi-dimensional formulations. Criteria for the location of zone boundaries must be established, and interfacial boundary conditions between zones must be developed. As with the multi-dimensional models, supplemental models may be required to adequately predict conditions at the zone boundaries. The relative advantages of multi-dimensional and multi-zone models are discussed in Chapter 5.

Pressure Gradient and the Apparent Suspension Density

Recall eq. (2.1) for the apparent suspension density:

$$\rho_{sa} = -\,\frac{1}{g}\frac{dp_g}{dz} \,. \tag{4.26}$$

As mentioned, ρ_{sa} is generally assumed to be representative of the cross-sectionally and temporally averaged true riser suspension density at a given height, i.e. $\rho_{sa} = \overline{\epsilon_p}\rho_p$. Moreover, the apparent suspension density is often assumed to be synonymous with the true cross sectional average of the suspension density. This assumption is not always reasonable, as will be seen from a discussion of necessary simplifications of the two-fluid equations required to obtain eq. (4.26).

Firstly assume that (i) the flow is steady ($\partial/\partial t = 0$) and vertical, (ii) the flow is fully-developed ($\partial \mathbf{v}_{zk}/\partial z = 0$ and $\partial \epsilon_k/\partial z = 0$) and axisymmetric ($\partial/\partial\theta = 0$), and (iii) the weight of the gas, $\epsilon_g\rho_g g$, is negligible in comparison to the weight of the solids, $\epsilon_p\rho_p g$. If the Model A eqs. (4.15) and (4.16) are added together, and these assumptions incorporated, we obtain

$$0 = (-\nabla p_g + \nabla\cdot \mathbf{T}_g) + (-\nabla p_c + \nabla\cdot \mathbf{T}_c) + \epsilon_p\rho_p\mathbf{g}\,. \tag{4.27}$$

Note that $\mathbf{M}_g^d + \mathbf{M}_p^d = 0$. Equation (4.27) applies to a point (x, y, z) (or (r, θ, z)) in the riser. If we define $\mathbf{T}_g + \mathbf{T}_c$ as $\mathbf{T}$, then the z-component equation of eq. (4.27), in cylindrical coordinates, becomes:

$$0 = -\frac{\partial p_g}{\partial z} - \frac{\partial p_c}{\partial z} + \frac{1}{r}\frac{\partial}{\partial r}(r\tau_{rz}) - \epsilon_p\rho_p g\,, \tag{4.28}$$

where τ_{rz} is the non-convective flux of combined gas-particle z-momenta in the r direction, which results in shear on a vertical plane. If the suspension flow is assumed to be locally homogeneous then $\partial p_c/\partial z$ may be assumed negligible compared to $\partial p_g/\partial z$, based on earlier discussions. (Alternatively, it may be viewed as an average collisional particle pressure over the entire riser cross-section, and eliminated in the next step.)

Consider the steady, fully-developed flow of gas and solids at a given height within the riser. From experimental investigations (Chapter 2), we know that typically a dilute suspension region of rapid upflow exists in the riser core, surrounded by a denser wall region where solids may flow downward. Furthermore, there is little difference in gas pressure between the core and the wall region at the same height, and the axial pressure gradient in both regions is similar. Therefore, from eq. (4.28), we may deduce that the shear force exerted between the core and

wall regions acts to retard the dilute core flow, and accelerate the slower wall flow. If eq. (4.28) is integrated over the entire riser cross-section, this gives

$$\frac{dp_g}{dz} = -\overline{\epsilon_p}\rho_p g + \tau_f \ , \tag{4.29}$$

where $\overline{\epsilon_p}$ is the cross-sectionally averaged particle volume fraction, i.e. $(\int \epsilon_p dA)/A$ over the whole cross-section. The term τ_f is a combined frictional shear force exerted on the gas-particle mixture by the wall, introduced by the integration as a boundary condition. Providing τ_f is small in comparison to the gravitational force, eq. (4.29) simplifies to (4.26), and ρ_{sa} is equal to the true suspension density, ρ_s. A similar analysis with the Model B equations yields the same result.

Clearly, a number of simplifying assumptions are required to develop the standard expression for apparent suspension density in a rigorous manner. It is important to note that apparent suspension densities tells us very little about the radial distribution of solids concentration or velocity. From the above discussion, we can conclude that apparent suspension density is only a justified approximation to the cross-sectionally averaged true suspension density at a given riser height if:

(1) the flow is steady and fully developed,

(2) there are no gas or particle recirculatory flows which result in significant radial pressure gradients,

(3) particle-wall and gas-wall shear forces may be neglected.

Fortunately, for much of the riser height in typical CFB units, these assumptions are reasonable (within ± 20 % accuracy, say), and the easily determined parameter ρ_{sa} is very useful. However, within 1–3 m of the riser base, and often near the riser exit, the axial gas pressure gradient cannot be used to estimate true suspension densities with any certainty (Weinstein and Li, 1989; Chapter 6).

Gas Inertia

For unsteady flow models, an approximation that is sometimes invoked is the omission of the gas inertial term on the l.h.s. of the gas momentum equation, i.e. $D(\epsilon_g \rho_g \mathbf{v}_g)/Dt$ is assumed to be zero, where D/Dt is the substantial derivative. This approximation is generally reasonable in bubbling beds, based on order of magnitude considerations (Garg and Pritchett, 1975; Pritchett *et al.*, 1978). It assumes that any difference in the magnitude of the large driving pressure gradient and retarding drag terms on the r.h.s. of the gas momentum equation is rapidly reduced by an almost instantaneous acceleration of the gas. Numerical simulations discussed by Gidaspow (1986) indicate that this assumption is reasonable for bubbling beds, except possibly close to high velocity gas jets entering near the distributor. For riser flow, much of the particle acceleration due to gas drag occurs in the denser turbulent bed region near the base of the riser, and models that assume zero gas inertia may also provide reasonable predictions.

4.4 Flow Instabilities: Bubbles and Clusters

A well known and widely investigated phenomenon in gas-fluidised beds is the formation and rise of voids or bubbles. It is generally accepted that bubbles form due to instabilities in the two-phase flow, and various studies have examined the instability mechanism. The majority of these studies begin with two-fluid equations of motion. In CFB risers, local non-homogeneities in the flow, or pockets of denser suspension surrounded by dilute suspension upflow, have been reported in experimental investigations, as discussed in Chapter 2. Some investigators have called these denser regions "clusters," and postulated that they form due to instabilities of two-phase flow at low suspension densities, typical of CFB risers. Here the theoretical evidence for the formation of clusters in unbounded dilute suspension flow is examined. As the majority of instability studies have focussed on bubble formation, these studies are first reviewed, and the implications for more dilute suspension flows discussed.

Most stability studies have used the standard technique of linear stability theory. The growth of an initial small voidage perturbation has been investigated using the one-dimensional

unsteady version of Model A, eqs. (4.24) and (4.25) (Jackson, 1971; Garg and Pritchett, 1975; Needham and Merkin, 1983; Jackson, 1985). Jackson (1985) reported the results of a general study that included the effects of solids phase pressure, p_c, shear viscosity, μ_c and bulk viscosity, κ_c on stability limits and initial disturbance growth rates. These parameters appeared in the groups $(\frac{4}{3}\mu_c + \kappa_c)$ and $dp_c/d\epsilon_p$. Although Jackson reported that increasing $(\frac{4}{3}\mu_c + \kappa_c)$ decreased the disturbance growth rate in a gas fluidised bed, the dense uniform suspension was always unstable over the range of values considered. Jackson used a constant value of $|dp_c/d\epsilon_p| = 2$ Pa. In contrast, Garg and Pritchett (1975), who used $|dp_c/d\epsilon_p| = G(\epsilon_p)$ as mentioned earlier, considered a wide range of values for $G(\epsilon_p)$. They found that the dense suspension was stable for $G(\epsilon_p) > 18$ kPa. This is of $O(10^4)$ greater than both estimated experimental values for $|dp_c/d\epsilon_p|$ later reported by these authors (Pritchett *et al.*, 1978) and Jackson's assumed value. Using the Garg and Pritchett method and a relation for particle collisional pressure, $p_c = \epsilon_p p_{c0}$, where p_{c0} was a constant "base" pressure (a relation not inconsistent with granular kinetic theory for dilute suspensions), Needham and Merkin (1983) found upper and lower limits of suspension voidage for instability to occur. Outside these limits, i.e. as $\epsilon_g \rightarrow 0$ (dense suspension) or $\epsilon_g \rightarrow 1.0$ (dilute suspension), the suspension was predicted to be stable. Unfortunately, Needham and Merkin did not give numerical results to assess this instability range for fluidised beds.

As Jackson (1985) points out, the theoretical values of $|dp_c/d\epsilon_p|$ required to stabilise a dense bed are at least several orders of magnitude greater than those estimated from experiments. Smaller Group A particles (say $d_p < 100\mu$m) in dense gas-particle suspensions generally fluidise uniformly over a range of gas velocities above minimum fluidisation. Although slower disturbance growth rates are predicted for these beds, linear stability theories still predict them to be unstable. This discrepancy is commonly attributed to particle cohesive forces, which are not included in the theories (Jackson, 1985). Particle cohesive forces are not expected to be important in risers (Chapter 3). Although linear stability theories only establish if a small disturbance begins to grow, and do not guarantee that bubbles (or clusters) form from the initial disturbance, complementary non-linear analyses for bubbling beds, including the two-fluid

models for transient motion, do predict the growth and motion of void regions in the dense bed with some similarities to bubbles (e.g. Fannucci *et al.*, 1979; Pritchett *et al.*, 1978; Gidaspow *et al.*, 1986).

From the linear stability analyses for dense fluidised beds it is known that particle phase stresses, including pressure due to collisions, play a significant role, and should be included in a stability analysis of a uniform dilute suspension. Furthermore, it has been observed that if the particle assemblage bulk modulus of elasticity, $G(\epsilon_p)$, is sufficiently large, the suspension is predicted to be stable.

More recently, Batchelor (1988) presented an analysis of the stability of fluidised beds that indicates there may be inadequacies in the two-fluid approach. His analysis also has important implications for the stability of dilute suspensions. Batchelor established the one-dimensional momentum equation for the unsteady mean motion of the particles largely from physical arguments, rather than beginning with continuum assumptions. All terms in his momentum balance could be equated with terms in the general two-fluid solid phase equation, except for the hydrodynamic diffusion of particles down a concentration gradient. In a bubbling bed, this term corresponds to the particles migrating into a void region due to their fluctuating motion, thereby reducing the likelihood of that void growing. Thus, whenever a particle concentration gradient appears, there is an "effective" force driving the particles to reduce that gradient. Similarly, in a dilute suspension this process will tend to reduce local concentration gradients. Its effect on dilute suspension stability may be even more important, as r.m.s. fluctuating particle velocities and particle mean free paths between collisions in these suspensions may be shown to be considerably greater than in a bubbling bed.

Batchelor combined the gradient diffusion and particle pressure gradient terms into a single bulk modulus of elasticity for the particle assemblage, $G(\epsilon_p)$. From order of magnitude considerations, he demonstrated that the gradient diffusivity term dominated the particle pressure gradient term. Thus it would appear that the large $G(\epsilon_p)$ values used earlier by Garg and Pritchett (1975) may have some physical basis. Batchelor demonstrated that his theory gave

results similar to the relatively successful correlation of Foscolo and Gibilaro (1984), for transition from uniform fluidisation to bubbling bed behaviour. Like Needham and Merkin (1983), he predicted a "window" of bed voidages in which the suspension would be unstable, and, in addition, provided supporting numerical values for gas fluidised beds.

Batchelor's study provides evidence that dilute suspensions above a lower limit of particle concentration, corresponding to some stability criterion, may be stable. In Chapter 5 experimental results are reviewed that support this assertion. As Batchelor points out, the particle gradient diffusion process is analogous to a non-ideal (real) gas phenomenon. This phenomena is not included in two-fluid momenta equations or in granular theories described next. For steady-state models, where either effects of local transients in solids concentration are accounted for by constitutive relations or locally uniform suspensions are assumed, particle gradient diffusion need not be included in model equations. However, for multi-dimensional unsteady riser flow studies, its inclusion should be considered. Based on an earlier study by Grace and Tuot (1979), and measured local non-uniformities in particle concentration, several CFB riser models have been proposed that assume clusters are present at all suspension concentrations (e.g. Ishii *et al.*, 1989; Horio and Takei, 1990). This approach is questionable, in view of both Batchelor's study, and the fact that Grace and Tuot (1979) assumed inviscid gas and solids phases, and did not include a collisional particle pressure term.

4.5 Granular Flow Theory

Granular flow theory is based on analogy between a flowing suspension of particles and a dense kinetic theory gas. In a hard-sphere single component kinetic theory gas the r.m.s. fluctuating component of molecular velocity, $\mathbf{c}_k$, is related to the gas temperature, i.e. $\frac{1}{2}m_p\mathbf{c}_k^2 = \frac{3}{2}k_BT_g$, where k_B is the Boltzmann constant and m_p, in this case, is the mass of a single molecule (Chapman and Cowling, 1970). By analogy, the "granular temperature," T_c, is defined by the relation $\frac{1}{2}\mathbf{c}_k^2 = \frac{3}{2}T_c$ (e.g. Jenkins and Savage, 1983). Thus "granular temperature" has units of specific kinetic energy (m^2/s^2) rather than temperature.

Using similar principles to those invoked for dense kinetic theory gases, differential mass, momentum, and "granular" or "pseudo-thermal" energy balances are derived for the particles in suspension, of similar form to the single-fluid continuum mass, momentum and thermal energy balance equations. The only additional term present in the granular energy equation, not found in the standard thermal energy balance, is an energy dissipation term due to inelastic particle collisions. Expressions corresponding to transport properties of the particles, i.e. solids shear and bulk viscosity, and granular energy conductivity, may be discerned from examination of the momentum and energy balances. These properties are functions of the particle "temperature."

Granular kinetic theories were primarily developed to predict flows of dense suspensions of particles. The total stress in the particle assemblage in a dense suspension (as in a dense gas) may be divided approximately into two contributions: momentum transfer which occurs during motion of particles between collisions, termed the *kinetic* component, and transfer of momentum over a distance separating the centres of colliding particles at the time of contact, called the *collisional* component. The collisional component may be shown to dominate in dense suspensions. However, in dilute suspension regions, such as those that exist throughout much of a CFB riser, the kinetic component becomes the dominant term, and collisional momentum transfer may approach zero. Several granular kinetic theories ignore the kinetic contribution in their final expressions (e.g. Jenkins and Savage, 1983; Savage, 1988), and these theories are not applicable for modelling dilute suspension flow[4].

For low density particle suspensions, the expressions for the phase transport properties simplify to the more familiar kinetic theory expressions for standard (dilute) gases, based on the assumption of molecular chaos. For example, for a suspension of uniformly-sized spherical particles of diameter d_p, the solid phase viscosity is (Chapman and Cowling, 1970),

$$\mu_c = \frac{5}{96}\rho_p \pi^{\frac{1}{2}} d_p T_c^{\frac{1}{2}} , \tag{4.30}$$

[4]This appears to be an oversight by Gidaspow *et al.* (1990), who use expressions of Jenkins and Savage (1983) in their CFB riser model.

where T_c is the granular temperature. The more complex general granular kinetic theory expressions (see Lun *et al.*, 1984), that account for "dense gas" effects also, and the simpler "dilute gas" kinetic theory equations, such as eq. (4.30), predict solids phase transport properties that are within 20% for suspension voidage, ϵ_g, greater than 0.95. The voidage $\epsilon_g = 0.95$ is the assumed boundary between a "dense" and "dilute" particle suspension in this study, based on further analysis in Chapter 8. "Collisional" momentum transfer, as defined above, is neglected in this study when $\epsilon_g > 0.95$.

Specific details of granular kinetic theory are contained in the papers of Jenkins and Savage (1983), Lun *et al.* (1984), Lun and Savage (1986), Walton and Braun (1986), Farrell *et al.* (1986), Jenkins (1986), and Savage (1988). These theories were originally developed to predict characteristics of simple flows, such as shear flows of identical smooth spheres. From here on, we only examine the possible adaptation of these theories to the more complex task of CFB riser modelling. All granular theories assume that the dominant force on a discrete particle is due to collisions with other particles. The effect of drag due to the mean gas flow through the suspension is assumed to influence the mean velocity of the particle assemblage, but not the fluctuating motion of individual particles. In other words, the change in a particle's velocity between collisions due to drag is assumed negligible. This is probably reasonable for larger particles in dense suspension in a bubbling bed, but it is generally not true for the smaller particles and the lower suspension densities in a CFB riser (see Chapters 3 and 8).

Between collisions, drag works to increase the particle's velocity in the direction of the gas flow, *and* decrease its velocity in other directions. Therefore, there is an additional dissipation of fluctuating particle energy that must be introduced into the granular energy equation. In fact, this dissipation is significant (Chapter 8; Pita and Sundaresan, 1991). This suggests that several of the key granular theory assumptions, such as invariant velocities between collisions, are rather crude approximations for typical riser flows. It is therefore important to recognise that kinetic theories are only approximate methods when applied to riser flow.

In granular theory a Newtonian stress tensor is assumed. However, unlike a gas, a suspension

generally gains a significant portion of its fluctuating energy from shearing of the particle assemblage. This is particularly the case near the wall in riser flow, where substantial changes in vertical mean particle velocity occur over distances that are shown in Chapter 8 to be of similar order of magnitude to the lateral mean free path of the particles. In this zone, there is a significant change in granular temperature, and transport properties linked to the temperature, due to particle shear. The solids flow in this zone is unlikely to be Newtonian, and even the continuum approach may be questioned, as discussed below.

Another problem arises when suspensions consisting of more than a single particle size and density are modelled by a kinetic theory analogy. In the kinetic theory of gas mixtures, the temperature of each constituent gas may be shown to be the same (Chapman and Cowling, 1970). Thus only one thermal energy balance is required. However, because the rate of energy dissipation of particles in suspension may vary by orders of magnitude with the size of the particle, the particles do not have the same granular temperature, and many of the results of kinetic theory for gas mixtures cannot be applied. Inconsistencies that arise when a common particle granular temperature is assumed are discussed in Chapter 8. Theories that assume a common granular temperature for different particle fractions (e.g. Farrell *et al.*, 1986) are probably limited to suspensions of narrow PSD or large particles (say $> 800\mu$m).

Granular kinetic theory cannot predict the fluctuating particle motion when the fluctuations are due largely to the influence of gas turbulence. As discussed in Chapter 3, this may be the case for the smaller particles often present in CFBs (say $< 60\mu$m). Although there appear to be several specific problems with the application of granular flow theories to CFB riser flow, the theory still represents a substantial advance in the understanding and modelling of particulate flows. The model presented in Chapter 8 utilises some granular flow concepts.

4.6 Limits of the Continuum Approach and Alternatives

Although a gas is, in fact, a collection of discrete molecules, it is commonly treated as a continuum. This approach is well justified by the kinetic theory of gases. From a fundamental

consideration of the distribution of molecular velocities, equations of mean motion and energy are derived by this theory with terms that correspond with the continuum equations. However, there are several underlying assumptions in general kinetic theory required to develop these equations. Firstly, there must be a sufficient number of molecules present within a local region for statistical mean properties of the molecules to be assumed that do not fluctuate with the individual molecular motion. For example, for hydrogen gas at standard conditions the mean free path of a molecule is 10^{-7}m, and there are 2.7×10^{19} molecules per cm^3 (Chapman and Cowling, 1970). Thus a "local" region is many orders of magnitude smaller than distances over which macroscopic changes in mean gas properties are measurable. Kinetic theory assumes that there is no loss of molecular kinetic energy during or between molecular interactions. For the general results of kinetic theory to apply, it must also be possible to express body forces on the molecules as gradients of potentials (e.g. gravitational or electrical potential).

To examine if a continuum representation is reasonable for particles in suspension these same criteria must be considered. Consider a typical dilute suspension of $\rho_s = 15$ kg/m^3 in a riser, consisting of particles of density $\rho_p = 2700$ kg/m^3 and diameter $d_p = 200$ μm. In this suspension there are 1.3×10^3 particles per cm^3. Using a particle r.m.s. fluctuating velocity of $O(1)$ m/s (Chapter 8), the mean free path can be shown to be order 5 mm. This distance is comparable to the distance over which significant changes in mean variables may be measured. Also, over this distance drag force is neither constant, nor expressible as the gradient of a potential. For large particles, drag may have negligible effect on the energy of a particle between collisions, and the kinetic theory assumption is satisfied. Very small particles closely follow the gas flow. As the gas may be modelled as a continuum, these small particles also behave as a continuum. However, as discussed earlier, intermediate size particles (say 50 to 250 μm) are affected by drag between collisions, but not to the extent that they closely follow the gas. The magnitude of fluctuating velocities of these particles may approach that of their mean slip velocity (Chapter 8; Pita and Sundaresan, 1991). Thus drag may significantly modify the distribution of fluctuating velocities, and tend to cause anisotropy in the distribution. Anisotropy may also result from

inelastic collisions when the particle assemblage is sheared.

It would therefore appear that at the lower particle concentrations found in CFB risers with intermediate size particles, the criteria for treating the flow as a continuum are not adequately satisfied. Nevertheless, it is not clear to what extent these inadequacies affect the accuracy of simulations based on two-fluid continuum approaches, and the majority of modellers still use two-fluid models. An alternative to a two-fluid approach is to treat the gas as a continuum and, from a large number of calculations of particle trajectories, discern mean solids phase flow properties. This method requires enormous computational power if one is to compute the solids behaviour throughout the entire flow field. Some empiricism is still required to describe the dynamics of particle-particle collisions and the probability of a collision.

A particle trajectory method is used in this study (Chapter 9) to examine the response of discrete particles to the large drag and lift forces present in the steep gas velocity gradients near a riser wall or streamer vertical surface. A substantial variation in particle trajectory is predicted, depending on the initial lateral particle velocity into this layer. The initial velocity is a component of the fluctuating particle velocity, and it is unlikely that this phenomena could be reasonably modelled by a continuum approach, which bases all transport properties on r.m.s. particle fluctuating velocities, and calculates lift and drag from the mean particle phase velocities. This is discussed further in Chapter 9.

Chapter 5

CFB RISER FLOW PREDICTION AND MODELLING APPROACHES

A summary of the various methods that have been utilised to predict CFB riser phenomena is presented. These vary from simple empirical methods, to complex multi-dimensional two-fluid flow models. The objective of the discussion is to outline the limitations and advantages of the various approaches, including the approach used in the two models developed in this study (Chapters 8, 10).

5.1 Empirical Correlations, One-Dimensional Models and Scaling Studies

A number of relatively simple methods to predict axial apparent suspension density have been proposed. As discussed in Chapter 2, Li and Kwauk (1980) fitted a sigmoidal density profile to their data, and developed a number of correlations to predict these density profiles. Rhodes and Geldart (1988) and Kunii and Levenspiel (1991) treated the CFB riser as a bubbling bed and freeboard. The suspension density in the "freeboard" was assumed to decay exponentially with height, and an empirical profile decay parameter was used to fit profiles to experimental data. Both these approaches were based on the concept of upward and downward motion of agglomerates or clusters of particles. Neither approach considered the substantial downflow of solids at the wall in risers, or the significant influence of riser entry and exit geometry. Relatively flat suspension density profiles are commonly observed in the middle and upper heights of the riser, suggesting that the core-wall particle interchange is nearly balanced over that height interval. The continuous decay assumed by Kunii and Levenspiel is inconsistent with this observation. Bolton and Davidson (1988) also treated the upper part of the riser as a freeboard, and assumed continuous decay of suspension density with height, which they

attributed to turbulent diffusion of particles out to the riser wall. The assumption that the riser can be divided into a dense bed in the bottom, with a "freeboard" region above, is questionable. The initial steep decay in suspension density profile with height in the riser typically occurs over a height of 1–3 m, and there is no clearly defined bed "surface." Consequently, the mechanisms and correlations for particle entrainment in bubbling beds do not apply. At higher U_g, there is often no characteristic "dense bed" suspension density, as the density profile decays steeply from the riser base, upward.

These simple methods for predicting riser suspension density profiles cannot account for the radial non-uniformity of solids distribution in the riser. For example, Wu (1989) measured similar differential pressures at two heights in a riser with very different radial solids distributions. As correlations for prediction of suspension density profiles omit parameters that are known to influence the riser flow, such as riser geometry, and do not account for radial non-uniformities in solids distribution, they cannot be considered reliable outside the range of conditions on which they were developed.

Fett and co-workers (Weiss and Fett, 1986; Weiss *et al.*, 1988; Fett *et al.*, 1991) have modelled the riser by dividing it into a series of well-mixed compartments, or "CSTRs," stacked on top of each other. There is no mention of how the vertical solids interchange between compartments is predicted. This approach has two disadvantages. Firstly, experimental tracer data (e.g. Bader *et al.*, 1988) indicate that the wall and core regions are not well-mixed. Secondly, one must assume a number of CSTRs to model the riser. By varying this number the model can be fitted to data, but consequently loses its predictive power.

Several experimental riser scale-up studies have been reported (Chang and Louge, 1991; Glicksman *et al.*, 1991), based on principles of dimensional similitude. Strict adherence to similarity principles limits the diameter of an elevated temperature riser that can be modelled by a pilot-scale cold unit to less than typical commercial riser diameters. Chang and Louge partly overcame this problem by using mixtures of helium and carbon dioxide as the fluidising gas, in place of air. Glicksman *et al.* obtained reasonable agreement between dimensionless suspension

density profiles in a pilot-scale combustor and a cold unit operating with steel spheres, except near the exit region. Despite their limitations, these studies are useful in identifying important hydrodynamic parameters in CFB risers.

5.2 The Two-Zone Core-Annulus Approach and Cluster and Strand Models

An alternative to a multi-dimensional representation is to divide the flow space into discrete zones. Assumptions that are specific to each zone can then be made, thereby simplifying the overall model. Flow within a zone is usually assumed to be one-dimensional. The division of two-phase flows into dilute and dense suspension regions, with a step change in concentration at the interface is a well-established approach, e.g. in bubbling fluidised beds and spouted beds. The two major disadvantages of this approach, compared to a multi-dimensional representation of the flow field, are that conditions for interchange of mass and momenta at the zone boundaries may have to be established, and it is not always obvious where or how to define the zone boundary.

Except in the bottom of the riser, there is a relatively abrupt transition between the dense suspension wall region and a dilute suspension core (see Chapter 2). Relatively flat gas and particle velocity profiles are reported for the core, and the bulk of the gas flows in this region. A two-zone core-wall division, shown in Figure 5.1, is therefore a reasonable representation of the radial gas and solids distribution over these heights. Moreover, though there is substantial heterogeneity in local solids concentration at the wall, the suspension is relatively uniform in the core (Chapter 2). The wall region thickness may approach zero at low solids circulation and/or high gas velocity, as the riser flow approaches dilute pneumatic conveying. In the bottom of the riser, the core-wall transition is usually not as abrupt, and local heterogeneity in solids concentration may be significant over the entire riser cross-section. A core/wall zone division at these heights is a much cruder approximation. When dividing the riser into core and wall zones, it is generally implicitly assumed that the flow is axisymmetric. This may not be a reasonable assumption, especially in larger commercial units.

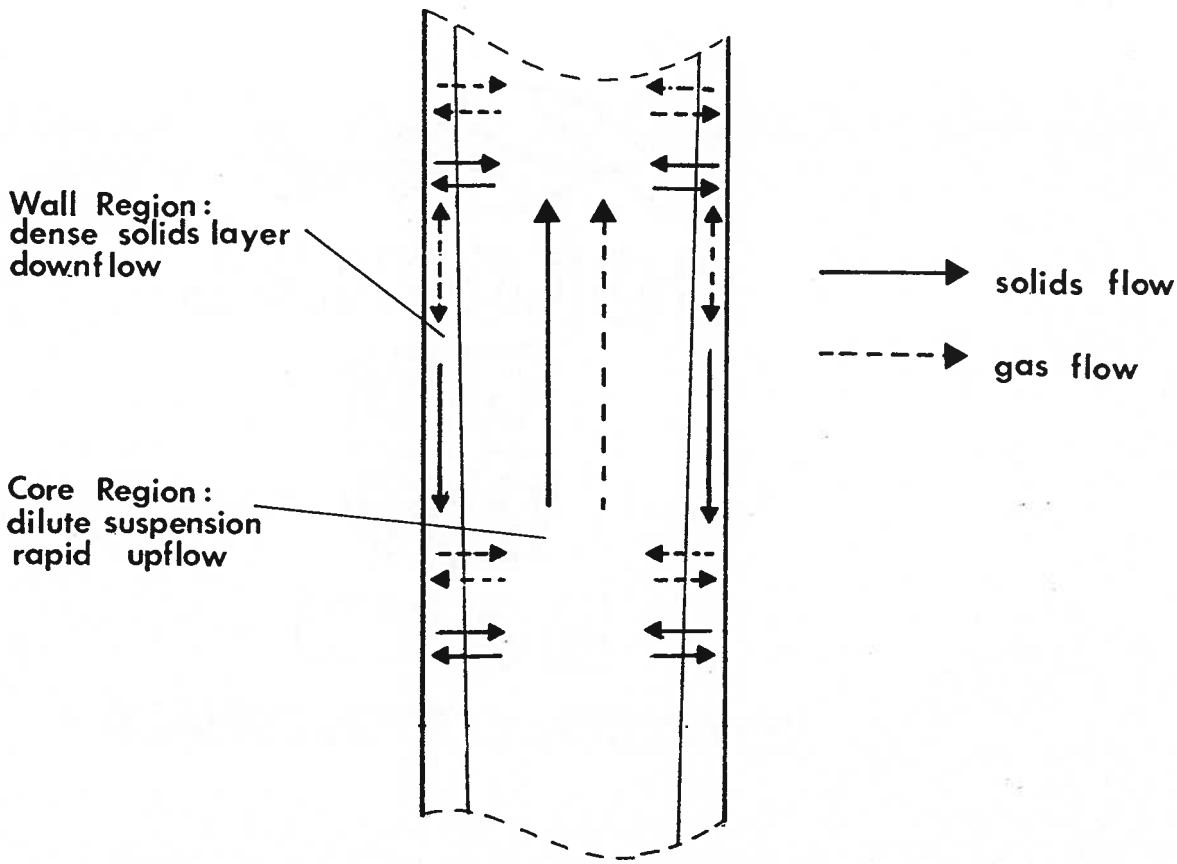

Figure 5.1: The regions and flow patterns assumed in two-zone core-wall modelling of riser flow.

Nakamura and Capes (1973) proposed a core-annulus model for fully-developed flow. They proposed momentum equations for each zone which included exchange of momentum between core and annulus. They assumed, without justification, that the solids were distributed between core and annulus in a manner that minimised the axial pressure drop. No wall-core particle exchange mechanisms were proposed to explain the particle transfer. Their model predicted wall downflows of solids that were an order of magnitude less than their measured data. Nevertheless, their work introduced a number of useful concepts that have been applied in subsequent models (e.g. Ishii *et al.*, 1989). Several simple core-annulus two-zone models have also been proposed (e.g. Berruti and Kalogerakis, 1989; Rhodes, 1990). These models feature simple mass balances developed to interpret rather than predict measured data. Uniform concentrations of solids are assumed in each zone.

To account for local heterogeneity in solids concentration Horio and co-workers (Ishii *et al.*, 1989; Horio and Takei, 1991) assume that the solids are distributed throughout the riser as dilute suspension and denser spherical solids clusters, as originally suggested by Yerushalmi *et al.* (1978). A major objection to this approach is that spherical clusters are a poor representation of solids structures observed near the riser wall. Wall streamers are very long thin sheets, that do not behave dynamically like spheres. In this study, denser solids structures detected in the core of the riser also appeared to be thin vertical strands. Wirth (1991) proposed dividing the riser into dilute suspension regions surrounding strands shaped like vertical pipe elements. Both approaches introduce the problem of describing the dynamics at the interface of the dense and dilute regions. Both models are still at the conceptual stage.

5.3 Multi-Dimensional Two-Fluid Models

A multi-dimensional approach to modelling riser flow has the advantage that radial gradients can be more reasonably represented. Furthermore, if the basic equations of motion and boundary conditions are "correctly" formulated, solution of the unsteady flow equations may show transients in the flow similar to those observed experimentally. Unfortunately there is no single

"correct" formulation, known to guarantee good results.

The current multi-dimensional models of two-phase gas-solid flow are based on two-fluid formulations, described in Chapter 4. As discussed, despite the mathematical rigour used in their development, the two-fluid modelling approach has limitations. Empirical relationships are required to describe gas-particle interaction and boundary conditions. In addition, as we will see in Chapter 9, the treatment of the solids phase as a continuum may not be reasonable near the riser wall. A further disadvantage is the enormous computational power, time and expense required for solution of these models.

Multi-dimensional two-fluid riser models assume either that particle collisions cause particle fluctuating motion, or that gas turbulence is the major influence on fluctuating particle motion. Although Jansen and Romate (1991) have outlined a model that accounts for both phenomena, no models have been developed that combine both. Furthermore, the effect of PSD on particle fluctuating motion has not been considered in these models.

The models of Gidaspow and co-workers (Gidaspow *et al.*, 1989; Tsuo and Gidaspow, 1990) and Sinclair and Jackson (1989) are based on particle collision theories. The Gidaspow model is an unsteady flow model, whilst the current version of the Sinclair and Jackson model assumes fully-developed steady flow. Gidaspow and co-workers report simulation results for CFB risers that show some transient behaviour which they liken to cluster flow. However, these "cluster" regions are very diffuse, and orders of magnitude larger than measured clusters. No phenomena like wall streamer flow has been predicted. Pita and Sundaresan (1991) report several problems with the Sinclair and Jackson model, including unsatisfactory sensitivity to inelasticity of particle collisions. Berker and Tulig (1986) propose a two-phase k-ϵ turbulence model for fully-developed riser flow, that incorporates a large degree of empiricism. Several other investigators (e.g. Militzer, 1986; Chen, 1989; Rizk and Elghobashi, 1989) have modelled very dilute suspension flows in a similar manner. Currently, none of the two-fluid multi-dimensional models has been developed to the stage where accurate predictions are assured.

Chapter 6

HYDRODYNAMIC TESTS AT AMBIENT TEMPERATURE

Riser reactor design, particle properties and operating conditions may differ significantly, even between units with similar applications. The majority of previous investigations into riser dynamics, such as those discussed in Chapter 2, have been primarily concerned with measuring the effects of superficial gas velocity, U_g, and solids recirculation rate, G_s, in a riser of fixed geometry and with a single particle type. However, several of these studies clearly demonstrate that changes in other parameters, such as exit design, may also have a substantial effect on riser solids flow and distribution. Furthermore, from a theoretical consideration of riser suspension flow (Chapters 3 and 4), one can identify additional factors that are likely to influence riser operations, such as particle size distribution (PSD), and which, hitherto, have not been investigated.

To advance our understanding of CFB hydrodynamics, and extend modelling efforts beyond models limited to particular riser geometries and particle types, there is clearly an urgent need for investigation into the effects on riser operation of parameters other than U_g and G_s. A selection of such tests are described in this Chapter. Riser exit and entry design, secondary air injection, particle density and PSD effects were studied. The tests were performed systematically, with care taken to minimise variation of all factors except the parameter under study. In addition, factors that may influence wall streamer stability were investigated.

6.1 Experimental Objectives

As modelling concepts and theories were developed in this study, questions arose which could not be answered by recourse to the available literature. At times an improved understanding

of a particular aspect of riser dynamics was needed before theories could be advanced, whilst often experimental support of modelling postulates and predictions was required. The cold unit test program was undertaken to specifically investigate a selection of effects that had been postulated to be important but not investigated, or to further other investigators' earlier preliminary observations of known key effects. Many of these earlier preliminary studies were not systematic and, in some cases, only suspension density profiles were measured, with no local solids concentration data reported.

As well as addressing certain modelling questions, this cold unit study was designed to generally improve our understanding of CFB dynamics. The matrix of tests performed, with control of key parameters such as mean particle size and particle shape, adds to the pool of reliable data for the development of correlations. Solids concentrations were estimated by several methods, including the most common method involving measurement of differential pressures. A comparison of these estimates in the riser exit and entry regions provides new insight into the possible flow patterns in these regions. The accuracy of estimating suspension densities from differential pressures in regions of accelerating or two-dimensional flows is examined. Also, a valuable benefit gained by visually observing the flow patterns of solids through the transparent riser wall of the cold unit is a better understanding and interpretation of data measured both in this study and reported by others. In many instances these observed flow patterns provide further insight into the fundamental mechanisms involved in pilot-scale riser cold flows, particularly at the riser wall. Some qualitative description of observed solids flows are provided in this chapter, and a further detailed description of the time-varying wall solids flow patterns and streamer motion is presented in the wall dynamics chapter (Chapter 9).

We first consider the motivation behind each of the cold unit tests. From consideration of the fundamental dynamics of riser flows presented in Chapter 3 and the equations of motion for suspensions given in Chapter 4, it is apparent that particle density and particle mean size should affect suspension flow patterns and solids distribution, with larger or heavier particles expected to travel up the riser more slowly than smaller, lighter particles. Although several

investigators have included two particle types in their CFB studies (e.g. Hartge *et al.*, 1986; Hartge *et al.*, 1988; Arena *et al.*, 1989), these investigators were primarily interested in the effects of G_s and U_g. No comprehensive direct comparison of the behaviour in a CFB of solids of similar size, PSD and shape, but dissimilar particle density had been performed. As particle density is a parameter that may be altered in some commercial operations (e.g. inert sands in CFB combustors), such a study is worthwhile.

There is also theoretical evidence that particle size distribution (PSD) has an effect on CFB dynamics. Recall the proposal that collisions amongst particles contribute to the observed lateral movement of particles out to the walls of the riser. One possible cause of collisions identified in this study is the difference in particle slip velocity of smaller and larger particles. Thus systems with wider PSD particles may exhibit higher collision frequencies, increased lateral particle motion, and increased particle deposition at the riser wall. Hence, widening PSD may increase the solids hold-ups in a riser at constant G_s and U_g. Although some effects of PSD on solids hold-up have been investigated by Nakamura and Capes (1976) for pneumatic conveying and by Sun and Grace (1990) for lower velocity turbulent fluidised beds, no similar study appears to exist for circulating fluidised beds. Particle segregation may also increase with wider PSDs, due to smaller or larger particles preferentially transferring out to the riser wall. Dry (1987) observed radial particle size segregation at typical CFB gas velocities in a riser operating with FCC catalyst of narrow PSD and mean size 71 μm. The influence of PSD width on segregation has not been investigated, and segregation in risers with larger particles, typical of CFB combustors, does not appear to have been reported.

It is known that CFB exit geometry can significantly affect the unit operation. In addition, it is likely that the design of several additional key riser features such as the shape of the riser base, the method and location of solids and air injections into the unit and the topography of wall surfaces also have a significant effect on gas and solids flow patterns within the riser.

As mentioned in Chapter 1, some CFB risers have narrow bottom or "base" sections that

increase in cross-sectional area with height, while in others the base section has a larger cross-section than the remainder of the riser column. Commercial size riser exits also vary both in geometry and cross-sectional area. Both Brereton (1987) and Jin *et al.* (1988) have investigated the effect of an abrupt and smooth exit on the suspension density profile within pilot-scale risers. The performance of entry geometries has not been compared, and there is insufficient data for the development of correlations to describe the variation in solids hold-up and flow between risers of different design.

As discussed in Chapter 1, some circulating fluidised bed applications involve addition of gas at heights above the primary gas distributor. For example, in circulating fluidised bed combustors, secondary air is injected between approximately 2 and 10 m above the base of the riser column. Despite its common use, the effect of secondary (or tertiary) gas injection on CFB riser hydrodynamics has not been thoroughly investigated. Brereton (1987) reported secondary air test results for one gas velocity and solids circulation rate. Wang and Gibbs (1990) investigated secondary air effects at low G_s. Further tests are performed in this study to complement these initial studies.

A key feature of CFB risers is the downflow of wall streamers. These streamers do not fall as continuous uninterrupted layers. Intermittently small areas of the streamers rapidly decelerate, to become almost stationary for a brief time of order 0.2 seconds, before re-commencing their downward motion. It is postulated in Chapter 9 that significant entrainment of particles from dense wall layers into the rapid core suspension upflow occurs from the sites of these disruptions. Although it is likely that the extent of streamer formation and disruption greatly affects key processes such as solids flow and distribution, and bed-wall heat transfer, factors influencing general streamer dynamics and the observed instabilities in streamer motion have not been investigated.

The specific objectives of the cold unit test program were to:

(i) observe the effect of varying PSD on solids hold-up within the riser, and compare this to trends predicted by particle-particle and gas-particle interaction theories,

(ii) test for particle size segregation by sampling solids from several locations around the CFB loop,

(iii) measure and compare axial solids hold-up and local solids concentrations within the riser for two different riser base section and exit section geometries,

(iv) measure the extent of angular and radial non-uniformity of solids distribution within the solids entry and exit regions and at the riser mid-height,

(v) determine the effect of secondary air injection flowrate and direction on solids hold-up within the riser,

(vi) investigate the influence of particle density on solids hold-up within the riser,

(vii) examine if the local transient motion of wall streamers is influenced by fluctuations emanating from distant points (e.g. pulses in solids return).

Not all factors were studied in these tests. The riser design and particle properties that were varied correspond to those typically varied by investigators in search of improved riser operation. The study focussed on determining particle distribution and motion and no study of gas mixing was performed. The tests designed to satisfy objectives (i) and (v) were considered preliminary in nature, in that the primary aim was to observe trends and qualitatively relate these to modelling concepts.

6.2 Experimental Apparatus and Procedure

6.2.1 Cold Unit Apparatus

The cold model circulating fluidised bed apparatus used in this investigation is shown schematically in Figure 6.1. It consists of a riser, two cyclones, a vessel for storage of recirculated particles, and an L-valve. Except for minor changes to the riser and addition of extra instrumentation, it is essentially the same as described by Burkell (1986) and Brereton (1987).

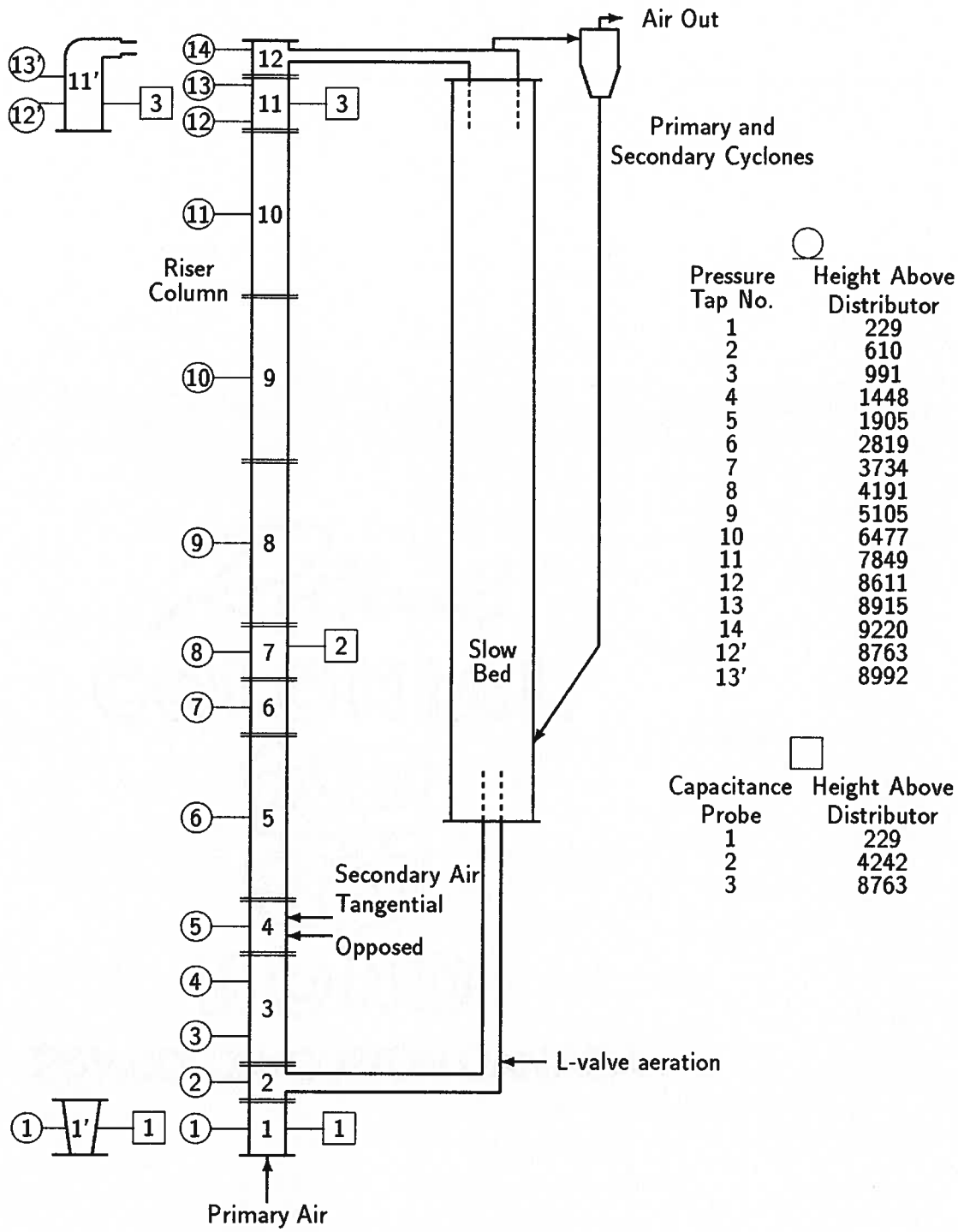

Figure 6.1: Schematic of cold unit CFB showing the heights of pressure measurement taps (circles) and capacitance probe ports (squares). The riser is drawn with the cylindrical entry and abrupt exit configuration. Alternative conical entry and smooth exit sections are shown at the correct height for their insertion. All dimensions in mm.

The riser is 9.3 m tall, 152 mm ID, and is constructed of transparent polyacrylic tubing ("Plexiglass"). It consists of individual flanged sections of lengths that are multiples of 457 mm, an exit section and a solids entry tee section. Particles are recirculated to near the base of the riser via an L-valve. The vertical and horizontal sections of the L-valve are also 152 mm ID. In this study, the centreline of the solids entry tee was located 610 mm above the base of the riser.

To study the effect of the riser base geometry, experiments were conducted with a cylindrical section of the same cross-sectional area as the riser, and with a conical section that increased from 89 mm ID to 152 mm ID. These 457 mm high, interchangeable entry sections, shown in Figure 6.2, were located between the riser primary air distributor and the solids entry tee (Figure 6.1). The two geometries were chosen as they are sufficiently different in design to produce a measurable difference in solids distribution, and because both are commonly found in CFB units. In addition, as the UBC combustor also has a base section which increases in cross-section with height, qualitative comparison of the performance of the hot and cold units could be made. Primary air was introduced into the cylindrical base section through a perforated 152 mm diameter plate with 6.3 mm diameter holes drilled on a 12.7 mm square pitch, providing 19% free area. For the conical base, a perforated 89 mm diameter plate with 8.7 mm holes drilled on a 12.7 mm triangular pitch was used, giving a free area of 43%.

Two riser exit sections were studied, a smooth and abrupt exit, as in the study by Brereton (1987). These are shown in Figure 6.3. Both sections consist of 152 mm ID vertical riser sections, and 102 mm ID exits to the primary cyclone.

Most of the solids leaving the top of the riser are captured by a primary cyclone of a constant internal diameter of 203 mm along its full height, which is designed for high solids throughput and efficiencies nominally greater than 98%. Gas and fine particles leaving the primary cyclone are passed through a secondary cyclone of conventional Stairmand high efficiency design. Solids captured by both cyclones fall into a solids storage column of 4.8 m total height and 343 mm inside diameter. The storage column is run as a low-velocity bubbling fluidised bed to ensure

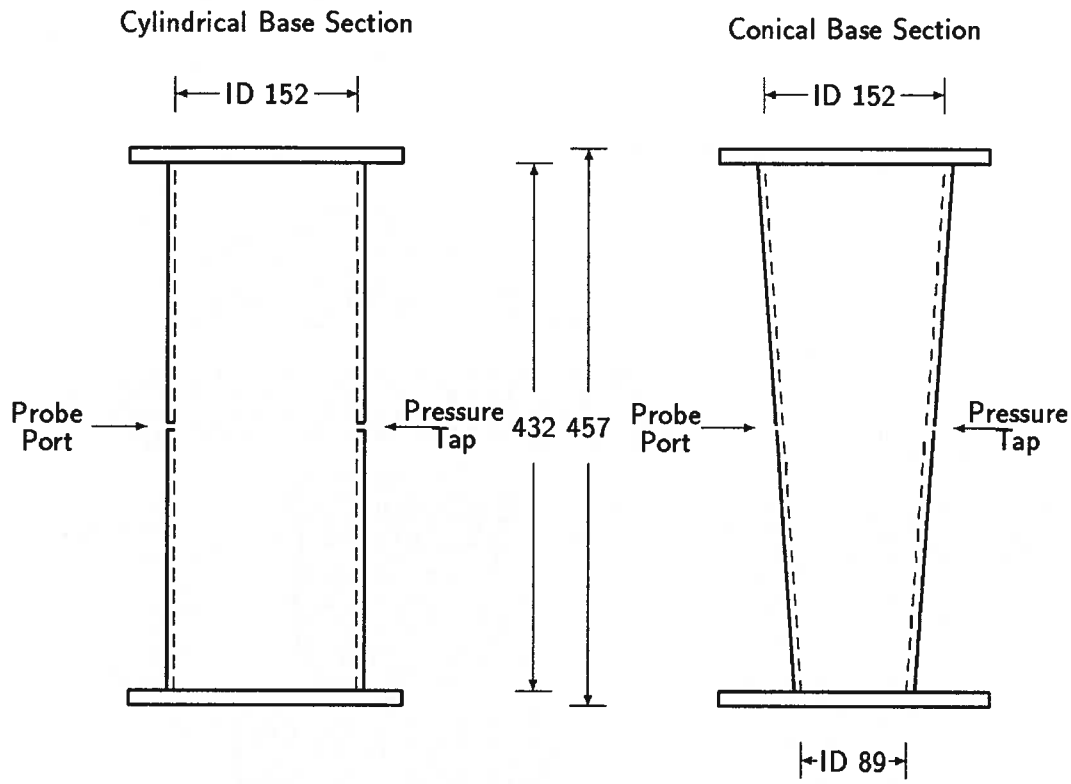

Figure 6.2: Base section geometries used in entry effect test runs. All dimensions in mm.

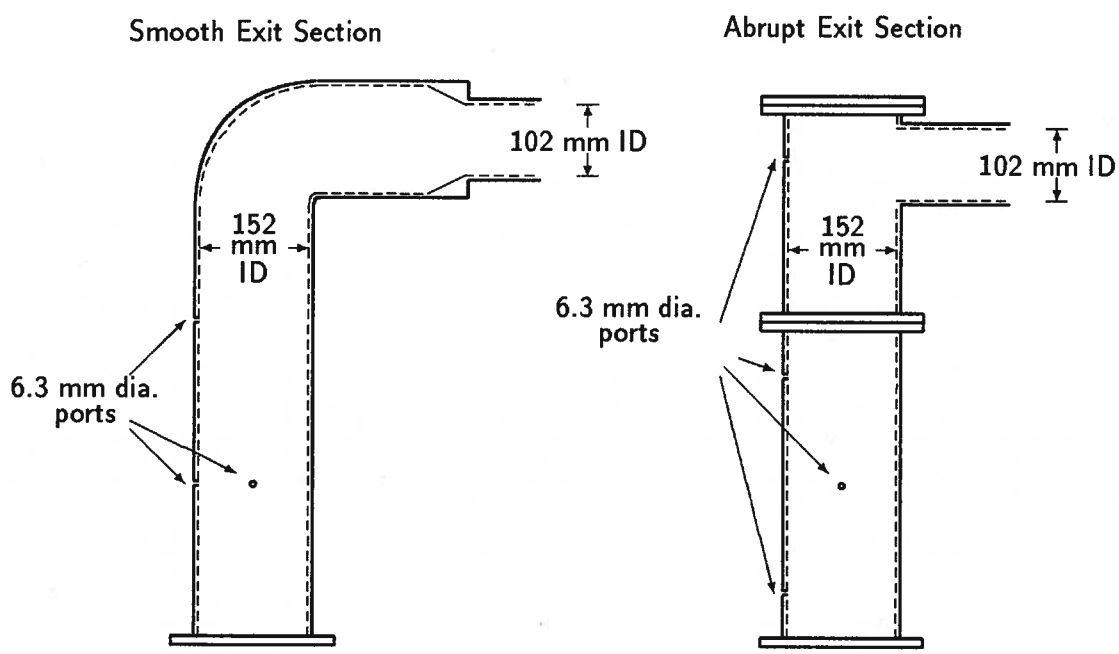

Figure 6.3: Riser exit section geometries used in exit effect test runs.

continuous return of the fine secondary cyclone solids. The bubbling bed height is typically 1.1 m. Solids from the storage column move down a 2.18 m long, 152 mm ID standpipe to an L-valve in packed bed flow. The L-valve was aerated at a point 114 mm above the centreline of the 0.9 m long, 152 mm ID horizontal L-valve section, through a port of 6.4mm ID. Separately controlled input of air at both inside elbow and outside elbow orientations, as shown in Figure 6.4, was required to minimise "stick-slip" flow in the L-valve, and to ensure good control of the solids flow into the riser.

In addition to primary air introduced at the base of the riser, secondary air was injected further up the riser in several of the experiments. Tangential (or "swirl") air injection ports were located 1981 mm above the primary air distributor, while radial (or "opposed") air was injected at a height of 1829 mm. At both levels air injection occurred through four identical 25.4 mm ports, each spaced evenly at 90° intervals around the riser circumference. The tangential air ports directed air tangential to the riser wall, thus creating swirl, while the radial ports directed air towards the riser axial centreline, as shown in Figure 6.5. Primary and secondary air were supplied by a 0.15 m^3/s, 50 kPag Sutorbuilt blower, model 7HV.

6.2.2 Axial Differential Pressure Measurements

Pressure profiles were determined using the pressure tap locations along the riser length shown in Figure 6.1. Each pair of adjacent taps was connected across a differential pressure transducer. Omega transducers of type PX162D (range 0 – 6.9 kPa), PX163D (range 0 – 1.245 kPa) and PX164D (range 0 – 2.49 kPa) were used. All transducers produce a voltage signal between 1 and 6 volts that is linearly proportional to the differential pressure.

6.2.3 Capacitance Probe

A needle capacitance probe was used to measure local variations in solids concentration within the CFB riser. The probe design is shown in Figure 6.6. It consists of an inner 1.3 mm diameter rigid stainless steel wire, which protrudes 4 mm from a surrounding sheath. The

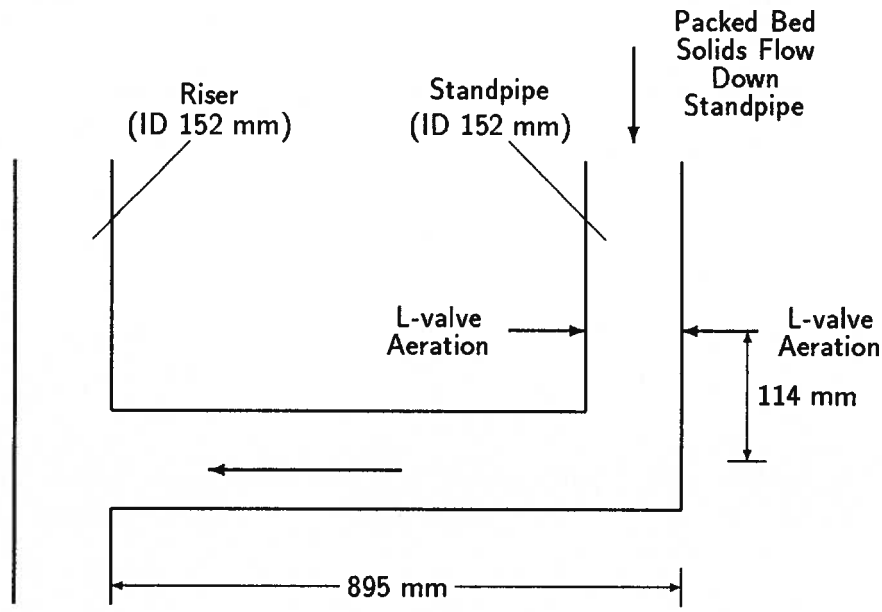

Figure 6.4: L-valve aeration positions for control of solids flow into the riser.

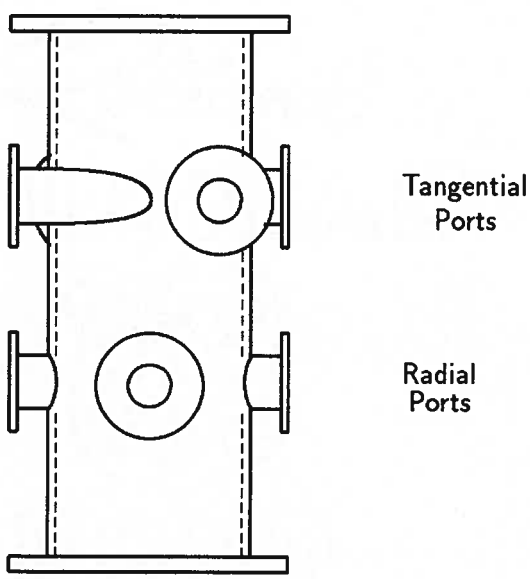

Figure 6.5: Configuration of the radial ("opposed") and tangential ("swirl") injection secondary air ports (Brereton, 1987).

sheath is composed of a 3.2 mm OD 2.2 mm ID brass tube and is press-fitted into a larger 6.4 mm OD 4.6 mm ID stainless steel bushing. The wire is insulated from the sheath by a magnesium oxide thermocouple insulator. The wire and insulator are held rigidly within the sheath using ceramic cement. The electrical connection at the non-measurement end of the probe is a BNC coaxial coupling. Further details of the probe are given by Brereton (1987).

The live wire tip and grounded outer sheath of the probe behave as a capacitor which, in combination with a tuning plug (Disa type 51E03), form a resonant circuit that controls the frequency of a transistorised oscillator (Disa type 51E02) (Figure 6.7). Variations in the dielectric constant of the medium surrounding the probe tip due to changes in solids concentration in that region alter the capacitance of the probe and consequently change the oscillator frequency. These frequency modulations are converted by a reactance converter (Disa type 51E01) to a voltage which is proportional to changes in probe capacitance. To reasonably estimate local solids concentrations over the range of solids volume fractions present in CFBs (0.0 to 0.5) the output from the probe may be assumed to be linearly proportional to the concentration of solids present (Brereton, 1987). Although the probe is capable of detecting capacitance changes at a frequency up to 100 kHz, in this study the probe output was logged at a rate of 100 Hz. The power spectra of capacitance probe signals given by Brereton (1987) and Louge *et al.* (1990) show that fluctuations in voidage within the riser occur predominantly at frequencies lower than 20 Hz. The probe was calibrated prior to each run by noting the change in output voltage as the probe was submerged in a loose-packed bed of the solids used in the tests. Stray capacitance effects on the probe due to the presence of the nearby non-conductive polyacrylic riser wall were found to be insignificant in an earlier investigation (Brereton, 1990)

6.2.4 Solids Sampling

Solids were withdrawn from the unit through a 4.93 mm ID, 6.35 OD tube (Figure 6.8). By rotating the curved tip of the tube through 180°, the tip could be oriented upwards or downwards. The gas-solid suspension withdrawn through the tube was passed through a small 20

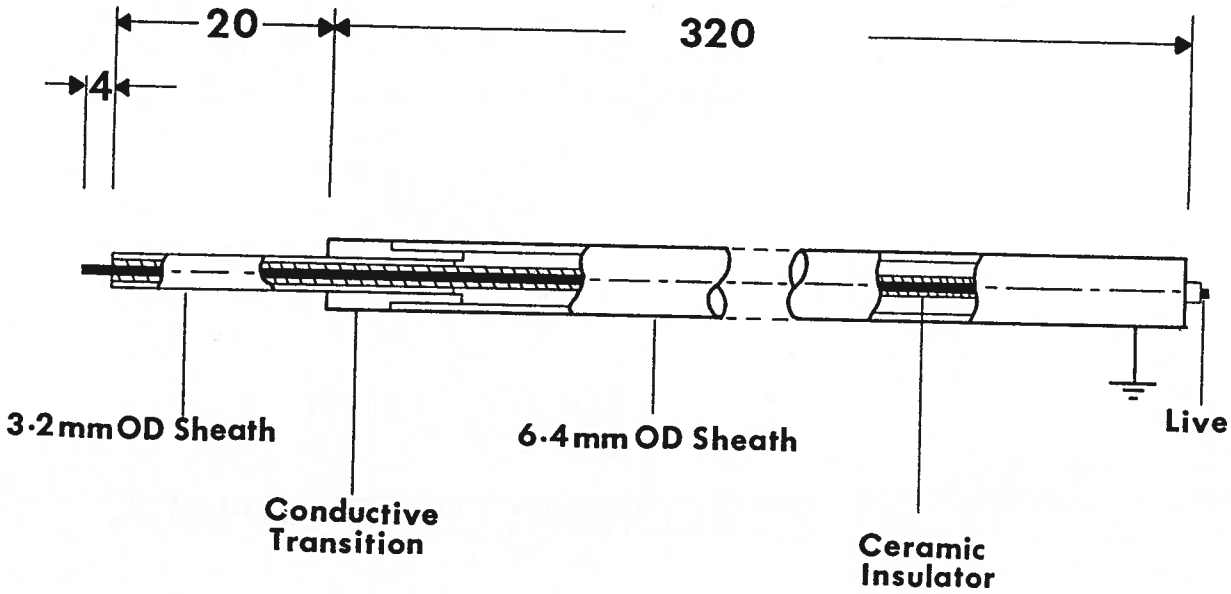

Figure 6.6: Needle capacitance probe. Dimensions in mm.

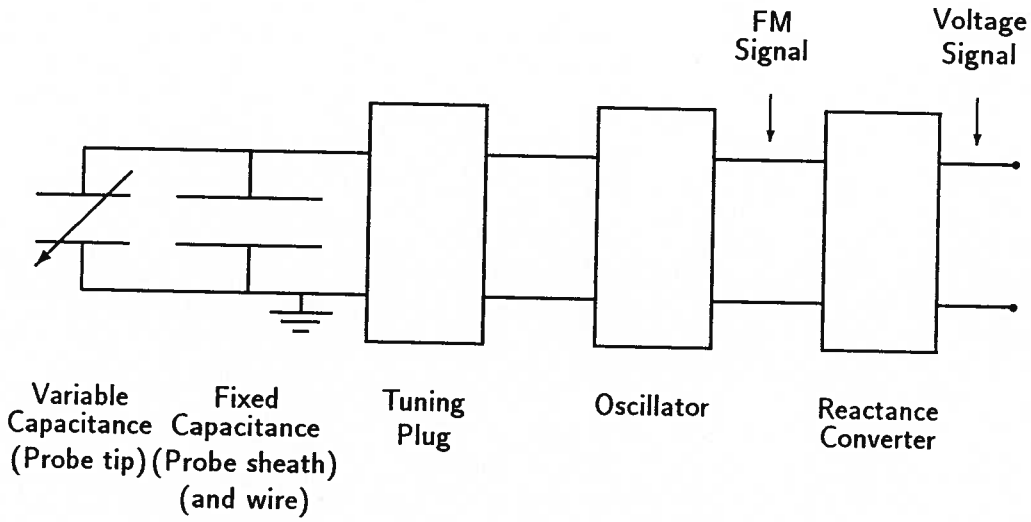

Figure 6.7: Block diagram of the capacitance probe system illustrating principal components.

mm ID portable cyclone to separate solids from gas. Samples were taken from mid-way up the riser and from the horizontal section between the riser exit and the primary cyclone. At the riser mid-height position, the tip was positioned at the wall, and both upflow and downflow samples were taken. The sample withdrawn in the 102 mm ID horizontal exit section was taken with the tip facing upstream along the section axis. Rapid solids flow toward the cyclone at the wall of this section was observed and, given the high gas velocities of $O(20\ \mathrm{m/s})$ in this section, it appeared likely that a well-mixed unidirectional flow of solids towards the cyclone existed. Thus the exit solids sample was assumed to be representative of the externally recycled solids stream. For comparison with the exit sample, a solids sample was also taken by draining some solids from a small orifice on the standpipe wall. Following the test runs the samples were sieved to obtain their size distributions.

6.2.5 Data Acquisition

Both the probe and the differential pressure transducer voltage outputs were directed to a multiplexer board (Omega type EXP-16). The multiplexer board was connected to an A/D data acquisition board (Omega type DAS-8) resident within an IBM XT compatible computer. A commercially available data analysis software package (LABTECH NOTEBOOK) was used for data logging. The probe signal was logged at 100 Hz for 20.48 s while the pressure transducer signals were logged at 2 Hz for 40 s (except for the cross-correlation tests described later). Higher logging durations or rates of the transducer outputs were found to have negligible effect on the average solids hold-ups calculated over the total sampling time. The differential pressures (Δp_g) were converted to apparent suspension densities (ρ_{sa}) as they were logged using the standard relationship $-\Delta p_g/\Delta z = \rho_{sa} g$ presented in Chapter 4, with Δz equal to the distance between taps.

Table 6.1: Properties of particles used in the cold unit tests

PARTICLE PROPERTY	PARTICULATE					
	Glass			Sand		
	Narrow	Standard	Bimodal	Ottawa	Olivine	Chromite[a]
Sauter mean dia. (μm)	230	218	233	160	177	148
Particle size spread[b] (μm)	28	69	142	39	95	91
Particle density (kg/m^3)	2470	2470	2470	2600	3220	4420
Bulk density (kg/m^3)	1380	1430	1430	1400	1580	2430
Dense-packed voidage	0.38	0.36	0.36	0.41	0.45	0.38
Loose-packed voidage	0.44	0.42	0.42	0.46	0.51	0.45
Angle of repose	23°	23°	22°	31°	34°	32°
Archimedes Number[c], Ar	1018	867	1059	361	605	486
$d_p^\star (= Ar^{1/3})$	10.1	9.5	10.2	7.1	8.5	7.9

[a]includes 3% by mass of zircon sand
[b]$(d_{84\%} - d_{16\%})/2$, where d is the particle diameter and % refers to the cumulative mass percent undersize
[c]evaluated at 25 °C

6.2.6 Test Procedure

Glass beads were used as particles in all experimental runs except for those when the effect of particle density was investigated. Glass beads were chosen because they had sphericities close to unity, thus eliminating one unknown in these runs, namely the effect of particle shape. They were also available in narrow size distributions, which could be combined to form mixtures of wider size distribution. For the tests in which the effect of particle density was examined, three sands, Ottawa (silica), Olivine (iron/magnesium silicate) and chromite sand were employed in succession. Densities of these sands were 2600 kg/m^3, 3220 kg/m^3 and 4420 kg/m^3 respectively. In order to improve visual observation of the particle flows through the riser and standpipe walls for the chromite particle run, 3% by mass of white zircon sand (ρ_p = 4200 kg/m^3) was mixed with the black chromite sand. These two sands had similar PSDs. Properties of all the particles used are given in Table 6.1, with "chromite" denoting the zircon/chromite mixture.

For each run, measurements were performed at two solids circulation rates (20 and 60 kg/m^{2}s) and two superficial air velocities (6.5 and 9.0 m/s). The solids circulation rate was estimated by timing downward movement of the solids in packed-bed flow in the vertical leg

of the L-valve, and calculating the solids mass flowrate from this velocity and the loose-packed bed voidage of the solids under study. This simple procedure has been shown by Burkell *et al.* (1986) to give results within about ± 10% of more accurately determined circulation measurements, such as collection of solids on a butterfly valve in the standpipe. From repeated measurements, it was estimated that loose-packed voidages were accurate to within ± 5%. Except for the chromite sand, these voidages are typical of documented voidages for sands and glass beads (e.g. Brown and Richards, 1970). The chromite sand voidages are slightly lower than typical values, possibly due to a relatively high fines content. Replicate timings of L-valve solids flow varied within ± 3%. Consequently, in this study the accuracy of the measured solids flow entering the base of the riser was assumed to be within ± 10%. Primary and secondary air flowrates were metered by sharp edged orifices. In each run the pressure was measured at intervals along the length of the riser, from which apparent suspension density profiles were computed. For three of the runs radial distribution of solids was measured using the capacitance probe. In two runs, samples were withdrawn for later size distribution analysis.

A summary of each run is given in Table 6.2. The four operating conditions studied in each run (2 solids fluxes × 2 superficial air velocities) are designated as conditions A, B, C and D, as defined in Table 6.2. In the discussion of test results, the pertinent run and condition are frequently referred to only by the run number and condition letter. Run 1 was the base case against which all other test results involving glass beads were compared. For this base case a cylindrical base geometry and abrupt exit were in place. Runs 1, 2 and 3 investigated the effect of PSD on the overall solids hold-up in the riser. In Run 1 narrow size distribution glass beads were used, whilst in Runs 2 and 3, respectively, "standard" and wide bimodal particle size distributions were employed. These distributions are plotted in Figure 6.9. The Sauter mean for each set of particles was nominally 230 μm (Table 6.1). In Runs 2 and 3 solids samples were withdrawn as described earlier.

In Run 4 the conical base section and abrupt exit were used with narrow PSD glass beads. In Run 5 the smooth exit section and cylindrical base section were in place. Comparison of results

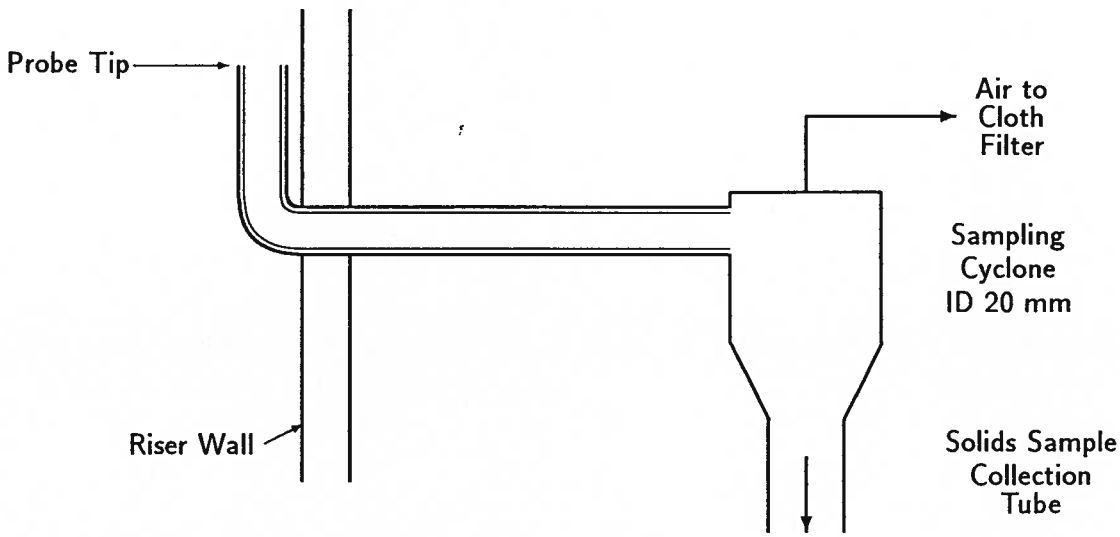

Figure 6.8: Schematic of solids sampling probe and solids collection system. Probe shown in position to capture wall solids downflow.

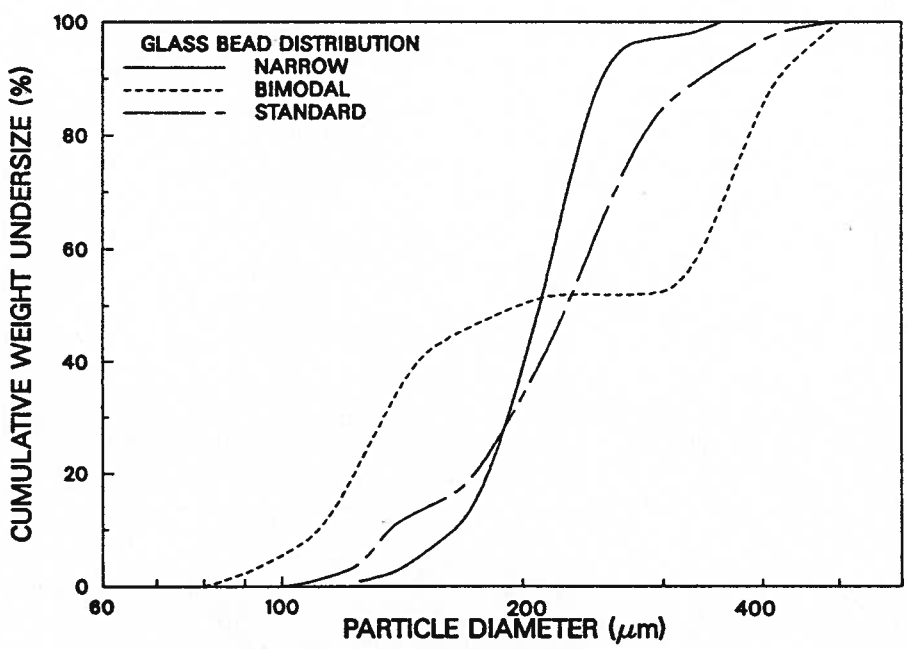

Figure 6.9: Cumulative particle size distributions of the three glass bead particle mixes studied.

Table 6.2: Summary of the cold unit tests performed

RUN NO. & CONDITIONS[a]	PARTICLES	RISER BASE	RISER EXIT	SEC. AIR RATIO[b]	SEC. AIR PORTS	TESTS PERF-ORMED[c]
1 (A–D)	Narrow	Cylindrical	Abrupt	—	—	AP, CP
2 (A–D)	Standard	Cylindrical	Abrupt	—	—	AP, SS
3 (A–D)	Bimodal	Cylindrical	Abrupt	—	—	AP, SS
4 (A–D)	Narrow	Conical	Abrupt	—	—	AP, CP
5 (A–D)	Narrow	Cylindrical	Smooth	—	—	AP, CP
6 (A–D)	Narrow	Cylindrical	Abrupt	1:1	Opposed	AP
7 (A, B)	Narrow	Cylindrical	Abrupt	1:2	Opposed	AP
8 (A–D)	Narrow	Cylindrical	Abrupt	1:1	Swirl	AP
9 (A–D)	Ottawa	Cylindrical	Abrupt	—	—	AP
10 (A–D)	Olivine	Cylindrical	Abrupt	—	—	AP
11 (A–D)	Chromite	Cylindrical	Abrupt	—	—	AP

[a]superficial air velocity and solids circulation rates as follows:
A: 6.5 m/s, 20 kg/m^{2}s; B: 9.0 m/s, 20 kg/m^{2}s; C: 6.5 m/s, 60 kg/m^{2}s; D: 9.0 m/s, 60 kg/m^{2}s
[b]secondary-to-primary air ratio
[c]AP = axial pressure profile; CP = capacitance probe traverse; SS = solids sampling

for Runs 1, 4 and 5 allowed the influence of riser geometry to be distinguished. Radial solids distributions were measured near the base for Runs 1 and 4 and near the exit in Runs 1 and 5. In all three runs, radial distribution of solids was measured approximately half way up the riser. Each radial traverse was performed in a horizontal plane, through the axial centreline of the riser from wall to wall. More measurements were made near the riser walls as it was anticipated that solids concentrations would change most abruptly in this region. Two horizontal traverses, perpendicular to one another, were performed when measurements were made near the exit or base.

In Runs 1, 6, 7 and 8 the effects of secondary air injection were investigated. The secondary-to-primary air ratios and method of secondary air injection are given in Table 6.2. In Runs 9, 10 and 11 the performance of the unit was assessed with the different sands. Measured apparent suspension density profiles were used to estimate solids hold-up in the secondary air and sand runs.

In an additional test, the probe was located at the wall, mid-way up the column. The output

of the pressure transducer that measured the pressure across the solids inlet tee and the probe were simultaneously logged at 100 Hz. By adjusting the split of L-valve air to the two aeration points a "stick-slip" flow in the standpipe was initiated. The differential pressure transducer detected the pulses in solids entering the unit. Auto- and cross-correlation analysis of the two signals was performed to determine if the behaviour of the solids at the riser wall is affected by the fluctuations in solids hold-up at the base of the riser.

6.3 Results and Discussion

6.3.1 Interpretation of Differential Pressure Results

In general, the apparent suspension density profiles were similar to those obtained in earlier CFB studies (e.g. Arena *et al.*, 1986; Brereton, 1987; Bader *et al.*; 1988). The profiles exhibited an initial rapid decay over the lower 1–3 m of the riser. Above this height the suspension density was approximately constant for about 4 m. Over the top 1–2 m a sharp increase in density was observed when the abrupt exit was in place. With the smooth exit the suspension densities towards the exit were similar to those in the mid-section of the riser.

For all runs, each condition was repeated several times to determine the reproducibility of the data. Figure 6.10 shows a typical set of profiles. These profiles were obtained in Run 1 with a solids circulation of 20 kg/m^{2}s and a gas velocity of 6.5 m/s (condition A). Prior to logging each of the profiles shown, the unit was shut down, and the test conditions then re-established. All profiles in Figure 6.10 are similar. Similar concordance of profiles was obtained in all runs. For profiles taken under nominally the same conditions the spread of the data at a given height was typically less than 25% of the mean value. However, the spread was more significant near the abrupt exit when in use. The curves fitted to the data points in Figure 6.10 are smoothed splines, computed by the DISSPLA graphics package (Computer Associates, N.Y.). This method was used to fit curves to all experimental density profiles presented in this study.

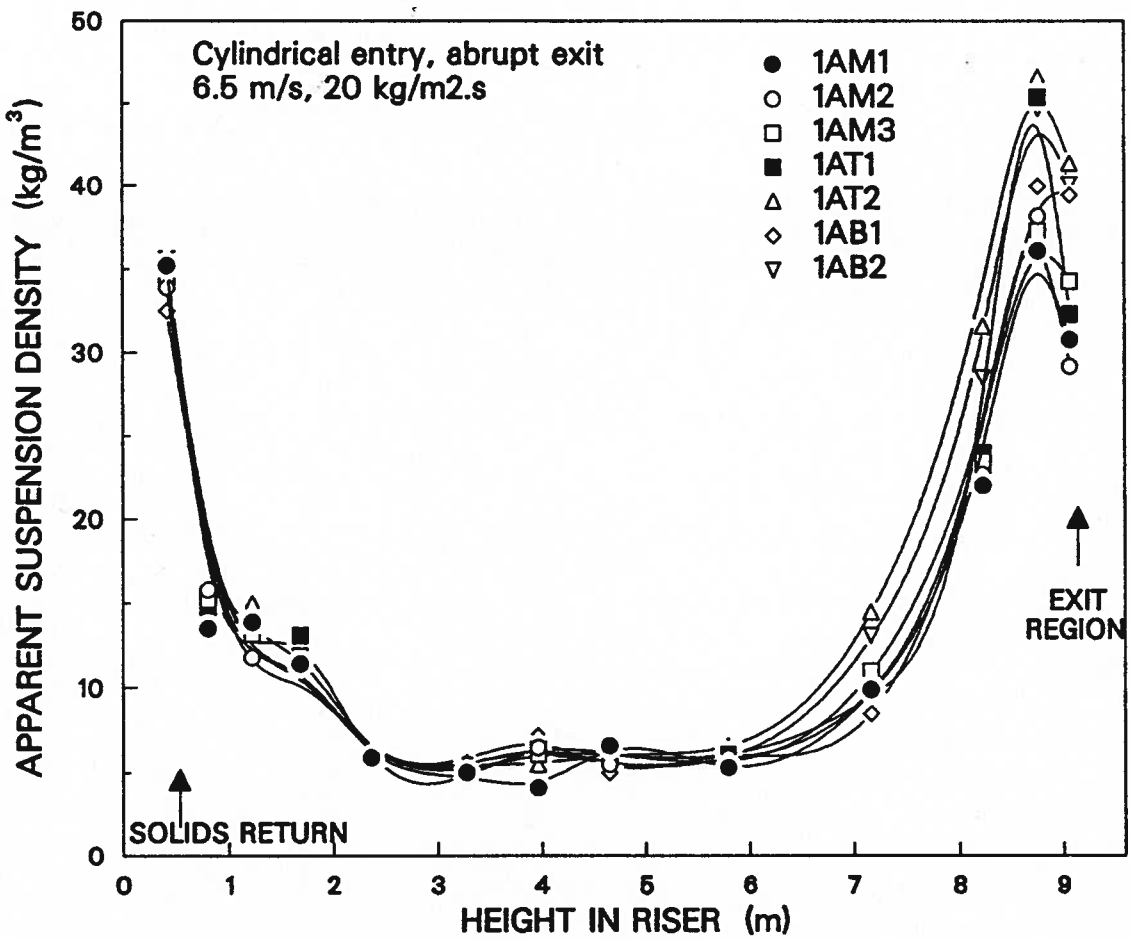

Figure 6.10: Example of the reproducibility of the experimental pressure profiles: apparent suspension density profiles measured for the seven repetitions of Run 1, condition A.

6.3.2 Analysis of Capacitance Probe Data

Two typical capacitance probe traces are plotted in Figure 6.11. Both traces were obtained for Run 1, condition C, with the probe located in the lower position, just below the solids return. The upper trace (a) was obtained with the probe tip at the riser wall, and the lower trace (b) with the probe tip in the centre of the riser. The probe voltage output is proportional to the solids concentration. Comparison of the two traces indicates that, in this case, the wall region contains a significantly higher concentration of solids than the riser core and that the solids concentration fluctuates considerably in the wall region.

Whenever dense downflowing sheets or "streamers" of particles were observed through the transparent riser wall, wall probe traces similar to Figure 6.11(a) were obtained. In the absence of solids downflow at the walls, the wall traces appeared more like those in Figure 6.11(b). In such cases, a rapid dilute suspension upflow across the entire riser cross-section was observed through the transparent riser walls. At the higher solids circulation rate (60 kg/m^{2}s), some denser solids structures were intermittently detected in the centre of the riser when the probe was located at the lower level near the base of the column. In such cases, the dense wall layer at this height was substantially thicker. Although the cross-sectionally averaged solids concentrations varied considerably with operating conditions, whenever dense sheets of solids were observed at the riser wall, capacitance probe traverses confirmed that solids were distributed radially between a relatively dilute core and a denser annular wall layer.

To obtain the time-averaged solids concentration for each trace, a baseline was fitted to the trace, which was assumed to correspond to zero solids volume. The area under the trace was then found by integration, and divided by the total sampling time to give the average voltage. This voltage was converted to solids concentration using the proportionality factor obtained from probe calibration (typically 5.3 volt/vol. fraction solids). This factor remained relatively constant ($\pm 5\%$) with subsequent probe recalibrations. When repositioning the probe between measurements, small shifts in the baseline voltage were sometimes observed. This appeared to be due to minor changes in fixed probe capacitance caused by slight flexing of the probe between

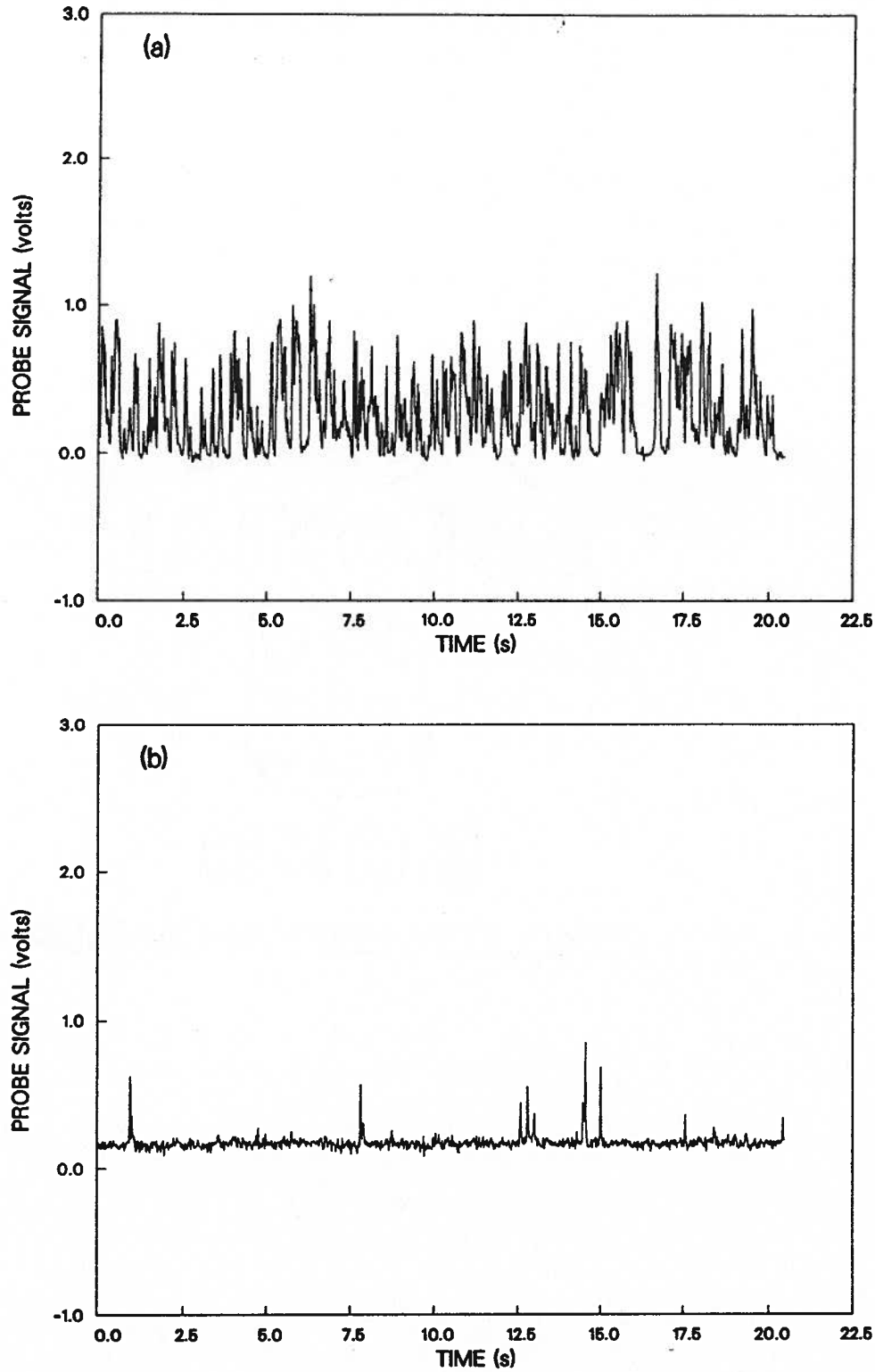

Figure 6.11: Typical traces produced by the capacitance probe with its tip (a) at the riser wall and (b) at the centre of the riser.

the tightly clamped non-measurement end of the probe and the riser wall fitting through which the probe passed. No problems were encountered with baseline shift during measurements at a fixed probe position.

There were two limitations on the accuracy of the data obtained from the capacitance probe. Firstly, the probe measuring volume was of the order of 30 mm^3 around the probe tip (i.e. tip length 4 mm). The probe was incapable of identifying non-homogeneity within this volume, and thus only gave an average value of solids concentration for this volume. Consequently, when falling sheets or "streamers" of wall particles thinner than about 4 mm fell over the probe tip, the probe did not give a true reading of the voidage of these sheets. Secondly, the accuracy with which a zero baseline could be fitted to the trace corresponded to approximately ± 0.4 vol.% solids ($\pm$ 10 kg/m^3 for glass particles). This estimate was obtained by comparing the suspension density determined from probe results with the apparent suspension density at the same height when low suspension densities were present at the mid-level of the riser. For such cases, local non-homogeneity in solids distribution was neither visually observed nor detected by the probe, and the similar probe traces for all radial traverse positions indicated that the suspension was relatively uniform over the entire riser cross-section. When such conditions occur the apparent suspension density is likely to provide a reasonable estimate of the true solids hold-up (see Chapter 4). Although several numerical schemes were employed to fit the probe signal baseline, they generally produced similar results to visual fits. From a comparison of probe signal fluctuations with gas flow only and fluctuations with streamers passing over the probe tip, the signal-to-noise ratio of the probe was estimated to be $O(30)$.

At higher suspension densities (say > 60 kg/m^3), or in regions of substantial particle acceleration, the "probe" suspension densities, with an estimated absolute error of ± 10 kg/m^3, are likely to provide superior estimates of the true suspension density in comparison to the apparent suspension density. This is assumed to be the case for densities measured near the entry and abrupt exit in this study. Also, as an additional comparison with the apparent and probe suspension densities measured at low G_s, a "uniform flow" suspension density ρ_{su} is calculated

at the riser mid-level. For these cases it is known from probe measurements that the mid-level suspension density was radially uniform and dilute (< 10 kg/m^3). The constant axial apparent suspension density profile at the mid-level in these cases indicated that the particles were fully accelerated. Therefore, ρ_{su} is calculated assuming negligible accelerative effects and estimating the average particle upward velocity, $\mathbf{v}$, to be equal to the superficial gas velocity U_g minus the terminal velocity of the Sauter mean particle size, $\mathbf{v}_t$, i.e.

$$\rho_{su} = \frac{G_s}{\mathbf{v}} + \frac{2 f_g \rho_g U_g^2}{g\, D} \tag{6.1}$$

Although gas-wall friction is allowed for, particle-wall friction is neglected. Numerical simulations of the suspension dynamics at mid-level in Chapter 8 indicate that this is reasonable for low riser suspension densities. The gas-wall Fanning friction factor is computed in the standard manner for single phase gas flow in a pipe. Capacitance probe results are discussed fully in the sections on exit and entry effects.

6.3.3 Entrance Effects

At low solids circulation rates, suspension densities between the primary air distributor and the solids entry tee were sufficiently low to allow visual observation of solids flow patterns in this riser region. The observed flow pattern is sketched in Figure 6.12. The solids in the L-valve horizontal section intermittently slipped down the surface of the packed bed advancing towards the riser. The initial trajectory of the dense packets of solids entering the riser was therefore determined by the angle of the surface of the advancing packed bed. Accelerated by gravity, these packets travelled downwards in a parabolic arc until they contacted the wall opposite the entry tee. On contacting this wall, the feed solids joined a downflowing wall solids stream moving towards the primary air distributor. As this solids stream fell, particles were stripped from it into a rapid dilute suspension upflow. The particles that fell as far as the distributor flowed across the distributor plate, where they were rapidly entrained by the high velocity air jets entering through the distributor plate holes. When operating at high U_g and low G_s

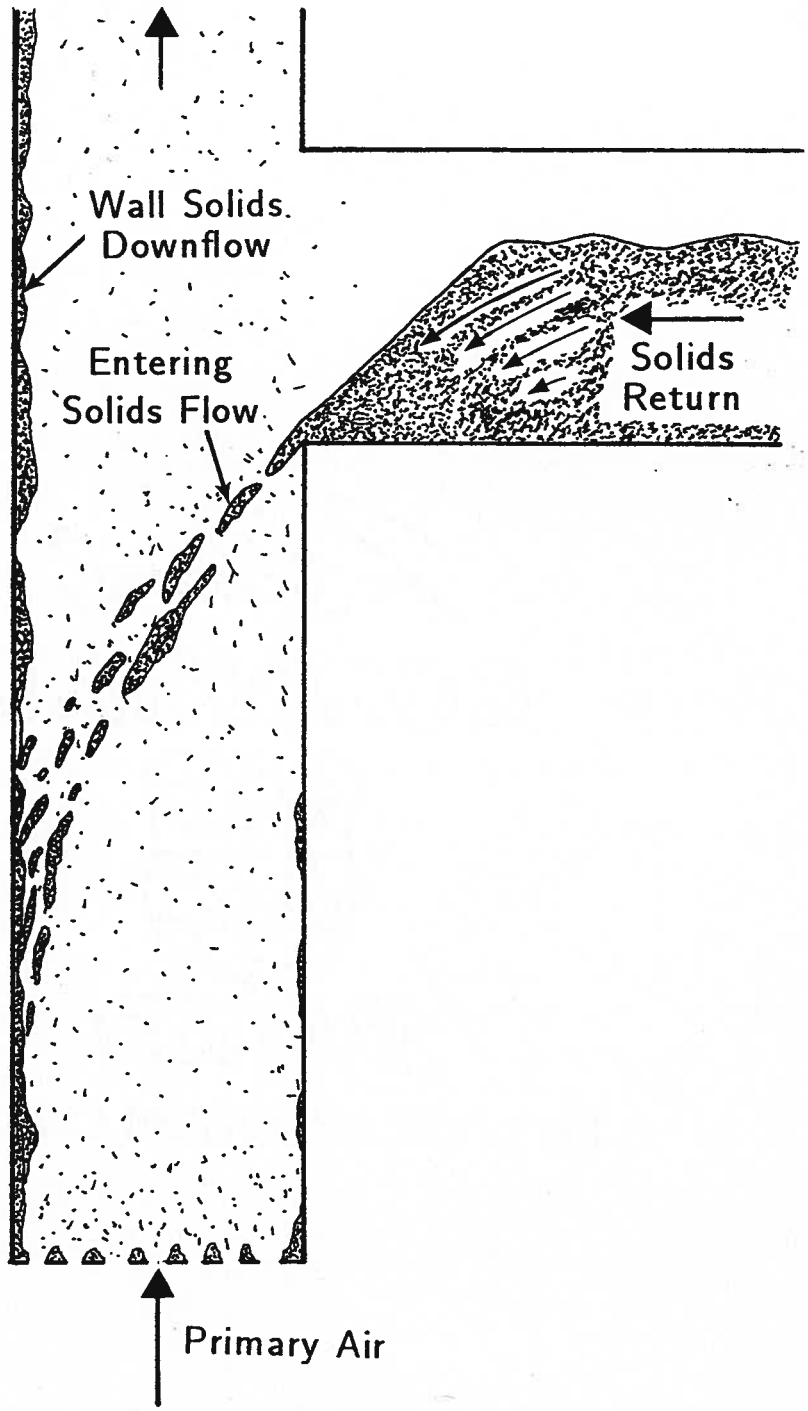

Figure 6.12: Observed flow pattern of solids in the entry region of the riser for low (20 kg/m^{2}s) solids return flux.

(condition B) with the conical entry section in place, the falling solids were completely stripped from the wall before they reached the distributor. Presumably, this was due to the higher gas velocities resulting from the reduced cross-section of the conical section.

Several important conclusions pertinent to design and modelling may be drawn from these simple qualitative observations. Dense clumps of solids introduced into the riser do not break up rapidly into a dilute suspension and accelerate up the riser. Instead, they accelerate downwards with a finite entrainment of individual particles or small clumps of particles from their surface. Consequently, for modelling purposes, it may be assumed that all entering solids initially move downward. The arc which the entering solids transcribe suggests that in a larger column the solids would not impact upon the opposite wall, but would fall within the central area of the riser. Solids entry geometries may be designed to improve feed solids dispersion. Feed solids could be introduced through downwardly angled ramps which direct solids towards different areas on the distributor, thereby improving radial distribution of solids. Vanes within these ramps could split the solids into smaller streams that disperse more rapidly upon entering the riser.

The apparent suspension density profiles for the cylindrical entry (Run 1) and conical entry (Run 4) are plotted in Figure 6.13[1]. By interpolating between time-averaged solids concentration data for perpendicular capacitance probe traverses, three-dimensional plots of solids concentration as a function of cross-sectional riser position were constructed. Figures 6.14 and 6.15 show these plots for the lower probe position for Runs 1 and 4, respectively. The cross-sectionally averaged "probe" suspension density at each height that a probe traverse was performed was estimated for each operating condition by integrating the respective concentration data over the full riser cross-section. Table 6.3 gives a comparison of these densities and the apparent suspension densities derived from pressure measurements for the lower and middle probe traverse positions.

[1]Note that "part profile" in the figure captions indicates that the ordinate scale has been reduced to improve resolution of the profiles above the dense lower region. The data points corresponding to high suspension densities in the base of the riser are generally off-scale in a "part profile".

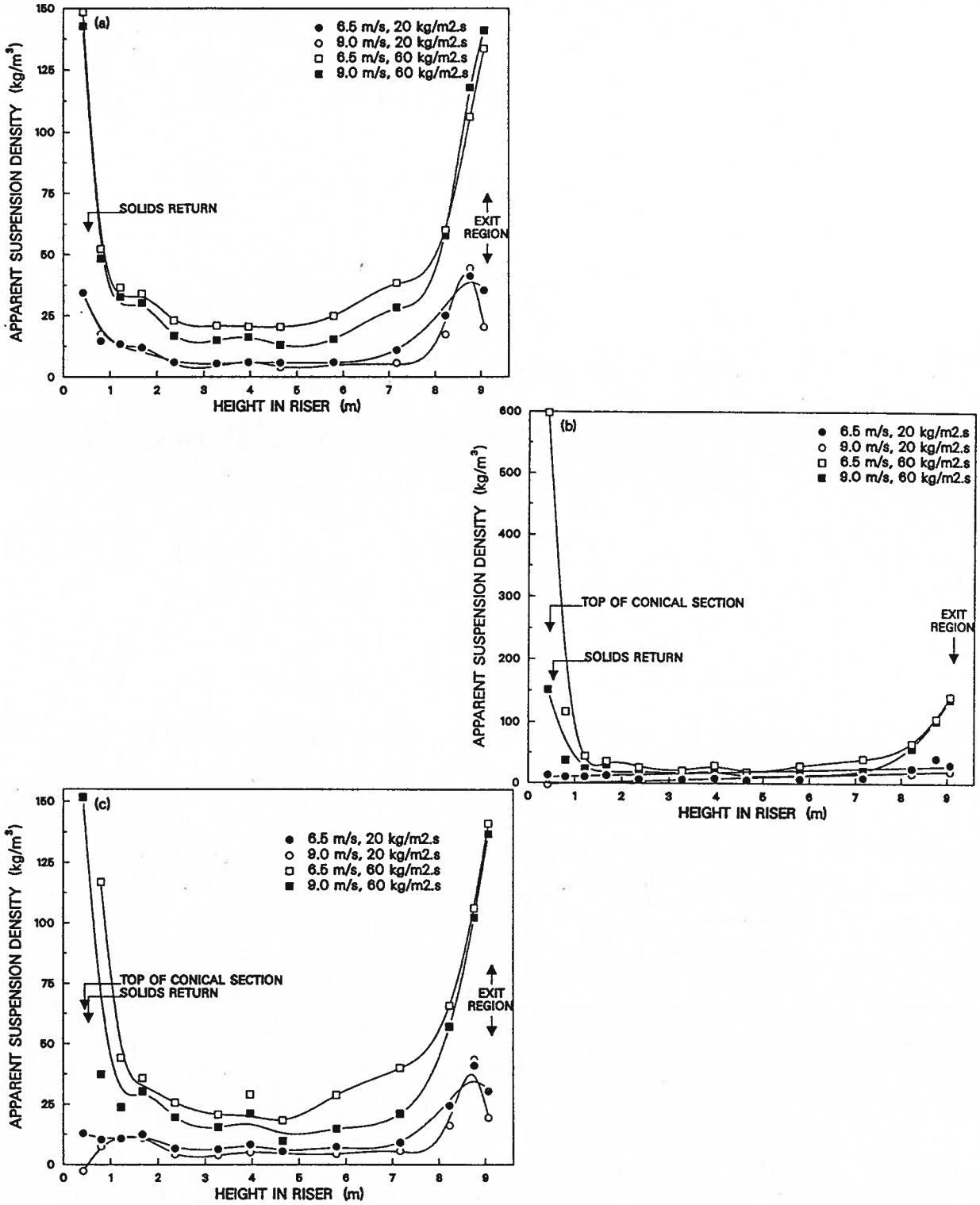

Figure 6.13: Apparent suspension density profiles for abrupt exit and (a) cylindrical entry (Run 1), (b) conical entry (full profile, Run 4) and (c) conical entry (part profile, Run 4).

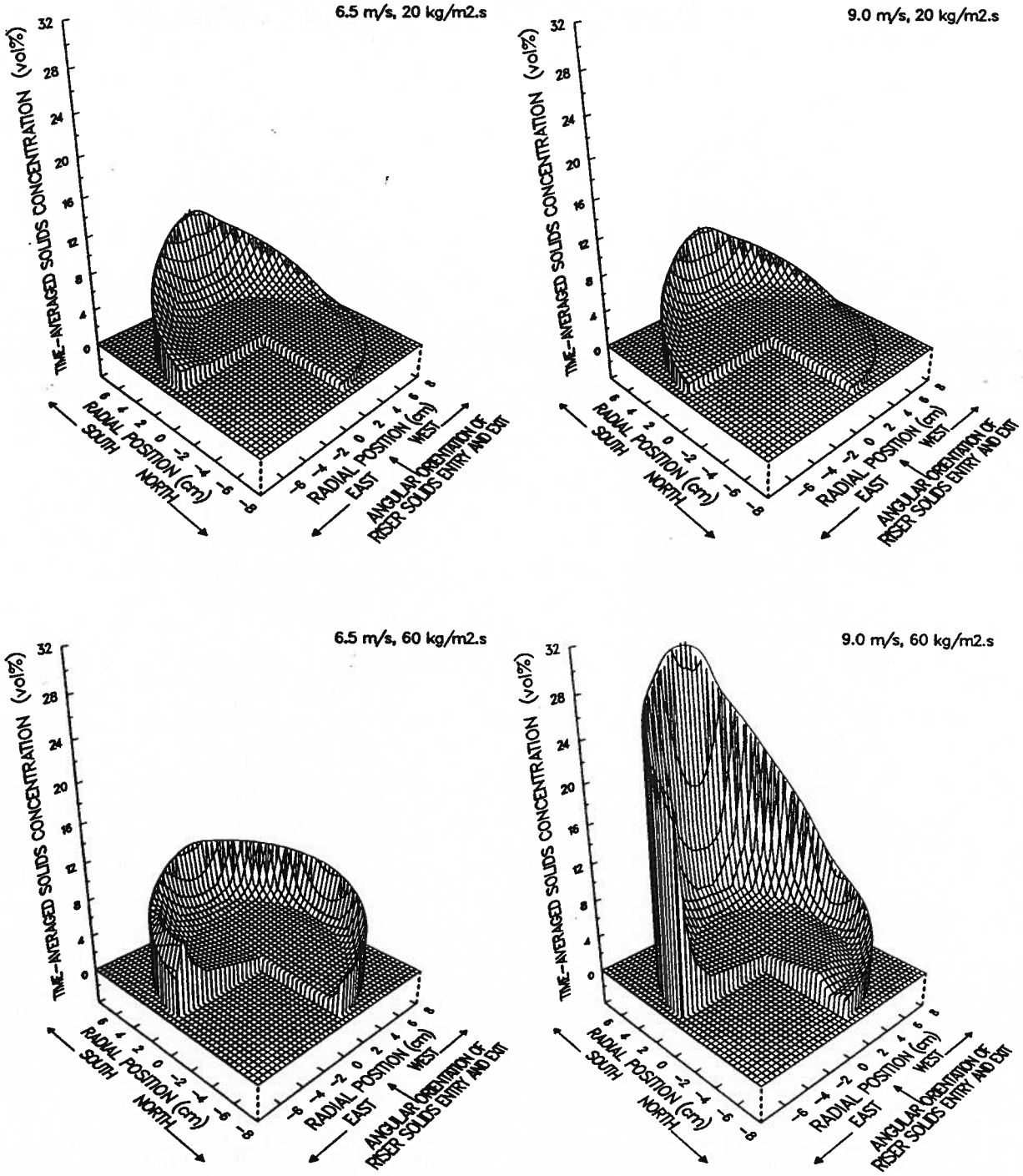

Figure 6.14: Measured radial solids concentration profiles for Run 1 (cylindrical entry, abrupt exit) at the lower probe position (229 mm above the distributor).

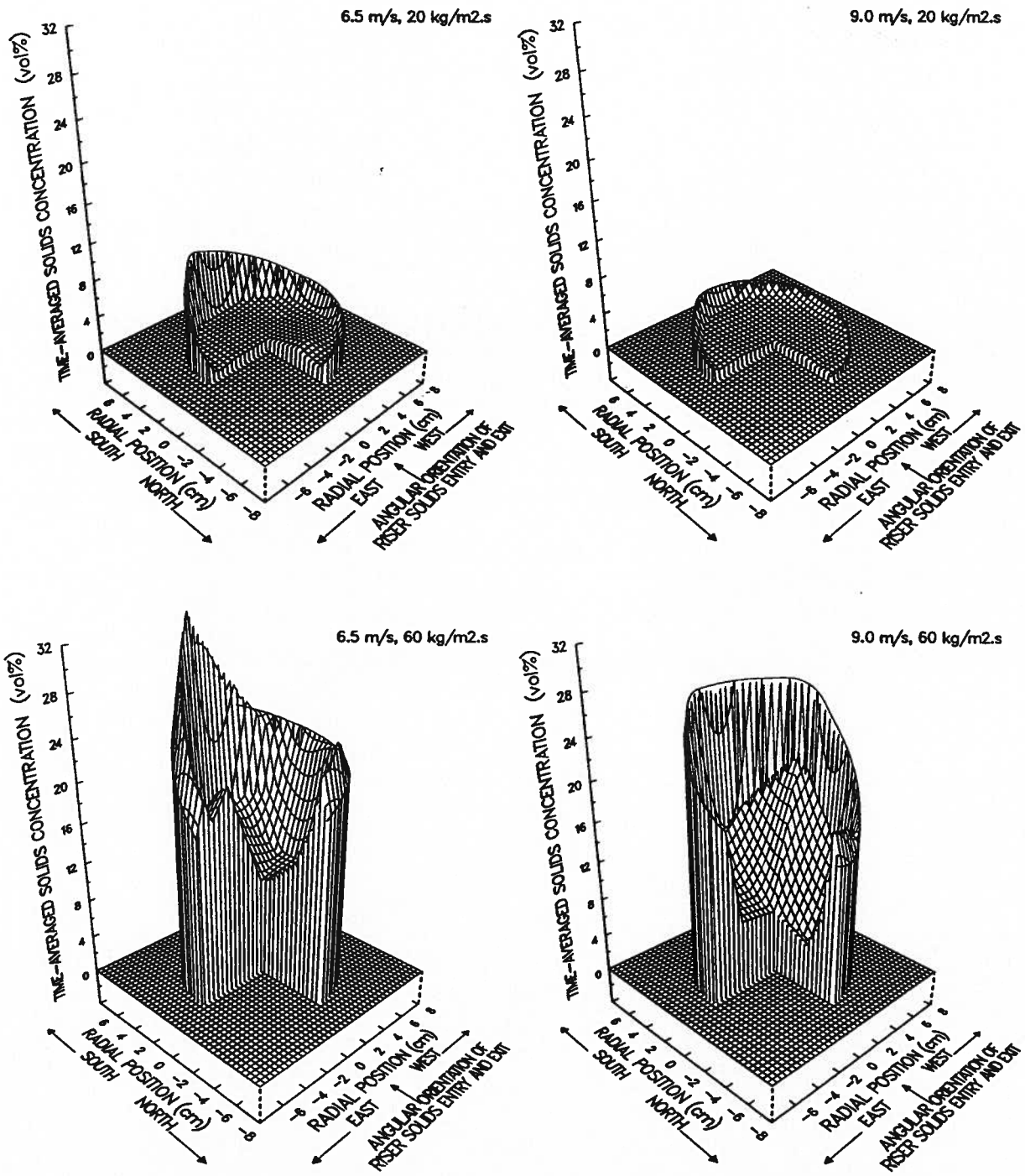

Figure 6.15: Measured radial solids concentration profiles for Run 4 (conical entry, abrupt exit) at the lower probe position (229 mm above the distributor).

Table 6.3: Comparison of suspension density estimates at lower and middle probe positions given by (i) differential pressure measurements (apparent suspension density), (ii) integration of capacitance probe data, and (iii) uniform dilute suspension upflow assumption (when applicable).

ENTRY GEOMETRY	CONDITION (see Table 6.2)	LOWER POSITION Density (kg/m^3)		MIDDLE POSITION Density (kg/m^3)		
		Apparent	Probe	Apparent	Probe	Uniform Flow
Cylindrical	A	34	50	6	8	5
Cylindrical	B	35	42	5	7	4
Cylindrical	C	148	85	20	27	–
Cylindrical	D	143	139	15	21	–
Conical	A	13	52	8	–	–
Conical	B	−3	37	7	–	–
Conical	C	598	454	22	16	–
Conical	D	152	339	16	16	–

In Run 1 a core-annulus solids flow structure was present over the lower and upper sections of the riser for all four conditions. However, there were very few wall streamers observed over the central sections of the riser when operating at the lower solids circulation of 20 kg/m^{2}s. At this solids circulation, the apparent suspension densities for both gas velocities were similar below a height of 7 m (Figure 6.13) suggesting that a slight decrease in solids hold-up over this height, likely to result from a higher gas velocity, was partially compensated for by an increase in gas-wall friction. At the higher G_s the solids hold-up in the riser was greater for U_g = 6.5 m/s than for U_g = 9.0 m/s. At G_s = 60 kg/m^{2}s and U_g = 6.5 m/s substantial wall solids downflow was observed mid-way up the column, whereas at G_s = 60 kg/m^{2}s and U_g = 9.0 m/s only thin "wisps" of streamers appeared at these heights. Similar intermediate level trends were observed when operating the riser with the conical base section (Run 4, Figure 6.13).

The apparent suspension density profiles for the conical base run exhibit some interesting effects near the bottom of the riser. At G_s = 20 kg/m^{2}s, the normal decaying profile is not observed. In fact, for condition B (9.0 m/s, 20 kg/m^{2}s) the apparent density is negative near

the base of the riser. This may be explained if separation of gas flow and formation of gas eddies occurs at the riser walls at this height. As the measured pressure is the riser pressure at the wall, a rapid downflow of gas at the wall would result in an increase in measured pressure with riser height. When the riser was operated with only gas flow through it, positive pressure gradients equivalent to negative apparent suspension densities were measured within 1 m of the distributor. This may be interpreted as a gas flow "entry length". This effect was far more pronounced with the conical entry in place than with the full area entry section. The pressure transducers were repeatedly checked to ensure they correctly zeroed with no gas flow in the column. As a result of this effect, apparent suspension densities in this region may significantly underestimate true solids hold-up. Table 6.3 supports this assertion for the conical base tests, for conditions A, B and D. For each of these cases the estimate of solids hold-up derived from capacitance probe traverses is significantly higher than the apparent suspension density derived from pressure profiles for the same conditions.

The conical entry section is generally assumed to be a design which enhances mixing and entrainment of downflowing solids into a rapid upflow by substantially increasing gas velocities just above the distributor in a region of reduced cross-section. Consequently, at similar operating conditions, one would expect a lower solids hold-up in a conical base compared to a cylindrical base. However, at $G_s = 20$ kg/m^{2}s, the results in Table 6.3 show solids concentrations to be comparable for the two entry geometries. At $G_s = 60$ kg/m^{2}s, solids concentrations are significantly higher in the conical section. It appears that not only is gas velocity important in particle re-entrainment, but so too is the surface area of the denser solids structures from which entrainment occurs. Significantly lower downflowing wall streamer velocities were observed in the conical section in comparison to further up the column, presumably due to higher gas velocities and interfacial shear force at the wall streamer-core interface in this region. It is likely that there was a substantial reduction in this interfacial area in the conical section, with a lateral expansion of the streamers into the core, due to both the actual decrease in the total riser cross section and the associated deceleration of the wall streamers. It is postulated

that at higher G_s the initial reduction in wall streamer surface area created by the converging walls of the conical base has a greater impact on entrainment than the associated increase in gas velocity. Consequently, the net entrainment of particles from the wall into the core (i.e. entrainment/unit area $\times$ interfacial area) at first decreases, and the wall layer thickens substantially until much higher gas velocities are achieved and a new mass balance between wall downflow, entrainment and core upflow are established with a core of greatly reduced cross-section.

Comparison plots of the cylindrical and conical entry density profiles (Runs 1 and 4) are given in Figure 6.16. For condition C, with the conical section in use, a relatively dense turbulent fluidised bed was established in the bottom 1 m of the column. In this case, instantaneous capacitance probe measurements in this region indicated that the core contained a dilute suspension much of the time. Figure 6.17 shows the probe trace at the axis of the riser in the conical section. It is evident that solids concentration in this region alternates very quickly between high and low levels, with little time in which intermediate concentrations are present. A large relatively void volume containing rapid particle upflow was frequently observed visually, briefly appearing on a portion of the wall of the conical section during this test. The radial position of this volume fluctuated, with no apparent pattern. The repeated passing of the volume vertical interface over the probe tip could account for some of the fluctuation seen in the probe trace. In contrast, similar fluctuations in traces, representing the solids concentration in the core of a turbulent fluidised bed, have been attributed to the axial motion of small clumps or "clusters" of particles over the measuring probe tip by some investigators (e.g. Horio *et al.*, 1988 and Yerushalmi *et al.*, 1978). In agreement with the findings of Abed (1983) the time-averaged solids concentration in the core of the turbulent fluidised bed established in this study was observed to be still significantly lower than at the walls (Figure 6.15). In comparison with the conical section run, a core-annulus solids distribution typical of "fast fluidisation" was established for condition C in the cylindrical base section.

As shown in Table 6.3, the apparent suspension density was higher than the "probe" suspension density for condition C when the conical entry section was in use. This is opposite to

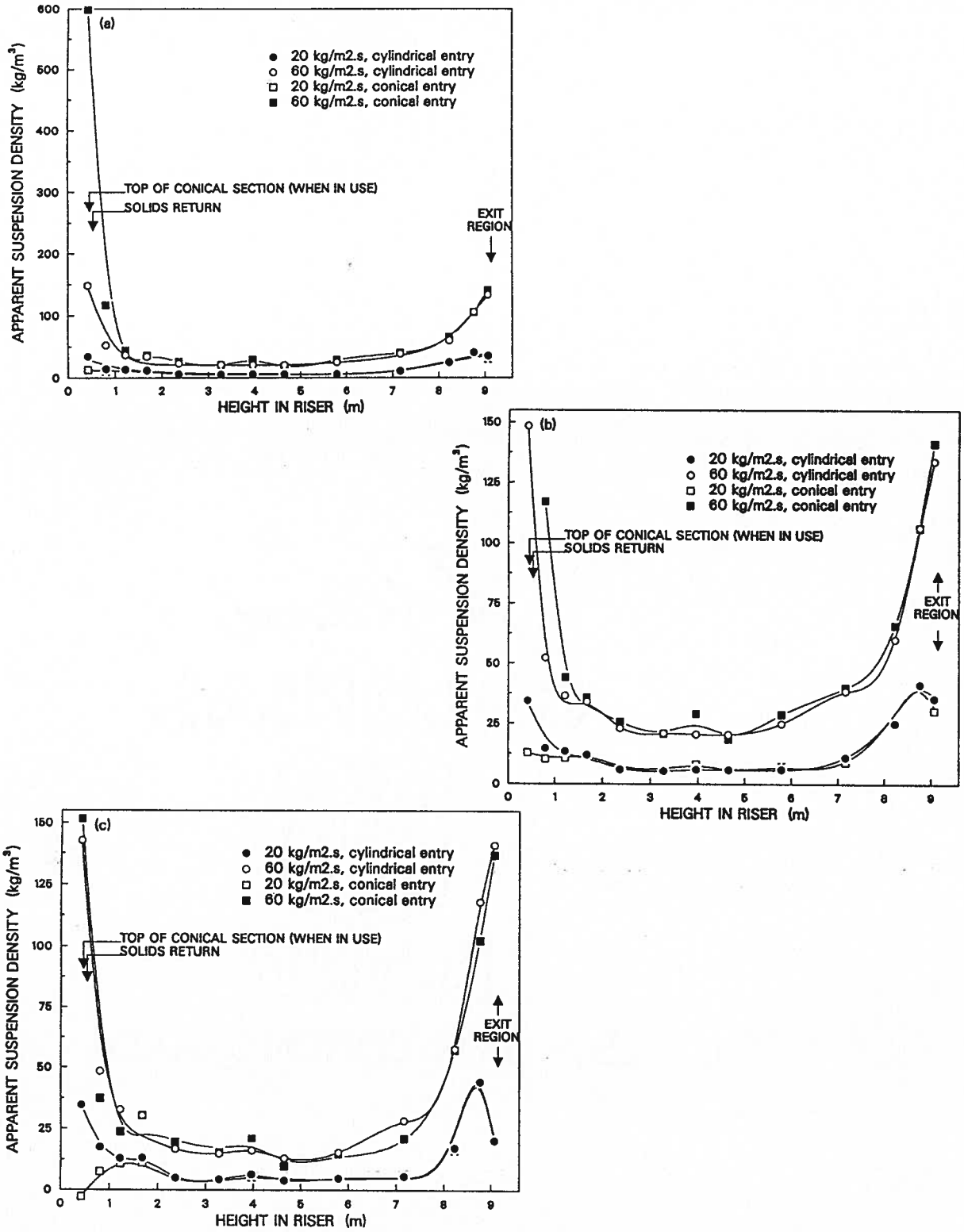

Figure 6.16: Comparison of apparent suspension density profiles for cylindrical and conical entry sections (Runs 1 and 4, abrupt exit): (a) $U_g = 6.5$ m/s (full profile), (b) $U_g = 6.5$ m/s (part profile), (c) $U_g = 9.0$ m/s.

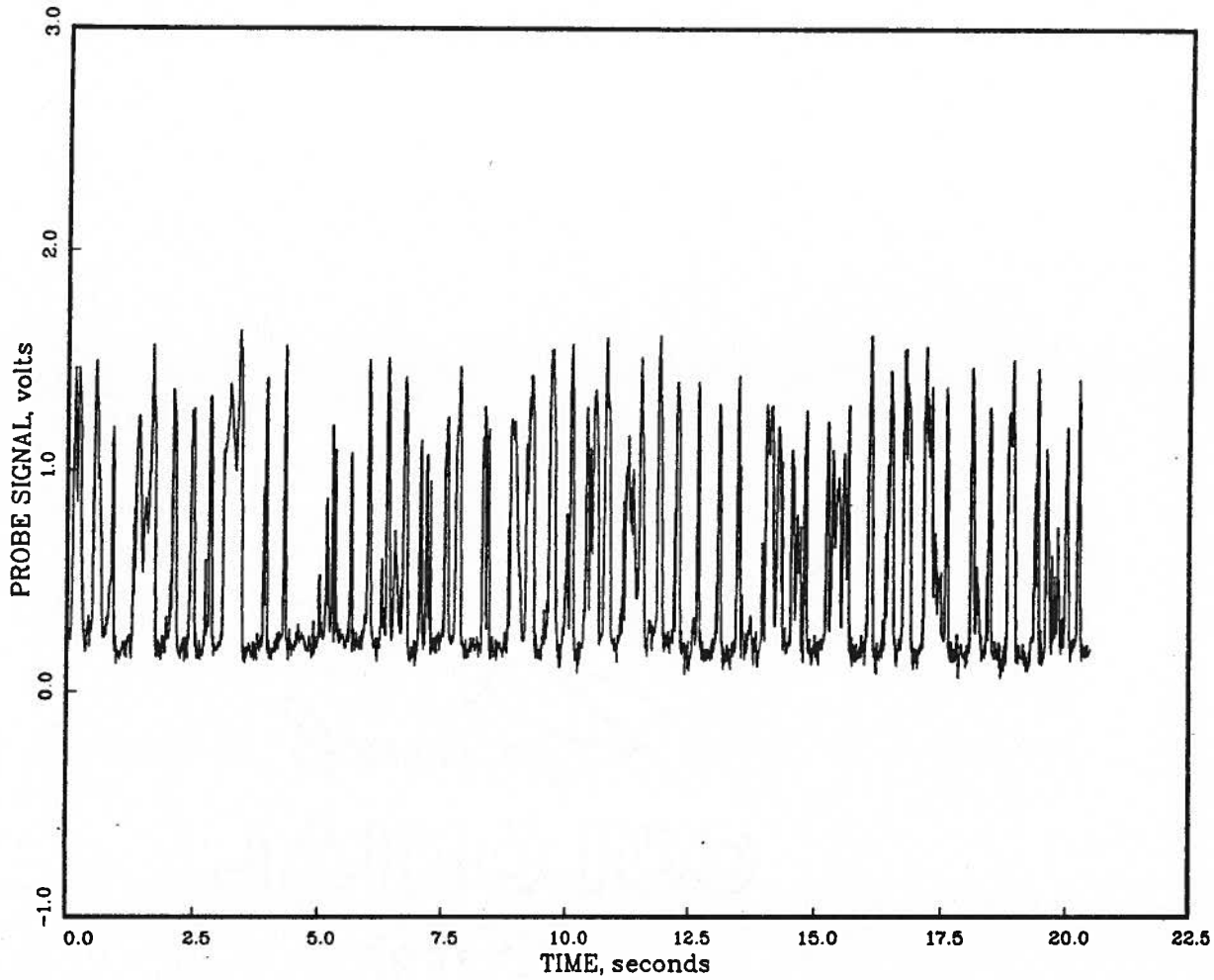

Figure 6.17: Capacitance probe trace for Run 4 (conical entry, abrupt exit), condition C, with the probe at the lower position, and the probe tip located at the centre of the riser.

observations for the other three conditions discussed previously. It is possible that the significantly higher solids concentration in the turbulent fluidised bed of condition C changes the gas flow patterns in the bottom of the column, and that gas flow separation does not occur in this case. An anomaly in Table 6.3, for which no explanation has yet been identified, is that the "probe" suspension density is higher for condition C than D for the cylindrical entry test. Intuitively one would expect a higher gas velocity to give lower solids concentrations. The solids concentration plot (Figure 6.14) shows a very high solids concentration on the wall opposite the entry for condition D.

In addition to the possible effects of entry region gas flow patterns discussed, particle acceleration effects, discussed in Chapter 4, may also have influenced measured pressure gradients in the riser entry region. In contrast to the effects of gas recirculating flow at the riser wall, particle acceleration results in higher measured pressure drops than one would expect due to solid hold-up alone. A possible further complication is that the location of the pressure taps on the riser circumference may also influence measured results when there is asymmetry in gas flow about the riser centreline, created by an asymmetry in solids re-entry. The test results indicate that apparent suspension density, based on wall tap pressure measurements, is only a very crude estimate of the true suspension density within approximately 1 m of the primary air distributor. It may grossly under- or over-estimate true solids hold-up depending on operating conditions and the geometry of the bottom of the riser. This result is important for riser reaction modelling because a significant portion of the total riser solids inventory is typically contained in this lower region and apparent suspension density is often equated with true suspension density when collecting data for such models.

The mid-height densities for each condition are in good agreement (Table 6.3), suggesting that in the middle section of the riser the apparent suspension density is a reasonable estimate of the true cross-sectionally averaged solids hold-up. This conclusion is consistent with the findings of Arena *et al.* (1986) and Hartge *et al.* (1986). Arena *et al.* (1986) compared solids hold-ups in a 41 mm ID, 6.4 m high riser column that were estimated both from pressure drop

measurements and from the mass of solids captured by a set of quick-closing valves. Good agreement between the methods was obtained at heights where average solids volume fractions were lower than approximately 0.04. Similarly, Hartge *et al.* (1986) obtained good agreement between γ-ray and pressure drop estimates of solids hold-up for solids volume fractions less than approximately 0.06. At higher solids volume fractions, typically found in the bottom section of the riser, both investigators reported differences in the results from their two methods of estimation. In this study solids volume fractions over the middle riser heights (approximately between $z = 1.5$ and $z = 7.5$ m) were less than 0.04.

An important observation from the density profile comparison plots for riser entry effect runs (Figure 6.16) is that, irrespective of the geometry used, at the same operating conditions the profiles are almost identical for $z > 1.5$ m. This observation is most noteworthy for condition C, where there were large differences in the solids hold-up and distribution in the entry section. These preliminary results suggest that the design of the CFB riser distributor and solids entry region generally does not greatly affect solids distribution in the middle and upper sections of the riser. This may not be true if the design and air blower characteristics lead to phenomena such as choking or slugging in the lower section. Bierl *et al.* (1980) also observed this apparent insensitivity of the middle and upper profile to the entry geometry. In their hydrodynamic investigation they employed two methods of solids return, both differing from those used in this study.

The plots of solids concentration as a function of cross-sectional position near the base of the riser (Figures 6.14 and 6.15) show extensive asymmetry in solids distribution. For all conditions and both geometries the solids concentration was much higher on the wall opposite the solids entry (south wall) than on the side of the solids entry (north wall). This is consistent with visual observations of solids flow patterns described earlier. Mid-way up the riser probe traverses did not detect any asymmetry in radial solids distribution about the riser axis, despite the maldistribution of solids at the riser base.

6.3.4 Exit Effects

The apparent suspension density profiles for the abrupt (Run 1) and smooth (Run 5) exits are given in Figures 6.13(a) and 6.18, respectively. Comparison plots of the profiles for the two runs appear in Figure 6.19. The three-dimensional cross-sectional solids concentration plots for the upper capacitance probe position (8763 mm above the distributor, 406 mm below the bottom of the exit) are plotted in Figures 6.20 and 6.21.

With the abrupt exit, the rapid core upflow resulted in a packed layer of solids on the roof of the riser. Solids in this layer moved radially outwards to the walls. Upon reaching the vertical riser walls, these solids then accelerated downwards. The wall solids initially fell from the roof as a continuous layer that covered the wall, but within 0.5 to 1.0 m below the riser exit disturbances to this layer were evident and rapid dilute suspension upflow could be seen intermittently on small areas of the wall. The apparent and "probe" suspension densities just below the abrupt exit are given in Table 6.4. Both these densities were substantially higher than suspension densities further down the riser, indicating that a high proportion of solids in the upflow were reflected internally within the riser upon reaching the exit height, rather than successfully exiting the riser. Most of these reflected solids were then re-entrained into the core flow as they descended along the wall.

With the abrupt exit there was a significant turndown in the apparent suspension density profile within 0.5 m of the riser exit for $G_s = 20$ kg/m^{2}s (conditions A and B). It is possible that a large gas eddy in the exit region accelerated the wall solids downward in this region, a phenomenon similar to that described for the conical entry section. Figure 6.22 shows possible gas flow patterns in the exit region that could account for the observed density profiles. These gas patterns were proposed by Brereton (1987) following study of riser operation with the same exit geometry. Although Brereton did not report turndowns in the density profile close to the exit, this is probably because fewer pressure tap locations near the exit were used in that study. The variation of apparent suspension densities between repetitions of the same case was greater over the top 1 m of the riser than below this height (e.g. see Figure 6.10). This may

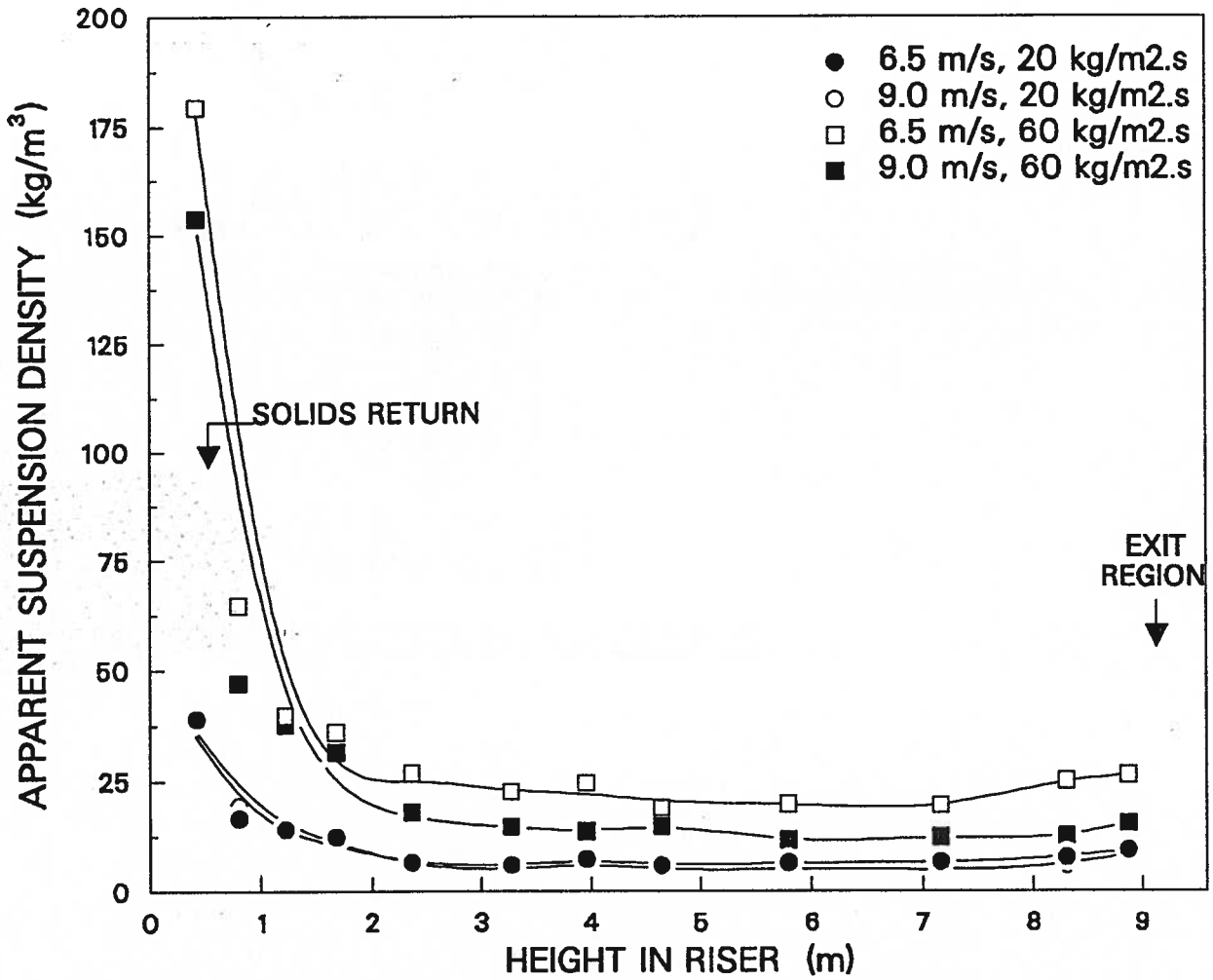

Figure 6.18: Apparent suspension density profiles for the smooth exit tests (Run 5, cylindrical entry).

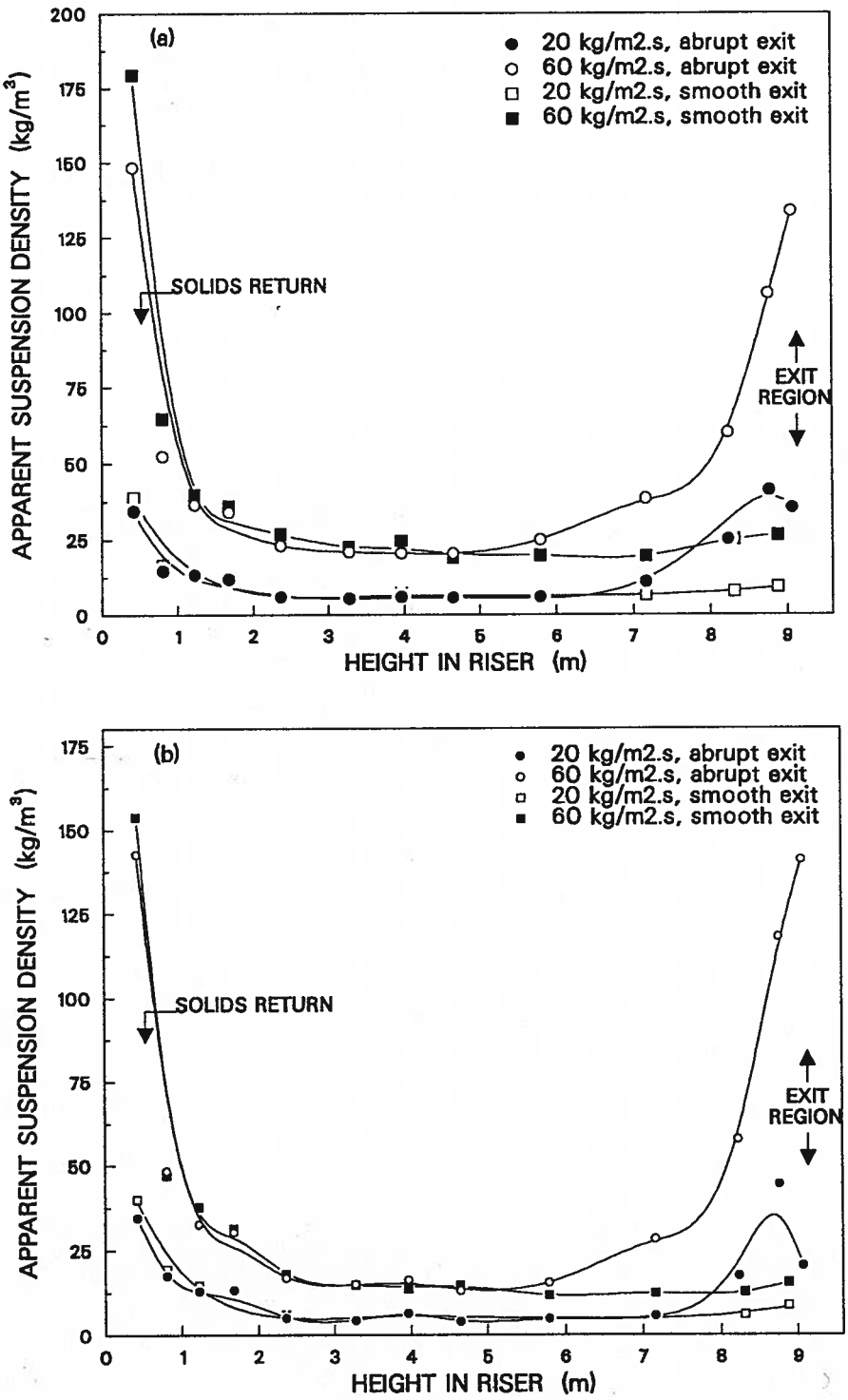

Figure 6.19: Comparison of the abrupt and smooth exit section apparent suspension density profiles (Runs 1 and 5, cylindrical entry): (a) $U_g = 6.5$ m/s, (b) $U_g = 9.0$ m/s.

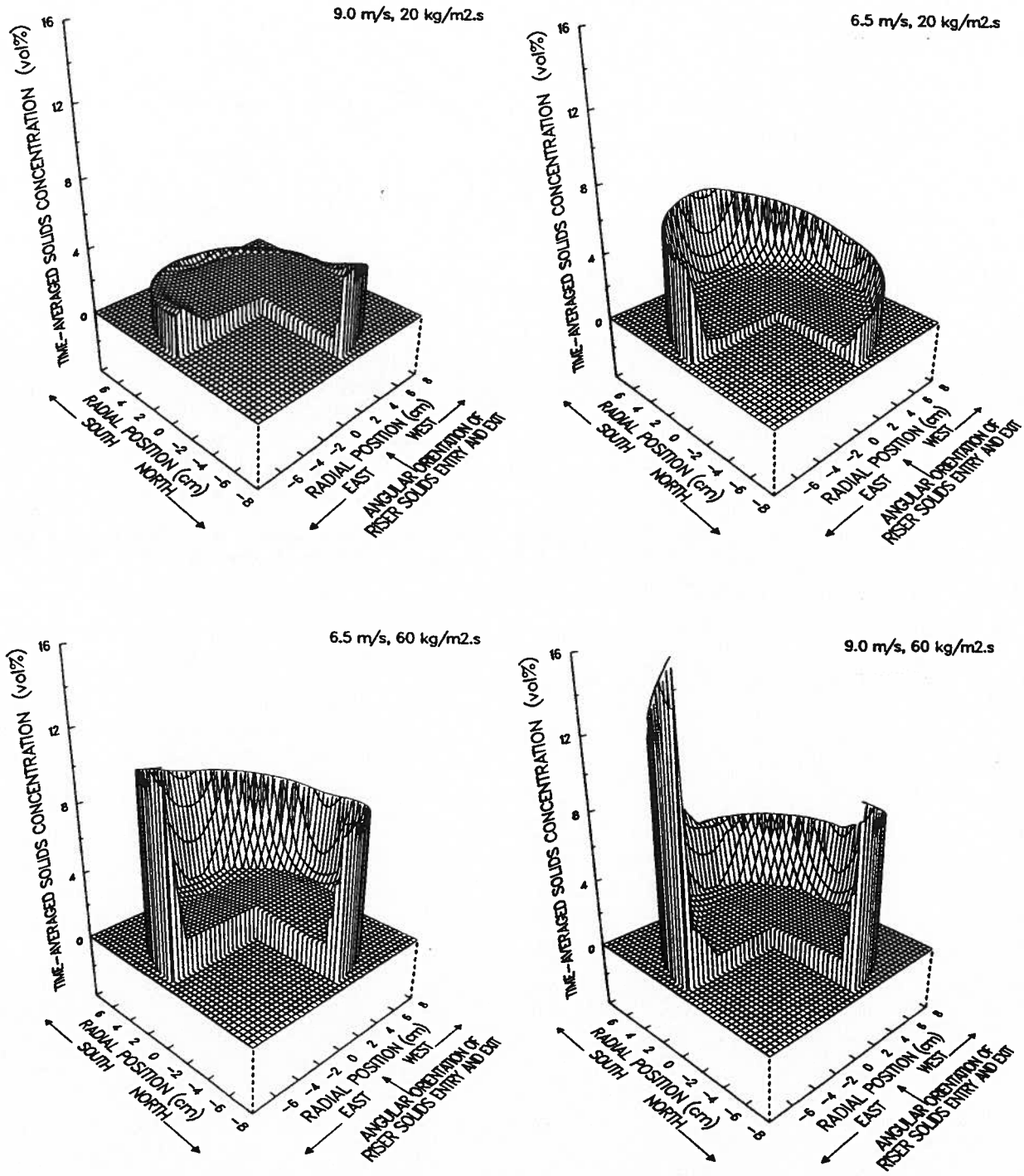

Figure 6.20: Measured radial solids concentration profiles for Run 1 (abrupt exit) at the upper probe position (8763 mm above the distributor).

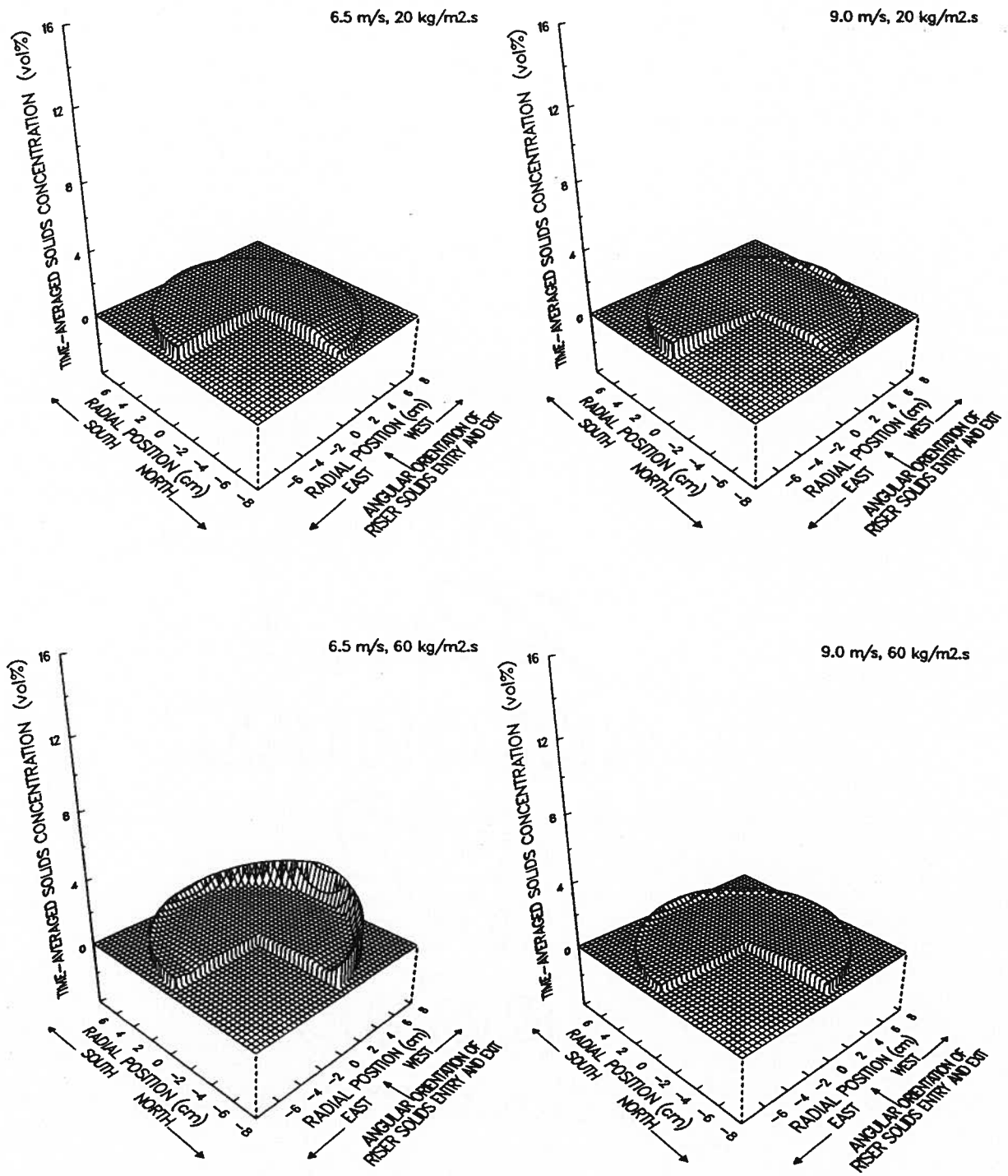

Figure 6.21: Measured radial solids concentration profiles for Run 5 (smooth exit) at the upper probe position (8763 mm above the distributor).

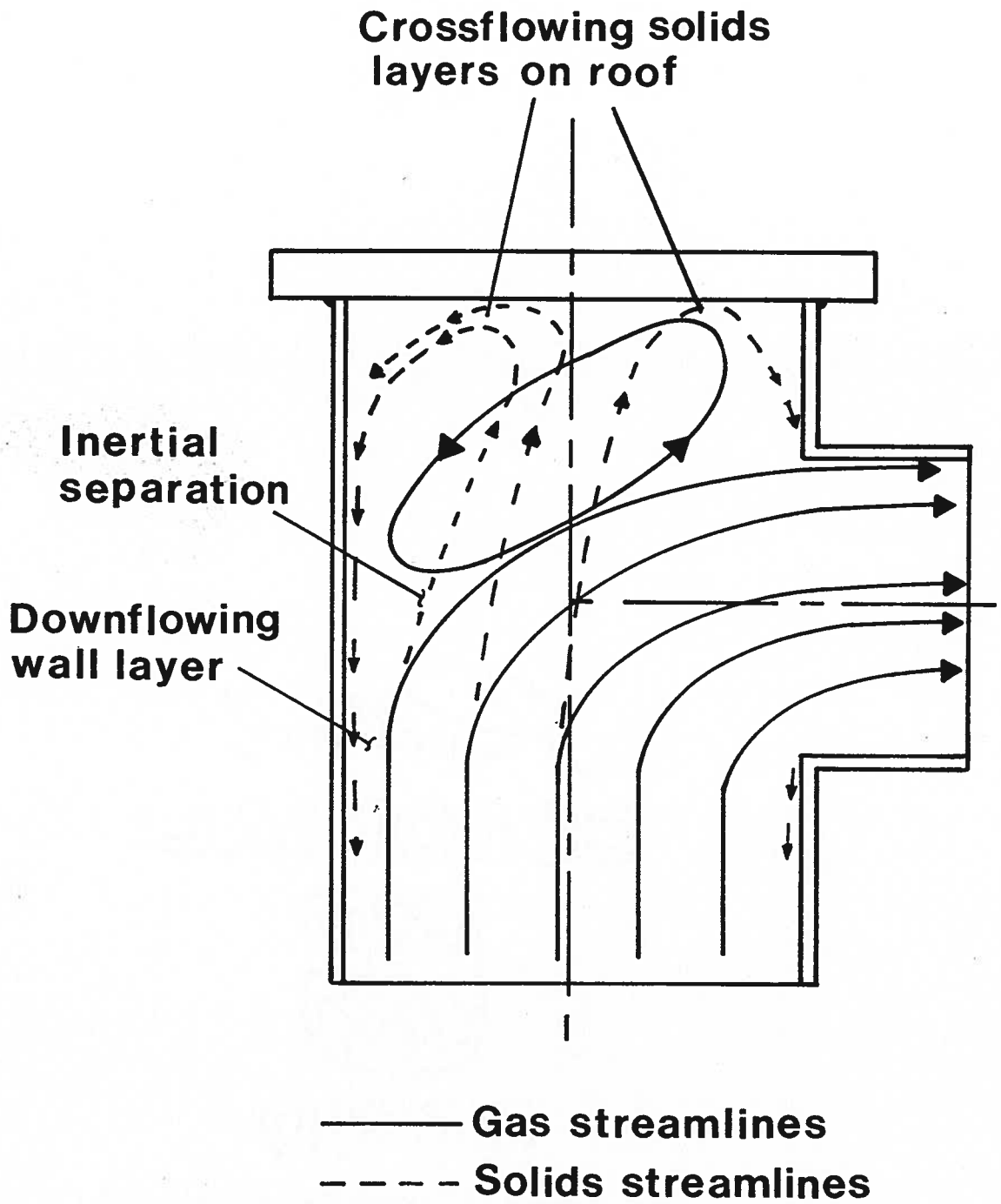

Figure 6.22: Possible gas flow patterns in the abrupt exit region proposed by Brereton (1987).

Table 6.4: Comparison of suspension density estimates at upper probe position given by (i) differential pressure measurements (apparent suspension density) and (ii) integration of capacitance probe data.

EXIT GEOMETRY	CONDITION (see Table 6.2)	UPPER PROBE POSITION Density (kg/m^3)	
		Apparent	Probe
Abrupt	A	41	36
Abrupt	B	44	34
Abrupt	C	106	84
Abrupt	D	118	75
Smooth	A	9	19
Smooth	B	8	13
Smooth	C	26	24
Smooth	D	15	14

have been caused by changes in the gas recirculation patterns near the exit, resulting from very small differences in the external solids recirculation or gas velocity between cases. This sensitivity was observed for profiles for all test runs when the abrupt exit was used. It should be noted that large changes in the apparent suspension density in the exit region for nominally the same conditions do not necessarily mean that the true solids hold-up in this region also varies substantially.

At G_s = 60 kg/m^{2}s the turndown of the suspension density profiles near the abrupt exit was no longer observed. For these two cases it is possible that the large re-entrainment rate of solids from the walls near the exit caused a significant pressure drop due to particle acceleration in the core. This assertion is supported by the data in Table 6.4. For G_s = 60 kg/m^{2}s with an abrupt exit, the apparent suspension density 0.4 m below the bottom of the exit is significantly greater than the true suspension density estimate from probe traverses. For the 20 kg/m^{2}s abrupt exit cases and for all smooth exit cases, the probe densities agree, within experimental error, with the apparent densities.

With the abrupt exit, the probe traverses 0.4 m below the bottom of the exit (upper probe position) detected a dense wall layer surrounding a dilute core, illustrated in Figure 6.20. The

core solids concentration was relatively uniform, and the core-annular wall region transition well defined. The maldistribution of solids around the circumference evident for condition D (9.0 m/s, 60 kg/m^{2}s) results from a single measurement at the east wall position, and therefore may not be significant. Some maldistribution around the riser perimeter is evident for conditions A, B and C. However, in contrast to the entry effect tests, there is no orientation where higher solids concentrations always occur. It was not possible to discern any solids maldistribution from visual observations. Changes in gas flow patterns around the exit may account for the observed changes in wall solids distribution between different conditions.

The solids concentrations for the smooth exit shown in Figure 6.21 are significantly lower than for the abrupt exit under equivalent conditions. This agrees with the trends observed in the apparent suspension density profile plots for the two exit geometries. With the smooth exit in place, the solids concentration was uniform across the entire riser for conditions A, B and D. However, some denser wall solids layers were detected for condition C (6.5 m/s, 60 kg/m^{2}s), suggesting that under some operating conditions even very smooth exits internally reflect a fraction of the upflowing solids back down the walls.

Comparison of apparent suspension density profiles for the two exits (Figure 6.19) demonstrates that, except within 3 m of the exit for the 60 kg/m^{2}s conditions and within 1.5 m for the 20 kg/m^{2}s conditions, the suspension density profiles coincide for the same condition. Thus, as was observed with the entry effect, the exit section geometry does not generally appear to affect the riser operation at all heights. Again, this agrees with the work of Bierl *et al.* (1980), who placed a sharp restriction to the riser flow just below the exit, and observed little change in the density profile within about 1.2 m of the exit. In contrast, Brereton (1987) reported a case where a significant difference in the entire density profile was measured for abrupt and smooth exits when running with sand. From the suspension densities given by Brereton, it appears that the riser base was operating close to the transition point to turbulent fluidisation with the smooth exit. Under the similar operating conditions with an abrupt exit, it is possible the small increase in wall solids downflow precipitated this transition, thus creating a turbulent

bed in the base of the riser.

The entry and exit regions of the riser may be viewed from a modelling perspective as boundary conditions that perturb the riser system away from some characteristic operating condition in the central riser heights. This operating condition may be assumed to be independent of entry and exit effects, but likely depends on many other variables such as operating conditions (e.g. solids circulation, superficial gas velocity and temperature) and properties of the particles (e.g. diameter, size distribution and density). If the entry or exit effect perturbation is large, it may be possible that the characteristic operating condition is not closely approached. The concept of a characteristic operating condition is used in a riser model discussed in Chapter 10. Exit and entry effects are further discussed in Chapter 9.

6.3.5 Effects of Secondary Air Addition

From a modelling viewpoint, secondary air injection may be considered as dividing the CFB riser into two separate systems: a high gas velocity riser above the secondary air ports ("secondary zone") and a lower gas flow region below the ports ("primary zone"). According to the qualitative description of solids flow patterns given in Chapter 2, several possible effects of secondary air injection may be postulated. Firstly, particles in dilute suspension travelling upwards, upon reaching the secondary air ports, should experience rapid upward acceleration due to the higher upward gas velocities created by the secondary air injection. This may result in a peak in the apparent suspension density profile that is not related to a change in the true solid hold-up near the ports. In addition, if there is substantial downflow of particles at the riser wall, then the secondary air injection may entrain some of these solids into the core suspension upflow. This would further enhance the particle acceleration effects and result in a real increase in solids hold-up near the secondary air ports. It would also reduce the wall downflow of solids into the primary zone and possibly cause a lower primary zone suspension density, and an associated lower upflux of solids from the primary zone. The overall effect on true solids hold-up just above the secondary air ports is likely a combination of all these effects.

In the first set of secondary air tests (Runs 6 and 7), secondary air was injected through opposed ports (Figure 6.5). In Run 6 the primary-to-secondary air ratio was set to 1:1 and all four conditions (A–D) were established. In Run 7 the primary-to-secondary air ratio was 2:1, and data were taken for conditions A and B ($G_s = 20$ kg/m^{2}s). The results from these tests were compared to Run 1 (no secondary air). The measured apparent suspension density profiles for Runs 1, 6 and 7 are plotted in Figure 6.23.

When operating at the lower solids circulation rate of 20 kg/m^{2}s, a negligible concentration of wall streamers was observed falling in the vicinity of or over the secondary air ports in Runs 1, 6 and 7. Despite this, the introduction of secondary air in Runs 6 and 7 produced a local peak in the apparent suspension density (i.e. differential pressure) profile at the height of the opposed secondary air ports. The peak was higher for a higher secondary air injection rate. As discussed in Chapter 4, gas inertia is generally significantly less than particle inertia in CFB risers. Therefore, the peak was likely due largely to the acceleration of upflowing core particles upon encountering the additional upward gas flow from the ports.

For operating condition D in Runs 1, 6 and 7, thin "streaks" of downflowing streamers were observed at the wall intermittently falling over the opposed secondary air ports. For condition C this downflow was substantial. At the 1:1 injection air ratio for condition C, a relatively dense turbulent fluidised bed was established over the bottom 1.0–1.5 m of the riser, as is evident from the suspension density profile (Figure 6.23). In this case the concentration of solids, particularly at the riser wall, was significantly higher than for other conditions with opposed flow, yet no peak in the profile was observed. This may be explained by the observation that wall streamers falling over the opposed air ports continued their downward motion, relatively undisturbed. Assuming that particle acceleration was a much smaller fraction of the total pressure drop for condition C due to the high concentration of solids at the wall, then the absence of a peak near the ports suggests that only a small fraction of wall solids are entrained into core upflow by opposed secondary air injection. Intuitively this seems reasonable, as one may expect from the direction of the opposed inflow that only wall solids that pass directly over the 25 mm

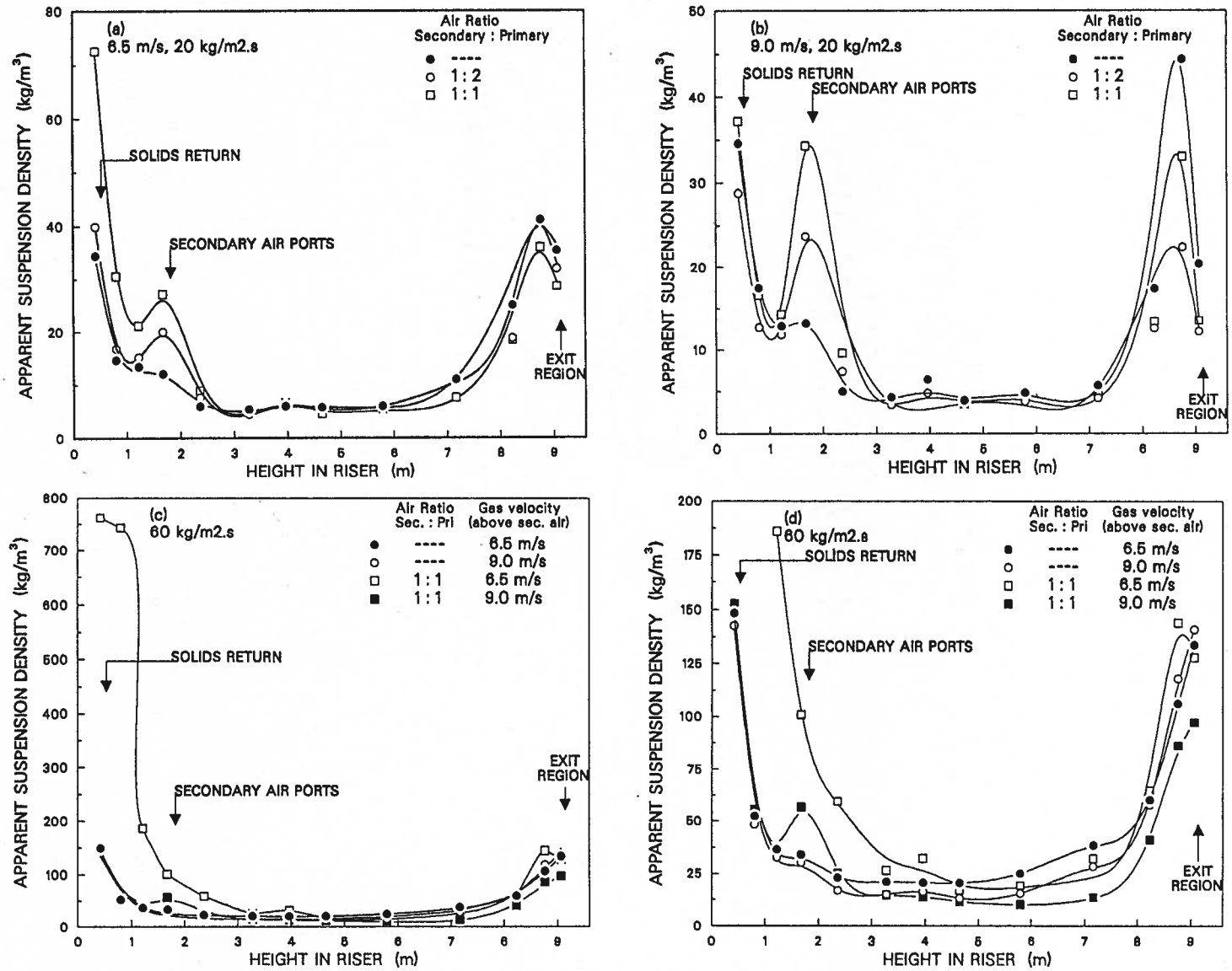

Figure 6.23: Comparison of the apparent density profiles for opposed secondary air injection tests (Runs 1, 6 and 7, abrupt exit): (a) condition A; (b) condition B; (c), (d) conditions C and D (full and part profiles).

diameter ports would be entrained. This assertion is strongly supported by noting that for the equivalent "swirl" flow created by tangential secondary air injection, a significant peak occurred in the apparent suspension density profile for condition C. In this case, although there was substantial downflow of wall solids in the middle heights of the riser, these solids were observed to be stripped off by the swirling air just above the tangential injection ports. A comparison of opposed air and swirl air injection run profiles (Runs 6 and 8) is given in Figure 6.24.

With opposed air injection, Figure 6.23 also demonstrates that, for the entire range of air ratios investigated, the profiles all converged (within experimental error) by 1 m above the secondary air injection ports. Wang and Gibbs (1990) and Brereton (1987) observed similar trends. However, within 0.5 m of the exit, the profiles diverge for several of the conditions. This again suggests that minor changes in riser operating conditions can greatly affect gas and/or solids flow patterns in the environs of an abrupt exit. The apparent suspension densities in the primary zone decrease with increasing primary-to-secondary air ratio for a secondary zone velocity of $U_g = 6.5$ m/s (conditions A and C). At a secondary zone velocity of $U_g = 9$ m/s (conditions B and D) this effect is negligible.

The transition from a dense turbulently fluidised bed present for condition C in Run 6 (opposed air, secondary-to-primary air ratio 1:1) to a more dilute bed occurred over a height of approximately 0.5 m (Figure 6.23). For Run 6, condition D, the solids in the primary zone were distributed in a core-annulus structure, but the primary zone appeared to be close to transition to a denser turbulent bed. With a small decrease in primary zone gas velocity a dense bed began to form from the primary air distributor upwards. It appeared that the primary air rate was no longer sufficient to rapidly entrain all the solids flowing down the walls and across the distributor plate into the core. At primary air gas velocities of 4.5 m/s, apparent suspension densities above approximately 200 kg/m^3 were typically associated with breakdown of the fast fluidised bed core-annulus structure to a denser turbulently fluidised bed. Although the primary zone in the 1:1 ratio, opposed flow, condition D case was close to transition to a denser turbulent bed, the apparent density was similar to that for the equivalent 0:1 ratio case

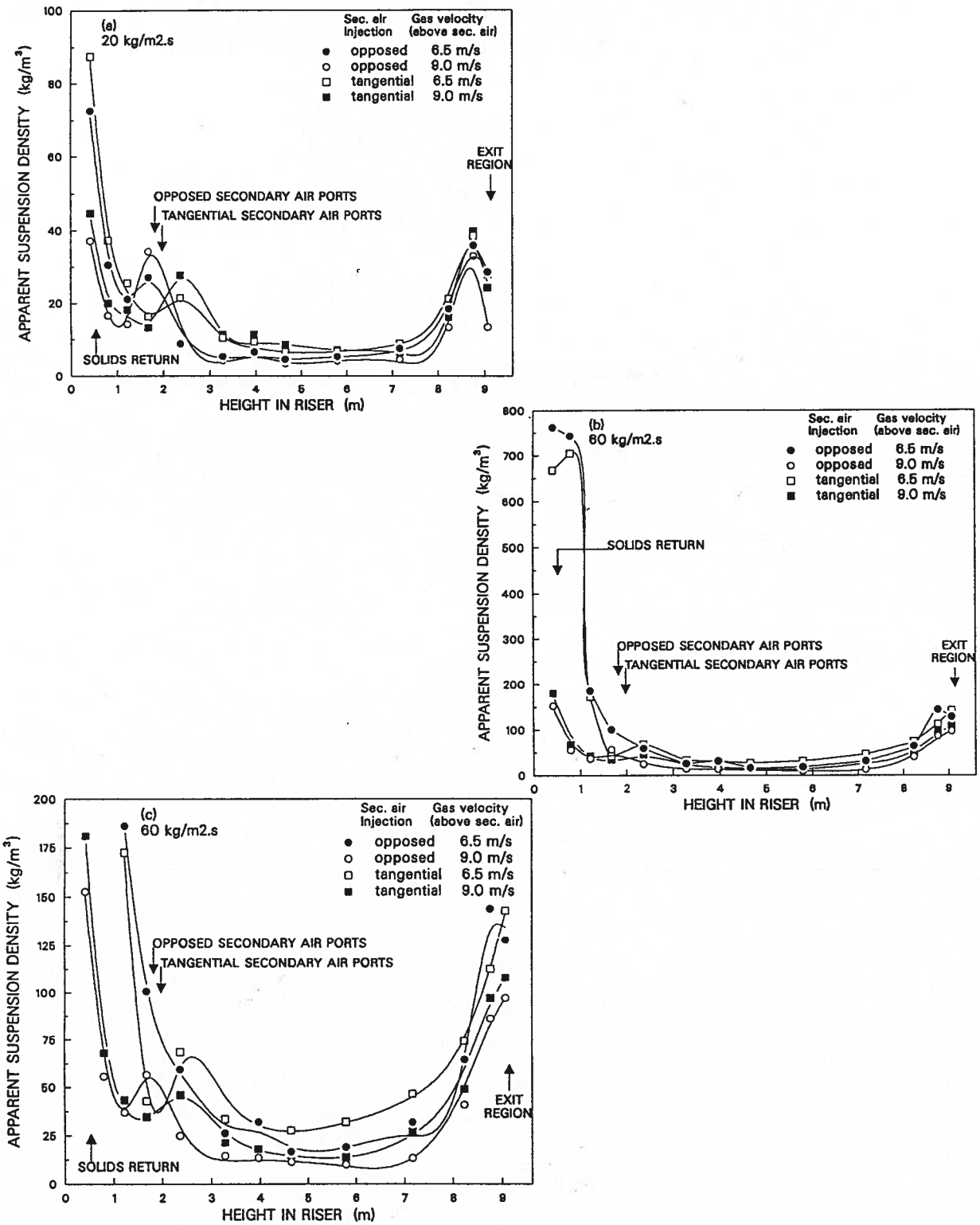

Figure 6.24: Comparison of apparent density profiles for opposed and tangential secondary air injection tests (Runs 6 and 8, secondary-to-primary air ratio 1:1, abrupt exit): (a) conditions A and B; (b), (c) conditions C and D (full and part profiles).

(i.e. no secondary air) (Figure 6.23). The 0:1 ratio case was not near transition. Evidently, apparent suspension density alone is not a good indicator of the possibility of the transition or "breakdown" of the well-defined fast bed core-annulus structure. It must be noted that the true suspension densities for these two cases may have been significantly different despite the similarity of the apparent densities.

In the swirl flow tests (Run 8, secondary-to-primary air ratio 1:1) with a high solids circulation rate (60 kg/m^{2}s), solids were observed falling at the walls at all heights of the riser except for a distance between 130 mm above the swirl ports and 80 mm below the ports. Over this 210 mm height around the ports the walls were swept clear by the swirling gas flow. At equivalent operating conditions, the swirl flow gave higher apparent suspension densities than the opposed flow along the entire riser height, except within 1 m of the ports (Figure 6.24). A similar trend was observed by Wang and Gibbs (1990). Considering the influence of relative rates of lateral transfer of particles between an upflowing core solids stream and a downflowing wall solids stream discussed in Chapters 2 and 5, this suggests that along the full length of the riser the swirl flow either increases the transfer of particles out to the wall or decreases particle re-entrainment from the wall. A decrease in wall particle entrainment seems less likely since the swirl flow was observed to locally entrain all the wall particles around the ports. An important observation is that the densities below the secondary air ports were higher for swirl flow than for opposed flow secondary air injection for conditions A, B and D, despite the apparent reduction of wall streamer downflow into the primary zone. It is possible that the swirl effect is also transmitted downwards into the primary zone as a result of gas viscous effects. When operating at condition C with swirl flow, a denser turbulent bed was present in the primary zone which may have damped the swirl, thereby reducing this effect. The increase in particle flow out to the walls may have been caused by the centrifugal forces on the particles in swirl flow, as suggested by Brereton (1987).

6.3.6 Influence of Particle Size Distribution (PSD)

"Standard" and "bimodal" glass particle size distributions (PSDs) were utilised in Runs 2 and 3, respectively. The results of these two runs were compared with the narrow distribution glass particle tests of Run 1. The particles in all three distributions were nearly spherical glass beads of particle density 2470 kg/m^3. The nominal Sauter mean diameter of all three distributions was 230 μm. Thus, all particle properties likely to affect the performance of the riser, except PSD, remained invariant during the three runs. Each PSD was also characterised by its "spread" (see Table 6.1). The spreads of the narrow, standard and bimodal distributions were, respectively 28, 69 and 142 μm.

The measured apparent suspension density profiles for the three runs are shown in Figure 6.25. At U_g = 9.0 m/s all three distributions gave similar profiles. However, at U_g = 6.5 m/s the bimodal distribution gave higher apparent suspension densities throughout the riser for condition C (60 kg/m^{2}s), and over a height of approximately 5.5 to 7.5 m for condition A (20 kg/m^{2}s). For all three distributions under condition C, streamers were observed cascading down the riser wall over the entire riser height, although they appeared very thin in the middle heights of the riser for the narrow and standard PSDs. For condition A the dense wall solids downflow extended from the exit to a height of approximately 7.0 m when running with the narrow and standard PSDs, and 5.0 m for the bimodal distribution.

To confirm the important result that the bimodal size distribution gave higher solids hold-up within the riser under some operating conditions, the data from which the condition A and C density profiles were derived were compared statistically. The apparent suspension density profiles plotted in Figure 6.25 are means of data from multiple cases of the same particle distribution and operating conditions. For example, Run 3, condition C was repeated six times. From the replications it was possible to estimate expected variations (i.e. sample standard deviations). By comparing the differences between the mean densities at a particular height for two different size distributions with the possible variation that could be expected between repetitions of the same case, the significance of these density differences was determined. The

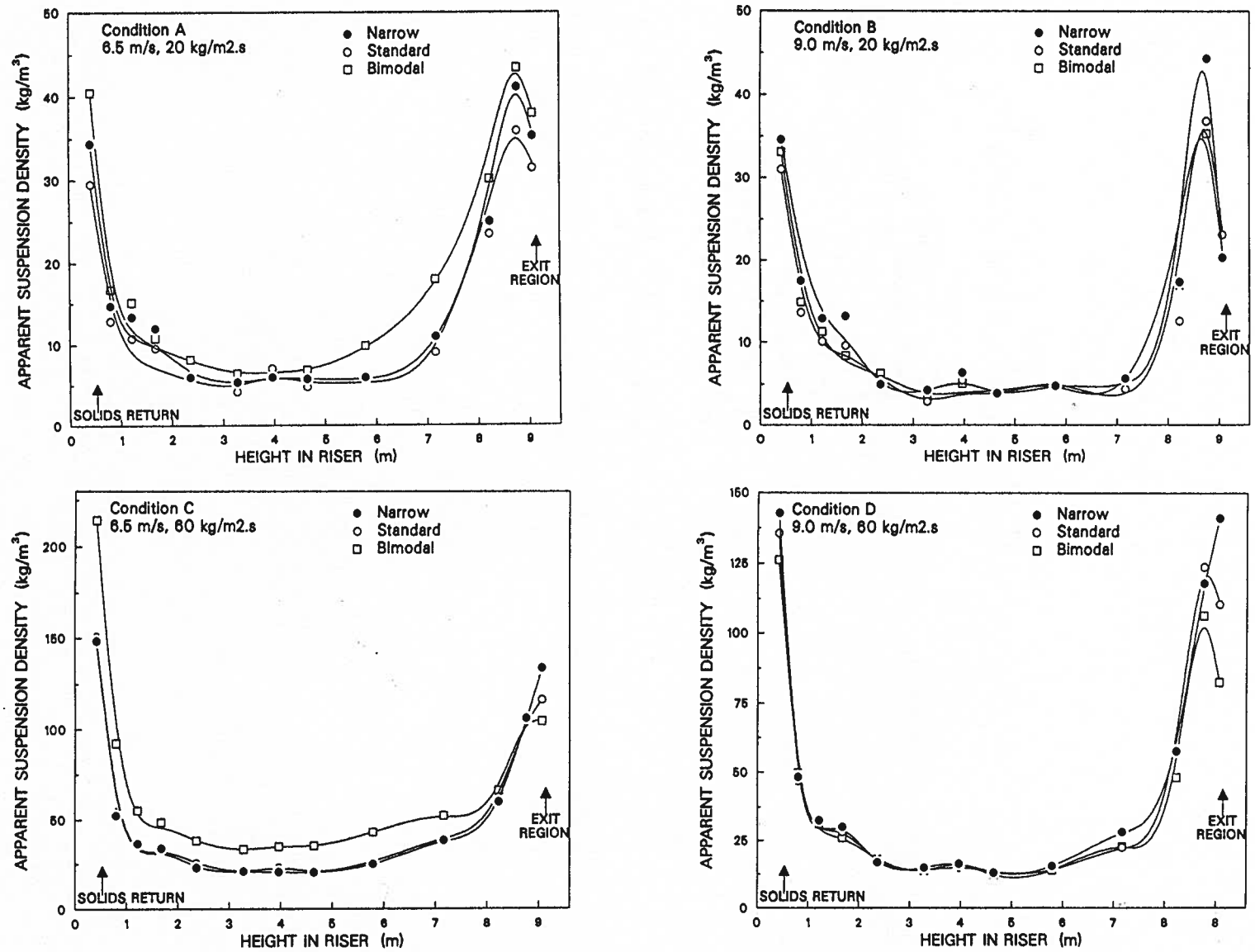

Figure 6.25: Comparison of the apparent density profiles for runs with narrow, standard and bimodal particle size distributions (Runs 1, 2 and 3; abrupt exit).

comparison was performed using an appropriate statistical test for this case, a Student's t-distribution comparison test. For condition C the apparent suspension density along the entire riser was significantly greater for the bimodal PSD than for the narrow distribution at a 99% confidence level. For condition A this result was true for riser heights below approximately 1.0 m and between 5.5 and 7.5 m. Full results of the statistical tests are given in Appendix B.

Size segregation of particles was investigated by sampling the solids upflow and downflow at the riser wall at $z = 4.2$ m for condition C, for both the standard and bimodal PSDs. Bierl *et al.* (1980), using a similar solids sampling probe in a 0.3 m diameter riser with FCC catalyst ($d_p = 61$ μm, $\rho_p = 1600$ kg/m^3), reported that changes in suction rate through their solids sampling probe had little effect on the capture rate of solids from within the riser, except when measuring wall solids downflow. They attributed this insensitivity to the dominance of solids momentum over gas momentum. For wall solids downflow samples they reduced the gas flow rate through the probe to the minimum level at which solids were drawn away from inside the probe tip, thereby avoiding blockage of the probe. They argued intuitively that, as there was negligible gas downflow at the wall, any withdrawal of gas through the probe with the captured falling solids would bias the measured mass flux. Although they did not investigate effects of probe suction on the sample size distribution, it seems likely that any bias of the mass flux measurement may also bias the sample size distribution. Similarly, in this study the solids were sampled non-isokinetically. However, following the recommendation of Bierl *et al.* (1980), when sampling solids downflow the gas flow through the probe was minimised. During sampling of the wall downflow, as wall streamers intermittently passed over the sampling probe tip, large pulses of solids were captured by the probe. The wall streamers appeared to behave as single entities, rather than as individual particles, suggesting that biasing of the size distribution due to probe suction was minimal. When sampling upflow, the capture rate was much lower and relatively steady. This suggests that the probe captured little of the downflow when orientated to capture solids upflow, and vice versa.

The riser wall sample PSDs were compared with samples taken from between the riser

exit and the primary cyclone, and from the standpipe. The gas exiting the secondary cyclone appeared free of dust. When this stream was filtered the solids capture was a negligibly small fraction of the total solids recirculation, indicating that particle attrition was minimal and the combined cyclone efficiency was close to 100%. Thus it was assumed that differences between standpipe and exit sample PSDs were representative of the random error involved in sampling and sieving. Repeated sieving of the same sample generally gave weight fractions in a given interval within ± 3% of each other. The size distributions of all samples are given in Figure 6.26. For the standard distribution tests the differences in PSD between all samples were comparable to the estimate of the random error (based on the exit and standpipe samples). For the wider bimodal PSD, a significantly greater weight fraction of large particles was measured at the wall than in the external solids recirculation. Furthermore, the solids downflow at the wall had a higher weight fraction of large particles than the upflow measured at the same riser position.

As discussed, the initial impetus behind the PSD tests was to support the theory that particle collisions are largely responsible for the lateral motion of particles out to the riser wall, where they are captured by a downflowing layer of solids, thereby increasing overall solids hold-ups within the riser. Collisions may result from the shearing of the particle assembly (e.g. slow wall particles re-entrained into the rapid flow riser core) and the response of the particles of differing size or density to the time-averaged gas velocity and the turbulent gas velocity fluctuations. The PSD tests were thus conducted assuming that increased collision frequencies and collisional energy transfers would result with the wider PSDs due to the greater spread in particle slip velocities in comparison to the narrow PSD. As discussed below, the experimental results are not entirely consistent with this theory, though some effort was initially made to qualitatively explain the results in terms of PSD collision effects. Later model simulations of the PSD tests, described in Chapter 8 (Section 8.15.3), provide an explanation for the observed trends. To improve the discussion of the PSD results in this chapter some of the results of the modelling work are pre-empted. In addition, the inadequacies of the PSD collision theory explanation for these tests are discussed.

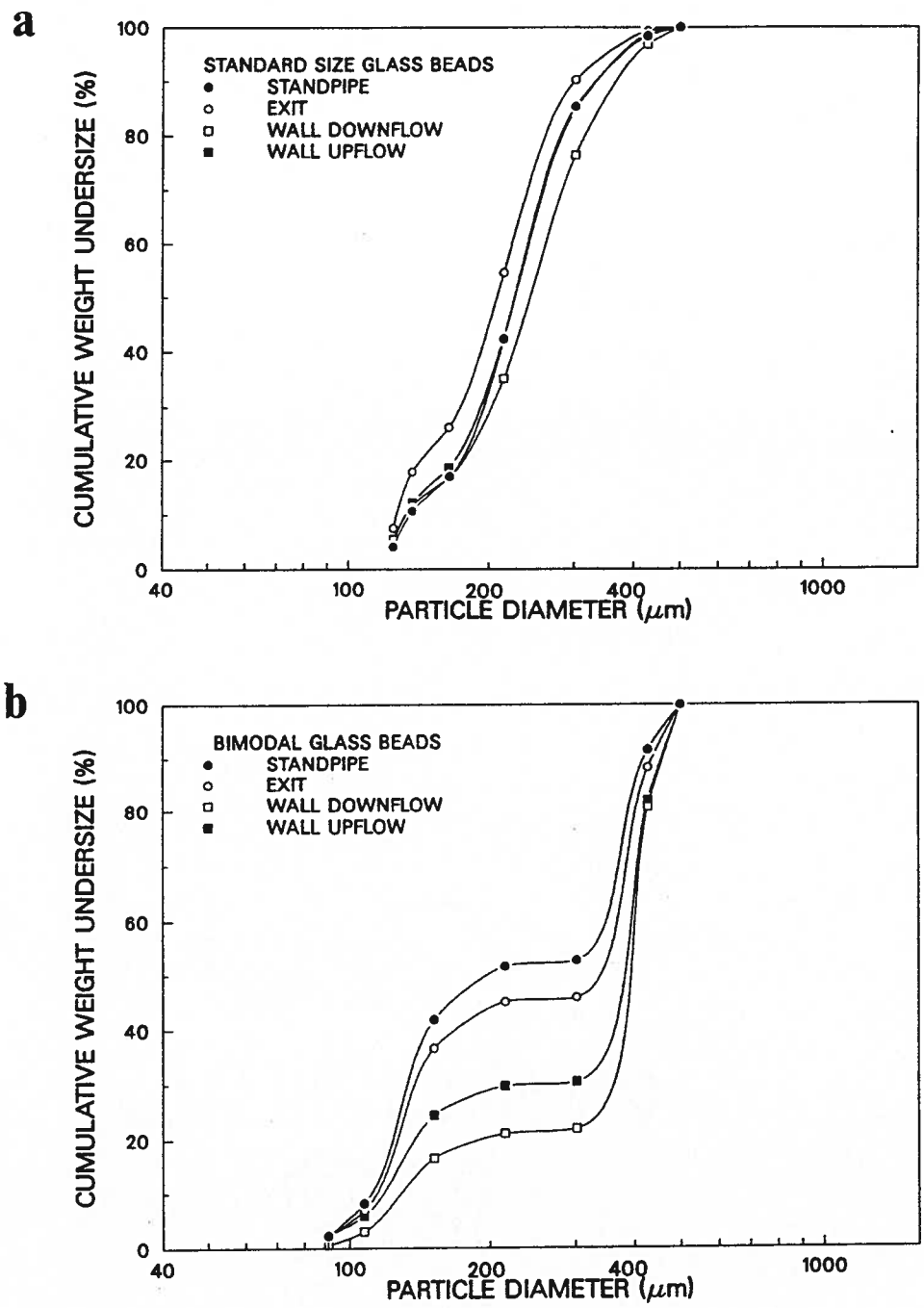

Figure 6.26: PSD's of riser wall, exit and standpipe samples: (a) standard, and (b) bimodal PSD tests. Condition C for both cases.

Table 6.5: Mean particle diameters and terminal velocities of the "small" and "large" size fractions of each glass bead PSD. Air properties at $T_g = 25$ °C assumed.

PROPERTY	NARROW		STANDARD		BIMODAL	
	small 45 wt%	large 55 wt%	small 45 wt%	large 55 wt%	small 45 wt%	large 55 wt%
Sauter mean dia. d_p (μm)	189	270	162	303	150	440
Terminal velocity[a] $\mathbf{v}_t$ (m/s)	1.27	2.00	1.04	2.29	0.95	3.38
$\mathbf{v}_t$(large) - $\mathbf{v}_t$(small) (m/s)	0.73		1.25		2.43	

[a]terminal velocity correlations for spheres from Grace (1986)

Firstly, consider the likely increase in collision frequency of the wider PSDs in comparison to the narrow PSD. The bimodal PSD (Figure 6.9) is a mixture of two narrow size distributions of Sauter mean diameter 150 μm (45 wt%) and 440 μm (55 wt%), with little overlap. If the same weight percent split (45:55) is made in the narrow size distribution, then the smaller fraction (45 wt%) has a Sauter mean diameter of 189 μm, while the larger particles (55 wt%) have a diameter of 270 μm. Corresponding values for the standard PSD are 162 μm and 303 μm. Terminal settling velocities of these particle sizes at ambient conditions are given in Table 6.5. A reasonable indicator of the frequency of particle collisions due to PSD effects is the difference in the terminal velocity for the small and large particle sizes for each PSD. If the gas-particle suspension is very dilute then the slip velocities of these particle sizes may actually be similar to their terminal velocities. Otherwise the relative magnitudes of the terminal velocities may be interpreted as the relative responses of the particles to gas flow between collisions. The difference in small and large particle terminal velocities for standard PSD is 70% greater than for the narrow PSD, whilst for the bimodal PSD this difference is 230%.

A precursory examination of the profiles given in Figure 6.25 reveals that PSD in most cases appears to have little influence on the apparent suspension density profiles, with two exceptions. For condition C the bimodal PSD suspension density is significantly greater than the profiles for the narrow and standard PSDs. Furthermore, the narrow and standard PSD profiles are almost identical. This is inconsistent with the core collision theory. If PSD effects were not significant then one would expect all profiles to be similar. If a wider PSD influenced solids hold-up by

increasing collision frequency, one would expect the standard PSD suspension densities to be greater than those for the narrow PSD. This inconsistency also occurs for condition A, although for this case the differences are not statistically significant for most heights, as discussed earlier. It appears that there is some other dynamical phenomenon that is influenced by PSD under some operating conditions.

The PSD test model simulations presented in Chapter 8 predict that whenever a significant concentration of wall streamers is present the particle lateral velocity fluctuations are largely due to collisions caused by the re-entrainment of slow wall particles into the rapid core upflow. Fluctuations due to gas turbulence and PSD effects are predicted to be secondary in comparison[2]. Differences in the measured suspension densities between PSDs occurred only at heights where a significant concentration of wall streamers was present. Model simulations of the condition C tests with the same suspension density, wall streamer thicknesses and voidages, and wall streamer re-entrainment rates gave core particle velocity fluctuations of similar magnitude for all PSDs. It may therefore be deduced that wall gas-particle dynamics led to the increase in suspension density observed with the bimodal PSD. It appears either that particles are captured at a higher rate by the wall streamers when using the bimodal PSD, or that the bimodal PSD wall streamers are more stable and less likely to be re-entrained.

The PSDs of the particles sampled at the wall for condition C shown in Figure 6.26 are further support for the wall dynamical explanation of the observed trends. The PSDs of the wall upflow and downflow show that the downflowing wall streamers contained more large-sized particles than were found in the upflow at the same location. It may be that larger particles are more successfully captured by the streamers, due to their considerably greater inertia in comparison to the particles they generally collide with at the streamer surface. Dry (1987) made a similar suggestion to account for measured radial particle size segregation in his tests. The absence of detectable wall segregation for the standard PSD (Figure 6.26) may be explained if one considers the masses of the large-sized particles in the 45:55 wt% PSD split (Table 6.5),

[2]This is not a general result. For wider PSDs and larger diameter risers, particle size/density distribution is predicted to have a significant influence on core dynamics even when there is substantial wall downflow of solids.

compared to the nominal mean-sized 230 μm particle for all three PSDs. The 440 μm particle mass is 7.0 times greater than the 230 μm particle, whilst the 303 and 270 μm particle masses are only 2.2 and 1.6 times greater, respectively. A 440 μm particle would thus be expected to "implant" itself more successfully in a falling wall streamer than the 303 or 270 μm particles, assuming a typical wall streamer particle size is 230 μm. Wall streamer dynamics are discussed further in Chapter 9.

The density profiles in Figure 6.25 for conditions B and D ($U_g = 9.0$ m/s) show short, high apparent suspension density, acceleration regions over the lower 1.5 m of the riser, and short, high density, exit regions within 1.5 m of the abrupt exit. Between these two regions negligible downflow of solids was observed at the walls, and the suspension densities for all three PSDs were similar. Likewise, for condition A, all PSD suspension densities were similar over the interval $z = 2.0$ to 5.0 m, corresponding roughly to the heights where streamers were absent. As discussed earlier, where there is dilute suspension upflow over the full riser cross-section, the apparent suspension density, ρ_{sa}, is a reasonable estimate of the true suspension density. Thus, changing the PSD had little effect on solids hold-up in the riser over the heights where wall streamers were absent.

Although suspension densities were similar for the three PSDs at heights without wall streamers, this does not imply that core collision frequencies and particle lateral fluctuating velocities were also similar. In fact, significant increases in particle fluctuating velocities with PSD spread were predicted in simulations of the PSD tests, with wall streamers absent (Chapter 8). However, the predicted contribution of the related particle-wall shear, due to particle-wall collisions, was only a small fraction of the total pressure drop. Thus, PSD had a negligible effect on apparent suspension densities in the model simulations, in agreement with experimental observations.

The difference between the riser wall region PSDs and the exit/standpipe PSDs shown in Figure 6.26(b) for the bimodal particle condition C test may be due to several factors including lateral particle size segregation, riser exit effects and differences in axial particle velocities up

the riser. Lateral segregation may result from differences in the lateral fluctuating velocities of particles of differing size, in addition to the preferential capture of larger particles in the wall streamers discussed previously. Different axial particle velocities due to differences in slip velocities of the smaller and larger particles may result in greater riser residence times for larger particles relative to smaller particles. Thus a greater fraction of large particles may reside within the riser compared with the packed-bed return solids flow in the standpipe. It is also possible that a higher fraction of smaller particles than larger particles are successfully accelerated by the gas flow through the abrupt exit 90° turn.

Assuming a negligible effect of particle collisions, particle slip velocities equal to terminal settling velocities, and uniform dilute suspension upflow of particles, the contribution of axial velocity variation to the observed PSD differences may be crudely estimated. Consider the representative large and small particles (45 wt% 150 μm and 55 wt% 440 μm) for the bimodal PSD given in Table 6.5. With slip velocities equal to $\mathbf{v}_t$, and $U_g = 6.5$ m/s (condition C), the upward velocities of the 150 μm and 440 μm particles are 5.55 and 3.12 m/s, respectively. For uniform flow of solids up the riser, the internal riser upflux equals G_s. Thus the suspension densities within the riser of the 150 μm and 440 μm particles for $G_s = 60$ kg/m^{2}s are, respectively, 4.9 kg/m^3 (0.45 $\times$ 60 kg/m^{2}s/5.55 m/s) and 10.6 kg/m^3. This corresponds to 32 wt% 150 μm particles and 68 wt% 440 μm particles within the riser. The measured values for particles in downflow at the riser wall for condition C, when expressed in terms of the two representative sizes, were 30 wt% for 150 μm particles and 70 wt% for 440 μm particles.

A comparison of the estimate and experimental results suggests that differences in axial particle velocity may account for much of the measured differences between wall and standpipe/exit PSDs. However, this overlooks particle-particle collisions within the riser, which are likely to increase the upwards velocities of larger particles and retard the upflow of the smaller particles. In dilute pneumatic conveying tests with glass beads of diameter 1.08 and 2.90 mm, Nakamura and Capes (1976) observed less segregation than predicted assuming no particle interaction. They attributed the difference to particle collisions. It has also been noted by several

investigators that large particles with terminal velocities far in excess of superficial fluidisation gas velocities exit from the top of both bubbling beds and circulating beds (e.g. Merrick and Highley, 1972; Geldart *et al.*, 1979; Goldblatt, 1991). This is generally attributed to the collisional impact of small, rapidly moving particles on the underside of the larger particles, thus propelling the larger particles upward.

The simulation of the bimodal condition C PSD test, presented in Chapter 8, included estimates of gas turbulence and collisional effects on the particles. Predicted mean upward core velocities of the 150 μm and 440 μm particles were about 4.9 and 4.4 m/s, respectively (Appendix F, "Output (c)"). Based on these velocities, a uniform suspension core upflow contains 42 wt% of 150 μm particles and 58 wt% of 440 μm particles, compared with the 55:45 wt% particle mixture in the standpipe. In contrast to the crude estimate above, this estimate indicates that the contribution of particle axial velocity variation to the measured segregation was small.

Visual observations of the solids flow near the abrupt riser exit used in the PSD tests indicated that very little of the core solids upflow was diverted through the 90° exit bend before first impacting on the riser roof. The fraction of the packed layer of solids on the roof that fell near the exit port was entrained by the gas flow out to the primary cyclone, whilst the remainder cascaded down the riser walls as streamers. This pattern of solids flow suggests that, for this exit geometry, segregation due to exit effect was probably not significant. Furthermore, between the exit height and the mid-height where the wall solids downflow sample was taken there was likely a substantial renewal of solids in the falling streamers. Thus, it appears that the difference between the wall PSDs and exit/standpipe PSDs for condition C was largely due to lateral particle size segregation.

6.3.7 Effect of Particle Density

The measured apparent density profiles for each of the sand runs are presented in Figure 6.27. General profile shapes and trends in suspension density variation with changes in operating

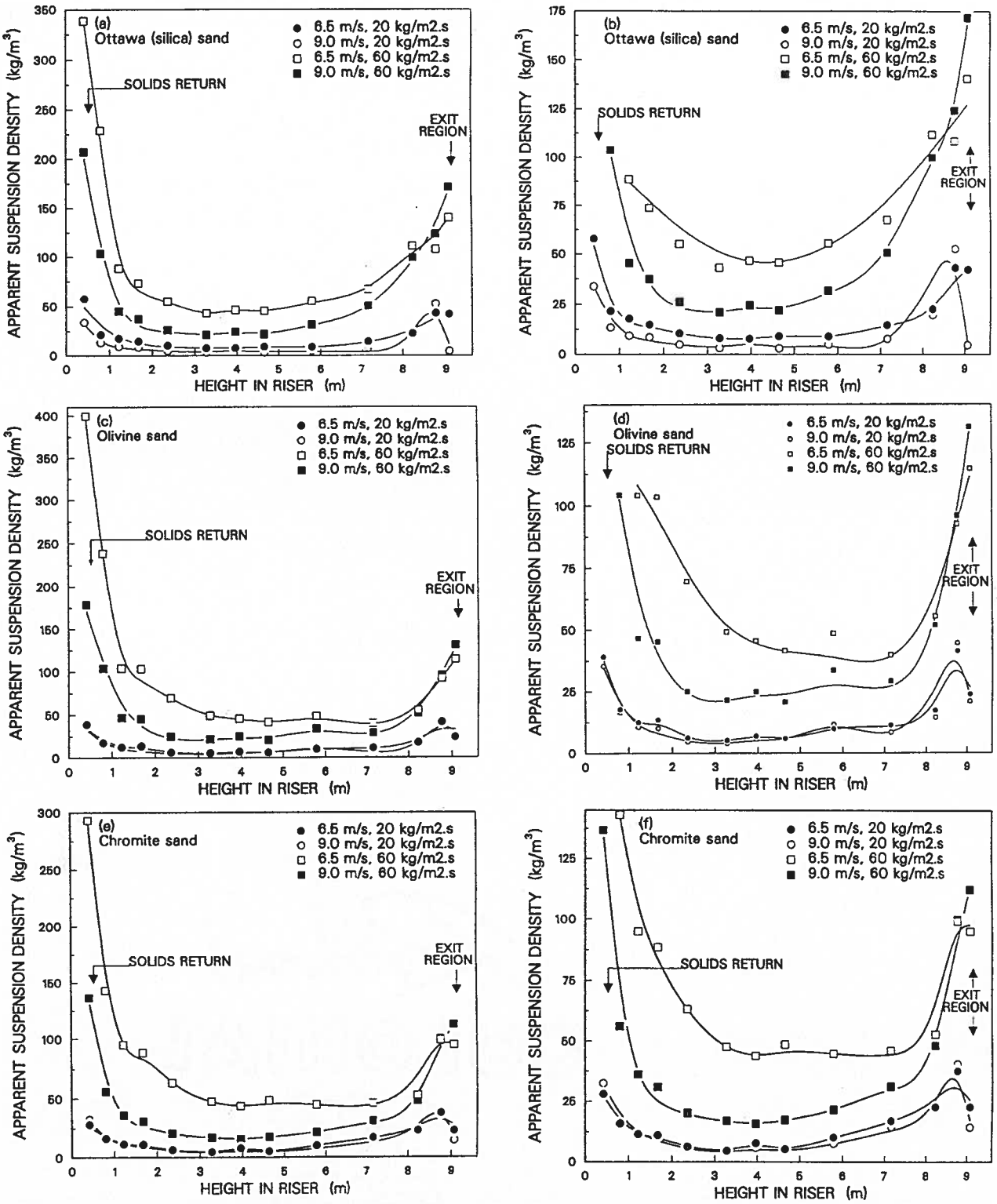

Figure 6.27: Apparent suspension density profiles for the particle density effect tests (riser abrupt exit and cylindrical entry): (a)-(b) Ottawa sand (Run 9); (c)-(d) Olivine sand (Run 10); (e)-(f) chromite sand (Run 11). (Part profiles in (b), (d) and (f) correspond, respectively, to full profiles in (a), (c) and (e).)

condition were similar to those observed for glass particles. With $G_s = 60$ kg/m^{2}s, decreasing the gas velocity from 9 m/s to 6.5 m/s caused an increase in apparent density throughout most of the riser. At a solids circulation of 20 kg/m^{2}s , decreasing the gas velocity from 9.0 m/s to 6.5 m/s caused only a slight increase in apparent density for the Ottawa sand, and had negligible effect for the Olivine and chromite sands. However, trends within 0.6 m of the riser exit varied substantially. At $G_s = 20$ kg/m^{2}s the profiles dropped away sharply to the last data point, whilst at $G_s = 60$ kg/m^{2}s this sudden decrease was not observed. There was also a cross-over in the two 60 kg/m^{2}s profiles (conditions C and D) within approximately 0.6 m of the riser exit. Once again, measured riser wall pressure gradients just below the riser exit did not always follow trends seen over the remainder of the riser height. These observed pressure gradients likely resulted from changes in three-dimensional gas flow patterns near the exit discussed earlier, rather than from true changes in solids hold-up.

Comparison of the apparent suspension density profiles for the different sands obtained under similar operating conditions is given in Figure 6.28. Despite significant differences in particle density, profiles for the same operating conditions are similar. Only two minor differences occur. At $G_s = 60$ kg/m^{2}s, the Ottawa sand exhibits a higher apparent density over the top 3.0 m of the riser than do the other two sands. Over the lower 1.0 m of the riser there is some variation between apparent suspension densities, although there is no consistent trend when all runs and conditions are considered.

Based on the glass particle test results and discussion, it is assumed that apparent suspension density is a reasonable approximation of true solids hold-up over the riser height of 1.5 m to 8.0 m. Consequently, apparent density ρ_{sa} may be related to the cross-sectionally averaged voidage, $\overline{\epsilon_g}$, by the expression

$$\rho_{sa} = \rho_p(1 - \overline{\epsilon_g}) \ , \tag{6.2}$$

where ρ_p is the particle density. As ρ_{sa} at a given height was approximately constant between different sands under the same conditions, eq. (6.2) implies that $(1-\overline{\epsilon_g})$ decreased proportionally with an increase in particle density ρ_p. This can be verified qualitatively for condition A. For

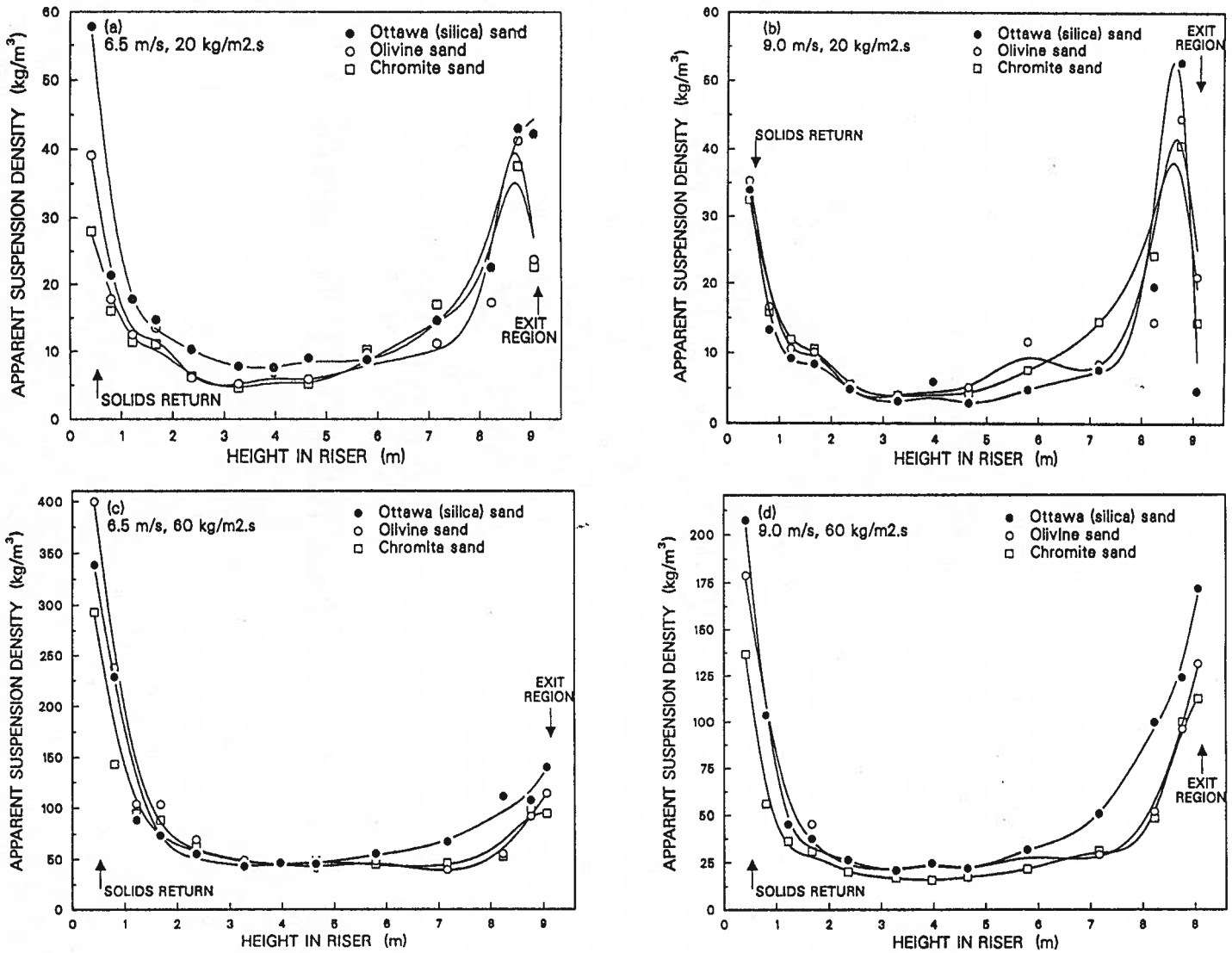

Figure 6.28: Comparison of the apparent density profiles for tests with Ottawa, Olivine and chromite sands (Runs 9, 10 and 11; abrupt exit and cylindrical entry): (a), (b), (c) and (d) correspond to conditions A, B, C and D, respectively.

Ottawa sand, a substantial concentration of falling wall streamers was observed mid-way up the column. With Olivine sand this concentration was far less, while no such solids structures were observed for the chromite sand. Thus, different radial distributions of solids may give the same apparent and/or true suspension density depending on the particle density of the solids in the riser. This highlights the need to consider radial solids distribution when modelling phenomena such as heat transfer, which depend greatly on the presence of downflowing dense solids layers at the riser wall.

The observed approximate variation of $(1 - \overline{\epsilon_g})$ with ρ_p may be reasonably explained by considering the changes in mean particle velocity up the riser with change in particle density. The terminal velocities for the Sauter mean sand particle sizes (Table 6.1) are 1.1 m/s, 1.4 m/s and 1.4 m/s for the Ottawa, Olivine and chromite sands, respectively. Assuming that the mean upward particle velocity, $\mathbf{v}_p$, is proportional to the difference between superficial gas velocity and particle terminal velocity of the Sauter mean sized particle (i.e. $\mathbf{v}_p \propto (U_g - \mathbf{v}_t)$), then the maximum difference in mean particle velocity of the three sands for U_g = 6.5 m/s is 6% (i.e. (1 - (6.5-1.4)/(6.5-1.1)) × 100%). This difference is less for a gas velocity of 9.0 m/s. For negligible creation or destruction of solids within the riser, the net solids upflux is equal to the external solids flux, G_s. This flux may also be expressed as

$$G_s = \rho_p(1 - \overline{\epsilon_g})\mathbf{v}_p \ . \tag{6.3}$$

Equation (6.3) indicates that at constant solids mass flux, an increase in particle density ρ_p results in a proportional decrease in $(1 - \overline{\epsilon_g})\mathbf{v}_p$. Particle density for Olivine sand is 20% higher than for Ottawa sand, while chromite sand has a particle density 41% higher than Ottawa sand. These variations ($\geq$ 20%) are significantly greater than the estimated decreases in solids velocity due to the increase in particle density ($\leq$ 6%), which suggests that the majority of the decrease in $(1 - \overline{\epsilon_g})\mathbf{v}_p$ will be due to a decrease in $(1 - \overline{\epsilon_g})$.

For larger or denser particles than those used in this study the magnitude of changes in particle velocities may be comparable or greater than the related changes in particle density. Thus, it is unlikely the similarity in profiles observed in this study is a "universal" result.

There are other differences between the three sands that may also have some effect on their behaviour in the riser. The size distributions, given in Figure 6.29, show that the PSD of the Ottawa sand is narrower than for the other two. None of the distributions are Gaussian (normal), and the chromite sand is bimodal. The Ottawa sand particle shape may be described as rounded-angular, while the Olivine and chromite sands are both angular.

Although the mean size of the Ottawa sand was significantly smaller than that of the narrow distribution glass particles, most other properties were similar. Both Ottawa sand and the narrow sized glass particles had similar particle densities and PSD widths. Comparison of the apparent suspension density profiles for the two types of particles is given in Figure 6.30. For all conditions except D the solids hold-up for Ottawa sand was significantly greater than for the narrow PSD glass particles. Of note is that the only Ottawa sand case where wall streamers were not observed over the entire riser height was condition B (U_g = 9.0 m/s, G_s = 20 kg/m^{2}s). A theory that suggests that smaller particles may be more likely to form downflowing wall streamers is presented in Chapter 9. The density profiles for the Ottawa sand were, in general, only slightly above those for the bimodal PSD glass particles.

In addition to the mean particle size, the other significant difference between the sands and the glass particles was their behaviour in packed-bed flow around the elbow of the L-valve. The glass generally flowed as one uniform plug, with very few shear planes and substantial slip between the polyacrylic wall of the L-valve and the particles in contact with this wall. In contrast, the sand particles exhibited little slip at the L-valve wall, and layers of sand moved far more freely over each other. It is possible that this different flow behaviour of the two solids types observed at loose-packed voidages also resulted in differing relative stabilities of the falling dense sheets of particles at the riser walls. Although the smaller sand particles (nominal mean 160 μm) may have been more affected by gas turbulence than the larger glass particles (230 μm mean size), the results presented in Chapters 3 and 8 suggest this effect was probably not significant.

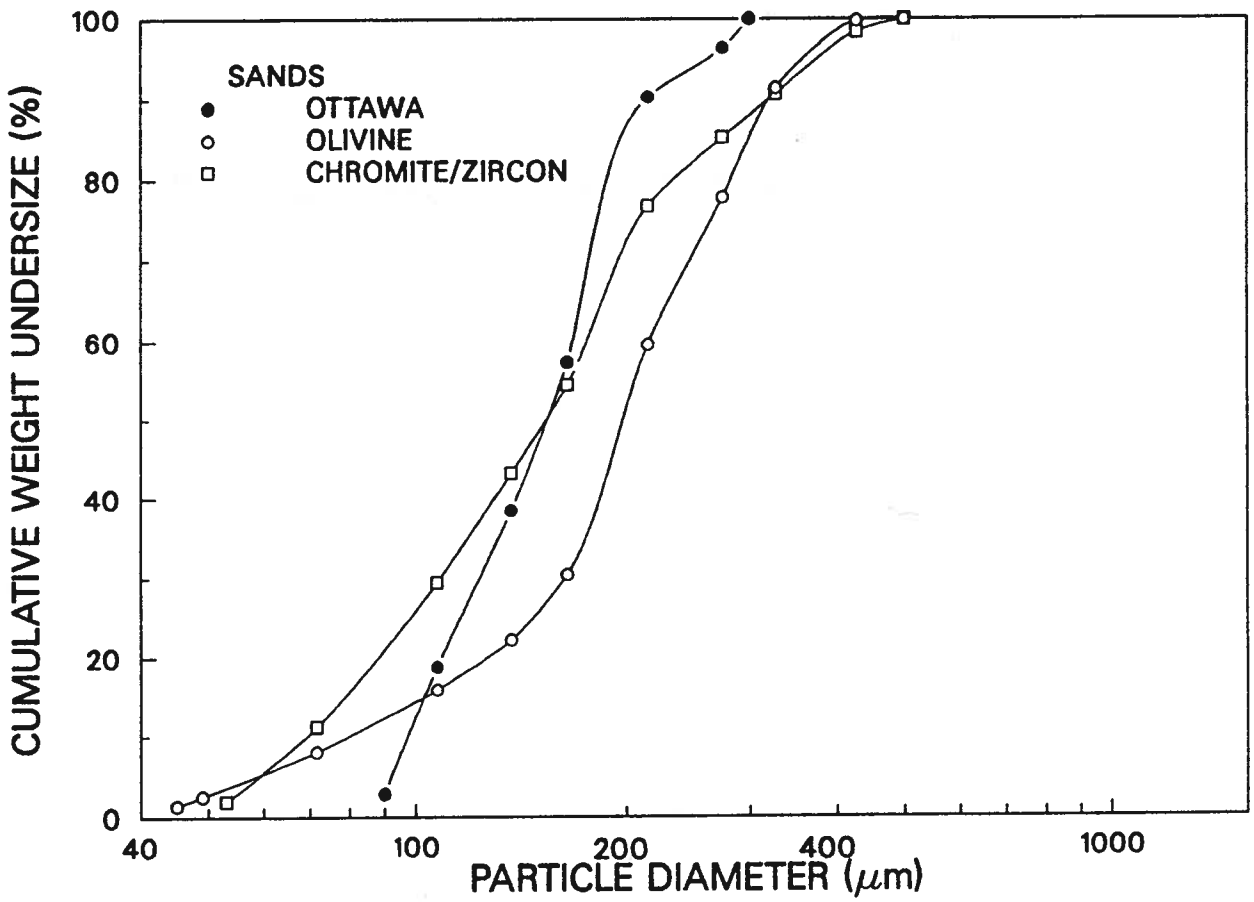

Figure 6.29: Particle size distributions of the Ottawa, Olivine and chromite sands (sampled from the standpipe after each run).

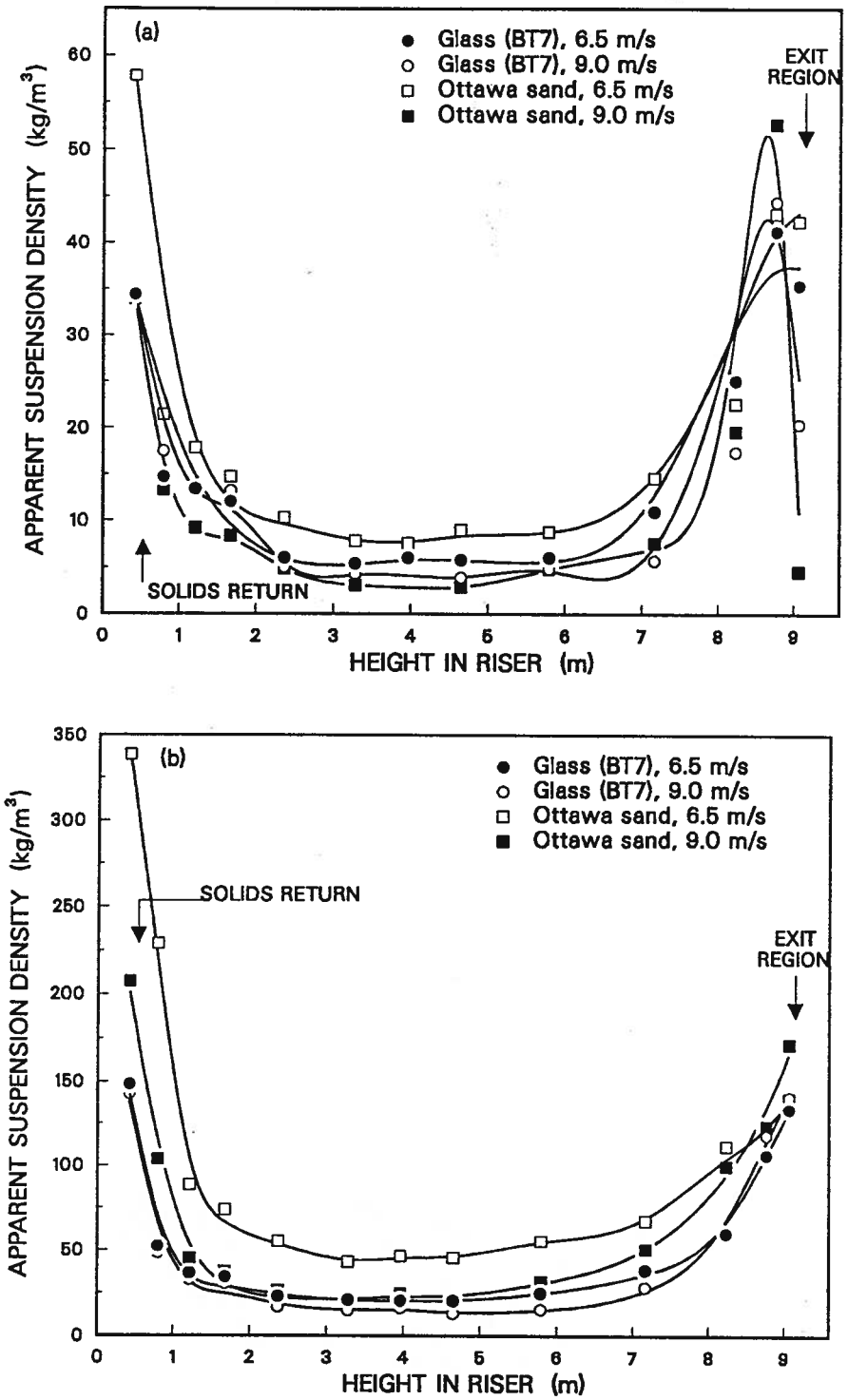

Figure 6.30: Comparison of the apparent density profiles for tests with narrow PSD glass particles and Ottawa sand (Runs 1 and 9, abrupt exit): (a) G_s = 20 kg/m^{2}s, (b) G_s = 60 kg/m^{2}s.

6.3.8 Time Series Analysis of Transients in Solids Concentration at the Riser Base and Mid-Height.

A time series study was undertaken to determine if the observed disruptions to the wall streamers are predominantly due to local factors, such as instabilities that may be inherent in riser gas-solids flow at the wall, or whether fluctuations distant from the position where the wall layer disruptions occur also have an influence. The capacitance probe tip was positioned at the riser wall at the mid-height position (4.24 m above the distributor). The probe voltage, proportional to the wall solids concentration, was logged for 20.48 seconds at a frequency of 100 Hz. Simultaneously, the voltage signal from the differential pressure transducer connected across the two lowest pressure taps (tap #1 at 0.23 m and #2 at 0.61 m) was logged at the same frequency and for the same duration. This second signal was proportional to the apparent density averaged over the riser volume between the taps. The solids from the standpipe returned between these two taps.

The differential pressure signal at the base of the riser was chosen as a possible indicator of "distant" perturbations for several reasons. Observed pulses in the returning solids flow into the riser coincided with peaks in the differential pressure, and it therefore appeared that the larger magnitude fluctuations in the pressure drop signal were representative of fluctuations in the true solids hold-up in this volume. It was also possible that generation of large-scale energetic turbulent eddies in the turbulently fluidised bed in the base of the riser would be represented by a component of the signal. It was thus postulated that pulses of solids concentration and/or gas pressure and gas turbulence generated near the riser base may then travel up the riser core and influence the downflowing wall streamers at mid-height. In addition to activity in the turbulent bed and pulses of returning solids, an additional possible source of pressure fluctuations in the base was the air blower. However, the blower pressure fluctuation frequency measured in a particle-free riser was about 80 Hz, which is significantly greater than the typical frequency of solids concentration fluctuations discussed earlier (<20 Hz), and suggests the blower used in this test did not influence the wall streamers.

The choice of base section differential pressure was also convenient because the solids recirculation flow could be deliberately pulsed by establishing a "stick-slip" flow in the L-valve. Thus it was possible to ascertain if an unsteady solids return flow had an effect on riser dynamics mid-way up the riser. From visual observation of solids flow in the standpipe, the period between pulses in the L-valve solids flowrate was estimated to vary within the range of 0.2 to 1.0 s.

Simultaneous logging of the two signals was performed for conditions C and D with narrow PSD particles (Run 1). The logged probe and transducer voltage signals obtained for the two conditions are plotted in Figure 6.31. The peaks in the capacitance probe trace for condition C correspond to the passing of downflowing sheets of wall particles over the probe tip. The brief periods of relatively constant low voltage correspond to times when the wall near the probe tip was exposed to dilute rapid suspension upflow. Generally the wall was exposed at locations where a disruption in the wall streamers occurred. Just above these exposed regions a streamer "wavefront" could be observed momentarily holding up before accelerating down over the probe. The probe trace for condition C is typical of a moderate concentration of wall streamers.

The probe signal for condition D indicates that a negligible concentration of downflowing wall streamers was present at the riser mid-height for this condition and that the probe tip was continuously in dilute suspension of a relatively uniform concentration. The corresponding autocorrelations for each of the four voltage signals are given in Figure 6.32 for lags between 0.0 and 1.0 s. Computation of auto- and cross-correlations was performed using the BMD02T statistical software package (Appendix C). The dashed lines in each plot correspond to approximate 95% confidence limits (Diggle, 1990; Box and Jenkins, 1970). It may be assumed that if an autocorrelation value for a given lag lies in the region between the dashed lines, then no significant autocorrelation of the signal occurs at that lag. Clearly evident in Figure 6.32 is the influence of the stick-slip L-valve flow on the differential pressure at the riser base. For condition C the dominant period of fluctuations in this pressure is approximately 0.55 s, while for

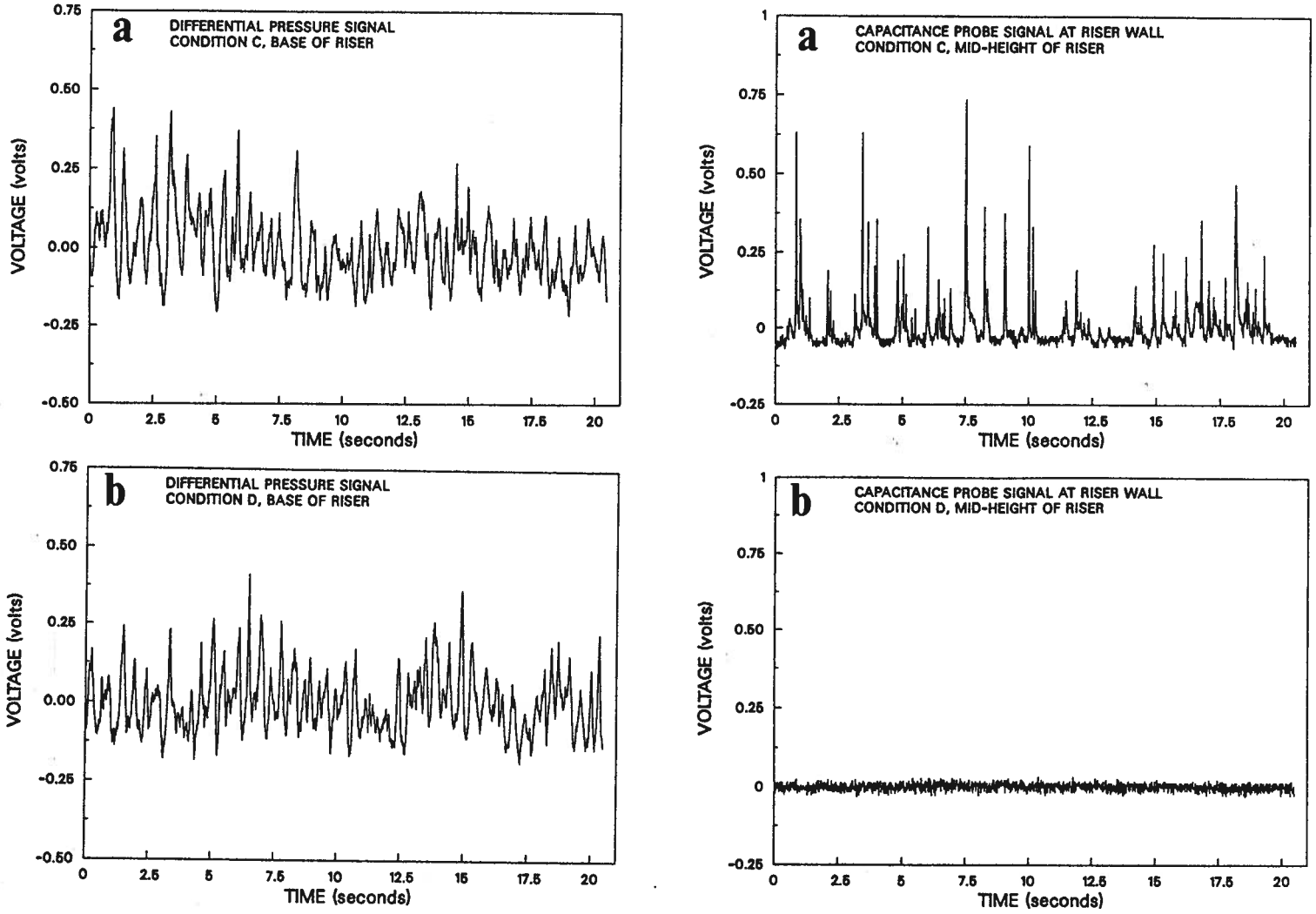

Figure 6.31: Simultaneously logged differential pressure and capacitance probe signals in Run 1 for (a) condition C, and (b) condition D. (Probe height 4.24 m. Δp_g heights 0.23–0.61 m.)

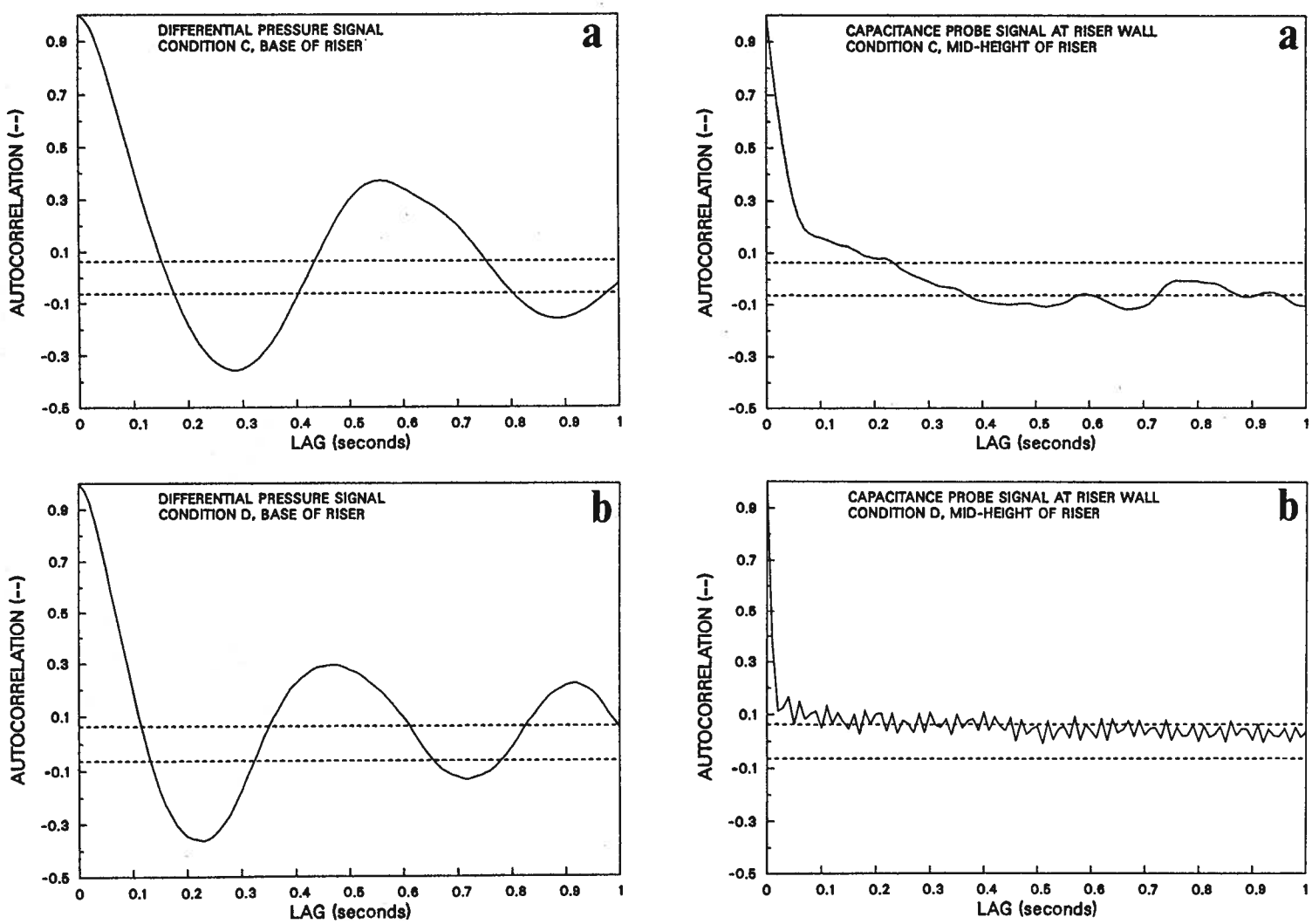

Figure 6.32: Autocorrelations of the differential pressure and capacitance probe signals in Run 1 for (a) condition C, and (b) condition D. Dashed lines correspond to 95% confidence limits. (Probe height 4.24 m. Δp_g heights 0.23–0.61 m.)

condition D it is approximately 0.45 s. The L-valve aeration was maintained constant for both conditions and the measured solids flux in both cases was 60 kg/m^{2}s. The observed difference in period indicates that when fluctuations about a constant mean value in L-valve solids flow occur (e.g. "stick-slip" flow), the period of these fluctuations is influenced by the dynamics within the riser. It is probable that a similar dependency also occurs for other non-mechanical solids return valves.

Neither of the two autocorrelation plots of the probe signal shows any significant autocorrelation at lags equivalent to the dominant periods of L-valve solids flow fluctuation. For condition C the probe signal exhibited some autocorrelation for lags up to 0.15 seconds, which corresponds to the order of time over which measurable concentration changes occurred at the wall when wall streamers were present. In contrast, virtually no significant autocorrelation of the condition D probe signal was observed over the time lags considered. Changes in concentration in the dilute suspension at the riser mid-height were very small and rapid in comparison to changes that occurred as wall streamers moved past the probe.

To confirm that no relationship existed between fluctuations in the riser base pressure and solids concentration mid-way up the column at the wall, the two signals were cross-correlated. Prior to cross-correlation, the signals were pre-whitened. Pre-whitening is necessary when one or both of the signals is strongly autocorrelated. Box and Jenkins (1970) show that, without signal pre-whitening, the cross-correlation may exhibit similar systematic patterns to that of the autocorrelations. This may be falsely interpreted as a strong cross-correlation between signals that are completely uncorrelated. Full details of signal pre-whitening are given in Appendix C. The cross-correlations for conditions C and D appear in Figure 6.33. There is no significant cross-correlation between the signals at any lag.

The time series analysis results have important implications for modelling of wall dynamics. The condition C results show that the large fluctuations that occur in the base of the riser and sometimes in the solids return inflow, do not influence the transient motion of wall streamers further up the riser. An alternative potential influence on streamer motion is the riser exit.

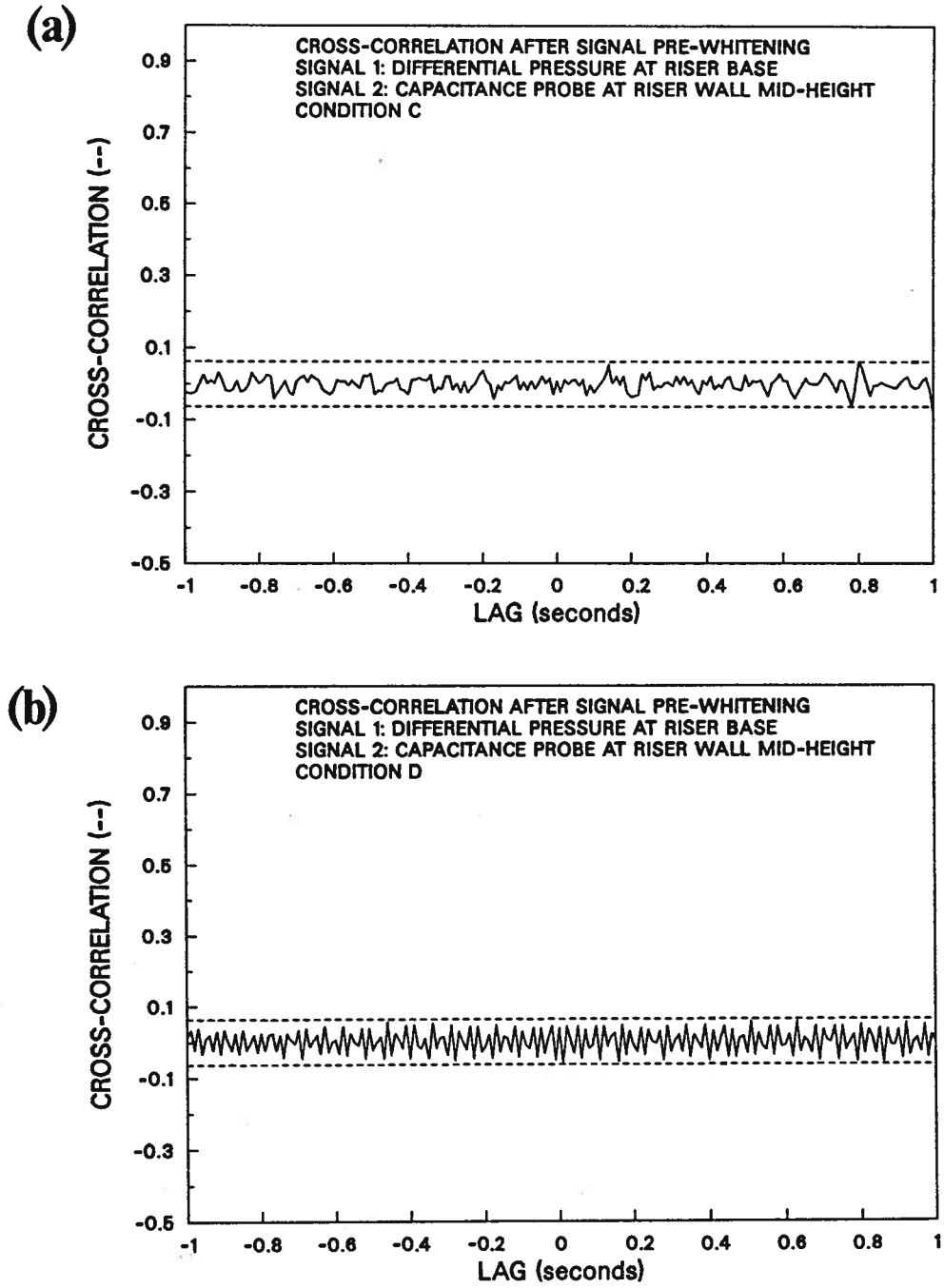

Figure 6.33: Cross-correlations of the differential pressure and capacitance probe signals in Run 1 for (a) condition C, and (b) condition D. Dashed lines correspond to 95% confidence limits. (Probe height 4.24 m. Δp_g heights 0.23–0.61 m.)

Instabilities initiated at the roof of the riser may grow as the streamers fall. However, at low G_s there are often no streamers at the upper levels of the riser, yet falling streamers closer to the base still exhibit their characteristic intermittent motion. Thus streamer instability may be triggered primarily by local factors. The condition D results show that large fluctuations in the solids concentration in the base of the riser do not appear to cause fluctuations of similar period in upflowing dilute suspension higher up the riser. Either pulses of solids are not ejected upwards from the relatively dense riser base region, or, if pulses do emanate from the base, these are damped quickly, so that the upflowing dilute suspension at mid-height is uncorrelated.

In Appendix C estimates of power spectra for the four signals are given. Coherence square estimates for the two conditions are also plotted. The only additional information contained in these frequency domain plots, not discernable from the time domain auto- and cross-correlations, is that the power spectra for the condition D probe signal shows a peak at approximately 40 Hz. The coherence square plots also show some minor peaks at this frequency. Frequencies at which individual dilute suspension particles impact on the probe tip are several orders of magnitude greater than 40 Hz. Power spectra of the probe signals obtained whilst vibrating the probe tip showed no peaks near 40 Hz. No explanation in terms of particle concentration fluctuation has been identified. It is assumed that the peaks may be due to riser column vibration, and the effect of this vibration on the probe signal output.

6.4 Conclusions

The cold unit tests resulted in a number of findings; some new and some supporting preliminary results of other investigators. Several of the key results, which are important for development of modelling concepts to follow, are:

(i) Significant radial non-uniformity and local heterogeneity in the solids concentration exist in the turbulent fluidised bed, in the bottom of a riser.

(ii) Apparent suspension density derived from axial pressure profiles may grossly under- *or* over-estimate true suspension density in regions of particle acceleration and recirculating gas flow.

(iii) Exit and entry geometry significantly affect solids distribution in a riser. Use of conical base sections may result in higher primary zone suspension densities, in contrast to the general design concept of the conical entry as a region of high gas velocity and particle entrainment, and low suspension density.

(iv) The method of secondary air injection may influence suspension densities within the riser.

(v) PSD can affect riser solids hold-up, though this may not necessarily be related to the influence of PSD on core particle collision frequency.

(vi) Instabilities in falling wall streamers may be primarily triggered by local factors, inherent in the gas-solid flow at the riser wall.

Chapter 7

PILOT-SCALE CFB COMBUSTOR HYDRODYNAMIC TESTS

In most commercial circulating fluidised bed applications, the riser operates at an elevated temperature. In contrast, the majority of riser hydrodynamic studies are performed at ambient temperature due to economic constraints and practical difficulties with adapting ambient temperature measurement techniques to high temperature environments. It is therefore desirable to confirm that the gas and solids flow patterns reported for ambient temperatures also occur at high temperatures. A series of hydrodynamic tests were performed to determine solids flow and distribution within the University of British Columbia (UBC) pilot-scale CFB combustor. In addition to the measurement of apparent suspension density profiles, capacitance probe traverse and erosion probe experiments were also conducted. The tests formed part of a larger study of the combustion of various fuels in a pilot-scale CFB combustor (Grace *et al.*, 1989a). The capacitance probe tests were part of the ongoing development of a high temperature probe, and only preliminary results are given. The hydrodynamic results have been utilised in scale-up and modelling studies (Senior and Brereton, 1990; Glicksman *et al.*, 1991). Parameter estimation for the semi-empirical model discussed in Chapter 10 is based on data presented in this chapter.

7.1 Experimental Equipment

The key features of the UBC pilot-scale combustor pertaining to the hydrodynamic tests are described here. A schematic of the entire facility is presented in Figure 7.1, and full details of the unit are given by Grace and Lim (1987) and Grace *et al.* (1989a). The riser reactor is a refractory lined chamber of 152 mm square cross-section, and overall height of 7.32 m, shown in Figure 7.2. The bottom tapers gradually on the inside, from a 51 mm $\times$ 152 mm cross-section

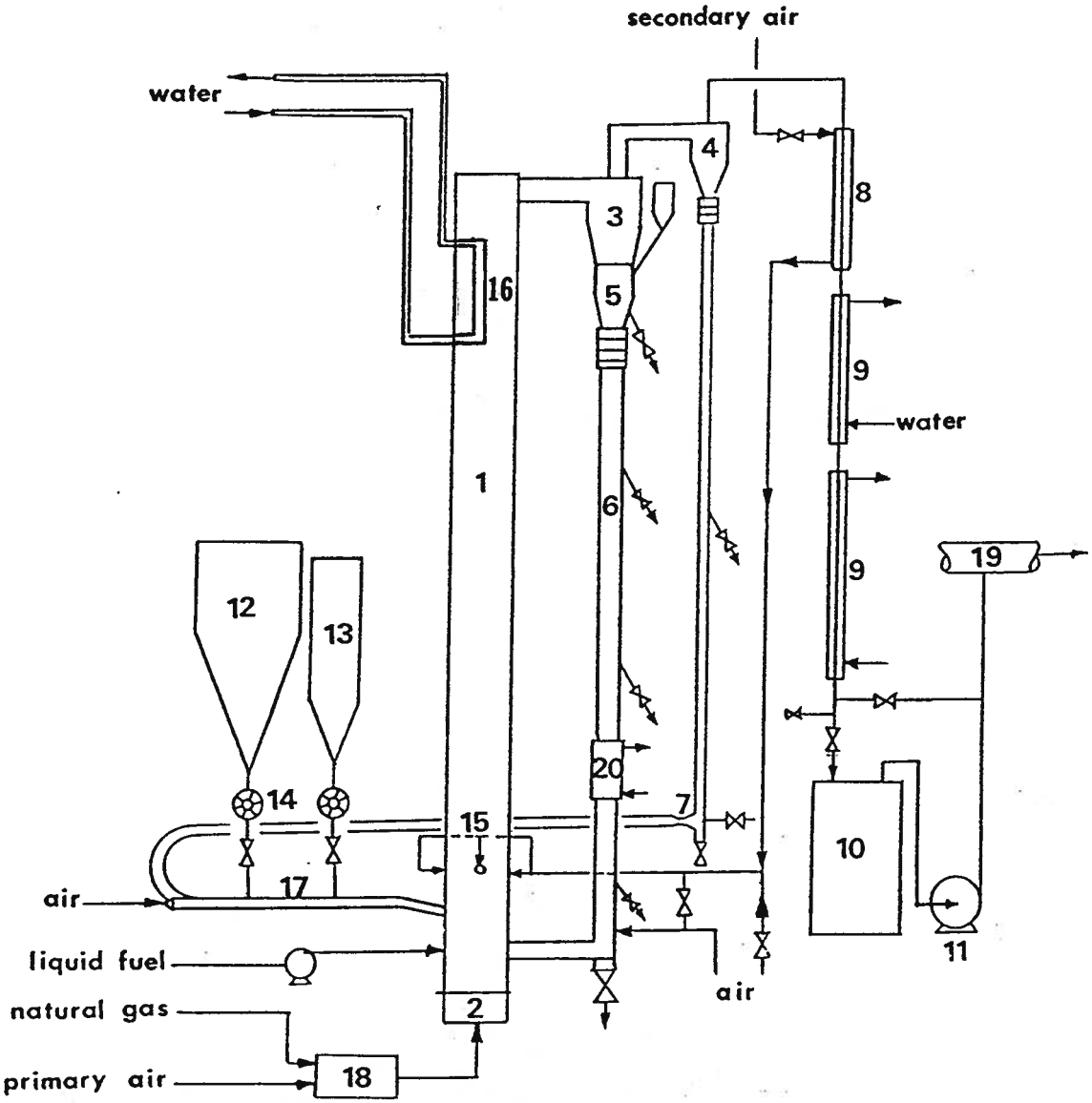

Figure 7.1: Simplified schematic diagram of the UBC circulating fluidised bed combustion facility.
1. Reactor; 2. Windbox; 3. Primary cyclone; 4. Secondary cyclone; 5. Recycle hopper; 6. Standpipe; 7. Eductor; 8. Secondary air preheater; 9. Flue gas coolers; 10. Baghouse; 11. Induced draught fan; 12. Fuel hopper; 13. Sorbent hopper; 14. Rotary valves; 15. Secondary air ports; 16. Reactor cooling tubes; 17. Pneumatic feed line; 18. External burner; 19. Ventilation; 20. Calorimetric section.

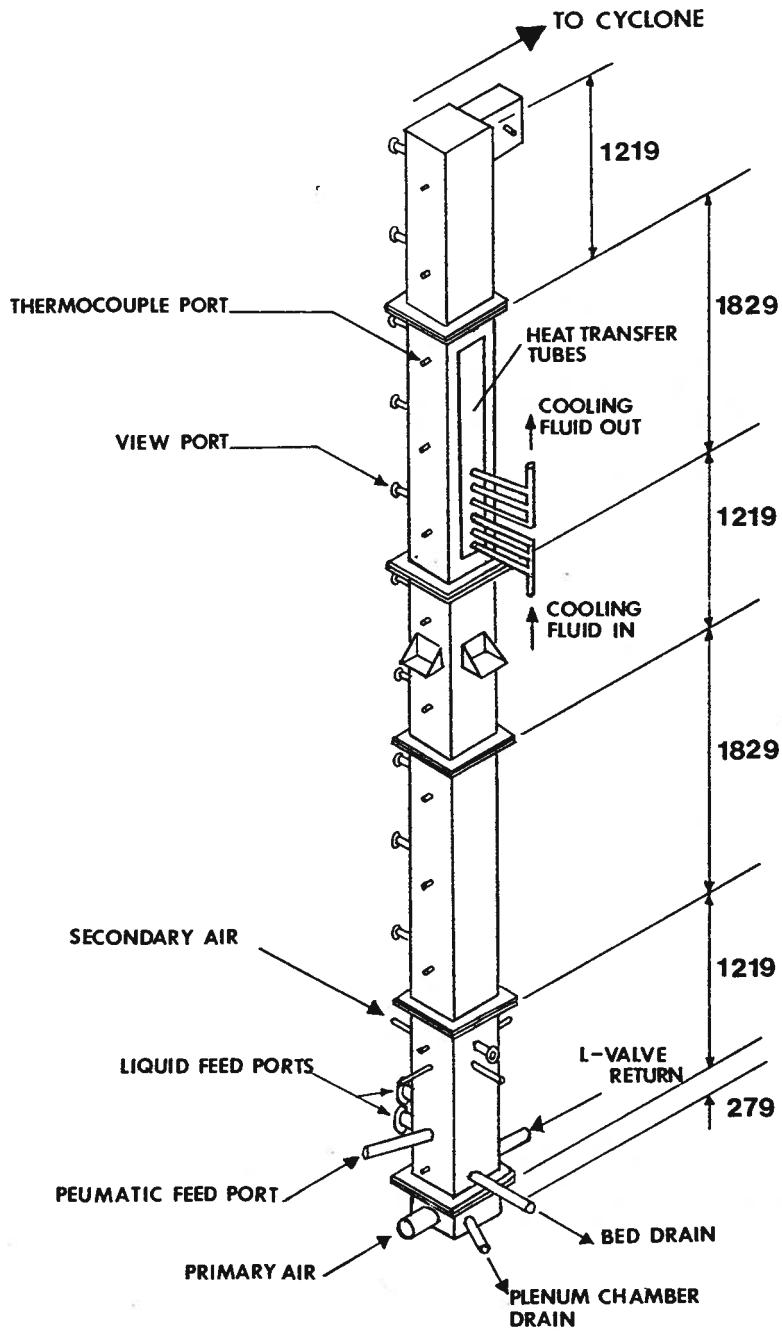

Figure 7.2: View of the riser reactor column. All dimensions in mm.

at the base to the full 152 mm × 152 mm cross-section at a height of 1.22 m. There are nine pressure tap locations at heights 51, 305, 813, 1067, 2134, 3353, 5182, 6401 and 7010 mm above the primary air distributor. In addition, there are eleven thermocouple ports and twelve 41 mm diameter probe ports, regularly spaced along the column. Solid fuels are fed pneumatically at a height of 540 mm above the distributor. The riser has an abrupt exit configuration (Figure 7.2). The exit port width and height are, respectively, 102 and 204 mm.

Gas and entrained solids exiting the top of the riser enter a medium efficiency primary cyclone of 305 mm ID. Solids captured by the primary cyclone are returned to the riser reactor at a height 152 mm above the distributor, via a 102 mm ID standpipe and non-mechanical solids flow L-valve. Gas and fine entrained solids pass from the primary cyclone to a 203 mm ID high efficiency secondary cyclone. Dusty gas leaving the secondary cyclone then passes through a baghouse. Solids captured by the secondary cyclone are returned continuously by a jet eductor system to the riser at 540 mm above the distributor. The mass flowrate of both this fine solids return stream and the fuel feed is small fraction of the L-valve solids return.

For the hydrodynamic tests, secondary air was injected through two pairs of opposed air ports, 914 mm above the primary air distributor. Heat was removed from the riser by passing either water or air through a vertical stainless steel tube bundle, located in the upper half of the riser (Figure 7.2). The solids recirculation rate, G_s, was estimated by calorimetry. The calorimetric section consists of a 584 mm long jacketed section of the standpipe. Cooling air is passed through the jacket, which is insulated on the outside. The mass flowrate of hot solids, which flow as a packed bed in the standpipe, is estimated from measurements of the cooling air flowrate, and the inlet and outlet temperatures of the cooling air and the solids (Burkell, 1986; Grace *et al.*, 1989a). To obtain a reasonable estimate of the heat loss from the solids in the jacketed section, inlet and outlet solids temperatures were measured at four radial positions.

7.2 Apparent Suspension Density Profiles

Apparent suspension density profiles were determined for the hot combustor in the same manner as for the cold unit. Gas differential pressures between pressure taps were measured by fast response transducers. Voltage outputs from these transducers were averaged over 10 s intervals, and converted to apparent suspension densities. This practice gave very stable suspension density results. Riser superficial gas velocity (based on total air flow), U_g, was varied in the range 5.7 to 10.5 m/s, with secondary-to-primary air ratios between 0.8 and 1.0. The estimated solids circulation rate, G_s, ranged from 19 to greater than 100 kg/m^3. The combustor fuel was sub-bituminous Alberta "Highvale" coal.

The start-up bed material for the test run was the same grade of Ottawa silica sand used in the cold unit tests ($\overline{d_p}$ = 160 μm, ρ_p = 2600 kg/m^3, see also Table 6.1). The PSD of the bed material collected after the test run had a Sauter mean diameter of 191 μm. The difference between start-up and bed drain samples is due to loss of fines and accumulation in the loop of inert ash particles originating in the coal feed. Highvale ash is predominantly composed of silica and alumina, and for reactive coals, such as Highvale, the mass fraction of carbon in the bed samples is always less than 1.0 wt%. Thus an average particle density for the bed material of 2650 kg/m^3 was assumed for model simulations described in Chapter 10.

Axial apparent suspension density profiles are shown in Figure 7.3. Suspension density profile data, corresponding to a nominal gas velocity of 7.3 m/s and a nominal solids circulation rate of 44 kg/m^{2}s, are also included in Figure 10.3 in comparison with model predictions. The profile shapes are similar to the abrupt exit profiles measured in the cold unit, i.e. there is an initial steep decrease over the lower part of the riser, followed by a relatively flat profile, and finally an increase again at the top of the riser. Similar trends occur for all U_g and G_s investigated. As in the cold unit, an increase in G_s caused a substantial increase in the apparent suspension density throughout the riser. In contrast, although there is a decrease in apparent suspension density when U_g is increased, the changes in density profile are not as significant (see Figure 10.3). The similarity between ambient and high temperature profiles near the exit

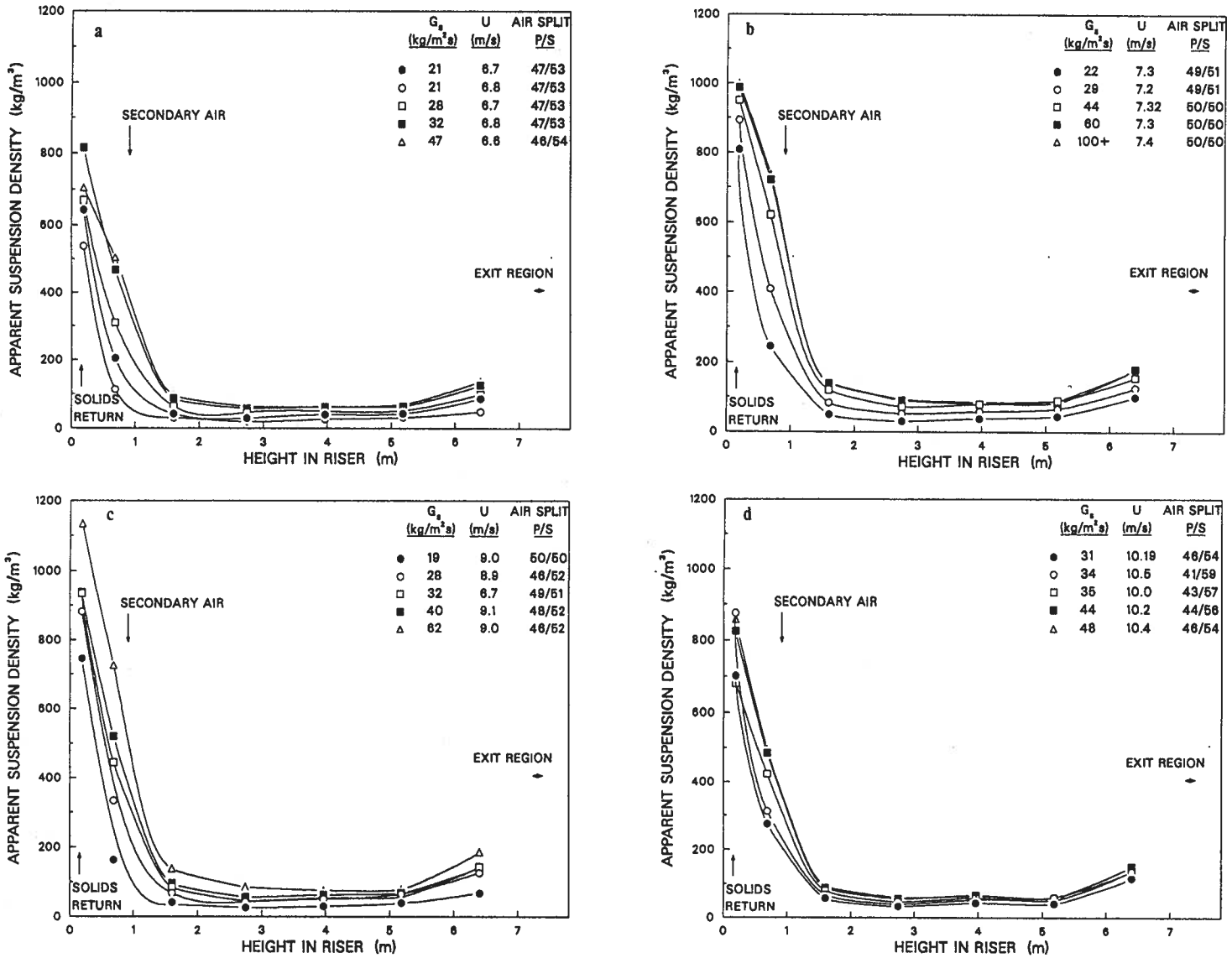

Figure 7.3: Apparent suspension density profiles measured in the UBC CFB combustor. Nominal superficial gas velocities: (a) 6.8, (b) 7.3, (c) 9.0, and (d) 10.3 m/s. ($T = 855 \pm 25$ °C, primary-to-secondary air ratios between 0.8 and 1.0, silica sand and Highvale coal.)

indicates that the abrupt exit also internally deflects a substantial fraction of the upflowing solids back down the riser. The high primary zone suspension densities, up to a height of about 1.5 m, are typical of a turbulent fluidised bed, and occur even at low G_s and high U_g. The formation of a turbulent bed in the tapered combustor base section is consistent with the observations in the tapered conical base section tests described in Chapter 6.

7.3 Capacitance Probe Study

The measurement of local solids concentration by capacitance probes was described in Chapter 6. Although capacitance probes have been used for a number of cold unit studies (e.g. Brereton, 1987; Louge *et al.*, 1990), they have not yet been widely applied to high temperature CFB units. One objective of the combustion studies was to develop a high temperature probe, suitable for use in a CFB combustor. Probe design and choice of construction materials are critical at combustor temperatures (800–900 °C range) due to the increased conductivity of dielectrics and weakening of metal components. As a cooled probe would be too bulky, and likely to interfere with the solids flow patterns, a "hot" probe was fabricated, shown in Figure 7.4. The needle and sheath are 304 stainless steel and, in the dimensions shown, were sufficiently strong to withstand the high temperature solids impacts for durations of $O(6\text{ h})$ before minor repairs were required. Several probes were rejected because they "shorted out" when the ceramic dielectric became conductive in the 550–600 °C range. Use of a high temperature magnesium oxide dielectric used in high temperature thermocouples overcame this problem.

Typical probe traces obtained at a height of 2.74 m are shown in Figure 7.5. Diesel fuel was used to maintain the combustor at approximately 870 °C. Nominal operating conditions were $U_g = 6.8$ m/s, $G_s = 40$ kg/m^{2}s, and primary-to-secondary air ratio, P/S = 80/20. The apparent suspension density, determined from the differential pressure measurements, was about 60 kg/m^3 at the probe traverse height. The probe was calibrated by inserting it into a sample of hot solids drained from the bed during the runs, and then noting the change in voltage output when it was rapidly removed from the sample. A typical loose-packed bed solids volume

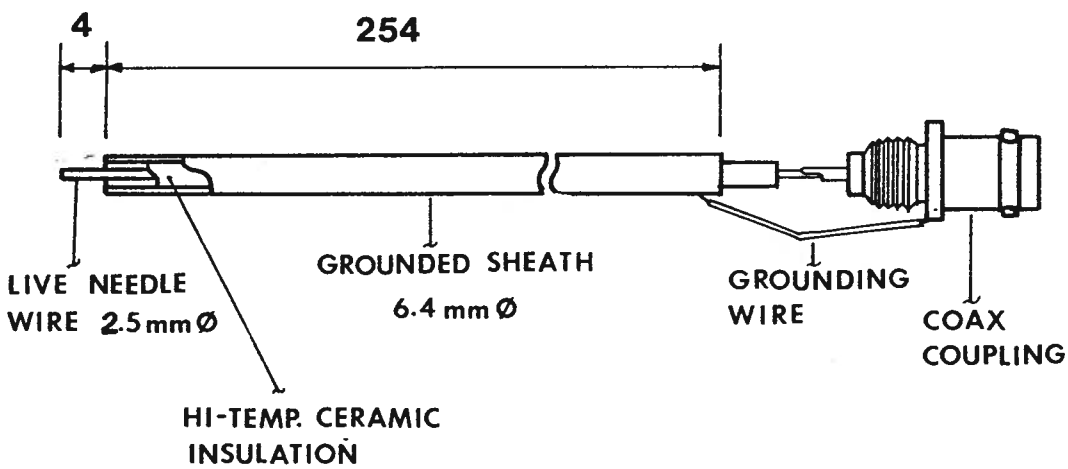

Figure 7.4: Capacitance probe used in the high temperature work. All dimensions in mm.

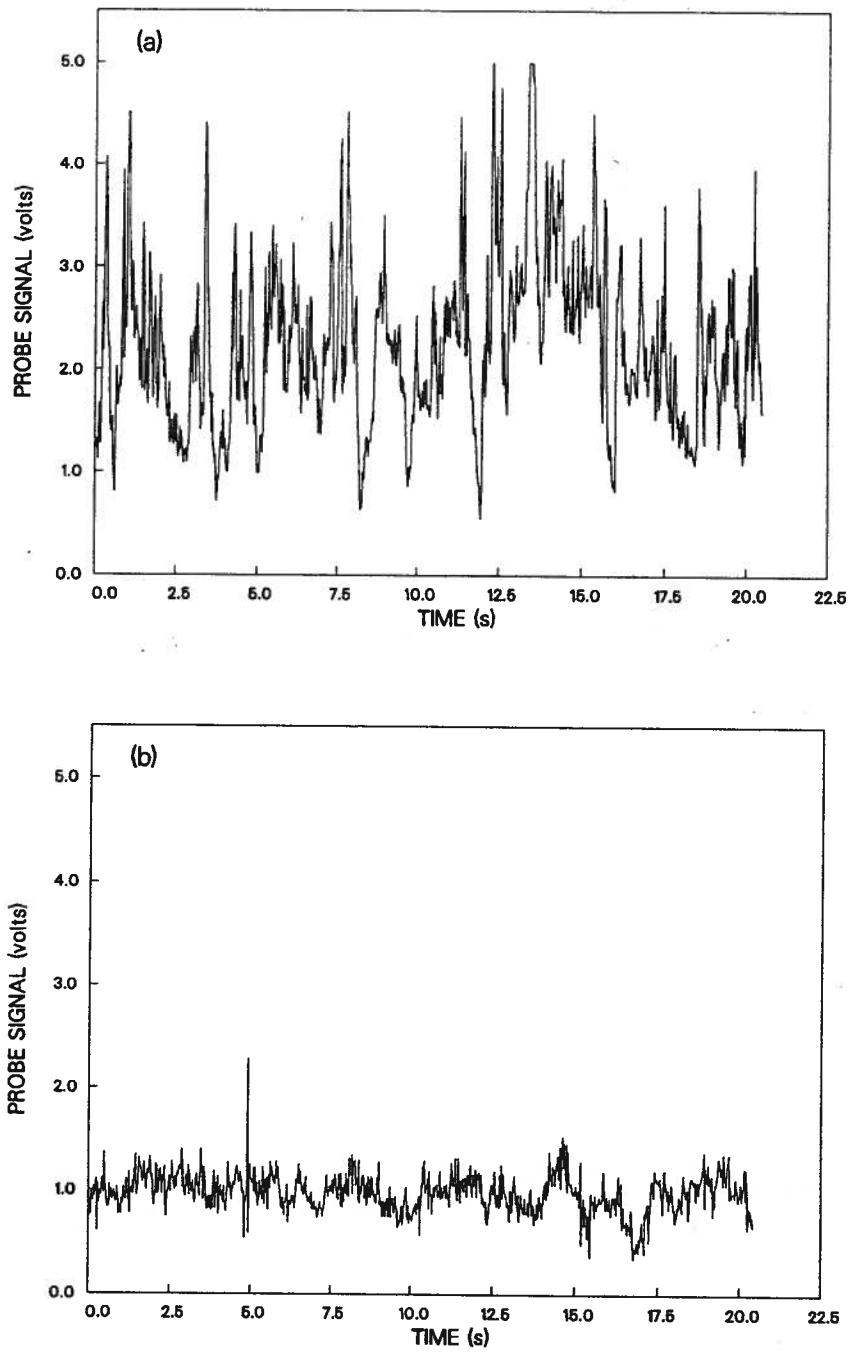

Figure 7.5: Typical traces produced by the high temperature capacitance probe with its tip (a) 5mm from the CFB combustor wall, and (b) at the centre of the combustor (76 mm from the wall). Measurement height, $z = 2.74$ m. (Combustor conditions: $U_g = 6.8$ m/s, $G_s = 40$ kg/m^{2}s, $T = 870$ °C, primary-to-secondary air ratio, P/S = 80/20.)

fraction of 0.58 was assumed for the hot solids. Calibration gave a 0.0 to 3.5 volt output over a range of 0.0 to 0.58 solids volume fraction.

By drawing a baseline through the lower points in the trace measured near the wall, and ignoring the sharpest peaks in the trace, which correspond to a negligible fraction of the total trace time, a crude estimate of the solids fraction of the denser solids structures may be made. The voltage signal varies by roughly 2.5 V, between the baseline (approximately zero solids fraction) and the periods of time over which the denser solids structures are detected. This was a typical result for the wall traces, and corresponds to a solids fraction of approximately 0.4 (i.e. 0.58×2.5 V / 3.5 V). Hartge *et al.* (1988) measured similar wall layer solids concentrations in a cold unit operating with CFB combustor ash. A solids volume fraction of 0.4 is thus assumed for wall streamers in the semi-empirical CFB combustor model described in Chapter 10.

Although voltage fluctuations in the trace at the centre of the combustor are clearly substantially less than near the wall, they are relatively large in comparison to traces in the centre of the cold unit (Figure 6.11). Significant problems with base line shift were frequently experienced, especially when the probe was in the core of the unit, and not all the fluctuations in the trace can confidently be attributed to solids concentration changes. For example, several of the largest voltage spikes in the wall trace are greater than the 3.5 V limit expected from the calibration tests. Furthermore, the probe was prone to "shorting out" when left for extended periods with the needle in the centre of the combustor. This did not appear to be due to any visually discernable damage to the probe, and the probe did not short out when heated to 900 °C in a Bunsen burner flame. Clearly, further development of the "hot" probe is required. Nevertheless, the traces clearly showed that average local suspension densities near the wall were greater than in the core of the combustor. Estimates of time-averaged suspension densities from the probe results were 450 and 140 kg/m^3 at the wall and centre of the riser, respectively. This centreline density is significantly greater than the apparent (cross-sectionally averaged) suspension density of 60 kg/m^3, measured at the traverse height, and further suggests that fluctuations in the probe output were not due solely to solids concentration fluctuations.

A possible cause of this additional fluctuation is probe vibration due to particle impacts.

7.4 Erosion Probe Results

Fresh stainless steel tubes of 9.5 mm OD were inserted horizontally at several axial locations into the combustor prior to three different test runs. Details of the composition of the fuels, high sulphur "H-Oil" pitch (two runs) and Highvale coal (one run) are given by Grace *et al.* (1989a). Nominal conditions for the runs were $T = 870$ °C, $G_s = 60$ kg/m^{3}s, and 16% excess air. Both 304 and 316 stainless steels were tested. The coal run and one pitch run lasted approximately one day, while the duration of the other pitch run was approximately two days. After exposure to the combustor, the tubes were removed and examined.

Most of the probes inserted in the combustor for the two day run were severely eroded, and bent upwards. They were generally too badly damaged to deduce erosion patterns. In contrast erosion patterns were observable on most of the probes resident in the combustor for one day. Normally, due to wall roughness and chipped refractory at the probe ports, the exact location of the wall was not discernable to any greater accuracy than ±4 mm.

Typical erosion patterns on the probes after one day of exposure are shown in Figure 7.6. The lower surface of the probes in the core of the combustor showed heavy pitted erosion due to impacts from upward moving particles. The tube wall (thickness 2 mm) was frequently fully eroded near the combustor centre (slightly off-centre in cooling tube region). On the upper surface of the probe a dark brown oxide layer formed with little erosion evident, except sometimes near the wall. Near the wall the oxide layer was often tinged with the colour of other compounds. For the pitch runs the interface between the dark brown oxide layer and metal exposed by erosion was often tinged a mustard yellow. The whole oxide layer in the wall region often had a dark red colour after exposure in the Highvale coal combustion run. The observed trends appeared to be independent of steel type. Wear patterns on the oxide layer, presumably due to a downward flux of particles, were often observed on the upper region of the probes near the combustor wall. These patterns usually extended between 10 and 20 mm from the

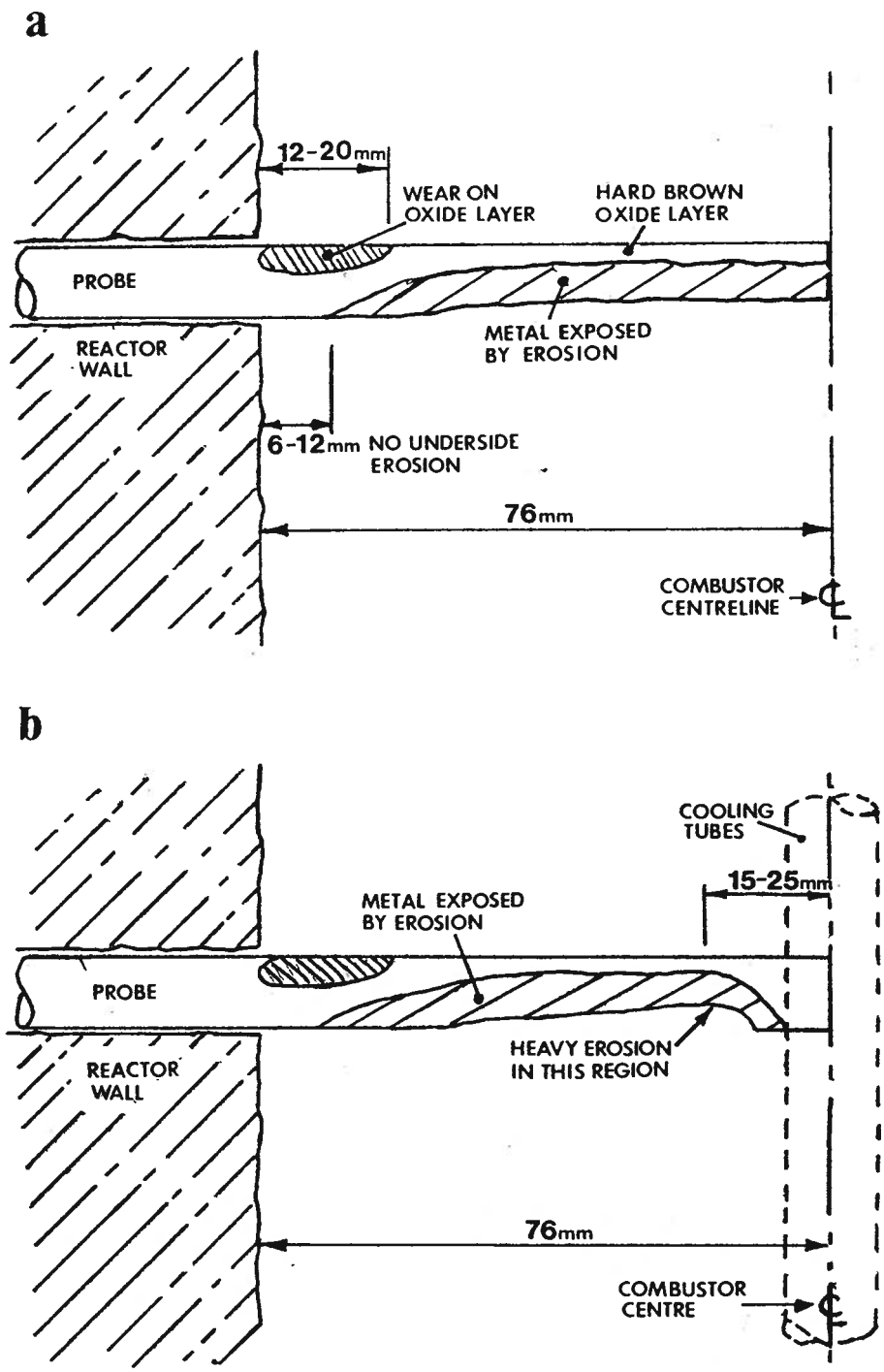

Figure 7.6: Erosion patterns observed on the erosion probes after a 24 hour exposure in the combustor: (a) typical pattern, and (b) pattern in the cooling tube region. (Highvale coal, $T = 870$ °C, $G_s = 60$ kg/m^{2}s, 304 stainless steel probe.)

wall. The erosion of the probe underside usually extended to within 6 to 12 mm from the wall (Figure 7.6). Hence there was a small region at the boundary between the outer annular region and the inner core, which experienced both upwards and downwards particle motion. Erosion is more strongly dependent on impact velocity than mass flux, and thus the erosion patterns are consistent with a rapid suspension upflow in the core and slower particle downflow at the wall.

7.5 Solids Flow and Distribution in the Pilot-Scale CFB Combustor

The test results clearly indicate that solids flow patterns in the hot pilot-scale unit are similar to those observed in cold unit risers, i.e. a relatively dense suspension downflow at the wall, and rapid more dilute suspension upflow in the core. From the extent of erosion on the probes it is clear that the magnitude of the wall downflow velocity is significantly lower than the core upflow velocity. The capacitance probe traces indicate interspersed regions of dilute and dense suspension at the wall, consistent with an intermittent disruption of the downflowing wall layer, as in cold units. The combustor abrupt exit appears to have the same effect on the solids flow patterns as the cold unit abrupt exit, described in Chapter 6.

Chapter 8

INTEGRATED PARTICLE COLLISION AND TURBULENT DIFFUSION MODEL FOR DILUTE SUSPENSION FLOWS

The model presented in this chapter predicts the key flow characteristics of gas-particle dilute suspensions in vertical flow in risers of constant cross-section. Such flows occur in the core of CFB risers and in dilute pneumatic conveying. In a "dilute" suspension it is assumed that the particles are uniformly distributed over a distance at least comparable to lengths characteristic of the dynamical interactions, such as energetic eddy sizes and particle mean free paths between collisions, but smaller than macroscopic distances such as the riser height. Furthermore, only binary particle collisions are assumed to occur in a dilute suspension. When non-homogeneity occurs in the particle distribution and it is possible to divide the overall flow into dilute flow regions interspersed with or surrounded by denser particle structures (as in a CFB core surrounded by wall streamers, within dilute transient channels in a turbulent bed, or inside bubbles in a bubbling bed), then the model is still applicable in the dilute regions. Obviously, appropriate boundary conditions between the dilute and denser regions are required. In this chapter, wall boundary conditions are presented for dilute CFB core flow considering both the cases of a bare wall and a wall covered by dense particle streamers. The CFB core flow is assumed to be radially uniform.

The primary aim of the model is to predict (i) the forces influencing the steady vertical velocities of both gas and particles, and (ii) the distribution of lateral particle velocities that result in the deposition of particles on the riser wall. These are key influences on the overall motion and distribution of solids within a CFB riser. From the discussion of the various dynamical gas-particle and particle-particle interactions in Chapters 3 and 4, it is evident that

there are many coupled effects that must be accounted for. A rigorous mathematical approach to formulating and solving the dynamical interaction equations to give the modulation of the turbulence energy spectrum and the full velocity distributions for all particles of various sizes, shapes and densities is clearly a mammoth task. Even for the highly idealised systems of "particles" in kinetic gas theory, where only collisions and field forces (e.g. gravitational, electrical) need be considered, the mathematics of even the simplest systems become complex (Chapman and Cowling, 1970). For particulate systems, such mathematical efforts are not warranted given the complexity of the systems and the many uncertainties involved in characterising both the particles (e.g. shape, elastic/plastic collision deformation, attrition, etc.) and the gas turbulence.

The modelling approach employed here characterises the gas turbulence in terms of its energetic eddies (see Chapter 3), discretises the particle phase into several size/density fractions, and assigns ensemble average r.m.s. fluctuating and mean velocity components to each fraction. The particles are assumed to be spherical in deriving expressions to predict particle scattering due to collisions. The net effect of particle-particle interactions within a given fraction or between particles of different fractions is assumed to be reasonably predicted by considering only interactions of particles possessing the appropriate ensemble average velocities. To predict lateral motion of particles, "fluctuating kinetic energy" balances for each fraction are developed. Based on the analysis in Chapter 3, a linear drag law is assumed for particle motion involving velocity changes of similar magnitude to the r.m.s. fluctuating velocities.

The accuracy of such an approach may be demonstrated by considering an equivalent approach often given in simple gas kinetic theory. Consider a box filled with a static gas (zero mean velocity) composed of molecules of the same type (say type 1) at a uniform, constant temperature. If the molecules are treated as elastic hard spheres, then kinetic theory predicts that the velocity distribution of the gas will be Maxwellian. If the r.m.s. velocity of the molecules is defined as $\mathbf{c}_1$, then the collision frequency (collisions per unit time and volume) amongst the type 1 molecules, Z_{11}, may be determined exactly by multiple integration over all possible

molecular encounters. The exact kinetic theory result is $Z_{11} = 2\sqrt{\pi/3}\,\sigma_1^2 \mathbf{n}_1^2 \mathbf{c}_1$ (Chapman and Cowling, 1970), where $\mathbf{n}_1$ is the number of molecules per unit volume and σ_1 is the collision radius ($\sigma_1 = 2r_{p1}$ in this case). The average number of collisions by *each* molecule per unit time is simply $Z_1 = 2Z_{11}/\mathbf{n}_1 = 4\sqrt{\pi/3}\,\sigma_1^2 \mathbf{n}_1 \mathbf{c}_1$. As the mean molecular velocity of the gas is zero, Z_1 may be estimated by considering the case of a single molecule with r.m.s. velocity $\mathbf{c}_1$ moving through a field of static molecules of concentration $\mathbf{n}_1$. This is the standard "bullets and targets" problem covered in many physics and chemistry texts (e.g. Levich, 1971; Adamson, 1979). The collision frequency in this case may be simply shown to be $Z_1 = \pi\sigma_1^2 \mathbf{n}_1 \mathbf{c}_1$. The estimated and exact relations for collision frequency only differ by a constant, which in the gas case results in the estimate underpredicting collision frequency by approximately 30%. In the following model, although exact relations are used where possible (e.g. for collision frequencies), some approximations similar to this example are employed.

From the discussion of Chapter 3 it is assumed that the gas turbulence production and dissipation rates are balanced. Changes in turbulence intensity with height are assumed to be influenced only by corresponding changes in the particle concentration and distribution with height (assuming walls of constant roughness), and convective transfer of gas turbulent energy is assumed negligible. In contrast, the convective component in the fluctuating kinetic energy balance equation is assumed to be significant. Whereas a gas eddy loses a substantial portion of its energy in one turnover time, τ_e, it is expected that a larger particle ($\tau_p \gg \tau_e$) will travel a substantial distance before losing its energy if it enters into a dilute region where collision frequency is low. In numerical simulations of the turbulent motion of discrete 250 μm glass particles in ambient temperature air flowing at 20 m/s in a 32 mm diameter vertical tube, Govan *et al.* (1989) predicted that the r.m.s. fluctuating velocity may take a much greater distance to develop than the mean axial velocity.

The model presented in this chapter has two key features that distinguish it from other detailed models for suspension flow: (a) it considers the coupled effects of gas turbulence and particle collision, and (b) it allows for multiple particle sizes or densities. Although the analysis

of Chapter 3 suggests that both turbulence and collisions may be important in determining suspension flow in CFB risers, no models appear to have been developed that include both effects. Jansen and Romate (1991) have, however, outlined a prospective model considering turbulence and collisions for suspension flows in FCCs, assuming a single particle size. The inclusion of multiple particle size or density fractions permits the representation of several phenomena that may be important in suspension flows, including particle segregation and the enhancement of collisional forces and particle velocity fluctuations due to increased particle collision frequency. This is particularly important in some systems. For example, in CFB combustion systems the fuel particles may be an order of magnitude larger than the inert bed particles (sand/ash/limestone). The carryover of very large particles from the freeboard of bubbling beds is likely only explainable in terms of particle collisions between large and small size fractions (Geldart *et al.*, 1979).

In the latter part of this chapter, a version of the suspension flow model for fully-developed flow in a riser core is proposed, using two-fluid equations of motion from Chapter 4. This model is coded in FORTRAN, and a number of simulations of the cold unit tests and other riser operations are presented. The results of these tests provided considerable insight into the fundamental dynamics of suspension flows in risers and justify many of the model assumptions.

8.1 Model Concepts

Many of the model concepts follow directly from Chapter 3, where it was shown that a typical energetic eddy contains many particles. It is assumed that when particle collisions are important in determining particle fluctuating motion, the collision process may conceptually be considered as occurring "inside" a typical energetic eddy ($\tau_k < \tau_r$). The gas turbulence is assumed to be isotropic and homogeneous and the mean gas and particle flows are vertical. Each particle fraction is assigned three characteristic velocities: a mean axial (z direction) velocity $\mathbf{v}_z$, an r.m.s. fluctuating velocity $\mathbf{c}_k$, and a mean "drift" velocity $\mathbf{c}_t$ due the effects of the gas turbulence. The concept is shown schematically in Figure 8.1. Particles either "fall" into the eddy (eddy

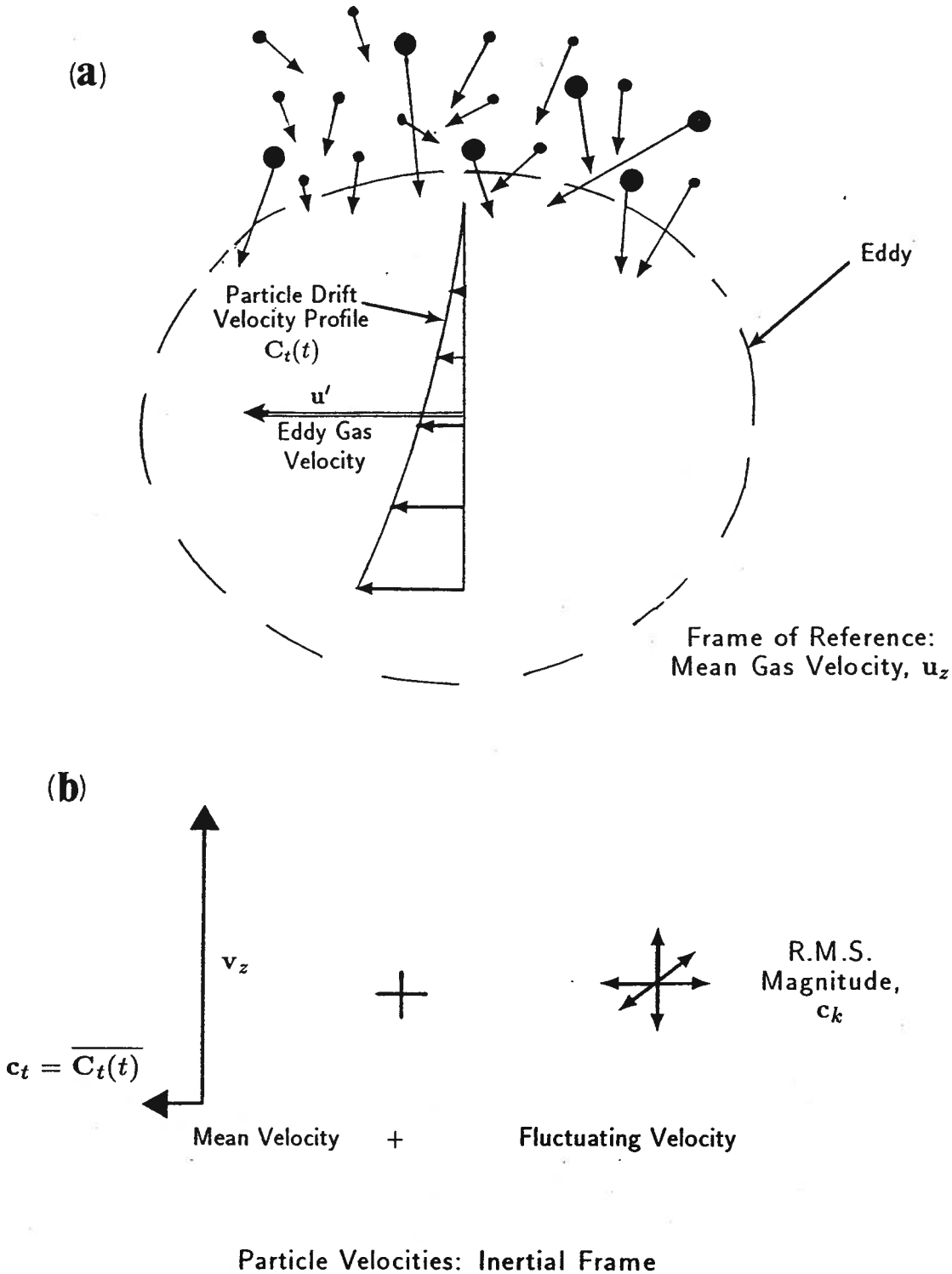

Figure 8.1: Schematic illustrating the proposed model concept of particle-particle interaction and gas-particle interaction inside an energetic eddy: (a) eddy drift velocities, (b) particle fraction velocity components.

frame of reference) from different eddies above or the eddy forms around the particles. It is assumed that these particles have come from regions where gas fluctuating velocities are uncorrelated, and hence the net drift velocity of the particles is zero upon entering the eddy. Particles within an eddy collide with one another due to both the distribution in fluctuating velocities and the different axial slip velocities of different fractions. During the time the particles are in the eddy they gain an additional component of velocity due to the drag force in the direction of the eddy gas velocity, $\mathbf{u}'$. The mean drift velocity, $\mathbf{c}_t$, is defined as the drift velocity of a particle averaged over the time in which it interacts with the eddy. The drift velocity, $\mathbf{c}_t$, depends on the particle response time and the eddy interaction time, both of which vary between fractions. Hence a relative velocity between fractions in the direction of the eddy gas flow arises, which further enhances the particle collision frequency.

The "fluctuating kinetic energy" of a single particle from particle fraction i is the kinetic energy of that particle calculated in a frame of reference travelling with the mean velocity $(\mathbf{v}_{zi} + \mathbf{c}_{\mathbf{t}i})$ of that fraction. The mean fluctuating kinetic energy per unit mass, K_i, of a particle fraction i is defined as the mean specific fluctuating kinetic energy of that fraction, averaged over all its constituent particles inside a typical energetic eddy. Hence,

$$K_i = \frac{\mathbf{c}_{ki}^2}{2}\,, \tag{8.1}$$

where $\mathbf{c}_{ki}$ is the r.m.s. fluctuating velocity. Therefore, the fluctuating kinetic energy of fraction i per unit suspension volume is $\rho_{si}K_i$. Although this definition of fluctuating energy is similar to the definition of temperature in kinetic gas theory, such terms as "granular temperature" are not used in this model because of the poor analogy between particulate phases with wide size distributions and multi-molecular gas mixtures. The limits of the kinetic theory gas analogy are discussed in Section 8.10.

The mean velocity of a cloud of particles may be defined as that portion of the particles' velocities that are correlated, and the fluctuating velocity as that portion that is uncorrelated. Therefore, the drift component velocity $\mathbf{c}_t$ of the particles has ambivalent properties, being both a mean and fluctuating velocity. Within an energetic eddy it is a component of the *mean*

velocity of the particles. In contrast, considering all eddies in a given region, each with gas fluctuating velocities in different directions, the corresponding distribution of $\mathbf{c}_t$ is another form of *fluctuating* particle velocity that occurs on a longer timescale than the collisional fluctuations within any given eddy. When the particles are within the eddy the mean drift velocity of each fraction does not contribute *directly* to the fluctuating kinetic energy of that fraction (indirectly it may increase collision frequency). However, upon leaving the eddy the particles are assumed to mix with particles from other eddies into a combined pool before being redistributed amongst the next set of eddies. As the particles of a given fraction enter this pool from energetic eddies of arbitrary orientation, the kinetic energy corresponding to the drift velocity becomes part of the fluctuating kinetic energy at this stage, and the particles enter their next eddy with zero net drift velocity. The drift velocity therefore transfers energy from the gas turbulence to the random fluctuating kinetic energy of the particles with a finite transfer time and energy level.

To determine the collisional r.m.s. fluctuating velocity $\mathbf{c}_k$ of each particle fraction, it is necessary to assume some form for the particle fluctuating velocity distribution. For the simplest case of motion of particles of a single size, assuming elastic particle-particle collisions, negligible interference of boundary conditions (such as entering streamer particles) and particle response times, τ_p, significantly greater than collision intervals, τ_k (i.e. small changes in particle velocity between collisions compared to changes due to collision), the particle motion is analogous to that of molecules in a hard-sphere kinetic theory of gas. In this case the velocity fluctuations are isotropic and the distribution Maxwellian due to the symmetry of the system and the principles of detailed balancing (Chapman and Cowling, 1970). Unfortunately there are several possible forces and effects in real particulate systems that may distort this ideal velocity distribution and cause anisotropy.

Particle-particle collisions are a mechanism by which particle fluctuating kinetic energy associated with one direction is redistributed in all directions (and dissipated by inelastic collisions). Therefore, when effects are present that tend to cause anisotropy in the particle fluctuating velocity distributions, the counter-balancing collision process continually works towards restoring

the system to isotropy. There are several effects that may cause anisotropy. In Chapter 3 it was predicted that discrete particles with type 2 motion in a turbulent gas flow may have axial r.m.s. fluctuating velocities up to twice that of the corresponding lateral r.m.s. velocities. However, even for the lowest type 2 particle concentrations typical of the core of CFB risers, the turbulence is expected to be substantially suppressed and particle fluctuating motion should be largely due to collisions (see Chapter 3). This suggests that anisotropy in type 2 particle fluctuations may not be significant. The fluctuations of small type 1 particles are isotropic in regions of isotropic gas turbulence and the response of type 3 particles to the turbulence is small. Consequently, the particle fluctuations due to gas turbulence are assumed to always be isotropic in the model. In this case $\mathbf{c}_t^2 = 3v_e^2$, where v_e is the average particle linear drift velocity within an eddy.

Oblique collisions arising from a difference in mean axial velocities between particles also increase the fluctuating velocity components of the particles as described in Chapter 3. In the period between collisions, a particle's velocity increases in the axial direction and decreases in the lateral directions due to drag by the gas. Consider first the case of nearly elastic collisions. If the collision interval τ_k is significantly less than the particle response time τ_p, then the input of kinetic energy to the system via axial forces between each collision is a small fraction of the total fluctuating kinetic energy: energy is then evenly distributed in all directions in the colliding particle system, and near isotropy in fluctuations is maintained. For typical CFB core suspension densities, this isotropy is always a good approximation for the larger particles and frequently also applicable for the smaller, more responsive particles (see Chapter 3). Furthermore, the collision frequency for a wall particle entering the core is likely to be orders of magnitude greater than the average core particle collision frequency because of the much greater relative velocities involved. Thus the large parcel of kinetic energy (relative to the core suspension frame of reference) introduced by each wall particle should generally be re-distributed rapidly amongst core particles.

For very small or light particles, τ_p is comparable to or less than τ_k. These particles have

lower average slip velocities than large particles, and are quickly accelerated axially and decelerated laterally by gas drag following collisions. Consequently they spend most of their time between collisions travelling at a velocity close to their impact velocity immediately before their next collision (see Chapter 3). As a result of their motion between collisions, these particles do not have a symmetrical Maxwellian (or Gaussian) fluctuating velocity distribution. However, providing suitable mean particle velocities are assigned to these small particles by using the concept of the velocity weighting factor, λ, introduced in Chapter 3, a particle fluctuating kinetic energy balance still gives reasonable estimates of the ensemble average r.m.s. fluctuating velocities for these particles. Small particles also tend to follow the gas flow around a larger target particle, thereby lowering the collision frequency. This is characterised by a collision efficiency parameter based on the data of Soo (1967). Collision frequencies for all particles are calculated assuming that the velocity distributions are Maxwellian. Although this is an approximation for small particles, the rapid response of such particles to gas fluctuations suggests that their fluctuating motion are largely determined by turbulence rather than particle-particle collisions. It must be stressed that, although Maxwellian velocity distributions are assumed, and several kinetic theory results pertaining to such distributions are used in the model development, direct analogy between the particles in suspension and a kinetic theory gas is not invoked. In fact, there are fundamental differences between these two systems as discussed later.

If the collisions are inelastic, particles lose a significant fraction of their fluctuating kinetic energy in a collision. Then the particle velocity fluctuations are expected to be anisotropic when the forces driving the collision process are anisotropic (i.e. drag due to mean gas flow or lateral gradients in particle vertical velocity). Only a fraction of each parcel of energy transferred to the colliding system in the axial direction is re-distributed into lateral fluctuations. Fortunately particles used in many CFB systems are either mineral particles or robust catalysts, both of which are relatively elastic materials. The possible extent of anisotropy for highly inelastic collisions is discussed later in this chapter. Particle fluctuating velocities in this model are always assumed to be isotropic.

The lateral flow of particles across any vertical plane, such as a core-wall boundary in a CFB, results from the distribution of fluctuating velocities in the lateral direction. Although the mean lateral velocity of any fraction is zero when averaged over all eddies and particles, there are always some individual particles near the interface that have a component of fluctuating velocity that carries them across before the next collision. The distribution of lateral velocities may be characterised by the r.m.s. fluctuating velocity $\mathbf{c}_k$ and the drift velocity $\mathbf{c}_t$. If all particles of a given fraction i inside each typical energetic eddy are assumed to have drift velocities of constant magnitude $|\mathbf{c}_{ti}|$ within an eddy, and the turbulence is isotropic, then a combined r.m.s. "fluctuating" velocity $\mathbf{c}$ may be defined by averaging either spatially (over a volume containing many eddies) or temporally, i.e.

$$\begin{aligned} \mathbf{c}_i^2 &= \overline{(\mathbf{c}_{ti} + \mathbf{C}_{ki}) \cdot (\mathbf{c}_{ti} + \mathbf{C}_{ki})} \\ &= \mathbf{c}_{ti}^2 + 2\,\overline{(\mathbf{c}_{ti} \cdot \mathbf{C}_{ki})} + \overline{(\mathbf{C}_{ki}^2)} \\ &= \mathbf{c}_{ti}^2 + \mathbf{c}_{ki}^2 \,, \end{aligned} \tag{8.2}$$

where $\mathbf{C}_{ki}$ is the instantaneous fluctuating velocity of a discrete type i particle within an eddy, and the distribution of all such velocities within an eddy is isotropic, as discussed. The direct relation between the combined r.m.s. fluctuating velocity $\mathbf{c}_i$ and the flow of particles across a vertical plane is derived in Section 8.9.

8.2 Ensemble Averaging of the Binary Particle Collision Process

8.2.1 Single Collisions between Two Spherical Particles

A typical collision between two spherical particles of respective masses m_{pA} and m_{pB} and diameters d_{pA} and d_{pB} is shown in Figure 8.2. The velocities the instant before impact are $\mathbf{V}_{1A}$ and $\mathbf{V}_{1B}$, and the scattering velocities immediately following collision are $\mathbf{V}_{2A}$ and $\mathbf{V}_{2B}$. The velocity of particle A relative to particle B is $\mathbf{V}_{AB}$ and the unit vector directed from the centre of particle A to the centre of particle B at the moment of impact is $\mathbf{k}$. Assuming that (i) particle rotation prior to collision is negligible, (ii) the contact area between particles upon

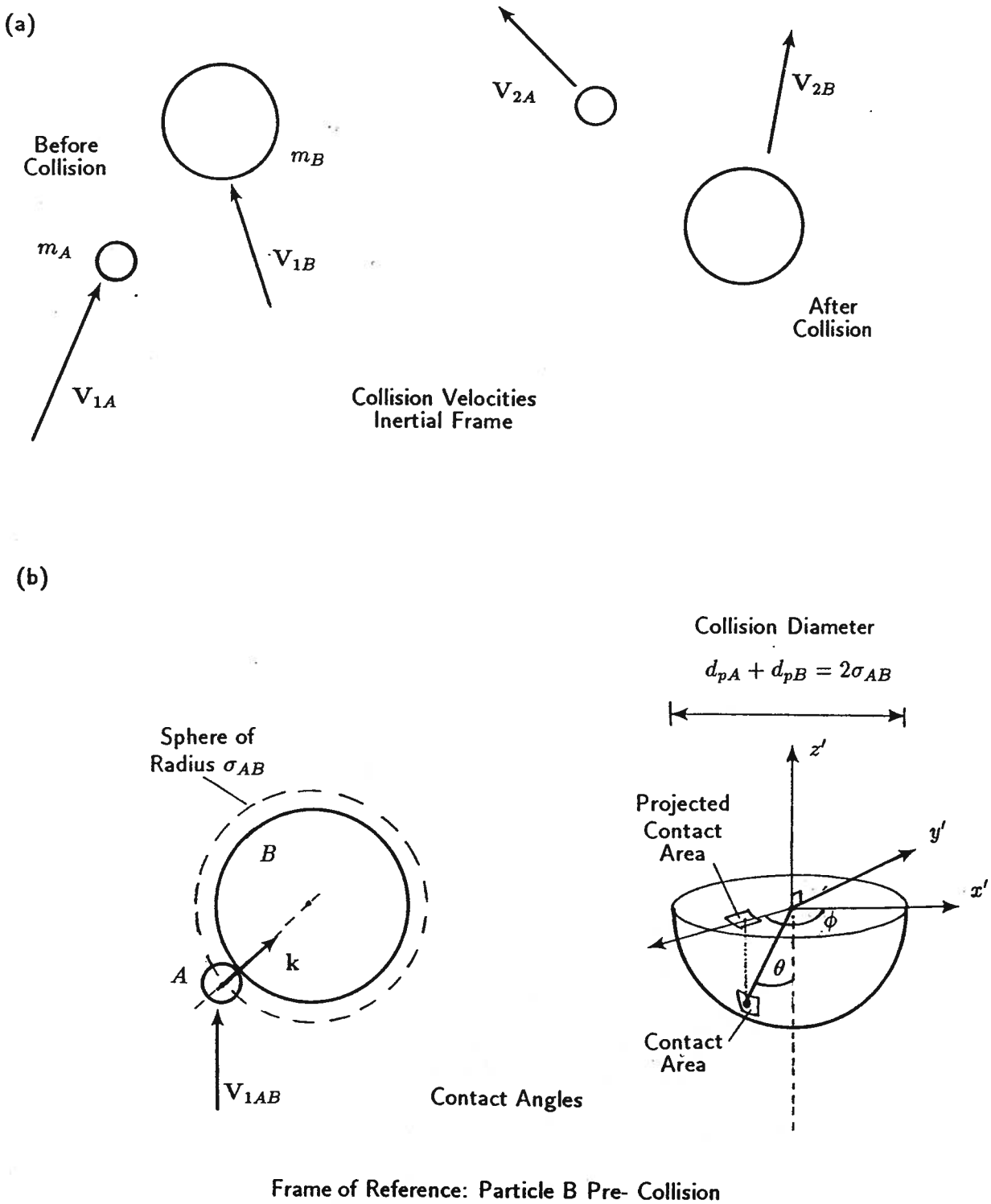

Figure 8.2: Typical binary particle collision: (a) collision velocities and (b) contact angles and collision radius.

impact is small and (iii) the particle surfaces are smooth, then the change in velocity of particle A relative to B will occur only in the direction of $\mathbf{k}$. For the components of relative velocity in this direction, the ratio of the relative velocity after collision to that before collision is termed the *coefficient of restitution*, e, i.e.

$$\mathbf{k} \cdot \mathbf{V}_{2AB} = -e\,(\mathbf{k} \cdot \mathbf{V}_{1AB}) \ . \tag{8.3}$$

The coefficient of restitution is dependent on the particle material. The maximum value, $e = 1.0$, corresponds to a perfectly elastic material. A special case of a head-on collision corresponding to $e = 0.0$ occurs when particles adhere to one another on impact. Particles smaller than those typically of interest in CFBs ($< 5\ \mu$m, say) may adhere upon impact due to close range surface forces (e.g. Rogers and Reed, 1984). Typical ranges for e at ambient temperature are 0.8 to 1.0 for glass particles and 0.2 to 0.6 for metal particles (Goldsmith, 1960; Nakamura and Capes, 1976; Govan *et al.*, 1989). As values for e at elevated combustor temperatures (800–900 °C) do not appear to have been measured, it is assumed they are similar to ambient temperature values, providing there is not a significant softening of the particles. Mineral sands and ashes that are typical of the inert particles predominant in CFB combustors would be expected to have values of e similar to glass based on hardness and crystalline structure. For devolatilising coals and combusting char, e may be very low due to plastic deformation and attrition during impact. It is normal to assume that e is constant for a given material, and several quite rigorous mathematical models for the collisions of single-sized large particles (i.e. no influence of gas turbulence) have been proposed based on this assumption (e.g. Jenkins and Savage, 1983; Louge *et al.*, 1991). Unfortunately e may also vary significantly with both the size of the particles and the approach velocities of the collision (Goldsmith, 1960; Beer and Johnston, 1976; Lun and Savage, 1986). Here we assume that e is constant for a given material. The variation in reported values of e ($O(\pm 20\%)$) suggests that the error introduced by this assumption is no greater than errors introduced by characterising the collision process in terms of r.m.s. velocities, as described earlier. It is debatable whether more rigorous mathematical approaches are justified in models where e is assumed to be a

material constant.

In a two-particle collision linear momentum is always conserved, i.e.

$$m_{pA}\mathbf{V}_{1A} = m_{pA}\mathbf{V}_{2A} - \mathbf{J} \ , \tag{8.4}$$

$$m_{pB}\mathbf{V}_{1B} = m_{pB}\mathbf{V}_{2B} + \mathbf{J} \ , \tag{8.5}$$

where $\mathbf{J}$ is the impulse of the force exerted by particle A on particle B. If the particle velocities before collision, $\mathbf{V}_{1A}$ and $\mathbf{V}_{1B}$, are known, then eqs. (8.3), (8.4) and (8.5) may be combined (see Appendix D) to give the respective particle velocities after collision,

$$\mathbf{V}_{2A} = \mathbf{V}_{1A} - \left(\frac{m_{pB}}{m_{pA} + m_{pB}}\right)(1+e)(\mathbf{k}\cdot\ \mathbf{V}_{1AB})\,\mathbf{k} \ , \tag{8.6}$$

$$\mathbf{V}_{2B} = \mathbf{V}_{1B} + \left(\frac{m_{pA}}{m_{pA} + m_{pB}}\right)(1+e)(\mathbf{k}\cdot\ \mathbf{V}_{1AB})\,\mathbf{k} \ . \tag{8.7}$$

Equations (8.6) and (8.7) extend the results presented by Jenkins and Savage (1983) for identical spherical particles to particles of different size/density.

Orthogonal axes with the origin at the centre of particle B are also shown in Figure 8.2. Note that the z' axis is parallel with the pre-collision relative velocity and is not necessarily in the vertical direction z. Therefore, there are no restrictions on the possible approach or scattering velocities of the particles thus far. If the unit vectors in the axis directions are $\boldsymbol{\delta}_x$, $\boldsymbol{\delta}_y$ and $\boldsymbol{\delta}_z$, and particle A contacts particle B such that particle A's centre lies at position $(\sigma_{AB}, \theta, \phi)$ as shown, then

$$\mathbf{k} = \sin\theta\,\cos\phi\,\boldsymbol{\delta}_x + \sin\theta\,\sin\phi\,\boldsymbol{\delta}_y + \cos\theta\,\boldsymbol{\delta}_z \ . \tag{8.8}$$

The components of the particles' post-collision velocities for this coordinate system may be found by substituting $\mathbf{k}$ into eq. (8.6) and resolving. For example, the x', y', and z' components for particle A are, respectively,

$$\mathbf{V}_{x2A} = \mathbf{V}_{x1A} - \frac{m_{pB}(1+e)}{2\,(m_{pA} + m_{pB})}\,|\mathbf{V}_{z1AB}|\sin 2\theta\cos\phi\,\boldsymbol{\delta}_x \ , \tag{8.9}$$

$$\mathbf{V}_{y2A} = \mathbf{V}_{y1A} - \frac{m_{pB}(1+e)}{2\,(m_{pA} + m_{pB})}\,|\mathbf{V}_{z1AB}|\sin 2\theta\sin\phi\,\boldsymbol{\delta}_y \ , \tag{8.10}$$

$$\mathbf{V}_{z2A} = \mathbf{V}_{z1A} - \frac{m_{pB}(1+e)}{(m_{pA}+m_{pB})}\mathbf{V}_{z1AB}\cos^2\theta \ . \tag{8.11}$$

Note that the choice of coordinate system in this case simplifies the expressions for scattering velocity components because $\mathbf{V}_{x1AB}$ and $\mathbf{V}_{y1AB}$ are both zero.

The change in kinetic energy of each particle due to a single collision is a function of both the energy transferred from one particle to the other and the energy lost in the collision. For particle A the energy change is

$$\Delta E_A = \frac{1}{2}m_{pA}\left(\mathbf{V}_{2A}\cdot\mathbf{V}_{2A} - \mathbf{V}_{1A}\cdot\mathbf{V}_{1A}\right) \ . \tag{8.12}$$

Substituting the expression for $\mathbf{V}_{2A}$ from eq. (8.6) into eq. (8.12) and re-arranging gives

$$\Delta E_A = \frac{m_{pA}m_{pB}(1+e)}{2(m_{pA}+m_{pB})}\left[\frac{m_{pB}(1+e)}{m_{pA}+m_{pB}}(\mathbf{k}\cdot\mathbf{V}_{1AB})^2 - 2(\mathbf{k}\cdot\mathbf{V}_{1AB})(\mathbf{k}\cdot\mathbf{V}_{1A})\right] \ . \tag{8.13}$$

Similarly, for particle B,

$$\Delta E_B = \frac{m_{pA}m_{pB}(1+e)}{2(m_{pA}+m_{pB})}\left[\frac{m_{pA}(1+e)}{m_{pA}+m_{pB}}(\mathbf{k}\cdot\mathbf{V}_{1AB})^2 + 2(\mathbf{k}\cdot\mathbf{V}_{1AB})(\mathbf{k}\cdot\mathbf{V}_{1B})\right] \ . \tag{8.14}$$

The net loss of kinetic energy in the collision is thus,

$$\begin{aligned}\Delta E &= \Delta E_A + \Delta E_B \\ &= \frac{m_{pA}m_{pB}(1+e)}{2(m_{pA}+m_{pB})}\left[(1+e)(\mathbf{k}\cdot\mathbf{V}_{1AB})^2 - 2(\mathbf{k}\cdot\mathbf{V}_{1AB})^2\right] \\ &= \frac{m_{pA}m_{pB}}{2(m_{pA}+m_{pB})}\left(e^2-1\right)(\mathbf{k}\cdot\mathbf{V}_{1AB})^2 \ . \end{aligned} \tag{8.15}$$

Note that if the collision is perfectly elastic ($e = 1.0$) then ΔE is zero as expected. For the special case of collision between particles of the same mass ($m_{pA} = m_{pB} = m_p$), eq. (8.15) simplifies to

$$\Delta E = \frac{m_p}{4}\left(e^2-1\right)(\mathbf{k}\cdot\mathbf{V}_{1AB})^2 \ , \tag{8.16}$$

which agrees with the result given by Jenkins and Savage (1983) for the collision of spherical particles of identical mass.

8.2.2 Average Collision Scattering Velocity for Invariant Incident Velocities

The outcome of a collision between two particles A and B with known incident velocities depends on the contact angle defined by $\mathbf{k}$. Consider all possible collisions in a uniform mixture of particles that involve type A particles with initial velocity $\mathbf{V}_{1A}$ and type B particles with initial velocity $\mathbf{V}_{1B}$. If particle A is travelling towards a target particle B, it will collide with B if its centre contacts a hemispherical volume around the centre of B of radius $\sigma_{AB} = (d_{pA}+d_{pB})/2$, as shown in Figure 8.2. Radius σ_{AB} is the "collision radius." The probability that the centre of particle A lies within a small surface area $(\sigma_{AB}^2 \sin\theta\, d\theta\, d\phi)$ on the hemisphere at the time of contact is the projected area of that surface on a plane perpendicular to $\mathbf{V}_{1AB}$, divided by the total projected area of the hemisphere on the same plane, i.e.

$$\begin{aligned} \Pr(\sigma_{AB}, \theta, \phi) &= \frac{(\sigma_{AB}\, \sin\theta\, d\phi)\,(\sigma_{AB}\, \cos\theta\, d\theta)}{\pi\sigma_{AB}^2} \\ &= \frac{\sin 2\theta}{2\pi}\, d\theta\, d\phi\,. \end{aligned} \tag{8.17}$$

From the probabilities of all possible outcomes of collisions involving particle A with incident velocity $\mathbf{V}_{1A}$ and particle B with incident velocity $\mathbf{V}_{1B}$, average scattering velocities may be defined, i.e. for a scattering velocity $\mathbf{V}$ this average is

$$\overline{\mathbf{V}} = \int_0^{\frac{\pi}{2}} \int_{-\pi}^{\pi} \mathbf{V} \left(\frac{\sin 2\theta}{2\pi}\right) d\phi\, d\theta\,. \tag{8.18}$$

Substituting the expression for $\mathbf{V}_{z2A}$ from eq. (8.11) into eq. (8.18) gives the average post-collision A velocity in the z' axis direction,

$$\begin{aligned} \overline{\mathbf{V}_{z2A}} &= \mathbf{V}_{z1A} - \int_0^{\frac{\pi}{2}} \int_{-\pi}^{\pi} \left(\frac{\sin 2\theta}{2\pi}\right) \left(\frac{m_{pB}(1+e)}{(m_{pA}+m_{pB})} \mathbf{V}_{z1AB} \cos^2\theta\right) d\phi\, d\theta \\ &= \mathbf{V}_{z1A} - \frac{m_{pB}\,(1+e)\,\mathbf{V}_{z1AB}}{2\,(m_{pA}+m_{pB})}\,. \end{aligned} \tag{8.19}$$

Similar integrations for the scattering velocities in the x'- and y'-axis directions give $\overline{\mathbf{V}_{x2A}} = \mathbf{V}_{x1A}$ and $\overline{\mathbf{V}_{y2A}} = \mathbf{V}_{y1A}$. Thus there is no change in A particle average velocity in the x' or y' directions. This is due to the symmetry of the collision process about the z' axis. In a frame of reference moving with the pre-collision B particle, the A particles always scatter with "radial"

velocities directed outwards from the z'-axis in the x'-y' plane shown in Figure 8.2. For every collision that produces a post-collision velocity in the radial $\boldsymbol{\delta}_r$ direction there is an equivalent collision producing scatter in the $-\boldsymbol{\delta}_r$ direction. Hence the average change in velocity of an A particle, $\overline{\Delta \mathbf{V}_A}$, is in the z' direction, and, from eq. (8.19),

$$\begin{aligned} \overline{\Delta \mathbf{V}_A} &= (\overline{\Delta \mathbf{V}_{z2A}} - \mathbf{V}_{z1A}) \\ &= -\frac{m_{pB}\,(1+e)\,\mathbf{V}_{z1AB}}{2\,(m_{pA}+m_{pB})} \,. \end{aligned} \tag{8.20}$$

An identical analysis for particle B gives

$$\overline{\Delta \mathbf{V}_B} = \frac{m_{pA}\,(1+e)\,\mathbf{V}_{z1AB}}{2\,(m_{pA}+m_{pB})} \,. \tag{8.21}$$

These velocity changes define an "average" collision for the case considered. Momentum in the z' direction is conserved in this average collision, i.e. $m_{pA}\overline{\Delta \mathbf{V}_A} + m_{pB}\overline{\Delta \mathbf{V}_B} = 0$. If a large number of collisions occur between clouds of A and B particles, with mean incident vector velocities $\mathbf{V}_{1A}$ and $\mathbf{V}_{1B}$, respectively, then the average change in velocity of both the A and B particles is in the z'-axis direction, i.e., the $\mathbf{V}_{1AB}$ direction. Also, $\overline{\mathbf{V}_{2AB}}$ is in this direction, since $\overline{\mathbf{V}_{2AB}} = \mathbf{V}_{1AB} + (\overline{\Delta \mathbf{V}_A} - \overline{\Delta \mathbf{V}_B})$. An effective *net* force between the clouds of A and B particles arises due to the collision process. This force is also directed along the z' axis.

Another quantity used later in the model development is the average change in the "radial" speed (x'-y' plane) of the particles. Although the average radial velocity change is zero, due to the symmetry of the collision process, the average change in the radial speed may be interpreted as a measure of the energy transferred from particle motion in the z' axis direction to motion perpendicular to this axis due to the "average" collision, which is an oblique collision.

For a single collision the radial velocity change for particle A is $\Delta \mathbf{V}_{rA} = \Delta \mathbf{V}_{xA} + \Delta \mathbf{V}_{yA}$. Re-arranging eqs. (8.9) and (8.10) gives

$$\Delta \mathbf{V}_{xA} = -\frac{m_{pB}(1+e)}{2\,(m_{pA}+m_{pB})}\,|\mathbf{V}_{z1AB}|\sin 2\theta \cos\phi\;\boldsymbol{\delta}_x \,, \tag{8.22}$$

and

$$\Delta \mathbf{V}_{yA} = -\frac{m_{pB}(1+e)}{2\,(m_{pA}+m_{pB})}\,|\mathbf{V}_{z1AB}|\sin 2\theta \sin\phi\;\boldsymbol{\delta}_y \,. \tag{8.23}$$

Therefore the change in radial speed ΔV_{rA} for particle A involved in a single collision is

$$\begin{aligned} \Delta V_{rA} &= \left(\Delta V_{xA}^2 + \Delta V_{yA}^2\right)^{\frac{1}{2}} \\ &= \frac{m_{pB}(1+e)}{2\left(m_{pA}+m_{pB}\right)} \left|\mathbf{V}_{z1AB}\right| \sin 2\theta \,. \end{aligned} \tag{8.24}$$

Averaging ΔV_{rA} over all possible collision outcomes by eq. (8.18) then gives,

$$\overline{\Delta V_{rA}} = \frac{\pi\, m_{pB}\,(1+e)\,|\mathbf{V}_{z1AB}|}{8\left(m_{pA}+m_{pB}\right)} \,. \tag{8.25}$$

Similarly,

$$\overline{\Delta V_{rB}} = \frac{\pi\, m_{pA}\,(1+e)\,|\mathbf{V}_{z1AB}|}{8\left(m_{pA}+m_{pB}\right)} \,. \tag{8.26}$$

The average velocities and speeds discussed thus far have been expressed in terms of velocities immediately before and following collision. However, the proposed model requires that the velocity of each particle fraction be expressed in terms of an average and r.m.s. fluctuating velocity. From the model postulate that when particle collisions significantly affect particle motion, the particle collision frequencies are generally greater than eddy interaction frequencies, it is expected that the local mean and fluctuating velocity distributions of each particle fraction within an eddy will be in pseudo steady-state, with changes in the average and r.m.s. velocities occurring over a period significantly greater than the period τ_k between collisions. In this "steady-state", an "average" particle representative of all particles in a given size fraction returns to its pre-collision velocity between collisions due to drag by the gas. As mentioned, for the collision of "average" A particles with "average" B particles, the velocity changes due to collisions, and relative pre- and post-collision velocities are all in the z' direction. An average A particle fluctuates between velocities $\mathbf{V}_{1A}$ and $\overline{\mathbf{V}_{2A}} = \mathbf{V}_{1A} + \overline{\Delta\mathbf{V}_A}$, where $\overline{\Delta\mathbf{V}_A}$ is given by eq. (8.20). For the average particle, there is no change due to collision in the x' and y' directions. Similarly, an average B particle velocity fluctuates between $\mathbf{V}_{1B}$ and $\overline{\mathbf{V}_{2B}} = \mathbf{V}_{1B} + \overline{\Delta\mathbf{V}_B}$, where $\overline{\Delta\mathbf{V}_B}$ is given by eq. (8.21).

The motion of a particle accelerated by a constant gas velocity over a fixed period τ_k was investigated in Chapter 3. If the average post-collision velocity is abbreviated as $\mathbf{V}_2$, then the

mean velocity of particle A when the A-B collision process is in a pseudo steady-state is given by eq. (3.27), i.e.

$$\mathbf{v}_A = (1 - \lambda_{AB})\,\mathbf{V}_{1A} + \lambda_{AB}\mathbf{V}_{2A}\ , \tag{8.27}$$

where $\mathbf{v}_A$ is the mean velocity between collisions, and the overbar in eq. (3.27) is omitted from here on for convenience. Similarly for particle B

$$\mathbf{v}_B = (1 - \lambda_{BA})\,\mathbf{V}_{1B} + \lambda_{BA}\mathbf{V}_{2B}\ . \tag{8.28}$$

Note that the subscript on λ_{AB} signifies that it applies to the mean period between collisions for A particles undergoing collision with B particles. (The subscripts 1 and 2 in eqs. (8.27) and (8.28) are the reverse of those in eq. (3.27), as in this case the velocity immediately before collision has been designated as the "initial" velocity.)

For the relationships in eqs. (8.20), (8.21), (8.25) and (8.26) to be applied in the model, the average changes in velocity and speed must be expressed in terms of the mean velocities $\mathbf{v}_A$ and $\mathbf{v}_B$. This task is made easier by noting that $\overline{\Delta V_{rA}} = \pi|\overline{\Delta \mathbf{V}_A}|/4$ and $\overline{\Delta V_{rB}} = \pi|\overline{\Delta \mathbf{V}_B}|/4$. Therefore only $(\overline{\Delta \mathbf{V}_A})$ and $(\overline{\Delta \mathbf{V}_B})$ in terms of $\mathbf{v}_A$ and $\mathbf{v}_B$ are required. Using the expressions for $\mathbf{v}_A$ and $\mathbf{v}_B$ in eqs. (8.27) and (8.28), and re-defining $(\overline{\Delta \mathbf{V}_A})$ and $(\overline{\Delta \mathbf{V}_B})$ as $\Delta\mathbf{v}_{AB}$ and $\Delta\mathbf{v}_{BA}$ from here on, gives after some manipulation (see Appendix D),

$$\Delta\mathbf{v}_{AB} = \frac{(1+e)\,m_{pB}\,(\mathbf{v}_B - \mathbf{v}_A)}{m_{pA}\,(2-\lambda_B) + m_{pB}\,(2-\lambda_A) - e\,(m_{pA}\lambda_B + m_{pB}\lambda_A)}\ . \tag{8.29}$$

Similarly,

$$\Delta\mathbf{v}_{BA} = \frac{(1+e)\,m_{pA}\,(\mathbf{v}_A - \mathbf{v}_B)}{m_{pA}\,(2-\lambda_B) + m_{pB}\,(2-\lambda_A) - e\,(m_{pA}\lambda_B + m_{pB}\lambda_A)}\ . \tag{8.30}$$

8.3 Collision Frequencies

According to the model formulation, each particle fraction within an energetic eddy may be assigned an axial velocity $\mathbf{v}_z$, a mean drift velocity $\mathbf{c}_t$ and a r.m.s. collisional fluctuating velocity $\mathbf{c}_k$. Therefore, within a *given* energetic eddy each particle fraction has a mean velocity $\mathbf{v}$ that is the vector sum $\mathbf{v}_z + \mathbf{c}_t$, and particles fluctuate about this mean with a r.m.s. fluctuating

velocity of magnitude of $|\mathbf{c}_k|$. A key assumption of the model is that the collisions within an eddy can be divided into type (i) collisions due to differences in mean velocity, and type (ii) collisions due solely to the collisional fluctuating velocities of individual particles. Clearly only type (ii) collisions may occur amongst particles of the same fraction.

To evaluate the collision frequency for type (i) collisions, each particle in a particular fraction is assigned the mean particle velocity corresponding to that fraction, and the fluctuating component is not considered. Considering a mixture of two particle types A and B, type (i) collisions correspond to a cloud of A particles, all with mean velocity $\mathbf{v}_A$ streaming though a cloud of B particles, all with velocity $\mathbf{v}_B$. (Note that this is the "bullets and targets" collision problem mentioned earlier. It is discussed in many texts on the kinetic theory of gases, e.g. Adamson (1979).) The average velocity changes due to this type of collision were discussed in the previous section. Let $\mathbf{n}_A$ and $\mathbf{n}_B$ be the respective numbers of particles per unit volume of A and B particles. In the frame of reference of the B particles, a single A particle moving through the B particle cloud will collide with a single B particle if their centres are within a distance equal to the collision radius σ_{AB} as the A particle passes by. In a unit of time the A particle sweeps along the axis of cylindrical volume $\pi\sigma_{AB}^2|\mathbf{v}_A - \mathbf{v}_B|$, and any B particles with centres lying inside this volume collide with the A particle. Hence the number of collisions which an A particle makes is the product of this volume and $\mathbf{n}_B$, i.e.

$$Z'_{A(B)} = \pi\sigma_{AB}^2\mathbf{n}_B|\mathbf{v}_A - \mathbf{v}_B| \ , \tag{8.31}$$

where the prime signifies a type (i) collision. Similarly,

$$Z'_{B(A)} = \pi\sigma_{AB}^2\mathbf{n}_A|\mathbf{v}_A - \mathbf{v}_B| \ . \tag{8.32}$$

Clearly, the total number of collisions per unit time between the A and B particles is $Z'_{AB} = \mathbf{n}_A Z'_{A(B)} = \mathbf{n}_B Z'_{B(A)}$, i.e.

$$Z'_{AB} = \pi\sigma_{AB}^2\mathbf{n}_A\mathbf{n}_B|\mathbf{v}_A - \mathbf{v}_B| \ . \tag{8.33}$$

For type (ii) collisions the differences in mean velocities of the particle fractions are assumed

to be zero. The distribution f of velocities for each fraction is assumed to be Maxwellian,

$$f = \mathbf{n}\left(\frac{3}{2\pi\overline{\mathbf{C}^2}}\right)^{\frac{3}{2}} \exp\left(-3\mathbf{C}^2/2\overline{\mathbf{C}^2}\right) , \tag{8.34}$$

where $\overline{\mathbf{C}^2} = \mathbf{c}_k^2$ in this study. The number of particles per unit volume with velocities in the range $\mathbf{C}$ to $(\mathbf{C} + d\mathbf{C})$ is $fd\mathbf{C}$. Consider a mixture of A and B particles with respective fluctuating velocity distributions f_A and f_B. The collisions between A particles with velocities in the range $\mathbf{C}_A$ to $(\mathbf{C}_A + d\mathbf{C}_A)$ and B particles with velocities in the range $\mathbf{C}_B$ to $(\mathbf{C}_B + d\mathbf{C}_B)$ are effectively type (i) collisions, and the collision frequency of such collisions is therefore equal to $\pi\sigma_{AB}^2|\mathbf{C}_A - \mathbf{C}_B| f_A f_B d\mathbf{C}_A d\mathbf{C}_B$. Thus the total collisions frequency Z''_{AB} for A-B type (ii) collisions is

$$Z''_{AB} = \int\int \pi\sigma_{AB}^2 \, |\mathbf{C}_A - \mathbf{C}_B| \, f_A f_B d\mathbf{C}_A d\mathbf{C}_B \, . \tag{8.35}$$

The integration is performed over the entire three-dimensional velocity spaces of the A and B particles. Chapman and Cowling (1970) perform this integration, giving

$$Z''_{AB} = \sqrt{\frac{8\pi}{3}}\mathbf{n}_A\mathbf{n}_B\sigma_{AB}^2\left(\mathbf{c}_{kA}^2 + \mathbf{c}_{kB}^2\right)^{\frac{1}{2}} \, . \tag{8.36}$$

The average number of type (ii) collisions per unit time for a single A particle is therefore $Z''_{A(B)} = Z''_{AB}/\mathbf{n}_A$. Similarly, $Z''_{B(A)} = Z''_{AB}/\mathbf{n}_B$.

For type (ii) collisions amongst particles of the same fraction, the collision frequency is determined in the same manner, except that results must be halved to avoid "double counting" each collision. Hence, for A-A particle collisions, eq. (8.36) gives

$$Z''_{AA} = 2\sqrt{\frac{\pi}{3}}\mathbf{n}_A^2\sigma_{AA}^2\mathbf{c}_{kA} \, . \tag{8.37}$$

Also, $Z''_{A(A)} = Z''_A = (Z''_{AA}/\mathbf{n}_A)$.

Although it would be convenient to simply add the expressions for type (i) and (ii) collision frequencies to obtain the total collision frequency between unlike fractions, this is incorrect. When there is a significant difference in the mean velocity of the two fractions, the number of collisions due to the fluctuating velocity is greatly reduced. This may be explained by

considering suspension upflow of A and B particles where the difference in mean velocities $|\mathbf{v}_A - \mathbf{v}_B|$ increases and the A particles travel faster than the B particles. At zero difference in mean velocity all different approaches between A and B particles due to the distribution of fluctuating velocities are possible. However, as the difference is increased to a stage where it is comparable to the r.m.s. fluctuations, the fluctuating velocity collisions involving the lower surface of the faster A particles and the upper surface of the slower B particles are no longer possible. With further increase in the mean difference, the number of possible collisions, excluding those solely attributable to the mean velocity difference, approaches zero.

To correctly evaluate the total collision frequency between unlike fractions A and B it is necessary to integrate over all approach velocities in a similar manner to eq. (8.35), except in this case the total vector velocity $\mathbf{v} + \mathbf{C}$ of each particle in the range $\mathbf{C}$ to $(\mathbf{C} + d\mathbf{C})$ must be considered, i.e.

$$Z_{AB} = \int\int \pi\sigma_{AB}^2 \, |\mathbf{v}_A + \mathbf{C}_A - \mathbf{v}_B - \mathbf{C}_B| \, f_A f_B \, d\mathbf{C}_A \, d\mathbf{C}_B \, , \tag{8.38}$$

The result of this integral, given by Abrahamson (1975), is

$$\begin{aligned} Z_{AB} \;=\; & \pi \mathbf{n}_A \mathbf{n}_B \sigma_{AB}^2 \frac{3\,(\mathbf{v}_A - \mathbf{v}_B)^2 + (\mathbf{c}_{kA}^2 + \mathbf{c}_{kB}^2)}{3\,|\mathbf{v}_A - \mathbf{v}_B|} \operatorname{erf}\left[\left(\frac{3}{2}\right)^{\frac{1}{2}} \frac{|\mathbf{v}_A - \mathbf{v}_B|}{(\mathbf{c}_{kA}^2 + \mathbf{c}_{kB}^2)^{\frac{1}{2}}}\right] \\ & + \sqrt{\frac{8\pi}{3}} \mathbf{n}_A \mathbf{n}_B \sigma_{AB}^2 \left(\mathbf{c}_{kA}^2 + \mathbf{c}_{kB}^2\right)^{\frac{1}{2}} \exp\left[\frac{-3}{2} \frac{(\mathbf{v}_A - \mathbf{v}_B)^2}{(\mathbf{c}_{kA}^2 + \mathbf{c}_{kB}^2)}\right] , \end{aligned} \tag{8.39}$$

where the error function, $\operatorname{erf}(x) = \frac{2}{\sqrt{\pi}} \int_0^x \exp(-t^2) dt$.

When the A and B particles have zero fluctuating velocities (i.e. $\mathbf{c}_{kA} = \mathbf{c}_{kB} = 0$), then the second r.h.s. term of eq. (8.39) approaches zero and the error function in the first term approaches 1.0. In this case the expression for Z_{AB} in eq. (8.39) correctly reduces to the type (i) collision expression for Z'_{AB} given by eq. (8.33). Similarly, when the difference in mean velocities is zero (i.e. $|\mathbf{v}_A - \mathbf{v}_B| = 0$), then Z_{AB} in eq. (8.39) reduces to the type (ii) collision expression for Z''_{AB} given in eq. (8.36). The first and second r.h.s. terms in eq. (8.39) may therefore be interpreted as the respective corrected collision frequencies of type (i) and (ii) collisions, Z'_{AB} and Z''_{AB}. Note that $Z'_{AA} = 0$, and Z''_{AA} is still given by eq. (8.37).

The properties of the collision frequency function Z_{AB} given in eq. (8.39) is explored further in Appendix D where a ratio of mean velocity difference to r.m.s. fluctuating velocity is defined as

$$\xi_{AB} = \frac{|\mathbf{v}_A - \mathbf{v}_B|}{(\mathbf{c}_{kA}^2 + \mathbf{c}_{kB}^2)^{\frac{1}{2}}} . \tag{8.40}$$

It is shown that for values of $\xi > 1.5$, the number of collisions attributable to the fluctuating velocities becomes insignificant compared with collisions due to the mean velocity difference. Also the approach of simply adding eqs. (8.33) and (8.36) to obtain the total collision frequency Z_{AB} between unlike particle fractions results in significant errors for $1.2 < \xi < 3.0$. Consequently, the more rigorously derived expressions for collision frequency are assumed for the model. In terms of ξ_{AB},

$$Z'_{AB} = \mathbf{n}_A \mathbf{n}_B \sigma_{AB}^2 \pi \, |\mathbf{v}_A - \mathbf{v}_B| \left(1 + \frac{1}{3\xi_{AB}^2}\right) \operatorname{erf}\left(\sqrt{\frac{3}{2}}\xi_{AB}\right) , \tag{8.41}$$

and

$$Z''_{AB} = \mathbf{n}_A \mathbf{n}_B \sigma_{AB}^2 \sqrt{\frac{8\pi}{3}} \left(\mathbf{c}_{kA}^2 + \mathbf{c}_{kB}^2\right)^{\frac{1}{2}} \exp\left(\frac{-3\xi_{AB}^2}{2}\right) . \tag{8.42}$$

In Appendix D an exponential function fit to the error function is given so that eq. (8.41) may be used in numerical model simulations.

8.4 Collision Efficiencies

In the model development thus far, the tendency for very small particles to follow the gas streamlines around the target particle has not been considered. This phenomenon decreases the collision frequency of such small particles. This reduction is normally characterised by the "collection efficiency" η, defined as the ratio of the number of small particles that collide with the target to the number that would have collided if uninfluenced by the local diverging gas flow around the target particle. The collection efficiency is often correlated with an inertial parameter I. For collisions of smaller A particles with larger B particles,

$$I_{AB} = \frac{\rho_{pA} \, \mathbf{v}_{sB} \, d_{pA}^2}{18 \, \mu_g \, d_{pB}} , \tag{8.43}$$

where $\mathbf{v}_{sB}$ is the gas velocity relative to the target B particle at a distance sufficiently upstream that divergence of the gas streamlines is still negligible (i.e. the slip velocity of B). Soo (1967) presented some experimental and theoretical data for η as a function of I. Although there is considerable scatter in these data, the efficiency η appears to correlate reasonably with I. In this study, these data were found to be approximately represented by the empirical correlation:

$$\begin{aligned} \eta_{AB} &= 0 && \text{for } \sqrt{I_{AB}} < 0.2 \\ \eta_{AB} &= \log_{10}\left(5\sqrt{I_{AB}}\right) && \text{for } 0.2 < \sqrt{I_{AB}} < 2.0 \\ \eta_{AB} &= 1 && \text{for } \sqrt{I_{AB}} > 2.0\,. \end{aligned} \tag{8.44}$$

Practically all energetic particle collisions in cold unit CFBs are likely to occur with efficiencies of 100%. Only for particles smaller than about 10 μm or for collisions involving negligibly small approach velocities are efficiencies significantly less than 100% predicted. In high temperature CFBs the increase in gas viscosity and associated increase in particle response may result in efficiencies less than 100% for the smallest size particles (say 20 to 50 μm) if the gas velocity relative to the large particle is less than 0.2 m/s. Some sample calculations for η are given in Appendix D. In the model development from here on, and in the numerical simulations, the expression for η in eq. (8.44) is included in the collision frequency term (i.e. $Z_{AB}(\text{corrected}) = \eta_{AB} Z_{AB}$). This approach is only a crude "first approximation," as changes in particle collision contact velocities due to the response of very small particles to the gas flow around the target particle are not considered. Nevertheless, for very small particles it probably provides reasonable order of magnitude estimates. It should be remembered that in the vast majority of collisions in risers η has a value of 1.0. Furthermore, the dominant influences on the fluctuating motion of very small particles are drag and gas tubulence.

8.5 Forces Between Different Particle Fractions

Consider collisions occurring repeatedly between particles from the A and B particle fractions, with mean velocities $\mathbf{v}_A$ and $\mathbf{v}_B$, respectively. The relative mean velocity between fractions

is thus $(\mathbf{v}_A - \mathbf{v}_B)$. Although individual collisions result in post-collision scattering velocities with components perpendicular to $(\mathbf{v}_A - \mathbf{v}_B)$, it has been shown above that the average velocity change for the A-B collision, obtained by averaging over all possible A-B particle contact angles, is in the direction of the mean relative velocity (eqs. (8.29) and (8.30)). As mentioned, this result is due to the symmetry of the collision process, which ensures that when all possible post-collision velocities are summed, components not aligned with $(\mathbf{v}_A - \mathbf{v}_B)$ cancel. Corresponding to the average velocity change is an impulse and momentum change, also in the direction of $(\mathbf{v}_A - \mathbf{v}_B)$. If a single A particle undergoes many collisions with a given frequency, then the product of the average momentum change due to an "average" A-B particle collision and this frequency closely approximates the actual effect of these collisions on the particle. One can then speak of an effective force or "collisional force" on the A particle.

Considering the model collision process in an energetic eddy, only type (i) collisions contribute to the force, as these collisions arise from differences in the mean velocities of the particle fractions. Forces due to individual type (ii) collisions cancel as the distribution of fluctuating particle velocities that cause type (ii) collisions is isotropic. Thus the collisional force $\mathbf{f}_{k_{A(B)}}$ on an A particle due to collisions with B particles is the change in momentum of the A particle due to type (i) collisions multiplied by the frequency of such collisions,

$$\mathbf{f}_{k_{A(B)}} = m_{pA}\, Z'_{A(B)}\, \Delta\mathbf{v}_{AB} \ , \tag{8.45}$$

where $\Delta\mathbf{v}_{AB}$ is given by eq. (8.29). The total force $\mathbf{F}_{k_{AB}}$ per unit volume of suspension on fraction A due to collisions with fraction B is

$$\mathbf{F}_{k_{AB}} = m_{pA}\, Z'_{AB}\, \Delta\mathbf{v}_{AB} \ . \tag{8.46}$$

The total force on fraction A due to all particle fractions is

$$\mathbf{F}_{k_A} = m_{pA} \sum_{j=1}^{n} Z'_{Aj}\, \Delta\mathbf{v}_{Aj} \ . \tag{8.47}$$

Now the average velocity change due to a collision for A particles, $\Delta\mathbf{v}_{AB}$, is proportional to (but *not* equal to) $(\mathbf{v}_B - \mathbf{v}_A)$ (eq. (8.29)). As $(\mathbf{v}_B - \mathbf{v}_A)$ may be resolved into components

$(\mathbf{v}_{zB} - \mathbf{v}_{zA})$ and $(\mathbf{c}_{tB} - \mathbf{c}_{tA})$, in the axial z and eddy drift velocity directions, respectively, $\Delta\mathbf{v}_{AB}$ may similarly be resolved into components $(\Delta\mathbf{v}_{AB})_z$ and $(\Delta\mathbf{v}_{AB})_t$. Therefore, for a given eddy, the average collision force $\mathbf{F}_{k_{AB}}$ may be resolved into two components $\mathbf{F}_{kz_{AB}}$ and $\mathbf{F}_{kt_{AB}}$ in the axial z and eddy drift velocity directions, i.e.

$$\mathbf{F}_{kz_{AB}} = m_{pA}\, Z'_{AB}\, (\Delta\mathbf{v}_{AB})_z \ , \tag{8.48}$$

and

$$\mathbf{F}_{kt_{AB}} = m_{pA}\, Z'_{AB}\, (\Delta\mathbf{v}_{AB})_t \ . \tag{8.49}$$

Both $\mathbf{v}_{zA}$ and $\mathbf{v}_{zB}$ are constant in direction and magnitude for all eddies at a given axial position z in the riser. Furthermore, the drift velocity components $\mathbf{c}_{tA}$ and $\mathbf{c}_{tB}$ are considered small enough in magnitude that a linear drag law may be used and the changes in velocity due to collision are comparable to the changes between collisions due to drag. Thus both the drag force and collision force may be resolved into axial and drift components that are linearly dependent on velocity, and the particle eddy drift velocities are in the direction of the gas eddy velocity.

In the vertical direction the model is only required to predict the mean velocities of the fractions, and it is therefore sufficient to characterise interparticle force between two fractions in this direction by summing all vertical forces over all eddy orientations to obtain a net vertical force. However, in the horizontal plane both the distributions of fluctuating particle velocity $\mathbf{C}_k$ and particle fraction drift velocity $\mathbf{c}_t$ are needed to characterise the lateral motion of particles. A net horizontal force will not suffice, as this force and the mean particle motion are zero in this plane. To estimate $\mathbf{c}_t$ it is necessary to consider gas-particle dynamics within the eddies. As the distributions of particle fluctuating velocity, eddy gas velocity and eddy particle fraction velocity are assumed isotropic in the horizontal plane, the average magnitude of these velocities in any horizontal direction equals that in all other horizontal directions. Therefore, to predict the lateral motion of gas and particles, the dynamics inside a typical or "model" energetic eddy are considered. The model eddy is assumed to have the same particle and gas motion

as the average of all eddies with drift gas velocities directed positively across a given vertical half-plane. Due to lateral isotropy, the net vertical force in this eddy equals the net vertical force averaged over all eddies.

For isotropic gas turbulence, the r.m.s. fluctuating gas velocities of the turbulence are equal in three mutually orthogonal directions. In terms of a Cartesian coordinate system with the z-axis directed vertically upward, the components of the eddy gas drift velocity $\mathbf{u}'$ of the model eddy are

$$\mathbf{u}' = u_e \boldsymbol{\delta}_x \ + u_e \boldsymbol{\delta}_y \ \pm u_e \boldsymbol{\delta}_z \ , \tag{8.50}$$

where u_e is the linear turbulence velocity. The orientation of the horizontal plane x and y axes is arbitrary and does not affect the analysis due to lateral isotropy. The $\pm$ sign on the z term is included to allow for vertical gas fluctuations in both directions. Similarly, the components of particle velocity for a given particle fraction are

$$\mathbf{v}_z + \mathbf{c}_t = v_e \boldsymbol{\delta}_x \ + v_e \boldsymbol{\delta}_y \ + \mathbf{v}_z \pm v_e \boldsymbol{\delta}_z \ , \tag{8.51}$$

where v_e is the linear particle drift velocity (i.e. $3v_e^2 = \mathbf{c}_t^2$) and $\mathbf{v}_z$ is the mean axial fraction velocity in direction $\boldsymbol{\delta}_z$.

Consider the interaction between two fractions A and B within the model eddy. With the aid of eq. (8.51), the approach speed between A and B may be written,

$$|\mathbf{v}_B - \mathbf{v}_A| = \left[(\mathbf{v}_{zB} - \mathbf{v}_{zA})^2 + 3\,(v_{eB} - v_{eA})^2 \pm 2\,(\mathbf{v}_{zB} - \mathbf{v}_{zA})\,(v_{eB} - v_{eA})\right]^{\frac{1}{2}} \ . \tag{8.52}$$

The difference in velocities between the fractions is

$$(\mathbf{v}_B - \mathbf{v}_A) = (\mathbf{v}_{zB} - \mathbf{v}_{zA}) + (v_{eB} - v_{eA})\ (\boldsymbol{\delta}_x + \boldsymbol{\delta}_y \pm \boldsymbol{\delta}_z\ ) \ . \tag{8.53}$$

Only the *net* force in the vertical direction is of interest, and therefore the properties of the model eddy may be further refined by assuming that it has approximate properties of a combination of the two possible eddies in eq. (8.50), with vertical fluctuations of equal magnitude but opposite direction. The velocity differences for A and B particles in this eddy, obtained

from an arithmetic average of the two possibilities given in eqs. (8.52) and (8.53), are

$$|\mathbf{v}_B - \mathbf{v}_A| = \frac{1}{2}\sqrt{(\mathbf{v}_{zB} - \mathbf{v}_{zA})^2 + 3\,(v_{eB} - v_{eA})^2 + 2\,(\mathbf{v}_{zB} - \mathbf{v}_{zA})\,(v_{eB} - v_{eA})}$$
$$+\frac{1}{2}\sqrt{(\mathbf{v}_{zB} - \mathbf{v}_{zA})^2 + 3\,(v_{eB} - v_{eA})^2 - 2\,(\mathbf{v}_{zB} - \mathbf{v}_{zA})\,(v_{eB} - v_{eA})}\,, \quad (8.54)$$

and

$$(\mathbf{v}_B - \mathbf{v}_A) = (\mathbf{v}_{zB} - \mathbf{v}_{zA}) + (v_{eB} - v_{eA})\,(\boldsymbol{\delta}_x + \boldsymbol{\delta}_y)\,. \quad (8.55)$$

An approximation for the approach speed expression in eq. (8.54) that is accurate within ± 10% for all combinations of $\mathbf{v}_A$, $\mathbf{v}_B$, v_{eA} and v_{eB} is

$$|\mathbf{v}_B - \mathbf{v}_A| = \sqrt{(\mathbf{v}_{zB} - \mathbf{v}_{zA})^2 + 3\,(v_{eB} - v_{eA})^2}\,, \quad (8.56)$$

Results from this expression agree exactly with those given by eq. (8.54) in the two limits where $\mathbf{v}_A = \mathbf{v}_B$ (i.e. identical slip velocities) and v_{eA} and v_{eB} are both zero (i.e. no turbulence effects). Equation (8.56) is adopted as a general expression for $|\mathbf{v}_B - \mathbf{v}_A|$ in the model eddy. Although the model eddy is still assumed to have isotropic drift velocities in all three orthogonal directions, by using eq. (8.56) the sign of the z-direction component no longer has an effect on the net force or collision frequency.

The collisional force on the A particle fraction due to collisions with the B fraction within the model eddy is given by eq. (8.46). Inserting the full expressions for Z'_{AB} and $\Delta\mathbf{v}_{AB}$ from eqs. (8.41) and (8.29) into eq. (8.46), and re-arranging, gives this force in terms of $(\mathbf{v}_A - \mathbf{v}_B)$ and $|\mathbf{v}_A - \mathbf{v}_B|$ (defined in eqs. (8.55) and (8.56)), i.e.

$$\mathbf{F}_{k_{AB}} = \frac{\pi\,\rho_{sA}\,\rho_{sB}\,\eta_{AB}\,\sigma_{AB}^2\,(1+e)(\mathbf{v}_B - \mathbf{v}_A)\,|\mathbf{v}_A - \mathbf{v}_B|}{m_{pA}\,(2-\lambda_B) + m_{pB}\,(2-\lambda_A) - e\,(m_{pA}\lambda_B + m_{pB}\lambda_A)}\left(1 + \frac{1}{3\xi_{AB}^2}\right)\mathrm{erf}\left(\sqrt{\frac{3}{2}}\xi_{AB}\right)\,, \quad (8.57)$$

where $\rho_s = \mathbf{n}m_p$, and ξ_{AB} and η_{AB} are defined in eqs. (8.40) and (8.44), respectively. The equivalent expression for $\mathbf{F}_{k_{BA}}$ may be obtained either by interchanging A and B subscripts in eq. (8.57) or using the identity $\mathbf{F}_{k_{BA}} = -\mathbf{F}_{k_{AB}}$. Note that the velocity weighting factor λ (i.e. λ_A or λ_B) is a function of the collision frequency Z' if the particle is small. When there are multiple particle fractions, the velocity weighting factor, λ_i, for an average fraction i particle, is based on the collision period, τ_{ki}, considering all type (i) collisions, i.e. $\tau_{ki} = 1/\sum_j Z'_{i(j)}$.

8.6 Particle Fraction Drift Velocities

The drift velocity gained by each particle fraction during its interaction time, τ_r, with an eddy in suspension flow is not only dependent on drag by the gas, but also on particle-particle collisional forces. To estimate the mean particle fraction drift velocity, v_e, the interactions of particles and gas within the model eddy are considered. Both clouds of larger particles with significant slip velocities that "fall" into an eddy and small particles which are present when an eddy forms are assumed to have zero drift velocity initially. The particle acceleration due to drag is initially much greater for the smaller particles, and a difference in drift velocities between fractions is quickly established. As the drift velocity difference increases, collisions between fractions that are not due solely to random velocity fluctuations arise, causing a net force that retards the smaller particles and accelerates the larger particles.

To determine the drift velocity of each fraction, the equations of motion for all fractions within the eddy must be solved. For fraction A the Lagrangian equation of motion is

$$\rho_{sA}\frac{d\mathbf{C}_{tA}}{dt} = \mathbf{F}_{Dt_A} + \sum_{i=1}^{n}\mathbf{F}_{kt_{Ai}} \ , \tag{8.58}$$

where $\mathbf{C}_t$ is the particle fraction drift velocity, $\mathbf{F}_{Dt_A}$ is the drag force on fraction A due to the eddy component of gas velocity, $\mathbf{F}_{kt_{Ai}}$ is the collision force on fraction A due to collision with fraction "i" particles (eq. (8.49)), and n is the total number of particle fractions. This equation must be solved up to a time equal to the interaction period τ_{rA}.

Solution of eq. (8.58) is difficult. The r.h.s. terms are not only a function of the dependent variable $\mathbf{C}_{tA}$ but also of all other fraction velocities ($\mathbf{C}_{ti}$) at the *same* position within the eddy. Simultaneous solution of n equations, corresponding to each of the n particle fractions, would be numerically intensive because it would be repeated many times as the eddies and particle properties varied with mean flow. Fortunately, a full velocity-time history of each fraction in the eddy is not required. Instead, an estimate of the *average* drift velocity $\mathbf{c}_{ti}$ of each fraction within an eddy is sufficient.

A reasonable estimate of the change in drift velocity over the interaction time is assumed

to be

$$\rho_{sA}\frac{\Delta \mathbf{C}_{tA}}{\tau_{rA}} = \mathbf{F}_{Dt_A} + \sum_{i=1}^{n} \mathbf{F}_{kt_{Ai}} \,, \tag{8.59}$$

with the drag and collisional forces now constant and evaluated at the average drift velocities ($\mathbf{c}_{ti}$). To determine the mean drift velocity, $\mathbf{c}_{tA}$ must be related to $\Delta \mathbf{C}_{tA}$. As the initial drift velocity is zero, a first estimate would be to assume that $\mathbf{c}_{tA} \approx \Delta \mathbf{C}_{tA}/2$. However, if the interaction time is large compared to the particle response times, then, regardless of the collision process, all particle velocities will be close to the gas velocity for much of the interaction time, i.e. $\mathbf{c}_{tA} \approx \Delta \mathbf{C}_{tA}$. To account for this an "eddy interaction velocity weighting factor" λ_e is introduced,

$$\mathbf{c}_{tA} = (1 - \lambda_e)\Delta \mathbf{C}_{tA} \,. \tag{8.60}$$

When collisional forces are significant, the exact expressions developed for λ in Chapter 3 are not valid. However, the general form of λ_e in eq. (8.60) may be deduced using a heuristic approach, and an approximate form assumed. Consider the collisional forces amongst the various particle fractions in an eddy due to drift velocity. This force retards the small particles and accelerates the larger particles. In contrast, the mid-sized particles experience both accelerative and decelerative forces due to large and small particle collisions. Hence, there is some mid-sized fraction that experiences little net collisional force and behaves as though it were accelerated by gas drag only. Furthermore, unless the suspension is very dilute, collisional forces due to drift increase rapidly whenever a smaller or larger fraction's drift velocity deviates substantially from this mid-size fraction velocity. Generally, although the smaller and larger fractions will still lead and lag the mid-size particles respectively, their average response to the eddy forces as they travel through the eddy will be similar to the mid-size particles. For the mid-size particle fraction which experiences negligible net collision force, the velocity weighting factor expressions in Chapter 3 (Table 3.5) are applicable. The velocity weighting factor for this mid-size particle fraction, denoted $\overline{\lambda_r}$, is based on this fraction's eddy interaction time, $\overline{\tau_r}$.

In contrast, when the suspension is very dilute, differences in particle drift velocity are likely to be comparable to the eddy gas fluctuating velocity. In this case, the collision frequency is very

low, the collision force on all fractions becomes negligible, and the weighting factors, λ_{ri}, for each fraction i may be evaluated from Table 3.5 assuming an interaction period of τ_{ri}. Hence the velocity weighting factor in eq. (8.60) may vary between $\overline{\lambda_r}$ at high collision frequencies ($\tau_k \ll \tau_r$) and λ_{ri} at very low collision frequencies ($\tau_k \geq \tau_r$). It is expected that collisions will not greatly influence the particle motion until the collision period becomes an order of magnitude less than the eddy interaction period. A relationship that gives such trends is

$$\lambda_e \approx \exp[-4\tau_k/\tau_r]\,\overline{\lambda_r} + (1 - \exp[-4\tau_k/\tau_r])\,\lambda_r\ , \tag{8.61}$$

where τ_k is the period between collisions, based on a sum of collision frequencies Z' with all other fractions.

8.7 Gas-Particle Interactions

The drag force exerted by gas flowing around a moving particle works to increase the velocity of the particle in the direction of the gas flow and decrease the particle velocity in all other directions. In a vertically flowing suspension the component of drag attributable to the mean gas and particle velocities results in the vertical motion of the particles and a decrease in the pressure of the gas. The component of force due to the fluctuating gas velocity (i.e. turbulence) and the mean particle velocity results in the particle acquiring the local drift velocity in the direction of the gas fluctuation, as discussed. At the same time the transfer of energy from the turbulent eddies to the particles reduces the turbulence intensity. To solve eq. (8.59) for the particle drift velocities, this modulation of the turbulence must be determined. A final effect of the drag is to reduce the fluctuating velocity component of the individual particles that is not aligned with the local gas velocity, thereby reducing the fluctuating kinetic energy of the particles. The analysis presented below to characterise gas-particle interactions is based on a similar analysis given by Louge *et al.* (1991).

According to the model formulation, the velocity components of the gas in the model eddy are

$$\mathbf{U} = \mathbf{u} + \mathbf{u}'\ , \tag{8.62}$$

and the velocity components of a single particle are

$$\begin{aligned} \mathbf{V} &= \mathbf{v}_z + \mathbf{c}_t + \mathbf{C}_k \\ &= \mathbf{v} + \mathbf{C}_k \,, \end{aligned} \tag{8.63}$$

where $\mathbf{v}$ is the mean particle velocity and $\mathbf{C}_k$ is the instantaneous fluctuating component due to collisions that corresponds to an r.m.s. velocity of $\mathbf{c}_k$. From eqs. (3.17) and (3.18) the drag force on the particle is

$$\begin{aligned} \mathbf{f}_D &= \frac{m_p(\mathbf{U} - \mathbf{V})}{\tau_p} \\ &= \frac{m_p(\mathbf{u} + \mathbf{u}' - \mathbf{v} - \mathbf{C}_k)}{\tau_p} \,. \end{aligned} \tag{8.64}$$

Over a range of particle velocities corresponding in magnitude to the eddy gas velocity, $\mathbf{u}'$, or the particle r.m.s. fluctuating velocity, $\mathbf{c}_k$, a linear drag law may be used. If the drag on a particle fraction in an average eddy is considered, then $\overline{\mathbf{C}_k} = 0$ and, as mentioned earlier, the total drag force per unit suspension volume may be divided into the axial drag $\mathbf{F}_{Dz}$ that is independent of gas turbulence, and the eddy drag force $\mathbf{F}_{Dt}$[1],

$$\begin{aligned} \mathbf{F}_D &= \frac{\rho_s(\mathbf{u} - \mathbf{v}_z)}{\tau_p} + \frac{\rho_s(\mathbf{u}' - \mathbf{c}_t)}{\tau_p} \\ &= \mathbf{F}_{Dz} + \mathbf{F}_{Dt} \,. \end{aligned} \tag{8.65}$$

The rate at which the gas performs work on a particle is $(\mathbf{f}_D \cdot \mathbf{V})$. This work can be expressed in terms of the components of velocity in eqs. (8.62) and (8.63). The net work by the gas on particles is then obtained by first averaging over all particles of a given particle fraction *within* a model eddy, and then averaging this result over all possible gas drift velocity directions of the model eddy. Due to the isotropy of both the particle collisional fluctuating velocity distribution within an eddy and the eddy gas and particle drift velocities amongst the eddies, the averages

[1] A empirical correction for suspension voidage effects on drag is introduced later. The correction does not alter the analysis here. For the dilute suspension concentrations considered in this model, the magnitude of the correction is small.

$\overline{\mathbf{C}_k}$, $\overline{\mathbf{c}_t}$ and $\overline{(\mathbf{u}' - \mathbf{c}_t)}$ are all zero. Therefore,

$$\begin{aligned}\overline{(\mathbf{f}_D \cdot \mathbf{V})} &= \frac{m_p}{\tau_p}\left[\overline{(\mathbf{u} - \mathbf{v}_z)\cdot \mathbf{v}_z} + \overline{(\mathbf{u}' - \mathbf{c}_t)\cdot \mathbf{c}_t} - \overline{\mathbf{C}_k^2}\right] \\ &= (\mathbf{f}_{Dz} \cdot \mathbf{v}_z) + \overline{(\mathbf{f}_{Dt} \cdot \mathbf{c}_t)} - \frac{m_p \mathbf{c}_k^2}{\tau_p} . \end{aligned} \tag{8.66}$$

The net energy transfer, S_{gp_A}, per unit suspension volume from the gas to the particles of fraction A is obtained from eq. (8.66):

$$\begin{aligned} S_{gp_A} &= \overline{(\mathbf{F}_D \cdot \mathbf{V})_A} \\ &= (\mathbf{F}_{Dz_A} \cdot \mathbf{v}_{zA}) + \overline{(\mathbf{F}_{Dt_A} \cdot \mathbf{c}_{tA})} - \frac{\rho_{sA}\, \mathbf{c}_{kA}^2}{\tau_{pA}} . \end{aligned} \tag{8.67}$$

As the gas velocity is generally greater than the particle velocities, the first two r.h.s. terms are the energy transfer from the gas to the particles due to mean gas flow and gas turbulence, respectively. The final r.h.s. term is the dissipation of the particle collisional fluctuating kinetic energy due to drag. The overbar has been retained on the turbulence work term to indicate that it is an average over the entire eddy.

Now consider the rate of reduction in gas turbulence energy due to the particles given in eq. (8.67), $\overline{(\mathbf{F}_{Dt_A} \cdot \mathbf{c}_{tA})}$. Although the force and velocity vectors are co-linear, the approximation $\overline{(\mathbf{F}_{Dt_A} \cdot \mathbf{c}_{tA})} \approx \overline{|\mathbf{F}_{Dt_A}|}\ \overline{|\mathbf{c}_{tA}|}$ may introduce a substantial error if the particles are small. Based on the assumption that the eddy gas velocity is relatively constant, Appendix D derives a suitable expression for the rate of energy reduction:

$$\begin{aligned}\overline{(\mathbf{F}_{Dt_A} \cdot \mathbf{c}_{tA})} &= \frac{\rho_s \overline{|\mathbf{u}' - \mathbf{c}_t|}\ \overline{|\mathbf{c}_t|}}{2\,(1 - \lambda_e)\,\tau_p} \\ &= \frac{3\rho_s\,(u_e - v_e)\,v_e}{2\,(1 - \lambda_e)\,\tau_p} , \end{aligned} \tag{8.68}$$

where λ_e is defined by eq. (8.61).

The analysis leading to the gas turbulent energy balance of eq. (3.60) does not allow for the effects of particle collisions. In addition, it is based on the assumption that particles interact with many eddies and that the particle fluctuating motion can therefore be predicted assuming diffusive motion. In contrast, it is also shown in Chapter 3 that the energetic gas

eddies within commercial scale CFBs are very large, suggesting that the particle motion may not be diffusive in larger units. The alternative approach presented in this chapter considers the motion of particles in a single typical energetic eddy with allowance for collisions, and should therefore provide more accurate results in large units and at higher suspension concentrations. In comparison to eq. (3.60), the model turbulent energy balance is

$$\begin{aligned} P_{gt} = \rho_g u_{e1} l_e \left(\frac{\partial \mathbf{u}}{\partial r}\right)^2 &\approx \frac{3}{2}\frac{\rho_g u_{e0}^2}{\tau_{e0}} \\ &\approx \frac{3}{2}\frac{\rho_g u_{e1}^2}{\tau_{e1}} + \sum_{i=1}^{n} \frac{3\rho_{si}\left(u_e - v_{ei}\right) v_{ei}}{2\left(1-\lambda_{ei}\right)\tau_{pi}}, \end{aligned} \tag{8.69}$$

where the summation is over all n particle fractions and, as in Chapter 3, subscript "0" denotes the particle-free condition and subscript "1" the particle-laden condition. The particle-free turbulence velocity, u_{e0}, may be estimated from correlations given in Chapter 3. Simultaneous solution of the n particle fraction drift equations of motion and the turbulent energy balance, eqs. (8.59) and (8.69), at a fixed point in the suspension, fully defines the gas-particle suspension turbulence characteristics at that point.

8.8 Particle Fluctuating Kinetic Energy Balance

There are two model pathways by which particles are assumed to derive particle fluctuating kinetic energy from the gas flow. Energy is first transferred from the gas to the mean particle flow due to drag. The difference in mass and size of particles in different fractions results in differences in the mean velocities between the fractions, in turn causing particle collisions. As discussed above, the average effect of these collisions can be expressed as a force between the fractions in the direction of the relative velocity between them. However, individual collisions are, in general, oblique, and individual particles scatter with components of velocity that are not in the direction of the relative velocity between fractions. Thus a portion of the energy imparted to the particles from the gas results in a force between the particle fractions, and a portion is promulgated as particle fluctuating kinetic energy. Particles may also respond to gas turbulence. When particles leave an eddy, they have drift velocities that are uncorrelated

with the drift velocities of particles leaving other eddies, assuming the turbulence is isotropic. At this point the energy of these particles due to their drift velocity becomes part of the total particle fluctuating kinetic energy, as discussed earlier. Thus there are two production terms for fluctuating kinetic energy: P_{kk} due to collisions resulting from mean differences in fraction velocities, and P_{kt} due to the direct effect of turbulence on the particles.

Collisions between particles are not only due to mean velocity differences, but also result from differences in the fluctuating velocity of individual particles. These collisions are assumed to alter only the fluctuating velocity of the particles involved. Thus such collisions result in a transfer of fluctuating kinetic energy within a given fraction and between different fractions. This transfer term, S_k, results in re-distribution of fluctuating kinetic energy amongst particle fractions. The production P_{kk} and transfer S_k of fluctuating kinetic energy depend on collisions of type (i) and (ii), respectively. If the collisions are not perfectly elastic, then dissipation of energy also occurs with each collision. The elasticity of the particles is therefore a measure of the effectiveness of the particle system to gain and retain fluctuating energy.

Fluctuating energy is dissipated by the gas as well as by inelastic collisions. Any component of particle velocity not aligned with the local gas flow will be reduced by gas drag. This reduction rate, developed in the previous section (eq. (8.66)), is

$$D_{kt} = \frac{\rho_s \, \mathbf{c}_k^2}{\tau_p} \, . \tag{8.70}$$

Production of fluctuating kinetic energy due to lateral gradients in the mean vertical particle velocities is assumed negligible, except near the boundary of the suspension flow, where this gradient steepens considerably due to wall effects. This is similar to the assumption that turbulence production in turbulent fluid flows occurs predominantly near the wall where the shear is greatest. The fluctuating kinetic energy due to wall effects is included in the model as a boundary condition, and it is assumed that there are no lateral gradients within the dilute suspension flow. Due to the very high approach velocities in CFB risers between slow particles entering from the wall and the rapid core upflow, and the resultant high frequency of energetic collisions, it is assumed that the fluctuating energy rapidly reaches into the centre of

the suspension flow in these units. This is again somewhat analogous to the relatively uniform core turbulence intensities observed in single-phase flows, and is consistent with the assumed lateral uniformity.

Although it is proposed that the current one-dimensional formulation for the fluctuating kinetic energy model is adequate for predicting key suspension flow characteristics providing that appropriate boundary conditions are included, the approach could simply be extended to two-dimensions by addition of shear production and energy conduction terms using the kinetic theory analogy. However, in this section only expressions for P_{kk}, P_{kt} and S_k are developed.

8.8.1 Production of Fluctuating Kinetic Energy due to Mean Velocity Differences

Earlier in this chapter expressions for average collision scattering velocities were presented based on a statistical consideration of all possible approach angles. For particle fractions A and B with mean velocities $\mathbf{v}_A$ and $\mathbf{v}_B$, it was shown that the average changes in velocity due to collision, $\Delta\mathbf{v}_{AB}$ and $\Delta\mathbf{v}_{BA}$, and the corresponding collision forces on both particles, were in the direction of $(\mathbf{v}_B - \mathbf{v}_A)$. However, though the "average" collision resulted in a zero *velocity* change in a direction perpendicular to $(\mathbf{v}_B - \mathbf{v}_A)$, the average change in *speed* perpendicular to $(\mathbf{v}_B - \mathbf{v}_A)$ was not zero because individual collisions produce some perpendicular component of scattering velocity. Thus repetition of the "average" collision can be interpreted as a process which results not only in a collision force, but also a spectrum of post-collision velocities of magnitude $\overline{\Delta V_r}$ (eqs. (8.25) and (8.26)), isotropically distributed in a plane perpendicular to this force. The mean of this distribution is zero, and thus the velocities contribute to the fluctuating kinetic energy.

For this model the contribution of each average collision to the fluctuating kinetic energy is assumed to correspond to the kinetic energy associated with the speed of the particle perpendicular to the force direction, $\frac{1}{2}m_p\overline{\Delta V_r}^2$. Thus, considering the collisions of A fraction particles with B fraction particles attributable to mean velocity differences, an approximation of the

production of fluctuating kinetic energy per unit volume P_{kk_A} for the A particles is

$$\begin{aligned} P_{kk_A} &= \frac{1}{2} m_{pA} Z'_{AB} \overline{(\Delta V_{r_{AB}})}^2 \\ &= \frac{1}{2} m_{pA} Z'_{AB} \left(\frac{\pi}{4} \Delta \mathbf{v}_{AB} \right)^2 , \end{aligned} \tag{8.71}$$

where $\overline{\Delta V_{r_{AB}}}$ corresponds to $\overline{\Delta V_{r_A}}$ given in eq. (8.25), Z'_{AB} is the A-B type (i) collision frequency due to mean velocity difference (eq. (8.41)), and $\Delta \mathbf{v}_{AB}$ is the average change in velocity given by eq. (8.29). An equivalent expression for P_{kk_B} may be obtained by interchanging A and B subscripts in eq. (8.71).

In Appendix D it is shown that $\Delta \mathbf{v}_{AB}$ is proportional to $(1+e)/(3-e)$ for large particles. For a perfectly elastic collision, $e = 1.0$, giving $(1+e)/(3-e) = 1.0$. As $e \rightarrow 0.0$, then $(1+e)/(3-e) \rightarrow 0.33$. Thus, from eq. (8.71), the maximum reduction in efficiency with which vertical energy prior to collision is re-directed into lateral energy post collision is approximately $(0.33)^2$, compared to an elastic collision efficiency of 1.0. This efficiency does not fall to zero because the average collision is oblique and energy is only lost in the direction of contact angle vector $\mathbf{k}$. If the particle velocity fluctuations are isotropic when collisions are elastic, then, as a crude approximation, it may be assumed that the magnitude of the lateral fluctuations in velocity is only 33% of the vertical fluctuations when $e = 0.0$. For small particles $\Delta \mathbf{v}_{AB}$ is proportional to $(1+e)$, and an equivalent analysis also predicts lateral fluctuations to be 50% of vertical fluctuations when $e = 0.0$. Generally e will be much greater than zero and, as mentioned above, anisotropy in fluctuations is not considered in the model.

8.8.2 Production of Fluctuating Kinetic Energy due to Gas Turbulence

The average energy transferred directly from the model eddy to a particle over time τ_r is $\frac{1}{2} m_p (\Delta \mathbf{C}_t)^2$, where $\Delta \mathbf{C}_t$ is related to the mean drift velocity, $\mathbf{c}_t$, by eq. (8.60). Hence the production of fluctuating energy P_{kt_A} per unit volume due to gas turbulence for a type A particle is

$$P_{kt_A} = \frac{\rho_{sA} \mathbf{c}_{tA}^2}{2\tau_{rA} (1 - \lambda_{eA})^2} . \tag{8.72}$$

8.8.3 Transfer of Energy between Particle Fractions due to Fluctuating Velocity Collisions

Collisions that result from the fluctuating component of the particles' velocities are classified as type (ii) collisions in the model, with a collision frequency of Z'' (eq. (8.42)). For type (ii) collisions the mean velocity differences between particle fractions are ignored, as effects due to mean velocity differences are assumed to have already been accounted for in type (i) collision analysis. Rather than consider the energy transfer and losses in all possible type (ii) encounters, a "typical" type (ii) collision is assumed in order to provide reasonable estimates of the overall effect of all such encounters.

If the mean velocity difference between fractions is zero, then eq. (8.36) gives the type (ii) collision frequency, obtained by considering all possible approach velocities. Evaluating the numerical constant in eq. (8.36) gives

$$Z''_{AB} = 0.9213\, \mathbf{n}_A \mathbf{n}_B \sigma_{AB}^2 \left(\mathbf{c}_{kA}^2 + \mathbf{c}_{kB}^2\right)^{\frac{1}{2}} . \tag{8.73}$$

If particles A and B are assumed to have fluctuating velocities of magnitude equal to their respective r.m.s. fluctuating velocities, $\mathbf{c}_{kA}$ and $\mathbf{c}_{kB}$, then a type (i) collision between these particles, with the incident velocities at right angles as shown in Figure 8.3, gives a very similar expression for collision frequency. From eq. (8.33),

$$Z''_{AB} = \mathbf{n}_A \mathbf{n}_B \sigma_{AB}^2 \left(\mathbf{c}_{kA}^2 + \mathbf{c}_{kB}^2\right)^{\frac{1}{2}} . \tag{8.74}$$

For exact agreement between eq. (8.73) and the collision frequency of the typical collision, particles A and B are assumed to collide at right angles in the "typical" collision with approach velocities of $\mathbf{w}_A = 0.9213\, \mathbf{c}_{kA}$ and $\mathbf{w}_B = 0.9213\, \mathbf{c}_{kB}$, respectively.

To calculate scattering velocities from this typical collision, the contact angle must also be defined. A coordinate system for the collision is shown in Figure 8.3. As in Figure 8.2, the orientation of the x', y', z' coordinate system is arbitrary. The dynamics of the collision are considered in the frame of reference of the B particle, and the approach velocity of the A

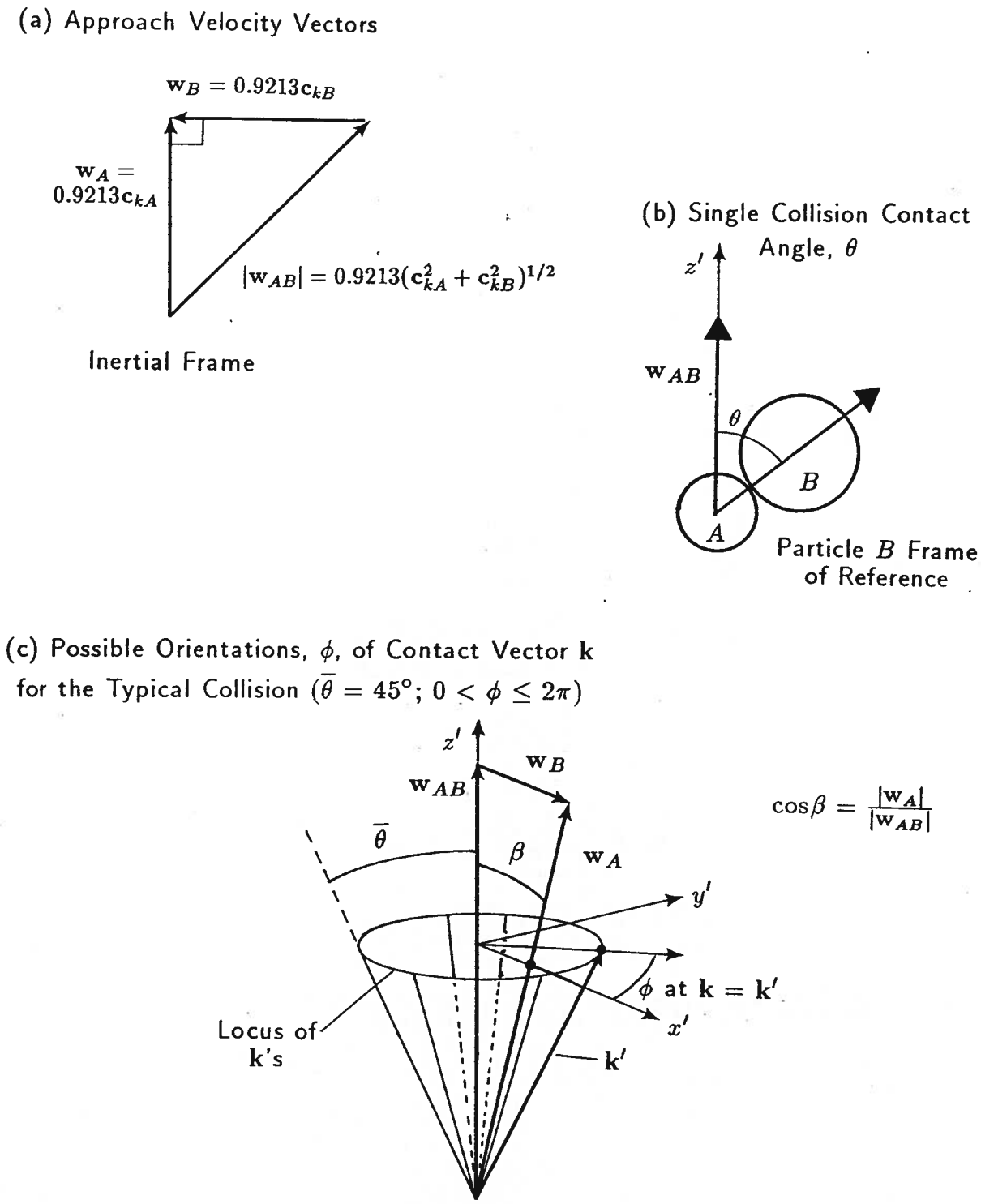

Figure 8.3: "Typical" type (ii) particle collision: (a) approach velocities, (b) contact angle for a single collision, and (c) possible particle orientations with a mean contact angle $\overline{\theta}$.

particle is $\mathbf{w}_{AB}$ in this frame. The collision process is symmetric about the z' axis. Thus the average contact angle is not a function of angle ϕ. The probability of a given contact angle surrounded by a differential contact area is given by eq. (8.17). The mean contact angle $\overline{\theta}$ may be defined assuming that 50% of collisions occur with contact angles less than $\overline{\theta}$. Thus

$$\begin{aligned} 0.5 &= \int_0^{\overline{\theta}} \int_{-\pi}^{\pi} \frac{\sin 2\theta}{2\pi} \, d\theta \, d\phi \\ &= \frac{1}{2}\left(1 - \cos 2\overline{\theta}\right) . \end{aligned} \tag{8.75}$$

Hence the average contact angle is 45°.

From the earlier analysis of energy transfer in a single collision (see eqs. (8.13) and (8.14)), it may be deduced that the energy transfer is a function of angle ϕ. To evaluate the average energy transfer in a typical collision it is necessary to sum the effects of typical collisions for all values of ϕ. In terms of the coordinate system in Figure 8.3, the vectors $\mathbf{w}_A$, $\mathbf{w}_{AB}$ and $\mathbf{k}$ for a single collision at angle ϕ become

$$\mathbf{w}_A = |\mathbf{w}_A| \cos\beta \, \boldsymbol{\delta}_z + |\mathbf{w}_A| \sin\beta \, \boldsymbol{\delta}_x \ , \tag{8.76}$$

$$\mathbf{w}_{AB} = |\mathbf{w}_{AB}| \, \boldsymbol{\delta}_z \ , \tag{8.77}$$

and

$$\mathbf{k} = \frac{1}{\sqrt{2}} \cos\phi \, \boldsymbol{\delta}_x + \frac{1}{\sqrt{2}} \sin\phi \, \boldsymbol{\delta}_y + \frac{1}{\sqrt{2}} \boldsymbol{\delta}_z \ , \tag{8.78}$$

where it has been assumed for convenience that the plane containing vectors $\mathbf{w}_A$ and $\mathbf{w}_B$ is the x'-z' plane. Therefore,

$$\mathbf{k} \cdot \mathbf{w}_{AB} = \frac{|\mathbf{w}_{AB}|}{\sqrt{2}} \ , \tag{8.79}$$

and averaging $(\mathbf{k} \cdot \mathbf{w}_A)$ over all orientations ϕ of the typical collision, gives

$$\begin{aligned} \mathbf{k} \cdot \mathbf{w}_A &= \frac{|\mathbf{w}_A|}{\sqrt{2}} \cos\beta + \frac{|\mathbf{w}_A|}{\sqrt{2}} \int_0^{2\pi} \cos\phi \, \sin\beta \, \frac{d\phi}{2\pi} \\ &= \frac{|\mathbf{w}_A|}{\sqrt{2}} \cos\beta \ . \end{aligned} \tag{8.80}$$

Also, $|\mathbf{w}_{AB}| \cos\beta = |\mathbf{w}_A|$, as shown in Figure 8.3. Substituting these expressions for $\mathbf{k}\cdot \mathbf{w}_A$ and $\mathbf{k}\cdot \mathbf{w}_{AB}$ into eqs. (8.13) and (8.14) gives an estimate of the average energy transfer for a type (ii) collision. For particle A the transfer is

$$\begin{aligned}\Delta E_A &= \frac{m_{pA} m_{pB}(1+e)}{2(m_{pA}+m_{pB})}\left[\frac{m_{pB}(1+e)}{m_{pA}+m_{pB}}(\mathbf{k}\cdot \mathbf{w}_{AB})^2 - 2(\mathbf{k}\cdot \mathbf{w}_{AB})(\mathbf{k}\cdot \mathbf{w}_A)\right] \\ &= \frac{m_{pA} m_{pB}(1+e)}{2(m_{pA}+m_{pB})}\left[\frac{m_{pB}(1+e)\mathbf{w}_{AB}^2}{2(m_{pA}+m_{pB})} - \mathbf{w}_A^2\right] . \end{aligned} \tag{8.81}$$

Similarly, for B,

$$\Delta E_B = \frac{m_{pA} m_{pB}(1+e)}{2(m_{pA}+m_{pB})}\left[\frac{m_{pA}(1+e)\mathbf{w}_{AB}^2}{2(m_{pA}+m_{pB})} - \mathbf{w}_B^2\right] . \tag{8.82}$$

Therefore a particle involved in a type (ii) collision may lose or gain energy depending on the masses, relative velocities and elasticity of the collision. In the specific case of collision of particles from the same fraction (i.e. same mass and r.m.s. fluctuating velocity), $\mathbf{w}_{AA}^2 = 2\mathbf{w}_A^2$, and there is no net energy transfer between particles if the collision is elastic. Adding ΔE_A and ΔE_B in eqs. (8.81) and (8.82) gives the same expression for the total energy loss as eq. (8.15).

The fluctuating kinetic energy transfer per unit volume, S_{kA}, for A particles, when considering only collisions with B particles, is therefore

$$\begin{aligned} S_{kAB} &= Z''_{AB}\,\Delta E_A \\ &= Z''_{AB}\frac{m_{pA} m_{pB}(1+e)}{2(m_{pA}+m_{pB})}\left[\frac{m_{pB}(1+e)\mathbf{w}_{AB}^2}{2(m_{pA}+m_{pB})} - \mathbf{w}_A^2\right] . \end{aligned} \tag{8.83}$$

8.8.4 The Differential Fluctuating Kinetic Energy Equation

The expressions for fluctuating kinetic energy production P_{kk} and transfer S_k were developed considering two particle fractions, A and B. When multiple particle fractions are present, the production and transfer terms for a given particle fraction are simply obtained by considering the interaction of this fraction with each other fraction in turn, and summing the individual contributions. For a system of n particle fractions, a differential fluctuating kinetic energy equation for a particle fraction "i" based on the production, transfer, and dissipation terms

discussed is

$$\frac{\partial}{\partial t}(\rho_{si}K_i) + \nabla \cdot (\rho_{si}K_i\mathbf{v}_{zi}) = P_{kt_i} - D_{kt_i} + \sum_{j=1}^{n}\left(P_{kk_{ij}} + S_{k_{ij}}\right) , \tag{8.84}$$

where $P_{kk_{ij}}$, P_{kt_i}, $S_{k_{ij}}$ and D_{kt_i} are given respectively by eqs. (8.71), (8.72), (8.83) and (8.70). Several of the terms in the model, such as those on the r.h.s. of eq. (8.84), were developed assuming that the mean gas and particle fraction velocities are in the vertical direction. Although the model applies to vertical mean flows, this is a minor limitation as the vast majority of gas-particle suspension reactors operate with mean flows in the vertical direction. To denote this model restriction, the velocity in the convective term of eq. (8.84) is shown with the subscript z.

8.9 Transfer of Particles across a Vertical Plane

The lateral transfer of particles in vertical suspension flow is due to both the collisional fluctuating velocities and the eddy drift velocities of the particles. In this section expressions for the number flow and mass flow of particles across a vertical plane are determined, using standard methods from the kinetic theory of gases (e.g. Chapman and Cowling, 1970). Only flow in one direction is considered. One such flow is the transfer of particles across a core-wall layer interface in a CFB riser. The average transfer of particles across this plane is a function of the r.m.s. fluctuating velocity, averaged over all eddy orientations. To calculate the transfer, it is assumed that the fluctuations are isotropic and that the particles all have a fluctuating velocity of magnitude $|\mathbf{c}|$, where $\mathbf{c}^2 = \mathbf{c}_t^2 + \mathbf{c}_k^2$.

Consider the transfer of particles from a given particle fraction across a small area ds in the x'-y' vertical plane shown in Figure 8.4, in the opposite direction to the z' axis, normal to the plane. As the particle velocity fluctuations are isotropic, only 50% of the particles have components of velocity towards ds. Furthermore, particles approach from all directions, depending on their velocity. The particles coming in from angle (θ, ϕ) move down a cylinder that has vertical sectional area ds, as shown. For isotropic fluctuations, the fraction of particles

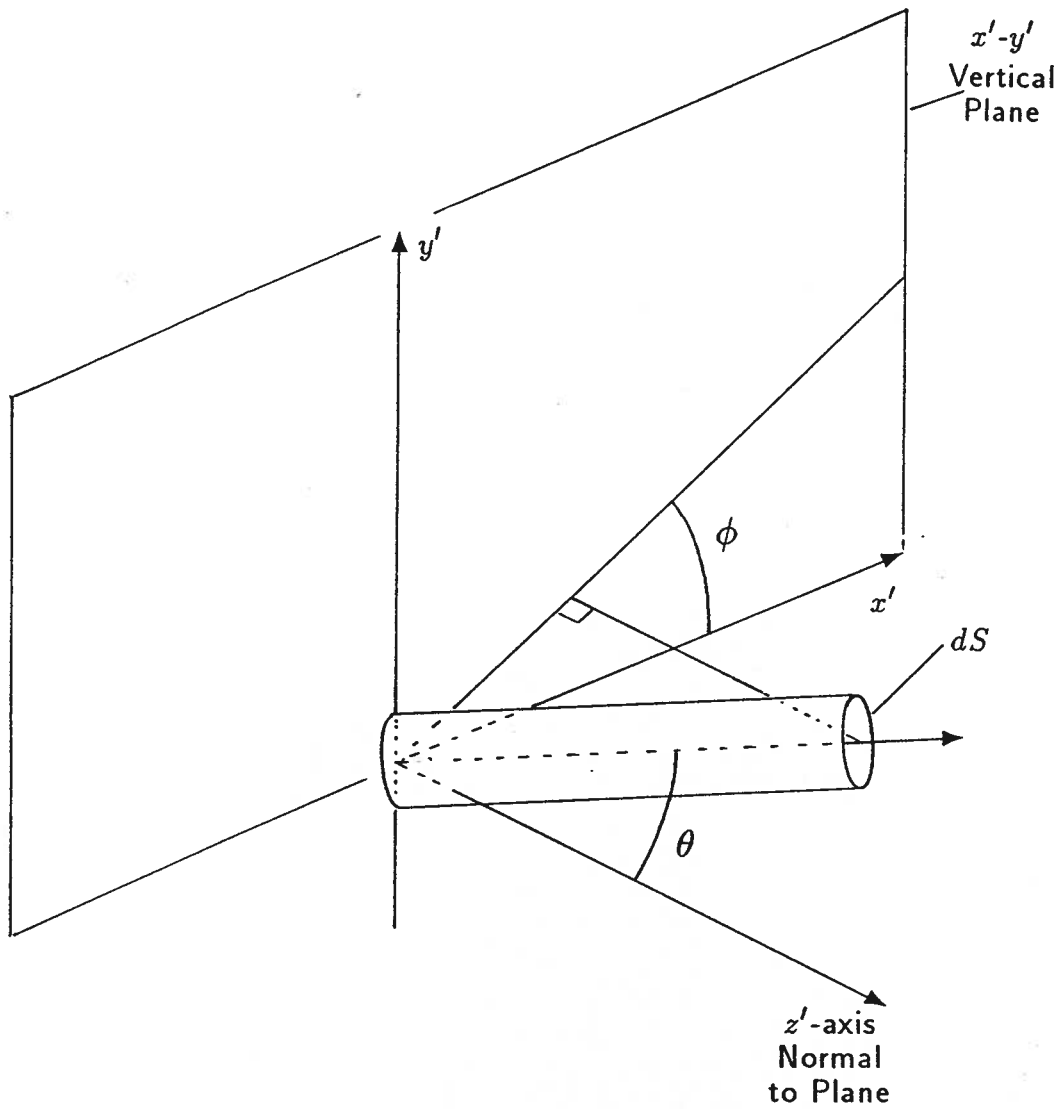

Figure 8.4: Lateral transfer of particles across a vertical plane.

coming from this angle is proportional to the fraction of particles that have velocity $\mathbf{c}$ in this direction, i.e. $\sin\theta\, d\theta\, d\phi/4\pi$. The velocity of these particles normal to the plane ds is $\mathbf{c}\cos\theta$. Therefore, the flow (number per unit time) crossing ds at the plane is $\mathbf{n}\sin\theta\, d\theta\, d\phi\, \mathbf{c}\cos\theta/4\pi$, where $\mathbf{n}$ is the number of particle per unit volume. Summing over all approach angles where the particle velocity is towards an area ds in the plane, and letting $ds \to 0$ gives the total number flow, N_c of particles per unit time per unit plane area, i.e.

$$\begin{aligned} N_c &= \mathbf{n}\,|\mathbf{c}| \int_{-\pi}^{\pi}\int_{0}^{\frac{\pi}{2}} \frac{\cos\theta\,\sin\theta}{4\pi}\, d\theta\, d\phi \\ &= \frac{\mathbf{n}|\mathbf{c}|}{4}\,. \end{aligned} \tag{8.85}$$

The rate of mass transfer, Q_c, per unit area across the plane is thus

$$Q_c = \frac{m_p\mathbf{n}\,|\mathbf{c}|}{4} = \frac{\rho_s\,|\mathbf{c}|}{4}\,. \tag{8.86}$$

For 50% of particles ($\mathbf{n}/2$) near the wall that have components of velocity that will carry them across the plane, the average velocity $\mathbf{W}_+$ normal to the plane is $(\frac{1}{4}\mathbf{n}\,|\mathbf{c}|)/(\frac{1}{2}\mathbf{n}) = |\mathbf{c}|/2$. As N_c, Q_c and $\mathbf{W}_+$ are functions of $\mathbf{c}$, they are expected to vary between different particle fractions.

8.10 Kinetic Theory Analogy

As mentioned in the general discussion of "granular kinetic theory" in Chapter 4, there are several obvious fundamental differences between a kinetic theory gas consisting of "hard-sphere" molecules and a mixture of particles. Collisions amongst molecules are elastic whilst collisions amongst particles generally are not. The fluctuating velocities of the molecules are many orders of magnitude greater than the mean velocity of the gas, whereas particle fluctuating velocities are expected to be $O(0.1)$ of typical mean velocities. Kinetic theory results are strictly valid only when the forces on the molecules may be expressed as gradients of potential (e.g. gravitational, electrical and magnetic). Gas-particle drag force does not satisfy this requirement. Nevertheless, if the particle collisions are nearly elastic, the particles are sufficiently large that drag force does not appreciably alter a particle's velocity between collisions and turbulence

does not significantly affect the particle motion, and a mixture of particles of similar size and particle density is present, then the gas kinetic theory analogy may be reasonable (Jenkins and Savage, 1983; Sinclair and Jackson, 1989; Louge *et al.*, 1991). Unfortunately, over the range of typical conditions observed in CFB risers, these restrictions are not always appropriate.

In dilute suspensions of small type (1) motion particles, the particle response time, τ_p, may be substantially less than the period between collisions, τ_k, and the particles respond significantly to the gas turbulence. In this case, the kinetic theory analogy is not applicable, and a suitable two-phase turbulent flow model is required. Also, there is no equivalent phenomenon to the anisotropy due to inelastic particle collisions, discussed earlier.

When the kinetic theory analogy is extended to particle mixtures of various sizes and densities, some practical problems arise. A corollary of the principle of equipartition of energy in gas mixtures is that the temperature (i.e. fluctuating molecular energy) of each component is equal to the temperature of the mixture (Chapman and Cowling, 1970). For a mixture of type 1 and 2 molecules (or particles), this may be written as

$$\frac{1}{2}m_{p1}\mathbf{c}_1^2 = \frac{1}{2}m_{p2}\mathbf{c}_2^2 \,. \tag{8.87}$$

Consider a binary system of 40 μm particles (type 1) and 230 μm particles (type 2) of the same particle density. If the r.m.s. fluctuating velocity of the 230 μm particles is $\mathbf{c}_2 = 0.2$ m/s, then eq. (8.87) predicts $\mathbf{c}_1 = 2.8$ m/s. A velocity of 2.8 m/s is an order of magnitude greater than typical measured fluctuating velocities discussed in Chapter 3. It would suggest substantial segregation of particles in a CFB riser, with a preponderance of fine particles at the riser wall. This is contrary to the segregation trends observed experimentally in this study (Chapter 6). Any particles with fluctuating velocities of this order would be expected to be rapidly decelerated due to drag, a factor not present in a kinetic theory gas. Consequently, although several modellers have employed the concept of a particle-phase temperature or "granular temperature" (e.g. Louge *et al.*, 1991), such terms are not used here.

An additional phenomenon for which there is no equivalent in kinetic theory is the production of fluctuating energy due to differences in the mean velocity of various fractions. Typical

differences in mean velocity of different gas components are much smaller than the fluctuating molecular velocities, whereas in suspension flows such differences may be comparable to r.m.s. velocities.

As discussed in Chapter 4, if the particle suspension is "dense," as in a bubbling bed or in wall streamers, transfer of momentum and energy over the distance separating the centres of the two colliding particles at the moment of impact becomes important, in addition to the transfer of momentum due to the distances travelled by particles between collisions. Chapman and Cowling (1970) give a criterion for estimating if a system of colliding particles is "dense" based on a factor $\varpi = (1-11\pi \mathbf{n} d_p^3/12)/(1-4\pi \mathbf{n} d_p^3/3)$. For particle systems this may also be expressed as $\varpi = (1-5.5\epsilon_p)/(1-8\epsilon_p)$, where ϵ_p is the solids volume fraction of the suspension. If $\varpi \gg 1.0$ the system is dense, whereas when $\varpi \approx 1.0$ the system is dilute. A typical dilute 10 kg/m^3 suspension of 230 μm particles of particle density $\rho_p = 2700$ kg/m^3, corresponds to a value of $\varpi = 1.0095$. For a 270 kg/m^3 suspension (volume fraction, $\epsilon_p = 0.1$) of the same particles, $\varpi = 2.25$. As stated in Chapter 4, in this study a dilute suspension is defined as a suspension of less than 0.05 volume fraction solids concentration, corresponding to $\varpi = 1.2$. With this limit, the error involved in neglecting "dense gas" effects is commensurate with general expected model accuracy. The model presented in this Chapter is assumed to be strictly applicable only for dilute (and very dilute) suspensions. It is assumed that this limit is reached before multi-particle collisions become prevalent. Collisional models for dense suspension flows based on kinetic theory analogies should assume the more general approach required for dense gases (Chapman and Cowling, 1970; Jenkins and Savage, 1983; Lun *et al.*, 1984; Savage, 1988).

8.11 Modelling Particle-Particle and Particle-Turbulence Interactions: Brief Comparison with Other Approaches

Several modellers have developed comprehensive models for the flow of fine particle suspensions in turbulent gas flows (e.g. Chen, 1989; Rizk and Elghobashi, 1989). These models generally involve extension of single-phase $k-\epsilon$ models to two-phases. (See Nallamsy (1987) for a review

of single-phase $k-\epsilon$ models.) As mentioned earlier, such models are limited to relatively dilute suspensions of small particles, and certainly do not cover the full range of conditions observed in CFBs.

Early models that accounted for the interaction of particles focussed on developing an expression for the collision force between particle fractions similar to that of eq. (8.57). Soo (1967) considered the case of head-on elastic collisions. Nakamura and Capes (1976) allowed for oblique collisions by using an empirical constant and also considered inelastic collisions. However, both Soo and Nakamura and Capes incorrectly assumed that the velocity of the particles immediately before each collision was equal to the mean velocity of the particles. Both approaches may produce errors up to $O(100\%)$, as discussed in Appendix D.

All the models developed with a fundamental approach to particle collision phenomena appear to use some form of analogy with kinetic theory. Louge *et al.* (1991) develop a granular temperature balance analogous to a thermal energy balance for gas flow. They assume that the response of the particles to the gas turbulence is negligible and obtain expressions for solid phase viscosity, pressure and thermal conductivity directly from dilute gas kinetic theory. Their model is limited to dilute flows of "relatively massive" particles. Interestingly, Louge *et al.* (1991) and Rizk and Elghobashi (1989) both compare their model predictions with the experimental data of Tsuji *et al.* (1984), despite proposing quite different mechanisms to explain the fluctuating particle motion. A likely explanation for this is discussed in Chapter 3.

Gidaspow and co-workers have applied the results of dense gas kinetic theory in order to develop expressions for solids phase transport properties (Ding and Gidaspow, 1990; Gidaspow *et al.*, 1990). Although Gidaspow *et al.* (1990) develop momentum equations for multiple particle size fractions, they assume only a single solids phase granular temperature, a questionable approach, as discussed earlier. They use the force expression of Nakamura and Capes (1976) for collisional force between particle fractions. Despite acknowledging the possible importance of forces due to collisions between particles from different fractions, they do not allow for the corresponding production of "granular energy" from such collisions. None of the models of

Gidaspow *et al.* considers the influence of gas turbulence on particle motion.

Sinclair and Jackson (1989) also introduce a granular temperature, which they term the pseudo-thermal energy. They do not account for turbulence effects, which they acknowledge may be important. Their theory is limited to fully-developed flow, again assumes only a single granular temperature and is not compared to experimental results. Their model qualitatively predicts division of solids into a denser wall region and a more dilute core. However, the Sinclair and Jackson model does not include a particle fluctuating energy dissipation term due to drag, shown to be important in later simulations in this Chapter. Pita and Sundaresan (1991) obtained significantly lower predicted fluctuating velocities from the Sinclair and Jackson model when they included this term, but the model no longer predicted a core-annulus solids distribution.

8.12 Model Boundary Conditions for Suspension Flow in the Core of a CFB Riser

In Chapter 5 a two-zone approach to modelling CFB risers was developed assuming rapid dilute suspension upflow in the core surrounded by an annular wall region that could contain dense streamers of particles. All core particle and gas properties were assumed to be uniform across a horizontal plane. The dilute suspension flow model presented in this chapter may be used to predict the flow dynamics within this core, providing boundary conditions for the core flow are known for the core-wall interface. To develop expressions for these boundary conditions, some preliminary model assumptions concerning wall effects are presented here. A detailed analysis of wall dynamics and a discussion of these assumptions appear in Chapter 9.

Recall that part of the riser wall is generally exposed to dilute suspension upflow due to disruptions to wall streamers. Consequently, two possible wall effects are assumed to influence the core flow. Firstly, individual core particles with lateral velocity components directed towards areas of exposed wall rebound from the wall back into the core flow. Secondly, where wall streamers are present, though many of the core particles passing into the wall region are absorbed into the falling streamers, a flow of particles from the streamers back into the core

also occurs, due to re-entrainment. These streamer particles have significantly lower vertical velocities than the fast flowing core particles, as streamers move predominantly downward. Factors generally affecting the mass transfer rate, Q_s, of particles from the wall streamers to the core are discussed in Chapter 9. The core suspension flow model simulations given later in this Chapter only consider the fully-developed flow case where there is zero net mass flow of particles across the core-wall interface. The fraction of the core-to-wall mass transfer that rebounds back into the core from a bare wall is defined as f_w, and the fraction captured by streamers is $(1 - f_w)$. Hence, for a core-to-wall solids mass flux of Q_c and a zero net core-wall mass flux, $Q_s = (1 - f_w)Q_c$ and $Q_r = f_w Q_c$, where Q_r is the mass flux of particles rebounding from a bare riser wall. Here f_w is assumed invariant with particle fraction size/density. This assumption is discussed later. Factors affecting f_w are analysed in Chapter 9.

In the following discussion, an analysis of the effect of a general "wall" particle on the core flow is first presented. The results of this analysis are then applied to the specific processes of particle-wall rebounds and streamer re-entrainment to develop boundary conditions for the shear force on the core and production/dissipation of core particle fluctuating kinetic energy due to wall effects.

8.12.1 Effects of Entering Wall Particles on Riser Core Flow

Johnson and Jackson (1987) discuss the relative effects of tangential frictional forces in particle-particle collisions and particle-wall collisions. They point out that particle-particle collisions in dilute suspensions are expected to involve point contacts for brief duration times, and that frictional forces tangential to the surfaces in contact are likely to be small compared to normal forces associated with the collision. In contrast, collisions of particles with a wall may involve multiple contact points if the wall is rough. Consequently, modellers of dilute suspension flow (e.g. Johnson and Jackson, 1987; Sinclair and Jackson, 1989; Tsuo and Gidaspow, 1990; Pita and Sundaresan, 1991) generally assume that frictional effects in particle-particle collisions can be neglected, but include terms for particle-wall friction. This approach is also adopted here.

The terms developed below for the change in core particle velocity and fluctuating kinetic energy due to a wall collision are conceptually similar to relations proposed by Sinclair and Jackson (1989).

A wall particle entering the core of a riser generally has a lower axial velocity than the majority of the upflowing core particles. A "rebound" particle, arriving after a wall collision, has been slowed by friction with the vertical wall during the wall-particle contact time, whilst particles entrained from downflowing wall streamers have significantly lower velocities than the core particles they first encounter. Collisions between a wall particle entering the core and core particles are oblique. Thus the wall-core particle collisions not only retard the mean vertical motion of each core particle fraction, but also result in the production of fluctuating kinetic energy within the core. A portion of the energy associated with the mean motion of the core particles is used to accelerate the wall particles, and a portion is converted to fluctuating kinetic energy.

An estimate of both the shear force on a given core particle fraction due to wall particles, and the associated creation of fluctuating kinetic energy within that fraction, is obtained by considering the collisions between particles from the given core fraction and average or "mean" wall particles of diameter d_{pw}, where d_{pw} is the Sauter mean diameter of the wall particles entering the core. As the Sauter mean diameter has the same surface area to volume ratio as the mixture, and the collision frequency between the upflowing core particles and the injected wall particles depends on the projected area of the wall particles, this is an appropriate choice. If Q_w is the mass flux of either rebound or streamer particles entering the core (i.e. $Q_w = Q_r$ or $Q_w = Q_s$), then

$$\begin{aligned} d_{pw} &= \frac{1}{\sum x_i/d_{pi}} \\ &= \frac{\sum Q_{wi}}{\sum Q_{wi}/d_{pi}} \\ &= \frac{Q_w}{\sum Q_{wi}/d_{pi}}, \end{aligned} \tag{8.88}$$

where the summation is over all particle fractions. The collision radius between a particle from

core fraction A and a mean wall particle is $\sigma_{Aw} = (d_{pA} + d_{pw})/2$.

Each core particle fraction is assumed to instantaneously accelerate the wall particles it interacts with up to the velocity of that core fraction. As approach velocities of wall streamer and core particles are several orders of magnitude greater than approach velocities for collisions amongst core particles, both the collision force and frequency briefly experienced by a wall streamer particle are orders of magnitude greater than that for collisions amongst core particles. Similarly, rebound particles returning from a rough wall are expected to have axial velocities significantly lower than core particle velocities, due to the retarding frictional force exerted on these particles in the wall collision. In both cases, the assumption of instantaneous change in wall particle velocity is probably reasonable and the contribution of drag to the wall particle acceleration is assumed negligible. Any small initial lateral velocity the wall particle may have in comparison to the vertical approach velocities involved is also neglected. If wall friction is very small, the rebounding particles may have similar mean velocities to the core particles, and drag may become important in determining the wall particle motion. However, in this case wall shear effects on the mean and fluctuating motion of the core particle suspension are expected to be small, and the accuracy of the estimates of wall particle shear and energy creation are not critical. The momentum and energy changes of core particles from a particular fraction that are scattered by a collision with a mean wall particle are assumed to be rapidly re-distributed throughout that core fraction by further core-core particle collisions.

The accelerated motion of a single mean-sized wall particle from an initial vertical velocity of $\mathbf{w}_0$, at the instant it enters the core, to a vertical velocity near that of the core fraction by repeated collisions is firstly considered. The particular core fraction under study is assumed to be solely responsible for the acceleration of that wall particle. To estimate the fluctuating kinetic energy generated by this process it is necessary to determine the number of collisions required to bring the wall particle up to near the core particle fraction velocity.

Let $\mathbf{w}_j$ be the vertical velocity of the wall particle after the jth collision with core particles from fraction "i" (i.e. j is a positive integer). As the accelerating wall particle travels more

slowly than the core particles, a different core particle hits the wall particle in each collision. On average these core particles have the mean vertical velocity of that fraction, $\mathbf{v}_{zi}$, which is essentially constant over the very short time period required to accelerate the wall particle. Since drag effects are assumed insignificant in the acceleration of the wall particle, there is no need to consider velocity weighting factors, and the velocities of the wall particle immediately prior to the $(j+1)$th collision equals that immediately after the jth collision. As the initial collisions are far more energetic than the later collisions, it is possible to obtain a reasonable estimate of the creation of fluctuating energy by only considering the effects of collisions up to the stage that the wall particle is within some fraction of the core particle fraction velocity. Here, a cut-off of $\mathbf{w}_j/\mathbf{v}_{zi} = 0.99$ has been set.

A wall particle typically gains a component of velocity in the lateral direction following each collision. The lateral direction of this component is random depending on the contact angle of the particles and it is therefore a form of fluctuating velocity. However, the average lateral velocity of the wall particle is neglected (as discussed earlier) and, to evaluate the vertical velocity change of the wall particle resulting from each collision, lateral components of velocity are assumed to be zero. Equation (8.20) gives the change in the average wall particle vertical velocity, $\Delta\mathbf{w}_j$, due to the jth collision in terms of the core and wall particle velocities immediately *before* the collision, i.e.

$$\begin{aligned} \Delta\mathbf{w}_j &= \frac{m_{pi}(1+e)(\mathbf{v}_{zi}-\mathbf{w}_{j-1})}{2(m_{pi}+m_{pw})} \\ &= \mathcal{R}_{wi}(\mathbf{v}_{zi}-\mathbf{w}_{j-1}) \ , \end{aligned} \tag{8.89}$$

where m_{pw} is the mass of the mean-sized wall particle. Using the constant parameter $\mathcal{R}_{wi}$, defined in eq. (8.89), the wall particle vertical velocity after each collision becomes

$$\begin{aligned} \mathbf{w}_0 &= 0 \\ \mathbf{w}_1 &= \mathbf{w}_0 + \mathcal{R}_{wi}(\mathbf{v}_{zi}-\mathbf{w}_0) \\ \mathbf{w}_2 &= \mathbf{w}_1 + \mathcal{R}_{wi}(\mathbf{v}_{zi}-\mathbf{w}_1) \\ \mathbf{w}_3 &= \ \ldots \end{aligned}$$

$$\mathbf{w}_m = \mathbf{w}_{m-1} + \mathcal{R}_{wi}\left(\mathbf{v}_{zi} - \mathbf{w}_{m-1}\right) , \tag{8.90}$$

where m is the number of collisions required to accelerate the wall particle up to $\mathbf{w}_m/\mathbf{v}_{zi} = 0.99$. In Appendix D a more useful form of eq. (8.90) is developed in which the wall particle velocity after each collision is not explicitly dependent on the velocity immediately before that particular collision,

$$\frac{\mathbf{w}_m}{\mathbf{v}_{zi}} = 1 - (1 - \mathcal{R}_{wi})^m \left(1 - \mathbf{w}_0/\mathbf{v}_{zi}\right) . \tag{8.91}$$

Substituting $\mathbf{w}_m/\mathbf{v}_{zi} = 0.99$ into eq. (8.91) gives $0.01 = (1 - \mathcal{R}_{wi})^m (1 - \mathbf{w}_0/\mathbf{v}_{zi})$. Thus the number of collisions for the wall particle to attain 99% of the core particle velocity is

$$m = \frac{-2 - \log_{10}|1 - \mathbf{w}_0/\mathbf{v}_{zi}|}{\log_{10}(1 - \mathcal{R}_{wi})} . \tag{8.92}$$

Typically m is $O(10^3)$ for small core particles, and $O(10)$ for large core particles. Note that it is also possible for a small portion of the mean wall particles to encounter particles from a slow moving core fraction (e.g. large coal particles in CFB combustors), and to be decelerated. Equation (8.92) is equally applicable for determining the number of collisions required to decelerate a mean wall particle, providing the absolute value of $(1 - \mathbf{w}_0/\mathbf{v}_{zi})$ is taken, as shown.

8.12.2 Force on Core Flow due to Entering Wall Particles

Again, consider mean wall particles that are all either rebound or streamer particles. The collision of a mean wall particle and core particle is a type (i) collision. Therefore, one possible estimate of the portion of wall particles, χ_{wA}, that collide with particles from a given core fraction A, is the collision frequency of type A particles with mean wall particles, divided by the total wall-core collision frequency. However, this approach overlooks the fact that smaller core particles must make many more collisions with a single mean-sized wall particle to fully accelerate it, than must the larger core particles. A considerably better estimate of the contribution of a given core fraction to accelerating the wall particles, that provides good results in later model simulations, is obtained by dividing the wall-core particle collision frequency of each core fraction by the number of collisions, m, required by each fraction to accelerate one

wall particle. The relative magnitudes of this parameter for each core fraction are then assumed equal to the proportion of wall particles accelerated by each core fraction, i.e. for core fraction A:

$$\chi_{wA} = \frac{(\mathbf{n}_A/m_A)\,\sigma_{Aw}^2|\mathbf{v}_{zA} - \mathbf{v}_{zw}|}{\sum_{j=1}^{n}(\mathbf{n}_j/m_j)\,\sigma_{jw}^2|\mathbf{v}_{zj} - \mathbf{v}_{zw}|}\,, \tag{8.93}$$

where m_j for the jth core fraction is given by eq. (8.92), and the specific term $\mathbf{v}_{zw}$ replaces the generic term $\mathbf{w}_0$ for the initial mean wall particle vertical velocity. Expressions for $\mathbf{v}_{zw}$ for rebound and wall streamer particles are developed later.

The rate of momentum transfer required to accelerate the wall particles by collision force is equal in magnitude to the decelerating force on the core particles. Hence the force per unit wall-core interfacial area (i.e. units of shear) on core particle fraction A due to the entry of wall particles into the core is

$$\tau_{wA} = \chi_{wA}\,Q_w\,(\mathbf{v}_{zw} - \mathbf{v}_{zA})\,. \tag{8.94}$$

8.12.3 Production of Core Particle Fluctuating Kinetic Energy due to Wall Particles

To estimate the production of fluctuating kinetic energy due to the acceleration of a single mean rebound or streamer wall particle by a given core particle fraction, the effects of each of the m collisions are summed. As with the production of fluctuating energy due to type (i) core particle collisions, the production of fluctuating energy in each wall-core particle collision is related to the lateral speed following a collision. The expression for the average change in radial speed in terms of particle velocities immediately prior to the collision is given in eq. (8.25). In terms of $\mathbf{w}$ and $\mathbf{v}_{zi}$, the mean change in radial speed of the wall particle, $\overline{\Delta W_{rj}}$, following the jth collision is

$$\begin{aligned}\overline{\Delta W_{rj}} &= \frac{\pi m_{pi}\,(1+e)\,|\mathbf{v}_{zi} - \mathbf{w}_{j-1}|}{8\,(m_{pi} + m_{pw})} \\ &= \frac{\pi}{4}\,\mathcal{R}_{wi}\,|\mathbf{v}_{zi} - \mathbf{w}_{j-1}|\,.\end{aligned} \tag{8.95}$$

Similarly, if $\mathcal{R}_{iw} = m_{pw}(1+e)/(2[m_{pi}+m_{pw}])$, then the average change in radial speed of a core particle from fraction i due to the jth wall-core collision is

$$\overline{\Delta V_{rij}} = \frac{\pi}{4}\mathcal{R}_{iw}\left|\mathbf{v}_{zi} - \mathbf{w}_{j-1}\right| . \tag{8.96}$$

Both the lateral velocity changes of the core and wall particles in each collision are assumed to contribute to the fluctuating kinetic energy of that core fraction, with the fluctuating energy of the wall particle transferring to the core particle fraction during each collision. This approximation accounts for the transfer of fluctuating kinetic energy from the wall particle back to the core particles in subsequent collisions and the contribution to the core particle fluctuating energy when the wall particles reach a final steady mean velocity, and become core particles. The fluctuating kinetic energy ΔE_i gained by the core particles in the m collisions with the wall particle is

$$\Delta E_i = \frac{m_{pi}\pi^2\mathcal{R}_{iw}^2}{32}\sum_{j=1}^{m}\left(\mathbf{v}_{zi} - \mathbf{w}_{j-1}\right)^2 . \tag{8.97}$$

Substituting eq. (8.91) into eq. (8.97) to eliminate $\mathbf{w}_{j-1}$ gives

$$\Delta E_i = \frac{m_{pi}\pi^2\mathcal{R}_{iw}^2\mathbf{v}_{zi}^2\left(1-\mathbf{w}_0/\mathbf{v}_{zi}\right)^2}{32}\sum_{j=1}^{m}\left(1-\mathcal{R}_{wi}\right)^{2m-2} . \tag{8.98}$$

Now $\mathcal{R}_{iw}/\mathcal{R}_{wi} = m_{pw}/m_{pi}$. Also the summation in eq. (8.98) is that of a geometric series, and thus eq. (8.98) may be simplified to

$$\Delta E_i = \frac{\pi^2}{32}m_{pw}\mathcal{R}_{iw}\mathbf{v}_{zi}^2\left[\frac{\left(1-\mathbf{w}_0/\mathbf{v}_{zi}\right)^2\left(1-\left(1-\mathcal{R}_{wi}\right)^{2m}\right)}{2-\mathcal{R}_{wi}}\right] . \tag{8.99}$$

Similarly, the fluctuating energy ΔE_w gained (and transferred) by the wall particle in m collisions is

$$\begin{aligned}\Delta E_w &= \frac{m_{pw}\pi^2\mathcal{R}_{wi}^2\left(1-\mathbf{w}_0/\mathbf{v}_{zi}\right)^2}{32}\sum_{j=1}^{m}\left(\mathbf{v}_{zi} - \mathbf{w}_{j-1}\right)^2 \\ &= \frac{\pi^2}{32}m_{pw}\mathcal{R}_{wi}\mathbf{v}_{zi}^2\left[\frac{\left(1-\mathbf{w}_0/\mathbf{v}_{zi}\right)^2\left(1-\left(1-\mathcal{R}_{wi}\right)^{2m}\right)}{2-\mathcal{R}_{wi}}\right] .\end{aligned} \tag{8.100}$$

Now $\mathcal{R}_{iw} + \mathcal{R}_{wi} = (1+e)/2$. Thus the total production of fluctuating kinetic energy ΔE in fraction i due to the single wall particle is

$$\begin{aligned} \Delta E &= \Delta E_w + \Delta E_i \\ &= \frac{\pi^2}{64} m_{pw} \mathbf{v}_{zi}^2 (1+e) \left[\frac{(1-\mathbf{w}_0/\mathbf{v}_{zi})^2 \left(1-(1-\mathcal{R}_{wi})^{2m}\right)}{2-\mathcal{R}_{wi}} \right] . \end{aligned} \tag{8.101}$$

Equation (8.101) is a general expression for the energy production as a function of m. Here m is specifically defined as the number of collisions for the wall particle to attain 99% of the core particle velocity. At this condition, $0.01 = (1-\mathbf{w}_0/\mathbf{v}_{zi})(1-\mathcal{R}_{wi})^m$. Therefore, $(1-\mathbf{w}_0/\mathbf{v}_{zi})^2(1-(1-\mathcal{R}_{wi})^{2m}) = (1-\mathbf{w}_0/\mathbf{v}_{zi})^2 - 0.0001$. The creation of energy is only significant when the entering wall particle is substantially slower than the core particles, i.e. when $\mathbf{w}_0/\mathbf{v}_{zi}$ is considerably less than 0.99. Consequently it is assumed that $(1-\mathbf{w}_0/\mathbf{v}_{zi})^2 - 0.0001 \approx (1-\mathbf{w}_0/\mathbf{v}_{zi})^2$, giving a simpler general expression for ΔE,

$$\Delta E = \frac{\pi^2 m_{pw} (\mathbf{v}_{zi} - \mathbf{w}_0)^2 (1+e)}{64 (2-\mathcal{R}_{wi})} . \tag{8.102}$$

The rate per unit core-wall interfacial area that wall particles of a specific type (i.e. rebound or streamer) enter the core and interact with a given core fraction i is $Q_w \chi_{wi}/m_{pw}$. Consequently, the production rate P_{kwi} of fluctuating kinetic energy for fraction i per unit interfacial area is

$$P_{kwi} = Q_w \chi_{wi} \frac{\pi^2 (1+e) (\mathbf{v}_{zi} - \mathbf{v}_{zw})^2}{64 (2-\mathcal{R}_{wi})} . \tag{8.103}$$

To further develop the boundary conditions for the riser core, the two different wall processes of particle rebounds and streamer re-entrainment must now each be examined in turn.

8.12.4 Core Particle-Wall Collisions and Rebound Particle Velocities

In this section the collision of core particles with a bare riser wall, and their rebound into the core, are considered. The riser wall may be exposed to core upflow, even at higher G_s, due to transient disruptions to the falling wall streamers (see Chapters 6 and 9). Over the periods when a section of wall is exposed to core flow, some core particles in a CFB pass into the wall

region where dense particle streamers may intermittently cascade downwards. Providing the wall region is relatively thin, these core particles rebound from the wall and re-enter the core upflow. Moreover, at very low particle concentrations or higher gas velocities typical of vertical dilute pneumatic conveying, wall streamers may not be present, except possibly near the solids entry location, and most of the wall is continually exposed to suspension upflow. In this case the "core" coincides with the total cross-section, and the wall region thickness is assumed negligible. The effect of the rebound particles on the core flow is modelled by considering the dynamics of an "average" rebound process. The wall is assumed to be sufficiently "flat" that specular reflection occurs at the wall. The wall collision is assumed at this stage to dominate any other effects on the particle motion, such as lift force, as the particle passes through the wall region. These other effects on particle-wall dynamics are discussed in Chapter 9.

An average wall collision is shown schematically in Figure 8.5. The z axis is in the vertical direction, while the x axis is aligned normal to the wall surface. When the particle hits the wall it loses kinetic energy in the x direction due to inelasticity of the wall collision, and in the y and z directions due to wall friction. On returning to the core flow, the rebounding particles generally have a lower mean vertical velocity than the core particles, and they exert a retarding force on the core suspension, as discussed. Hence the rebounding particles lose fluctuating energy when they hit the wall and cause collisions upon re-entering the core that result in the production of fluctuating energy.

The forces and fluctuating energy reduction associated with a wall collision are estimated assuming that the particles from a given core fraction i, which collide with the wall, have an average pre-collision component of velocity in the x and y directions of magnitude $|\mathbf{W}_+| = |\mathbf{c}_i|/2$ (i.e. $|\mathbf{W}_{+x}| = |\mathbf{W}_+|$ and $|\mathbf{W}_{+y}| = |\mathbf{W}_+|$). The corresponding post-collision components are denoted $\mathbf{W}_{-x}$ and $\mathbf{W}_{-y}$.

If the coefficient of restitution for a wall-particle collision is e_w, the particle x-momentum change due to a wall collision is $m_{pi}(1 + e_w)\mathbf{W}_+$. The x-direction ("normal") force on the particle that causes this change also results in a frictional shear force on the particle in the z

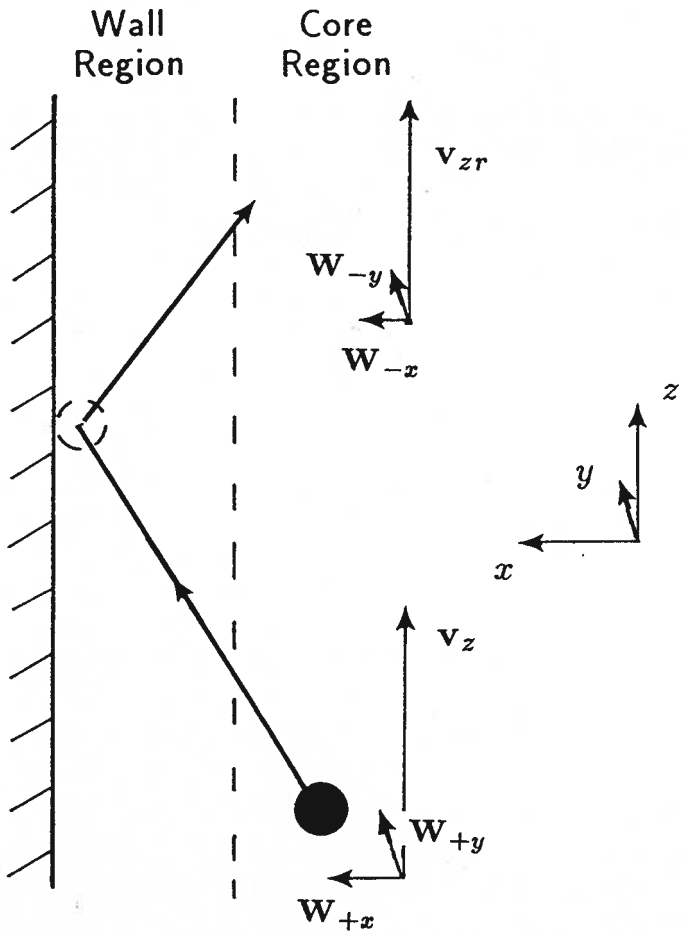

Figure 8.5: Collision of a core particle with the riser wall.

direction. It is assumed that the fast travelling particle generally slides during its brief contact time with the wall. Thus, applying Coulomb's law of friction, the change in z-direction particle momentum due to a wall collision is $-\mu_w m_{pi}(1+e_w)\mathbf{W}_+$, corresponding to a change in axial velocity of

$$\Delta \mathbf{v}_{zi} = -\mu_w(1+e_w)\mathbf{W}_+ \ , \tag{8.104}$$

where μ_w is the coefficient of sliding friction for the particle-wall contact.

The vertical fluctuating component of velocity of a particle is typically at least an order of magnitude smaller than the mean vertical velocity. Thus a reasonable estimate of the vertical velocity of a rebound particle from particle fraction i is $(\mathbf{v}_{zi} - \Delta\mathbf{v}_{zi})$. Furthermore, a mean rebound wall particle may be defined, whereby returning mean-size rebound particles have the same axial momentum as the sum of axial momenta of the rebounding particles from all fractions. Such mean rebound particles exert the same force on the core as exerted by the individual fractions. The average axial velocity of this mean rebound wall particle is

$$\mathbf{v}_{zr} = \frac{\sum Q_{ri}(\mathbf{v}_{zi} - \Delta\mathbf{v}_{zi})}{Q_r} \ , \tag{8.105}$$

where the summation is over all particle fractions, and, hence, $\sum Q_{ri} = Q_r$.

Expressions for d_{pw}, χ_{wi}, $\boldsymbol{\tau}_{wi}$ and P_{kwi} (eqs. (8.88), (8.93), (8.94), (8.103)), were developed earlier that apply to either type of wall particle. Therefore substituting $\mathbf{v}_{zr}$ from eq. (8.105) into these expressions (and replacing generic subscript "w" by subscript "r") gives d_{pr}, χ_{ri}, $\boldsymbol{\tau}_{ri}$ and P_{kr_i}. Thus, the force per unit core-wall area due to returning rebound wall particles on a given core particle fraction A is

$$\boldsymbol{\tau}_{rA} = \chi_{rA}\, Q_r\, (\mathbf{v}_{zr} - \mathbf{v}_{zA}) \ . \tag{8.106}$$

Similarly, the production rate P_{kr_i} of fluctuating kinetic energy in core fraction i per unit interfacial area due to rebound particles is

$$P_{kr_i} = Q_r \chi_{ri} \frac{\pi^2(1+e)\,(\mathbf{v}_{zi} - \mathbf{v}_{zr})^2}{64\,(2-\mathcal{R}_{ri})} \ . \tag{8.107}$$

The number of collisions required to accelerate a rebound particle is given by eq. (8.92), with $\mathbf{v}_{zr} = \mathbf{w}_0$.

In addition to the creation of fluctuating kinetic energy due to collisions on their return to the core, individual rebound particles also lose fluctuating kinetic energy due to the friction and inelasticity of the wall collision. This diminishes the fluctuating components of velocity of the particles returning from the wall to the core.

For a typical wall collision, the magnitudes of the x component of velocity of the rebounding particle before and after the wall collision are $|\mathbf{W}_{+x}| = |\mathbf{W}_+|$ and $|\mathbf{W}_{-x}| = e_w|\mathbf{W}_+|$. Thus the energy change due to the inelasticity of the wall collision is $-m_p(1-e_w^2)\mathbf{W}_+^2/2$. The magnitude of the y component of fluctuating velocity before impact is also assumed to be $|\mathbf{W}_+|$. As $|\mathbf{v}_{zi}| \gg |\mathbf{W}_+|$, the change in this velocity due to friction is $\Delta\mathbf{W}_y \approx \mathbf{W}_+|\Delta\mathbf{v}_{zi}|/|\mathbf{v}_{zi}|$. Generally $\Delta\mathbf{v}_{zi} \ll \mathbf{v}_{zi}$, and hence $\Delta\mathbf{W}_y \ll \mathbf{W}_{+y}$. Thus $(\mathbf{W}_{+y}^2 - \mathbf{W}_{-y}^2) \approx -(2\ |\mathbf{W}_+|\ |\Delta\mathbf{W}_y|)$. This corresponds to a change in energy in the y-direction of $-m_p\mathbf{W}_+^2|\Delta\mathbf{v}_z|/|\mathbf{v}_z| = -m_p\mu_w(1+e_w)|\mathbf{W}_+|^3/|\mathbf{v}_z|$. Although the z fluctuating component of the particle is typically much smaller than the mean velocity, this fluctuating component will also be reduced by friction. The loss in fluctuating energy in the z direction is assumed to be equal to the loss in the y direction. The net change ΔE_r in the energy of a single core particle due to a wall collision is therefore

$$\Delta E_{ri} = \frac{-m_{pi}}{2}(1+e_w)\mathbf{W}_+^2\left[(1-e_w) + \frac{2\mu_w|\mathbf{W}_+|}{|\mathbf{v}_{zi}|}\right] . \tag{8.108}$$

Now the rate at which particles from fraction i rebound from the wall per unit wall-core interfacial area is Q_{ri}/m_{pi}. Consequently, the dissipation of fluctuating kinetic energy in particle fraction i due to direct collisions is

$$D_{kr_i} = \frac{Q_{ri}}{2}(1+e_w)\mathbf{W}_{+i}^2\left[(1-e_w) + \frac{2\mu_w|\mathbf{W}_{+i}|}{|\mathbf{v}_{zi}|}\right] . \tag{8.109}$$

8.12.5 Entry of Wall Streamer Particles into the Riser Core

In pilot-scale risers, average wall streamer downward velocities of O(-1 m/s) are typically measured. It is assumed that wall streamer velocities in commercial-size CFBs are similar in

magnitude. This assumption is discussed later, with the model parametric test results. As already mentioned, it is postulated in this study that an important mechanism by which streamer particles are re-entrained involves the transient disruption of the streamers due to instabilities. When a disruption occurs, the streamers are observed to briefly remain nearly stationary at the wall, whilst particles rapidly entrain into the core. Based on this observation, the simple boundary condition assumed for this model is that the initial vertical velocity of entrained streamer particles, $\mathbf{v}_{zs}$, is zero. Some particles are also likely to be entrained from the interface of the falling wall streamers, though visual observations and empirical modelling work in this study indicate that they may be a minor fraction of the total streamer particle entrainment. (see Chapters 9 and 10). Furthermore the initial vertical velocities of such particles, which may be expected to be similar to wall streamer velocities, are normally almost an order of magnitude less than core particle velocities. Thus the assumption that $\mathbf{v}_{zs} = 0$ is probably reasonable for all streamer particles entering the core, in lieu of a far more detailed analysis of wall streamer dynamics.

From visual observations of local particle re-entrainment from streamer disruptions, it is further assumed that streamer re-entrainment does not discriminate between particle size, and that the composition of particles entering the core is thus the same as that in the streamers from which the particles are drawn. The fraction of particles reaching the streamers from the core that are captured, $(1 - f_w)$, is also assumed to be independent of particle size/density. Although this is a rather crude assumption, there are substantial difficulties in predicting the capture rate of particles by streamers as a function of size and mass, as discussed in Chapter 9.

As for the rebound particles, expressions for d_{ps}, χ_{si}, τ_{si} and P_{ks_i} for streamers are given by eqs. (8.88), (8.93), (8.94) and (8.103), following substitution of $\mathbf{v}_{zs} = 0$ into these expressions and replacement of subscript "w" by subscript "s". The force per unit core-wall area due to entrained wall streamer particles on a given core particle fraction A is

$$\tau_{sA} = -\chi_{sA} Q_s \mathbf{v}_{zA} \,. \tag{8.110}$$

Similarly, the production rate P_{ks_i} of fluctuating kinetic energy in core fraction i per unit

interfacial area due to rebound particles is

$$P_{ks_i} = Q_s \chi_{si} \frac{\pi^2 (1+e) \mathbf{v}_{zi}^2}{64\,(2 - \mathcal{R}_{si})} \,. \tag{8.111}$$

The number of collisions required to accelerate a streamer particle is given by eq. (8.92), with $\mathbf{v}_{zs} = 0$.

The fluctuating kinetic energy associated with the core particles that are captured by wall streamers represents a loss of energy from the core flow. For fully-developed flow, the rate of particles from fraction i captured per unit core-wall region interface is $Q_{si}/m_{pi} = (1 - f_w)Q_{ci}/m_{pi}$. The kinetic energy of each captured particle is $m_{pi}\mathbf{c}_{ki}^2/2$. Thus, for core fraction i, the loss of core fluctuating energy per unit core-wall interfacial area due to streamer capture is

$$D_{ks_i} = Q_{si} \frac{\mathbf{c}_{ki}^2}{2} \,. \tag{8.112}$$

8.13 Riser Core Model Mass, Momenta and Energy Equations

The particle-particle collision and turbulent diffusion model described earlier in this Chapter is a general model for vertical dilute gas-solid suspension flows, that may be extended to two or three dimensions, as mentioned. However, at this stage we limit the model to a one-dimensional form for steady fully-developed flows. This limit is not overly restrictive, as the suspension flow in a riser is generally close to the fully-developed condition over much of the riser height. The boundary conditions just presented are developed specifically to be incorporated into the one-dimensional fully-developed flow model. The model is equally applicable for vertical pneumatic conveying lines, although it is termed a "riser core" model. Note that the core-wall region division applies to solids distribution. Thus, when there are no wall streamers, the wall region thickness is zero and the "core" corresponds to the full riser cross-section.

A basic assumption of the comprehensive riser core model presented in this chapter and of a simpler semi-empirical model described in Chapter 10 is that the convective suspension flow is only in the vertical z direction, and radial gradients in pressure, volume fraction and velocity

are zero across the entire riser core cross section. This riser modelling approach was discussed in Chapter 5. To obtain the model equations in a form suitable for numerical simulation, it is necessary to first integrate the pertinent differential mass, momenta and energy equations over the core cross-sectional area. The shape of the core region cross-section is assumed to be the same as the riser cross-section (i.e. square or circular). Although the objective of the simulations is the prediction of the steady fully-developed flow characteristics, these results are obtained by solution of the steady, developing-flow equations, as described below.

The two-fluid mass and momenta equations presented in Chapter 4 are used to model the flow. For steady one-dimensional flow, the phase k (gas or solid) differential mass balance equation (i.e. continuity equation), eq. (4.21), becomes

$$\frac{d|\epsilon_k \rho_k \mathbf{v}_{zk}|}{dz} = 0 \,, \tag{8.113}$$

where the mass transfer, $\dot{m}_k$, between phases is assumed to be zero, as discussed in Chapter 4. Similarly, the phase k differential momentum equation for steady one-dimensional flow is given by eq. (4.23)[2]:

$$\epsilon_k \rho_k \mathbf{v}_{zk} \frac{d|\mathbf{v}_{zk}|}{dz} = -\,\epsilon_k \frac{dp_k}{dz}\boldsymbol{\delta}_z + \left(\frac{4}{3}\mu_k + \kappa_k\right)\left(\epsilon_k \frac{d^2\mathbf{v}_{zk}}{dz^2} + \frac{d\epsilon_k}{dz}\frac{d\mathbf{v}_{zk}}{dz}\right) + \epsilon_k \rho_k \mathbf{g} + \mathbf{M}^d_{zk} \,. \tag{8.114}$$

Recall that these equations were developed assuming isothermal and incompressible flow of both gas and solid phases. Before integration, several simplifications to the momentum equation are first introduced. It is assumed that the effects of particle viscosity on the acceleration of the particle fractions are negligible in comparison to gravitational, collisional and drag forces. Also the component of particle pressure gradient due to collisions, dp_{ci}/dz, is assumed negligible (i.e. $dp_{pi}/dz = dp_g/dz$) and the gas is assumed to be inviscid. These simplifications are reasonable for steady developing flows, as discussed in Chapter 4. The terms omitted from the momentum equation by these simplifications all include $d\mathbf{v}_{zk}/dz$. For fully-developed flow, this term approaches zero. Thus the proposed simplifications have no effect on the accuracy of the final fully-developed flow predictions.

[2]This is the "Model B" form described in Chapter 4. Due to subsequent simplifications, the initial choice of Model A or B forms does not affect the analysis.

With these simplifications the momentum equation for phase k becomes

$$\epsilon_k \rho_k \mathbf{v}_{zk} \frac{d|\mathbf{v}_{zk}|}{dz} = -\epsilon_k \frac{dp_g}{dz} \boldsymbol{\delta}_z + \epsilon_k \rho_k \mathbf{g} + \mathbf{M}_{zk}^d \,. \tag{8.115}$$

The model differential mass, momentum and particle fraction fluctuating kinetic energy equations, eqs. (8.113), (8.115), and (8.84), are integrated over the riser core cross-section in Appendix D for the general case that the core cross-sectional area, A_{cr}, varies with axial height in the riser.

As mentioned, to solve the model equations for fully-developed flow, the more general developing flow model equations are solved. The solution advances up the riser from an initial assumed condition at $z = 0$, until the suspension flow becomes fully-developed. The developing flow equations used to obtain this final condition are subject to two restrictions: the net mass flux of gas and particles across the core-wall boundary is assumed to be zero, and the core cross-sectional area is assumed to be constant. Both these conditions are consistent with a fully-developed flow, and do not affect the accuracy of the fully-developed flow predictions. (To extend the model to predict actual riser developing flows, these restrictions would have to be relaxed, and a wall region dynamics model introduced to give the independent rate of particle return from streamers into the core.) Subject to these restrictions, the integrated gas phase mass balance, eq. (D.58), in Appendix D simplifies to

$$\frac{d\,|\epsilon_g \mathbf{u}_z|}{dz} = 0 \,. \tag{8.116}$$

Similarly, the integrated mass balance for particle fraction i, eq. (D.59), simplifies to

$$\frac{d\,|\epsilon_{pi} \mathbf{v}_{zi}|}{dz} = 0 \,. \tag{8.117}$$

The integrated gas and particle fraction momentum equations, eqs. (D.66) and (D.67), and integrated particle fluctuating kinetic energy equation, eq. (D.68), are unchanged by the restrictions, and are, respectively:

$$\rho_g \epsilon_g \mathbf{u}_z \frac{d|\mathbf{u}_z|}{dz} = \left[-\epsilon_g \frac{dp_g}{dz} \boldsymbol{\delta}_z + \epsilon_g \rho_g \mathbf{g} + \mathbf{M}_g^d \right] + \frac{\mathcal{P}_{ca}}{A_{cr}} \boldsymbol{\tau}_g \,, \tag{8.118}$$

$$\rho_{pi}\epsilon_{pi}\mathbf{v}_{zi}\frac{d|\mathbf{v}_{zi}|}{dz} = \left[-\epsilon_{pi}\frac{dp_g}{dz}\boldsymbol{\delta}_z + \epsilon_{pi}\rho_{pi}\mathbf{g} + \mathbf{M}_{pi}^d\right] + \frac{\mathcal{P}_{ca}}{A_{cr}}\left[\boldsymbol{\tau}_{ri} + \boldsymbol{\tau}_{si}\right] , \tag{8.119}$$

$$\rho_{pi}\epsilon_{pi}|\mathbf{v}_{zi}|\frac{dK_i}{dz} = \left[P_{kt_i} - D_{kt_i} + \sum_{j=1}^{n}\left(P_{kk_{ij}} + S_{k_{ij}}\right)\right] + \frac{\mathcal{P}_{ca}}{A_{cr}}\left[P_{kr_i} + P_{ks_i} - D_{kr_i} - D_{ks_i}\right] . \tag{8.120}$$

To simplify the numerical solution of the model, three final changes to the momentum equations are introduced. Firstly, the gas inertial term, $\rho_g\epsilon_g\mathbf{u}_z(d|\mathbf{u}_z|/dz)$, is neglected. This is probably reasonable for developing riser core flow equations, as discussed in Chapter 4, and does not affect the fully-developed flow results. Secondly, the gravitational force on the gas, $\epsilon_g\rho_g g$, is assumed negligible in comparison to the drag. This is a standard assumption that is justified by noting that the magnitude of the drag force is comparable to the gravitational force on the solids in suspension, $\epsilon_p\rho_p g$. In turn, $\epsilon_p\rho_p g$ is typically at least an order of magnitude greater than $\epsilon_g\rho_g g$. Finally, the effect that the gas pressure gradient has on the particles in the dilute core suspension is assumed to be negligible, as discussed in Chapter 3. Thus the pressure gradient term is omitted from the particle fraction equations, and the full pressure gradient is transferred to the gas momentum equation. With these assumptions, the final gas and particle fraction momentum equations used in the model simulations are, respectively,

$$\frac{dp_g}{dz}\boldsymbol{\delta}_z = \mathbf{M}_g^d + \frac{\mathcal{P}_{ca}}{A_{cr}}\boldsymbol{\tau}_g , \tag{8.121}$$

and

$$\rho_{pi}\epsilon_{pi}\mathbf{v}_{zi}\frac{d|\mathbf{v}_{zi}|}{dz} = \epsilon_{pi}\rho_{pi}\mathbf{g} + \mathbf{M}_{pi}^d + \frac{\mathcal{P}_{ca}}{A_{cr}}\left[\boldsymbol{\tau}_{ri} + \boldsymbol{\tau}_{si}\right] , \tag{8.122}$$

Note that for fully-developed core suspension flows, ϵ_g is generally greater than 0.98, and the difference between eqs. (8.118) and (8.121) is very small. Even at much lower ϵ_g, in bubbling beds, Bouillard *et al.* (1989) reported that there was little difference between the predictions of a model with ∇p_g solely in the gas momentum equation, and a model with $\epsilon_g\nabla p_g$ in the gas equation and $\epsilon_p\nabla p_g$ in the solids phase equation.

The riser core flow model represents all the effects of the wall layer on the core flow by a set of boundary conditions assumed to act at the core-wall region interface. In lieu of a wall region

dynamic model for streamer formation and motion, the thickness of the wall region, the fraction of the wall covered by wall streamers, and the voidage of the wall streamers are input into the model. These may be determined experimentally, as in Chapter 6, using a capacitance probe. Alternatively, they may be varied until the core pressure gradient matches the experimentally determined pressure gradient. The wall region thickness is defined as the average streamer thickness. The flow of gas in the wall region is assumed to be negligible, and thus the core interstitial gas velocity is:

$$|\mathbf{u}_z| = \frac{U_g A_t}{\epsilon_g A_{cr}} , \tag{8.123}$$

where U_g is the riser superficial gas velocity at the given operating temperature, T_g, and A_t is the total riser cross-section (assumed constant).

Due to their transient motion, portions of the wall streamers occasionally protrude into the core, thereby increasing the shear force on the core gas flow. The gas shear force, τ_g , is approximated in the model by assuming that shear at the core-wall interface on the core gas flow is similar to the shear that would occur with single-phase gas flow through a roughened pipe of cross-sectional area A_{cr}. As the height of the streamer disruptions are likely to be of similar magnitude to the average streamer thickness, the height of the (equivalent sand) roughness elements is crudely estimated by the average thickness of the wall streamers. Although average streamer velocities are of O(-1 m/s), no correction is made for the fact that the streamers are not a static wall because the local protrusions into the core caused by disruptions to the streamers appear to have velocities close to zero, as discussed earlier. If the average streamer thickness is less than the actual wall roughness, the wall roughness is used for calculating the shear. As discussed in Chapter 3, an increase in gas shear is also likely to increase the gas turbulent energy production. This is allowed for in the model in the same manner as described in Chapter 3. Gas frictions factors are predicted by the Blasius equation for smooth pipes, and correlations given by Davies (1972) for roughened pipes.

It is also assumed in the model that the fractional coverage of the riser wall by streamers is equal to the fraction of particles leaving the core that are captured by streamers, $(1 - f_w)$. As

discussed above, not all particles leaving the riser core in the direction of an area of exposed riser wall rebound into the core, as some of these particles are engulfed by falling streamers. Similarly, not all particles that hit the streamer surface are captured. Nevertheless, measured streamer thicknesses are typically relatively thin in the fully-developed flow region and the corresponding streamer voidages are significantly greater than, say, loose-packed bed voidages. Thus, as a first approximation, this assumption may be reasonable. Also, as a streamer is a relatively thin flat layer (i.e. the streamer thickness is at least an order of magnitude less than its width or length), the fraction of the wall region cross-section occupied by streamers may be reasonably estimated by the fractional wall coverage by streamers. Experimental wall streamer data for streamer voidage and thicknesses measured in the cold unit tests are given in Table 8.6 below.

As mentioned, if there are no wall streamers, the wall region thickness is assumed to be negligible, the core boundary becomes the riser wall, and the core cross-section coincides with the total riser cross-section. In this case the riser flow is equivalent to a pneumatically conveyed dilute suspension flow, the core flow does not depend on streamer property model inputs, and the model is fully predictive. Thus detailed pneumatic conveying data may be used to assess the accuracy of the model. Simulations of the data of Nakamura and Capes (1976) are presented in Section 8.15.3 below.

As discussed above, we neglect radial gradients in gas and particle velocities in the core. Furthermore, the change in gas velocity between core and wall regions, which must occur over a layer of finite thickness, is represented by a step change at the core-wall region interface. Suitable boundary conditions, consistent with this representation, have been developed for all of the important effects on the core flow discussed in Chapter 4, except lift force. Lift on a particle depends on the gradient of the gas velocity near the wall or streamer interface, and cannot be modelled with the one-dimensional approach. The effects of lift force near the wall are investigated in Chapter 9. In anticipation of the results of that analysis, it shall be assumed that lift is significant only very close to the wall, and affects whether particles deposit on the wall,

are captured by wall streamers, or rebound back into the core flow. By inputting predetermined fractions of particles that rebound or are captured by streamers, the need to model these lift force effects is circumvented here. The development of the expression for dissipation of particle fluctuating kinetic energy of the rebound particles due to friction and inelasticity of the wall collision, D_{kr}, did not consider the effects of lift or drag in a gas shear layer near the wall. For small particles or low magnitudes of fluctuating velocity, these effects are shown in Chapter 9 to be significant. In the model simulations described later in this chapter, it is assumed that D_{kr} is generally a reasonable estimate of the actual loss of fluctuating kinetic energy of the rebound particles. This assumption is reviewed in Chapter 9. Later simulations show that D_{kr} is always a minor component of the energy balance, and may often be neglected.

As the radial gradient in gas velocity is assumed to be zero *within* the riser core, shear induced lift force is not included in the particle fraction interaction force, $\mathbf{M}_{pi}^{d}$. Thus the two interaction forces on a particle fraction are drag, due to the mean axial gas flow, and the collisional force, due to collisions arising from differences between the mean axial velocities of the particle fractions, i.e.

$$\mathbf{M}_{pi}^{d} = \mathbf{F}_{Dz_i} + \sum_{j=1}^{n} \mathbf{F}_{kz_{ij}} \ , \tag{8.124}$$

Hence, the drag on the gas is

$$\mathbf{M}_{g}^{d} = -\sum_{j=1}^{n} \mathbf{F}_{Dz_j} \ , \tag{8.125}$$

To account for suspension effects not considered for discrete particles, the drag expression for a single particle is multiplied by a correction factor proposed by Foscolo and Gibilaro (1984), and later adjusted by Mastorakos *et al.* (1989) for use with interstitial velocities:

$$\mathbf{F}_{Dz_j} = \frac{\rho_{pi}\epsilon_{pi}\left(\mathbf{u}_z - \mathbf{v}_{zi}\right)}{\tau_{pi}\,\epsilon_g^{1.8}} \ . \tag{8.126}$$

For dilute suspension flow, the correction is small. The same correction is applied for the calculation of $\mathbf{F}_{Dt_j}$.

A summary of all the model equations in their final form is given in Table 8.1. The model consists of $(4n + 3)$ algebraic and differential equations. The equations are written in terms

Table 8.1: Riser core model equations

Mass Balances, eqs. (8.116), (8.117):

Gas	$d\left\|\epsilon_g \mathbf{u}_z\right\| / dz$	$=$	0
Particle fraction	$d\left\|\epsilon_{pi} \mathbf{v}_{zi}\right\| / dz$	$=$	0

Axial Momentum Balances, eqs. (8.121), (8.122), (8.124), (8.125):

Gas	$dp_g/dz\ \boldsymbol{\delta}_z$	$=$	$-\sum_{j=1}^{n} \mathbf{F}_{Dz_j} + \mathcal{P}_{ca} \boldsymbol{\tau}_g / A_{cr}$
Particle fraction	$\rho_{pi}\epsilon_{pi}\mathbf{v}_{zi}\dfrac{d\left\|\mathbf{v}_{zi}\right\|}{dz}$	$=$	$\epsilon_{pi}\rho_{pi}\mathbf{g} + \mathbf{F}_{Dz_i} + \sum_{j=1}^{n} \mathbf{F}_{kz_{ij}} + \dfrac{\mathcal{P}_{ca}}{A_{cr}}\left[\boldsymbol{\tau}_{ri} + \boldsymbol{\tau}_{si}\right]$

Particle Fraction Fluctuating Kinetic Energy Balance, eq. (8.120):

$$\rho_{pi}\epsilon_{pi}\left|\mathbf{v}_{zi}\right|\frac{dK_i}{dz} = \left[P_{kt_i} - D_{kt_i} + \sum_{j=1}^{n}\left(P_{kk_{ij}} + S_{k_{ij}}\right)\right] + \frac{\mathcal{P}_{ca}}{A_{cr}}\left[P_{kr_i} + P_{ks_i} - D_{kr_i} - D_{ks_i}\right]$$

Gas Turbulence-Particle Interaction Equations, eqs. (8.69), (8.59), (8.60):

Gas	$\dfrac{\left\|\mathbf{u}_0'\right\|^3}{1.6\sqrt{3}\, l_e}$	$=$	$\dfrac{\left\|\mathbf{u}_1'\right\|^3}{1.6\sqrt{3}\, l_e} + \dfrac{1}{\rho_g}\displaystyle\sum_{j=1}^{n}\dfrac{\epsilon_{pj}\rho_{pj}\left\|\mathbf{u}_1' - \mathbf{c}_{tj}\right\|\ \left\|\mathbf{c}_{tj}\right\|}{2\left(1-\lambda_{ej}\right)\tau_{pj}}$
Particle fraction	$\dfrac{\epsilon_{pi}\rho_{pi}\mathbf{c}_{ti}}{\tau_{ri}\left[1-\lambda_{ei}\right]}$	$=$	$\mathbf{F}_{Dt_i} + \sum_{j=1}^{n} \mathbf{F}_{kt_{ij}}$

Volume Conservation Equation:

$\epsilon_g + \sum_{j=1}^{n} \epsilon_{pi} = 1$

of $(4n+4)$ constrained variables, $(\epsilon_g \mathbf{u}_z)$, $(\epsilon_{pi}\mathbf{v}_{zi})$, $\mathbf{u}_z$, $\mathbf{v}_{zi}$, K_i, $\mathbf{u}_1'$, and $\mathbf{c}_{ti}$. One of the volume fractions may be defined in terms of the other volume fractions by use of the volume conservation equation, also shown in Table 8.1. Hence there are $(4n+3)$ independent variables in the model, and the model is fully determined.

8.14 Riser Core Flow Model Solution — Program CIRCOR

In this section the numerical methods used to solve the core riser model equations are outlined. The model is solved by the FORTRAN program, CIRCOR. Program documentation, sample input files, and full listing of the FORTRAN code are given in Appendix E. The basic steps of the program CIRCOR are performed by various FORTRAN subroutines given in Appendix E, as well as by the main program. The program has a modular structure. Many of the subroutines perform general functions, and are also used in other models, such as the model WALSTF, described in Chapter 9. The documentation in Appendix E describes which routines are needed to execute a particular model, and the preamble to each routine provides a description of its functions. The names of the subroutines that perform each step in the solution algorithm below are listed on the same line as the step number.

The program is capable of handling two types of particles (type "1" and type "2"), as well as multiple fractions of each type. For example, the behaviour of a mixture of various sizes of CFB combustor inert (sand/ash) and coal particles may be simulated.

8.14.1 Solution Algorithm

Step 1 DATIN, ERINIT

The input riser geometry, particle properties and operating condition data are read in. Included in the input are the following constants used in the discussion below: gas superficial velocity, U_g; solids circulation rate, G_s; wall streamer velocity, $\mathbf{v}_d$; wall streamer voidage, ϵ_{gd}; fractional wall coverage by wall streamers, $(1-f_w)$; core cross-sectional area, A_{cr}; and riser cross-sectional area, A_t. Error flags are all set to "no error" status.

Step 2 AIRPRO

Gas density and shear viscosity are calculated, based on the riser mean temperature.

Step 3 FEDSIZ, CIRCOR

The input PSD sieve data (or equivalent) for the type 1 particles is converted to a cumulative mass distribution. The distribution is then divided into n_1 fractions of equal weight %, and the mean particle diameters of each of these fractions are calculated. If type 2 particles are to be included in the calculation ($n_2 > 0$), the same procedure is performed for these particles. The overall weight ratio of type 1 to type 2 particles in the mixture is an input to the model. The default assumption that the particle PSD for a given particle type is to be divided into equal mass fractions may be overwritten in CIRCOR. Similarly, the size of a given fraction may be overwitten (see instructions in CIRCOR listing, in Appendix E). The weight fraction, X_i, of each particle fraction in the total initial or "feed" particle mixture is calculated.

Step 4 ICONDS

The values of the independent variables are initialised. A value of 0.98 is assumed for the core voidage, ϵ_g. Using this value, the core interstitial gas velocity, $\mathbf{u}_z$, may be calculated by eq. (8.123). The initial weight fractions of the particle fractions in the core and streamers are set equal to those calculated in *Step 3*, and all particle fractions are assumed to have the same initial core axial velocity, $\mathbf{v}_{zi}$. (It is assumed that the PSD data are obtained from a sample representative of the whole bed, such as a standpipe sample.) The mass flux of particles in dilute suspension in the thin wall region may be neglected in comparison to the mass flux of dense streamers in this region, and the upward flux of particles in the much larger core region. Therefore, by mass balance, the initial axial velocity is $\mathbf{v}_{zi} = (G_s A_t / A_{cr} \epsilon_p \overline{\rho_p}) - (\epsilon_{gd} \mathbf{v}_d (1 - f_w)(A_t - A_{cr})/A_{cr})$, where $\epsilon_p = (1 - \epsilon_g)$, and $\overline{\rho_p}$ is a average particle density based on the relative proportions of type 1 and 2 particles. The initial values of particle fraction fluctuating energies, K_i, are set to small, but non-zero, values. The choice of these values is arbitrary, providing they are physically feasible, i.e. non-negative. Small positive initial K_i values reduce computational time in the initial stages of the calculation. The initial absolute gas pressure is

set to standard atmospheric pressure.

Step 5 CIRCOR

The riser height to which the solution has advanced, z, is set to the initial height, $z_1 = 0$. Accuracy and step size parameters for the solution of the differential equations are set. A "macro" incremental height, $\Delta z = 0.2$ m, is assumed for interim reporting of the solution as it advances upwards.

Step 6 ODERKF, FHLBRG

The model differential equation (D.E.) solver takes a "micro" step in height from z to $z + \delta z$, commensurate with the accuracy and step size parameters.

Step 7 SYSTEQ

The process involving the evaluation of the r.h.s. of the differential equations at $z + \delta z$ for the values of variables, $(\epsilon_g \mathbf{u}_z)$, $(\epsilon_{pi} \mathbf{v}_{zi})$, $\mathbf{u}_z$, $\mathbf{v}_{zi}$, K_i, $\mathbf{u}_1'$, and $\mathbf{c}_{ti}$ supplied by the D.E. solver begins. "First guess" values for the particle-laden gas turbulence intensity, $\mathbf{u}_1'$, and particle fraction eddy drift velocities, $\mathbf{c}_{ti}$ are assumed first time (when $z = 0$) or set to the values obtained at the old height, z, in subsequent calculations.

Step 8 SYSTEQ, GASTUR

The constant particle-free gas turbulence properties are calculated.

Step 9 PARTUR, DRAGON, DYNCOL, DGAUSS

The $(n + 1)$ algebraic turbulence interaction equations are solved by Newton's method, to obtain the values for $\mathbf{u}_1'$ and $\mathbf{c}_{ti}$, corresponding to height $z + \delta z$. The solution method is iterative. The Newton's method augmented Jacobian matrix for the algebraic equations is repeatedly assembled in PARTUR, and solved by Gauss elimination in DGAUSS. Drag and collision forces, and terms in derivatives of expressions for these forces, are also repeatedly calculated in DRAGON and DYNCOL. Convergence is tested for in PARTUR. (A more detailed description of the application of Newton's method, including some necessary simplifications, is given in Appendix D).

Step 10 DYNCOL, PARTUR

The fluctuating kinetic energy balance terms due to particle collisions and turbulence, P_{kk}, S_k, P_{kt} and D_{kt} are evaluated at $z + \delta z$.

Step 11 WALCON

The shear and fluctuating kinetic energy balance terms due to wall rebound and streamer particles, τ_r , τ_s , P_{kr}, P_{ks}, D_{kr} and D_{ks} are evaluated at $z + \delta z$.

Step 12 SYSTEQ

The r.h.s. values for the model D.E.s are assembled for the D.E. solver. Each time the solution advances a distance Δz up the riser from z_1, the full details of the model solution at that height are reported.

Step 13 ODERKF, FHLBRG

If the solution accuracy criteria are satisfied, then $z_{new} = z_{old} + \delta z$, and the solution advances. Otherwise, δz is reduced. If the solution has not advanced to $z_1 + \Delta z$, then *Steps 6–12* are repeated.

Step 14 CIRCOR, ERCHEK

The starting height for the next "macro" integration step is set; i.e. $z = z_{1,new} = z_{1,old} + \Delta z$. *Steps 6–13* are repeated until the solution has advanced up the riser to some final limiting height. (This height is set at 4.0 m in the CIRCOR code version in Appendix E.) If minor problems were detected during the calculation process, these are reported.

8.14.2 Program Development and Execution

The program CIRCOR and its auxiliary subroutines are written in standard, portable FORTRAN 77. The program has run on an IBM 3081/63 (under MTS) and an IBM 3090 (under AIX/370). The logical input/output unit assignments are described in Appendix E.

The most numerically intensive operation in the program is the solution of the algebraic equations for the gas-particle turbulence properties, which is repeated for every integration step up the riser. As mentioned above, and detailed in Appendix E, Newton's iterative method was used to solve these non-linear equations. The solution is supervised by the routine PARTUR. No

convergence problems have been experienced with this method. A "first guess" estimate of the gas-particle turbulence properties is required for the Newton's method solution. If this guess is not close to the solution for the first call of PARTUR, up to $O(100)$ iterations may be required for convergence within 1% tolerance. For subsequent calls, gas-particle turbulence properties saved from prior solutions are used as starting guesses, and convergence typically occurs within 8 iterations. In an earlier version of CIRCOR, a Gauss-Seidel method was used to solve the non-linear equations. This method resulted in computation times of $O(4)$ greater than those for the Newton's method solution, and occasional convergence problems were experienced.

The differential equations are solved by a Runge-Kutta Fehlberg method, that compares 4th and 5th order Runge-Kutta solutions to estimate the accuracy of the numerical integration and control error. This is a standard numerical technique (Carnahan *et al.*, 1969; Bowen, 1988). When the initial starting estimate of the voidage for the fully-developed flow solution was set to a level significantly less than the final solution value (e.g. $\epsilon_g = 0.9$ at $z = 0$), occasional problems were encountered with the Runge-Kutta Fehlberg method, due to the stiffness of the equations in the initial stages of solution. Although this problem could be easily overcome by using a D.E. solver for stiff equations (e.g. "LSODE," Hindmarsh, 1983), it is computationally less expensive to simply re-run the problem with a more realistic starting value for ϵ_g. For starting values of $\epsilon_g = 0.98$, the Runge-Kutta method has performed reliably. The current version of the CIRCOR program calculates the solution from zero height up to a height of 4.0 m. Fully-developed flows are generally predicted after the solution has advanced 1.5 m, and have always been achieved within 4.0 m. A possible improvement to reduce computation time was investigated by including test criteria for the fully-developed flow condition, and halting the solution once fully-developed flow was achieved. However, this had little effect on execution time, as most of the program computation was devoted to calculations in the initial heights where the flow was developing.

The program has been written with error checking and diagnostic capabilities. The current

version has relatively few checks that test for possible problems in execution. Two error severities are allowed for. If a minor error occurs, the program execution continues, and a warning message is written at the end of the execution. For a major error, the program stops, and the error message is printed. The inclusion of checks for "bad" or unreasonable input data is a straightforward task, that would be required should the program be run by users not fully familiar with the model and typical CFB terms.

The program can calculate riser core dynamics for square or circular riser cross-sections. The gas turbulence may be "turned off" by changing the value of an integer flag in routine PARTUR. When the turbulence is set to zero, the solution of the algebraic gas-particle turbulence equations is not required, and program execution is considerably faster. For mixtures of large particles that are not affected by the turbulence, this is a useful time-saving feature. CIRCOR has been run successfully with as many as 40 particle size fractions.

8.15 Riser Core Model Simulations

Several simulations of experimental data and a number of parametric studies were undertaken to evaluate the model CIRCOR, and investigate possible interesting scale-up and particle property effects. Both the cold unit PSD tests, described in Chapter 6, and the binary particle mixture pneumatic conveying tests of Nakamura and Capes (1976) were simulated to evaluate the model. As CIRCOR is fully predictive for pneumatic conveying conditions (i.e. no wall streamer properties to be measured or assumed), simulation of these data provide a good validation test for the model. The simulation of the cold unit tests, using measured streamer properties, provides additional insight into the trends observed in these tests, that could not be adequately explained by simpler intuitive argument.

The simplest test for the particle fluctuating kinetic energy balance of the model would be to compare model predictions with measured particle fluctuating velocities in typical riser operations. Unfortunately, the few published results of direct measurements of particle fluctuating velocities in vertical suspension flows have been performed in small bench-scale units and at

solids circulations and suspension densities significantly lower than those typical of CFB riser operations. At this stage, indirect, less precise, and less satisfactory means must be found to evaluate this component of the model. For example, a significant force on the riser core flow that directly influences the core gas pressure gradient in a pilot-scale unit is the shear force due to re-entraining streamer particles (see Chapter 4). In fully-developed suspension flows, the lateral flux of core particles due to collisions and turbulence equals the flux of particles back into the core of rebounding particles and particles entrained from wall streamers. Thus, the predicted pressure gradient in the core is a function of the magnitude of the core particle fluctuating velocities. If the model is run with known streamer properties, and predicts core pressure gradients that are similar to the measured values, then it may be deduced that the predicted fluctuating particle velocities are reasonable. Based on this approach, predicted pressure gradients are compared with measured values for both experiments of Nakamura and Capes and the cold unit tests performed in this work.

The model results reported below are divided into four sections. Firstly the model output for a typical pilot-scale CFB operation at ambient temperature is explained, and the importance of the various influences on particle motion is considered. The model simulations of the data of Nakamura and Capes, and the cold unit test results are presented in the following sections. Finally, the parametric test results are discussed. In particular, the effects of riser diameter, particle size distribution, particle coefficient of restitution and gas temperature are examined.

8.15.1 Interpretation of the CIRCOR Model Output

The output from the model CIRCOR is divided into two sections. In section "A" the input riser geometry, operating conditions, and general particle properties are restated. In section "B" the model predictions for fully-developed flow in the riser core are given. Examples of the section A and B outputs are given in Tables 8.2 and 8.4, respectively, for a riser with a circular cross-section and 0.15 m diameter. The definitions of most of the symbols in the model output are obvious, e.g. `TAUP` $= \tau_p$, `EG` $= \epsilon_g$, etc.. A full list of the definitions of these model output

Table 8.2: Sample output from model CIRCOR: Operating conditions and particle properties.

```
CIRCULATING FLUIDISED BED RISER CORE MODEL - CIRCOR
---------------------------------------------------
SECTION A: INPUT; OPERATING CONDITIONS
--------------------------------------
RISER DIAMETER                    0.152  M       PARTICLE PROPERTY              TYPE 1  TYPE 2
RISER CROSS SECTION            CIRCULAR          DENSITY (KG/M3)                2700.   1400.
WALL ROUGHNESS                      2.5  MM      PARTICLE COEFF. RESTITUTION     0.90    0.70
NET SOLIDS CIRCULATION RATE         60.  KG/M2.S PARTICLE-WALL COEFF. REST.      0.58    0.58
GAS TEMPERATURE                    298.  K       SPHERICITY                      0.95    0.75
GAS PRESSURE                    101325.  PA      WALL COEFF. SLIDING FRICTION    0.80    0.75
GAS VISCOSITY                 0.18E-04  KG/M.S
GAS DENSITY                      1.187  KG/M3
STREAMER FRACTIONAL WALL COVERAGE 0.40
WALL REGION THICKNESS             5.00  MM
```

symbols is given in Table 8.3.

The operating conditions for the model run results given in Tables 8.2 and 8.4 are T_g = 25 °C, U_g = 7.0 m/s, and G_s = 60 kg/m^2 s. A streamer wall fractional coverage of 0.4 and wall region thickness of 5 mm has been assumed. The particles are a mixture of 95 wt% type 1 particles, with a density typical of sand or ash particles, and 5 wt% type 2 particles, with a density typical of coal. This mixture was chosen to demonstrate the importance of allowing for particle collisions when predicting the motion of a relatively small fraction of reactive particles that have sizes and/or densities very different from the mixture average. The particle densities and size distributions in this example are typical of particles present in a CFB combustor burning an anthracite. Particle-particle and particle-wall coefficients of restitution, and particle-wall coefficients of sliding friction are consistent with published values for these particle types (Goldsmith, 1960; Brown and Richards, 1970; Nakamura and Capes, 1976).

The initial type 1 particle PSD has been divided into five particle fractions of equal wt% (see "FEED"). The initial 5 wt% of type 2 particles has been further divided into fractions of 1.25, 2.5, and 1.25 wt%, with mean sizes of 40 μm, 250 μm and 2000 μm, respectively. Based on the assumed wall region thickness, the core superficial gas velocity is 8.02 m/s.

The first block of data in Table 8.4 details the gas mean flow and turbulence properties. For gas flow without particles in the core (but with a roughened "wall" due to the wall region), the

Table 8.3: Symbol definitions for a standard CIRCOR model output. (Symbols listed in the order they appear in the output.)

UOC	UZC	UPF	UPL	TAUGF	TAUGL	EG	PG	XP	RHOP	VZC
U_{0cr}	$\mathbf{u}_z$	$\mathbf{u}_0'$	$\mathbf{u}_1'$	τ_{e0}	τ_{e1}	ϵ_g	p_g	d_{pi}	ρ_{pi}	$\mathbf{v}_{zi}$
TAUP	TAUR	EP	CT	FDT	FKT	PKK	SK	PKT	DKT	PKS
τ_{pi}	τ_{ri}	ϵ_{pi}	$\mathbf{c}_{ti}$	$\mathbf{F}_{Dt_i}$	$\mathbf{F}_{kt_i}$	P_{kk_i}	S_{k_i}	P_{kt_i}	D_{kt_i}	P_{ks_i}
PKR	DKR	DKS	PW/AC	CK	FKZ	FDZ	SFS	SFR	GRF	FDGAS
P_{kr_i}	D_{kr_i}	D_{ks_i}	$\mathcal{P}_{ca}/A_{cr}$	$\mathbf{c}_{ki}$	$\mathbf{F}_{kz_i}$	$\mathbf{F}_{Dz_i}$	$\boldsymbol{\tau}_{si}$	$\boldsymbol{\tau}_{ri}$	$\epsilon_{pi}\rho_{pi}\mathbf{g}$	$\mathbf{F}_{Dz}$
SFGC	SFSCT	SFRCT	RHOPA	RHOPT	CKT	Z1T	Z2T	VWK	FPATH	
$\boldsymbol{\tau}_g$	$\boldsymbol{\tau}_s$	$\boldsymbol{\tau}_r$	ρ_{sa}	$\rho_{s_{cr}}$	$\mathbf{c}_i$	$\sum_j Z'_{i(j)}$	$\sum_j Z''_{i(j)}$	λ_i	Λ_i	

FEED = Input mass fraction of particles, X_i (e.g. fractions in standpipe)
CORE = Core mass fraction of particles for fully-developed flow, $x_i = \epsilon_{pi}\rho_{pi}/(\sum_i \epsilon_{pi}\rho_{pi})$
WALL = Mass fraction based on flux to wall, $Q_{ci}/\sum_i Q_{ci}$

predicted turbulence intensity, $\mathbf{u}_0' = 0.94$ m/s. The reduction in intensity of this turbulence due to modulation by the particles is 25% (i.e. $100\,[1-(.81/.935)^2]$). The particle laden energetic eddy decay time is $\tau_{e1} = 0.055$ s. The predicted responses of the particles to the turbulence are given in the next block. For all the particles, except for the 40 μm type 2 particles, crossing trajectory effects are significant, i.e. $\tau_r \ll \tau_{e1}$. These particles exhibit type 3 motion (Chapter 3), and respond very little to the turbulence.

In contrast, the 40 μm particles respond significantly to the turbulence ($\mathbf{c}_t/\mathbf{u}_1' = 0.39/0.81$). However, the response of these particles in the particle mixture is very different from that which would occur were these particles alone in the riser gas flow. As discrete particles, the slip velocity would be $O(0.1$ m/s), and they would closely follow the local gas flow ($\tau_p \ll \tau_{e1}$). In the particle mixture their vertical motion is retarded by collisions with larger particles, and, in this case, the mean slip velocity is 1.2 m/s. Although crossing trajectory effects significantly reduce the interaction time, τ_r, the 40 μm particles still have adequate time to respond fully to

Table 8.4: Sample output from model CIRCOR: Fully-developed flow solution. (See Table 8.3 for symbol definitions.)

```
CIRCULATING FLUIDISED BED RISER CORE MODEL - CIRCOR
---------------------------------------------------
SECTION B: RESULTS
------------------
GAS FLOW AND TURBULENCE
    UOC    UZC    UPF    UPL   TAUGF  TAUGL   EG    PG
    M/S    M/S    M/S    M/S     S      S     --    PA
   8.019  8.074  0.935  0.810  0.048  0.055  0.993  101325.

PARTICLE-TURBULENCE INTERACTION
  XP   RHOP    VZC   TAUP   TAUR    EP       CT       FDT      FKT
  UM   KG/M3   M/S   S      S       --       M/S      N/M3     N/M3
  133. 2700.  5.407  0.063  0.006  0.00122  0.0355   41.1825  -2.6195
  188. 2700.  5.289  0.106  0.006  0.00124  0.0237   25.2369   2.1189
  219. 2700.  5.241  0.134  0.006  0.00126  0.0198   20.2498   3.1122
  259. 2700.  5.191  0.172  0.006  0.00127  0.0162   16.0319   3.6290
  343. 2700.  5.111  0.259  0.005  0.00129  0.0115   10.8767   3.6760
   40. 1400.  6.861  0.004  0.013  0.00012  0.3920   16.8660  -9.8581
  250. 1400.  5.350  0.072  0.006  0.00031  0.0317    4.8088  -0.1422
 2000. 1400.  4.772  0.636  0.005  0.00018  0.0040    0.3144   0.0836

PARTICLE FLUCTUATING ENERGY BALANCE
(i) PKK   (ii) SK    (iii)PKT   (iv) DKT   (v) PKS    (vi) PKR   (vii) DKR   (viii)DKS   SUM (i
  KG/MS3    KG/MS3     KG/MS3     KG/MS3    *PW/AC     *PW/AC     *PW/AC      *PW/AC     to viii)
                                            KG/MS3     KG/MS3     KG/MS3      KG/MS3      KG/MS3
 0.63E+01   0.57E+02   0.14E+01  -0.95E+02  0.44E+02   0.12E+01  -0.37E+01  -0.11E+02  -0.13E-04
 0.15E+01  -0.15E+02   0.65E+00  -0.34E+02  0.53E+02   0.85E+00  -0.15E+01  -0.53E+01  -0.67E-05
 0.84E+00  -0.31E+02   0.46E+00  -0.22E+02  0.56E+02   0.71E+00  -0.10E+01  -0.38E+01  -0.51E-05
 0.59E+00  -0.41E+02   0.32E+00  -0.14E+02  0.57E+02   0.56E+00  -0.75E+00  -0.28E+01  -0.39E-05
 0.47E+00  -0.45E+02   0.17E+00  -0.74E+01  0.54E+02   0.31E+00  -0.49E+00  -0.20E+01  -0.29E-05
 0.28E+02   0.24E+01   0.20E+01  -0.35E+02  0.22E+01   0.79E+00  -0.71E-01  -0.22E+00   0.14E-06
 0.31E+00  -0.28E+01   0.15E+00  -0.52E+01  0.80E+01   0.17E+00  -0.14E+00  -0.48E+00  -0.65E-06
 0.95E-03  -0.51E+00   0.16E-02  -0.12E+00  0.70E+00   0.24E-05  -0.15E-01  -0.58E-01   0.77E-07

PARTICLE AXIAL MOMENTUM BALANCE
  VZC     CK        FKZ       FDZ       SFS       SFR      GRF      SUM
                                        *PW/AC    *PW/AC
  M/S     M/S       N/M3      N/M3      N/M3      N/M3     N/M3     N/M3
  5.4073 1.3459   -50.265   141.766   -48.626   -10.620 -32.255  -0.000
  5.2890 1.0376     3.773    89.369   -51.906    -8.260 -32.976  -0.000
  5.2409 0.9291    19.228    72.584   -51.490    -7.043 -33.279  -0.000
  5.1915 0.8390    30.535    58.206   -49.454    -5.691 -33.596  -0.000
  5.1105 0.7398    40.185    40.359   -42.880    -3.536 -34.128  -0.000
  6.8605 0.9420   -42.281    48.944    -2.291    -2.699  -1.673  -0.000
  5.3504 0.9200    -2.874    16.824    -8.124    -1.537  -4.289  -0.000
  4.7723 0.5514     1.698     1.288    -0.581    -0.000  -2.404  -0.000

GAS FORCE BALANCE, PARTICLE AND GAS WALL SHEAR, SUSPENSION DENSITY
      FDGAS     SFGC      SFSCT     SFRCT     RHOPA     RHOPT
      N/M3      N/M3      N/M3      N/M3      KG/M3     KG/M3
    -469.340  -15.218  -255.353  -39.386   49.3943   17.7982

PARTICLE COLLISION FREQUENCY, MEAN FREE PATHS AND MASS FRACTIONS
  XP      CKT       Z1T       Z2T       FPATH    VWK     FEED    CORE    WALL
  UM      M/S       1/S       1/S       MM       --      WT%     WT%     WT%
  133.   1.3463   216.069   208.767   3.1691   0.5000  19.00   18.47   25.70
  188.   1.0379   384.112   264.227   1.6008   0.5000  19.00   18.89   20.25
  219.   0.9293   494.712   298.303   1.1719   0.5000  19.00   19.06   18.30
  259.   0.8392   652.067   346.126   0.8407   0.5000  19.00   19.24   16.68
  343.   0.7399  1060.657   463.586   0.4854   0.5000  19.00   19.55   14.94
   40.   1.0203   121.005    26.653   6.9098   0.3483   1.25    0.96    1.01
  250.   0.9206   603.312   375.793   0.9402   0.5000   2.50    2.46    2.34
 2000.   0.5514 31926.485  6012.683   0.0145   0.5000   1.25    1.38    0.78
```

gas eddies. However, the motion of these particles in the gas eddy flow direction is also limited by collisions with larger particles that respond more slowly to the eddy gas velocity. Thus these particles exhibit only *partial* response to the gas turbulence, a phenomenon that could not be predicted from single particle fraction models.

Similarly, the effect of collisions on the large 2000 μm type 2 particles is profound. The terminal settling velocity of a particle of this size and density is in excess of the interstitial gas velocity in the riser core, and drag, alone, could not upwardly convey such a particle. However, due to collisional force, the steady upward velocity in fully-developed flow is 4.8 m/s for this example, approximately 0.5 m/s less than the mean-size particle axial velocity.

The next block of data contains all the terms in the particle fluctuating kinetic energy balance. The terms describing energy gain/loss due to boundary conditions have been multiplied by $\mathcal{P}_{ca}/A_{cr}$, so that they are in the same units as the other terms, i.e. per unit volume of core suspension. Thus the relative importance of the various energy gain/loss processes may be established by comparing the magnitude of the respective terms in the output. For the sample output in Table 8.4, the dominant energy creation process in the core is the effect of entering wall streamer particles (P_{ks}). This is a general result for pilot-scale risers, *providing* wall streamers are present. In this case, the production of kinetic energy due to turbulence, P_{kt}, and type (i) particle collisions, P_{kk}, is minor for small particles, and negligible for the larger particles. Both P_{kk} and P_{kt} are predicted to become more significant with an increase in riser diameter, to the extent that they may dominate P_{ks} in commercial-size risers, as discussed later. The transfer of energy due to type (ii) collisions, S_k, is generally from the larger to the smaller size fraction particles. Kinetic energy reduction is predominantly due to drag (D_{kt}), and type (ii) collisions (S_k), when these collisions are inelastic. Wall rebound effects are secondary, but not negligible, providing some of the riser wall is exposed for such collisions.

A compilation of the magnitude of the forces in the axial momentum equation, given in Table 8.4, indicates that all forces are significant. The collisional force, on the small and large particle fractions is of similar magnitude to the gravitational force on the particles in these

fractions. The magnitude of the collisional fluctuating velocities varies from $O(1.0$ m/s) for the smaller particles, to $O(0.7$ m/s) for the larger particles. Clearly, these results are not consistent with the kinetic theory principle of equipartition of energy, discussed earlier.

The "gas force balance" results show that drag is the dominant force on the gas. The gas shear contribution to the gas pressure gradient is only 3% (100% $\times$15/470). The core gas pressure gradient, given as the equivalent apparent suspension density, ρ_{sa}, is 49 kg/m^3. The true core suspension density, ρ_s, is 18 kg/m^3. The total shear force on the core particles due to re-entering wall particles ($\tau_r + \tau_s$) is significant, as it is of a similar order of magnitude to the total core drag.

In the final block of data in Table 8.4, the total fluctuating velocities of the particles, $\mathbf{c}$, are given. There is little difference between $\mathbf{c}$ and the corresponding $\mathbf{c}_k$ values given earlier in the table, even for the 40 μm type 2 particle fraction. Although the 40 μm particle fraction partially responds to the turbulent gas velocity fluctuations, both the direct ($\mathbf{c}_t$) and indirect (P_{kt}) contributions to total fluctuating velocity for this fraction are small. Hence the effects of turbulence on particle fluctuating motion are minor in this example. Examples where gas turbulence significantly influences fluctuations of all particle fractions are presented later.

The mean free path, Λ_i, of the particles in a given fraction is based on the total fluctuating velocity and collision frequency, i.e. $\Lambda_i = \mathbf{c}_i / \sum_j (Z'_{i(j)} + Z''_{i(j)})$. Note that the predicted mean free paths of the particles in Table 8.4 are of similar magnitude to the expected gas wall layer thicknesses for pilot-scale units discussed in Chapter 3. The values of Λ in Table 8.4 are also typical of Λ in CFB combustors. At lower suspension densities, when wall streamers are first experimentally observed, the predicted particle mean free paths are generally of magnitude similar to, or greater than, the estimated gas wall layer thicknesses. The implications of this observation are discussed in Chapter 9.

The particle mass fraction data in the output (i.e. terms `FEED`, `CORE`, and `WALL`) refer, respectively, to the relative masses of a given fraction in the initial "feed" (e.g. standpipe), X_i, in the core at fully-developed flow conditions, x_i, and in the lateral flux of particles into

Table 8.5: Comparison of CIRCOR model results for: (i) $G_s = 20$ kg/m^{2}s, no wall coverage by streamers, and (ii) $G_s = 60$ kg/m^{2}s, 40% wall coverage by streamers.

Particle Fraction			Case (i) $G_s = 20$ kg/m^{2}s, $(1 - f_w) = 0.0$				Case (ii) $G_s = 60$ kg/m^{2}s, $(1 - f_w) = 0.4$			
$\rho_{p1} = 2700$ kg/m^3			$\mathbf{u}_z = 7.0$ m/s; $\mathbf{u}_0' = 0.73$ m/s				$\mathbf{u}_z = 8.1$ m/s; $\mathbf{u}_0' = 0.94$ m/s			
$\rho_{p2} = 1400$ kg/m^3			$\mathbf{u}_1' = 0.71$ m/s; $\epsilon_g = 0.999$				$\mathbf{u}_1' = 0.81$ m/s; $\epsilon_g = 0.993$			
d_p	type	X	$\mathbf{v}_z$	$\mathbf{c}_k$	$\mathbf{c}$	Λ	$\mathbf{v}_z$	$\mathbf{c}_k$	$\mathbf{c}$	Λ
(μm)	(–)	(wt%)	(m/s)	(m/s)	(m/s)	(mm)	(m/s)	(m/s)	(m/s)	(mm)
133	1	19.0	5.77	0.36	0.37	10.6	5.41	1.35	1.35	3.2
188	1	19.0	5.54	0.25	0.25	4.1	5.29	1.04	1.04	1.6
219	1	19.0	5.43	0.21	0.21	2.6	5.24	0.93	0.93	1.2
259	1	19.0	5.30	0.19	0.19	1.7	5.19	0.84	0.84	0.8
343	1	19.0	5.11	0.22	0.22	1.1	5.11	0.74	0.74	0.5
40	2	1.25	6.78	0.30	0.67	31.9	6.86	0.94	1.02	6.9
250	2	2.50	5.67	0.29	0.29	3.1	5.35	0.92	0.92	0.9
2000	2	1.25	4.30	0.44	0.44	0.1	4.77	0.55	0.55	0.01
Conditions common to both cases: $D = 0.15$ m; $T_g = 25$ °C; $U_g = 7.0$ m/s. For full input conditions, see Table 8.2 and Appendix F.										

the wall region, $Q_{ci}/\sum Q_{ci}$. For this case, there is little difference between the core and feed weight fractions. Proportionally, slightly more smaller than larger particles are predicted to transfer into the wall region. (However, in reality it is more likely that the larger particles will be successfully captured by streamers, as discussed in Chapter 9.)

The results in Tables 8.2 and 8.4 illustrate many of the features of the model. However, it is important to note that the number of parameters that are predicted by CIRCOR to significantly affect riser core dynamics is large, and few unqualified general conclusions are possible. The simulation just described was repeated for $G_s = 20$ kg/m^{2}s and no wall streamers. All other input variables were unchanged. The full output for this run is given in Appendix F. Selected data for both runs are summarised in Table 8.5. Based on the cold unit tests, in which particle properties and operating conditions were similar, the fractional wall coverages assumed for the two runs are likely to be reasonable estimates.

The general trends evident in Table 8.5 are all consistent with the model concepts. At the lower G_s (case (i)), the voidage is higher, and there is less modulation of the gas turbulence

intensity. The fluctuating particle velocities are lower, and the spread in axial particle velocities about the mean increases, as the suspension becomes more dilute, and collision frequencies reduce. Note that the core interstitial gas velocity, $\mathbf{u}_z$, is significantly higher than U_g for $G_s = 60$ kg/m^{2}s because of a 5 mm thick wall region, and consequent reduction in core area. The mean slip velocity of the particles increases from $O(1.5$ m/s) to $O(2.5$ m/s) with the increase in G_s, due to the shear force exerted by entrained streamer particles at the higher G_s.

A greater effect on the fluctuating velocities of the small particles, in comparison to the larger particles, is predicted as the solids circulation is increased from $G_s = 20$ to $G_s = 60$ kg/m^{2}s. This occurs because of the significant influence of entraining wall streamer particles on core motion in case (ii). The smaller particles gain more fluctuating kinetic energy from collisions with streamer particles because they travel faster than the larger core particles. Note, that at $G_s = 20$ kg/m^{2}s, and in the absence of streamers, the larger particles are predicted to have slightly higher fluctuating velocities than particles of average size. Also, for case (i), gas turbulence is predicted to make a significant contribution to the total fluctuating velocity of particles in the 40 μm size fraction. The predicted mean free paths of average size particles in case (i) are of $O(3$ mm), and much greater than this for the smaller particles.

The full case (i) results given in Appendix F (Output "(a)") show that the velocity weighting factor, λ, for both the 133 and 40 μm particles falls below the "large" particle value of 0.5. In fact, $\lambda = 0.1$ for 40 μm particles, and particles of this size are predicted to rapidly approach a slip velocity equal to their terminal settling velocity after each collision. The significant change in velocity between collisions for these particles is contrary to the assumptions of granular kinetic theory, discussed in Chapter 4.

The model CIRCOR was run with a number of different size fractions to establish how many fractions are required to accurately model a given PSD. The model was run with only type 1 particles, with a spread in particle size similar to cases (i) and (ii). The PSD was discretised into 1, 3, 9, and 27 fractions. The results between the runs with 9 and 27 fractions only varied by $O(\pm\ 2\%)$. In all results described in subsequent sections, the type 1 PSD has been

discretised into 9 fractions. More fractions may be required for particle mixtures with very wide PSDs. Results with only 3 fractions were still generally within $O(\pm\ 20\%)$ of the results with 27 fractions, whereas single particle fraction results deviated considerably from multiple particle fraction results, unless wall shear forces dominated core motion. In particular, significantly lower particle fluctuating velocities and turbulence modulation were frequently predicted using one particle fraction. It appears that even a crude allowance for PSD effects is worthwhile, unless the PSD is very narrow.

8.15.2 Simulation of Nakamura and Capes (1976) Pneumatic Conveying Experiments

Nakamura and Capes (1976) performed a number of vertical pneumatic conveying experiments with binary particle mixtures of small and large particles. They investigated the effect of particle collisions on the relative masses, x_A and x_B, of the small "A" particles and large "B" particles within a 76 mm diameter conveying line. These weight fractions were then compared to the initial weight fractions of small and large particles fed to the line, X_A and X_B. Experiments with both steel and glass beads were performed. G_s, U_g, and the mass fraction of smaller particles in the feed, X_A, were varied systematically. Nakamura and Capes compared their experimental results with a relatively simple model where separate axial momentum balances for the small and large particles were proposed, with a collisional force interaction term included.

Two of the Nakamura and Capes tests were simulated using CIRCOR. In test (a), the behaviour of a mixture of 1.08 and 2.90 mm diameter glass beads was investigated at $G_s = 24$ kg/m^{2}s, over a range of superficial gas velocities from 12 to 25 m/s. In test (b), the flow of a mixture of 0.54 and 2.34 mm diameter steel beads was simulated at $G_s = 75$ kg/m^{2}s, over a range for U_g of 12 to 30 m/s. The mass fraction, X_A, of smaller particles in the feed in the two tests was 32 wt% and 49 wt%, respectively. These cases were chosen because a reasonable number of both small and large particles were present, G_s values were relatively high in comparison to other Nakamura and Capes tests, and the experimental scatter was

relatively small.

The CIRCOR model predictions and experimental measurements for x_A/X_A are shown in Figures 8.6(a) and 8.6(b). The vertical dotted lines in the figures are the terminal settling velocities for the larger B particles, $\mathbf{v}_{tB}$, calculated using correlations in Table 3.2. Nakamura and Capes fitted their model to the data by including an empirical factor in their collision force expression, which was found to vary between tests. A coefficient of particle-wall sliding friction, $\mu_w = 0.58$ (Goldsmith, 1960; Brown and Richards, 1970) was used in the CIRCOR model runs.

The CIRCOR model accurately predicts the magnitude of x_A/X_A at the higher superficial gas velocities. With decreasing U_g, it predicts a fall-off in x_A/X_A at velocities that are about 10% higher than those reported experimentally. The fall-off in x_A/X_A corresponds to the onset of choking, i.e. the gas velocity is no longer high enough to transport the solids, and the larger particles begin to accumulate in the line. The difference in experimental and predicted fall-off gas velocities may be due to greater drag on the particles than predicted by standard drag curve correlations. Using Chapter 3 equations, the Kolmogorov eddy size in the Nakamura and Capes experiments may be estimated to be of $O(100\ \mu\text{m})$. Thus, the enhancement of drag due to small-scale turbulence, discussed in Chapter 3, is likely to occur in this case. In fact, the particles are only 10% smaller than predicted energetic eddy sizes in this line. For all simulations of the Nakamura and Capes data, the turbulence intensity was of $O(1.5)$ m/s. The predicted response of the large particles used in the experiments was negligible.

Nakamura and Capes also reported measured pressure gradients for several of their glass bead tests. The predicted and measured apparent suspension densities for the glass bead case in Figure 8.6(a) are given in Figure 8.7. The dashed line corresponds to the results of the Nakamura and Capes model. To fit the model to the data, Nakamura and Capes used an empirical particle-wall friction factor, including a factor assumed to be constant for each particle size and type. However, this factor varied considerably, even for particles of different size but the same density.

The CIRCOR model predictions in Figure 8.6 are very good at low suspension density. At

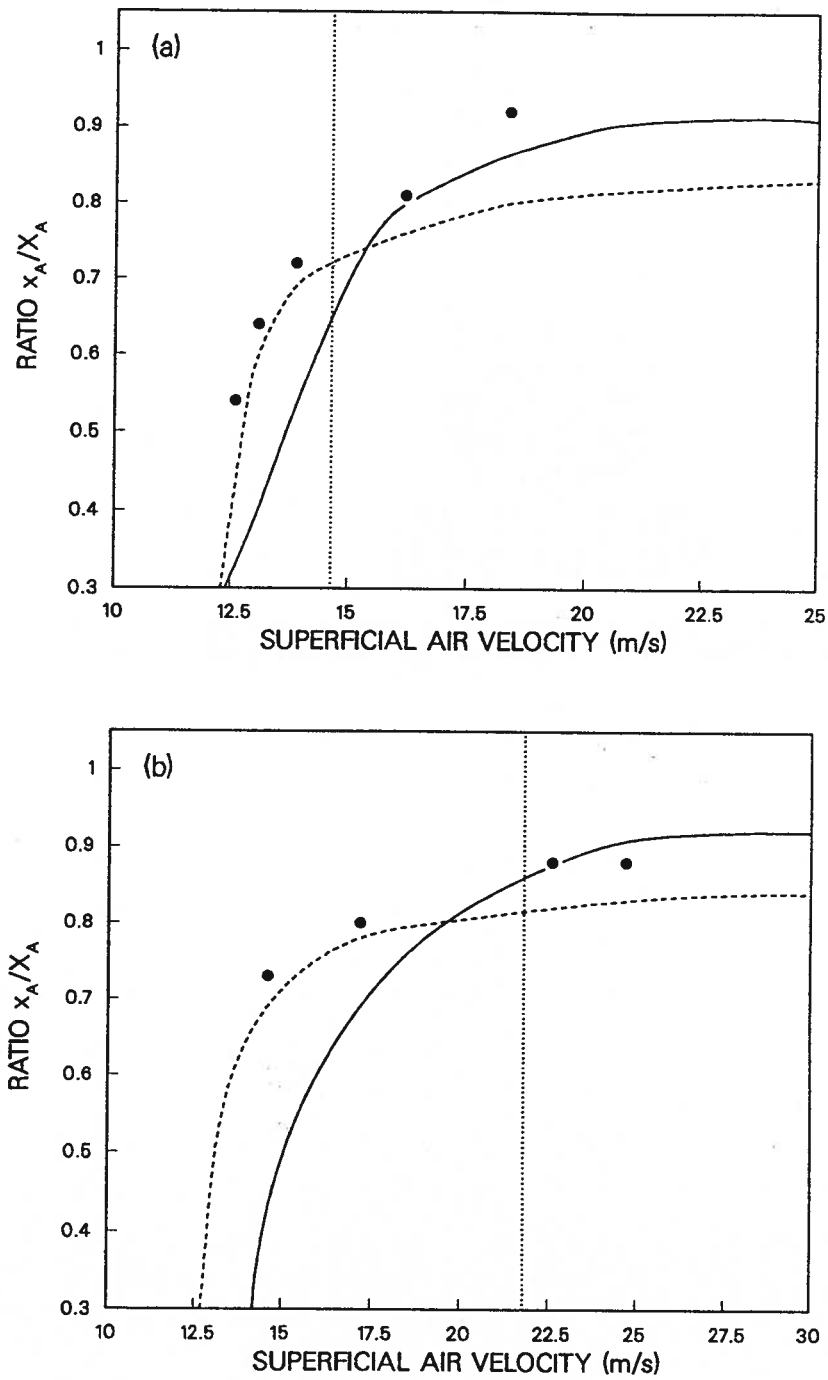

Figure 8.6: Simulation of the vertical pneumatic conveying tests of Nakamura and Capes (1976). Ratios of riser-to-feed particle mass fractions, x_A/X_A.
(a) Glass beads (d_{pA} = 1.08 mm, d_{pB} = 2.90 mm, ρ_p = 2900 kg/m^3, μ_w = 0.58, e = 0.9, e_w = 0.8, $\mathbf{v}_{tB}$ = 14.7 m/s, X_A = 32 wt%); (b) Steel beads (d_{pA} = 535 μm, d_{pB} = 2.34 mm, ρ_p = 7800 kg/m^3, μ_w = 0.58, e = 0.5, e_w = 0.6, $\mathbf{v}_{tB}$ = 21.8 m/s, X_A = 49 wt%)
(Solid lines: CIRCOR predictions; Dashed lines: Nakamura and Capes model prediction; Symbols: experimental results; Dotted line: $U_g = \mathbf{v}_{tB}$.)

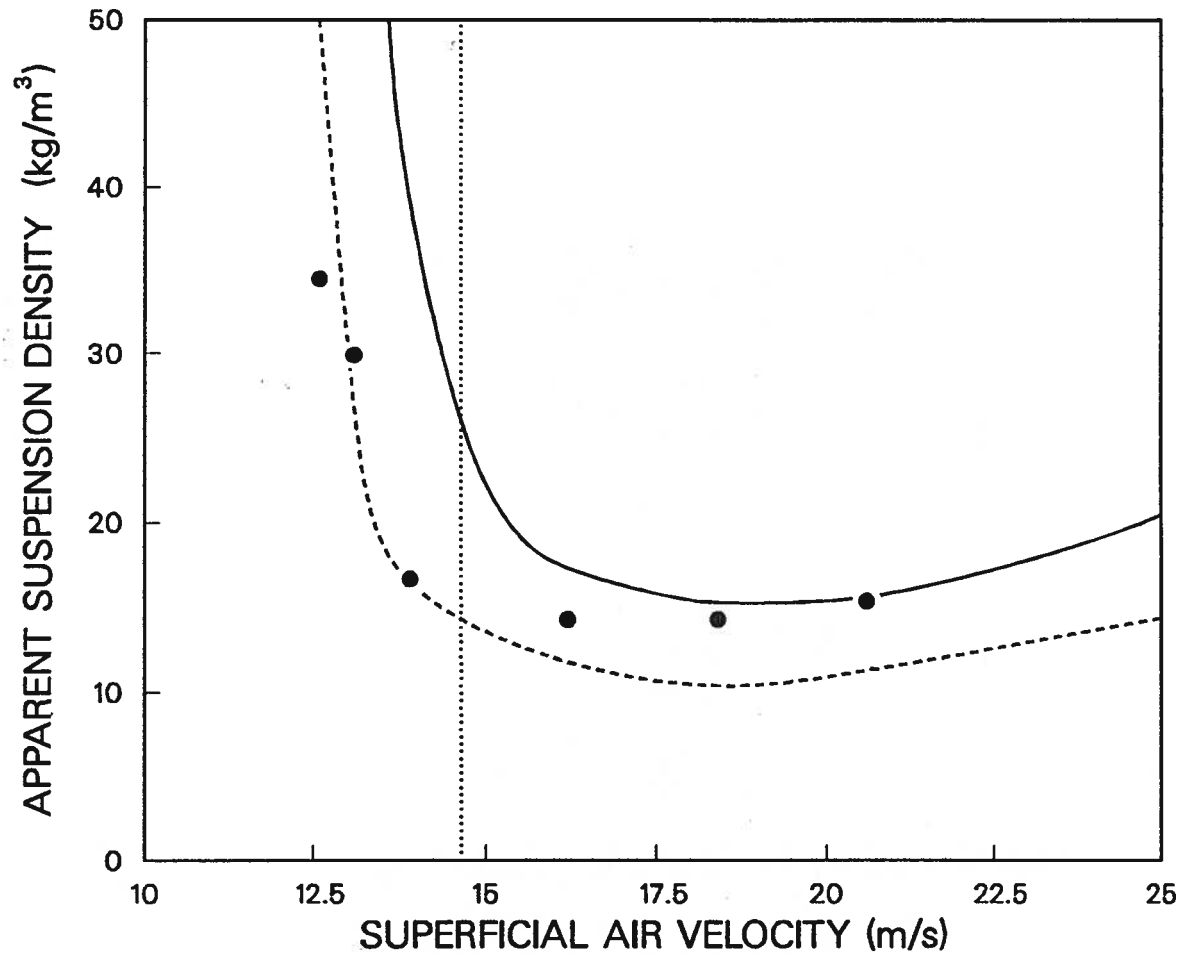

Figure 8.7: Simulation of the vertical pneumatic conveying tests of Nakamura and Capes (1976). Apparent suspension densities for glass bead tests. ($d_{pA} = 1.08$ mm, $d_{pB} = 2.90$ mm, $\rho_p = 2900$ kg/m^3, $\mu_w = 0.58$, $e = 0.9$, $e_w = 0.8$, $\mathbf{v}_{tB} = 14.7$ m/s, $X_A = 32$ wt%)
(Solid lines: CIRCOR predictions; Dashed lines: Nakamura and Capes model prediction; Symbols: experimental results; Dotted line: $U_g = \mathbf{v}_{tB}$.)

these densities, particle r.m.s. fluctuating velocities of $O(0.9)$ and (0.3) m/s were predicted for the 1.08 mm and 2.90 mm particles, respectively. The magnitude of the calculated wall friction force retarding the particles was about 20% of the total drag on the particles. Drag and wall gas shear accounted for approximately 50% of the pressure gradient at these low suspension densities. Thus particle friction was predicted to have a minor, but significant, effect on measured pressure gradient. An order of magnitude increase in the predicted fluctuating velocities would have resulted in much higher predicted than measured pressure gradients. Thus, it may be concluded that fluctuating velocities are not significantly overpredicted by the model. The difference between the predicted and experimental gas velocities, attributed to drag enhancement, results in the differences in choking velocities shown in Figure 8.7.

Whilst the model predictions of the data of Nakamura and Capes are not ideal, they are encouraging. Without using fitting parameters, the model has accurately reproduced the trends in the data, and given reasonable predictions for all the data ($\pm$ 20%, based on U_g). As discussed, it is contended that the discrepancy is due to turbulence effects on particles that occur only in small diameter lines, and are not accounted for in the model.

8.15.3 Simulation of the Cold Unit PSD Tests

The narrow, standard and bimodal glass bead PSD cold unit tests (Runs 1, 2, 3), described in Chapter 6, were simulated by the core riser model. The measured apparent suspension densities between riser heights of 2.0 and 6.0 m were relatively constant in these runs (Figure 6.25), suggesting that the flow in this part of the riser was close to fully-developed. Details of the riser geometry, operating conditions, and particle properties are given below and in Chapter 6. At the riser mid-height sampling position ($z = 4.2$ m), wall streamers were only detected by the capacitance probe for condition C, (although thin "wisps" were occasionally visually observed for condition D runs). The alternating regions of dilute suspension and dense streamer were clearly evident in the probe traces, and the interface between these regions was relatively abrupt for the mid-height traces. The wall streamer solids fraction, $(1 - \epsilon_{gd})$, the average streamer

Table 8.6: Model simulations of the cold unit PSD test results: Suspension densities and shear force magnitudes.

	Experimental				Model simulation			
Run & Condition	ρ_{sa} (kg/m^3)	$\overline{\rho_s}$ (kg/m^3)	r_{an} (mm)	f_w (–)	ρ_{sa} (kg/m^3)	$\overline{\rho_s}$ (kg/m^3)	$\frac{(\mathcal{P}_{ca}\tau_r)}{(A_{cr}\mathbf{F}_{Dz})}$ (%)	(τ_r/τ_g) (%)
$1A$	6	8	0	1.0	4.8	4.2	1	8
$2A$	6	–	0	1.0	4.8	4.1	2	18
$3A$	7	–	0	1.0	5.2	4.7	4	30
$1B$	5	7	0	1.0	4.0	2.8	1	4
$2B$	4	–	0	1.0	4.0	2.7	3	8
$3B$	5	–	0	1.0	4.3	2.9	5	14
$1C$	20	27	3.0	0.8	24	22	8	170
$2C$	20	–	3.0	0.8	24	19	9	200
$3C$	35	–	4.5	0.7	38	26	10	300
$1D$	15	21	0	1.0	10	8.0	1	11
$2D$	15	–	0	1.0	10	8.0	3	18
$3D$	15	–	0	1.0	10	8.5	4	33
$3C^\star$	–	–	3.0	0.8	27	21	11	280

Particle PSDs used in runs: 1: Narrow; 2: Standard; 3: Bimodal (PSDs in Figure 6.9).
U_g and G_s for conditions A-D: A: 6.5 m/s, 20 kg/m^{2}s;
B: 9.0 m/s, 20 kg/m^{2}s; C: 6.5 m/s, 60 kg/m^{2}s; D: 9.0 m/s, 60 kg/m^{2}s.
Constant operating conditions and properties:
$D = .15$m, $T_g = 25$ °C, $\rho_p = 2500$ kg/m^3, $e = 0.9$, $e_w = 0.8$, $\mu_w = 0.58$, $\epsilon_{gd} = 0.86$.
Condition $3C^\star$: same r_{an} and f_w as in conditions $1C$, $2C$.

thickness, r_{an}, and the fraction of wall covered at any instant by wall streamers, $(1 - f_w)$, were estimated for condition C from these probe traces. The estimates appear in Table 8.6. Calculated wall streamer properties from different traces for the same run typically agreed within ± 30%. The values of $(1 - \epsilon_{gd})$, estimated from the probe traces, were in the range of 0.11 to 0.17, and a constant value of 0.14 was used in the model simulations. Note that the corresponding wall streamer voidage (0.86) is significantly greater than loose-packed voidages.

The predicted and measured cross-sectionally averaged suspension densities, $\overline{\rho_s}$, and apparent suspension densities, ρ_{sa}, are compared in Table 8.6. Experimental values of $\overline{\rho_s}$ are

estimated from probe traverses (Table 6.3). Full traverses were not performed for the standard and bimodal PSDs. Model values of $\overline{\rho_s}$ are estimated from the predicted core suspension density, $\rho_{s,cr}$, and the wall streamer input information, assuming that the density of the dilute suspension in the wall region is similar to the density in the core, i.e. $\overline{\rho_s} = \rho_{s,cr}(q + (1-q)f_w) + \rho_{sd}(1-q)(1-f_w)$, where $q = A_{cr}/A_t$. Clearly, when there are no wall streamers, the predicted uniform core suspension density equals the cross-sectionally averaged suspension density. The apparent suspension density given by the model is based on the predicted core pressure gradient. The dimensionless expression $(\mathcal{P}_{ca}\tau_r)/(A_{cr}\mathbf{F}_{Dz})$, in Table 8.6, is the ratio of the total shear force on the core particles in suspension, due to rebound particles (i.e. particle-wall friction effects), to the total drag on the core particles. (τ_r/τ_g) is the ratio of particle-wall friction to gas-wall friction. Both gas-wall and particle-wall friction contribute to the total pressure gradient in the core, as may be demonstrated by adding the gas and particle equations of motion to eliminate the drag term.

Table 8.7 gives the predicted mean gas velocity, and mean and r.m.s. fluctuating particle velocities, corresponding to the runs shown in Table 8.6. The particle PSDs were discretised into 9 fractions of equal initial wt% for the model simulations. Results for the smallest, median and largest size fractions are shown. For all simulations, the direct response of the particles to gas turbulence was negligible, compared to $\mathbf{c}_k$.

The measured streamer thicknesses and wall coverage were about the same for the narrow and standard PSD condition C runs. However, the streamers were thicker, and covered more of the wall, in the condition C bimodal PSD test, as shown in Table 8.6. In an additional model simulation of the bimodal PSD, run $3C^\star$ in Table 8.6, it was assumed that the wall streamer properties were the same as for the condition C narrow and standard PSD simulations.

The predicted and measured apparent suspensions densities are in close agreement for all condition C runs. Note, that for runs $1C$ and $2C$, where the same wall streamer properties were used, predicted apparent suspension density is similar, despite significant differences in the narrow and standard PSDs. This is because the dominant influence on production of particle

Table 8.7: Model simulations of the cold unit PSD test results: Mean and fluctuating velocities.

Run	Model simulation results							
	$\mathbf{u}_z$	$\mathbf{v}_z$	d_p			$\mathbf{c}_k$		
		M	S	M	L	S	M	L
	(m/s)	(m/s)	(μm)	(μm)	(μm)	(m/s)	(m/s)	(m/s)
$1A$	6.5	4.8	158	237	293	0.27	0.12	0.15
$2A$	6.5	4.9	92	234	417	0.43	0.19	0.23
$3A$	6.5	4.3	114	365	570	0.53	0.21	0.27
$1B$	9.0	7.2	158	237	293	0.30	0.15	0.17
$2B$	9.0	7.3	92	234	417	0.47	0.21	0.28
$3B$	9.0	6.7	114	365	570	0.55	0.23	0.34
$1C$	7.1	4.9	158	237	293	0.83	0.62	0.54
$2C$	7.1	5.0	92	234	417	0.88	0.65	0.54
$3C$	7.4	4.6	114	365	570	1.13	0.74	0.64
$1D$	9.0	7.3	158	237	293	0.29	0.15	0.16
$2D$	9.0	7.5	92	234	417	0.46	0.20	0.20
$3D$	9.0	7.0	114	365	570	0.53	0.20	0.22
$3C^\star$	7.1	4.5	114	365	570	0.92	0.66	0.57

Particle feed PSD discretised into 9 fractions of equal wt%.
S, M, and L, denote smallest, median-size, and largest size fraction, respectively.
See Table 8.6 for run conditions and particle properties.

fluctuating kinetic energy in all condition C simulations was the effect of re-entraining wall streamer particles into the core. In all cases, greater than 80% of particle fluctuating kinetic energy production in the core was due to collisions caused by entering streamer particles (P_{ks}). The corresponding kinetic energy production due to PSD effects, P_{kk}, was less than 15% of the total production. When the bimodal PSD was simulated in run $3C^{\star}$ with the *same* wall streamer thicknesses and coverage as for the narrow and standard PSDs, the predicted apparent suspension densities were similar for all three PSDs, as shown in Table 8.6. The dominance of energy production due to streamer particles, P_{ks}, is further illustrated in Table 8.7. The spread in the r.m.s. fluctuating velocities of the respective particle sizes for runs $1C$, $2C$, and $3C^{\star}$ is significantly less than the spread between runs $3C^{\star}$ and $3C$. As discussed in Chapter 6, as the lateral flux of particles outwards to the walls is proportional to $\mathbf{c}$ ($= \mathbf{c}_k$ in this case), it may be deduced from these results that PSD effects on core dynamics cannot, alone, explain the greater concentration of wall streamers measured in run $3C$, compared to runs $1C$ and $2C$.

From the predicted ratios of $(\mathcal{P}_{ca}\tau_r)/(A_{cr}\mathbf{F}_{Dz})$ and (τ_r/τ_g) given in Table 8.6, it may be concluded that the contribution of particle-wall shear to the pressure gradient is minor when there are no wall streamers (conditions A, B, and D). (This result was used in justifying the omission of τ_r from eq. (6.1).) Consequently, although τ_r and $\mathbf{c}_k$ are predicted to vary significantly with PSD for conditions A, B and D as shown in Tables 8.6 and 8.7, the effect on the predicted pressure gradient and apparent suspension density is negligible. This explains the similarity of apparent suspension density profiles for these conditions discussed in Chapter 6. The measured and predicted apparent suspension densities agree closely for conditions A and B. The apparent suspension density is underpredicted for condition D. It may be that the thin wisps of streamers discussed earlier contributed to an increase in the pressure gradient. Also, recall that both the model predictions and the suspension density measurements are only assumed to be accurate within $O(\pm\ 20\%)$.

The presence of wall streamers indirectly increases the shear force due to core particles impacting on bare regions of the riser wall, because significantly higher core particle fluctuating

velocities result from streamer particle entrainment. When streamers are present (condition C), the force on the core due to wall-core particle shear, ($\mathcal{P}_{ca}\boldsymbol{\tau}_r$), is predicted to be up to 10% of the total drag in the core, ($A_{cr}\mathbf{F}_{Dz}$).

As discussed in Chapter 6, a proportionally higher weight fraction of large particles was measured in the wall streamers, compared to the external solids recirculation in the standpipe during run $3C$. The run $3C$ model simulation predicted axial velocities of 4.9 and 4.4 m/s for fractions of size 150 μm and 440 μm, respectively. In Chapter 6 these values were used to demonstrate that differences in axial slip velocities could not explain the measured differences between wall and standpipe sample PSDs. In general, the predicted magnitudes of $\mathbf{c}_k$ in Table 8.7 are greater for smaller particles. Thus greater fluxes to the riser wall are predicted for small particles than for large particles. If particle capture by streamers and entrainment from streamers is independent of particle size or density, then the fraction of small particles in the streamers would be expected to be higher than elsewhere in the riser. This is contrary to the cold unit test experimental measurements. Hence it appears that large particles are more successfully captured and/or retained by wall streamers, as suggested in Chapter 6. Note that the higher values of $\mathbf{c}_k$ for the small particles also indicate that the small particles have a proportionately higher fraction of the total fluctuating kinetic energy of the suspension than the mid-size or large particles. However, also shown in Table 8.7, is that $\mathbf{c}_k$ for the large particle fractions may be greater than that for the mid-size particles (conditions A, B and D).

The model simulations of the cold unit PSD tests provides considerably more insight into the experimental trends described in Chapter 6 for the PSD tests. The relatively good prediction of apparent suspension densities provide a further indication that fluctuating velocity predictions are at least order of magnitude correct.

8.15.4 Parametric Test Results

The effect of varying particle coefficient of restitution, e, particle-wall coefficient of restitution, e_w, particle-wall coefficient of sliding friction, μ_w, mean gas temperature, T_g, and riser diameter,

D, were investigated by parametric testing. In the majority of the tests, a PSD and particle density typical of sands and ash in CFB combustion units was used. The Sauter mean diameter of the PSD was 205 μm and the particle density was 2700 kg/m^3. Several simulations with fine FCC catalyst at typical FCC operating conditions were also performed. The influence of gas turbulence on the results was examined, using the model feature for "turning off" the turbulence, mentioned earlier. For all runs a riser of circular cross-section was assumed. In the simulations involving sand particles, the *direct* contribution of particle drift velocity, $\mathbf{c}_t$, to the combined (total) particle fluctuating velocity, $\mathbf{c}$, was always negligible, i.e. $\mathbf{c}_t^2 \ll \mathbf{c}_k^2$. Consequently, all results for fluctuating particle motion for the sand cases are given in terms of $\mathbf{c}_k$. Note, however, that the *indirect* contribution of turbulence to $\mathbf{c}_k$, via the term P_{kt} in the collisional fluctuating energy balance, is not always negligible for the sand particles, as discussed below. For the smaller and lower density FCC particles, $\mathbf{c}_t$ was of similar magnitude to $\mathbf{c}_k$, and results for both $\mathbf{c}$ and $\mathbf{c}_k$ are given in these cases.

All tests involving the sand particles were variations of two base cases, "(i)" and "(ii)." The base case conditions were the same as those described in Section 8.15.1, except that no type 2 particles were included. The PSD was discretised into 9 fractions of equal initial wt%. In case (i), G_s was 20 kg/m^{2}s, and it was assumed that there were no wall streamers. For case (ii) G_s was set to 60 kg/m^{2}s, and a fractional wall coverage by streamers of 40% was assumed. A pilot-scale riser diameter of 0.15 m, superficial gas velocity of 7.0 m/s, and ambient operating temperature were assumed for the base cases. Further details of the low G_s case (i) and high G_s case (ii) conditions are given in Table 8.2 and Appendix F, respectively.

For the various case (ii) simulations it was necessary to assume wall streamer properties. The fractions of wall covered by streamers and streamer thicknesses assumed for the sand base cases and FCC simulations were both typical of those observed experimentally. The variation of these base case streamer values in each series of tests for a given parameter ensured that the predicted effect of that parameter was conservative. The most noteworthy findings of the parametric tests are summarised below. Additional results are given in Appendix F.

Particle Coefficient of Restitution

In this series of tests, the respective wall streamer properties assumed for base cases (i) and (ii) were used for all model runs, and only the particle coefficient of restitution, e, was varied. Significant effects of e were predicted over the range 1.0 to 0.4, the range of experimentally observed values (Goldsmith, 1960). Figure 8.8 shows the effect of e on particle r.m.s. fluctuating velocity, averaged over all the fractions, i.e $\mathbf{c}_k^2 = (\sum_i \mathbf{c}_{ki}^2)/n$. This average $\mathbf{c}_k$ value is normalised with respect to the average fluctuating velocity at $e = 1$; $\mathbf{c}_k^2/\mathbf{c}_{k(e=1)}^2$ is the fractional reduction in specific particle fluctuating kinetic energy of the core suspension due to inelasticity of the particles. The reduction in core particle fluctuating velocity is not as great in case (i) because the production of fluctuating energy due to P_{kt} is of $O(25\%)$, and D_{kt} is the dominant energy reduction term. Both these terms are independent of e. However, for case (ii), energy production is dominated by streamer-core particle collisions (term P_{ks}), and energy loss due to inelastic collisions (measured by $\sum_i S_{kki}$) becomes significant.

Apparent suspension densities for the e parametric tests are given in Table F.1. For case (i), the significant changes in $\mathbf{c}_k$ with e had a negligible effect on the core apparent suspension density because particle-wall friction effects were small (as in the condition A, B and D cold unit test simulations described above). However, for case (ii), with streamers present, the core apparent suspension density changed significantly, from $\rho_{sa} = 55$ kg/m^3 for $e = 1.0$ to $\rho_{sa} = 38$ kg/m^3 for $e = 0.4$. This was due to the reduction in shear on the core arising from less lateral particle transfer between core and streamers. For case (ii), the true core suspension density remained relatively constant at $\rho_s = 18$ kg/m^3 as e was varied.

In all case (i) simulations it was assumed that there were no wall streamers present, regardless of the value of e. Wall streamer formation probably relies on both the rate at which particles reach the wall, and the probability of particles staying close to the wall for a sufficient time for an accumulation of particles to occur. Although a constant particle-wall coefficient of restitution, e_w, was assumed for the e parameter tests, it is more likely that particles of low e also exhibit lower values of e_w. The case (i) predictions indicate that fluxes of particles out to

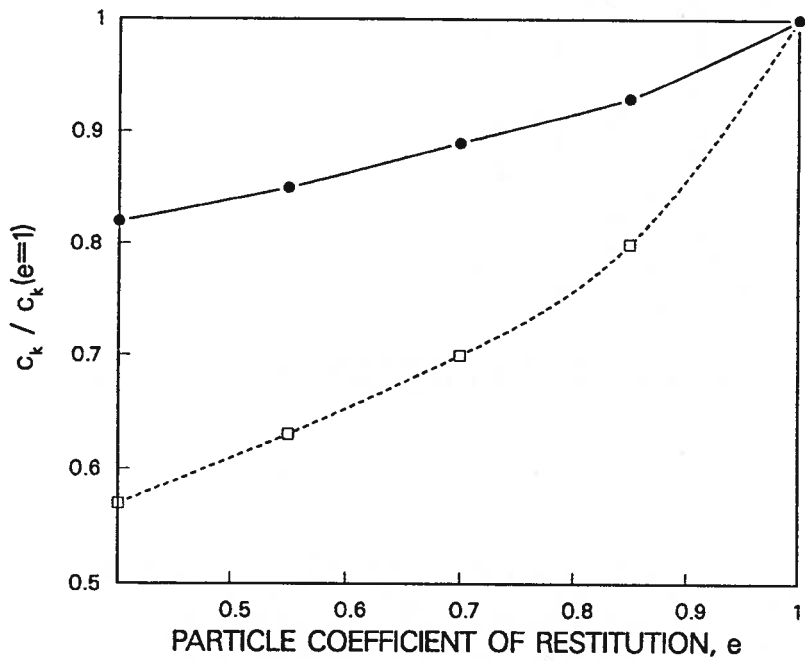

Figure 8.8: Predicted effect of particle coefficient of restitution, e, on the average particle fluctuating velocity within the riser core. Solid line: $G_s = 20$ kg/m^{2}s, case (i). Dashed line: $G_s = 60$ kg/m^{2}s, case(ii). ($T_g = 25$ °C. Other conditions: as given in Table 8.8.)

the walls are greater from suspensions of nearly elastic particles. However, it is also probable that these particles are more likely to rebound off the wall back into the core flow. Thus, it is unclear if wall streamers are more likely to nucleate with suspensions of inelastic or nearly elastic particles. Streamer formation is discussed in Chapter 9. The discussion of case (i) results from here on assumes no streamer formation. Similarly, for case (ii) results, it is assumed that $G_s = 60$ kg/m^{2}s is sufficiently high for wall streamers to be present in all simulations.

In the case (ii) simulations the assumption of constant wall streamer coverage and thickness results in conservative estimates of the effect of e. In reality, the streamer thickness and wall coverage are both likely to increase with an increase in $\mathbf{c}_k$, thereby resulting in even greater differences between particles of low and high e. It may be concluded that particle coefficient of restitution (or some similar measure of the energy loss involved in particle collisions) has a significant effect on the behaviour of a suspension. Louge (1991) presented experimental results that are consistent with this prediction. He observed an increase in solids hold-up in a CFB riser after applying a thin surface coating to particles to alter their collisional properties. The particle shape and density were not significantly changed by the coating. Possible effects of differences in particle elasticity should be considered when scaling CFB risers from bench-scale cold units using relatively inelastic particles (e.g. steel beads, $e \approx 0.6$) to larger units using nearly elastic particles (e.g. sands, $e > 0.9$).

Both the effect of e_w and μ_w were also investigated in parametric tests. Apparent suspension densities for the μ_w parametric tests appear in Table F.1. Only the dissipation of fluctuating kinetic energy due to core particle collisions with the wall, D_{kr}, depends on e_w. The predicted magnitude of D_{kr} in model simulations was always minor in comparison to other energy dissipation terms. Consequently, e_w had little effect on the case (i) and (ii) predictions. However, as mentioned above, it may play a key role in streamer formation. Particle-wall friction coefficients, μ_w, of 0.10 and 0.90 were assumed, in addition to the base case value of 0.58. For these values, the effect of μ_w was negligible for case (i), as the predicted particle-wall friction shear force, τ_r , was small in comparison to other forces on the core. For case (ii), a small effect of

changing μ_w was predicted, due to the greater magnitude of $\mathbf{c}_k$. An increase in ρ_{sa} from 46 to 49 kg/m^3 was predicted for case (ii) when μ_w was increased from 0.10 to 0.90 (see Table F.1).

Riser Temperature

Temperature parametric tests were run for riser temperatures from 25 to 1000 °C. Firstly, a 0.15 m diameter riser was considered. The high temperature simulations were thus typical of combustion conditions in the pilot-scale CFB combustor described in Chapter 7. The assumed wall streamer properties were not varied is these simulations. In a second set of tests, model predictions at gas temperatures of 25 °C and 850 °C were compared for risers of diameter 0.5, 1.0 and 4.0 m.

The results for the 0.15 m diameter riser are given in Table 8.8. Note that both the apparent and true suspension densities, ρ_{sa} and ρ_s, apply to the riser core. The particle r.m.s. fluctuating velocity, $\mathbf{c}_k$, and mean velocity, $\mathbf{v}_z$, are average values for the suspension. The temperature affects both the mean axial velocity of the particles, and the response of the particles to gas turbulence. Between 25 and 1000 °C, the mean slip velocity of the mineral sand particles varied from approximately 1.6 to 1.2 m/s. At the assumed superficial velocity of 7.0 m/s, this resulted in relatively little change in suspension density. The effect of turbulence on the fluctuating velocity of the particles was secondary compared to the effects of particle collisions. The indirect (P_{kt}) contribution of the gas turbulence accounted for between about 5 and 15% of the particle collisional fluctuating velocity, $\mathbf{c}_k$. As the particle response to the turbulence increased with temperature, the turbulence was increasingly modulated. The net effect was that the magnitude of particle fluctuations due directly to turbulence, $\mathbf{c}_t$, was always significantly less than the magnitude of particle velocity fluctuations due to collisions.

Table 8.8 results show that the overall effect of gas temperature on mean and fluctuating motion in the 0.15 m diameter riser was small. However, the turbulence intensity was substantially decreased as the temperature increased. This indicates that gas mixing may be poorer in high temperature risers in comparison to cold units. Cold unit CFB gas tracer data may

Table 8.8: Predicted effects of gas temperature on gas and particle motion in a pilot-scale riser.

	Case (i), $G_s = 20$ kg/m^{2}s					Case (ii), $G_s = 60$ kg/m^{2}s				
T_g (°C)	$(\mathbf{u}_1'/\mathbf{u}_0')^2$ (%)	ρ_{sa} (kg/m^3)	ρ_s (kg/m^3)	$\mathbf{v}_z$ (m/s)	$\mathbf{c}_k$ (m/s)	$(\mathbf{u}_1'/\mathbf{u}_0')^2$ (%)	ρ_{sa} (kg/m^3)	ρ_s (kg/m^3)	$\mathbf{v}_z$ (m/s)	$\mathbf{c}_k$ (m/s)
25	96	4.7	3.7	5.4	0.26	88	47	18	5.2	0.90
150	92	4.7	3.7	5.4	0.27	83	46	18	5.2	0.90
300	89	4.3	3.7	5.4	0.27	76	46	18	5.3	0.90
450	85	4.1	3.6	5.6	0.27	69	46	18	5.3	0.91
600	76	3.9	3.6	5.6	0.26	62	46	18	5.4	0.92
850	66	3.8	3.5	5.7	0.25	50	46	17	5.5	0.94
1000	60	3.7	3.5	5.8	0.25	38	47	17	5.6	0.94

Case (i): $\mathbf{u}_0' \approx 0.7$ m/s, $\mathbf{u}_z = 7.0$ m/s.
Case (ii): $\mathbf{u}_0' \approx 0.9$ m/s, $\mathbf{u}_z = 8.0$ m/s.
Cases (i) and (ii): $U_g = 7.0$ m/s, $D = 0.15$ m, $\rho_p = 2700$ kg/m^3, $\overline{d_p} = 205$ μm, $e = 0.85$, $e_w = 0.8$, $\mu_w = 0.58$, PSD given in Table 8.4.

require correction, before being used to predict gas mixing in elevated temperature risers.

Relatively little change in particle mean and fluctuating motion with temperature change was predicted also for larger diameter risers at 25 °C and 850 °C. Results of those simulations appear in Table F.2. It appears that the motion of particles of size and density typical of sand particles in CFB combustion units, is relatively insensitive to gas temperature for gas velocities of $O(7$ m/s$)$. Turbulence effects are secondary at low temperatures, and are predicted to remain relatively minor as temperature increases, due to modulation of the turbulence by the particles. Nevertheless, these turbulence effects are not insignificant, as discussed below. For smaller or lighter particles, turbulence may dominate collision effects, and particle motion may be strongly dependent on gas temperature. Examples of such particles are fine carbon particles in CFB combustors, and catalyst in FCC risers. Model simulations with 40 μm coal particles were discussed earlier, and FCC simulations are given below.

Riser Diameter

The investigation of riser diameter or "scale-up" effects predicted by the model was divided into three series of tests. In series 1, the ambient temperature case (i) and (ii) simulations

were performed, with riser diameters of 0.15, 0.5, 1.0 and 4.0 m. In series 2, these tests were repeated with T_g = 850 °C. As mentioned in the previous section, the only significant effect of temperature increase within a given riser was a decrease in turbulence intensity. Given the similarity of series 1 and 2 results, only the high temperature results are discussed here. In the series 3 tests, the high temperature series 2 tests were repeated with the turbulence "turned off" in the model, to evaluate the contribution of gas turbulence to particle motion. Additional results for the three series of tests are provided in Table F.2, Appendix F.

For the case (ii) simulations, the wall streamer average thickness was assumed to increase proportionally with the diameter of the riser. Consequently, the core superficial velocity in case (ii) was constant for all riser diameters. The fractional wall coverage by streamers was maintained at 40% for the case (ii) runs. The riser gas superficial velocity was 7.0 m/s for all runs.

The model simulations of pilot-scale units discussed above predict that a major influence on the core gas and particle motion in these units is the entrainment of wall streamer particles into the core. Shearing of the particle assemblage in a pilot-scale riser is the dominant mechanism which imparts fluctuating kinetic energy to larger particles that do not respond significantly to gas turbulence. The wall region thickness in larger units is a small fraction of the total riser diameter (e.g. Couturier *et al.*, 1989, 1991), as is generally also the case in small pilot-scale risers. The cross-sectional area occupied by the core suspension increases approximately in proportion to the riser cross-sectional area. However, the core-wall region interface available for entrainment of streamer particles only increases in proportion to the riser diameter, D. Unless the wall streamers fall substantially faster in a large unit, a reduction in the magnitude of the effect of wall streamers on the core is expected, as D increases.

It is unlikely that streamers could fall with sufficient velocity in a large riser to maintain the same effect of shear on the core as in a pilot-scale riser. Consider the effect of streamers on the core flow in a pilot-scale 0.15 m diameter riser and a large 4.0 m diameter riser. For the total effect of shear on the core in a 4.0 m diameter unit due to wall streamers to equal

that in a pilot-scale 0.15 m diameter unit, the shear force per unit area would have to increase by a factor of about (4/.15). It is known that streamers in the 0.15 m unit fall with mean velocities of $O(1 \text{ m/s})$. Thus streamers would have to fall with velocities of approximately 30 m/s in the 4.0 m unit to match the shear effects of streamers with velocities of 1 m/s in the 0.15 m diameter unit. Such velocities at the wall a very unlikely, given wall and gas shear effects. Objects free-falling in a vacuum for the full height of a typical large CFB combustor ($\approx$ 40 m) would only just attain this velocity before reaching the bottom. The limited number of measurements in larger units indicate that streamer velocities in large units are similar in magnitude to those in small units (Couturier *et al.*, 1991). Thus, it may be concluded that a reduction of the effects of the wall streamers on the core occurs as the riser diameter increases. It is implicitly assumed in the model that the magnitude of wall streamer velocities in risers of all diameters is significantly less than typical riser core velocities. Consequently, a decrease in wall effects with riser diameter is also predicted by the model.

Figure 8.9 shows the apparent and true core suspension densities predicted by the model for case (ii). The apparent density for $D = 0.15$ m is significantly greater than the true core density, due to the effect of wall streamer particle entrainment. An increase in D results in the difference between ρ_{sa} and ρ_s substantially diminishing. The predicted difference between ρ_{sa} and ρ_s was small for all diameters considered in the "bare-wall" case (i) simulations, due to the minor contribution of particle-wall friction to pressure gradient in these runs. Figure 8.10 shows the dependence of the average fluctuating particle velocity on D for cases (i) and (ii). For case (ii), $\mathbf{c}_k$ decreases substantially as D increases, due to the reducing contribution of entrained streamer particles on core particle collisions. As there are no streamers in case (i), little effect of diameter is observed.

The predicted decrease in importance of wall effects on core dynamics with an increase in D is further illustrated in Figure 8.11. The two curves referred to the left ordinate give the fraction of fluctuating kinetic energy production due to core "type (i)" collisions between particles from different fractions, $P_{kk}/\sum P_k$, where $\sum P_k$ is an abbreviation for the total production,

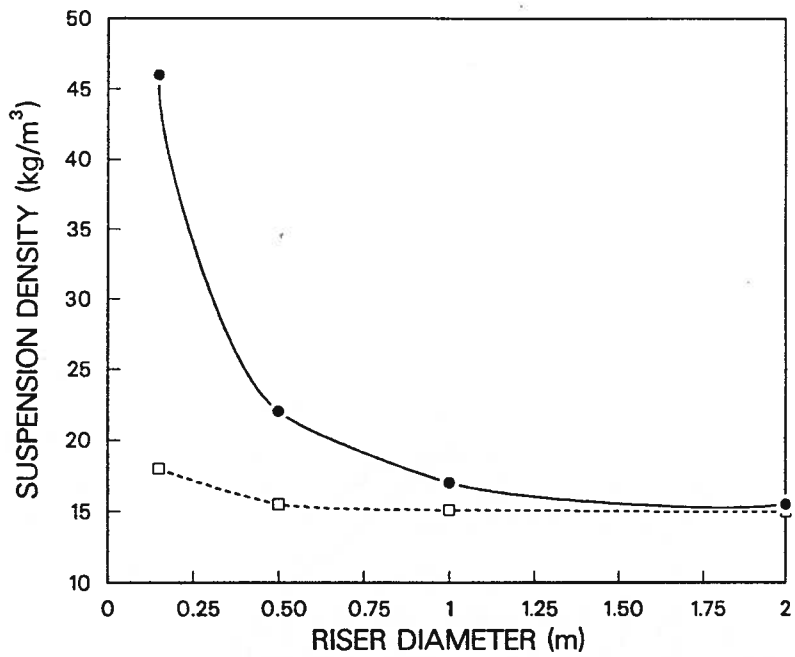

Figure 8.9: Variation of apparent and true core suspension densities with riser diameter. Solid line: apparent core suspension density, ρ_{sa}. Dashed line: true core suspension density, ρ_s. (Case (ii), $G_s = 60$ kg/m^{2}s, $T_g = 850$ °C. Other conditions: as given in Table 8.8.)

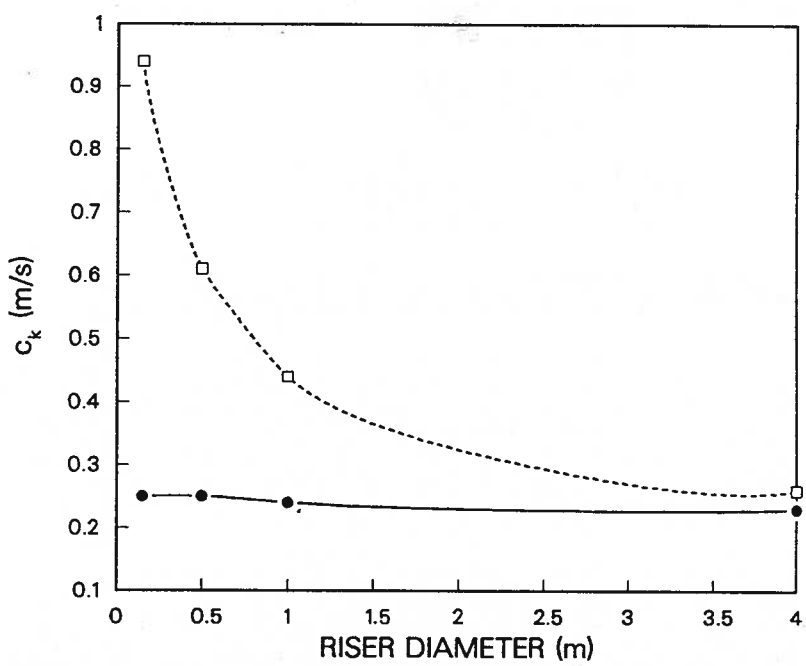

Figure 8.10: Variation of average particle r.m.s. fluctuating velocity with riser diameter. Solid line: $G_s = 20$ kg/m^{2}s, case (i). Dashed line: $G_s = 60$ kg/m^{2}s, case(ii). ($T_g = 850$ °C, Other conditions: as given in Table 8.8.)

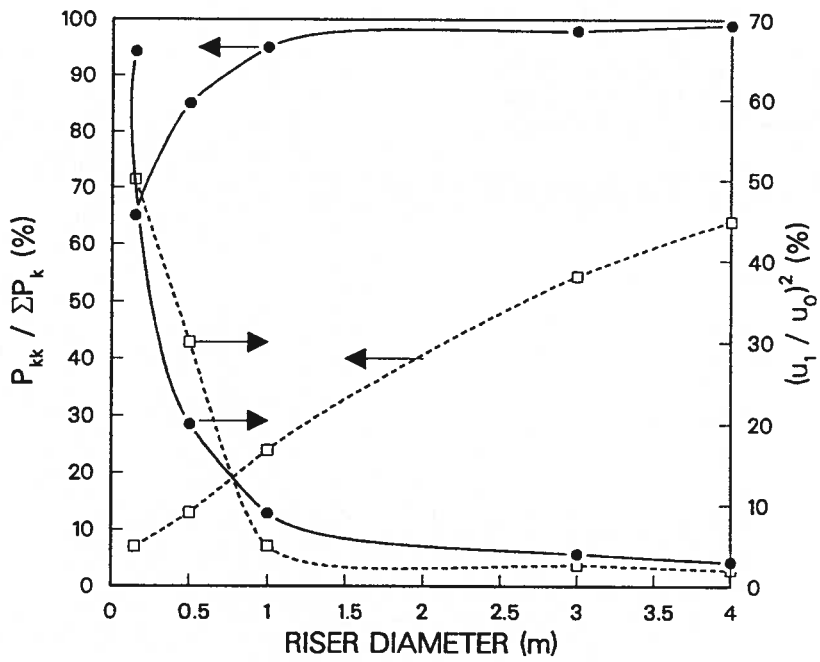

Figure 8.11: Riser diameter effects on (a) the contribution of particle "type (i)" collisions to total particle fluctuating kinetic energy production in the riser core ($P_{kk}/\sum P_k$), and (b) the reduction in core gas turbulence intensity due to particles, $(\mathbf{u}_1'/\mathbf{u}_0')^2$. Solid lines: G_s = 20 kg/m^{2}s, case (i). Dashed lines: G_s = 60 kg/m^{2}s, case(ii). (T_g = 850 °C, Other conditions: as given in Table 8.8.)

$(P_{kk} + P_{kt} + P_{ks} + P_{kr})$. Recall that P_{kk} is dependent on the PSD spread. When there are no wall streamers (case (i)), P_{kk} is always the dominant production term. For small diameter units the energy production due to turbulence, P_{kt}, accounts for much of the additional production in case (i). In the pilot-scale riser case (ii) simulation, core fluctuating energy production is largely due to entraining wall streamers (term P_{ks} in the energy balance). However, as riser diameter increases in case (ii), the relative contribution of P_{kk} increases from approximately 10% to greater than 65% in a 4.0 m diameter unit. These results indicate that PSD effects on fluctuating particle motion and particle deposition on riser walls are important in larger diameter risers, at least for the particles considered.

The curves in Figure 8.11 referred to the right ordinate give the predicted reduction in turbulence intensity due to the presence of the particles. As the riser diameter increases, the size of energetic eddies are predicted to increase, thereby providing additional time for particles passing through these eddies to gain some component of velocity in the direction of the eddy gas fluctuation. As particles increasingly respond to the eddies, they also increase the gas turbulent energy dissipation rate, and average gas turbulence intensities are lowered. Substantially lower turbulence intensity levels are predicted for large diameter risers than for pilot-scale units, due to modulation of the larger eddies. This phenomenon, first discussed in Chapter 3, suggests that gas mixing may be relatively poor in large diameter commercial risers compared to pilot-scale units.

The predicted contribution of gas turbulence to the average fluctuating particle kinetic energy for cases (i) and (ii) was evaluated by comparing the second series of model simulations with the third series, where the turbulence was "turned off" ($\mathbf{u}_1' = 0$). The resulting trends, given in Figure 8.12, differed for cases (i) and (ii). In the "bare wall" riser case (i), turbulence effects account for approximately 25% of the fluctuating particle energy in the pilot-scale unit. However, as the riser diameter was increased, and the particles increasingly responded to the eddies, the gas turbulence intensity decreased rapidly, to a level that was significantly less than the magnitude of the particle velocity fluctuations. The net result was a reduction in gas

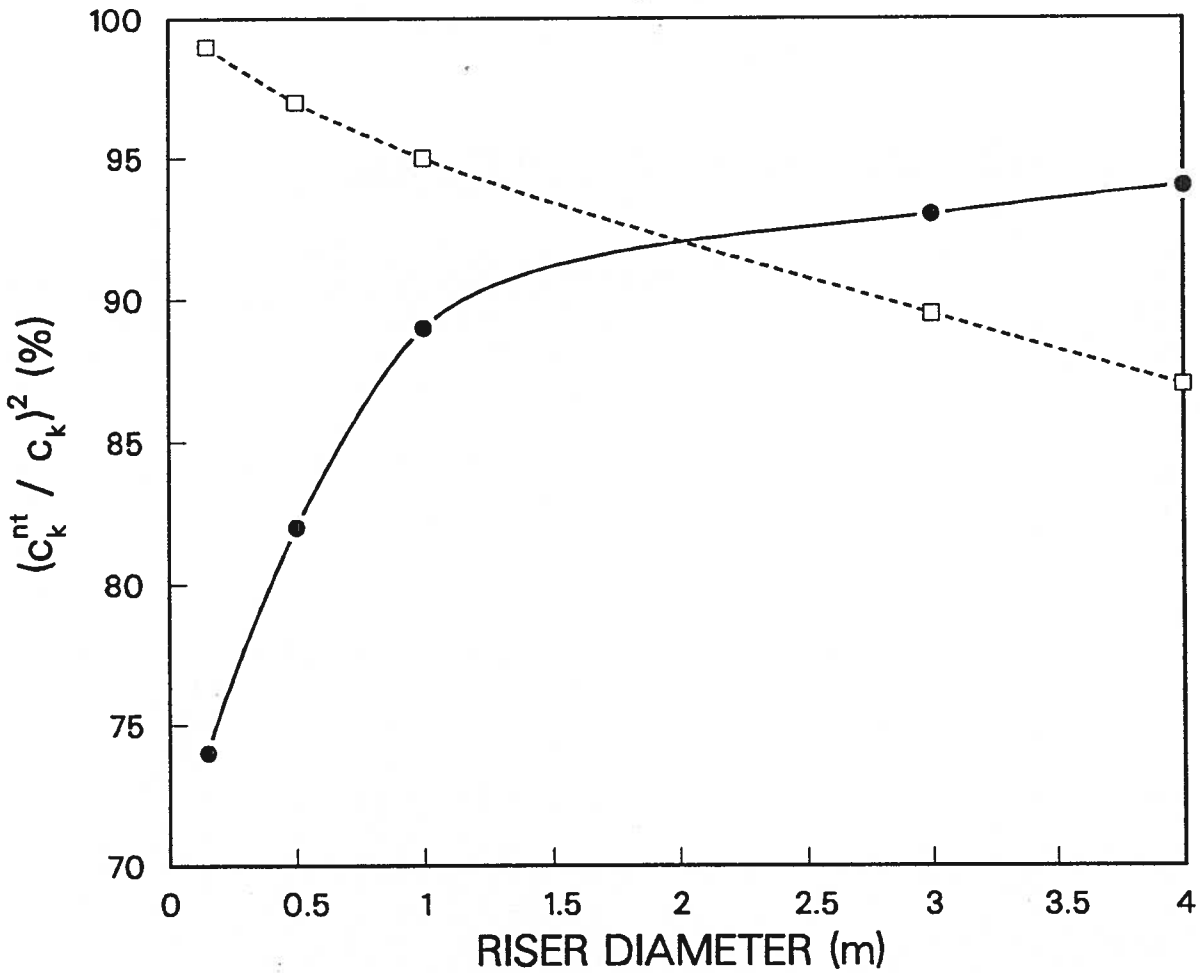

Figure 8.12: Influence of gas turbulence on specific particle fluctuating kinetic energy at T_g = 850 °C. Solid lines: G_s = 20 kg/m^{2}s, case (i). Dashed line: G_s = 60 kg/m^{2}s, case (ii). (Superscript *nt* denotes model simulations with preset zero gas turbulence intensity.)

turbulence effects on the overall fluctuating energy of the particles for larger diameter risers. In case (ii), the production of fluctuating energy in the pilot-scale risers was due predominantly to streamer particle entrainment, as discussed. However, wall "roughness," due to the wall streamers for all case (ii) runs, resulted in significantly higher gas turbulence energy production rates than in case (i). Although turbulence modulation also increased with riser diameter in case (ii), both predicted particle-free and particle-laden turbulence intensities were higher than in case (i). As D increased, and wall effects decreased, gas turbulence intensity remained sufficiently high to have a minor effect on the fluctuating particle motion.

The reduction in $\mathbf{c}_k$ with an increase in riser diameter shown in Figure 8.10 for case (ii) indicates that particle deposition per unit area of riser wall is less in larger units. However, the reduced shear on the wall streamers in larger units may also result in lower particle re-entrainment back into the core. The net effect on wall region thickness and the concentration of particles in wall streamers in large units is not obvious. If we assume that streamers in large units fall at similar velocities to streamers in pilot-scale units, it may be shown that r_{an}/D, i.e. the wall region thickness relative to the total riser diameter, and/or average streamer density, decrease as D increases. The apparent suspension density, ρ_{sa}, may be assumed to be radially invariant in regions of fully-developed riser flow (see Chapter 4). Model predictions indicate that ρ_{sa} decreases with D, for otherwise constant operating conditions. Consequently, for ρ_{sa} to continue to reasonably approximate the cross-sectionally averaged suspension density in large diameter risers, the proportion of particles in dense streamers to that in the dilute core suspension must also decrease, i.e. r_{an}/D must decrease and/or streamer voidage must increase.

Hydrodynamic wall layer thicknesses of $O(10)$ mm were measured in a 0.15 m $\times$ 0.15 m square pilot-scale CFB combustor in this study (Chapter 7), so that r_{an}/D =7%. Stevens (1990) measured regions of solids downflow within about 0.2 m of the wall in the 4.0 m $\times$ 4.0 m square Chatham demonstration CFB boiler. Unfortunately, there was only one measurement near the wall, and it is not possible to accurately determine the wall region thickness from the

results. Knowlton (1990) proposed that the riser core may operate at choking conditions, and assumed an annular wall region filled with suspension at loose-packed voidage. Although his method predicts r_{an}/D to be almost constant with scale-up, the approach is questionable given variations in measured time-averaged wall region voidages, and the large lateral flux of particles required to maintain such thick, dense wall layers in larger diameter units.

The first important benefit of these riser diameter parametric tests is an understanding of the likely trends when a small unit is scaled up. As discussed, the assumed wall streamer thicknesses for these tests are not critical if the wall region remains a small fraction of the total riser diameter, and the wall streamers fall with similar velocities. Regardless of the streamer properties, similar results are then obtained for the core flow because of the reduction in wall effects with increasing riser diameter. The apparent suspension density and fluctuating particle kinetic energy in the riser core are both expected to decrease with increasing riser diameter. Recall from Chapter 4 the evidence suggesting that a uniform dilute suspension may be stabilised by the particle phase "pressure." For a dilute suspension this pressure is proportional to the particle fluctuating energy (Chapman and Cowling, 1970; Chapter 4). Thus the results suggest that formation of clusters or free streamers within the core may be more likely in a large diameter unit than in a pilot-scale unit.

A second important result from the tests is that both PSD and gas turbulence effects are predicted to be significant, though generally secondary in importance to wall shear effects. A substantially greater reduction of the gas turbulence intensity is expected in large units than in smaller risers. These results apply to sand particles with a PSD that is narrower than often present in CFB combustion systems, and a particle density and/or mean diameter that are significantly greater than the particles in many other CFB applications. (PSD or gas turbulence may be the dominant influence on particles in other CFB riser applications.)

Clearly, a wall dynamics model is required to complement the core model before quantitative predictions of scale effects are possible. Scale-up effects on wall region dynamics are further discussed in Chapter 9.

FCC Riser Simulations

The conditions in the fully-developed flow region of a FCC riser core were simulated, assuming a net solid circulation of 200 kg/m^{2}s and a superficial gas velocity of 9.0 m/s. A riser with a circular cross-section and diameter of 1.0 m was assumed, operating at a mean gas temperature of 450 °C. The FCC catalyst properties were those given by Yerushalmi *et al.* (1978). The particle density was 1070 kg/m^3, and Sauter mean particle diameter was 49 μm. Approximately 90 wt% of the particles had diameters between 25 and 100 μm. Values typical of relatively elastic particles were assumed for e, e_w, and μ_w (0.8, 0.7, and 0.58, respectively). Wall coverage by streamers and average streamer thickness were assumed to be 70% and 50 mm, respectively. The objective of the simulations was to investigate the relative importance of particle collisions and gas turbulence on the particle fluctuating motion in the core. Hence, accuracy of these assumed properties was not critical to the study.

The riser was simulated with both turbulence effects included, and with zero turbulence intensity. Full model outputs are given in Appendix F. Figure 8.13 gives the predicted particle r.m.s. fluctuating velocities in the riser core for the different particle sizes. With turbulence included, the total fluctuating particle velocity, $\mathbf{c}$, was about 0.51 m/s, and the collisional fluctuating particle velocity was about 0.2 m/s. Without gas turbulence, $\mathbf{c}_k$ (equal to $\mathbf{c}$ in this case) was about 0.1 m/s for all particle sizes. The model clearly predicts that turbulence is the major contributor to the fluctuating motion of the particles.

The particle-free turbulence intensity, $\mathbf{u}'_0$, and the particle-laden turbulence intensity, $\mathbf{u}'_1$, were predicted to be 1.4 and 0.47 m/s, respectively. The small, low density FCC particles responded almost fully to the turbulent eddies, i.e. $\mathbf{c}_t \approx 0.47$ m/s for all particle sizes. These small particles thus resided within an eddy for the duration of the eddy lifetime. This motion was termed "type 1" motion in Chapter 3. These small particles have less effect on reducing the turbulence intensity than larger less responsive particles which pass through several eddies during the typical eddy decay lifetime, as discussed in that Chapter.

From Figure 8.13, it may be deduced that the *direct* response of the particles to the gas

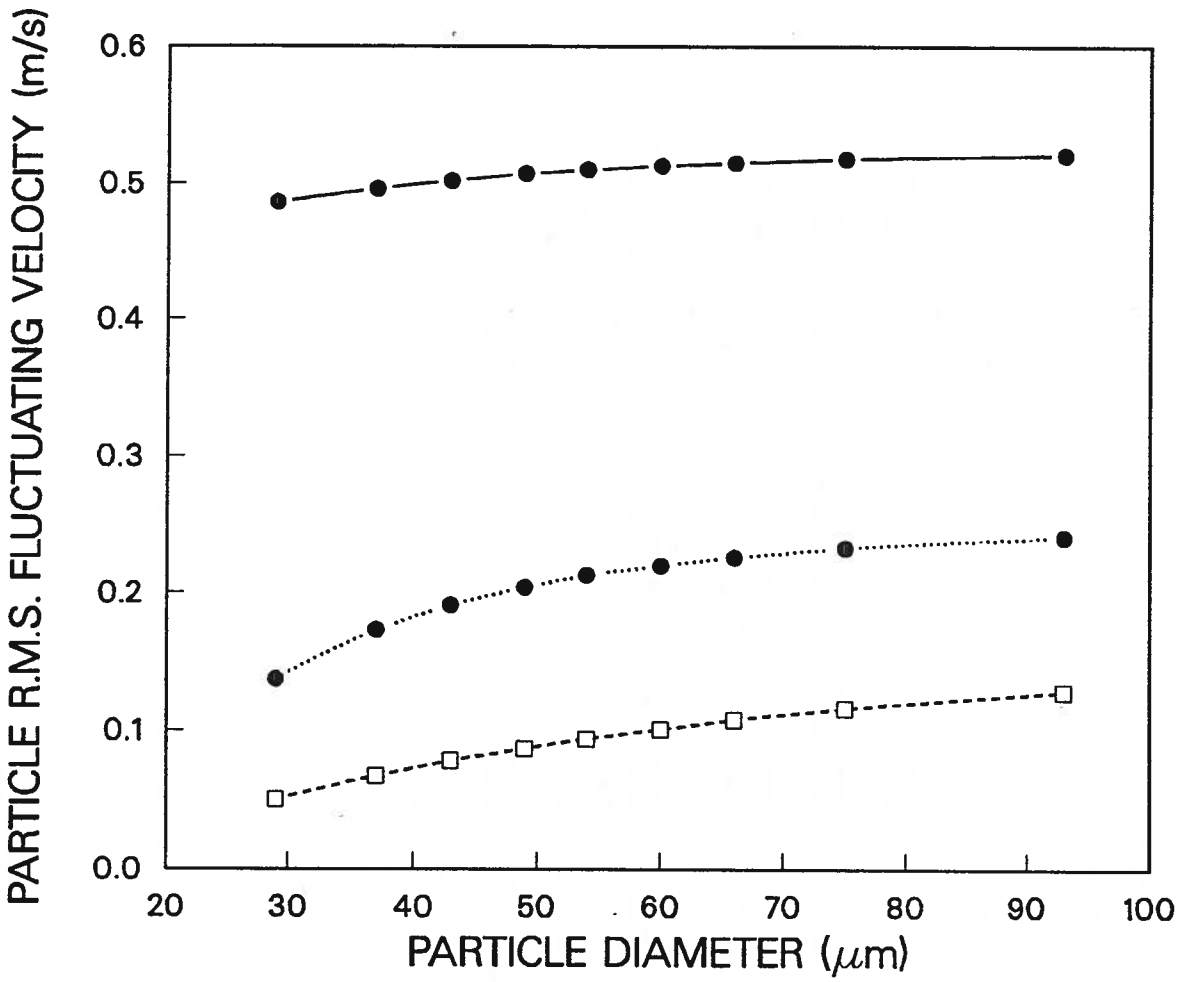

Figure 8.13: Predicted particle r.m.s. fluctuating velocities in the core of a 1.0 m diameter riser operating with fine FCC catalyst. Solid line: $\mathbf{c}$. Dotted line: $\mathbf{c}_k$. Dashed line: $\mathbf{c}_k$ without gas turbulence. ($G_s = 200$ kg/m^{2}s; $U_g = 9.0$ m/s; $T_g = 450$ °C; $\overline{d_p} = 49$ μm; $\rho_p = 1070$ kg/m^3.

turbulence accounts for approximately 85% of the total r.m.s. particle fluctuating velocity ($(0.47/0.51)^2$). Furthermore, the enhancement of collisions due to *indirect* gas turbulence effects increases the collisional fluctuating velocity by approximately 50%. From these predictions, it is clear that gas turbulence significantly influences particle motion in risers operating with small particles that respond rapidly to gas velocity changes.

8.16 Conclusions

A general one-dimensional model for vertical dilute suspension flows has been developed that considers the coupled effects of gas turbulence and particle collisions on the motion of the suspension. Multiple particle fractions of differing sizes and densities are included in the formulation. Fluctuating kinetic energy balances for each particle fraction are established that incorporate terms for PSD and gas turbulence effects. The gas turbulence is represented by characteristic energetic eddies. The transfer of gas turbulence energy to responsive particles results in the modulation of the turbulence intensity.

Boundary conditions for dilute suspension flow within the core of a CFB riser include effects on the core flow of both the exposed riser wall and falling dense particle wall streamers. Equations for the fully-developed flow version of the riser core model are derived from the more general model and the two-phase equations of motion given in Chapter 4. This fully-developed riser core flow model is coded in a FORTRAN program, "CIRCOR." The model requires either experimental or assumed values for wall streamer properties, in lieu of a comprehensive wall region riser sub-model. For flows where there is a negligible concentration of wall streamers, the model is fully predictive, and requires no input of riser dynamical variables.

The model reasonably simulated both Nakamura and Capes (1976) vertical pneumatic conveying data for binary particle mixtures and the experimental trends for the cold unit PSD tests described in Chapter 6. Both predictions relied on reasonable calculated values of the magnitude of the fluctuating particle velocity. The results are encouraging. Predicted fluctuating particle velocities varied in magnitude from approximately 0.2 to 1.0 m/s. A number of

parametric tests were performed to evaluate the model and to investigate the effect of various particle properties on core dynamics.

In its current form, the model is limited by the need to provide information about the wall streamers. Nevertheless, it still provides considerable insight into the fundamental dynamics of riser suspension flows and represents a sound basis for further modelling. The predictions lead to several significant conclusions for riser suspension flows:

- Both turbulence and particle collisions may significantly influence the fluctuating motion of the particles.
- Collisions, due to shearing of the particle assemblage and differences in mean particle velocity (PSD effects), are the major causes of fluctuating motion for larger mineral or sand particles, such as those present in CFB combustors.
- The response of small, low density particles, such as FCC catalyst, to the gas turbulence is a dominant influence on their fluctuating motion.
- The mean and fluctuating motion of particles whose size and/or density differ significantly from the average may deviate considerably from the average particle motion.
- Turbulence intensity is likely to decrease with an increase in riser diameter or gas temperature.

Chapter 9

RISER WALL DYNAMICS, ENTRY EFFECTS AND EXIT EFFECTS

Numerous examples of the importance of the riser base geometry, exit geometry, and the riser walls on the behaviour of gas-solid suspension flow have appeared in preceding chapters. "Wall effects" include the formation and transient motion of dense sheets of particles, or "streamers" near the wall. Streamer downflow is a key feature of CFB risers, that substantially influences all riser operating characteristics, including overall solids hold-up, gas and solids mixing and bed-to-wall heat transfer. Similarly, the exit and entry design can significantly affect the riser performance, as mentioned in Chapter 2 and investigated in Chapters 6 and 7. Despite the recognised importance of the exit and entry design, few published preliminary studies of exit and entry effects exist (see Chapter 6). Although a number of studies have measured solids concentrations, mass fluxes and particle velocities near the wall, fundamental wall dynamics are poorly understood. It is assumed in this chapter that wall streamers are distinct from the far more dilute core suspension, with abrupt boundaries between the two regions at any instant. Thus "separated flow" is assumed, with regions of dilute and dense suspension "phases." This approach was discussed in Chapter 5.

In the first part of this chapter, the fundamental dynamics of streamer formation and motion are considered. The cold unit test results clearly demonstrate that there exists a "threshold" below which streamers are no longer detected at the wall, at heights where the flow is close to fully-developed. A mechanism for streamer formation is investigated that accounts for this observation. A detailed account of the streamer motion observed in the cold unit tests is also presented, and plausible mechanistic explanations for the motion are examined. The challenges involved in modelling exit and end effects are considered below, after reviewing the pertinent

experimental results in Chapters 2, 6, and 7.

A number of explanations for observed wall, exit and entry effects are advanced, and critically evaluated. From the discussion it is apparent that fundamental theoretical approaches to modelling these phenomena pose formidable problems. It is proposed that a more pragmatic semi-empirical approach be adopted to include these effects in practical "engineering" models. Irrespective of the approach taken, additional experimentation is required to better understand and correlate these phenomena. Several simple correlations are tentatively advanced, based on the limited number of pilot-scale data measured in this study. These correlations are incorporated in a semi-empirical predictive model described in Chapter 10.

9.1 Riser Wall Layer Dynamics and Wall Streamer Formation

An interesting feature of CFB risers is that streamers form at the walls, despite the very high riser core gas and particle axial velocities, and the relatively large particle fluctuating velocities predicted for the core by the model CIRCOR. One might expect the particles travelling rapidly up the core to simply bounce off the wall at high speed, and continue their upward motion. Indeed, from observing the operation of the cold unit riser in this study, this appears to be the case at lower suspension densities. However, as solids circulation rate, G_s, is increased in the cold unit, one begins to observe thin "wisps" of particles appearing at the wall. These have substantially lower velocities than the core suspension flow. Further increase in G_s results in these wisps intermittently appearing, thickening a little, and falling short distances, before being re-entrained. At yet greater values of G_s, part of the wall is covered with quite dense sheets of particles that often fall distances of $O(1\text{ m})$ before disintegrating.

For streamers to form at the riser wall, particles must (a) reach the wall, and (b) be held at or near the wall for a sufficient time for some particle accumulation to occur. Although these two criteria may appear obvious, there are many situations where they are not satisfied by most particles in the core suspension flow, as discussed below. A simplistic approach would be to assume that inelastic particle-wall collisions cause streamer formation, i.e. particles hit the wall,

lose their component of velocity normal to the wall, and fall downwards. Several modellers have incorporated this assumption in order to "force" streamer formation (e.g. Tsuo and Gidaspow, 1990). Although the energy lost by a particle in a wall collision certainly contributes to streamer formation, it cannot fully explain it. Nor can it explain the absence of streamers at low G_s. Particles that hit the wall do not lose all their kinetic energy normal to the wall, as particle-wall coefficients of restitution, e_w, are not zero. For particles to concentrate at the wall sufficiently for streamers to form, it is reasonable to expect that lateral velocities near the wall would have to decrease by at least an order of magnitude, in comparison to core particle lateral velocities. For wall collisions to cause this, e_w would have to be less than 0.1, which is not the case. In fact, relatively elastic mineral particles, such as sand, lose very little of their lateral velocity in a wall collision, as was clearly evident from viewing cold unit operation in this study.

9.1.1 Particle Trajectory Equations in the Wall Layer

Several studies of particle trajectories in a gas wall layer (Ishii, 1984; Kallio, 1989), have established the importance of shear-induced lift under some conditions. It is proposed that the shear-induced lift force on the particles is generally the major cause of particle accumulation near the wall, often causing streamer formation. To investigate this possibility, the motion of discrete CFB particles in riser vertical gas wall layers is modelled. To calculate the particle trajectories, a number of simplifying assumptions are made. Firstly, it is assumed that the core suspension density is low, corresponding to the conditions at which streamers first begin to form (e.g. case (i): $G_s = 20$ kg/m^{2}s, $U_g = 7.0$ m/s, in Table 8.5). The gas wall layer thickness and velocity profile at these low suspension densities are assumed to be relatively unaffected by the presence of the particles, and are calculated by the Law of the Wall relations, eq. (3.37). The particle trajectories are calculated from a starting position at the outer edge of the buffer layer (i.e. the turbulent core-buffer zone interface, at $y^+ = 30$). Wall layer thicknesses corresponding to $y^+ = 30$ are given in Table 3.7 for fully-developed gas flow in three typical risers. These wall layer thicknesses and typical mean free paths of particles for dilute suspensions, calculated

in Chapter 8 (see Table 8.5), are of similar order of magnitude. As a first approximation, the trajectories of particles in this wall layer are calculated by neglecting collisions with other particles. Clearly, if particles do accumulate at the wall, this assumption is not reasonable. However, the aim of the study is only to establish if and when particles are likely to accumulate at the wall, a necessary precursor to streamer formation.

Drag, lift and gravitational forces act on the particles. For this study, the Saffman (1965) lift force expression, eq. (3.15), is used to calculate the lift on the discrete particle in the absence of an alternative, more appropriate equation. As mentioned in Chapter 3, there is little theoretical basis for using this expression in a turbulent flow wall layer and at $Re_p > 1$. However, Hall (1988) compared measured lift force on particles close to a flat wall with those calculated by the Saffman equation, and concluded that the Saffman expression predicted lift force within a factor of 2 for $Re_p < O(200)$. A number of other particle trajectory models also use the Saffman expression in the wall layer (e.g. Govan *et al.*, 1989; Kallio, 1989).

The wall layer is assumed to be sufficiently thin, compared to the total riser diameter, that wall curvature effects may be ignored for risers of circular cross-section. Thus the particle trajectory equation,

$$m_p \frac{d\mathbf{v}}{dt} = \mathbf{f}_D + \mathbf{f}_L - m_p g \ , \tag{9.1}$$

is divided into z and y components, corresponding to the vertical direction and direction normal to the wall, respectively:

$$\frac{d\mathbf{v}_z}{dt} = \frac{1}{m_p}(\mathbf{f}_{Dz} + \mathbf{f}_{Lz}) - g \ , \tag{9.2}$$

$$\frac{d\mathbf{v}_y}{dt} = \frac{1}{m_p}(\mathbf{f}_{Dy} + \mathbf{f}_{Ly}) \ . \tag{9.3}$$

The x-direction velocity component is assumed to be zero, as it has no effect on the y- or z-components, and does not affect particle accumulation at the wall. The particles are assumed to be spherical. A linear drag approximation is *not* used, as the particle velocity and response time, τ_p, change significantly over the trajectories considered. Thus total drag, $\mathbf{f}_D$, is first calculated by eq. (3.17), and then split into y and z components. The gas flow is assumed to

be only in the vertical direction, and the flow-shear induced lift force on the particle, $\mathbf{f}_L$, due to the gradient in the gas velocity, is directed normal to the wall (Saffman, 1965; Ishii, 1984), i.e. $\mathbf{f}_{Lz}$ is zero, and

$$\mathbf{f}_{Ly} = 6.46\frac{d_p^2}{4}\sqrt{\rho_g \mu_g \frac{d\mathbf{u}_z}{dy}}\ (\mathbf{v}_z - \mathbf{u}_z)\ . \tag{9.4}$$

Note that if the particle leads the gas ($\mathbf{v}_z > \mathbf{u}_z$), then the lift force on the particle is directed towards the wall; the reverse is true for $\mathbf{v}_z < \mathbf{u}_z$. Simple differentiation of the Law of the Wall expressions with respect to y gives the gas velocity gradient, $d\mathbf{u}_z/dy$. Particle rotation effects are assumed negligible, as discussed in Chapter 3 (see also Hinze, 1972; Ishii, 1984). For particles within several particle diameters of the wall, there is a small enhancement of drag on the particle due to wall effects (Rizk and Elghobashi, 1989). However, Kallio (1989) reported that this had little effect on calculated particle trajectories in the wall layer. It is neglected here in view of the likely magnitude of inaccuracies introduced by other assumptions. For example, gas turbulence is likely to affect particle motion in the buffer layer, and trajectories calculated by eqs. (9.2) and (9.3) are only approximations. There is also evidence that particles may be influenced by unsteady gas motion in the viscous sub-layer, as discussed below.

For all trajectories calculated, particles were assumed to start with vertical slip velocity equal to terminal settling velocity, $\mathbf{v}_t$. Correlations for $\mathbf{v}_t$ (Grace, 1986) appear in Table 3.2. The initial lateral velocity of the particle, $\mathbf{v}_y$ at $t = 0$, was varied for each particle size considered. The change in particle velocity due to a collision with the wall was calculated using expressions developed in Chapter 8 for "rebound" particles, i.e. $\mathbf{v}_{yf} = -e_w\mathbf{v}_{yi}$, and $\mathbf{v}_{zf} = \mathbf{v}_{zi} - \mu_w(1 + e_w)\mathbf{v}_{yi}$. Here "$i$" denotes the pre-collision velocity, and "f" the post-collision velocity. For all tests, values for e_w and μ_w were taken as 0.7 and 0.8, respectively. The trajectories of particles that collide with the wall are followed until these particles either escape from the buffer layer, or lose all their lateral velocity, which may occur for very small particles, when $\mathbf{v}_s \approx 0$. This study is distinguished from several earlier particle trajectory studies near walls because typical CFB conditions are specifically assumed, wall collisions are modelled in detail, and particle trajectories following wall collisions are considered.

9.1.2 Solution of the Particle Trajectory Equations

Particle trajectories were calculated by solving four simultaneous ordinary differential equations, eqs. (9.2) and (9.3), and the particle displacements corresponding to these two equations, dz/dt and dy/dt. The equations are solved by the model "WALSTF." The r.h.s. values of the D.E.s are evaluated in subroutine DIFSTF, and the gas velocity profile is determined in subroutine PROFIL. A standard non-proprietary D.E. solver for stiff systems of equations, "LSODE" (Hindmarsh, 1983), was used. The FORTRAN code listing of WALSTF, and all ancillary subroutines (except LSODE) are given in Appendix E. The code is well-documented; definitions of all common block variables are also included in program documentation.

In addition to the input for the riser operating conditions (logical unit 11 input file CBUSE3, Appendix E), the particle diameter, d_p, initial lateral velocity, $\mathbf{v}_{y0}$, and initial starting distance from the wall, y_0, were also defined prior to the model run (logical unit 12 input file CBWAL3, Appendix E).

9.1.3 Calculated Particle Trajectories

Trajectories were calculated for particles in the gas wall layer of the three "typical" risers considered in Chapter 3: (a) $D = 0.15$ m, $T_g = 25$ °C; (b) $D = 0.15$ m, $T_g = 870$ °C; and (c) $D = 4.0$ m, $T_g = 870$ °C. Particles with diameters 40 μm, 230 μm, and 500 μm were considered, all with a particle density of 2700 kg/m^3. These are the same three "representative" particles assumed throughout Chapter 3.

Particle trajectories calculated for a 230 μm particle in the 0.15 m diameter ambient temperature riser are plotted in Figures 9.1 and 9.2. Initial lateral particle velocities of -4, -5 and -6 cm/s, were assumed (curves (i), (ii), and (iii)). The predicted lift force on the particles along their trajectory pathways is given in Figure 9.3. Note that the trajectories are for the centre of the particles. When the particles collide with the wall, their centres are a distance of $d_p/2$ from the wall. When particles first start moving towards the wall, their axial velocities are less than the local axial gas velocity (Figure 9.2(b)). Thus both drag and lift work to reduce

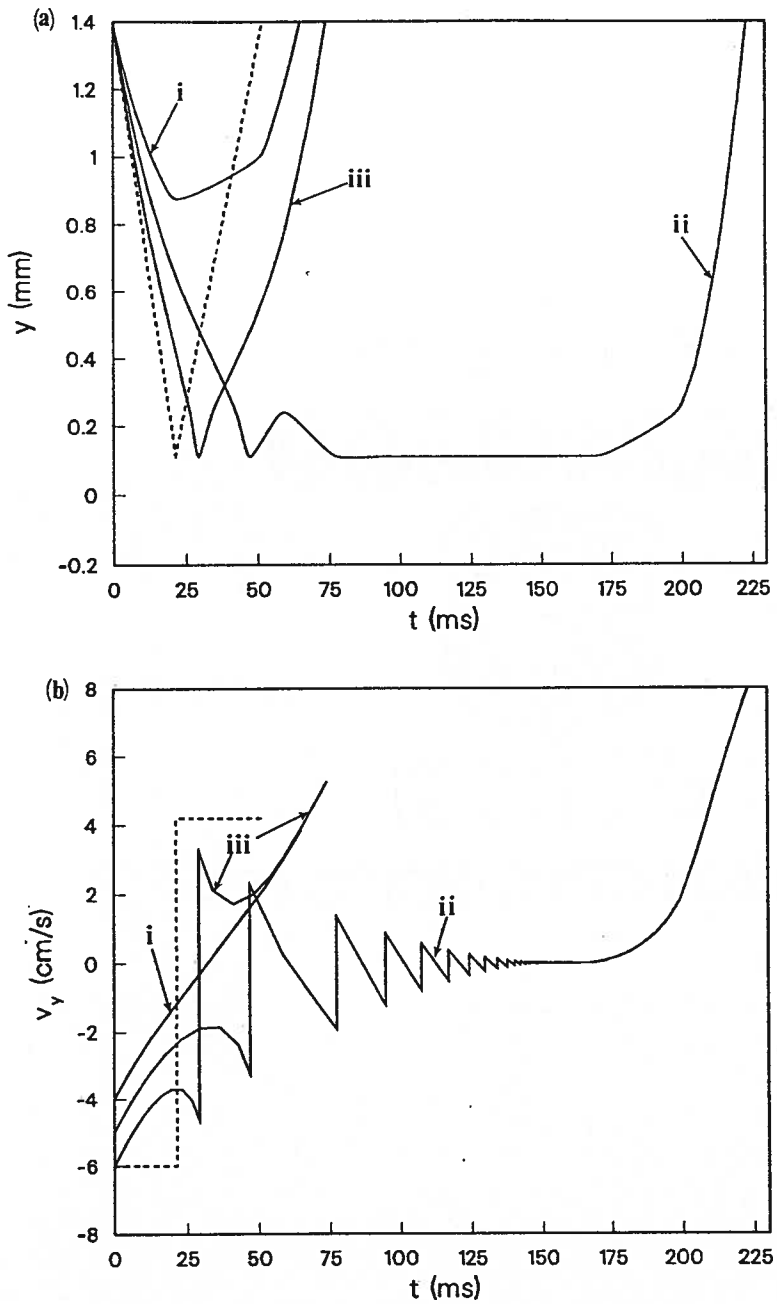

Figure 9.1: Predicted trajectory of a 230 μm diameter particle in the vertical wall layer of a pilot-scale cold unit riser: (a) particle displacement, y, and (b) particle velocity, $\mathbf{v}_y$, perpendicular to the riser wall vs time, t. Initial lateral velocity, $\mathbf{v}_{y0}$: (i) -4 cm/s, (ii) -5 cm/s, (iii) -6 cm/s. Particle trajectory with zero drag and lift given by the dashed line. (Riser conditions: $U_g = 6.5$ m/s, $D = 0.15$ m, $\rho_p = 2700$ kg/m^3, $T_g = 25$ °C, outer edge of buffer layer at $y_0 = 1.4$ mm.)

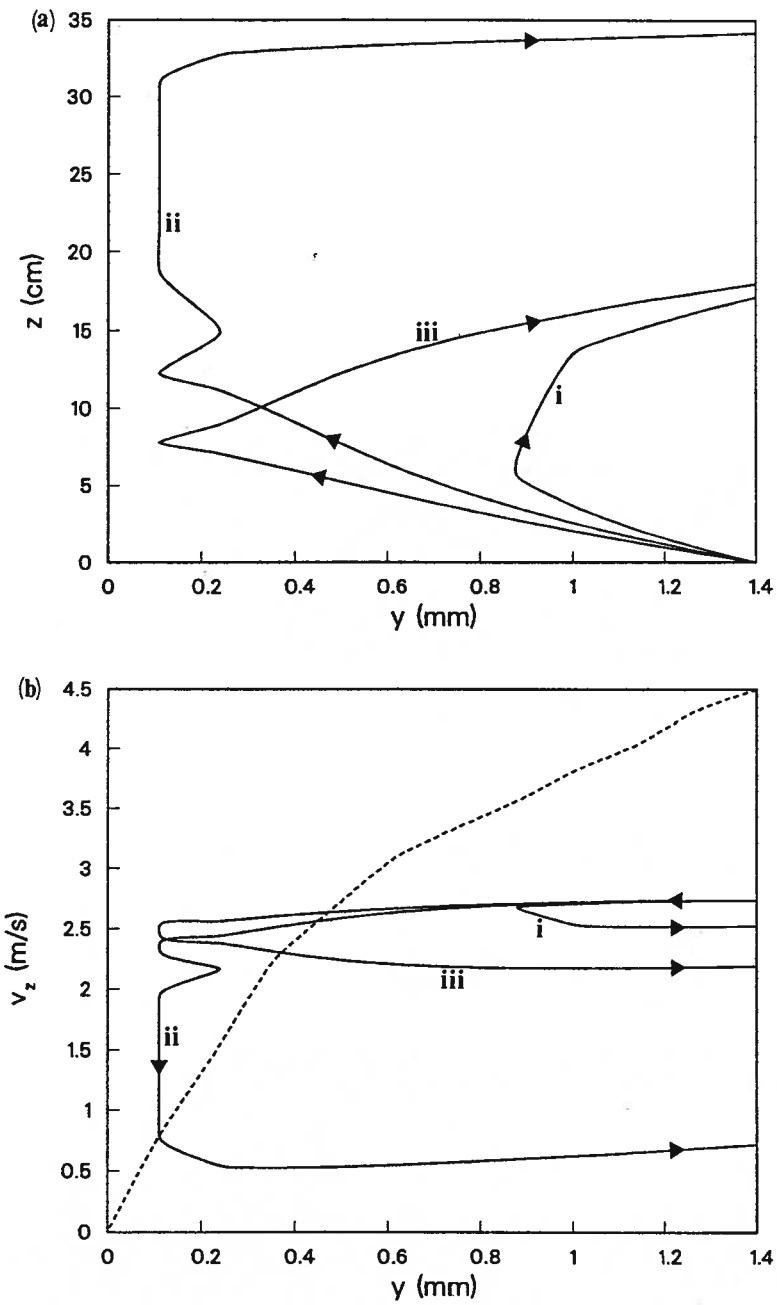

Figure 9.2: Predicted trajectory of a 230 μm diameter particle in the vertical wall layer of a pilot-scale cold unit riser: (a) axial particle displacement, z, and (b) axial particle velocity, v_z, vs lateral distance from the riser wall, y. Initial lateral velocity, v_{y0}: (i) -4 cm/s, (ii) -5 cm/s, (iii) -6 cm/s. Arrows indicate direction of motion. Dashed line is the "Law of the Wall" gas velocity profile. (Riser conditions: $U_g = 6.5$ m/s, $D = 0.15$ m, $\rho_p = 2700$ kg/m^3, $T_g = 25$ °C, outer edge of buffer layer at $y_0 = 1.4$ mm.)

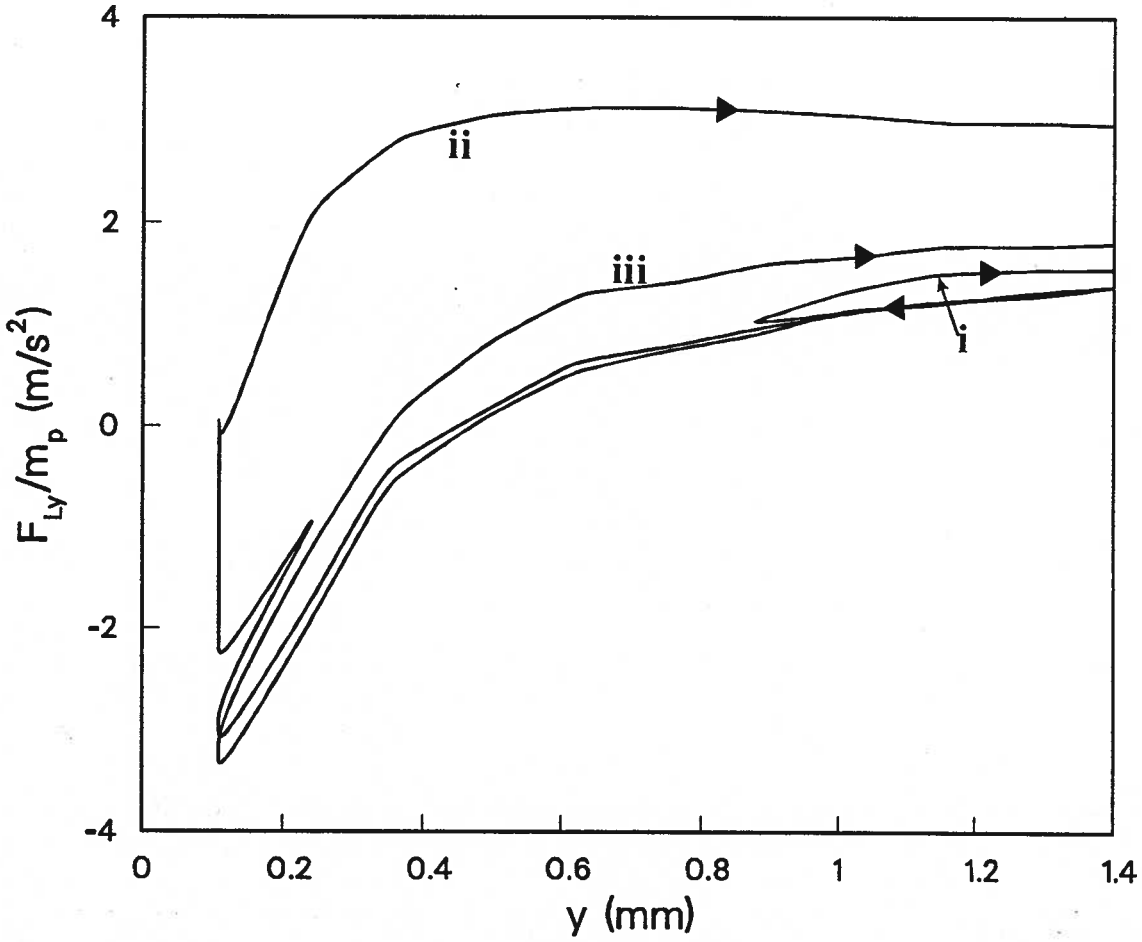

Figure 9.3: Predicted variation of lift force along the trajectory of a 230 μm diameter particle in the vertical wall layer of a pilot-scale cold unit riser. Initial lateral velocity, v_{y0}: (i) -4 cm/s, (ii) -5 cm/s, (iii) -6 cm/s. Arrows indicate direction of motion. (Riser conditions: $U_g = 6.5$ m/s, $D = 0.15$ m, $\rho_p = 2700$ kg/m^3, $T_g = 25$ °C, outer edge of buffer layer at $y_0 = 1.4$ mm.)

the magnitude of the velocity component, $\mathbf{v}_y$, directed towards the wall. The initial lateral velocity, $\mathbf{v}_{y0}$, of -4 cm/s for particle "(i)" is not sufficient for this particle to overcome these forces. It is fully decelerated before reaching the wall, and forced out of the wall layer. In contrast, particle (iii), with a higher initial lateral velocity, overcomes this force, and as it nears the wall its axial velocity exceeds the local gas axial velocity. Thus the sign of the lift force changes, and lift now propels particle (iii) towards the wall (Figures 9.1(b) and 9.3). After particle (iii) collides with the wall, it still leads the gas flow. Lift retards the lateral motion of the particle, and works to hold it in a narrow layer close to the wall. However, particle (iii) still has sufficient momentum after the wall collision to escape from this region, and re-enters the region of positive lift, further from the wall.

Particle (ii) initially behaves like particle (iii). However, after colliding with the wall, it does not have sufficient momentum to overcome the lift force. It is repeatedly driven back to the wall, and makes multiple wall collisions (Figure 9.1). Eventually, it loses all its lateral velocity due to collision energy losses, and it slides upwards along the wall (Figure 9.2). When wall friction has reduced the vertical velocity of the sliding particle below the local gas velocity (evaluated at the particle centre), the lift force changes sign, and the particle is swept away from the wall, and out of the wall layer.

The dashed lines in Figure 9.1 show the trajectory of the particle for $\mathbf{v}_{y0} = -6$ cm/s, without drag or lift force effects, but including the velocity change of the wall collision. (Almost identical pathways were also obtained for $\mathbf{v}_{y0} = -4$ cm/s and -5 cm/s, when lift and drag effects were excluded.) These results support the earlier assertion that inelastic wall collisions cannot solely explain the retention of particles at the wall. In Figure 9.3, the magnitude of the lateral lift force is divided by the particle mass for direct comparison with the magnitude of gravitational effects. Lateral accelerations due to lift acting close to the wall are about 25% of axial gravitational acceleration, for the conditions considered. Lateral drag ($\mathbf{f}_{Dy}$) was an order of magnitude less than lift for this example. Clearly, lift force on particles near the wall of a riser can be significant, and should be incorporated in comprehensive riser models.

A possible mechanism for streamer formation may be established by considering the change in concentration of a cloud of particles projected towards the wall, assuming these particles have trajectories similar to those shown in Figures 9.1 and 9.2. A substantial reduction in the lateral velocity of a portion of these particles is predicted to occur close to the wall. This results in an increase in particle concentration in the cloud. This increase is greatest in a thin layer next to the wall, the region of maximum gas velocity gradient and lift force. It is thus proposed that streamers nucleate when a fraction of the particles, with appropriate initial lateral velocities and sizes, concentrate within a distance of several particle diameters from the wall, due to the effects of drag and lift force, and energy lost in the wall collision. Other particles, with individual lateral velocities that are too great for their trajectories to be significantly influenced by drag and lift near the wall, begin to collide with these particle close to the wall. The energy and lateral velocity lost due to these collisions further increases the particle concentration of the wall layer.

Note that the particle concentration close to the wall need not be very high before the frequency of particle interactions becomes significant. This is evident from typical particle separations in denser suspensions. Consider a dense-packed bed of uniformly-sized spherical particles. The voidage and average distance between the centres of the particles in this bed are approximately 0.26 and d_p, respectively, assuming hexagonal close packing. If this bed is then uniformly expanded to a voidage of 0.9, the mean separation of the particle centres becomes approximately $2d_p$ (i.e. $d_p(.74/.1)^{1/3}$), and at a voidage of 0.97 the separation is still only $3d_p$. These separations correspond to mean free paths, Λ, between collisions of order d_p. For example, for the uniform spheres in this example, $\Lambda \approx 5d_p$ at $\epsilon_g = 0.97$ (Chapman and Cowling, 1970). Wall streamers typically have voidages of 0.9 or less (Chapters 2 and 6).

The concentration increase of particles in a thin wall layer only explains the "nucleation" of streamers. It does not necessarily ensure that layers of particles will commence falling down the wall. The discrete particle (ii) axial velocity profile in Figure 9.2(b) suggests that even discrete particles that lose all their lateral velocity, and slide along the wall, will be entrained

back into the core flow before beginning to fall, due to the change in direction of lift. Streamer downwards motion may be explained by noting that the lift force on individual particles in a sheet of particles is substantially less than that on a lone discrete particle. Hall (1988) measured reductions of almost an order of magnitude in the lift force on a particle at a flat solid boundary, when other particles were placed nearby.

The qualitatively described proposed mechanisms for particle concentration increase in a thin wall layer and the commencement of downward motion of this layer are consistent with a threshold condition, below which wall streamers are not observed, as detected in experimental tests. For an improved fundamental understanding of particle re-entrainment from riser walls, the dynamics of the turbulent shear layer at the wall must be considered. A key feature of turbulent wall layers, that accounts for much of the turbulent energy production in the entire flow, is the phenomena of turbulent bursting in the wall layer (Kline *et al.*, 1967; Heidrick *et al.*, 1977). Rashidi *et al.* (1990) propose that particles are "ejected" from the wall by these turbulent bursts. They found that the particle ejection rate was significantly reduced when the particles lay entirely within the viscous sub-layer. In the cold unit glass bead tests, this was the case for $U_g = 6.5$ m/s, but not for the thinner sub-layer at $U_g = 9.0$ m/s. Recall, that no streamers were observed in the fully-developed flow regions of the riser in the $U_g = 9.0$ m/s tests. Unfortunately, the limited understanding of the turbulent burst process (Heidrick *et al.*, 1977; Rashidi *et al.*, 1990) precludes detailed quantitative modelling of particle re-entrainment from turbulent wall layers, and necessitates empirical approaches for predicting such phenomena.

The extent of concentration of particles in a thin layer close to the wall may be estimated by comparing the actual time spent in that region with the time the particles would have spent there if drag and lift did not influence their velocity. Assume that the thin "wall layer" region thickness is $2d_p$. For particle (iii) in Figure 9.1(a), the actual time spent within $2d_p$ of the wall is approximately 30 ms. Were the particle to experience no lift or drag, *and* collide elastically with the wall, this time would be 15 ms. Thus the particle concentration in the wall layer approximately doubles. A similar analysis for the particle (ii) trajectory predicts the

concentration of these particles to increase by a factor of approximately 10 (200 ms vs. 20 ms).

The trajectory results in Figures 9.1, 9.2 and 9.3 illustrate the proposed concepts of streamer formation. However, it is important to note that the particle trajectories calculated in this study were strongly dependent on initial *lateral* and *axial* velocities and particle size. For the 230 μm diameter cold unit trajectories discussed, significant concentration of the particles at the wall was only predicted for initial lateral velocities varying from 0.045 to 0.055 m/s, i.e. over a narrow range of 0.01 m/s. For the 40 μm particles in the cold unit, an order of magnitude particle concentration increase near the wall was predicted over the much wider range of 0.03 to 0.22 m/s, for initial axial slip velocities equal to $\mathbf{v}_t$. This suggests that smaller particles in a wide PSD particle mixture are the primary instigators of streamer formation in cold pilot-scale units. For 500 μm particles, no range of particle lateral velocities was found at which the particles were slowed significantly close to the wall, given the assumed initial vertical velocity.

The trajectory results are consistent with reported particle measurements near the wall in bench-scale vertical gas-solid suspension flow experiments. Using a laser Doppler technique, Lee and Durst (1982) measured a particle-free region close to the wall when pneumatically conveying both 400 and 800 μm diameter glass beads. Axial velocities of these particles were less than the gas velocity up to very close to the wall, suggesting that the lift force was predominantly directed away from the wall. However, for 100 and 200 μm glass beads, they measured a cross-over in the axial velocity profiles near the wall, and detected particles at the wall. As in this study, Lee and Durst attributed the measured trends to shear flow-induced lift force. Tsuji *et al.* (1984) also measured a cross-over in axial velocity profiles for smaller diameter particles (see Chapter 3).

The calculated trajectories indicate that particles are more likely to accumulate at the wall if they initially approach the wall with axial velocities greater than the local gas velocity, since this causes the lift force to be towards the wall. The calculations further suggest that larger particles, with lower axial velocities, are less likely to form streamers than smaller particles, *providing* that the smaller particles have sufficient lateral velocity to reach the thin region of

wall-directed lift. (However, once streamers form, the larger particles may play a key role in their growth, as discussed below.) The cold unit experimental test results indicate that streamer formation is more likely to occur as G_s is increased, and/or U_g is decreased. This may be explained by the streamer formation mechanism described. An increase in G_s results in higher suspension densities in the core of the riser, higher fluxes of particles out to the wall, and thus a greater probability of streamers nucleating. Prior to streamer formation, increasing G_s may also flatten the particle axial velocity profile due to increased particle "viscous" shear across the riser, thereby increasing the width of the wall region where the incoming core particles lead the gas. A decrease in U_g raises the core suspension density and decreases the shear and core-directed lift force on slowed particles in nucleating streamers close to the wall. This reduction in shear and lift forces may lower the threshold concentration required for streamers to begin falling. The particles may also modulate the gas velocity gradient and flow characteristics at the wall, though these effects are not well understood.

This discussion of particle trajectories has applied thus far to pilot-scale cold unit risers. Calculated typical wall shear layer thicknesses for larger, ambient temperature riser operations are not significantly greater than in the pilot-scale units. However, as shown in Table 3.7, order of magnitude increases in wall layer thicknesses are expected for high temperature risers, compared to cold units. Correspondingly, gas velocity gradients near the wall are reduced at high temperature by an order of magnitude.

Figure 9.4 gives the trajectory of a 230 μm particle starting at the outer edge of the buffer layer in a 4.0 m diameter riser operating at 850 °C and U_g = 7.0 m/s. The initial particle lateral velocity is -14 cm/s, and the initial axial particle slip velocity is again assumed to equal the particle terminal velocity. In the wider wall shear layer, the particle has more time to respond to the changing gas velocity as it moves towards the wall. Consequently, although the particle still leads the gas near the wall, the difference between the particle axial velocity and gas velocity is not as great, compared to the pilot-scale cold unit. The magnitude of the lift force near the wall is less than 5% of the gravitational force, and is comparable in magnitude

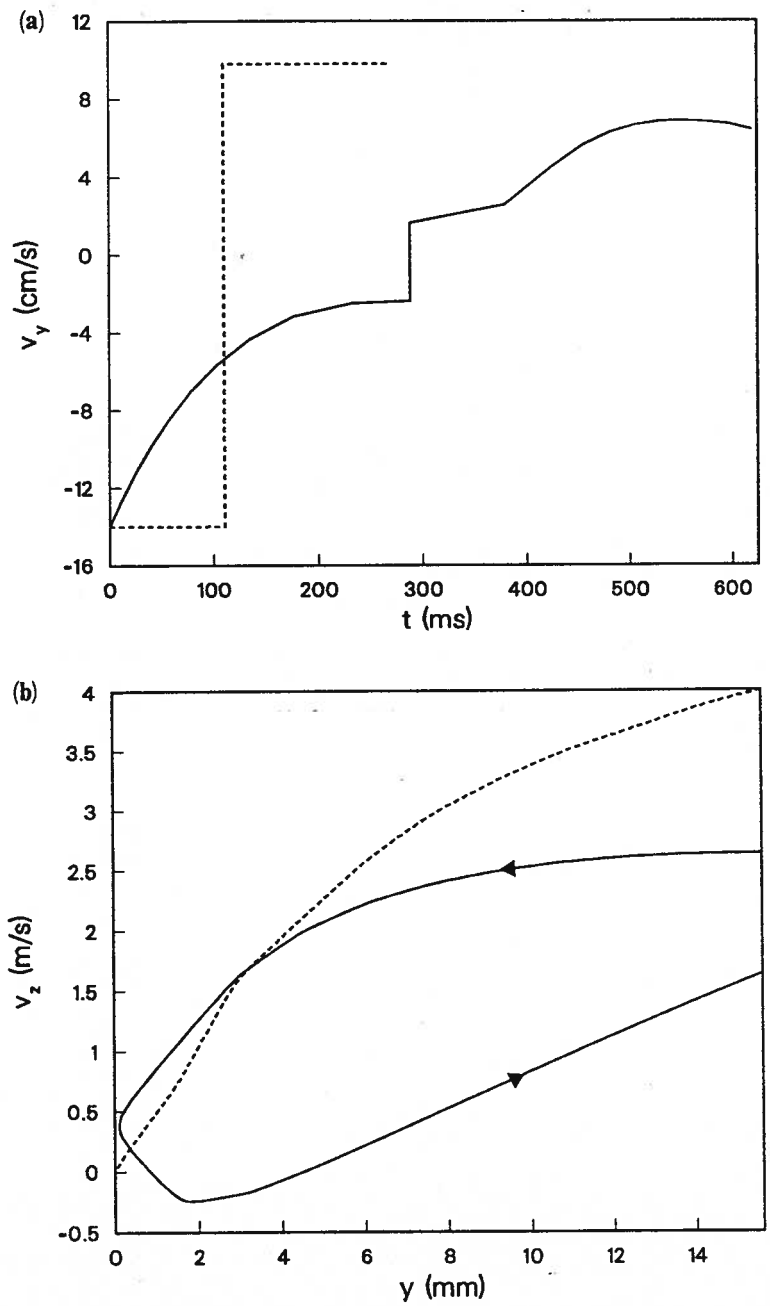

Figure 9.4: Predicted trajectory of a 230 μm diameter particle in the vertical wall layer of a commercial CFB boiler: (a) particle velocity perpendicular to the wall, $\mathbf{v}_y$, vs time, t, and (b) axial particle velocity, $\mathbf{v}_z$ vs displacement from the wall, y. Initial lateral velocity, $\mathbf{v}_{y0} = -14$ cm/s. Arrows indicate direction of motion. Particle trajectory with zero drag and lift given by the dashed line in (a). Gas velocity profile given by dashed line in (b). (Riser conditions: $U_g = 6.5$ m/s, $D = 4.0$ m, $\rho_p = 2700$ kg/m^3, $T_g = 870$ °C, outer edge of buffer layer at $y_0 = 15.6$ mm.)

to the lateral component of drag on the particle. For the assumed initial axial velocity, and starting distance from the wall, no initial lateral velocities were found where the particle made multiple collisions with the wall.

Although some concentration increase is expected near the wall of the 230 μm particles with the high temperature trajectory in Figure 9.4, it is not nearly as substantial as in the cold unit. Also the predicted lower magnitudes in lift force increase the relative importance of the inelasticity of the wall collision and drag for reducing particle velocities near the wall. Note that a negative axial velocity is predicted for the 230 μm particle close to the wall. This result applied also for the 500 μm particles in the high temperature wall layer, although it did not occur at low temperature. It is *not* associated with a particle concentration increase, and does not indicate that dense streamers will form. It indicates that downflow of relatively dilute suspension at the wall may frequently occur in high temperature risers, but is unlikely to be detected at ambient temperatures. This observation does not diminish the importance of streamers in high temperature riser dynamics. When streamers are present, they account for the majority of the solids mass downflux in the riser, due to their much greater suspension density than the dilute suspension.

Unrealistically high initial lateral velocities of $O(-5$ m/s) were required for the 40 μm particles to reach the wall in the high temperature trajectory calculations, due to the effects of drag. As mentioned, the effect of particle collision across the wall layer was neglected in the trajectory calculations. For the thicker high temperature wall layers, neglect of collisions may not be reasonable, considering the mean free paths of particles, presented in Chapter 8. Indeed, it appears that collisions in the high temperature wall layer may play an important role in increasing the axial velocity of particles close to the wall, and projecting the smaller particles towards the wall. As discussed above, particles that approach the wall with higher axial velocities are more greatly influenced by lift towards the wall, and thus more likely to nucleate streamers. The greater response of small particles to the gas flow at high temperature demonstrates that it is not necessarily the *smallest* fraction that most contributes to streamer

formation, but rather the smaller fractions that have sufficient inertia to reach the wall.

The lower gas velocity gradient at the wall in high temperature risers, and associated reduced lift force on the particles, suggests that particle concentrations do not have to be as high for streamers to nucleate and begin falling at high temperatures, compared to ambient temperatures. However, the lower gas velocity gradient also probably reduces the concentration close to the wall of particles projected towards the wall from the core. Consequently, it is unclear whether streamers are more or less likely to form in high temperature risers, compared to ambient temperature units.

Substantial changes in particle velocity near the riser wall, over distances comparable to one mean free path, were often predicted, at both ambient and elevated temperatures. The changes were strongly dependent on particle size, mass and initial velocity. Similar results are also likely to apply at other locations in the riser where there are large gas velocity gradients, i.e. streamer-dilute suspension interfaces, and near the surface of larger "clusters." It appears that the basic assumptions of the continuum and granular kinetic theories for modelling the particle phase behaviour, discussed in Chapter 4, do not strictly apply in these shear layers, at least at low riser suspension densities. The particles do not behave as a continuum in these layers, and their mean and r.m.s. fluctuating velocity cannot be assumed to reasonably represent the behaviour of all the particles. Multi-dimensional two-fluid continuum models may not adequately predict the relatively abrupt transitions in particle concentration and velocity between dense and dilute suspension regions, often detected in riser flows. The transitions from core upflow to wall downflow predicted by continuum riser models under development (Gidaspow *et al.*, 1990; Tsuo and Gidaspow, 1990; Pita and Sundaresan, 1991) are very gradual, and occur over radial distances comparable to $0.25R$. Measured transition region thicknesses are typically at least two orders of magnitude less than this (Chapter 2). For this reason, the alternative modelling approach of dividing the riser into core and wall zones was suggested in Chapter 5. If continuum models are applied across the full riser cross-section, empirical corrections for non-continuum effects may be required to obtain accurate predictions. Clearly, a fundamental approach to wall

layer dynamics modelling, whereby PSD, velocity distributions, particle-particle collisions, and gas velocity profile changes due to the particles are all considered, is very complex.

In the riser core flow model presented in Chapter 8, expressions for τ_r and D_{kr} at the core boundary were proposed for particles rebounding from the bare riser wall, neglecting the effects of drag and lift near the wall. As already mentioned, once wall streamers form, they dominate rebound wall effects on the core. Thus the accuracy of τ_r and D_{kr} predictions is only important when there is a negligible concentration of wall streamers. Particles held close to the wall by lift for a period significantly longer than would occur without lift effects lose more axial velocity (Figure 9.2(b)), and thus exert greater shear on the core flow when they return. Discrete particle trajectory calculations indicate that the majority of the glass beads used in the PSD tests were not greatly influenced by drag and lift in the wall layer. Thus, if the smaller fraction of particles, which did concentrate at the wall, did not significantly interfere with other particles rebounding from the wall, then τ_r and D_{kr} were probably reasonably estimated. This appears to be the case for the condition A and B simulations (G_s = 20 kg/m^{2}s). However, for condition D, thin "wisps" of particles were occasionally observed at the wall, suggesting that the riser was operating close to the condition of streamer formation, and interference of "rebound" particles reaching the wall was significant. Thus the predicted τ_r for condition D may have been low, explaining the discrepancy between the measured and predicted apparent suspension density in this case. Effects of wall layer drag and lift on the large particles used in the Nakamura and Capes (1976) experiments were predicted to be negligible by the particle trajectory model.

9.2 Wall Streamers

A preliminary discussion of wall streamer motion was included in Chapter 2. A more detailed description of streamer motion is presented here, based on cold unit visual observations. Given the similarity of wall solids flux measurements and capacitance probe traces from various cold unit risers and CFB combustors, it is likely that the transient motion of wall streamers in all

units is similar to the qualitatively described motion.

9.2.1 Transient Streamer Motion, Particle Capture and Particle Re-Entrainment

Wall streamers do not fall as continuous flat sheets. Intermittently localised regions of the streamers are disrupted; the motion and break-up of streamers appears to be a fluctuating stochastic process. The power spectra of capacitance probe signals are relatively broad, and no dominant break-up frequencies have been detected (Brereton, 1987). Steps 1 to 6 in Figure 9.5 illustrate the observed process of streamer disruption in the cold unit tests. Initially the streamer-core interface appears relatively undisturbed (Step 1). These flat streamers accelerate rapidly, from about - 0.5 m/s to between -1.5 and -3 m/s, over a period of order 1.0 s. Suddenly, a "bulge" in the flat streamer forms in a localised region. Although not visually discernable, a perturbation to the flat streamer surface (Step 2) undoubtedly precedes the observed bulge. The bulge then grows quickly, and protrudes into the core of the riser, often by a distance comparable to the initial streamer thickness. It also decelerates rapidly, its rapid growth probably due to particles falling into the disrupted region from above (Step 4). Some falling particles also divert around the disrupted area (Step 4A), thereby migrating around the riser circumference. Particles that were ahead of the disruption continue their rapid downward motion, exposing bare riser wall to dilute suspension upflow immediately below the disrupted area. As the bulge protrudes further into the riser core, particles are stripped of the leading "wavefront" of the bulge into the core flow at a high rate. As abruptly as the bulge forms, and holds up, the almost static particles in the leading edge of the bulge re-commence downward motion, passing over the region of exposed wall below (Steps 5 and 6). The period that the riser wall is exposed by a disruption is typically $O(0.5\text{ s})$. However, this period varies substantially with each disruption, and the bulges may stay relatively static at the wall, or even slowly climb up the wall, for a period up to $O(2\text{ s})$.

The faster falling streamers appear more likely to disrupt. With the abrupt exit in place, sheets of particles falling down the walls from the riser roof were not observed to disrupt until

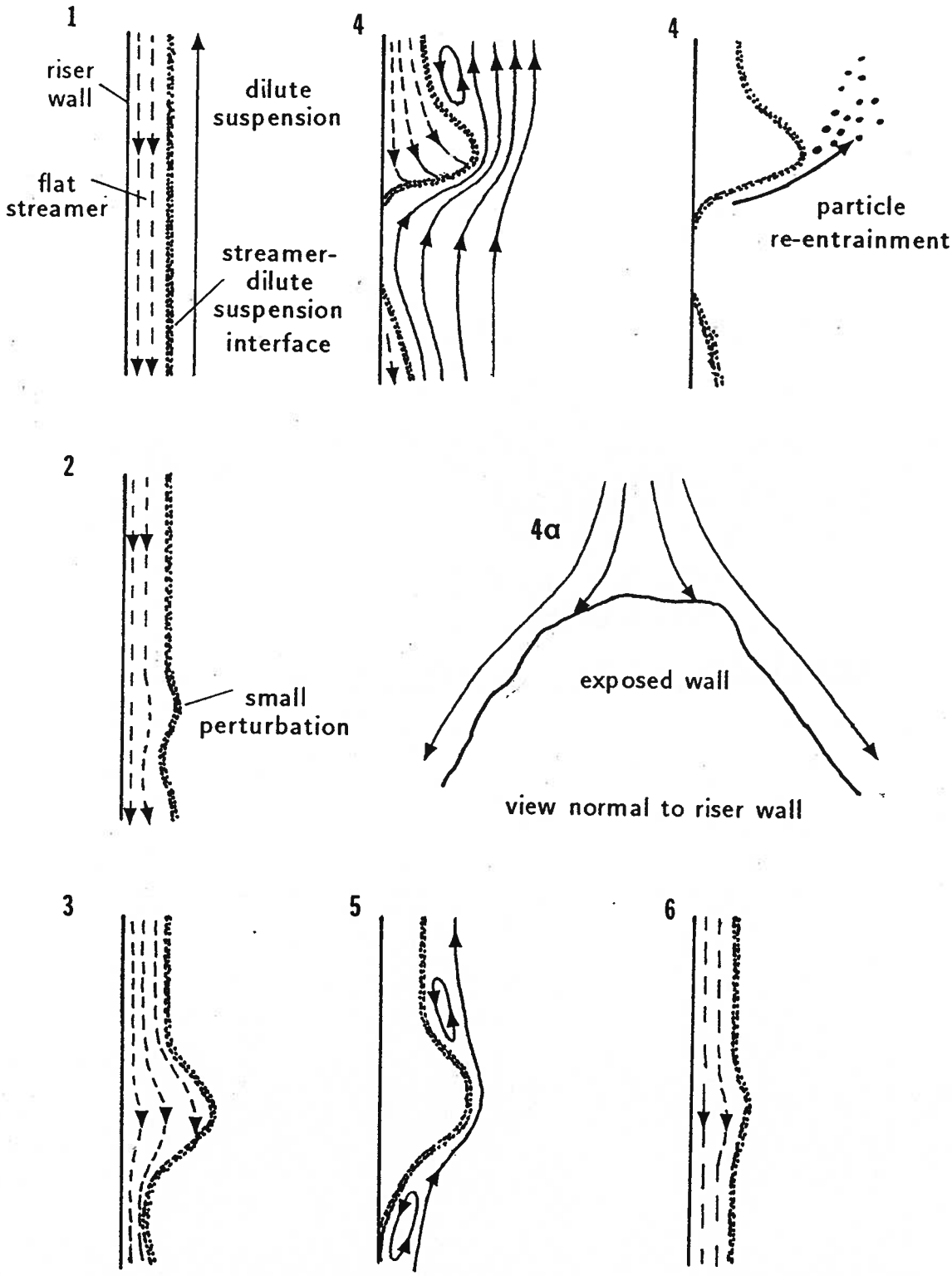

Figure 9.5: Illustration of the intermittent process of wall streamer disruption observed in cold unit tests. Dashed lines: proposed streamer particle streamlines. Thin solid lines: proposed gas streamlines in dilute suspension.

they had accelerated over a distance of about 0.5 m from the roof. The proposed streamlines shown in Figure 9.5 suggest a possible explanation for the described cycle of bulge growth, hold up, and re-commencement of downward motion. With the initial formation of a bulge, core gas flow separation at the rear of the bulge may occur, thus greatly increasing form drag, and causing the rapid deceleration of the solids in the disrupted region. As faster falling solids feed into the bulge from above, it grows and protrudes further into the core. Its density also increases rapidly as particles compact in the bulge. The leading wavefront becomes steeper, its mass increases, and less gas is able to percolate through the streamer. The core gas flow must divert around an increasingly larger protrusion, and it may even eventually separate from the wall at the leading wavefront edge. Particles then begin to fall over the exposed riser wall. This tentatively proposed mechanism does not explain "bulge" initiation, discussed below. Note that if streamers are relatively thick, "necking" of the streamers below the disruption is likely, without bare wall being exposed to core flow, i.e. Step 4 in Figure 9.5 would be by-passed.

Many of the properties of CFB risers may be related to the complex stochastic motion of the wall streamers. Streamer velocity, density, and lateral exchange of particles between the predominantly rapid core upflow and denser wall downflow are all likely to depend on the transient motion of streamers. The acceleration of particle streamers prior to disruption indicates that streamer velocities would be substantially higher if not for the intermittent rapid deceleration at local disruptions. Disruptions also significantly increase the shear force on the core gas flow, as discussed in Chapter 8. The observed intermittent entrainment of particles from the leading wavefront of the streamer disruptions into the core appears to be a major mechanism for particle re-entrainment. This mechanism projects particles much further into the core flow than would occur with "diffusive" re-entrainment. Transient streamer motion also results in a substantial fraction of the wall being exposed to dilute core suspension flow, even at relatively high suspension densities. This has important implications for bed-to-wall heat transfer in CFB boilers.

In the same cold unit riser as used in this study, Wu (1989) estimated fractions of time

local regions of riser wall were exposed to dilute suspension flow and denser suspension of solids volume fraction ranging from 0.1 to 0.5. Wu's tests were performed at $U_g = 7.0$ m/s with "Ottawa" silica sand. His results, reproduced in Figure 9.6, show that the average density of streamers increases significantly with the riser apparent suspension density. A substantial fraction of wall is exposed to dilute suspension up to relatively high suspension densities, and the streamer voidages rarely approach the loose-packed value. These results agree with Chapter 6 measurements. Thus local streamer velocities, voidages and wall coverage not only vary temporally, but the average streamer voidage and wall coverage may also vary substantially with G_s and U_g.

The intermittent motion of streamers affects streamer voidages. Average streamer voidages are greater than the loose-packed voidage because streamers go through cycles of compacting just above the disruptions, and expanding as they accelerate between disruptions. As mentioned in the discussion on streamer formation, particles in streamers with a voidage of 0.9 are separated by approximately $2d_p$, where d_p is an average particle size. A falling streamer may therefore be expected to "cushion" core particles that impact with the streamer surface. An average size core particle that rebounds vigorously from the bare wall may, in comparison, lose much of this energy when it hits the streamer surface, due to this cushioning effect, involving a large number of low energy scattering collisions within the streamer. Larger (or denser) particles probably embed themselves in the streamer due to their greater inertia than the average size particles at the streamer surface. In contrast, if small particles hit mean-size particles at the streamer surface they are likely to rebound into the riser core. Most capture of energetic small particles probably occurs when these particles successfully pass through the interstices between streamer particles at the streamer surface. Hence, the larger particles that reach the streamer surface from the core may be more successfully captured by the streamers than the smaller particles. As discussed in Chapter 6, this is a likely explanation for the relatively high proportion of large particles measured at the cold unit riser wall.

Certainly not all particles that reach the streamer surface from the core will be captured;

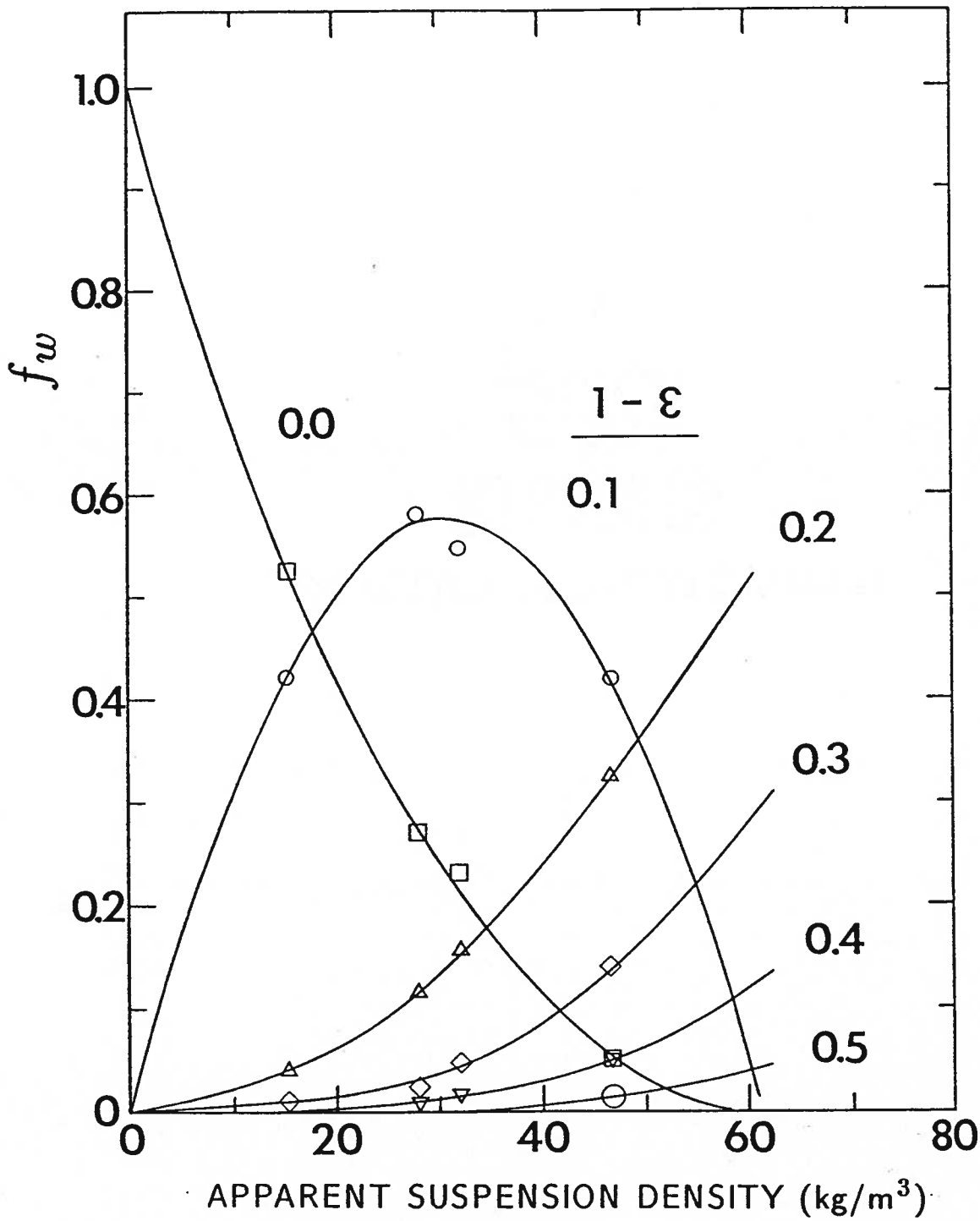

Figure 9.6: Time fraction, f_w, of wall coverage by streamers of different voidages, ϵ_g, versus apparent suspension density, estimated by Wu (1989). (U_g = 7.0 m/s, T_g = 25 °C, d_p = 170 μm, ρ_p = 2650 kg/m^3) (At $1 - \epsilon_g = 0$ the wall is exposed to dilute suspension upflow.)

some of these particles will rebound back into the core. The proportion of rebound particles is likely to increase as the relative velocities between the core particles and streamers increases, i.e. as U_g increases. However, unlike the densely packed annulus in a spouted bed, the assemblage of particles in a streamer is likely to capture a significant fraction of the core particles that reach the core-streamer interface. Whereas particles may be dislodged from the annulus of a spouted bed by impinging core particles (Lefroy and Davidson, 1969), this mechanism is unlikely to be significant at the riser core-streamer interface because the particles in the higher voidage streamers are generally not in contact. In addition to the capture of particles by lateral transfer across the vertical core-streamer interface, it is possible that some particles will intermittently be captured in the leading wavefront of a disruption. However, the rapid compaction of particles in this wavefront, and the high local gas velocity tangentially across it, suggest that capture rates there may be relatively small compared to capture elsewhere on the streamer surface.

Although streamer voidages suggest that particles are rarely in direct contact with one another in the streamer, the average particle spacing is still several orders of magnitude less than in the core. In view of the substantial interaction between particles of different sizes predicted for the dilute core (Chapter 8), it appears likely that particles in streamers all move with similar velocities, i.e. the upward "percolation" of small particles relative to the bulk of the particles in the streamer is likely negligible. Thus motion of the streamers can be assumed to be independent of the PSD.

In addition to the stages of streamer disruption shown in Figure 9.5, it is possible that thick streamers may bulge so rapidly into the core flow when disrupted, that "clumps" of the protrusion are sheared off, as well as individual particles. This may be one mechanism by which "clusters" form. It may also be an indicator of the transition from a well-defined core-annulus fast fluidised bed structure to a turbulent fluidised bed. In small diameter risers, disruptions to the wall layer may bridge across the full riser diameter as G_s is increased, corresponding to the onset of "choking."

Though the assumption that the riser is isothermal is often reasonable for most of the riser

volume at elevated temperatures (Chapter 4), significant temperature gradients may exist in a narrow layer at the wall (Leckner, 1991). Given the expected differences in ambient and elevated temperature wall layer thicknesses, temperature gradient may need to be considered in CFB combustor models.

9.2.2 Instability of Wall Streamers

There is poor understanding of the instability mechanisms that cause wall streamer disruption. Although there are substantial difficulties involved with a fundamental stability study of streamer motion, it is worth considering several plausible instability mechanisms to establish possible influences on the rates of streamer disruption and particle re-entrainment.

The study of instabilities in laminar flows generally results in challenging mathematical and numerical problems. The standard approach, that has produced successful results for several flows, including single phase boundary layers, is the "method of small disturbances" or "method of normal modes" (Schlichting, 1968). A small perturbation to the laminar flow is assumed to occur. For incompressible Newtonian fluids, the behaviour of the flow following the perturbation is described by the Orr-Sommerfeld equation, the cornerstone equation for linear stability of viscous flows. This equation is derived from the Navier-Stokes equation. If the perturbation grows, then the flow is unstable. The Orr-Sommerfeld equation is difficult to solve, even by numerical methods, and frequently the inviscid form of this equation, the Rayleigh equation, is assumed.

Two general instability mechanisms may be identified as possible causes of streamer disruptions; boundary layer instability and shear layer instability. The well-known phenomenon of boundary layer instability is first considered. When a fluid flows parallel to a flat plate, instabilities in the fluid laminar boundary layer at the surface of the plate begin to appear a finite distance, x, from the plate's leading edge. This distance can be predicted from linear stability analysis, and corresponds to a critical value of the boundary layer Reynolds number, $Re_x = U_\infty x/\nu$, where U_∞ is the undisturbed fluid velocity distant from the plate. It is also

known that a sufficient condition for instability to occur in the flat-plate boundary layer is an inflection in the velocity gradient of the fluid in the boundary layer. However, the instabilities take a finite time to grow, and the point at which instabilities first occur is upstream of the measured transition point to turbulent flow. The stability analysis only establishes if the flow is initially unstable to a small perturbation, and gives no indication if or how fast the instability may grow beyond the initial stage, as non-linear effects become important. This is a limitation of all linear stability analyses.

If the wall streamers are assumed to be a pseudo-fluid with no surface tension, then there are some superficial similarities between the streamers and a fluid boundary layer. There will certainly be friction on the streamer particles in contact with the wall as they fall. However, unlike the fluid-wall boundary, substantial slip may occur at the particle-wall interface. In addition, as the streamer accelerates, both its density and pseudo- or solids-phase viscosity are likely to change significantly. Thus the streamer is not a constant density and viscosity fluid. At the core interface to the streamer, there is also a large shear on the streamer due to gas shear and core particle impingement and capture. Although there may be a significant lateral velocity gradient in the wall streamer axial velocity profile, it does not involve a point of inflection, characteristic of instability in boundary layers. Rather, it is probably an extremum, as the magnitude of the downward velocity within the streamer may be higher than at either the wall or core interfaces. In view of these differences, a *direct* analogy between a boundary layer and a falling streamer is not valid.

If a "boundary layer" transition in the streamer does result in the observed streamer disruptions, then it may be expected that the roughness of the wall has some effect on the rate of disruption. However, again a direct fluid analogy is not possible. When relatively dense sheets of particles fall over a very rough wall (e.g. refractory in a CFBC boiler) powder mechanics studies (Brown and Richards, 1970) suggest that a vertical slip plane may occur several particle diameters from the wall. Thus the bulk of the streamer falls down a "wall" with an effective roughness equivalent to the size of the particles in the suspension, and the effect of

wall roughness may not be as great as expected.

Streamer instability may alternatively be due to the shear in the core-streamer interfacial region. The simplest representation of this shear layer is a step change in particle velocity and concentration at a vertical streamer-core interface. If the streamers and core suspension are treated as unbounded inviscid fluids with zero surface tension, in steady parallel flow, then the "step-change" interfacial shear layer is predicted to always be unstable, irrespective of the relative axial velocities of the core and streamers. This is Kelvin-Helmholtz instability (Yih, 1965; Hewitt and Hall-Taylor, 1970; Drazin and Reid, 1981). Bierl *et al.* (1980) proposed this mechanism for instability of gas jets in two-phase gas-solid flows. Although it is known that very high shear rates, such as at the streamer-core interface, are often associated with flow instabilities, this treatment of the core-streamer interfacial shear layer is an oversimplification. The streamer density and velocity are not expected to be constant at the interface. Also the higher density streamer "fluid" and low density core "fluid" are not unbounded, and the thickness of the shear layer between these fluids is finite. Finally, the expected capture of core particles by the streamers suggests non-convective momentum transfer effects, i.e. viscosity may need to be considered. In instability studies, such variations from ideal steady inviscid flow may have a profound effect on the results. Drazin and Reid (1980) show that an inviscid shear layer of finite thickness may be unstable or stable, depending on its thickness, and the exact form of the velocity profile across the shear layer. They also point out that, although viscosity generally dissipates the energy of disturbances and stabilises flows, momentum diffusion can make parallel shear flows unstable, despite predicted stability of the equivalent inviscid flow.

A phenomenon that has similarities to the observed instability of streamers is the instability of the liquid annulus in gas-liquid annular flow (Dukler, 1972). Although wall no-slip condition and surface tension effects obviously influence the growth and behaviour of the disturbance waves in a liquid annulus, it is possible that the initial cause of instability of particle streamers and the liquid annulus are similar. Hewitt and Hall-Taylor (1970) presented an inviscid stability analysis for bounded steady gas-liquid vertical annular flow, and also discussed results of more

realistic stability analyses for gas-liquid flow, based on the Orr-Sommerfeld equation. They reported inconclusive results, even for the more detailed approaches. Despite many theoretical gas-liquid flow investigations of the disruption of the liquid layer, and associated droplet re-entrainment and flooding, predictions of these phenomena are still essentially empirical (e.g. Wallis, 1970a, 1970b; McCoy and Hanratty, 1977; Whalley and McQuillan, 1985; Martin and Azzopardi, 1985; Moalem Maron and Brauner, 1987; Binder and Hanratty, 1991).

In comparison to gas-liquid flow, there are many more difficulties in applying linear stability theory to predict streamer instability, including unsteady velocity, density and viscosity, and the basic problem of defining the phases and the phase transport properties. For example, should the streamer and core flow be assumed to be pseudo-fluids, or should a two-phase equivalent of the Orr-Sommerfeld equation be derived? The limited success of the gas-liquid annular flow stability studies, the general limitations of linear stability theory, and the uncertainties in applying stability theory to gas-solid separated two-phase flow, clearly indicate that an empirical approach will initially be more successful for prediction of streamer behaviour. Nevertheless, a qualitative understanding of the possible instability mechanism aids in developing empirical approaches.

Although the possibility that the wall influences the stability of streamers cannot be dismissed, the limited evidence available suggests that the instabilities are more likely to originate in the shear layer at the core-streamer interface. The shear on streamers due to capture of core particles at this interface can be estimated from core conditions predicted by the core dynamics model CIRCOR (Chapter 8). With streamers present at the wall, average predicted fluctuating velocities, $\mathbf{c}$, and core suspension densities, $\rho_{s,cr}$, are $O(0.8\ \mathrm{m/s})$ and $O(20\ \mathrm{kg/m^3})$, respectively (e.g. condition C in Table 8.7 and Appendix F). These values correspond to a core-to-streamer mass flux of 4.0 $\mathrm{kg/m^2s}$ ($0.8 \times 20\ /\ 4$, by eq. (8.86)). Combining this result and a conservative value of 5.0 m/s for the difference between axial core and streamer velocities, gives a shear on the streamers of 20 $\mathrm{N/m^2}$. The maximum riser wall shear measured by Van Swaaij *et al.* (1970) for pneumatic conveying at very high G_s and U_g was 8 $\mathrm{N/m^2}$, and typical values

were an order of magnitude less. Shear in parallel flow is a well-established cause of instability (Yih, 1965; Hewitt and Hall-Taylor, 1970; Drazin and Reid, 1981). In contrast, a mechanism for streamer instability due to the wall shear and particle motion within the streamer is not obvious. Finally, Wu (1989) investigated the behaviour of falling streamers in a cold unit riser with a flat wall, and a simulated "membrane waterwall" geometry, consisting of raised vertical tubes and recessed fins between the tubes. Relatively stable downflow of streamers was observed in the recessed areas, whilst the crowns of the tubes were largely swept clear of streamer particles. As the shear force on the raised tube crowns was likely to be substantially higher than on the recessed regions (i.e. a steeper velocity gradient between core and wall regions), Wu's observations suggest that core-streamer shear significantly influences streamer stability.

The wall streamer cold unit test study (Chapter 6) indicated that wall streamer instability is caused predominantly by local phenomena. As mentioned in Chapter 3, Louge *et al.* (1990) found little effect of the gas superficial velocity on the frequency of measured wall layer solids concentration fluctuations, and suggested that disruption of the wall layer may not be related to gas turbulence. However, the characteristic frequencies of the energetic eddies predicted in Chapter 8 are similar to the reported frequency range (1–20 Hz) for solids concentration fluctuations in the wall layer (Brereton, 1987; Louge *et al.*, 1990), and the possibility of a link cannot yet be excluded. There are a number of other possible sources of perturbations to the wall streamers that could also trigger the observed disruptions, including wall roughness, and minor fluctuations in the core velocity, pressure or concentration due to local suspension dynamics. Clearly, further experimental investigation into the rates of streamer disruption is required before general qualitative predictive correlations can be developed for streamer behaviour.

9.2.3 Modelling Wall Streamer Phenomena

At this stage there are too many unknowns for detailed modelling of wall streamer dynamics, so that rather crude empirical correlations must suffice. Two important quantities which are required for CFB riser modelling are a measure of the extent of disruption of the streamers,

and the related particle entrainment rate from the streamers to the core. If we assume that core-streamer interfacial shear causes the observed streamer disruptions, pertinent variables for correlating these phenomena are characteristic (or average) core and streamer suspension densities and axial velocities, the average wall streamer thickness, and, possibly, the gas viscosity and/or density. Although stability analysis also suggests a characteristic maximum growth rate "wavenumber" for the disturbances of the streamer should be included, there is no method for estimating this quantity. General stability study results suggest that wall layer disruption will increase with increasing shear between the core and wall layers (Drazin and Reid, 1981), and may increase with wall layer thickness (Hewitt and Hall-Taylor, 1970).

A relatively simple approach to characterising wall streamer behaviour, that is incorporated in the semi-empirical predictive CFB riser model described in Chapter 10, is based on observed similarities between gas-liquid annular flow and riser flow, and the expected effects of shear and wall streamer thickness on streamer stability and particle entrainment. Wallis (1970a, 1970b) observed that the gas-liquid interface in gas-liquid annular flow became increasingly disrupted as the liquid layer thickness increased, and thereby as the liquid-gas interfacial shear increased. He plotted an interfacial friction factor, f_i, against the dimensionless liquid layer thickness, r_{an}/D, and observed that the relationship was nearly linear. The relationship

$$f_i = f_{i0}\left(1 + \Psi\frac{r_{an}}{D}\right) , \tag{9.5}$$

fitted his data well, where f_{i0} was a smooth pipe Fanning friction factor, based on the gas-droplet flow in the core, and Ψ was a proportionality constant. The interfacial friction was defined by Wallis to be

$$\tau_i = \frac{1}{2}\rho_{gl}\mathbf{u}_{gl}^2 f_i , \tag{9.6}$$

where the subscript gl denotes a "combined phase" gas-droplet property for the core, and τ_i includes both effects of gas shear and impacting core droplets on the liquid layer.

As the streamers observed in the cold unit tests in this study appeared to be increasingly disrupted and protrude further into the core flow as streamer thicknesses increased, it is assumed

that similar relationships to eqs. (9.5) and (9.6) may reasonably predict τ_i on the wall streamers due to rapid dilute suspension upflow in the core. Relationships for combined phase gas-particle ("*gp*") core density and velocity that are consistent with the Wallis approach are:

$$\rho_{gp} = \frac{\mathbf{u}_{cr}\,\epsilon_{gu}\,\rho_g + \mathbf{v}_{cr}\,\epsilon_{pu}\,\rho_p}{\mathbf{u}_{cr}\,\epsilon_{gu} + \mathbf{v}_{cr}\,\epsilon_{pu}}\ , \tag{9.7}$$

and

$$\mathbf{u}_{gp} = \mathbf{u}_{cr}\,\epsilon_{gu} + \mathbf{v}_{cr}\,\epsilon_{pu}\ , \tag{9.8}$$

where ϵ_{pu} and ϵ_{gu} are the particle and gas volume fractions in the core, respectively, and the subscript u denotes dilute suspension upflow. Replacing $\mathbf{u}_{gl}$ in eq. (9.6) by the core combined phase velocity, $\mathbf{u}_{gp}$, gives an expression for the shear force, τ_i , on the streamers. Note that, according to the Wallis method, f_{i0} is the smooth pipe Fanning friction factor, evaluated at the combined phase core density, ρ_{gp}, and superficial velocity, $U_{gp} = \mathbf{u}_{gp}\,A_{cr}/A_t$.

A simple empirical relationship for particle re-entrainment from streamers can be derived if it is assumed that the interfacial shear on the streamers is proportional to the vertical momentum change of the solids stripped from the streamers, i.e.

$$\tau_i \ \propto k_d\,\rho_{sd}\,(\mathbf{v}_{cr} - \mathbf{v}_d)\ , \tag{9.9}$$

where subscript d denotes dense streamer downflow, and $\mathbf{v}_d$ is the streamer velocity; k_d is the streamer-to-core lateral solids mass transfer coefficient, and ρ_{sd} is the suspension density of the streamers. Thus the streamer-to-core mass flux, Q_s, is $k_d\,\rho_{sd}$. An average constant value for ρ_{sd} is assumed in Chapter 10. Generally $|\mathbf{v}_d| \ll |\mathbf{v}_{cr}|$, so that $\mathbf{v}_d$ is neglected in eq. (9.9). By substituting eq. (9.6) into eq. (9.9) to eliminate τ_i , introducing a proportionality constant, Ω, and re-arranging, we obtain an expression for the streamer-to-core mass transfer coefficient:

$$k_d = \Omega\,\frac{\rho_{gp}\mathbf{u}_{gp}^2}{2\rho_d\mathbf{v}_{cr}}\,f_{i0}\left(1 + \Psi\frac{r_{an}}{D}\right)\ . \tag{9.10}$$

The proportionality constants Ω and Ψ are defined as the "viscous shear entrainment factor" and "wall layer disturbance factor," respectively.

It is assumed that there is a low, continuous re-entrainment rate of particles from the streamers to the core when the streamers are very thin. This is due to a combination of shear induced lift force on the relatively flat vertical streamer interfaces, described earlier for nucleating streamers, and the effects of impinging core particles. Evaluating k_d from eq. (9.10) as the wall layer thickness, r_{an}, approaches zero gives the contribution of this continuous entrainment mechanism to the total streamer-to-core flux, and explains the label for Ω. As wall streamers grow thicker, and increasingly disrupt, the entrainment rate increases due to the intermittent entrainment from disrupted regions on the streamers. The wall layer disturbance factor is a measure of the enhancement of the entrainment rate due to these disruptions. Values for the constants Ω and Ψ, and a simple empirical method for estimating the streamer surface area and coverage, are presented in Chapter 10.

9.3 Exit Effects

The geometry of the riser exit has a large influence on the solids distribution in the upper part of the riser, as discussed in Chapters 2, 6 and 7. Abrupt exits internally reflect a substantial portion of the arriving core solids down the riser walls, whilst smooth exits allow the majority of the solids upflow to leave the riser. Hence, the riser exit may be considered as an inertial separator of solids. The flow patterns observed near abrupt exits are typically complex, asymmetric and dependent on G_s and U_g. Also the Chapter 6 results demonstrate that smooth exits do not divert 100% of the dilute solids upflow out of the riser, the fraction of solids reflected internally being dependent on G_s and U_g.

It is also likely that the fraction of core particles that exit the riser is dependent on particle size and density. A greater fraction of smaller particles, which follow the gas flow more closely, are expected to exit, in comparison to larger particles. Thus segregation of particles may result. This segregation is likely to decrease as the suspension density of the core upflow increases and particle collision frequency increases. A fundamental approach to prediction of gas-solid suspension dynamics in the exit region probably requires consideration of PSD effects

and three-dimensional flow patterns. This is a challenging task, likely to require enormous computation.

Given the limited amount of exit effect data and the difficulties of comprehensive fundamental modelling of exit region flows, simple empirical approaches must be employed. As mentioned, the primary effect of the exit on overall riser dynamics is the internal reflection of solids down the riser walls. A secondary effect is the possible segregation of particles. Currently there are very few data for solids reflection and no data for estimation of segregation effects.

A crude estimate of the fraction of solids reflected internally, R_f, may be made by assuming that the riser cross-section just below the exit may be divided into regions of wall streamer downflow (subscript "d") and dilute suspension upflow (subscript "u"). The suspension density, ρ_{st}, averaged over the total riser cross-section at a given riser height, is:

$$\rho_{st} = \frac{1}{A_t} \left(A_u \, \rho_{su} + A_d \, \rho_{sd} \right) \ , \tag{9.11}$$

where ρ_{su} and ρ_{sd} are the suspension densities in the upflow and downflow regions, respectively. Also, by simple volume and mass conservation principles,

$$A_t = A_u + A_d \ , \tag{9.12}$$

and

$$G_s A_t = \mathbf{v}_u \, A_u \, \rho_{su} + \mathbf{v}_d \, A_d \, \rho_{sd} \ , \tag{9.13}$$

where $\mathbf{v}_u$ and $\mathbf{v}_d$ are the velocities of the dilute and dense suspension. Creation/destruction of particle mass has been assumed negligible. With these assumptions, the fraction of solids travelling upwards in dilute suspension reflected down the walls as dense streamers is

$$R_f = \left| \frac{\mathbf{v}_d \, A_d \, \rho_{sd}}{\mathbf{v}_u \, A_u \, \rho_{su}} \right| \ . \tag{9.14}$$

A more useful form of eq. (9.14) for estimating R_f from experimental data is obtained by substituting eqs. (9.11), (9.12) and (9.13) into eq. (9.14) to eliminate A_u, A_d, ρ_{su} and ρ_{sd}:

$$R_f = \frac{(G_s/\mathbf{v}_u - \rho_{st})}{(G_s/\mathbf{v}_d - \rho_{st})} \ . \tag{9.15}$$

Table 9.1: Estimated exit reflection coefficients, R_f, for cold unit riser and high temperature CFB combustor tests.

Riser	Exit	U_g (m/s)	G_s (kg/m^{2}s)	r_{an}/D (-)	$\mathbf{v}_u$ (m/s)	ρ_{st} kg/m^3	R_f (-)
cold	abrupt	6.5	20	0.06	6.6	41	0.64
cold	abrupt	9.0	20	0.06	9.8	44	0.67
cold	abrupt	6.5	60	0.075	7.2	106	0.61
cold	abrupt	9.0	60	0.075	10.6	118	0.65
cold	smooth	6.5	20	0.0	4.7	9	0.17
cold	smooth	9.0	20	0.0	7.2	8	0.20
cold	smooth	6.5	60	0.02	5.0	26	0.17
cold	smooth	9.0	60	0.0	4.7	15	0.03
hot	abrupt	6.8	32	0.07	6.6	174	0.83
hot	abrupt	7.4	22	0.06	7.6	204	0.86
hot	abrupt	8.9	28	0.07	9.1	165	0.85
hot	abrupt	8.7	32	0.09	9.3	200	0.86
hot	abrupt	10.2	31	0.08	10.9	205	0.85
hot	abrupt	10.0	35	0.09	11.0	205	0.85
Assumed constant streamer velocity, $\mathbf{v}_d = -1.1$ m/s							
Cold unit:		$A_t = 0.0181$ m^2, $D = 0.15$ m, circular cross-section $T = 25$ °C, $\overline{d_p} = 230$ μm, $\rho_p = 2500$ kg/m^3, $\mathbf{v}_t = 1.8$ m/s Narrow PSD glass bead tests, Chapter 6					
Combustor:		$A_t = 0.0232$ m^2, $D = 0.15$ m, square cross-section $T = 845$ °C, $\overline{d_p} = 205$ μm, $\rho_p = 2700$ kg/m^3, $\mathbf{v}_t = 1.1$ m/s UBC pilot-scale CFB combustor tests, Chapter 7					

G_s, $\mathbf{v}_d$ and ρ_{st} may be directly measured, and $\mathbf{v}_u$ can be calculated from estimates of the core gas velocity and particle slip velocity. This approach is used to the characterise exit effect in Chapter 10. R_f is termed the "exit reflection coefficient." Abrupt or small area exits have high values of R_f, whilst smooth or large area exits have low values.

Estimated R_f values for the narrow PSD glass bead tests (Chapter 6) and for some of the UBC combustor hydrodynamic tests (Chapter 7) appear in Table 9.1. A wall streamer velocity of -1.1 m/s was assumed for all calculations. To estimate the velocity of the particles in dilute suspension, $\mathbf{v}_u$, it was assumed that the gas velocity in the dilute suspension region was approximately $U_g A_t / A_u$, i.e. there was negligible gas flow in the dense streamer region.

A_u/A_t was approximated by $(1 - r_{an}/D)^2$ for risers of both square and circular cross section. Slip velocities of particles in the dilute core suspension were assumed to be equal to the terminal settling velocity of the Sauter mean size particle, $\mathbf{v}_t$. Thus it was assumed that $\mathbf{v}_u = U_g A_t/A_u - \mathbf{v}_t$. For the cold unit tests, the wall layer thicknesses, r_{an}, were measured just below the exit by capacitance probe. However, r_{an} was not measured near the exit in the combustor tests, so that alternative method for estimating A_u had to be used. In this case, a constant streamer suspension density of 1050 kg/m^3 was assumed. This value was typical of measured wall streamer densities lower in the combustor, and was consistent with the high apparent suspension densities measured just below the riser exit. An expression for A_u was derived by combining eqs. (9.12), (9.13) and (9.14), to eliminate A_d and $\mathbf{v}_u$:

$$\frac{A_u}{A_t} = 1 + \frac{G_s R_f}{\mathbf{v}_d \, \rho_{sd} (1 - R_f)} \, . \tag{9.16}$$

Equations (9.15) and (9.16) were then solved iteratively to obtain A_u and R_f. Measured apparent suspension densities, ρ_{st}, were used in all calculations. Values of R_f based on the "probe" suspension densities for the cold unit tests varied by approximately -10% from the values based on ρ_{st}.

The methods used to calculate experimental values of R_f from eq. (9.15) are crude. From the Chapter 8 modelling results, it is likely that the slip velocities of particles in dilute suspension upflow are greater than the terminal settling velocity due to collisions with re-entrained streamer particles. Similarly, although the assumed value of $\mathbf{v}_d$ is a reasonable rough approximation, values of $\mathbf{v}_d$ have been measured in the range from -0.5 to -2.0 m/s, as discussed in Chapter 2. The calculated R_f values are probably only accurate within about $\pm$ 0.2. For example, in the cold unit tests with the smooth exit and $G_s = 20$ kg/m^{2}s, no wall streamers were detected at the wall, yet the estimate of R_f indicates that a small amount of reflection occurred. Nevertheless, the calculated R_f values demonstrate that abrupt exits reflect significantly more solids than smooth exits and R_f is a reasonable indicator of the exit effect.

Although it is possible that R_f varies with U_g and G_s, as well as the exit geometry, the values calculated for each respective exit in Table 9.1 are relatively constant. In fact, R_f calculated for

all the combustor hydrodynamic results fell within the range 0.85 ± 0.03. In the cold unit tests with the abrupt exit, it appeared the majority of the upflowing particles impacted on the dense layer of particles held on the riser roof, rather than diverting out of the riser with the gas flow. The particles that then fell down the riser wall in dense particle sheets and over the exit port opening were swept out of the riser. Based on this observation, a crude estimate of the fraction of upflowing particles that exit the riser with an *abrupt* exit geometry is the fraction of the riser circumference that is cut away for the port to the cyclone (or equivalent solids capture device). The exit port width is 102 mm for both the combustor and the cold unit abrupt exits. For the circular cold unit cross section, this corresponds to a 102 mm chord, or a cut away of 23% of the circumference. For the combustor the exit port width is 17% of the square perimeter. Values of R_f for the combustor and cold unit, estimated from this method, are thus 0.83 and 0.77, respectively, similar to the calculated R_f values in Table 9.1.

9.4 Entry Effects

The solids and gas flow patterns in the entry region near the base of the riser are complex and difficult to characterise. As demonstrated in Chapter 6, a core-annulus structure often exists at low G_s, and a relatively dense turbulent fluidised bed may form as G_s is increased or as U_g is decreased. Radial non-uniformity also exists in the time-averaged solids distribution in a turbulent fluidised bed, though the wall-core region interface is not as well defined, and the low density suspension regions in the bed stochastically form, meander about, and break up. This behaviour of the transient solids structures suggests that even relatively complex two-fluid models for turbulent beds may have to include some crude approximations.

It is known that the apparent and true suspension densities of the entry region are dependent on G_s, U_g, riser base geometry, and particle properties (Chapter 6). Furthermore, riser entry dynamics may be influenced by riser diameter, design of the primary air distributor and the method used to return solids to the riser. Unfortunately, most measurements in the riser entry region are based on axial pressure gradients, which can be poor indicators of true solids hold-up

in this region of high gas and particle acceleration (Chapter 6).

There have been no attempts to predict details of the gas and solids flow and distribution near the base of the riser. This is not surprising, given the complex flow patterns. Tsuo and Gidaspow (1990) assumed a gas-solid plug flow of fixed voidage as a boundary condition at the base of the riser for their multidimensional unsteady-flow two-fluid model simulations. This boundary condition is inconsistent with the measured solids distribution in this study. Other two-fluid models (e.g. Sinclair and Jackson, 1989; and the Chapter 8 riser core model) are limited to prediction of flows further up the riser.

Predictions in the literature of riser phenomena near the riser base are almost exclusively directed at estimating cross-sectionally averaged solids hold-up. Several very simple correlations have been proposed to predict the apparent suspension density in this region. These correlations are simple empirical fits to data, although attempts at justifying their form have appeared, based on crude one-dimensional representations of the solids distribution and flow (e.g. Kwauk *et al.*, 1986). They cannot be applied reliably outside the range of conditions for which they were developed, as discussed in Chapter 5. They are based on measured apparent suspension densities, and thus predict apparent suspension densities. Possible differences between true average suspension density and apparent suspension density should also be kept in mind when applying these correlations.

The most often cited simple correlations for apparent suspension density are those proposed by Kwauk and coworkers (Li and Kwauk, 1980; Li *et al.*, 1982; Kwauk *et al.*, 1986). They correlated apparent suspension density data measured in a 90 mm diameter cold unit riser with several particle types, and reported "sigmoidal" shaped density profiles, that generally decayed from an initial dense bed at the base to a dilute suspension towards the riser exit. To predict the average solids fraction, ϵ_{pr}, in the dense bed region they proposed the correlation

$$\epsilon_{pr} = 0.2513 \left(\frac{18 Re_{sr} + 2.7 Re_{sr}^{1.687}}{Ar} \right)^{-0.4037} , \tag{9.17}$$

where Ar is the particle Archimedes number, and the Reynolds number, Re_{sr} is based on gas

and particle superficial velocities, i.e.

$$Re_{sr} = \frac{d_p \rho_g}{\mu_g} \left(U_g - \frac{G_s (1 - \epsilon_{pr})}{\rho_p \epsilon_{pr}} \right) . \tag{9.18}$$

The correlations proposed by Kwauk *et al.* have been used in several simple modelling studies to predict density profiles (e.g. Zhang *et al.*, 1991). Hartge *et al.* (1986) measured density profiles for both fine sand and alumina particles in risers of diameter 0.4 m and 0.05 m and compared their results with predictions of the Kwauk correlations. The solids volume fractions in the base of the riser were underpredicted by more than 50%, and the experimental and predicted trends were quite different. In this study, the accuracy of eq. (9.17) for predicting the measured apparent suspension densities in the base of the CFB combustor (Chapter 7) was examined. The prediction accuracy was poor, and predicted trends did not correspond to measured trends. The results are summarised in Appendix G.

For the semi-empirical model described in Chapter 10, an alternative empirical relationship for predicting the cross-sectionally averaged solids volume fraction near the base of the riser was developed in this study:

$$\epsilon_{pr} = c_0 \left(U_g^\star \right)^{c_1} \left(\frac{G_s}{\rho_p (U_g - \mathbf{v}_t)} \right)^{c_2} , \tag{9.19}$$

where $U_g^\star$ is the dimensionless superficial gas velocity, $U_g(\rho_g^2/\mu_g\, g\, \Delta\rho)^{1/3}$. The coefficients c_0, c_1, and c_2 were obtained by a non-linear regression fitting of this relationship to the UBC pilot-scale combustor data described in Chapter 7; they are, respectively, 2.11, 0.292, and 0.366. This relationship gave a far superior fit than the Kwauk formulation. It also gave reasonable predictions of suspension densities in the bottom of a larger prototype CFB combustor, as described in Chapter 10. The non-linear regression method and accuracy of the fit for the experimental data are described in Appendix G.

Despite the usefulness of eq. (9.19) in this study, it has limitations similar to those pertaining to the Kwauk correlations, i.e. it was developed from data measured in one riser, with only a single particle type, and a relatively narrow temperature range. Its use should therefore be limited to relatively small diameter CFB combustors. Interestingly, Chiu (1991) successfully

correlated the suspension density in the base of a commercial CFB combustor using eq. (9.19), but with a different set of coefficients.

Clearly, modelling of riser dynamics near the base of the riser is in the early conceptual stages, and additional experimental data are required to advance these studies. In particular solids flux and distribution measurements are needed. The possible next step to improve empirical predictions of solids hold-up in this region is to recognise that there is substantial solids flow into the base of the riser due both to the external solids return *and* to wall streamer downflow. Thus factors that influence wall streamer motion may need to be included in the correlations. The results of Chapter 8 suggest that the contribution of streamer downflow to the total solids influx into the base region may decrease as riser diameter increases. Deposition of particles at the wall and particle downward mass flux near the wall may also be influenced by particle properties and PSD, as discussed in Chapter 8.

The changes in the solids and gas flow patterns in the transition region, from a relatively dense turbulent fluidised bed in the lower part of the riser to the well-defined core-annulus structure in the middle and upper parts of the riser, are also not well understood and have not been investigated beyond the measurement of apparent suspension density profiles. A possible mechanism for "cluster" formation is the upward projection of clumps of particles from the turbulent fluidised bed into the core of the riser above. The transition typically occurs over a height of several metres, and it is incorrect to model this region as an abrupt interface. At this stage one must again rely on simple empirical relations for prediction of apparent suspension density in this region, such as the "sigmoidal" density profile equation of Kwauk *et al.* (1986). An alternative density profile relationship is presented in Chapter 10 for use in the semi-empirical CFB model described there.

9.5 Conclusions

A mechanism for wall streamer formation has been proposed, which includes the effect of shear induced lift force on the particles. The particle trajectory calculations in a wall shear

layer support this proposal. They also clearly demonstrate the significant effect of lift force on particle motion close to the riser wall and indicate that continuum representations of the particle phase near the wall may not be accurate. A detailed discussion of wall streamer dynamics highlights the difficulties of fundamental approaches to modelling streamer motion. The complex flow patterns in the riser entry and exit regions have also been described, and the challenging problems associated with modelling these flows reviewed. Simple methods for characterising streamer dynamics, exit effect, and solids hold-up in the riser entry region have been presented. Concepts for future modelling of these phenomena have also been introduced.

Chapter 10

A SEMI-EMPIRICAL PREDICTIVE CFB MODEL

A predictive semi-empirical model is presented that incorporates the major features described in earlier chapters. Streamers are assumed to fall at the walls, surrounding a rapid dilute suspension upflow. Empirical methods described in Chapter 9 are used to predict the entry region apparent suspension density, the exit effect, and particle entrainment from wall streamers into the dilute suspension upflow. Details of the model are also given by Senior and Brereton (1990, 1992).

This model was developed prior to some of the more fundamental theoretical and experimental modelling work described in Chapters 3, 6 and 8. It contains several assumptions that, in hindsight, are relatively crude. Nevertheless, none of the more fundamental work invalidates the model, and such assumptions are necessary to develop working predictive models. For example, a constant fluctuating particle velocity magnitude, **c**, of 0.8 m/s was set for the dilute core suspension in this model. Although **c** varies in the CIRCOR model predictions in Chapter 8, 0.8 m/s is a good estimate of the average of predicted **c** values with wall streamers present.

The model was developed for two reasons. Firstly, there was a need for an "engineering design" model to predict key phenomena in CFB combustors, such as bed-to-wall heat transfer coefficients. Consequently, particular attention was focussed on generating a realistic mathematical description of solids distribution and renewal at the riser walls, and CFB combustor data were used for model development. The model was fitted to UBC 115 kW_{th} pilot-scale combustor data, and successfully predicts data provided by Studsvik Energy of Sweden from their 2.5 MW_{th} combustor (Adams *et al.*, 1989). Hydrodynamic data predicted by this model

have been utilised in a heat transfer model (Senior and Brereton, 1990) for prediction of local and average bed-to-wall heat transfer coefficients. Although the model was developed primarily for prediction of CFB combustors, it may be adapted to other CFB applications. A second purpose of the model development was to provide a "testing ground" for a number of hydrodynamic concepts proposed in this study, such as possible mechanisms of lateral particle transfer between dilute core upflow, and dense streamer downflow.

10.1 Model Concepts and Formulation

The solids flow patterns and distribution within pilot-scale and commercial-size CFB combustors were discussed in Chapters 2 and 7. Recall that these units generally operate with relatively low G_s, compared to other CFB applications, such as FCC units, and have staged air injection. Except for a relatively dense region in the lower 1–3 m, the riser may be divided into a core region of dilute suspension rapid upflow, and a wall region, containing dense downflowing wall streamers. The transient stochastic motion of streamers, described in Chapter 9, results in exposure of the vertical membrane waterwall heat transfer surfaces to dilute suspension upflow, even at relatively high apparent suspension densities. Sauter mean particle sizes typically range from 100 to 400 μm, and average particle densities are approximately 2700 kg/m^3.

An important objective when developing this model was to minimise the number of model parameters, and give these physical significance. All model parameters presented below are assumed to be invariant, except for the exit reflection coefficient, R_f, which characterises the effect of the exit geometry (Chapter 9). It is assumed that experimental axial apparent suspension density profiles used to develop the model were reasonable estimates of true cross-sectionally averaged suspension density, except, possibly, for the turbulent fluidised bed region in the lower primary zone of the riser. As mentioned in Chapter 9, solids flow patterns in this region are complex and difficult to characterise. As heat transfer to exposed membrane walls occurs principally above the secondary air ports in a CFB combustor, and heat transfer through refractory

can be predicted by other means, detailed information regarding lateral solids flow and distribution in the lower region is normally not required for predictions of bed-to-wall heat transfer coefficients. Hence, only a bulk density profile is predicted by the model in this region for computation of overall reactor pressure drop.

As discussed in Chapter 2, the shape of riser axial apparent suspension density profiles may vary, depending on the riser exit configuration. Typical profile shapes are shown in Figure 10.1. Profiles typically exhibit an initial rapid decay in the lower 1 to 3 m above the solids return. In this *developing flow* region, upflowing core particles experience both large upward gas drag and vigorous interaction with other particles and clusters. The steep decline in suspension density with height is likely due to a combination of particle acceleration and net radial movement of solids from the upflowing core suspension to the predominantly downflowing wall region.

Above the developing flow region, core solids volume fractions are very low (i.e. < 0.015, see Chapters 2 and 6). In this *"developed flow"* region, changes in core particle vertical velocity with height are small[1]. Measured time-averaged velocities of the wall streamers also do not vary greatly with height. Despite only small velocity variations in the "developed flow" region of these two countercurrent solids streams, significant variations in axial suspension density are often observed. For the decaying profile shown in Figure 10.1, there must exist a net transfer of solids from upflowing core to downflowing wall streams. Conversely, in reactors with a constricted or abrupt exit, such that the suspension density increases with height at the top, the net transfer must be towards the core. This is only possible if there are two different mechanisms for transfer of particles, one to account for movement of core particles outwards to the walls, and one explaining the re-entrainment of falling wall streamer solids back into the core. Both mechanisms must be present, irrespective of reactor geometry.

The mechanisms by which upflowing core particles are deposited at the riser wall were modelled in detail in Chapter 8. The larger, relatively dense particles used in CFB combustors

[1]In a true fully-developed suspension flow there would be no change in the density or velocity with height. The term "developed flow" is used informally here to denote that changes in the core in this region are small compared with changes in the core lower in the riser.

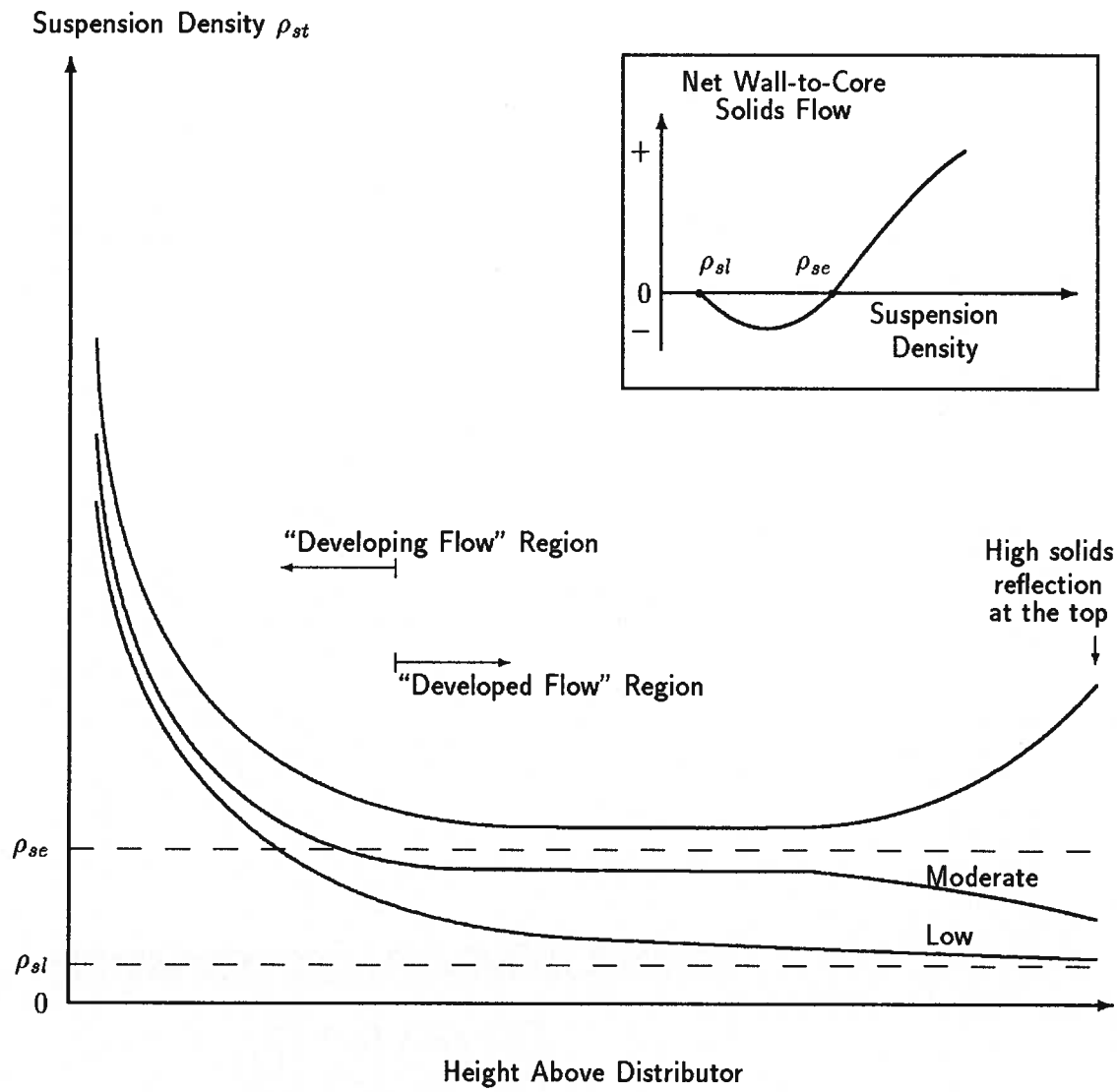

Figure 10.1: Variations in density profile shape due to internal solids reflection at the top of reactor, and (inset) net lateral solids flow in the "developed flow" region that arises from this end effect.

are predicted to reach the wall primarily due to oblique particle collisions. Gas turbulence is expected to be a secondary effect. The description of the dynamic behaviour of falling wall streamers in Chapter 9 suggests solids are continuously re-entrained from these structures. As discussed, this re-entrainment rate is believed to be greatly enhanced as streamers grow thicker, with instabilities causing local disruptions.

Analysis of cold unit density profiles (Bierl *et al.*, 1980; Brereton, 1987; Chapter 6) indicates that when considerable reflection occurs at the top, suspension densities in the developed flow region are higher throughout the riser than for low top reflection cases (Figure 10.1), but that ρ_{st} generally approaches some limit in the mid or lower regions of the riser, just above the developing flow region. This suggests that there is a condition of zero net cross-flux of solids. The suspension density, ρ_{se}, at zero cross-flux must be a function of the particle interchange mechanisms, streamer and core axial velocities, and individual suspension concentrations in the core and wall regions. Thus ρ_{se} is likely to be a function of solids circulation rate and gas flowrates. Furthermore, for a given set of hydrodynamic parameters, an increase in reactor height increases the likelihood that ρ_{se} will be approached in the central section of the reactor. In some cases, such as the low reflection case shown in Figure 10.1, the concentration of particles within the riser may be very low. When this occurs the individual transfer rates between core and wall are so small, that ρ_{se} is not closely approached within the "developed flow" region.

If the CFB is operated with very low G_s, then it behaves under dilute pneumatic conveying conditions. As mentioned earlier, in such cases, negligible downflowing wall solids are observed, despite a finite core solids concentration. There must also exist, therefore, a lower suspension density, ρ_{sl}, where both the wall layer and the net cross-flux approach zero simultaneously. At suspension concentrations below ρ_{sl} there is only dilute upflow, and no mechanism by which solids may be removed or added to this stream. For this condition, the suspension density profile must be constant with height above a short acceleration zone. Drawing on these postulates, we can construct a qualitative plot of cross-flux versus suspension density, shown in the Figure 10.1 inset, that accounts for all the suspension density profile trends seen in the developed flow region.

It is assumed that the riser is isothermal, the gas and particle densities are constant, and the rates of creation/destruction of gas and particle mass are negligible. These common modelling assumptions were discussed in Chapter 4. Although non-isothermality may occur within CFB combustors operating at low load or with high-volatile fuels, temperature variations are unlikely to affect hydrodynamics, except at the lowest loads. The particles are represented as uniform spheres of the Sauter mean particle size. Variations in particle dynamics due to PSD effects are not considered.

A core-annulus representation of the solids flow structure is assumed from the secondary air inlet to the top of the reactor. The model core region contains a dilute upflowing suspension that is radially uniform in concentration. The few particle clusters that have been detected in the CFB combustor core above the secondary air ports (Couturier, 1991; Chapter 7) are much lower in density than wall streamers, and constitute a minor fraction of the total solids mass flow. The wall region above the secondary air inlets is composed of upflowing dilute suspension interspersed with downflowing denser wall streamers. The wall streamers are assumed to be semi-elliptic in cross-section as shown in Figure 10.2, and to maintain a constant width-to-thickness ratio $\mathcal{K}$ as they grow; $\mathcal{K}$ is termed the *elliptic factor*[2]. Thus, as the wall region increases in thickness, so too does the fractional coverage of the wall by streamers. Sensitivity studies show that the magnitude of $\mathcal{K}$ has only a small effect on the predicted density profile. Note that the structures shown in Figure 10.2 are time-averaged representations of actual wall phenomena, and the instantaneous solids concentration, local thickness of streamers, and solids and gas velocity actually fluctuate randomly at any position in the wall region, as discussed. Although a square cross-section is shown in Figure 10.2, the model also handles risers with circular cross-section. For both cases, the wall layer thickness is assumed to be a small fraction of the total riser diameter, and the core region cross-section is assumed to remain geometrically similar to the shape of the riser cross-section.

The wall is assumed fully covered when the wall layer thickness, r_{an}, exceeds a thickness

[2]More precisely, $\mathcal{K}$ is the width-to-thickness ratio of the corresponding full ellipse.

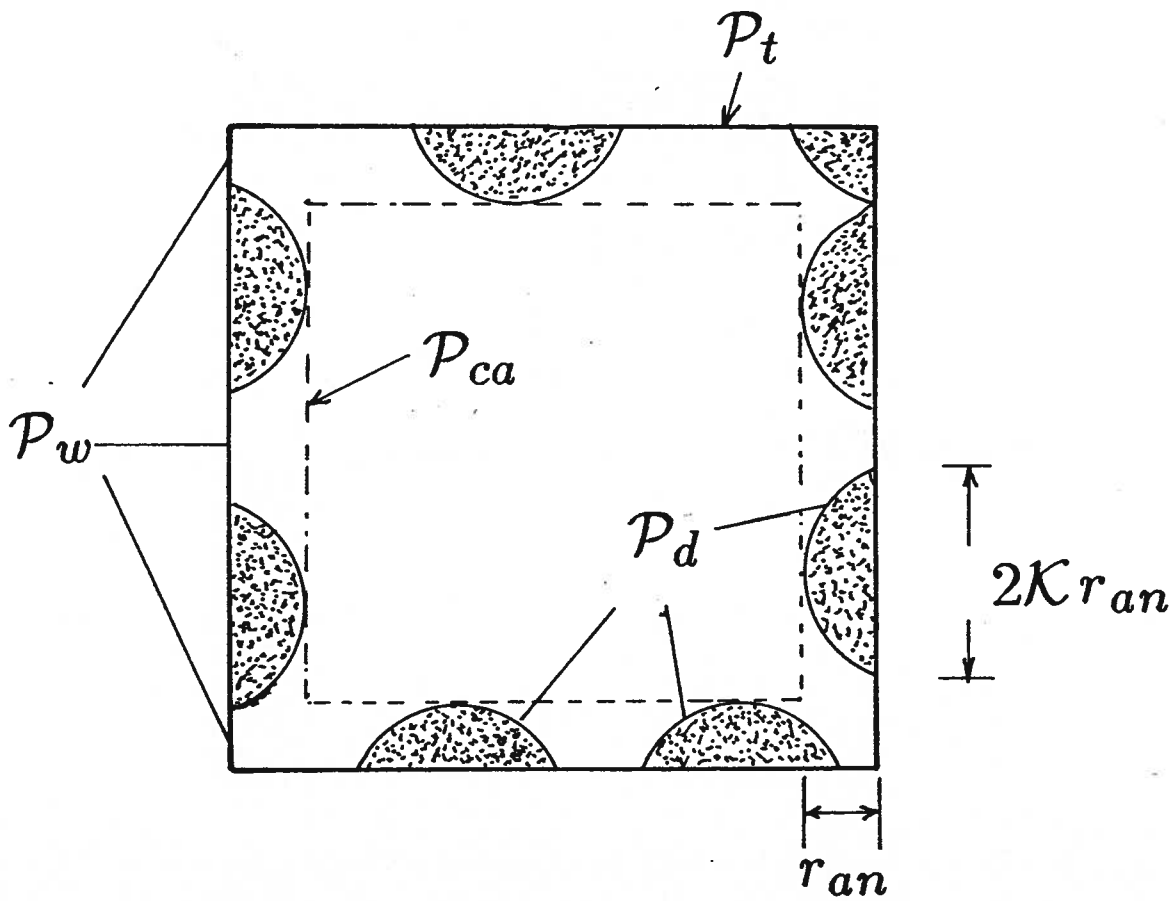

Figure 10.2: Reactor cross-section showing semi-elliptical streamers assumed by the model, and defining the model region perimeters: $\mathcal{P}_t$, total; $\mathcal{P}_d$, interface between streamers of semi-elliptic cross section and dilute suspension; $\mathcal{P}_w$, wall exposed to dilute suspension; $\mathcal{P}_{ca}$, core-wall region; r_{an}, wall layer thickness; $\mathcal{K}$, width-to-thickness shape factor of the wall streamers.

r_{max}. For streamer thicknesses greater than r_{max} the streamers join into one downflowing dense wall layer that retains the "roughened" interfacial area (plan view) that occurs at $r_{an} = r_{max}$. Estimation of r_{max} is discussed later. The dilute suspension particles interspersed within and amongst the downward falling streamers may be considered simply as core particles that have a lateral velocity that has brought them into a region where they may be captured by the downward falling dense streamers. Therefore, the suspension density and vertical velocity of particles in dilute suspension near the wall are assumed to be the same as in the central regions of the reactor. As the wall region typically occupies a small fraction of the total riser cross-section, the dilute suspension upflow in the wall region is likewise a small fraction of the total dilute suspension upflow. Dilute suspension upflow is denoted by subscript "u," and dense streamer downflow by subscript "d," as in Chapter 9.

As mentioned, the riser is divided into a *"developing flow"* and *"developed flow"* zones. It is assumed that most of the density profile decay in the lower part of the developing flow region is due to particle acceleration, with core-to-wall flux accounting for a significant portion of the decay towards the top of this region. Hence, core particles are assumed to have closely approached a final steady vertical speed, $\mathbf{v}_u$, at some height below the top of the developing flow region. For computational convenience, this height is set equal to the height of the secondary air inlets. The constant velocity, $\mathbf{v}_u$, is the difference between a mean core gas superficial velocity (averaged over the full riser height, with allowance for changing core cross-section) and the particle terminal settling velocity. Although this is a crude approximation, as discussed in Chapter 9, the magnitudes of typical particle slip velocities in the riser core are small compared to the absolute upward core suspension velocity, and the error in estimating of $\mathbf{v}_u$ is not expected to be greater than $O(\pm 20\%)$.

The constant gas volumetric flow above the secondary air ports is assumed to be the gaseous flowrate with 50% of the fuel combusted. Below the secondary air ports, gas flow is approximated by the primary air flowrate. The periodic presence of dilute suspension in the wall region above the secondary air ports suggest that a small fraction of the total gas volumetric

flow travels up in this region. A simple time-averaged gas velocity profile is assumed for the dilute suspension in the wall region. The gas velocity is assumed to be zero at the wall (no slip condition), and to increase linearly across the wall region so that it matches the core velocity at the core-wall region interface. It is assumed that there is no radial variation in the core gas velocity. The volumetric downflow of gas entrained with wall streamers is assumed negligible.

The model wall streamers have a constant voidage and fall with constant velocity, $\mathbf{v}_d$. The streamer voidage is set to 0.6, based on capacitance probe results presented in Chapter 7. As discussed in Chapter 9, the present level of understanding of the factors affecting instantaneous and time-averaged wall streamer velocity and density precludes detailed modelling of these quantities. In heat transfer studies (Senior and Brereton, 1990), reasonable predictions of heat transfer coefficients were obtained with the model described here with $\mathbf{v}_d = -1.1$ m/s. Note that, although ρ_{sd} and $\mathbf{v}_d$ are both assumed to be constant, the thickness of the wall region, r_{an}, and the dilute suspension density, ρ_{su}, both vary with riser height as a result of the interchange of solids between the core and wall.

10.2 Model Equations

Above the secondary air ports, simple mass and volume conservation relationships may be written for the particles at a given riser height, z, based on division of the solids flow into dilute suspension and dense streamer regions, and the assumptions of constant gas and particle velocities and densities, and negligible creation of mass. These relationships, first presented in Chapter 9 (eqs. (9.11), (9.12) and (9.13)) are:

$$A_t \, \rho_{st} = A_u \, \rho_{su} + A_d \, \rho_{sd} \, , \tag{10.1}$$

$$A_t = A_u + A_d \, , \tag{10.2}$$

and

$$G_s A_t = \mathbf{v}_u \, A_u \, \rho_{su} + \mathbf{v}_d \, A_d \, \rho_{sd} \, . \tag{10.3}$$

Furthermore, a simple differential mass balance over incremental height dz for the dilute suspension region gives:

$$\mathbf{v}_u \frac{d(A_u \rho_{su})}{dz} = \dot{m}_d - \dot{m}_u \ , \tag{10.4}$$

where $\dot{m}_d$ is the solids lateral mass transfer rate (kg/s per m reactor height) from streamers to dilute suspension, and $\dot{m}_u$ is its counterpart, from dilute suspension to streamers. A similar relationship for a differential height of dense streamer region may likewise be derived.

Equation (10.3) may be differentiated to give

$$\mathbf{v}_u \left(\rho_{su} \frac{dA_u}{dz} + A_u \frac{d\rho_{su}}{dz} \right) = -\mathbf{v}_d \, \rho_{sd} \frac{dA_d}{dz} \ . \tag{10.5}$$

This result is based on the assumption of constant wall streamer suspension density. Also, assuming the total reactor cross-section does not vary over the reactor height for which the model is assumed to apply, we may write

$$\frac{dA_d}{dz} = -\frac{dA_u}{dz} \ . \tag{10.6}$$

Combining eqs. (10.5) and (10.6) to eliminate dA_d/dz, and then substituting the resulting equation into eq. (10.4) to eliminate dA_u/dz gives the model differential equation for the dilute suspension density, ρ_{su},

$$A_u \frac{d\rho_{su}}{dz} = \left(\frac{1}{\mathbf{v}_u} - \frac{\rho_{su}}{\mathbf{v}_d \, \rho_{sd}} \right) (\dot{m}_d - \dot{m}_u) \ . \tag{10.7}$$

Simple manipulation of eqs. (10.1–10.4) gives the other unknowns, ρ_{st}, A_u and A_d in terms of ρ_{su} and known constants. Solution of eq. (10.7) constitutes solution of the model.

General expressions may be written for $\dot{m}_d$ and $\dot{m}_u$:

$$\dot{m}_d = \mathcal{P}_d \, k_d \, \rho_{sd} \ , \tag{10.8}$$

$$\dot{m}_u = \mathcal{P}_{ca} \, k_u \, \rho_{su} \tag{10.9}$$

where $\mathcal{P}$ is the interfacial area per unit reactor height (i.e. perimeter) specific to the particular transfer mechanism, and k_d and k_u, are lateral mass transfer coefficients.

Recall eq. (9.10) for the lateral flux coefficient, k_d, for particle entrainment from streamers:

$$k_d = \Omega \, \frac{\rho_{gp} \, \mathbf{u}_{gp}^2}{2\rho_{sd} \, \mathbf{v}_u} \, f_{i0} \left(1 + \Psi \frac{r_{an}}{D}\right) . \tag{10.10}$$

As discussed, this relationship predicts a steady low entrainment rate of particles from thin relatively undisturbed streamers. As streamers grow thicker, they are assumed to increasingly disrupt, and particle re-entrainment is enhanced. Fitting of the model to the UBC combustor data (Chapter 7) suggests that this enhancement is quite substantial for typical CFB streamer thicknesses ($\Psi \, r_{an}/D$ typically assumes values between 4 and 20). Clearly, the wall layer disturbance factor, Ψ, is a key model parameter.

The interchange of solids between wall streamers and dilute core is also dependent on the interfacial areas across which the solids move, as shown in Figure 10.2. It is assumed that solids entrainment from streamers into the core is proportional to the surface area of the streamers exposed to dilute suspension. Knowledge of the total streamer cross-sectional area, A_d, and elliptic factor, $\mathcal{K}$, permits computation of the streamer interfacial area (per unit height), $\mathcal{P}_d$, and wall layer thickness, r_{an}:

$$r_{an} = 2\sqrt{\frac{A_d \, r_{max}}{\pi \, s_x D}} , \tag{10.11}$$

and

$$\mathcal{P}_d = \frac{\pi \, r_{an} \, s_x D}{2 \, r_{max}} \sqrt{\frac{1 + 1/\mathcal{K}^2}{2}} , \tag{10.12}$$

where $s_x D$ is the total reactor perimeter, $\mathcal{P}_t$. Although some core particles move outwards towards areas of "bare" wall, it is assumed that the majority of these particles will normally be captured by falling streamers before they reach (or rebound from) the wall because of the large relative vertical velocities of streamers and core particles in comparison to the slow lateral movement of core particles. The core particles are therefore assumed to transfer across a core-wall region interface as shown in Figure 10.2.

The nucleation of wall streamers was discussed in Chapter 9. Based on that analysis, it is postulated that there always exist thin regions at the wall where some particles may briefly reside for a finite time, before being disturbed by the gas flow. As a result, there is always a

finite particle coverage on "bare" areas of wall. If falling streamers are not present to capture these particles, the rate at which particles deposit on the bare wall equals the rate at which they return to the core. When sufficient numbers of particles reside at any instant on the bare walls, streamers nucleate, and sections of the very thin wall layer begin to fall. The model assumes that at this point the walls are close to fully covered by a very thin layer of particles of suspension density ρ_{sd}. As defined earlier, the limiting suspension density of the core at this point is ρ_{sl}. At suspension density ρ_{sl}, the streamer interfacial area $\mathcal{P}_d$ is zero, $\mathcal{P}_{ca} = \mathcal{P}_t$, and there is a balance between the particles entrained from the "bare" wall and those depositing at the wall. Furthermore, as the wall layer interface is effectively a flat streamer, the equation for wall-to-core flux coefficient (eq. (10.10)), evaluated at ρ_{sl}, should give the entrainment from wall to core. Thus, at $\rho_{su} = \rho_{st} = \rho_{sl}$, the net core-wall flux is zero ($\dot{m}_u = \dot{m}_d$) and

$$\mathcal{P}_t \, k_{d0} \, \rho_{sd} = \mathcal{P}_t \, k_u \, \rho_{sl} \; , \tag{10.13}$$

where k_{d0} is the wall-to-core mass transfer coefficient evaluated at ρ_{sl}, corresponding to zero wall layer thickness ($r_{an} = 0$), i.e.

$$\begin{aligned} k_{d0} &= k_d(r_{an} = 0) \\ &= \Omega \frac{\rho_{gp} \mathbf{u}_{gp}^2}{2 \, \rho_{sd} \, \mathbf{v}_u} f_{i0} \; . \end{aligned} \tag{10.14}$$

$\mathbf{u}_{gp}$, ρ_{gp} and f_{i0} are calculated at $\rho_{st} = \rho_{sl}$ according to eqs. (9.7) and (9.8).

Equations (10.13) and (10.14) define the important model relationship between the limiting dilute suspension density, ρ_{sl}, and the wall layer viscous shear entrainment factor, Ω. The parameter ρ_{sl} may be physically measured by reducing reactor solids circulation until a negligible number of wall streamers are detected. Then, with estimates of k_u, and values for hydrodynamic parameters $\mathbf{u}_{cr}$, ρ_{su}, $\mathbf{v}_u$, ρ_g, ρ_p and ρ_{sd}, the parameter Ω may be calculated.

At typical wall streamer thicknesses, essentially all the dilute suspension particles crossing the core-wall boundary of perimeter $\mathcal{P}_{ca}$, as shown in Figure 10.2, are expected to be captured by falling streamers. Conceptually, the dilute suspension interspersed with the streamers may be described as a region that is continually swept clear of particles by streamers, and then

rapidly replenished with dilute suspension from the core. However, when the streamers are thin and substantial regions of bare wall are exposed to dilute suspension, some of the dilute suspension particles also deposit on the bare wall areas by the mechanism described earlier. Assuming that any solids transferring to the bare wall at a rate exceeding $k_u \rho_{sl}$ become part of the streamer flow, then the re-entrainment per unit height from the bare walls is still given by $k_{d0} \rho_{sd}$ multiplied by the bare wall perimeter $\mathcal{P}_w$. However, when streamers are present, it is likely that some particles leaving the bare walls will be captured by streamers before reaching the core. It is assumed that the fraction of particles which successfully reach the core from the bare walls is proportional to the fraction of reactor perimeter that is bare, $\mathcal{P}_w/\mathcal{P}_t$. This fraction varies linearly from unity at zero wall layer thickness to zero whenever the wall layer thickness exceeds r_{max}. Thus the rate of particle transfer from bare wall to core is $(\mathcal{P}_w^2/\mathcal{P}_t)\, k_{d0}\, \rho_{sd}$.

The core-to-wall lateral mass transfer coefficient, k_u, is equal to $\mathbf{c}/4$ (Chapter 8), where $\mathbf{c}$ is the r.m.s. fluctuating velocity of particles in the dilute core suspension. It is assumed that k_u is constant in the "developed flow" region. When this model was first developed, a heuristic argument was presented to justify this assumption, based on the postulate that wall streamers did not substantially influence the fluctuating motion of the core particles in the "developed flow" region (Senior and Brereton, 1992). The results of Chapter 8 indicate that this postulate is only reasonable in larger diameter commercial size combustors. Nevertheless, changes in dilute and dense region suspension densities in the "developed flow" region are relatively small, in comparison to the developing flow region, and use of a constant average value for k_u in this region is probably reasonable. As mentioned, $\overline{\mathbf{c}} = 0.8$ m/s (i.e. $k_u = 0.2$ m/s) was assumed for the developed flow region in model simulations. With this value, the model accurately fitted the UBC combustor experimental density profiles, and provided data that gave good results in heat transfer modelling (Senior and Brereton, 1990). The order of magnitude agreement between this empirically determined value and values of $\mathbf{c}$ predicted by the comprehensive CIRCOR model (Chapter 8) is encouraging, and suggests that the semi-empirical model provides a reasonable representation of riser solids flows.

In the developing flow zone, above the secondary air ports, suspension densities, wall layer thicknesses, and particle re-entrainment rates are greater than higher up in the riser. Consequently, the core particle collision frequency and the lateral core-to-wall mass flux of particles are expected to be greater in this zone. In addition, the projection of particles into this zone from the relatively dense primary zone, and the effect of secondary air injection, may further enhance lateral fluctuating particle motion in this zone. Consequently k_u is greater than in the developed flow zone. In addition, in the developing flow zone, k_u is allowed to vary with core suspension density, ρ_{su}.

Combining the equations for the various model lateral solids interchanges gives the expression for the net wall-to-core solids mass transfer,

$$(\dot{m}_d - \dot{m}_u) = (\mathcal{P}_d k_d + \mathcal{P}_c k_{d0})\, \rho_{sd} - \mathcal{P}_{ca} k_u \rho_{su} \ , \tag{10.15}$$

where $\mathcal{P}_c = \mathcal{P}_w^2/\mathcal{P}_{ca}$. Note that eq. (10.15) gives a curve similar to that in the Figure 10.1 inset. A number of alternative forms of eq. (10.15) were tried during model development that did not give this curve. They are discussed by Senior and Brereton (1990).

Rather than attempt detailed modelling to predict a bulk apparent suspension density profile, $\rho_{st}(z)$, in the developing flow region, it is assumed that the profile decays exponentially from the location at which the solids enter the reactor to the top of the developing flow region. A curve shape that accurately fitted the experimental suspension density profile trends over the developing heights is:

$$\frac{\rho_{st} - \rho_{sf}}{\rho_{s0} - \rho_{sf}} = \exp(-\zeta(z - z_0)) \ , \tag{10.16}$$

where ζ is a decay constant and ρ_{s0} is a reference constant density (800 kg/m^3). Parameters ρ_{sf} and z_0 depend on the hydrodynamic conditions. They are defined by constraining the curve given by eq. (10.16) to pass through suspension densities at two points; the suspension density at the solids return location, ρ_{sr}, and the suspension density at the top of the developing flow region, which equals the density at the bottom of the developed flow region. This task is complicated somewhat by the fact that the position of the developed flow-developing flow transition interface is also a model variable.

The solids volume fraction, ϵ_{pr}, of the turbulent fluidised bed at the solids return location is calculated using eq. (9.19), with U_g set equal to the primary zone superficial gas velocity. The suspension density at the solids return location, ρ_{sr}, equals $\epsilon_{pr}\rho_p$. As the solids return is generally close to the primary air inlet, the model only deals with phenomena above this height. The entry of the solids into the reactor therefore corresponds to the *lower boundary condition* of the model. The riser exit provides the *upper boundary condition*, with the reflection coefficient, R_f, specifying the fraction of solids travelling upward in the dilute suspension that are reflected back down the riser walls as streamers. The relation between R_f and the dilute suspension and dense streamer flows just below the exit is given by eq. (9.14).

To match the density at the top of the developing flow region with that at the bottom of the developed flow region, the location of the top of the developing flow region must first be defined. Values for $k_u(z)$ may be calculated from the developing flow density profile eq. (10.16), that simultaneously satisfy eqs. (10.1), (10.3) and (10.7). These values are always higher than the constant k_u value used in the developed flow region, but asymptotically approach the constant value as computation progresses up the reactor. The top of the developing region is defined as the location at which (i) the developed and developing flow region densities are virtually the same, and (ii) the core-to-wall mass transfer coefficient k_u, computed for the developing flow region, matches the constant coefficient of the developed flow region. Density ρ_{sf} (eq. (10.16)) and the height of the developing flow region are iteratively varied until the "matching" criteria are satisfied within a 2% tolerance. This fully defines the profile given by eq. (10.16).

Experimentally it is observed that the degree of solids internal reflection at the reactor exit can significantly affect the solids hold-up throughout much of the riser (Brereton, 1987). The matching criteria chosen for this model are consistent with this observation because of the dependence of ρ_{sf} on densities in the developed flow region. Generally ρ_{sf} is close to the zero cross-flux suspension density, ρ_{se}, for cases of moderate and high top reflection, and may assume values between ρ_{se} and ρ_{sl} for low reflection (Figure 10.2).

The prediction of the density profile in the developing flow region of the reactor relies on two

purely empirical equations (eqs. (10.16) and (9.19)). These equations adequately correlated the UBC combustor data presented in Chapter 7 for the specific conditions studied and reasonably predicted the available Studsvik data (Adams *et al.*, 1989) given below. However, they should be used with caution, in view of the limitations of simple empirical relations, discussed in Chapter 9.

10.3 Model Solution

The model is solved by the FORTRAN program RHOQUE. Program and ancillary subroutine codes are listed in Appendix G. The code is well documented, and includes definitions of all common block variables and key subroutine variables. Consequently, only a brief overview of the model operation is given here. There are two input files for the user. USERIN is a general input file for running different cases, and is the only file that most users need to change. The file PROGIN contains the key hydrodynamic parameters and should only be changed after some familiarity is gained with the model. Samples of the user input files are also given in Appendix G. File ERMSSG contains diagnostic messages. Should the program detect an input error or should numerical routines within the code not converge, appropriate messages from ERMSSG are reported as output. Most major input errors are detected by the program.

The main program RHOQUE supervises the solution process. Firstly all data are read via subroutine DATIN. Then gas and particle properties are computed (subroutines AIRPRO, SAUTER, and TERVEL). Subroutine SOLAIR supervises overall model convergence. Subroutines DENBED and UGCORE, respectively, compute solids hold-up and distribution, and gas flowrates in each region. They must be repeatedly called until the gas flowrates assumed for each call to DENBED converge to the correct value. Within DENBED there is a further iterative loop as the developing flow suspension density profile and the developed flow profile are matched. Details of a bed-to-wall heat transfer sub-model developed by Brereton to utilise data predicted by RHOQUE are given by Senior and Brereton (1990).

10.4 Results

The model was evaluated in three stages. Firstly, the model parameters were determined. Values for the majority of the parameters were obtained directly from experimental measurements in CFB combustors. Those parameters that were not directly measurable were adjusted in model simulations of the UBC combustor runs (Chapter 7) until predictions and experimental data agreed closely. All model parameters were then varied in turn to check that the trends predicted by the model agreed with experimental observation and/or model postulates. Finally, using the model parameters based on UBC combustor data (except for reflection factor, R_f, which varies with unit geometry), the predictive capability of the model was evaluated by comparing model predictions with experimental data obtained from the Studsvik prototype unit (Kobro, 1985; Adams *et al.*, 1989).

10.4.1 Model Fitting and Parameter Estimation

The model parameters may be summarised as follows:

(i) ρ_{sl}, the limiting suspension density below which a downflowing wall layer no longer occurs.

(ii) Ω, the viscous shear entrainment factor: fully defined by eqs. (10.13) and (10.14) if ρ_{sl} is known.

(iii) r_{max}, the minimum wall layer thickness at which 100% coverage of the riser wall by streamers occurs.

(iv) $\mathcal{K}$, wall streamer elliptic factor.

(v) Ψ, the wall layer disturbance factor; a key parameter that characterises how the wall layer is disturbed as it grows thicker.

(vi) k_u, the core-to-wall solids mass transfer coefficient; characterises the extent of particle transfer from core to wall. Higher values give greater decay rates of suspension density towards ρ_{se}, the density corresponding to zero net cross-flux.

(vii) ζ, the developing flow region density profile decay constant in eq. (10.16).

(viii) R_f, the fraction of upflowing solids which return down the walls rather than leaving via the riser exit.

(ix) ρ_{sd}, the suspension density of the wall streamers; assumed constant.

(x) $\mathbf{v}_d$, the wall streamer velocity; assumed constant.

Note that parameters (i), (iii) and (viii)–(x) can be directly measured, or simply estimated from measurements. Parameter (ii) is calculated from other parameters by eq. (10.14). Parameters (iii), (v), (vi) and (vii) are determined in this study by fitting the model to hydrodynamic data. Parameter (iv) exists only to characterise streamer shape, and parametric studies indicate it has negligible effect if ≥ 2. In this study $\mathcal{K}$ was set equal to 2. $\mathcal{K} \leq 1.5$ would imply the presence of streamers of almost semi-circular cross-section. All model parameters except R_f and r_{max} are assumed fixed for all CFB combustors. The parameter ρ_{sl} was set at 2 kg/m^3. This is a typical suspension density for dilute pneumatic conveying (Knowlton, 1986), and corresponds roughly to the suspension densities measured in the cold unit tests when streamers first began to form. Parameters ρ_{sd} and $\mathbf{v}_d$ were set to $0.4\rho_p$ and -1.1 m/s, respectively, as discussed above. $\zeta = 2.0$ ensured a good fit of eq. (10.16) to the data. R_f was set to 0.86 for all the UBC combustor simulations, based on the experimental estimates of R_f given in Chapter 9.

Two UBC combustor data sets were used to determine the unknown parameters Ψ, k_u, ζ and r_{max}, corresponding to cases where U_g and G_s were varied independently. For all runs, the combustor temperature was 850 °C ± °25 C. A very good match between predicted and experimental apparent suspension density profiles was obtained by simple trial and error adjustment of Ψ, k_u and ζ, as shown in Figure 10.3. Table 10.1 gives the combustor operating conditions and model input parameters for the UBC test run with $G_s = 44$ kg/m^{2}s and $U_g = 7.3$ m/s, corresponding to one of the profiles in Figure 10.3. The good fit obtained and the accuracy of the experimental profile data (± 20%) precluded any more detailed fitting processes. Although good fits to the experimental density profiles were obtained irrespective of the value for r_{max},

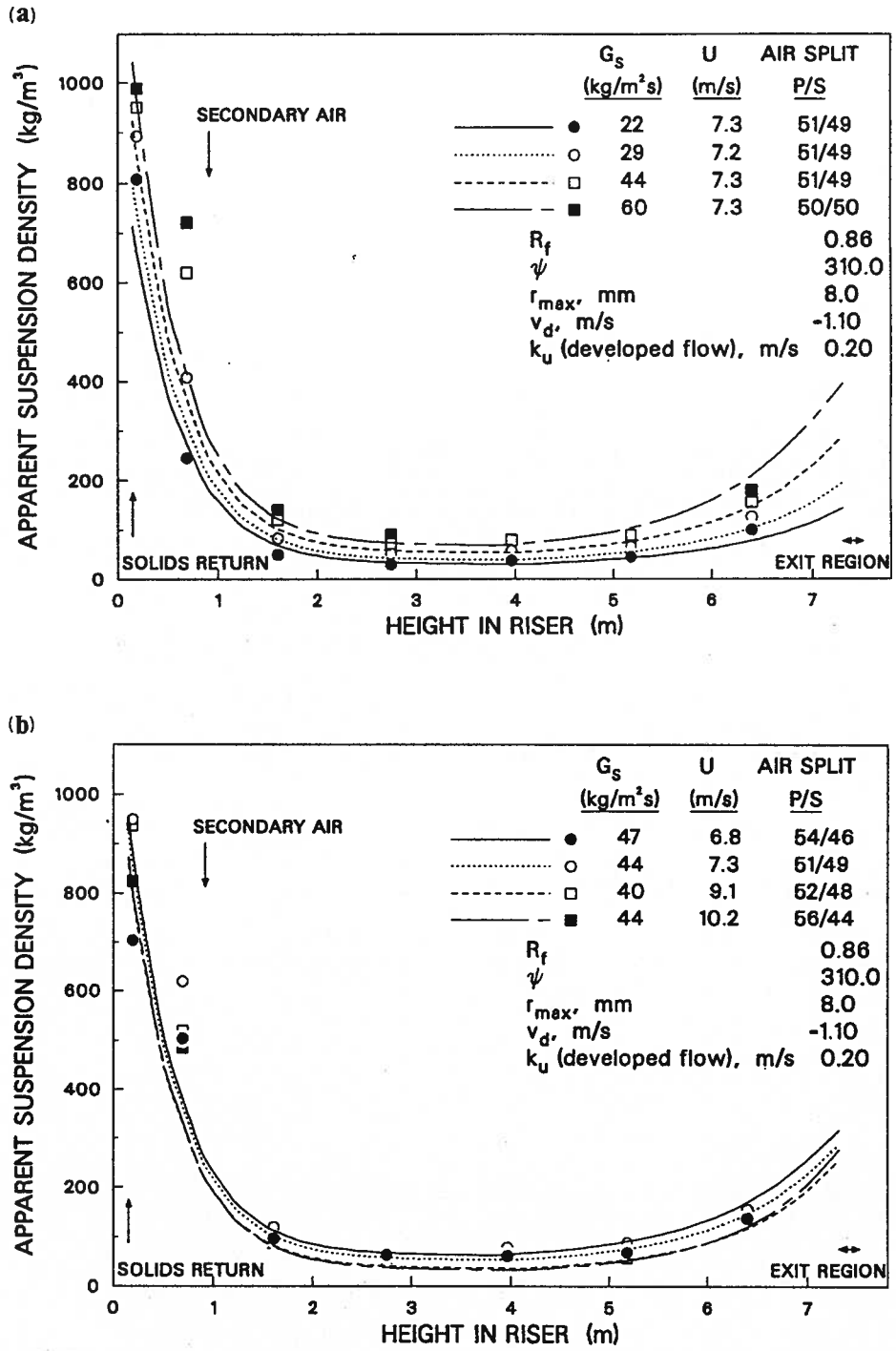

Figure 10.3: Comparison of model and experimental suspension density profiles for the UBC combustor with a nominal primary-to-secondary air ratio (P/S) of 50/50: (a) nominal superficial gas velocity 7.3 m/s; (b) nominal solids circulation rate 40 kg/m^{2}s. Symbols: experimental data. Curves: model predictions.

Table 10.1: Operating conditions and model parameters for the UBC and Studsvik combustors simulated by the solids flow model, RHOQUE.

Combustor	Studsvik	UBC	Units
Geometry			
Riser cross-sectional area	0.425	0.0232	m^2
Height of secondary air ports	1.000	0.914	m
Height to bottom of riser exit	6.050	7.315	m
Combustion Conditions			
Net solids flux	43.5	43.7	kg/m^2s
Nominal superficial gas velocity	6.2	7.3	m/s
Mean combustor gas temperature	845	845	°C
Bed particle density	2700	2650	kg/m^3
Sauter mean particle diameter	0.205	0.191	mm
Hydrodynamic Parameters			
Wall solids layer disturbance factor, Ψ	310	310	–
Riser top reflection coefficient, R_f	0.10	0.86	–
Wall streamer velocity	-1.1	-1.1	m/s
Minimum streamer thickness at 100% coverage	8	8	mm

heat transfer predictions (Senior and Brereton, 1990) were found to be a strong function of this parameter. A constant value of r_{max} = 8.0 mm was assumed for both UBC and Studsvik combustors. Although it is possible that r_{max} varies with riser diameter, there are currently no full-scale data available to confirm this, as discussed in Chapter 8. In addition, the wall surface may influence the stability of wall streamers, as discussed in Chapter 9, and thus streamers may be more stable on membrane waterwall surfaces than on flat walls. Although a single value for Ψ used in this study allowed good prediction of all density profiles considered, it is possible that Ψ may vary with the wall surface topography.

10.4.2 Parametric Testing and Validation

An extensive series of parametric tests was performed with the model. The trends predicted by the model in these tests were all consistent with experimentally observed trends and/or expected results based on model concepts. Important results are summarised here. Other details of the parametric tests are given by Senior and Brereton (1990). For the parametric study base case, a combustor of square cross-section, with the same geometry as the UBC combustor was assumed, except that R_f was set to 0.4. The base case operating conditions were T = 850 °C, U_g = 7.2 m/s, primary-to-secondary air ratio, P/S = 1/1, and G_s = 40 kg/m^{2}s. Particle properties were d_p = 200 μm and ρ_p = 2700 kg/m^3. All model parameters ((i)–(x)), except R_f, were set to the values discussed above.

The model predicted an increase in the reactor bulk suspension density throughout the reactor when the solids circulation was increased or the gas velocity decreased. Decreasing temperature within typical combustor temperature ranges had little effect on the suspension profile. However a large decrease in gas temperature (to 450 °C) produced an increase in the solids hold-up in the unit, due to the lower gas viscosity at the lower temperature, which decreased both the core solids velocity and the solids re-entrainment rate from the wall streamers. Significantly larger or heavier particles also gave greater solids hold-ups because of lower core solids velocities of these particles.

Of note was the effect of varying the solids top reflection factor, shown in Figure 10.4(a). A reflection factor of 0.90 gave the expected increase in density profile towards the exit. However, at $R_f = 0.40$, a gently decaying profile towards the exit was predicted, despite substantial internal reflection of solids at the top of the riser. This suggests that only very abrupt exits produce the upturn in the density profile towards the exit that is sometimes reported. The effect of increasing the wall layer disturbance factor is to increase the re-entrainment rate from a streamer of a given thickness, and, physically, may be viewed as destabilising the wall streamers. When this occurs, fewer solids remain within the reactor, resulting in lower solids hold-ups. This was clearly seen in the parametric studies (Figure 10.4(b)).

The final stage of testing the model was to compare the model's predictions with experimental results from a larger unit. The Studsvik prototype combustor has a very large exit region (Kobro, 1985), which allows adequate time for most particles to decelerate and divert out to a U-beam separator. Consequently, a low value of reflection coefficient R_f would be expected for this unit. A value of 0.10 was assumed. Without changing any of the other model parameters, the Studsvik prototype cases were simulated. Density profile results are given in Figure 10.5. Experimental and predicted density profiles are closely matched over the heights for which Studsvik data were available. Given the significant difference between the UBC and Studsvik combustor cross-sections, exit geometries, general solids hold-up and density profile shapes, the close agreement is encouraging.

The model predicts solids distribution and motion within the riser, in addition to the riser apparent suspension density profile. Figure 10.6 shows the wall coverage by streamers predicted by the model for the two cases of Table 10.1. For these small pilot and prototype units, as much as 25% of the wall is predicted to be exposed at any instant to dilute suspension upflow at suspension densities as high as 140 kg/m^3. The variation of wall coverage with riser height is very different for the two units, due to exit effects. These results are important for the understanding and prediction of local and overall bed-to-wall heat transfer coefficients. The measured variation of bed-to-wall heat transfer with height in the Studsvik prototype unit was

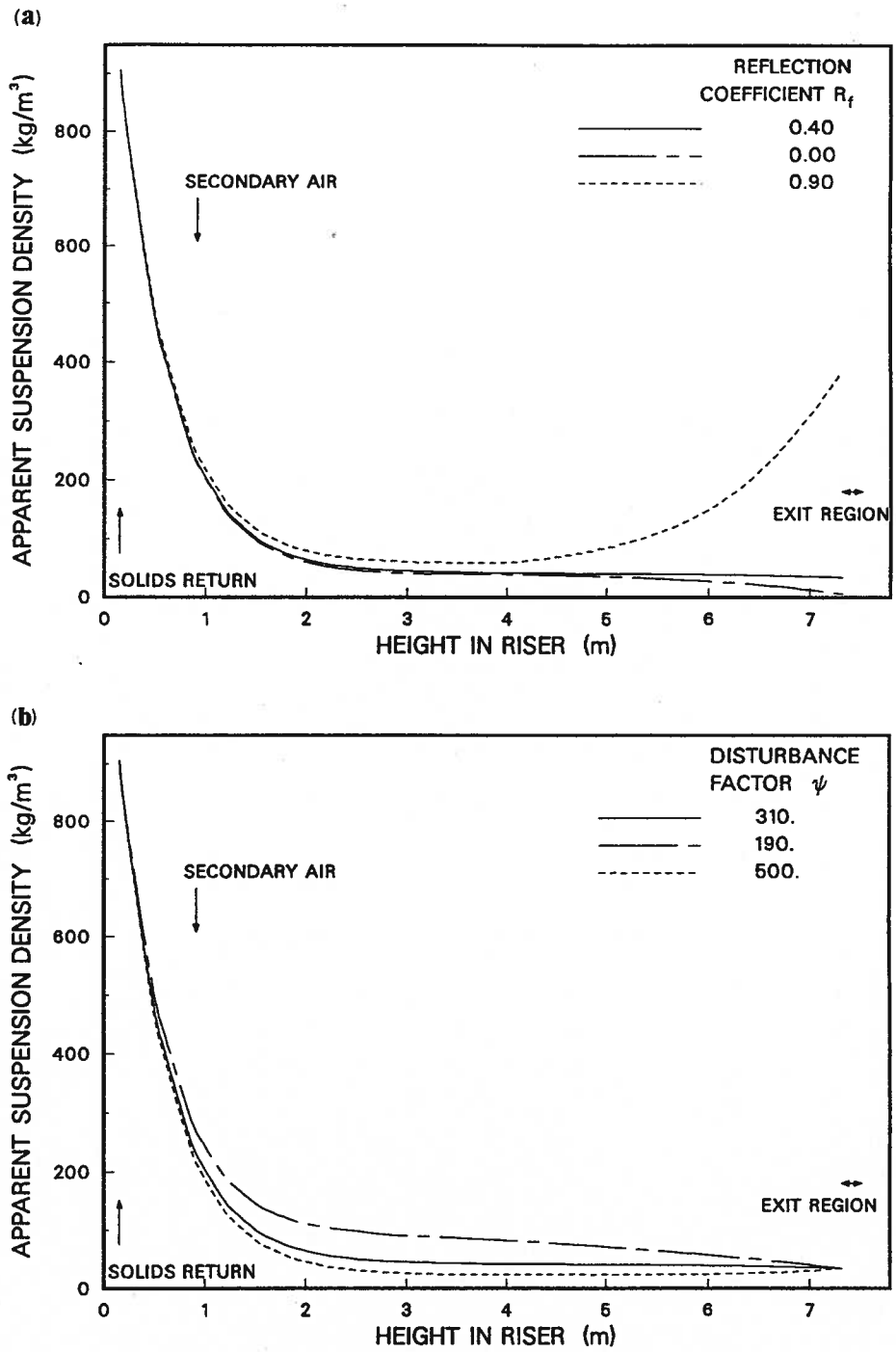

Figure 10.4: Parametric studies: effect on the apparent suspension density profile of (a) exit reflection factor, and (b) wall layer disturbance factor. (Riser conditions: $T = 850$ °C; $U_g = 7.2$ m/s; primary-to-secondary air ratio P/S = 1/1; $G_s = 40$ kg/m^{2}s; $d_p = 200$ μm; and $\rho_p = 2700$ kg/m^3; UBC combustor geometry).

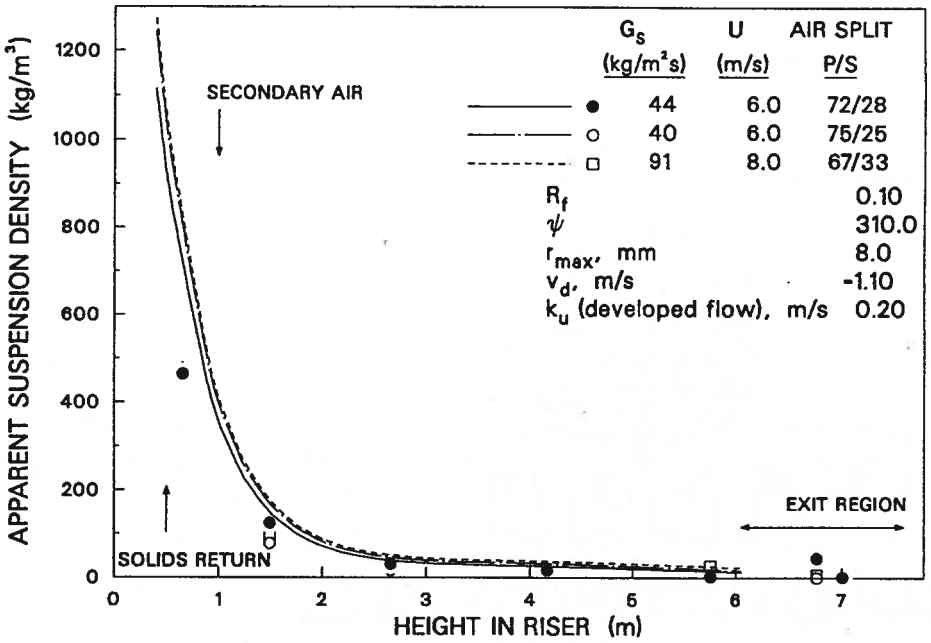

Figure 10.5: Comparison of model predictions and experimental suspension density profiles for the Studsvik prototype CFB combustor. Nominal primary-to-secondary air ratio (P/S) 70/30. See Table 10.1 for additional conditions. Symbols: experimental data. Curves: model predictions.

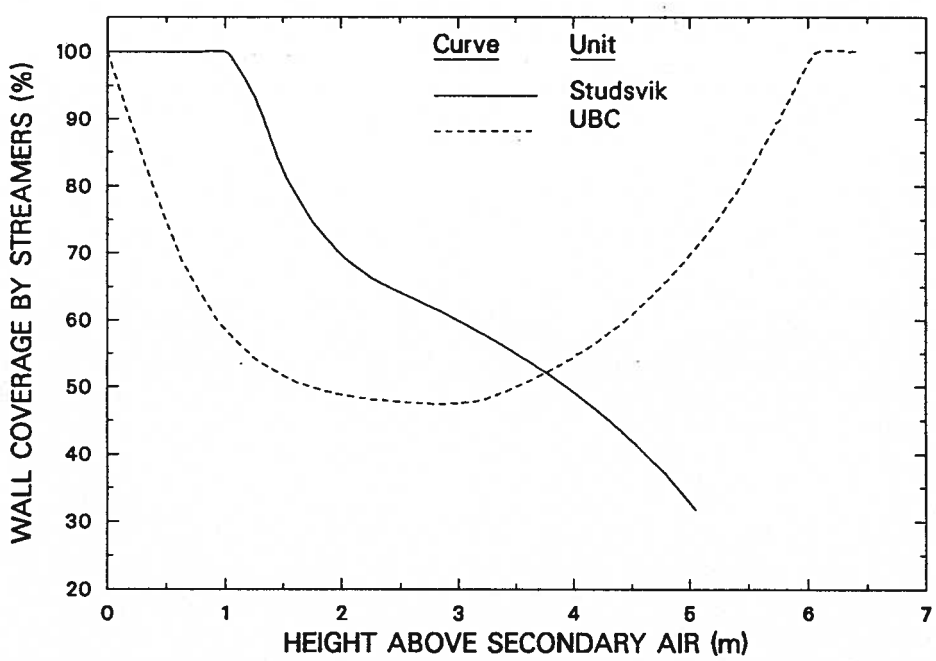

Figure 10.6: Calculated wall coverage by downflowing streamers for cases given in Table 10.1.

successfully predicted using data supplied by this model in the bed-to-wall heat transfer sub-model mentioned earlier. Chiu (1991) has reported good results using the model to predict solids flow and distribution in commercial scale units.

10.5 Conclusions

A semi-empirical model has been developed that predicts the flow and distribution of solids above the secondary air ports in a CFB combustor and the overall hold-up of solids within the combustor. The proposed mechanisms and relationships for solids internal reflection at combustor exits and interchange of solids between dense downflowing wall solids and dilute suspension upflow successfully account for suspension density profiles with abrupt and smooth exits. The model has performed well in comparisons with experimental data undertaken thus far. While encouraging results have been obtained, more testing and fundamental study of CFB dynamics are required to justify some of the model assumptions and parameters. The rudimentary approach to modelling suspension density below the secondary air ports also needs further development.

Chapter 11

CONCLUSIONS AND RECOMMENDATIONS

11.1 Overall Conclusions

Experimental and theoretical studies have been carried out to improve the understanding of the fluid and particle mechanics in CFB risers and to develop mathematical models to represent riser gas-particle suspension flows.

Cold unit riser tests in a column of 152 mm diameter confirmed the significant influence of riser exit and entry section geometries on solids flow and distribution within the riser. When a tapered base section of smaller cross-section than the riser was used, substantially higher suspension densities were often observed over the lower heights of the riser, in comparison to when a base section of uniform cross-sectional area was in place. The limitations of average suspension density estimates from measured pressure gradient were demonstrated. In particular, it was found that these estimates may vary substantially from more accurate estimates of true solids hold-up in the lower 1–2 m of the riser. A study of the relation between fluctuating signals measured at several locations in the riser suggested that the transient motion of wall streamers was largely due to local flow instabilities. A core-annulus distribution of solids in the riser was measured when wall streamers were present, in the turbulent fluidised regions at the bottom of the riser as well as at greater heights. A core-annulus distribution was also detected in preliminary hydrodynamic tests in a CFB pilot-scale combustor of cross section 152 mm $\times$ 152 mm.

Gas-particle and particle-particle interactions of importance have been considered. Order of magnitude estimations have helped with the assessment of the relative importance of different phenomena. Existing methods have been extended to estimate the response of discrete particles

to gas turbulence. The results of this analysis provided insight into the complex phenomenon of particle-turbulence interaction, and reasonably explain trends in existing LDV suspension flow data.

A comprehensive computer code for dilute suspension flow (CIRCOR) has been developed, which allows for gas turbulence-particle interactions, and particle collisions. Shear of the overall particle assemblage is modelled as a boundary condition. The effects of differing responses of particles of different size and density to the mean and fluctuating gas flow are incorporated by discretising the PSD into a number of particle fractions, and developing terms for interaction between fractions. Particle fraction fluctuating kinetic energy balances enable prediction of the r.m.s. fluctuating motion of particles within each fraction. This fluctuating motion in the core of a riser is directly related to the rate of lateral particle transfer to the walls. With the addition of suitable boundary conditions for fully-developed suspension flow, the model is used to predict details of riser core flow. Good results have been obtained in validation tests, in comparison with limited experimental data available. Correct order of magnitude particle fluctuating velocities (0.1–1.0 m/s) are predicted, and the model successfully explains initially puzzling trends observed in the cold unit tests.

The development of CIRCOR appears to be the first concerted effort aimed at determining the relative importance of gas turbulence and particle collisions on the fluctuating motion of the particles. The model simulations indicate that gas turbulence significantly influences the motion of suspensions of small, low density particles, such as FCC catalyst. In contrast, particle collisions are predicted to be the main mechanism by which larger denser particles, such as CFB combustor particles, gain fluctuating components of velocity. Several trends that are important for scale-up emerge from the model simulations. A substantial reduction in gas turbulence intensity with an increase in both riser diameter and temperature is predicted. Lower fluctuating particle velocities are predicted in the core of larger units due to less shearing of the particle assemblage. With the reduction in particle assemblage shear, PSD effects are expected to become more important in determining fluctuating particle motion in larger diameter units.

The CIRCOR model simulations support the assertion that a direct analogy between gas kinetic theory and an assemblage of colliding particles in suspension can be misleading. Equipartition of fluctuating energy between different particle size fractions in a suspension does not occur, due to the significant influence of drag. Therefore extension of existing granular kinetic theories to incorporate PSD effects is not a straightforward task.

Mechanisms for the formation of wall streamers have been proposed, supported by calculations of discrete particle trajectories in regions of steep gas velocity gradient near the riser wall. They indicate that shear flow-induced lift force in these regions may be significant, and further suggest that "non-continuum effects" in the particle phase may exist in these layers. These effects are not allowed for in two-fluid model formulations. A predictive semi-empirical solids flow model for CFB combustors, RHOQUE, is presented, based on the two-zone core-annulus approach. By incorporating suitable empirical methods into the model for prediction of the interchange between the core and annulus, and exit and entry effects, the majority of apparent suspension density profile shapes reported in the CFB literature may be predicted. Constants needed for the model were obtained by fitting to the UBC pilot-scale combustor, and predictions agree closely with data from a larger prototype CFB combustor.

11.2 Recommendations for Future Work

The simulations in this study indicate that a number of interesting and important changes may occur with scale-up and increasing temperature. More data are needed from larger and high temperature CFB risers to corroborate these findings. Wall layer properties, core region gas mixing and the effects of PSD on suspension density profile in large units should be investigated, and compared to data from smaller diameter units.

The complexity of the suspension flows in the wall region and near the base of the riser suggests that some empiricism will always be required to predict characteristics of these regions. Carefully planned experiments are required to develop these sub-models. For example, particle tracers injected into wall streamers could be followed to estimate particle re-entrainment

rates from streamers into the core flow. The influence of wall roughness and surface topography could be also investigated, to simulate surfaces in commercial units. Conditions under which significant heterogeneity in solids distribution in the riser core first arises should also be explored. Moreover, there is some evidence that dense or turbulent beds form more readily in small diameter units. This should be investigated to establish if the "dense bed" region is a pilot-scale unit phenomenon. The expected reduction in gas turbulence intensity with an increase in riser diameter suggests that improved gas mixing may be obtained in larger units if the riser is sub-divided into a number of vertical compartments of smaller diameter. This feature already exists in CFB combustors that have vertical "wing-wall" heat transfer surfaces inside the riser reactor.

Whilst the predictions obtained from both models developed in this study are encouraging, further improvements could be implemented. The riser core model CIRCOR could be extended to allow for non-uniform velocity profiles, thereby better representing the observed radial profiles of gas and solids velocity in the riser core. Addition of a comprehensive wall layer sub-model to CIRCOR would allow prediction of developing flows in the riser. Both these modifications to CIRCOR are relatively straightforward theoretical exercises, but challenging from a numerical point of view. The rudimentary approach to modelling the bottom (primary zone) region in the semi-empirical model RHOQUE should be improved, using additional combustor data from other CFB combustor units.

NOMENCLATURE

Symbol	Definition	Units
A	cross-sectional area	m^2
Ar	Archimedes number, $\mathbf{v}_t^3\rho_g^2/\mu_g g\Delta\rho$	–
a_P	particle projected area	m^2
a_p	particle surface area	m^2
$\mathbf{C}$	instantaneous fluctuating component of particle velocity	m/s
$\mathbf{C}_k$	instantaneous collisional fluctuating component of particle velocity	m/s
$\mathbf{C}_t$	instantaneous particle fraction drift velocity	m/s
C_D	particle drag coefficient	–
$\mathbf{c}$	combined r.m.s. fluctuating particle velocity	m/s
$\mathbf{c}_k$	collisional r.m.s. fluctuating particle velocity	m/s
$\mathbf{c}_t$	mean particle fraction drift velocity	m/s
c_0, c_1, c_2	correlation coefficients	–
D	CFB riser or reactor (hydraulic) diameter	m
D_{gt}	turbulence energy dissipation rate (per unit volume)	J/m^3s
D_{kr}	particle fluctuating kinetic energy dissipation by wall collisions	J/m^2s
D_{ks}	particle fluctuating kinetic energy dissipation by streamer capture	J/m^2s
D_{kt}	particle fluctuating kinetic energy dissipation due to drag	J/m^3s
$\mathcal{D}$	long time diffusion coefficient	m^2/s
d_p	particle diameter	m
$d_p^\star$	dimensionless particle diameter (Table 3.2)	m
d_{sv}	particle surface/volume diameter	m
d_s	diameter of sphere having same surface area as particle	m
d_v	volume-equivalent particle diameter	m
ΔE	kinetic energy change	J

Symbol	Definition	Units
e	coefficient of restitution for particle-particle collisions	–
e_w	coefficient of restitution for particle-wall collisions	–
$\mathbf{F}_D$	gas drag force on particles in suspension (per unit volume)	N/m^3
$\mathbf{F}_k$	collisional force per unit suspension volume	N/m^3
$\mathbf{f}_D$	gas drag force on a particle	N
$\mathbf{f}_k$	average collisional force on a single particle	N
$\mathbf{f}_L$	lift force on a single particle	N
$\mathbf{f}_S$	particle force – see eq (3.14)	N
f	Maxwellian velocity distribution – see eq. (8.34)	$1/s^3$
f_g	Fanning friction factor for gas flow	–
f_i	core-annulus interfacial friction factor	–
f_{i0}	smooth pipe friction factor	–
f_w	mass fraction of total wall-to-core transfer due to wall rebounds	–
$G(\epsilon_p)$	particle assemblage bulk modulus of elasticity	N/m^2
G_s	net solids circulation flux (based on total riser cross-sectional area)	$kg/m^2\,s$
$\mathbf{g}$	gravitational acceleration	m/s^2
g	magnitude of acceleration of gravity, $\lvert\mathbf{g}\rvert$	m/s^2
$\mathbf{I}$	unit tensor	–
I	inertial parameter – see eq. (8.43)	–
I_R	$\mathbf{v}_s/u_e$, velocity ratio: particle slip to gas turbulence intensity	–
$\mathbf{J}$	impulse of the particle-particle collision force	kg m/s
K	particle fraction fluctuating kinetic energy (per unit particle mass)	m^2/s^2
$\mathcal{K}$	wall streamer cross-section elliptic shape factor	–
$\mathbf{k}$	unit vector directed between particle centres at impact	–

Symbol	Definition	Units
$\mathbf{k}$	unit normal vector directed outward across phase interface	–
k	wall roughness	m
k_d	streamer-to-core lateral particle mass transfer coefficient	m/s
k_{d0}	wall-to-core particle mass transfer coefficient in the limit $r_{an} \to 0$	m/s
k_u	core-to-streamer lateral particle mass transfer coefficient	m/s
k_B	Boltzmann constant, 1.38×10^{-23}	J/K
Δk	single particle fluctuating kinetic energy creation by collision	J
L	riser (or pipe) length	m
l_e	characteristic energetic eddy size	m
$\mathbf{M}$	phase interfacial momentum source term	N/m^3
$\mathbf{M}^d$	total interfacial drag between phases	N/m^3
m	no. of collisions to accelerate mean wall particle to core velocity	–
$\dot{m}$	mass rate of formation per unit volume	kg/m^3 s
$\dot{m}_d$	mass transfer rate from dense streamers to dilute suspension upflow	kg/m s
$\dot{m}_u$	mass transfer rate from dilute suspension upflow to dense streamers	kg/m s
m_p	mass of a single particle	kg
m_s	solids loading ratio (mass flow solids/mass flow of gas)	–
N	number flux of particles	$1/m^2s$
$\mathbf{n}$	number of particles per unit volume	$1/m^3$
n	number of core particle fractions	–
P_{gt}	gas turbulence energy production rate (per unit volume)	J/m^3s
P_{kk}	particle fluctuational kinetic energy production by collision	J/m^3s
P_{kr}	particle fluctuational kinetic energy production by rebound particles	J/m^2s
P_{ks}	particle fluctuational kinetic energy production by streamer particles	J/m^2s

Symbol	Definition	Units
P_{kt}	particle fluctuational kinetic energy production by gas turbulence	J/m^3s
Pr	probability	–
$\mathcal{P}_c$	$\mathcal{P}_w^2/\mathcal{P}_{ca}$	m
$\mathcal{P}_{ca}$	perimeter of the riser core region	m
$\mathcal{P}_d$	streamer-dilute suspension interface perimeter	m
$\mathcal{P}_t$	riser cross-section perimeter	m
$\mathcal{P}_w$	wall perimeter exposed to dilute suspension upflow	m
p	pressure	N/m^2
p_g	gas pressure	N/m^2
Q_c	mass flux of particles from core to wall region	kg/m^2s
Q_r	mass flux of particles from wall rebounds to core region	kg/m^2s
Q_s	mass flux of particles from wall streamers to core region	kg/m^2s
Q_w	total mass flux of particles from wall to core region	kg/m^2s
R	(hydraulic) radius of riser	m
R_f	riser exit reflection coefficient	–
R_{Lg}	Lagrangian auto-correlation for gas flow	–
Re_D	pipe or riser gas flow Reynolds number, $\rho_g D U_g/\mu_g$	–
Re_p	particle Reynolds number, $\rho_g d_p\lvert\mathbf{U}-\mathbf{V}\rvert/\mu_g$	–
Re_{sr}	Reynolds number for Kwauk *et al.*(1986) correlation, eq. (9.18)	–
Re_t	particle terminal velocity Reynolds number, $\rho_g d_p \mathbf{v}_t/\mu_g$	–
Re_v	particle Reynolds number, $\rho_g d_v\lvert\mathbf{U}-\mathbf{V}\rvert/\mu_g$	–
$\mathcal{R}_{wi}$, $\mathcal{R}_{iw}$	see eq. (8.89)	–
r	radial distance from riser vertical axis	m
r_{an}	wall region thickness, perpendicular to the riser wall	m

Symbol	Definition	Units
r_{max}	lower limit of wall region thickness for full coverage by streamers	m
r_p	particle radius	m
S_k	particle fluctuational kinetic energy transfer by type (ii) collisions	J/m^3s
S_{gp}	net energy transfer from the gas to the particles per unit volume	J/m^3s
s	surface area	m^2
s_x	riser cross section shape factor (π for circular; 4 for square)	–
$\mathbf{T}$	deviatoric stress tensor	N/m^2
T	temperature	°C
T_g	gas temperature	°C
T_c	particle "granular" temperature	m^2/s^2
$\mathcal{T}$	integral timescale	s
t	time	s
$\mathbf{U}$	instantaneous interstitial gas velocity	m/s
U_g	gas superficial velocity	m/s
$U_g^\star$	dimensionless gas superficial velocity, $U_g(\rho_g^2/\mu_g\, g\, \Delta\rho)^{1/3}$	m/s
U_0	cross-sectionally averaged gas velocity	m/s
$\mathbf{u}$	(time-averaged) interstitial gas velocity	m/s
$\mathbf{u}_c$	mean axial centreline gas velocity	m/s
$\mathbf{u}_{gp}$	combined gas-particle phase velocity – see eq. (9.8)	m/s
$\mathbf{u}'$	fluctuating component of interstitial gas velocity	m/s
$\mathbf{u}_\star$	wall friction velocity	m/s
u	r.m.s. fluctuating gas velocity	m/s
u_e	(linear) turbulence velocity	m/s
u_x, u_y, u_z	x, y, z components of r.m.s. fluctuating gas velocity	m/s

Symbol	Definition	Units
u_κ	Kolmogorov sized eddy velocity scale	m/s
$\mathbf{V}$	instantaneous particle velocity	m/s
$\overline{\mathbf{V}}$	average particle velocity	m/s
$\Delta\mathbf{V}$	change in velocity	m/s
V_c	control volume	m^3
ΔV	change in speed	m/s
ΔV_r	collisional change in speed perpendicular to the initial relative velocity	m/s
$\mathbf{v}$	(time-averaged) particle velocity	m/s
$\mathbf{v}_k$	mean velocity of the kth phase	m/s
$\mathbf{v}'$	fluctuating component of particle velocity	m/s
$\mathbf{v}_s$	slip velocity	m/s
$\mathbf{v}_t$	terminal velocity of particle in stagnant gas	m/s
$\mathbf{v}_t^\star$	dimensionless terminal velocity (Table 3.2)	m/s
$\mathbf{v}_z$	mean vertical particle fraction velocity	m/s
$\Delta\mathbf{v}_z$	change in mean vertical velocity of core particle due to a wall collision	m/s
$\mathbf{v}_{zr}$	vertical velocity of mean rebound particle re-entering core flow	m/s
$\mathbf{v}_{zs}$	vertical velocity of mean streamer particle re-entering core flow	m/s
$\Delta\mathbf{v}_{AB}$	average change in particle A velocity in A-B particle collision	m/s
v_e	linear particle turbulence velocity	m/s
$\mathbf{W}_+$	average lateral velocity of particles across vertical plane	m/s
ΔW	change in speed of wall streamer particle due to core collision	m/s
$\mathbf{w}_j$	mean wall particle velocity after jth core collision	m/s
$\Delta\mathbf{w}_j$	average change in wall particle velocity due to jth core collision	m/s
X_i	feed or initial mass fraction (ith fraction)	–

Symbol	Definition	Units
$X(t)$	displacement at time t	m
∇X_k	see eq. (4.7)	1/m
$\mathcal{X}_j$	dimensionless mean wall particle velocity after jth core collision	–
x_i	mass fraction (ith fraction)	–
x, y	orthogonal coordinates in a horizontal plane	m
x', y', z'	orthogonal Cartesian coordinates	m
y^+	dimensionless distance from wall, $y\mathbf{u}_*/\nu$	–
Z_{AA}	collision frequency amongst type A particles	$1/\mathrm{m}^3\mathrm{s}$
Z_{AB}	collision frequency between A and B type particles	$1/\mathrm{m}^3\mathrm{s}$
Z_A	collision frequency of a discrete A particle with A particles	1/s
$Z_{A(B)}$	collision frequency of a discrete particle A with B particles	1/s
$\mathcal{Z}$	dimensionless collision frequency – see eq. (D.35)	–
$\mathcal{Z}^{\#}$	estimated dimensionless collision frequency – see eq. (D.38)	–
z	vertical coordinate	m
z_0	reference height – see eq. (10.16)	m

Greek Letters

Symbol	Definition	Units
$\boldsymbol{\delta}_r, \boldsymbol{\delta}_\theta, \boldsymbol{\delta}_z$	cylindrical coordinate unit vectors in r-, θ-, z-axis direction	–
$\boldsymbol{\delta}_x, \boldsymbol{\delta}_y, \boldsymbol{\delta}_z$	unit vectors in x-, y-, z-axis (or x'-, y'-, z'-axis) direction	–
$\boldsymbol{\Gamma}_k$	see eq. (4.10)	$\mathrm{N/m^3}$
ϵ	volume fraction (i.e. voidage for gas phase)	–
$\bar{\epsilon}$	cross-sectionally averaged volume fraction	–
ϵ_{pr}	solids volume fraction at solids return location	–
ϵ_t	turbulent energy dissipation rate (per unit mass)	$\mathrm{m^2/s^3}$
ζ	suspension density profile decay constant – see eq. (10.16)	–
η	small particle collection efficiency on larger target	–
η_κ	Kolmogorov eddy length scale	m
Θ	particle collision-response time interval ratio, $\exp(-\tau_k/\tau_p)$	–
θ	time lag	s
θ	polar coordinate angle between x- and r-axes	–
κ	bulk viscosity	kg/m s
Λ	particle mean free path	m
λ	particle velocity weighting factor	–
λ_e	eddy interaction particle velocity weighting factor	–
λ_r	particle velocity weighting factor based on period τ_r	–
$\bar{\lambda}$	mid-size particle velocity weighting factor	–
μ	shear viscosity	kg/m s
μ_w	wall-particle coefficient of sliding friction	–
ν	kinematic viscosity	$\mathrm{m^2/s}$
ν_t	eddy viscosity	$\mathrm{m^2/s}$
ξ	mean to r.m.s. fluctuating velocity ratio	–

Symbol	Definition	Units
$\boldsymbol{\Pi}$	total stress tensor	N/m^2
ϖ	$(1 - 11\pi \mathbf{n} d_p^3/12)/(1 - 4\pi \mathbf{n} d_p^3/3)$	–
ρ_g	gas density	kg/m^3
ρ_{gp}	combined gas-particle phase density – see eq. (9.7)	m/s
ρ_k	phase k density	kg/m^3
ρ_p	particle density	kg/m^3
ρ_s	suspension density	kg/m^3
ρ_{sa}	apparent suspension density	kg/m^3
ρ_{sd}	suspension density of dense suspension downflow	kg/m^3
ρ_{se}	riser suspension density at condition of zero net wall-core mass flux	kg/m^3
ρ_{sf}	density defined by eq. (10.16)	kg/m^3
ρ_{sl}	lowest riser suspension density at which wall streamers form	kg/m^3
ρ_{sr}	riser suspension density at solids return location	kg/m^3
$\rho_{st}(z)$	riser suspension density at height z (i.e. cross-sectional average)	kg/m^3
ρ_{su}	uniform dilute upflow suspension density	kg/m^3
ρ_{s0}	see eq. (10.16)	kg/m^3
$\Delta\rho$	$\rho_p - \rho_g$	kg/m^3
σ	collision radius	m
$\boldsymbol{\tau}_i$	total shear force on riser wall streamers due to core flow	N/m^2
$\boldsymbol{\tau}_{ij}$	non-convective flux of j-momentum across plane with normal $\boldsymbol{\delta}_i$	N/m^2
$\boldsymbol{\tau}_{ij}$	shear force per unit area in jth direction on plane with normal $\boldsymbol{\delta}_i$	N/m^2
$\boldsymbol{\tau}_r$	force (per unit interfacial area) on core due to wall rebound particles	N/m^2
$\boldsymbol{\tau}_s$	force (per unit interfacial area) on core due to wall streamer particles	N/m^2
$\boldsymbol{\tau}_f$	combined gas-particle frictional shear force on riser wall	N/m^2

Symbol	Definition	Units
τ_d	particle drift time	s
τ_e	characteristic energetic eddy decay time	s
τ_k	time interval between collisions for a particle	s
τ_p	particle relaxation time	s
τ_r	particle interaction time	s
τ_κ	Kolmogorov timescale	s
Φ	ratio Lagrangian/"Eulerian moving with the mean flow" integral timescales	–
φ	particle volume	m^3
χ_{ri}	fraction of wall rebound particles that collide with core fraction i	–
χ_{si}	fraction of wall streamer particles that collide with core fraction i	–
ψ	particle sphericity	–
Ψ	wall layer disturbance factor	–
Ω	viscous shear entrainment factor	–

Subscripts

Symbol	Definition
A, B	particle fraction A, B, respectively
AB	velocity: A relative to B
AB	velocity change, collision frequency and force: A-B interaction
$A(B)$	effect of fraction B on discrete A particle
an	riser annular wall region
c	particle-particle collision contribution or component
ca	riser core-annular wall region interface
cr	riser core region
d	dense suspension downflow
E	"Eulerian moving with the mean flow" frame of reference
L	Lagrangian frame of reference
f	final condition
g	gas
i, j	particle fraction i, j, respectively
i	initial condition
k	phase (gas or solid)
p	particle
r	rebound from wall; or lateral or perpendicular to initial velocity
s	wall streamer
t	energetic eddy (or in the direction thereof); or total riser-cross section
u	dilute suspension upflow
ud	dilute suspension-dense streamer interface

Symbol	Definition
w	wall or wall region
z	vertical (axial) direction
0, 1	particle-free and particle-laden condition, respectively
1, 2	initial and final condition, respectively

Superscripts

Symbol	Definition
$\mathbf{T}$	transpose of a tensor
$'$	type (i) collision
$''$	type (ii) collision

REFERENCES

Abed, R., The characterization of turbulent fluid-bed hydrodynamics, *Fluidization*, ed. D. Kunii and R. Toei, Engineering Foundation, N.Y., pp. 137–144 (1983).

Abrahamsen, A.R. and Geldart, D., Behaviour of gas fluidized beds of fine powders, *Powder Technol.*, **26**, 35–65 (1980).

Abrahamson, J., Collision rates of small particles in a vigorously turbulent fluid, *Chem. Eng. Sci.*, **30**, 1371–1379 (1975).

Adams, C.K., Gas mixing in fast fluidised beds, *Circulating Fluidized Bed Technology II*, ed. P. Basu and J.F. Large, Pergamon, pp. 299–306 (1988).

Adams, C., Morris, M., Colmano, R. and Epis, G., Full-load firing of coal, oil and gas in a circulating fluidised bed, *Proc. 10th Int. Conf. on Fluidized Bed Combustion*, ASME, pp. 107–119 (1989).

Adamson, *A Textbook of Physical Chemistry (2nd. ed.)*, Academic Press, N.Y. (1979).

Anderson, T.B. and Jackson, R., A fluid mechanical description of fluidized beds, *I&EC Fundam.*, **6**, 527–539 (1967).

Arena, U., Cammarota, A. and Pistone, L., High velocity behavior of solids in a laboratory scale circulating bed, in *Circulating Fluidized Bed Technology*, ed. P. Basu, Pergamon, Toronto, pp. 119–125 (1986).

Arena, U., Cammarota, A., Massimilla, L. and Pirozzi, D., The hydrodynamic behaviour of two different circulating fluidized bed units of different sizes, *Circulating Fluidized Bed Technology II*, ed. P. Basu and J.F. Large, Pergamon, Oxford, pp. 223–230 (1988).

Arena, U., Cammarota, A., Marzocchella, A. and Massimilla, L., Solids flow structures in a two-dimensional riser of a circulating fluidized bed, *J. Chem. Eng. Japan*, **22** (3), 236–241 (1989).

Arena, U., Malandrino, A., Marzocchella, A. and Massimilla, L., Flow structures in the risers of laboratory and pilot CFB units, *Circulating Fluidized Bed Technology III*, ed. P. Basu, M. Horio and M. Hasatani, Pergamon, pp. 137–144 (1991).

Asali, J.C. and Hanratty, T.J., Interfacial drag and film height for vertical annular flow, *A.I.Ch.E. J.*, **31**(6), 895–902 (1985).

Bader, R., Findlay, J. and Knowlton, T.M., Gas/solids flow patterns in a 30.5-cm-diameter circulating fluidized bed, in *Circulating Fluidized Bed Technology II*, ed. P. Basu and J.F. Large, Pergamon, Oxford, pp. 123–137 (1988).

Batchelor, G.K., A new theory for the instabilty of a uniform fluidized bed, *J. Fluid Mech.*, **193**, 75–110 (1988).

Bedford, A. and Drumheller, D.S., Theories of immiscible and structured mixtures, *Int. J. Engng. Sci.*, **21**(8), 863–960 (1983).

Beer, F.P. and Johnston, E.R, *Mechanics for Engineers: Dynamics (3rd. ed.)*, McGraw-Hill (1976).

Bendat, J.S. and Piersol, A.G., *Engineering applications of correlation and spectral analysis*, Wiley, N.Y. (1980).

Berker, A. and Tulig, T.J., Hydrodynamics of gas-solid flow in a catalytic cracker riser: Implications for reactor selectivity performance, *Chem. Eng. Sci.*, **41**, 821–827 (1986).

Berruti, F. and Kalogerakis, N., Modelling the internal flow structure of circulating fluidized beds, *Can. J. Chem. Eng.*, **67**, 1010–1014 (1989).

Bierl, T.W., Gajdos, L.J., McIver, A.E. and McGovern, J.J., Studies in support of recirculating bed reactors for the processing of coal, Final Report for work performed under U.S. D.O.E. Contract No. AC01–76ET10525, Carnegie-Mellon University, Pittsburgh (1980).

Binder, J.L. and Hanratty, T.J., A diffusion model for droplet deposition in gas/liquid annular flow, *Int. J. Multiphase Flow*, **17**, 1–11 (1991).

Bird, R.B., Stewart, W.E. and Lightfoot, E.N., *Transport Phenomena*, Wiley, N.Y. (1960).

Bolton, L.W. and Davidson, J.F., Recirculation of particles in fast fluidized risers, *Circulating Fluidized Bed Technology II*, ed. P. Basu and J.F. Large, Pergamon, Oxford, pp. 139-146 (1988).

Bouillard, J.X., Lyczkowski, R.W., Folga, S., Gidaspow, D. and Berry, G.F., Hydrodynamics of erosion of heat exchanger tubes in fluidized bed combustors, *Can. J. Chem. Eng.*, **67**, 218–229 (1989).

Bowen, B.D., Numerical methods, CHML 553 graduate course notes, University of British Columbia (1988).

Box, G.E.P. and Jenkins, G.M., *Time Series Analysis Forecasting and Control*, Holden-Day, San Francisco (1970).

Brereton, C.M.H., Fluid mechanics of high velocity fluidized beds, Ph.D. dissertation, University of British Columbia (1987).

Brereton, C.M.H., Private communication, University of British Columbia (1990).

Brown, R.L. and Richards, J.C, Principles of powder mechanics, Pergamon (1970).

Burkell, J.J., Solids circulation rate measurement in a circulating fluidized bed, M. A. Sc. thesis, University of British Columbia (1986).

Chapman, S. and Cowling, T.G., *The Mathematical Theory of Non-Uniform Gases (3rd. ed.)*, Cambridge U. Press (1970).

Chandok, S.S. and Pei, D.C.T., Particle dynamics in solids-gas flow in a vertical pipe, *Prog. Heat and Mass Transfer*, **6**, 465–474 (1972).

Chang, H. and Louge, M., Dynamic scale-up of circulating fluidized beds, *Proc. 11th Int. Conf. on Fluidized Bed Combustion*, ASME, pp. 1215–1218 (1991).

Carnahan, B., Luther, H.A. and Wilkes, J.O., *Applied Numerical Methods, Wiley*, N.Y. (1969)

Chen, C.P., Scaling and modeling of turbulent suspension flows, in *Constitutive relationships and models in continuum theories of multiphase flows*, NASA Conference Publication 3047, pp. 139–146 (1989).

Chiu, J., Private communication, ABB Combustion Engineering, CT, U.S.A. (1991).

Clift, R., Particle-particle interactions in gas-particle systems, *I. Chem. E. Symp. Ser.*, No. **91**, 27–41 (1985).

Clift, R. and Gauvin, W.H., Motion of entrained particles in gas streams, *Can. J. Chem. Eng.*, **49**, 439–448 (1971).

Clift, R., Grace, J.R. and Weber, M.E., *Bubbles, Drops and Particles*, Academic Press (1978).

Couturier, M.F., Doucette, B. and Poolpol, S., A study of gas concentration, solids loading and temperature profiles within the Chatham CFB combustor, Report to Energy, Mines and Resources Canada, Energy Research Laboratories, CANMET (1989).

Couturier, M.F., Doucette, B. and Poolpol, S., Temperature, gas concentration and solid mass flux profiles within a large circulating fluidized bed combustor, *Proc. 11th Int. Conf. on Fluidized Bed Combustion*, ASME, pp. 107–114 (1991).

Csanady, G.T., Turbulent diffusion of heavy particles in the atmosphere, *J. Atmos. Sci.*, **20**, 201–208 (1963).

Davidson, J., The two-phase theory of fluidization: Successes and opportunities, A.I.Ch.E. Annual Meeting, Chicago, Illinois, Nov. 11–16 (1990).

Davies, J.T., *Turbulence Phenomena*, Academic Press, New York (1972)

Diggle, P.J., *Time Series: A Biostatistical Introduction*, Clarendon Press, Oxford (1990).

Ding, J. and Gidaspow, D., A bubbling fluidization model using kinetic theory of granular flow, *A.I.Ch.E. J.*, **36**(4), 523–538 (1990).

Drazin, P.G. and Reid, W.H., *Hydrodynamic stability*, Cambridge U. Press, Cambridge (1981).

Drew, D.A., Mathematical modeling of two-phase flow, *Ann. Rev. Fluid Mech.*, **15**, 261–291 (1983).

Dry, R.J., Radial particle size segregation in a fast fluidised bed, *Powder Techol.*, **52**, 243–250 (1987).

Dukler, A.E., Characterization, effects and modeling of the wavy gas-liquid interface, *Prog. Heat and Mass Transfer*, **6**, 207–234 (1972).

Engstrom, F. and Lee, Y.Y., Future challenges of circulating fluidized bed combustion technology, *Circulating Fluidized Bed Technology III*, ed. P. Basu, M. Horio and M. Hasatani, Pergamon, pp. 15–26 (1991).

Fanucci, J.B., Ness, N. and Yen, R.-H., On the formation of bubbles in gas-particulate fluidized beds, *J. Fluid Mech.*, **94**, 353–367 (1979).

Farrell, M., Lun, C.K.K. and Savage, S.B., A simple kinetic theory for granular flow of binary mixtures of smooth, inelastic, spherical particles, *Acta Mech.*, **63**, 45–60 (1986).

Fett, F.N., Burkle, K.J., Dersch, J., Scholer, J., Edelmann, H. and Heinbockel, I., Progress in fluidised bed modelling, *Second Int. Symp. Coal Combustion*, Beijing (1991).

Foscolo, P.U. and Gibilaro, L.G., A fully predictive criterion for the transition between particulate and aggregative fluidization, *Chem. Eng. Sci.*, **39**, 1667–1675 (1984).

Garg, S.K. and Pritchett, J.W., Dynamics of gas-fluidized beds, *J. Appl. Phys.*, **46**, 4493–4500 (1975).

Geldart, D., Types of gas fluidization, *Powder Technol.*, **7**, 285–292 (1973).

Geldart, D. (ed.), *Gas Fluidization Technology*, Wiley, N.Y. (1986).

Geldart, D., Cullinan, J., Georghiades, S., Gilvray, D. and Pope, D.J. The effects of fines on entrainment from gas fluidized beds, *Trans Instn. Chem. Engrs.*, **57**, 269–275 (1979).

Gidaspow, D., Hydrodynamics of fluidization and heat transfer: Supercomputer modeling, *Appl. Mech. Rev.*, **39**(1), 1–23 (1986).

Gidaspow, D., Syamlal, M. and Seo, Y., Hydrodynamics of fluidization of single and binary size particles: Supercomputer modeling, in *Fluidization V*, ed. K. Ostergaard and A. Sorenson, Engineering Foundation, pp. 1–8 (1986).

Gidaspow, D., Tsuo, Y.P. and Luo, K.M., Computed and experimental cluster formation and velocity profiles in circulating fluidized beds, in *Fluidization VI*, ed. J.R. Grace, L.W. Shemilt and M.A. Bergougnou, Engineering Foundation, pp. 81-88 (1989a).

Gidaspow, D., Tsuo, Y.P. and Ding, J., Hydrodynamics of circulating and bubbling fluidized beds, *Proc. EPRI Workshop on Materials Issues in Circulating Fluidized-Bed Combustors*, GS-6747, Research Project 979-25, Argonne National Lab., U.S.A. (1989b).

Gidaspow, D., Ding, J. and Jayaswal, U.K., Multiphase Navier-Stokes equation solver, presented at the ASME Fluids Engineering Division Spring Meeting, University of Toronto (1990).

Givler, R.C., A interpretation for the solid phase pressure in slow, fluid-particle flows, *Int. J. Multiphase Flow*, **13**, 717–722 (1987).

Glicksman, L.R., Westphalen, D., Brereton, C. and Grace, J., Verification of the scaling laws for circulating fluidized beds, *Circulating Fluidized Bed Technology III*, ed. P. Basu, M. Horio and M. Hasatani, Pergamon, pp. 119–124 (1991).

Goldblatt, W.M., Electromagnetic induction sensing of individual tracer particles in a circulating fluidised bed, Ph.D. dissertation, University of British Columbia (1991).

Goldsmith, W., *Impact: The theory and physical behaviour of colliding solids*, Arnold, London (1960).

Gore, R.A. and Crowe, C.T., Effect of particle size on modulating turbulent intensity, *Int. J. Multiphase Flow*, **15**, 279–285 (1989).

Govan, A.H., A simple equation for the diffusion coefficent of large particles in a turbulent gas flow, *Int. J. Multiphase Flow*, **15**, 287–294 (1989).

Govan, A.H., Hewitt, G.F. and Ngan, C.F., Particle motion in a turbulent pipe flow, *Int. J. Multiphase Flow*, **15**, 471–481 (1989).

Grace, J.R., Contacting modes and behaviour classification of gas-solid and other two phase suspensions, *Can. J. Chem. Eng.*, **64**, 353–363 (1986).

Grace, J.R., Heat transfer in circulating fluidized beds, *Circulating Fluidized Bed Technology*, ed. P. Basu, Pergamon, pp. 63–81 (1986a).

Grace, J.R. and Tuot, J., A theory for cluster formation in vertically conveyed suspensions of intermediate density, *Trans. I. Chem. E.*, **57**, 49–54 (1979).

Grace, J.R. and Lim, C.J., Circulating fluidized bed combustion of coal, woodwastes and pitch, Final report prepared for Energy, Mines and Resources Canada, Contract 24ST.23440-6-9007, University of British Columbia (1987)

Grace, J.R., Brereton, C.M.H., Lim, C.J., Legros, R., Zhao, J., Senior, R.C., Wu, R.L., Muir, J.R. and Engman, R., Circulating fluidized bed combustion of Western Canadian fuels, Final Report for Energy Mines and Resources Canada, Contract 52SS.23440–7–9136, (1989a).

Grace, J.R., Zhao, J., Wu, R., Senior, R., Legros, R., Brereton, C. and Lim, C.J., Spatial variations inside a pilot scale circulating fluidized bed combustion unit, *Proc. EPRI Workshop on Materials Issues in Circulating Fluidized-Bed Combustors*, GS-6747, Research Project 979-25, Argonne National Lab., U.S.A. (1989b).

Haider, A. and Levenspiel, O., Drag coefficient and terminal velocity of spherical and nonspherical particles, *Powder Technol.*, **58**, 63–70 (1989).

Hall, D., Measurements of the mean force on a particle near a boundary in turbulent flow, *J. Fluid Mech.*, **187**, 451–466 (1988).

Hartge, E.-U., Li, Y. and Werther, J., Analysis of the local structure of the two phase flow in a fast fluidized bed, in *Circulating Fluidized Bed Technology*, ed. P. Basu, Pergamon, Toronto, pp. 153–160 (1986).

Hartge, E.-U., Rensner, D. and Werther, J., Solids concentration and velocity patterns in circulating fluidized beds, in *Circulating Fluidized Bed Technology II*, ed. P. Basu and J.F. Large, Pergamon, Oxford, pp. 165–180 (1988).

Heidrick, T.R., Banerjee, S.B. and Azad, R.S., Experiments on the structure of turbulence in fully developed pipe flow. Part 2. A statistical procedure for identifying "bursts" in the wall layers and some characteristics of flow during bursting periods, *J. Fluid Mech.*, **82**, 705–723 (1977).

Herb, B., Tuzla, K. and Chen, J., Distributions of solid concentrations in circulating fluidized bed, *Fluidization VI*, ed. J.R. Grace, L.W. Shemilt and M.A. Bergougnou, Engineering Foundation, pp. 73-80 (1989).

Hetsroni, G., Particles-turbulence interaction, *Int. J. Multiphase Flow*, **15**, 735–746 (1989).

Hewitt, G.F. and Hall-Taylor, N.S., *Annular Two-Phase Flow*, Pergamon Press, Oxford (1970).

Hindmarsh, A.C., ODEPACK, a systematized collection of ODE solvers, in *Scientific Computing, Vol. 1*, ed. R. Stepleman *et al.*, IMACS/North Holland Publishing Co., Amsterdam, pp. 55-64 (1983).

Hinze, J.O., Turbulent fluid and particle interaction, *Prog. Heat and Mass Transfer*, **6**, 433–452 (1972).

Hinze, J.O., *Turbulence (2nd. ed.)*, McGraw-Hill, N.Y. (1975).

Homsy, G.M., Jackson, R. and Grace, J.R., Mechanics of fluidized beds: Report of IUTAM Symposium at Stanford University, *J. Fluid Mech.*, in press (1992).

Horio, M., Taki, A., Hsieh, Y.S. and Muchi, I., Elutriation and particle transport through the freeboard of a gas-solid fluidized bed, in *Fluidization*, ed. J.R. Grace and J.M. Matsen, Plenum, pp. 509–518 (1980).

Horio, M., Morishita, K., Tachibana, O. and Murata, N., Solid distribution and movement in circulating fluidized beds, in *Circulating Fluidized Bed Technology II*, ed. P. Basu and J.F. Large, Pergamon, Oxford, pp. 147–154 (1988).

Horio, M. and Takei, Y., Macroscopic structure of recirculating flow of gas and solid in circulating fluidized beds, *Circulating Fluidized Bed Technology III*, ed. P. Basu, M. Horio and M. Hasatani, Pergamon, pp. 207–212 (1991).

Hutchinson, P., Hewitt, G.F. and Dukler, A.E., Deposition of liquid or solid dispersions from turbulent gas streams: a stochastic model, *Chem. Eng. Sci.*, **26**, 419–439 (1971).

Hyppanen, T., An experimental and theoretical study of multiphase flow in a circulating fluidized bed, Doctoral dissertation, Lappeenranta University of Technology, Finland (1989).

Ishii, H., Nakajima, T. and Horio, M., The clustering annular flow model of circulating fluidized beds, *J. Chem. Eng. Japan*, **22**(5), 484–490 (1989).

Ishii, M., *Thermo-fluid dynamic theory of two-phase flow*, Eyrolles, Paris (1975).

Ishii, M. and Kocamustafaogullari, G., Two-phase flow models and their limitations, in *Advances in Two-Fluid Flow and Heat Transfer*, ed. M. Ishii, Martinus Nijhoff, 1–14 (1983).

Ishii, R., Motion of small particle in a gas flow, *Phys. Fluids*, **27**, 33–41 (1984).

Jackson, R., Fluid mechanical theory, Chapter 3 in *Fluidization*, ed. J.F. Davidson and D. Harrison, Academic Press, London (1971).

Jackson, R., Hydrodynamic stability of fluid-particle sytems, Chapter 2 in *Fluidization (2nd. ed.)*, ed. J.F. Davidson, R. Clift and D. Harrison, Academic Press (1985).

Jansen, G.H. and Romate, J.E., Modelling of two-phase riser flow, IUTAM Meeting on Fluidization, Stanford, CA, U.S.A. (July, 1991)

Jenkins, J.T., Rapid flows of granular materials, in *Non-Classical Continuum Mechanics*, ed. R.J. Knopps and A.A. Lacey, Cambridge U. Press, pp. 213–235 (1986).

Jenkins, J.T. and Savage, S.B., A theory for the rapid flow of identical, smooth, nearly elastic, spherical particles, *J. Fluid Mech.*, **130**, 187–202 (1983).

Jin Y., Yu Z., Qi C. and Bai D., The influence of exit structures on the axial distribution of voidage in fast fluidized bed, *Fluidization '88 Science and Technology (Third China-Japan Symposium)*, ed. M. Kwauk and D. Kunii, Science Press, Beijing, pp. 165–173 (1988).

Johnson, P.C. and Jackson, R., Frictional-collisional constitutive relations for granular materials, with application to plane shearing, *J. Fluid Mech.*, **176**, 67–93 (1987).

Kallio, G.A., Wall-impact velocities of particles in the turbulent boundary layer, *Third Int. Symp. of Gas-Solid Flow*, UCLA, San Diego, CA, U.S.A., 1–6 (1989).

Kline, S.J., Reynolds, W.C., Schraub, F.A. and Runstadler, P.W., The structure of turbulent boundary layers, *J. Fluid Mech.*, **30**, 741–773 (1967).

Knowlton, T.M., Solids transfer in fluidized systems, Chapter 12 in *Gas Fluidization Technology*, ed. D. Geldart, Wiley, N.Y. (1986).

Knowlton, T.M., Hydrodynamics and nonmechanical solids recycle and discharge systems in circulating fluidized beds, *Proc. EPRI Workshop on Materials Issues in Circulating Fluidized-Bed Combustors*, GS-6747, Research Project 979-25, Argonne National Laboratory, Argonne, USA (1989).

Kobro, H., Description of Studsvik's fast fluidised bed prototype, Studsvik report EM-85/2 (1985).

Krzywanski, R.S., Multi-dimensional modelling of a spouted bed, Ph.D. dissertation, University of British Columbia (1992).

Kunii, D. and Levenspiel, O., Flow modelling of fast fluidized beds, *Circulating Fluidized Bed Technology III*, ed. P. Basu, M. Horio and M. Hasatani, Pergamon, pp. 91–98 (1991).

Kwauk, M., Wang N., Li Y., Chen B. and Shen Z., Fast fluidization at ICM, in *Circulating Fluidized Bed Technology*, ed. P. Basu, Pergamon, Toronto, pp. 33-62 (1986).

Leckner, B., Heat transfer in circulating fluidized bed boilers, *Circulating Fluidized Bed Technology III*, ed. P. Basu, M. Horio and M. Hasatani, Pergamon, 27–37 (1991).

Lefroy, G.A. and Davidson, J.F., The mechanics of spouted beds, *Trans. I. Chem. E.*, **47**, 120–128 (1969).

Lee, S.L. and Durst, F., On the motion of particles in turbulent duct flows, *Int. J. Multiphase Flow*, **8**, 125–146 (1982).

Levich, B.G., *Theoretical Physics, Vol. 2*, North-Holland (1971).

Levy, Y. and Lockwood, F.C., Laser Doppler measurements of flow in freeboard of a fluidized bed, *A.I.Ch.E. J.*, **29**(6), 889–895 (1983).

Li, J., Tung, Y. and Kwauk, M., Method of energy minimisation in multi-scale modeling of particle-fluid two-phase flow, in *Fluidization '88 Science and Technology: Third China-Japan Symposium*, ed. M. Kwauk and D. Kunii, Science Press, Beijing, pp. 89–101 (1988).

Li, J., Tung, Y. and Kwauk, M., Multiphase modeling of two-phase flow, Institute of Chemical Metallurgy, Academia Sinica (1989).

Li, Y. and Kwauk, M., The dynamics of fast fluidization, in *Fluidization*, ed. J.R. Grace and J.M. Matsen, Plenum, pp. 537–544 (1980).

Li, Y., Chen, B., Wang, F. and Wang, Y., Hydrodynamic correlations for fast fluidization, *Proc. First China-Japan Symposium on Fluidization*, pp. 124–134, Hangzhou, China (1982).

Louge, M., IUTAM Symposium at Stanford University, July 1–3 (1991).

Louge, M., Lischer, D.J. and Chang, H., Measurements of voidage near the wall of a circulating fluidized bed riser, *Powder Technol.*, **62**, 269–276 (1990).

Louge, M.Y., Mastorakos, E. and Jenkins, J.T., The role of particle collisions in pneumatic transport, in press, *J. Fluid Mech.* (1991).

Lun, C.K.K., Savage, S.B., Jeffrey, D.J. and Chepurniy, N., Kinetic theories for granular flow: inelastic particles in Couette flow and slightly inelastic particles in a general flow field, *J. Fluid Mech.*, **140**, 223–256 (1984).

Lun, C.K.K. and Savage, S.B., The effects of an impact velocity dependent coefficient of restitution on stresses developed by sheared granular materials, *Acta Mech.*, **63**, 15–44 (1986).

McCoy, D.D. and Hanratty, T.J., Rate of deposition of droplets in annular two phase flow, *Int. J. Multipahse Flow*, **3**, 319–331 (1977).

Martin, C.J. and Azzopardi, B.J., Waves in vertical annular flow, *Physico-Chem. Hydro.*, **6**, 257–265 (1985).

Mastorakos, E., Louge, M. and Jenkins, J.T., The role of particle collisions in pneumatic transport, in *Constitutive Relationships and Models in Continuum Theories of Multiphase Flows*, NASA conference publication CP-3047 (1989).

Merrick, D. and Highley, J., Particle size reduction and elutriation in a fluidized bed process, *A.I.Ch.E. Symposium Series*, No. 137, **70**, pp. 366–378 (1972).

Millitzer, J., Numerical prediction of the fully developed two-phase (air-solids) flow in a pipe, *Circulating Fluidized Bed Technology*, ed. P. Basu, Pergamon, Toronto, pp. 173–183 (1986).

Min, K., Intensity of particle motion in solid-gas suspension flow, *J. Appl. Physics*, **38**, 564–567 (1967).

Moalem Maron, D. and Brauner, N., The role of interfacial mobility in determining the interfacial shear factor in two-phase wavy film flow, *Int. Comm. Heat Mass Transfer*, **14**, 45–55 (1987).

Molodstof, Y. and Muzyka, D.W., A similar profile regime in the vertical fully developed flow of gas-solid suspensions, *Int. J. Multiphase Flow*, **17**, 573–583 (1991).

Monceaux, L., Azzi, M., Molodtsof, Y. and Large, J.F., Particle mass flux profiles and flow regime characterization in a pilot scale fast fluidized bed unit, *Fluidization V*, ed. K. Ostergaard and A. Sorenson, Engineering Foundation, pp. 337-344 (1986).

Murray, J.D., On the mathematics of fluidization: Part 1. Fundamental equations and wave propagation, *J. Fluid Mech.*, **21**, 465–493 (1965).

Nakamura, K. and Capes, C.E., Vertical pneumatic conveying: a theoretical study of uniform and annular particle flow models, *Can. J. Chem. Eng.*, **51**, 39–46 (1973).

Nakamura, K. and Capes, C.E., Vertical pneumatic conveying of binary particle mixtures, in *Fluidization Technology, Vol. 2*, ed. D.L. Keairns, Hemisphere, Washington, pp. 159–184, (1976).

Nallamsy, M., Turbulence models and their applications to the prediction of internal flows, *Comp. & Fluids*, **15**, 151–194 (1987).

Needham, D.J. and Merkin, J.H., The propagation of a voidage disturbance in a uniformly fluidized bed, *J. Fluid Mech.*, **131**, 427–454 (1983).

Owen, P.R., Pneumatic transport, *J. Fluid Mech.*, **39**, 407–432 (1969).

Pita, J.A. and Sundaresan, S., Gas-solid flow in vertical tubes, *A.I.Ch.E. J.*, **37**(7), 1009–1018 (1991).

Pritchett, J.W., Blake, T.R. and Garg, S.K., A numerical model of gas fluidized beds, *A.I.Ch.E. Symposium Series*, **74**, vol. 176, 134–148 (1978).

Prosperetti, A. and Jones, A.V., Pressure forces in disperse two-phase flow, *Int. J. Multiphase Flow*, **10**, 425–440 (1984).

Rashidi, M., Hetsroni, G. and Banerjee, S., Particle-turbulence interaction in a boundary layer, *Int. J. Multiphase Flow*, **16**, 935–949 (1990).

Reeks, M.W., On the dispersion of small particles suspended in an isotropic turbulent fluid, *J. Fluid Mech.*, **83**, 529–546 (1977).

Reh, L., The circulating fluid bed reactor — A key to efficient gas/solid processing, *Circulating Fluidized Bed Technology*, ed. P. Basu, Pergamon, Toronto, pp. 105–118 (1986).

Rhodes, M.J., The upward flow of gas/solid suspensions. Part 2: A practical quantitative flow regime diagram for the upward flow of gas/solid suspensions, *Chem. Eng. Res. Des.*, **67**, 30–37 (1989).

Rhodes, M.J., Modelling the flow structure of upward-flowing gas-solids suspensions, *Powder Technol.*, **60**, 27–38 (1990).

Rhodes, M.J. and Geldart, D., The upward flow of gas/solid suspensions. Part 1: A model for the circulating fluidized bed incorporating dual level gas entry into the riser, *Chem. Eng. Res. Des.*, **67**, 20–29 (1989).

Rhodes, M.J., Zhou, S., Hirama, T. and Cheng, H., Effect of operating conditions on longitudinal solids mixing in a circulating fluidized bed riser, *A.I.Ch.E. J.*, **37**, 1450–1458 (1991).

Rizk, M.A. and Elghobashi, S.E., A two-equation turbulence model for dispersed dilute confined two-phase flows, *Int. J. Multiphase Flow*, **15**, 119–133 (1989).

Rogers, L.N. and Reed, J., The adhesion of particles undergoing an elastic-plastic impact with a surface, *J. Phys. D: Appl. Phys.*, **17**, 677–689 (1984).

Saffman, P.W., The lift on a small sphere in a slow shear flow, *J. Fluid Mech.*, **136**, 31–62 (1965).

Savage, S.B., Streaming motions in a bed of vibrationally fluidized dry granular material, *J. Fluid. Mech.*, **194**, 457–478 (1988).

Schaub, G., Reimert, R. and Albrecht, J., Investigations of emission rates from large scale CFB-combustion plants, *Proc. 10th Int. Conf. on Fluidized Bed Combustion*, ASME, pp. 685–691 (1989).

Schlichting, H., *Boundary-layer theory (6th ed.)*, McGraw-Hill, New York (1968).

Senior, R.C. and Brereton, C., Modelling of circulating fluidised bed flow structure and heat transfer, Report to Studsvik Energy of Sweden, University of British Columbia (1990).

Senior, R.C. and Brereton, C., Modelling of circulating fluidised-bed solids flow and distribution, *Chem. Eng. Sci.*, **47**, 281–296 (1992).

Sha, W.T. and Soo, S.L., On the effect of $P\nabla\alpha$ term in multiphase mechanics, *Int. J. Multiphase Flow*, **5**, 153–158 (1979).

Sinclair, J.L. and Jackson, R., Gas-particle flow in a vertical pipe with particle-particle interactions, *A.I.Ch.E. J.*, **35**, 1473–1486 (1989).

Soo, S.L., *Fluid dynamics of multiphase sytems*, Blaisdel, Waltham, MA (1967).

Stevens, D., Evaluation of cyclone modification and combustor operation in the Chatham CFB boiler, Progesss Report, University of New Brunswick (1990).

Stuhmiller, J.H., The influence of interfacial pressure forces on the character of two-phase flow model equations, *Int. J. Multiphase Flow*, **3**, 551–560 (1977).

Sun, G. and Grace, J.R., The effect of particle size distribution on the performance of a catalytic fluidized bed reactor, *Chem. Eng. Sci.*, **45**, 2187–2194 (1990).

Taylor, I.G., Diffusion by continuous movements, *Proc. Lond. Math. Soc.*, **151**, 196–212 (1921).

Tennekes, H. and Lumley, J.L., A first course in turbulence, MIT Press, Cambridge, MA (1972).

Tsuji, Y., Morikawa, Y. and Shiomi, H., LDV measurements of an air solid two-phase flow in a vertical pipe, *J. Fluid Mech.*, **139**, 417–434 (1984).

Tsuo, Y.P. and Gidaspow, D., Computation of flow patterns in circulating fluidized beds, *A.I.Ch.E. J.*, **36**(6), 885–896 (1990).

Uhlherr, P.H.T.U. and Sinclair, C.G., *Proc. Chemeca '70*, Butterworths, Melbourne, **1**, 1–13 (1970).

Van Deemter, J.J. and Van der Laan, E.T., Momentum and energy balances for dispersed two-phase flow, *Appl. Sci. Res.*, **A10**, 102 (1960).

Van Swaaij, W.P.M., Buurman, C. and Van Breugel, J.W., Shear stresses on the wall of a dense gas-solids riser, *Chem. Eng. Sci.*, **25**, 1818–1820 (1970).

Wang, X.S. and Gibbs, B.M., Hydrodynamics of a circulating fluidized bed with secondary air injection, *Circulating Fluidized Bed Technology III*, ed. P. Basu, M. Horio and M. Hasatani, Pergamon, pp. 225–230 (1991).

Wallis, G.B., Annular two-phase flow. Part1: A simple theory, *J. Basic Eng., Trans. ASME*, 59–72 (1970a).

Wallis, G.B., Annular two-phase flow. Part2: Additional effects, *J. Basic Eng., Trans. ASME*, 73–82 (1970b).

Walton, O.R. and Braun, R.L., Stress calculations for assemblies of inelastic spheres in uniform shear, *Acta Mech.*, **63**, 73–86 (1986).

Weinstein, H., Avidan, A.A., Jean-Louis, J. and Meller, M., Axial variations in a transported high velocity fluidized bed, A.I.Ch.E. Fall Annual Meeting, New Orleans, LA (1981).

Weinstein, H., Graff, R.A., Meller, M. and Shao, M.J., The influence of the imposed pressure drop across a fast fluidized bed, *Proc. IV Int. Fluidization Conf.*, Kashikojima, Japan (1983).

Weinstein, H., Schnitzlein, M. and Graff, R.A., Radial variation in void fraction in a fast fluidized bed, *Fluidization V*, ed. K. Ostergaard and A. Sorenson, Engineering Foundation, pp. 329-336 (1986).

Weinstein, H. and Li, J., An evaluation of the actual density in the acceleration section of vertical risers, *Powder Techol.*, **57**, 57–59 (1989).

Weiss, V. and Fett, F.N., Modeling the decomposition of sodium bicarbonate in a circulating fluidized bed reactor, *Circulating Fluidized Bed Technology*, ed. P. Basu, Pergamon, Toronto, pp. 167–173 (1986).

Weiss, V., Scholer, J. and Fett, F.N., Mathematical modeling of coal combustion in a circulating fluidized bed reactor, *Circulating Fluidized Bed Technology II*, ed. P. Basu and J.F. Large, Pergamon, pp. 289–298 (1988).

Wells, M.R. and Stock, D.E., The effects of crossing trajectories on the dispersion of particles in a turbulent flow, *J. Fluid Mech.*, **136**, 31–62 (1983).

Werther, J., Hartge, E.-U., Kruse, M. and Nowak, W., Radial mixing of gas in the core zone of a pilot scale CFB, *Circulating Fluidized Bed Technology III*, ed. P. Basu, M. Horio and M. Hasatani, Pergamon, pp. 593–598 (1991).

Whalley, P.B. and McQuillan, K.W., Flooding in two-phase flow: The effect of tube length and artificial wave injection, *Physico-Chem. Hydro.*, **6**, 3–21 (1985).

Williams, J.J.E. and Crane, R.I., Particle collision rate in turbulent flow, *Int. J. Multiphase Flow*, **9**, 421–435 (1983).

Wirth, K.-E., Fluid mechanics of circulating fluidized beds, *Chem. Eng. Technol.*, **14**, 29–38 (1991).

Wu, R.L., Heat transfer in circualting fluidized beds, Ph.D. dissertation, University of British Columbia (1989).

Yerushalmi, J., Cankurt, N.T., Geldart, D. and Liss, B., Flow regimes in vertical gas-solid contact systems, *A.I.Ch.E. Symp. Ser.*, No. 176, **74**, pp. 1–13 (1978).

Yih, C.-S., *Dynamics of Nonhomogeneous Fluids*, MacMillan, N.Y. (1965).

Zhang, H., Xie, Y., Chen, Y. and Hasatani, M., Mathematical modelling for longitudinal voidage distribution of fast fluidized beds, *Circulating Fluidized Bed Technology III*, ed. P. Basu, M. Horio and M. Hasatani, Pergamon, pp. 151–156 (1991).

Appendix A

Drag Enhancement due to Turbulence: An Analysis of the Data of Tsuji *et al.* (1984)

Turbulence effects can result in large increases in the particle drag coefficient above that given by the standard drag curve *providing* the scale of turbulence is smaller than the particle. Clift *et al.* (1978) present several correlations for prediction of this drag modification. For Re_p values less than 50, Clift *et al.* cite the relation proposed by Uhlherr and Sinclair (1970),

$$C_D = 162\, I_R^{1/3} Re_p^{-1} \,, \tag{A.1}$$

where $I_R = u_e/\mathbf{v}_s$, and the limits for the relation are $0.05 < I_R < 0.5$. Although Clift *et al.* qualitatively describe some effects of turbulence on the flow around a spherical particle, the underlying cause of the drag increase is not fully understood. At Re_p greater than $O(10^3)$, the freestream turbulence may cause a transition to turbulence in the particle boundary layer at lower Re_p than given by the standard drag curve. This transition results in a decrease in the particle drag.

We consider the response of 200 μm particles to gas turbulence in the experiment of Tsuji *et al.* (1984), discussed in Chapter 3. Except in a small region near the core of the riser, I_R was generally much greater than 0.5. However, the importance of drag enhancement can be demonstrated by considering a 200 μm particle in Tsuji's experiment travelling with a slip velocity equal to its terminal velocity of 0.7 m/s in a gas flow of turbulence velocity $u_e = 0.35$ m/s (equivalent to $I_R = 0.5$ and the lowest levels of centreline turbulence in Tsuji's experiment). For this case $Re_t = 9.4$, which gives $C_D = 4.6$ and $\tau_p = 0.07$ s when using a standard drag correlation. In contrast, the Uhlherr and Sinclair correlation gives $C_D = 13.8$ and $\tau_p = 0.02$

s. Thus the particle response is a factor of three times faster, and response time is now comparable to the energetic eddy decay time. In the riser of Tsuji *et al.*, substantial reduction in turbulence intensity with particle loading was observed at $r/R > 0.4$ as shown in Figure 3.2. Assuming that the slip velocity at $r/R = 0.6$ for the Figure 3.2 conditions was similar to those shown in Figure 3.3, crude estimates of $\mathbf{v}_s$ and u_e at this radial location are 0.25 m/s and 0.5 m/s, respectively, giving $I_R = 2.0$. If the Uhlherr and Sinclair correlation is assumed to give reasonable estimates when extended to $I_R = 2.0$, then one obtains $C_D = 61$ and $\tau_p = 0.015$ s for this case. As $\tau_e \approx 0.01$ s and $\tau_d = \mathbf{v}_s/l_e = 0.013$ this particle should respond significantly to the turbulence. If the standard drag curve had been used, the corresponding values of $C_D = 9.7$ and $\tau_p = 0.1$ s would have indicated little response of these particles. For particles at radial positions where $r/R > 0.6$ (i.e. within an area that is 64% of the riser cross-section), r.m.s turbulence velocities are even higher (Figure 3.2), and even greater enhancement of drag is possible.

The overall reduction in turbulence energy may be crudely estimated by integrating the Tsuji *et al.* 200 μm data from Figure 3.2. For solids loadings m_s of 1.3 and 3.2, this reduction is approximately 40% and 70%, respectively. These solids loading correspond to approximate suspension densities ρ_s of 1.7 and 4.1 kg/m^3, assuming $\rho_s = m_s \rho_g U_0/(U_0 - \mathbf{v}_t)$. Such densities are low, even for the more dilute regions of a CFB. This result confirms the theoretical assertion that only a small loading of responsive solids is required to greatly reduce turbulence levels (providing turbulence energy production is not increased by other phenomena). As Tsuji *et al.* did not provide a solids velocity profile for the data in Figure 3.2 and the Uhlherr and Sinclair correlation is not strictly valid at the high values of I_R corresponding to the Tsuji *et al.* tests, it is not possible to directly predict turbulence reduction using eqs. (3.54) and (3.61). However, using these equations with the above estimate of $\tau_p = 0.015$ s gives similar order-of-magnitude turbulence reductions. Without allowance for drag enhancement ($\tau_p \approx 0.1$ s), reductions of less than 2% are predicted, irrespective of the slip velocity assumed.

Appendix B

Cold Unit CFB Tests: Statistical Analysis of Density Profile Results for Runs 1 and 3

The apparent suspension density profiles shown in Figure 6.25 for the size distribution tests (Runs 1, 2 and 3 – Table 6.2) indicate that when running with bimodal PSD particles, higher suspension densities occurred throughout the riser for condition C, and over some riser column heights for condition A. Each density profile shown in Figure 6.25 was obtained by interpolating between the thirteen data points shown as symbols in the plots. In turn, each suspension density point is the mean of several repetitions of the same run and condition. For example, run 1, condition A, was repeated seven times. The measured densities for each repetition for the lowest data point height (0.42 m above the distributor) are given in Table B.1. Also tabulated is the corresponding mean value of these density values (34.4 kg/m^3).

To determine if the difference between the narrow and bimodal PSD suspension density at a given height was statistically significant, the mean densities for the narrow and bimodal particle runs for that height were compared assuming a Student t distribution of the measured density values. As no difference between narrow and standard PSD densities were observed, the standard particle run results were not included in the analysis, and results pertaining to the narrow PSD were assumed equally applicable to the standard PSD.

The statistical comparison method may be demonstrated by considering the (sample) mean apparent suspension densities for the lowest data point height (0.42 m) for the bimodal and narrow particle distributions run under condition A. Let μ_1 and μ_2 be the population mean densities of the bimodal and narrow particles, respectively, for the 0.42 m height. The test may be defined statistically as:

Table B.1: Apparent suspension densities measured for repetitions of the narrow and bimodal PSD runs: level 1 ($z = 0.42$ m), condition A.

Cold Unit Tests: Runs 1 and 3 Condition A (6.5 m/s, 20 kg/m^{2}s) Densities at height $z = 0.42$, mid-way between taps 1 & 2		
REPETITION	SUSPENSION DENSITY (kg/m^3)	
	bimodal	narrow
1	37.9	35.2
2	39.8	33.9
3	43.9	34.3
4		35.0
5		34.2
6		32.5
7		35.6
mean	40.5	34.4

1. Null hypothesis H_0: $\mu_1 = \mu_2$ or $\mu_1 - \mu_2 = 0$.

2. Alternative hypothesis H_1: $\mu_1 > \mu_2$ or $\mu_1 - \mu_2 > 0$ (one-tailed test).

3. Test significance level: $\alpha = 0.01$ (99% confidence level).

Furthermore, it is assumed that the two population standard deviations are equal, i.e. $\sigma_1 = \sigma_2$. The appropriate test statistic is

$$T = \frac{(\overline{X}_1 - \overline{X}_2) - 0}{S_p\sqrt{\frac{1}{n_1} + \frac{1}{n_2}}} \tag{B.1}$$

where $\overline{X}_1$ and $\overline{X}_2$ are the sample means and n_1 and n_2 the number of bimodal and narrow condition repetitions, respectively. The combined or "pooled" sample variance is defined as:

$$S_p^2 = \frac{(n_1 - 1)S_1^2 + (n_2 - 1)S_2^2}{(n_1 + n_2 - 2)} \tag{B.2}$$

where S_1 and S_2 are the individual sample variances, i.e.

$$S_j^2 = \frac{\sum_{i=1}^{n_j}(X_{ij} - \overline{X}_j)}{n_j - 1} \ . \tag{B.3}$$

The test degrees of freedom is $\nu = (n_1 + n_2 - 2)$.

For the data in Table B.1, n_1(bimodal) = 3 and n_2(narrow) = 7. Hence $\nu = 8$ and at a significance level of $\alpha = 0.01$, the critical T_α value is 3.143. Thus the critical region for the test is $T > T_\alpha$. If the computed T value lies in this critical region, then the null hypothesis may be rejected at a 99% confidence level, which is equivalent to stating that the bimodal particle run density is significantly greater than the narrow particle run density at the riser column height under consideration. Substitution of Table B.1 values into equations (B.1), (B.2) and (B.3) gives $\overline{X}_1 = 40.5$, $\overline{X}_2 = 34.4$, $S_1^2 = 9.4$, $S_2^2 = 1.06$, $S_p = 1.77$, and hence, $T = 5.02$. Thus, for this example, we reject H_0, and assume for condition A at height 0.42 m that the bimodal run density is significantly greater than the narrow PSD run density, at the assumed confidence level of 99%.

The statistical comparison of narrow and bimodal particle run densities was performed for all thirteen heights for conditions A and C. Results are summarised in Tables B.2 and B.3, respectively. The test result is given in the tables as a decision to accept or reject the null hypothesis. Two confidence levels ($\alpha = 0.05$ and $\alpha = 0.01$) were considered. For condition C, the bimodal PSD densities were significantly greater than the narrow PSD densities for all riser heights and both confidence levels. For condition A, Table B.2 and Figure 6.25 suggest that there was no significant difference between the two PSDs over the approximate height intervals of 8.5 – 9.0 m (just below the riser exit) and 1.0 – 5.0 m (although densities at several heights in this range were significantly different). For conditions B and D the same statistical approach confirmed that no significant difference between bimodal and narrow particles existed at these conditions, as expected from visual inspection of the Figure 6.25 density profiles.

Table B.2: Statistical comparison of apparent suspension densities for narrow (Run 1) and bimodal (Run 3) PSD tests: condition A.

$n_1 = 3$	$T_{\alpha=.05} = 1.94$	Condition A
$n_2 = 7$	$T_{\alpha=.01} = 3.14$	

Height		Statistic (1 = bimodal, 2 = narrow)						Reject H_0?	
no.	m	$\overline{X}_1$	S_1^2	$\overline{X}_2$	S_2^2	S_p	T	$\alpha = .05$	$\alpha = .01$
1	0.42	40.5	9.4	34.4	1.1	1.8	5.0	yes	yes
2	0.80	16.7	0.8	14.7	0.5	0.7	3.9	yes	yes
3	1.22	15.2	1.1	13.4	0.9	1.0	2.6	yes	no
4	1.68	10.8	0.3	12.0	0.4	0.6	-2.9	no	no
5	2.36	8.2	0.3	6.0	0.2	0.3	10.4	yes	yes
6	3.28	6.5	0.1	5.4	0.1	0.3	4.9	yes	yes
7	3.96	6.8	0.0	6.0	1.0	0.8	1.4	no	no
8	4.65	6.9	0.8	5.8	0.3	0.6	2.5	yes	no
9	5.79	9.9	2.2	6.0	0.2	0.8	6.8	yes	yes
10	7.16	17.9	7.6	11.0	4.4	2.3	4.4	yes	yes
11	8.23	30.1	3.6	25.0	12.9	3.3	2.3	yes	no
12	8.76	43.5	0.5	41.2	18.5	3.7	0.9	no	no
13	9.08	38.1	1.1	35.4	24.2	4.4	0.9	no	no

Table B.3: Statistical comparison of apparent suspension densities for narrow (Run 1) and bimodal (Run 3) PSD tests: condition C.

$n_1 = 6$		$T_{\alpha=.05} = 1.80$							Condition C
$n_2 = 7$		$T_{\alpha=.01} = 2.72$							
Height		Statistic (1 = bimodal, 2 = narrow)						Reject H_0?	
no.	m	$\overline{X}_1$	S_1^2	$\overline{X}_2$	S_2^2	S_p	T	$\alpha = .05$	$\alpha = .01$
1	0.42	214.3	1700.4	148.4	44.4	28.2	4.2	yes	yes
2	0.80	92.3	441.1	52.3	10.9	15.0	4.8	yes	yes
3	1.22	55.1	61.9	36.5	1.9	5.4	6.2	yes	yes
4	1.68	48.6	51.3	34.0	0.9	4.9	5.4	yes	yes
5	2.36	38.1	33.2	23.0	1.3	4.0	6.8	yes	yes
6	3.28	33.3	22.8	20.9	1.0	3.3	6.7	yes	yes
7	3.96	34.9	39.4	20.5	5.3	4.6	5.7	yes	yes
8	4.65	35.3	23.6	20.4	3.1	3.5	7.6	yes	yes
9	5.79	43.0	27.1	24.9	9.3	4.2	7.8	yes	yes
10	7.16	52.3	22.0	38.4	18.8	4.5	5.6	yes	yes
11	8.23	66.2	21.5	60.0	76.3	7.2	1.6	no	no
12	8.76	107.8	52.7	106.3	32.0	6.4	0.4	no	no
13	9.08	104.6	173.2	133.8	116.3	11.9	-4.4	no	no

Appendix C

Cold Unit CFB Tests: Time Series Analysis Results

C.1 Signal Pre-Whitening

The simple method of signal pre-whitening used in the cold unit testwork time series analyses is described by Diggle (1990). A time series may be written as $\{y(t_i), i = 1, \ldots, n\}$, where $y(t_i)$ is the observed value at time t_i and n is the total number of observations. The time increments between observations in this study were equal (0.01 sec). For brevity $y(t_i)$ is abbreviated as y_t. Smoothed values s_t of the time series were calculated as:

$$s_t = (y_{t-1} + y_t + y_{t+1})/3\,. \tag{C.1}$$

The pre-whitened signal r_t was then calculated by subtracting the smoothed value from the corresponding original time series value, i.e. $r_t = y_t - s_t$. Plots of the pre-whitened (or residual) signals for the cold unit tests are given in Figure C.1. The success of signal pre-whitening may be determined by calculating the autocorrelation of the pre-whitened signal. If the autocorrelation rapidly decays to values that are not significantly different from zero, and no obvious trends are present in the autocorrelation, then signal pre-whitening has been successful. Autocorrelation plots of the pre-whitened signals are given in Figure C.2. The dashed lines correspond to 95% confidence limits. Autocorrelation values within these limits may be assumed zero at this confidence level. The figure shows that signal pre-whitening was adequate in this case. Hence alternative methods of pre-whitening (e.g. Box and Jenkins, 1970) were not required.

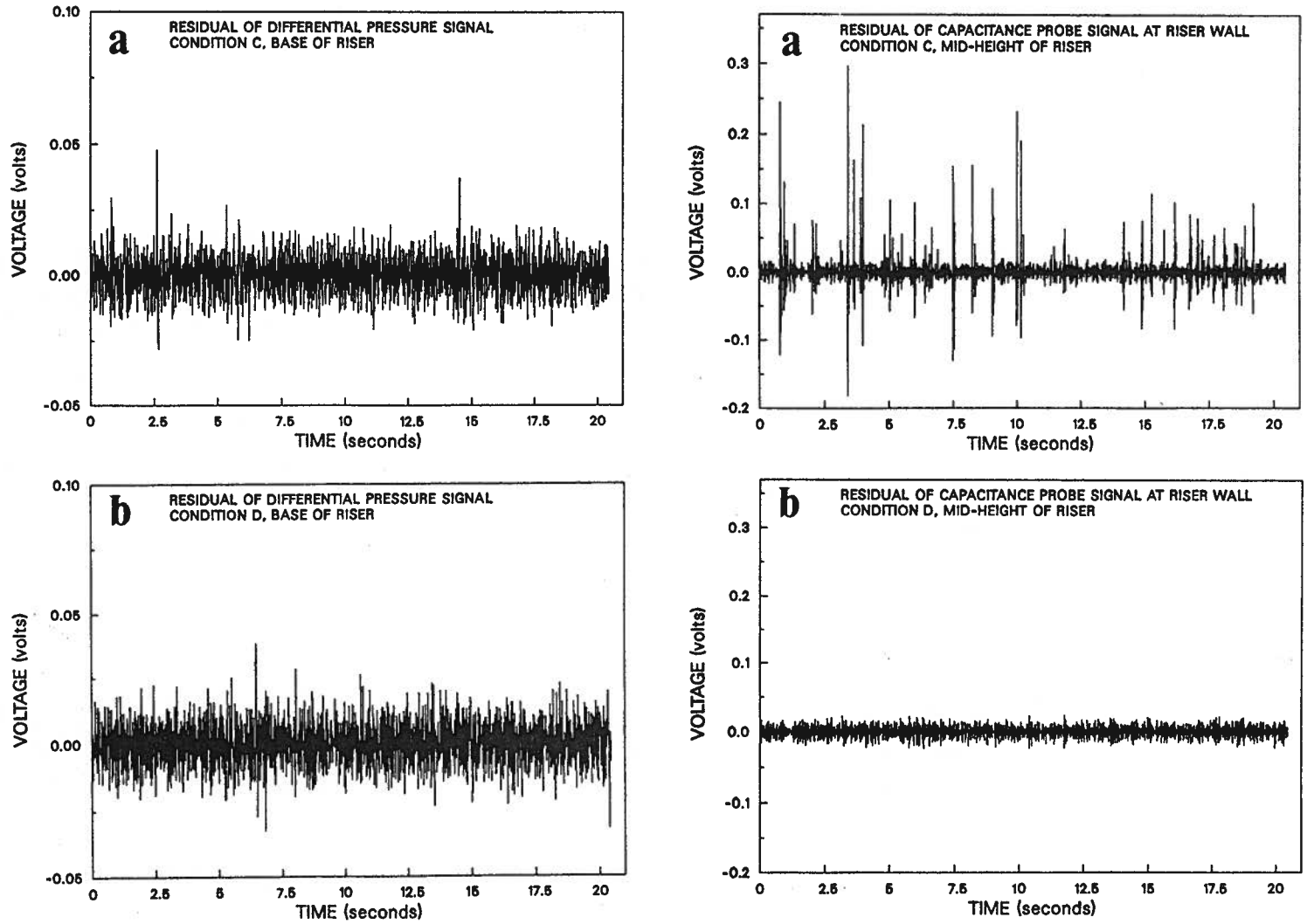

Figure C.1: Run 1 differential pressure and wall capacitance probe signals after pre-whitening: (a) condition C, and (b) condition D. (Probe height 4.24 m. Δp_g heights 0.23–0.61 m.)

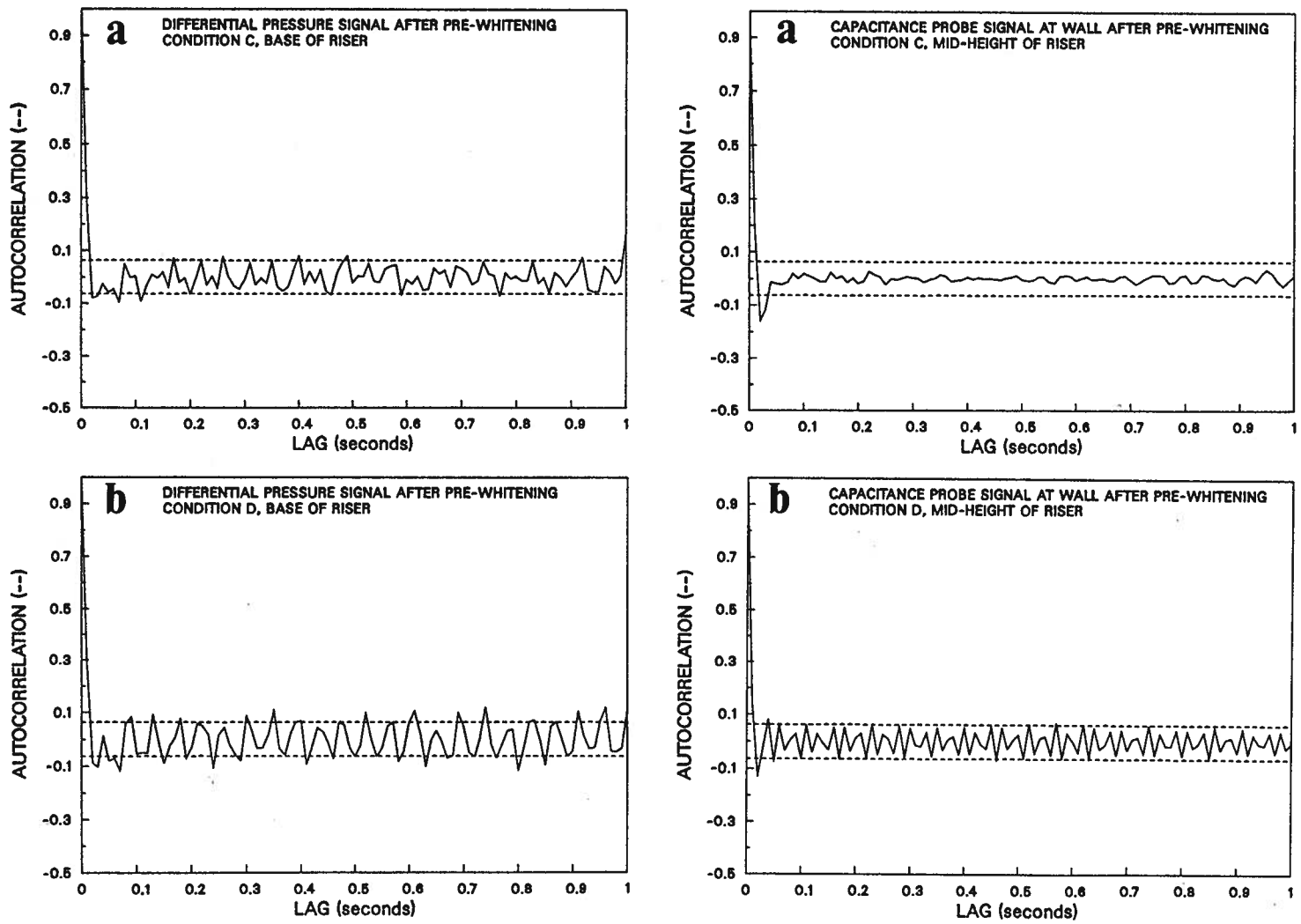

Figure C.2: Autocorrelations of the Run 1 differential pressure and capacitance probe signals after pre-whitening: (a) condition C, and (b) condition D. Dashed lines correspond to 95% confidence limits. (Probe height 4.24 m. Δp_g heights 0.23–0.61 m.)

C.2 Statistical Software

The time series statistical software used to compute time and frequency domain statistics in this study was the BMD02T software package, available on the University of British Columbia computing system. Many references exist on time series analysis (e.g. Box and Jenkins, 1970; Diggle, 1990; Bendat and Piersol, 1980) which present the relevant equations coded in this package and the background theory required to interpret the results.

C.3 Power Spectra and Coherence Square Estimates

The power spectra for each of the four time series (prior to pre-whitening) studied in the cold unit testwork are given in Figure C.3. The coherence square plots ("normalised" versions of the cross-spectra) are shown in Figure C.4. No dominant frequency is evident in the spectra, except at a frequency of about 40 Hz. The peaks at this frequency are unlikely to correspond to any physical fluctuation in solids concentration within the riser, and may be a result of vibration of the riser column or capacitance probe device, and its effect on the probe output signal. The corresponding phase data of the coherence square estimates exhibited extreme scatter with no discernable trends.

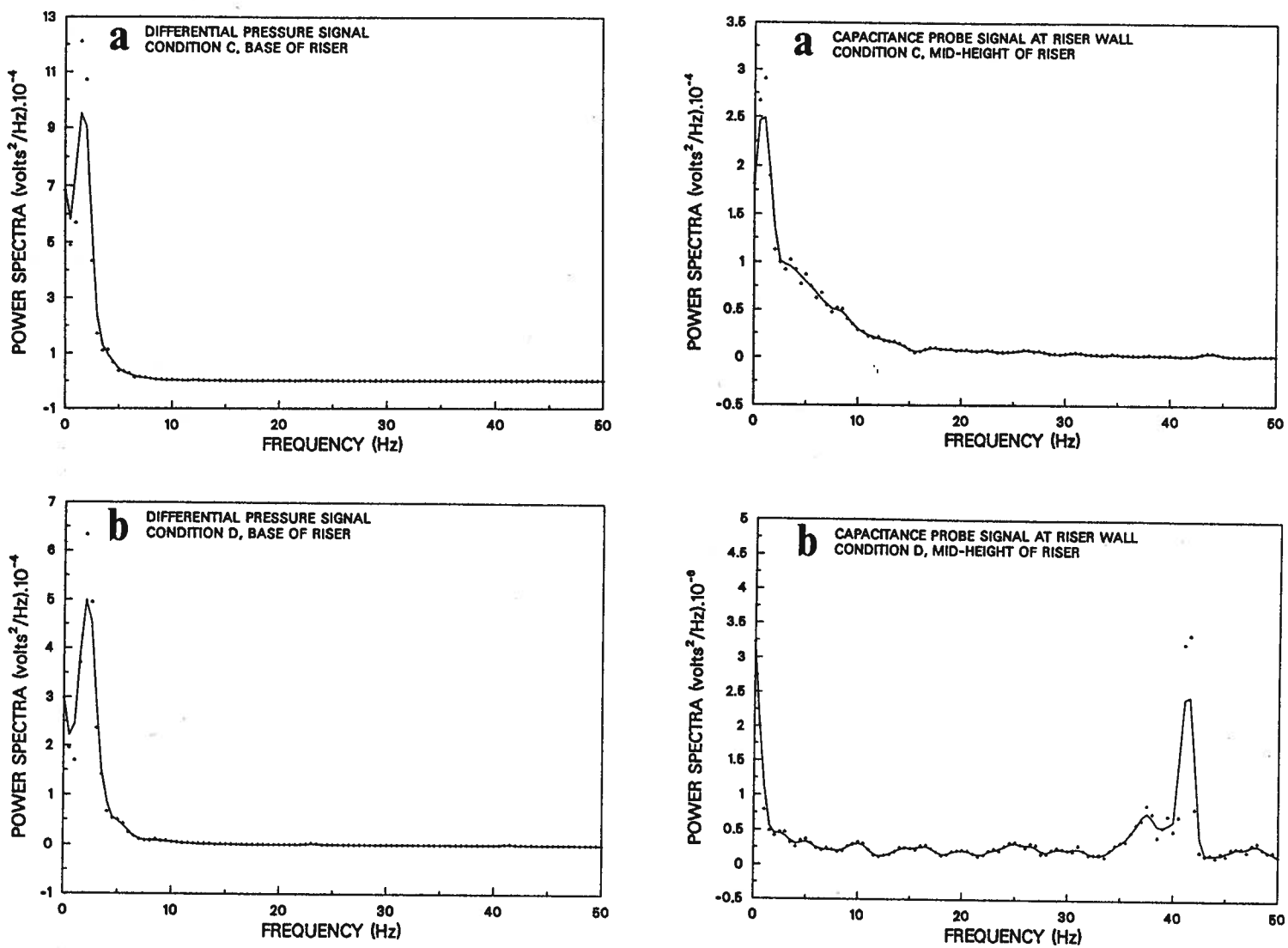

Figure C.3: Power spectra of the Run 1 differential pressure and capacitance probe signals: (a) condition C, and (b) condition D. (Probe height 4.24 m. Δp_g heights 0.23–0.61 m.)

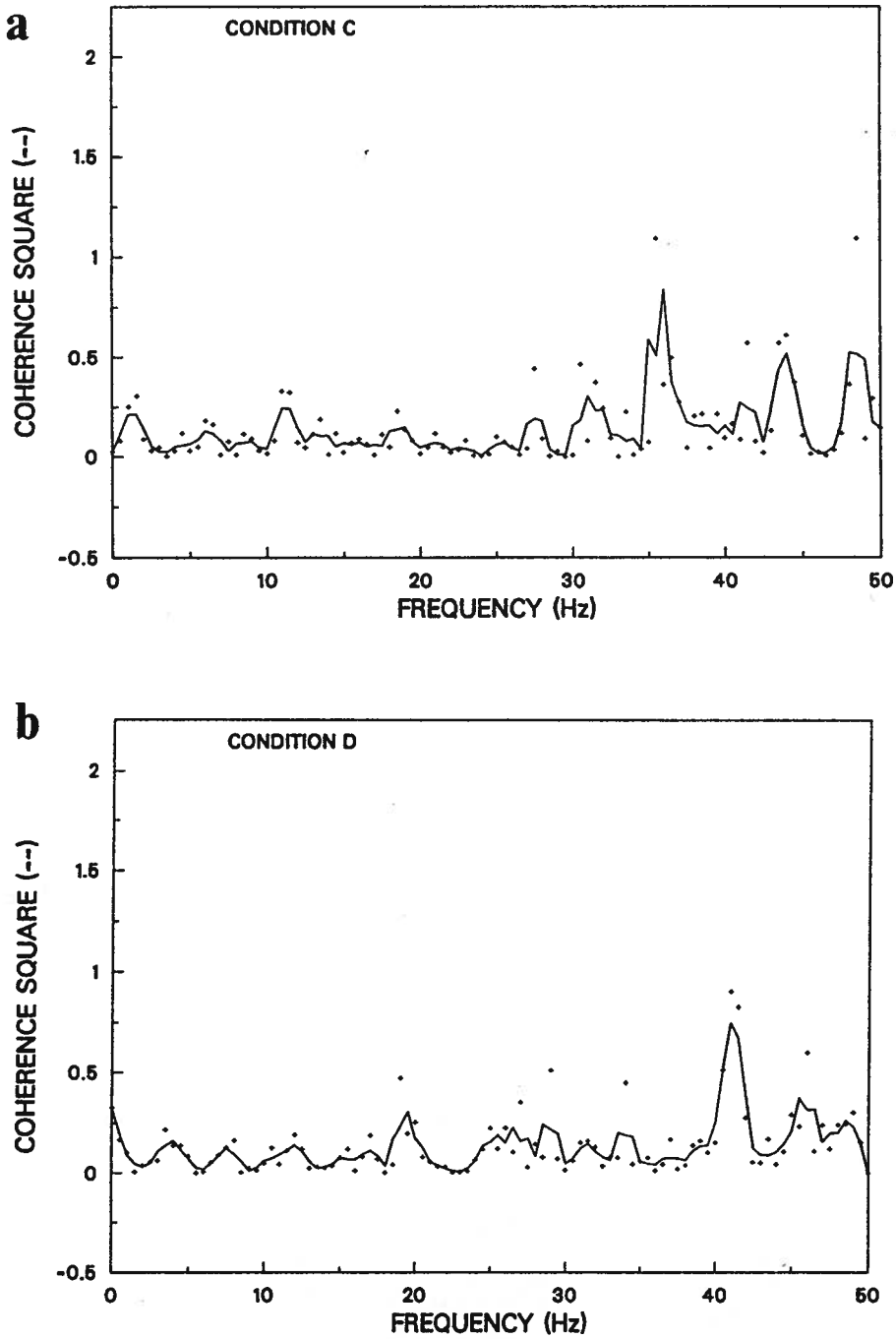

Figure C.4: Coherence square estimates of the Run 1 differential pressure and capacitance probe signals: (a) condition C, and (b) condition D. (Probe height 4.24 m. Δp_g heights 0.23–0.61 m.)

Appendix D

Particle Collision and Turbulent Diffusion Model Development

D.1 Scattering Velocities in a Single Binary Particle Collision

Consider the collision of a spherical particle A of mass m_{pA} with another spherical particle B of mass m_{pB}. The pertinent dynamic variables for the collision process are:

$\mathbf{V}_1$ = velocity prior to collision;

$\mathbf{V}_2$ = velocity post collision;

$\mathbf{V}_{AB}$ = velocity of particle A relative to particle B;

$\mathbf{k}$ = unit vector directed from the centre of particle A to the centre of particle B at time of contact;

$\mathbf{J}$ = impulse of the force exerted by particle A on particle B.

Conservation of linear momentum for the collision process gives

$$\begin{aligned} m_{pA}\mathbf{V}_{2A} &= m_{pA}\mathbf{V}_{1A} - \mathbf{J} \\ m_{pB}\mathbf{V}_{2B} &= m_{pB}\mathbf{V}_{1B} + \mathbf{J} \,, \end{aligned} \tag{D.1}$$

If it is assumed that the particles are smooth (i.e. no friction in particle-particle contacts) and the coefficient of restitution e for the collision is constant regardless of approach velocity or particle size, then

$$\mathbf{k} \cdot \mathbf{V}_{2AB} = -e\,(\mathbf{k} \cdot \mathbf{V}_{1AB}) \,. \tag{D.2}$$

It is assumed that the velocities prior to collision are known, and that the (scattering) velocities post-collision are required. From eq. (D.1),

$$\frac{\mathbf{J}}{m_{pA}} = \mathbf{V}_{1A} - \mathbf{V}_{2A} \ , \tag{D.3}$$

and

$$\frac{\mathbf{J}}{m_{pB}} = \mathbf{V}_{2B} - \mathbf{V}_{1B} \ . \tag{D.4}$$

Combining these two expressions gives the impulse $\mathbf{J}$ in terms of the relative particle velocities pre- and post-collision,

$$\mathbf{J} = \left(\frac{m_{pA} m_{pB}}{m_{pA} + m_{pB}} \right) (\mathbf{V}_{1AB} - \mathbf{V}_{2AB}) \ . \tag{D.5}$$

Now $\mathbf{J}$ is in the same direction as $\mathbf{k}$ since the particle velocities only change normal to the plane of contact. Thus

$$|\mathbf{J}| = (\mathbf{J} \cdot \mathbf{k}) \ , \tag{D.6}$$

and

$$\mathbf{J} = (\mathbf{J} \cdot \mathbf{k}) \ \mathbf{k} \ . \tag{D.7}$$

Substituting the expression for $\mathbf{J}$ in eq. (D.5) into the term $\mathbf{J} \cdot \mathbf{k}$ gives

$$(\mathbf{J} \cdot \mathbf{k}) = \left(\frac{m_{pA} m_{pB}}{m_{pA} + m_{pB}} \right) (\mathbf{V}_{1AB} - \mathbf{V}_{2AB}) \cdot \mathbf{k} \ . \tag{D.8}$$

Further substitution of eq (D.2) into this equation to eliminate $(\mathbf{V}_{2AB} \cdot \mathbf{k})$ gives

$$(\mathbf{J} \cdot \mathbf{k}) = \left(\frac{m_{pA} m_{pB}}{m_{pA} + m_{pB}} \right) (1 + e)(\mathbf{V}_{1AB} \cdot \mathbf{k}) \ . \tag{D.9}$$

Inserting this expression for $(\mathbf{J} \cdot \mathbf{k})$ into eq. (D.7) gives the impulse $\mathbf{J}$ in terms of known pre-collision variables,

$$\mathbf{J} = \left(\frac{m_{pA} m_{pB}}{m_{pA} + m_{pB}} \right) (1 + e)(\mathbf{V}_{1AB} \cdot \mathbf{k}) \mathbf{k} \ . \tag{D.10}$$

Finally, substituting this expression for $\mathbf{J}$ into the momentum balance expressions, eq. (D.1), gives the respective particle velocities post-collision in terms of the pre-collision velocities ($\mathbf{V}_{1A}$,

$\mathbf{V}_{1B}$ and $\mathbf{V}_{1AB}$), the coefficient of restitution e and the impact angle (defined by $\mathbf{k}$),

$$\begin{aligned}\mathbf{V}_{2A} &= \mathbf{V}_{1A} - \left(\frac{m_{pB}}{m_{pA}+m_{pB}}\right)(1+e)(\mathbf{k}\cdot\mathbf{V}_{1AB})\mathbf{k} \\ \mathbf{V}_{2B} &= \mathbf{V}_{1B} + \left(\frac{m_{pA}}{m_{pA}+m_{pB}}\right)(1+e)(\mathbf{k}\cdot\mathbf{V}_{1AB})\mathbf{k}\,. \end{aligned} \tag{D.11}$$

D.2 Collisional Velocity Changes of "Average" Particles

Consider the fluctuating motion of two "average" particles A and B undergoing collision repeatedly with each other. Assume that particle A velocity fluctuates between a pre-collision velocity $\mathbf{V}_{1A}$ and post collision velocity $\mathbf{V}_{2A}$, with gas drag between collisions balancing the force exerted on A during collision. The mean velocity between collisions for A is $\mathbf{v}_A$ and the magnitude of the fluctuations is $\Delta\mathbf{v}_{AB} = \mathbf{V}_{2A} - \mathbf{V}_{1A}$. Similarly particle B's velocity fluctuates between a pre-collision velocity $\mathbf{V}_{1B}$ and post-collision velocity of $\mathbf{V}_{2B}$, with a mean velocity between collisions of $\mathbf{v}_B$ and fluctuation magnitude $\Delta\mathbf{v}_{BA} = \mathbf{V}_{2B} - \mathbf{V}_{1B}$.

From Chapter 8,

$$\mathbf{V}_{2A} = \mathbf{V}_{1A} - \frac{m_{pB}(1+e)(\mathbf{V}_{1A}-\mathbf{V}_{1B})}{2(m_{pA}+m_{pB})}\,. \tag{D.12}$$

$$\mathbf{V}_{2B} = \mathbf{V}_{1B} + \frac{m_{pA}(1+e)(\mathbf{V}_{1A}-\mathbf{V}_{1B})}{2(m_{pA}+m_{pB})}\,. \tag{D.13}$$

$$\mathbf{v}_A = (1-\lambda_A)\mathbf{V}_{1A} + \lambda_A\mathbf{V}_{2A}\,, \tag{D.14}$$

$$\mathbf{v}_B = (1-\lambda_B)\mathbf{V}_{1B} + \lambda_B\mathbf{V}_{2B}\,, \tag{D.15}$$

$$\Delta\mathbf{v}_{AB} = -\frac{m_{pB}(1+e)(\mathbf{V}_{1A}-\mathbf{V}_{1B})}{2(m_{pA}+m_{pB})}\,, \tag{D.16}$$

and

$$\Delta\mathbf{v}_{BA} = \frac{m_{pA}(1+e)(\mathbf{V}_{1A}-\mathbf{V}_{1B})}{2(m_{pA}+m_{pB})}\,, \tag{D.17}$$

where λ is the velocity weighting factor defined in Chapter 3 (Table 3.5) and m_p is the particle mass. For development of a collision model the changes in velocity $\Delta\mathbf{v}_{AB}$ and $\Delta\mathbf{v}_{BA}$ are required in terms of the mean velocities $\mathbf{v}_A$ and $\mathbf{v}_B$, which may be achieved by manipulation of eqs. (D.12 – D.17) in the following manner.

Re-arranging eqs. (D.14) and (D.15) gives

$$\mathbf{V}_{2A} = \frac{\mathbf{v}_A}{\lambda_A} - \frac{\mathbf{V}_{1A}(1-\lambda_A)}{\lambda_A}\,, \tag{D.18}$$

and

$$\mathbf{V}_{2B} = \frac{\mathbf{v}_B}{\lambda_B} - \frac{\mathbf{V}_{1B}(1-\lambda_B)}{\lambda_B}\,, \tag{D.19}$$

Subtracting eq. (D.18) from eq. (D.12) to eliminate $\mathbf{V}_{2A}$, and re-arranging gives

$$\mathbf{v}_A\left[2\left(m_{pA}+m_{pB}\right)\right] = \mathbf{V}_{1A}\left[2m_{pA}+m_{pB}\left(2-\lambda_A\left(1+e\right)\right)\right] + \mathbf{V}_{1B}\left[m_{pB}\lambda_A\left(1+e\right)\right]\,. \tag{D.20}$$

Similarly, subtracting eq. (D.19) from eq. (D.13) to eliminate $\mathbf{V}_{2B}$, and re-arranging gives

$$\mathbf{v}_B\left[2\left(m_{pA}+m_{pB}\right)\right] = \mathbf{V}_{1B}\left[2m_{pB}+m_{pA}\left(2-\lambda_B\left(1+e\right)\right)\right] + \mathbf{V}_{1A}\left[m_{pA}\lambda_B\left(1+e\right)\right]\,. \tag{D.21}$$

Substituting eq. (D.21) into (D.20) to eliminate $\mathbf{V}_{1B}$ gives

$$\begin{aligned}
&\mathbf{v}_A\left[2\left(m_{pA}+m_{pB}\right)\right]\left[2m_{pB}+m_{pA}\left(2-\lambda_B\left(1+e\right)\right)\right] = \\
&\quad \mathbf{V}_{1A}\left[2m_{pA}+m_{pB}\left(2-\lambda_A\left(1+e\right)\right)\right]\left[2m_{pB}+m_{pA}\left(2-\lambda_B\left(1+e\right)\right)\right] \\
&\quad +\mathbf{v}_B\left[2\left(m_{pA}+m_{pB}\right)\right]\left[m_{pB}\lambda_A\left(1+e\right)\right] - \mathbf{V}_{1A}\left[m_{pA}m_{pB}\lambda_A\lambda_B\left(1+e\right)^2\right]\,.
\end{aligned} \tag{D.22}$$

Collecting like terms and re-arranging to give $\mathbf{V}_{1A}$ explicitly in terms of $\mathbf{v}_A$ and $\mathbf{v}_B$,

$$\mathbf{V}_{1A}\Upsilon = 2\left(m_{pA}+m_{pB}\right)\left[\mathbf{v}_A\left(2m_{pB}+m_{pA}\left(2-\lambda_B-e\lambda_B\right)\right) - \mathbf{v}_B m_{pB}\lambda_A\left(1+e\right)\right]\,, \tag{D.23}$$

where

$$\begin{aligned}
\Upsilon &= \left[2m_{pB}+m_{pA}\left(2-\lambda_B-e\lambda_B\right)\right]\left[2m_{pA}+m_{pB}\left(2-\lambda_A-e\lambda_A\right)\right] - \left[m_{pA}m_{pB}\lambda_A\lambda_B\left(1+e\right)^2\right] \\
&= 2\left[m_{pA}^2\left(2-\lambda_B\left(1+e\right)\right)+m_{pB}^2\left(2-\lambda_A\left(1+e\right)\right)+m_{pA}m_{pB}\left(4-\left(1+e\right)\left(\lambda_A+\lambda_A\right)\right)\right]
\end{aligned} \tag{D.24}$$

Similarly, substituting eq. (D.20) into (D.21) to eliminate $\mathbf{V}_{1A}$, collecting like terms and re-arranging gives $\mathbf{V}_{1B}$ explicitly in terms of $\mathbf{v}_A$ and $\mathbf{v}_B$,

$$\mathbf{V}_{1B}\Upsilon = 2\left(m_{pA}+m_{pB}\right)\left[\mathbf{v}_B\left(2m_{pA}+m_{pB}\left(2-\lambda_A-e\lambda_A\right)\right) - \mathbf{v}_A m_{pA}\lambda_B\left(1+e\right)\right]\,. \tag{D.25}$$

Inserting the relations for $\mathbf{V}_{1A}$ and $\mathbf{V}_{1B}$ from eqs. (D.23) and (D.25) into eq. (D.16) and re-arranging gives the required particle A velocity change $\Delta\mathbf{v}_{AB}$ solely in terms of the mean particle velocities $\mathbf{v}_A$ and $\mathbf{v}_B$, i.e.

$$\Delta\mathbf{v}_{AB} = \frac{2\left(m_{pA}+m_{pB}\right)\left(1+e\right)m_{pB}\left(\mathbf{v}_B-\mathbf{v}_A\right)}{\Upsilon} . \tag{D.26}$$

Now the expression for Υ in eq. (D.24) may be factorised giving

$$\Upsilon = 2\left(m_{pA}+m_{pB}\right)\left[m_{pA}\left(2-\lambda_B\right)+m_{pB}\left(2-\lambda_A\right)-e\left(m_{pA}\lambda_B+m_{pB}\lambda_A\right)\right] . \tag{D.27}$$

Consequently,

$$\Delta\mathbf{v}_{AB} = \frac{\left(1+e\right)m_{pB}\left(\mathbf{v}_B-\mathbf{v}_A\right)}{m_{pA}\left(2-\lambda_B\right)+m_{pB}\left(2-\lambda_A\right)-e\left(m_{pA}\lambda_B+m_{pB}\lambda_A\right)} . \tag{D.28}$$

Similarly,

$$\Delta\mathbf{v}_{BA} = \frac{\left(1+e\right)m_{pA}\left(\mathbf{v}_A-\mathbf{v}_B\right)}{m_{pA}\left(2-\lambda_B\right)+m_{pB}\left(2-\lambda_A\right)-e\left(m_{pA}\lambda_B+m_{pB}\lambda_A\right)} . \tag{D.29}$$

When collisions occur amongst "small" particles, the mean particle velocity of each particle is approximately equal to its pre-collision velocity, and $\lambda \to 0$ (see Chapter 3). In this case eqs (D.28) and (D.29) correctly reduce to eqs. (D.16) and (D.17). If both particle types in the collision are "large", $\lambda \approx 0.5$ and eqs. (D.28) and (D.29) reduce to

$$\Delta\mathbf{v}_{AB} = \frac{2\left(1+e\right)m_{pB}\left(\mathbf{v}_B-\mathbf{v}_A\right)}{\left(3-e\right)\left(m_{pA}+m_{pB}\right)} . \tag{D.30}$$

and

$$\Delta\mathbf{v}_{BA} = \frac{2\left(1+e\right)m_{pA}\left(\mathbf{v}_A-\mathbf{v}_B\right)}{\left(3-e\right)\left(m_{pA}+m_{pB}\right)} . \tag{D.31}$$

D.3 Collision Frequencies

In Chapter 8 it is shown that for collisions between type A particles, with mean velocities $\mathbf{v}_A$ and r.m.s. fluctuating velocities $\mathbf{c}_{kA}$, and type B particles, with mean velocities $\mathbf{v}_B$ and r.m.s. fluctuating velocities $\mathbf{c}_{kB}$, the total number of collisions per unit time and volume is

$$\begin{aligned} Z_{AB} &= \pi \mathbf{n}_A \mathbf{n}_B \sigma_{AB}^2 \frac{3\left(\mathbf{v}_A-\mathbf{v}_B\right)^2+\left(\mathbf{c}_{kA}^2+\mathbf{c}_{kB}^2\right)}{3\left|\mathbf{v}_A-\mathbf{v}_B\right|} \operatorname{erf}\left[\left(\frac{3}{2}\right)^{\frac{1}{2}} \frac{\left|\mathbf{v}_A-\mathbf{v}_B\right|}{\left(\mathbf{c}_{kA}^2+\mathbf{c}_{kB}^2\right)^{\frac{1}{2}}}\right] \\ &\quad + \sqrt{\frac{8\pi}{3}} \mathbf{n}_A \mathbf{n}_B \sigma_{AB}^2 \left(\mathbf{c}_{kA}^2+\mathbf{c}_{kB}^2\right)^{\frac{1}{2}} \exp\left[\frac{-3}{2}\frac{\left(\mathbf{v}_A-\mathbf{v}_B\right)^2}{\left(\mathbf{c}_{kA}^2+\mathbf{c}_{kB}^2\right)}\right] . \end{aligned} \tag{D.32}$$

If the ratio of mean velocity difference to r.m.s. velocity for the A-B mixture is defined as

$$\xi_{AB} = \frac{|\mathbf{v}_A - \mathbf{v}_B|}{(\mathbf{c}_{kA}^2 + \mathbf{c}_{kB}^2)^{\frac{1}{2}}} , \tag{D.33}$$

then eq. (D.32) may be re-written

$$\begin{aligned} Z_{AB} &= \mathbf{n}_A \mathbf{n}_B \sigma_{AB}^2 \left\{ \pi \left|\mathbf{v}_A - \mathbf{v}_B\right| \left(1 + \frac{1}{3\xi_{AB}^2}\right) \operatorname{erf}\left(\sqrt{\frac{3}{2}}\xi_{AB}\right) \right. \\ &\quad \left. + \sqrt{\frac{8\pi}{3}} \left(\mathbf{c}_{kA}^2 + \mathbf{c}_{kB}^2\right)^{\frac{1}{2}} \exp\left(\frac{-3\xi_{AB}^2}{2}\right) \right\} . \end{aligned} \tag{D.34}$$

A dimensionless version of eq. (D.34) is

$$\frac{Z_{AB}}{\mathbf{n}_A \mathbf{n}_B \sigma_{AB}^2 \left(\mathbf{c}_{kA}^2 + \mathbf{c}_{kB}^2\right)^{\frac{1}{2}}} = \pi \left(\xi_{AB} + \frac{1}{3\xi_{AB}}\right) \operatorname{erf}\left(\sqrt{\frac{3}{2}}\xi_{AB}\right) + \sqrt{\frac{8\pi}{3}} \exp\left(\frac{-3\xi_{AB}^2}{2}\right) . \tag{D.35}$$

As discussed in Chapter 8, the first and second r.h.s. terms of eq. (D.34) may be interpreted as the dimensionless collision frequency due respectively to the mean velocity difference (type (i) collisions) and the fluctuating velocities of the two particle types (type (ii) collisions). Denoting these as $\mathcal{Z}'_{AB}$ and $\mathcal{Z}''_{AB}$ gives

$$\mathcal{Z}'_{AB} = \pi \left(\xi_{AB} + \frac{1}{3\xi_{AB}}\right) \operatorname{erf}\left(\sqrt{\frac{3}{2}}\xi_{AB}\right) , \tag{D.36}$$

and

$$\mathcal{Z}''_{AB} = \sqrt{\frac{8\pi}{3}} \exp\left[\frac{-3\xi_{AB}^2}{2}\right] . \tag{D.37}$$

The relative magnitudes of type (i) and (ii) collision frequencies may be compared when expressed in the dimensionless form of eqs. (D.36) and (D.37). The dimensionless collision frequencies $\mathcal{Z}'_{AB}$, $\mathcal{Z}''_{AB}$ and $\mathcal{Z}_{AB} = \mathcal{Z}'_{AB} + \mathcal{Z}''_{AB}$ are plotted in Figure D.1 as a function of ξ_{AB}. Also shown is a total collision frequency $\mathcal{Z}^{\#}_{AB}$ obtained by adding the collision frequencies for type (i) and (ii) collisions without allowance for the interaction of mean and fluctuating velocities (as initially suggested in Chapter 8), i.e.

$$\mathcal{Z}^{\#}_{AB} = \pi\xi_{AB} + \sqrt{\frac{8\pi}{3}} . \tag{D.38}$$

Figure D.1 demonstrates that when ξ is greater than about 1.5 the fluctuating velocity components of the two particle types have negligible influence on the frequency of A-B collisions

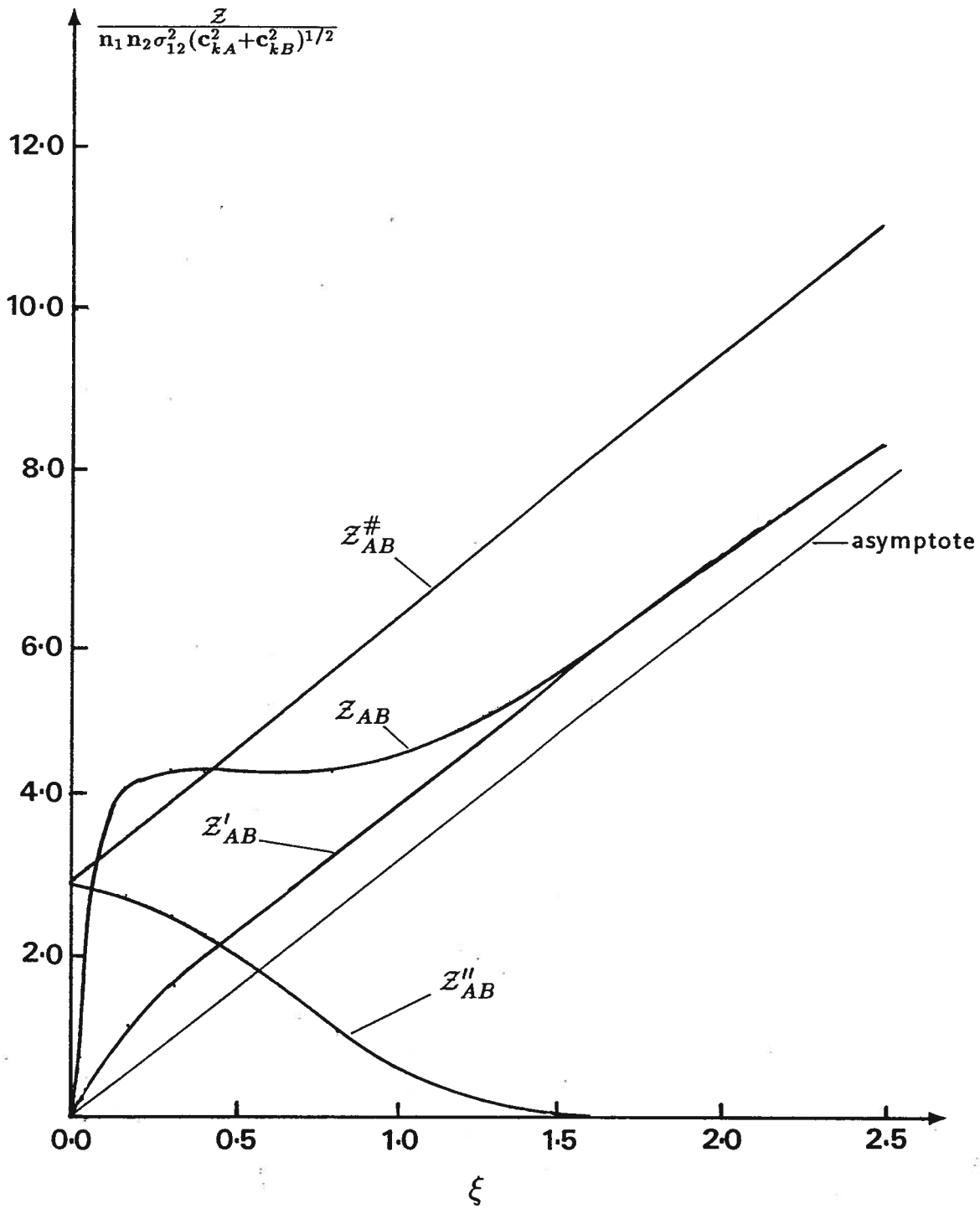

Figure D.1: Dimensionless collision frequencies for collisions between unlike (A and B) particles predicted by eqs. (D.36), (D.37) and (D.38).

regardless of the magnitude of these fluctuations. In this case, the use of mean velocities for each fraction to characterise the dynamic interactions between fractions should provide a complete and accurate representation of these interactions. In contrast, when the difference in mean velocity between the fractions is as low as 20% of the r.m.s. velocity fluctuations ($\xi = 0.2$), the effect of the mean velocity difference on total collision frequency, $\mathcal{Z}_{AB}$, is still significant. The estimates of collision frequency, $\mathcal{Z}^{\#}_{AB}$, given by eq. (D.38) result in significant errors for total collision frequency over a range of ξ of about 1.2 to 3.0. This is due to the failure of eq. (D.38) to account for the reduction in fluctuating velocity collision frequency $\mathcal{Z}''_{AB}$ as the mean velocity difference increases.

The presence of the error function in the collision frequency expressions makes it less amenable for use in numerical simulations. An alternative exponential expression for the error function is

$$\mathrm{erf}\left(\sqrt{\frac{3}{2}}\xi_{AB}\right) \approx 1 - \exp\left(-1.4\sqrt{\frac{3}{2}}\xi_{AB}\right) . \tag{D.39}$$

This expression estimates the error function with an error less than 10% in the region where collisions due to mean velocity differences become significant ($\xi > 0.2$), and an error less 1% when such collisions dominate ($\xi > 3.0$).

D.4 Collision Efficiencies

In Chapter 8 a correlation is proposed for estimating the collision efficiency η_{AB} of a smaller A particle approaching a larger B particle target in terms of an inertial parameter I_{AB}:

$$\begin{aligned} \eta_{AB} &= 0 && \text{for } \sqrt{I_{AB}} < 0.2 \\ \eta_{AB} &= \log_{10}\left(5\sqrt{I_{AB}}\right) && \text{for } 0.2 < \sqrt{I_{AB}} < 2.0 \\ \eta_{AB} &= 1 && \text{for } \sqrt{I_{AB}} > 2.0 . \end{aligned} \tag{D.40}$$

The parameter I_{AB} is defined as

$$I_{AB} = \frac{\rho_{pA}\, \mathbf{v}_{sB}\, d_{pA}^2}{18\, \mu_g\, d_{pB}} , \tag{D.41}$$

Table D.1: Particle collection efficiencies predicted by eq. (D.40).

Air Temperature T_g (°C.)	Target Particle Slip Velocity $\mathbf{v}_{sB}$ (m/s)	Inertial Parameter I_{AB} (-)	Collection Efficiency η_{AB} (%)
25	0.2	10	100
25	0.05	3	90
850	0.2	4	100
850	0.1	2	86
850	0.05	2	70

Approach particle A: $d_p = 40\mu$m, $\rho_p = 2700$ kg/m^3.
Target particle B: $d_p = 250\mu$m, $\rho_p = 2700$ kg/m^3.

where $\mathbf{v}_{sB}$ is the slip velocity of the target B particle.

Although η_{AB} is generally equal to 1.0 for collisions in CFB's, it may fall below unity for very small approach particles and low gas slip velocities around the target particle. For vertical suspension flow the lowest likely target particle slip velocities are of similar magnitude to the terminal velocity of the small particles. The target particle slip will usually be much greater than this. Table D.1 gives some typical values of η_{AB} for a 250 μm target particle and particle slip velocities of 0.1 and 0.2 m/s. The approach particle size and density are assumed to be 40 μm and 2700 kg/m^3, respectively.

D.5 The Energy Transfer to Particles by the Energetic Gas Eddies

Consider the motion of a particle that is accelerated by a gas eddy for the duration of its eddy interaction time τ_r. Assume that the gas eddy velocity $\mathbf{u}'$ is constant for the duration of the interaction and that the particle has an initial drift velocity $\mathbf{C}_t = 0$. Furthermore, assume that there is no collisional force on the particle and a linear drag law applies. Solution of the equation of motion for this case, given in Chapter 3 (with $\mathbf{C}_t$ in this case equal to $\mathbf{v}'$ in Chapter 3), is

$$\mathbf{C}_t = \mathbf{u}'\left(1 - \exp\left[-\tau_r/\tau_p\right]\right) . \tag{D.42}$$

From eqs. (3.23) and (3.25), the mean particle velocity is,

$$\overline{\mathbf{C}_t} = \mathbf{u}'\left(1 - \frac{\tau_p}{\tau_r}\right)\left(1 - \exp\left[-\tau_r/\tau_p\right]\right) , \tag{D.43}$$

The instantaneous power transfer from the eddy to the particle due to gas drag is $\mathbf{f}_{Dt} \cdot \mathbf{C}_t$, where $\mathbf{f}_{Dt} = m_p(\mathbf{u}' - \mathbf{C}_t)/\tau_p$. Hence the average transfer over time τ_r is

$$\begin{aligned}
\overline{\mathbf{f}_{Dt} \cdot \mathbf{C}_t} &= \frac{m_p}{\tau_p \tau_r} \int_0^{\tau_r} (\mathbf{u}' - \mathbf{C}_t) \cdot \mathbf{C}_t dt \\
&= \frac{m_p}{\tau_p} \frac{|\mathbf{u}'|^2 \tau_p}{2\tau_r} [1 - \exp(-\tau_r/\tau_p)] \, [1 - \exp(-\tau_r/\tau_p)] \, . \qquad \text{(D.44)}
\end{aligned}$$

Estimating the instantaneous power by $\overline{\mathbf{f}_D} \cdot \overline{\mathbf{C}_t}$ gives,

$$\begin{aligned}
\overline{\mathbf{f}_D} \cdot \overline{\mathbf{C}_t} &= \frac{m_p}{\tau_p} \left(\mathbf{u}' - \overline{\mathbf{C}_t}\right) \cdot \overline{\mathbf{C}_t} \\
&= \frac{m_p}{\tau_p} \frac{|\mathbf{u}'|^2 \tau_p}{2\tau_r} [1 - \exp(-\tau_r/\tau_p)] \left[2\left(1 - \frac{\tau_p}{\tau_r} \exp(-\tau_r/\tau_p)\right)\right] \, , \qquad \text{(D.45)}
\end{aligned}$$

where $\overline{\mathbf{u}' - \mathbf{C}_t} = \mathbf{u}' - \overline{\mathbf{C}_t}$, as $\mathbf{u}'$ is constant. Equations (D.44) and (D.45) differ. For small particles ($\tau_p \ll \tau_r$), eq. (D.45) overpredicts the average power transfer by 100%. For large particles ($\tau_p \gg \tau_r$) the two expressions give the same result. For eq. (D.45) to give the correct power transfer, it must be divided by a parameter $\mathcal{F}$,

$$\mathcal{F} = \frac{2\left(1 - \frac{\tau_p}{\tau_r} \exp(-\tau_r/\tau_p)\right)}{1 - \exp(-\tau_r/\tau_p)} \, . \qquad \text{(D.46)}$$

Comparison of eq. (D.46) and the expression for the velocity weighting factor λ in eq. (3.26) shows that $\mathcal{F} = 2(1 - \lambda)$. Hence the correct expression for the average power transfer from the gas to the particle in terms of the average particle drift velocity $\mathbf{c}_t$ ($= \overline{\mathbf{C}_t}$) is

$$\overline{\mathbf{f}_{Dt} \cdot \mathbf{C}_t} = \frac{m_p \, |\mathbf{u}' - \mathbf{c}_t| \;\; |\mathbf{c}_t|}{2\tau_p (1 - \lambda_r)} \, , \qquad \text{(D.47)}$$

where the subscript on λ_r denotes that it is based on the eddy interaction time τ_r.

Consider the same eddy and particle, but with significant particle collisional forces influencing the particle motion. In Chapter 8 an approximate velocity weighting factor λ_e was introduced for this particle motion. Therefore, to allow for possible effects of particle collisions on the drift motion of particles within an eddy, λ_r in eq. (D.47) should be replaced by the more general weighting factor λ_e. Note that $\lambda_e \to \lambda_r$ as the effect of collisions becomes negligible.

D.6 Effect of Slow Particles Entering the Core on the Core Particle Fluctuating Kinetic Energy

D.6.1 Number of Collisions Required to Accelerate a Slow Particle

The following equation was developed in Chapter 8 to describe the vertical velocity $\mathbf{w}_j$ of a slower particle introduced into the core after the jth collision with faster core particles from fraction i, each with vertical velocity $\mathbf{v}_{zi}$,

$$\mathbf{w}_j = \mathbf{w}_{j-1} + \mathcal{R}_{wi}\left(\mathbf{v}_{zi} - \mathbf{w}_{j-1}\right) , \tag{D.48}$$

where $\mathcal{R}_{wi}$ is a constant, specific to the particle masses and coefficient of restitution. To simplify the following analysis $\mathcal{R}_{wi}$ shall be abbreviated as $\mathcal{R}$ and $\mathbf{w}_j/\mathbf{v}_{zi}$ defined as $\mathcal{X}_j$. In terms of these parameters, the velocity after m collisions can be expressed in terms of velocities after earlier collisions by repeatedly applying eq. (D.48),

$$\begin{aligned}
\mathcal{X}_m &= \mathcal{R} & & +(1-\mathcal{R})\mathcal{X}_{m-1} \\
\mathcal{X}_m &= \mathcal{R}+ & \mathcal{R}\left[(1-\mathcal{R})\right] & +(1-\mathcal{R})^2\mathcal{X}_{m-2} \\
\mathcal{X}_m &= \mathcal{R}+ & \mathcal{R}\left[(1-\mathcal{R})+(1-\mathcal{R})^2\right] & +(1-\mathcal{R})^3\mathcal{X}_{m-3} \\
\mathcal{X}_m &= \mathcal{R}+ & \mathcal{R}\left[(1-\mathcal{R})+\ \ldots\ +(1-\mathcal{R})^{j-1}\right] & +(1-\mathcal{R})^j\mathcal{X}_{m-j} \\
\mathcal{X}_m &= \text{(i)}+ & \text{(ii)} & +\text{(iii)} .
\end{aligned} \tag{D.49}$$

Term (ii) in eq. (D.49) is the sum of a geometric sequence. By definition $0.0 < \mathcal{R} < 1.0$, and thus $0.0 < (1-\mathcal{R}) < 1.0$. Therefore this sequence always converges. For $\mathcal{X}_m$ expressed in terms of $\mathcal{X}_{m-j}$, term (ii) may be simplified by summing this series , i.e.

$$\begin{aligned}
\mathcal{R}\left[(1-\mathcal{R})+\ \ldots\ +(1-\mathcal{R})^{j-1}\right] &= \mathcal{R}(1-\mathcal{R})\left[\frac{1-(1-\mathcal{R})^{j-1})}{1-(1-\mathcal{R})}\right] \\
&= (1-\mathcal{R})\left[1-(1-\mathcal{R})^{j-1}\right] \\
&= \left[(1-\mathcal{R})-(1-\mathcal{R})^j\right] .
\end{aligned} \tag{D.50}$$

Thus eq. (D.49) becomes

$$\mathcal{X}_m = \mathcal{R} + (1-\mathcal{R}) - (1-\mathcal{R})^j(1-\mathcal{X}_{m-j})$$

$$= \quad 1-(1-\mathcal{R})^j(1-\mathcal{X}_{m-j})\,. \tag{D.51}$$

Now, when $m-j=0$, $\mathcal{X}_{m-j}=\mathcal{X}_0$, where $\mathcal{X}_0$ is the known initial velocity of the slow particle before its first collision. Therefore, in terms of $\mathcal{X}_0 = \mathbf{w}_0/\mathbf{v}_{zi}$, eq. (D.51) becomes

$$\mathcal{X}_m = 1-(1-\mathcal{R})^m\,(1-\mathcal{X}_0)\ . \tag{D.52}$$

This fully defines the velocity of the wall particle after m collisions in terms of m, known constant $\mathcal{R}$ and the initial slow particle dimensionless vertical velocity $\mathcal{X}_0$. For wall streamer particles it is assumed that $\mathcal{X}_0 = 0$. Typically, for core particles rebounding after a collision with the wall, $0.0 < \mathcal{X}_0 < 1.0$.

D.7 Integration of Differential Mass, Momentum and Particle Fluctuating Energy Equations

In Chapter 8 differential mass and momentum balance equations for the gas and particle phases for vertical suspension flow in the core of a riser are presented. In addition, a fluctuating kinetic energy differential balance is developed for the particles. Radial uniformity of all dependent variables is assumed across the entire core cross-section. It is also assumed that the mass creation rate of each phase, $\dot{m}_k$, is zero. Boundary conditions at the core-wall region interface are also given.

In the following analysis a general integration of each of these balance is performed over core cross-sectional area, A_{cr}, subject to these boundary conditions. The general integration assumes that A_{cr} may vary with height, z, up the riser, and that the net mass, momentum or fluctuating energy interchange between core and wall regions is not necessarily zero. To simplify the presentation, the succinct vector forms of the differential balances are used, keeping in mind that convective flow of gas and particles is only in the vertical z-direction. The rate of change in the core cross-sectional area with height is assumed to be sufficiently small that the core-wall region interface may be assumed to be vertical. Thus, since the flow is vertical, only non-convective transfer of mass, momenta or energy may occur across this interface.

D.7.1 Mass Balances

From eq. (4.21) in Chapter 4, the differential mass balance for the steady flow of phase k with $\dot{m}_k = 0$ is

$$\nabla\cdot\ (\epsilon_k \rho_k \mathbf{v}_k) = 0 \tag{D.53}$$

Phase k may be either the gas or a particle fraction i. Assuming all phases are incompressible, and integrating this equation over a differential core volume, $\Delta V_{cr} = A_{cr}\,\Delta z$, gives

$$\rho_k \iiint_{V_{cr}} \nabla\cdot\ (\epsilon_k \mathbf{v}_k)\, dV_{cr} = \mathcal{P}_{ca} Q_k\, \Delta z\ , \tag{D.54}$$

where $\mathcal{P}_{ca}$ is the core-annular wall region interfacial area per unit height (which equals the core region perimeter at height z). Q_k is the net rate of mass transfer across this interface and *into* the core per unit area. By Gauss' theorem,

$$\iiint_{V_{cr}} \nabla\cdot\ (\epsilon_k \mathbf{v}_k)\, dV_{cr} = \iint_{s_{cr}} \hat{\mathbf{n}}\cdot\ (\epsilon_k \mathbf{v}_k)\, ds_{cr}\ , \tag{D.55}$$

where s_{cr} is the surface area of volume V_{cr}, and $\hat{\mathbf{n}}$ is the unit normal directed outwards across ds_{cr}. As convective flow is assumed to occur only in the vertical z direction, it is only necessary to integrate over the upper and lower horizontal surfaces of the volume V_{cr}, i.e.

$$\iint_{s_{cr}} \hat{\mathbf{n}}\cdot\ (\epsilon_k \mathbf{v}_k)\, ds_{cr} = A_{cr}\epsilon_k \mathbf{v}_{zk}|_{z+\Delta z} - A_{cr}\epsilon_k \mathbf{v}_{zk}|_z\ . \tag{D.56}$$

By substituting the r.h.s. of eq. (D.56) for the l.h.s. of eq. (D.54), dividing the resulting equation by Δz, and assuming $\Delta z \to 0$, the integrated mass balance for phase k flow in the core is obtained:

$$\rho_k \frac{d\,|A_{cr}\epsilon_k \mathbf{v}_{zk}|}{dz} = \mathcal{P}_{ca} Q_k\ . \tag{D.57}$$

For flow of the gas phase, the mass balance becomes

$$\rho_g \frac{d\,|A_{cr}\epsilon_g \mathbf{u}_z|}{dz} = \mathcal{P}_{ca} Q_g\ . \tag{D.58}$$

The mass balance for the ith particle fraction is

$$\rho_{pi} \frac{d\,|A_{cr}\epsilon_{pi} \mathbf{v}_{zi}|}{dz} = \mathcal{P}_{ca}\,(Q_{ri} + Q_{si} - Q_{ci})\ . \tag{D.59}$$

Mechanisms resulting in the lateral mass fluxes, Q_{ri}, Q_{si}, Q_{ci}, are discussed in Chapter 8.

D.7.2 Momentum Balances

The momentum balance for phase k proposed for the core riser model, eq. (8.115), written in vector form with $\dot{m}_k = 0$, is

$$\nabla\cdot\ (\epsilon_k \rho_k \mathbf{v}_k \mathbf{v}_k) = -\ \epsilon_k \nabla p_g + \epsilon_k \rho_k \mathbf{g} + \mathbf{M}_k^d\ . \tag{D.60}$$

The same assumptions apply as in the mass balance derivation. Integrating this equation over the differential core volume, $\Delta V_{cr} = A_{cr}\,\Delta z$, gives

$$\rho_k \iiint_{V_{cr}} \nabla\cdot\ (\epsilon_k \rho_k \mathbf{v}_k \mathbf{v}_k)\, dV_{cr} = \iiint_{V_{cr}} \left(-\epsilon_k \nabla p_g + \epsilon_k \rho_k \mathbf{g} + \mathbf{M}_k^d\right) dV_{cr} + \mathcal{P}_{ca}\,(\boldsymbol{\tau}_k\ + Q_k \mathbf{v}_k)\ \Delta z\ , \tag{D.61}$$

where $\boldsymbol{\tau}_k$ is the shear force exerted on the phase k core flow, and $Q_k \mathbf{v}_k$ is the change in phase k core momentum due to mass gain from the wall region.

Using Gauss' theorem, the l.h.s. of eq. (D.61) becomes

$$\begin{aligned} \iiint_{V_{cr}} \nabla\cdot\ (\epsilon_k \mathbf{v}_k \mathbf{v}_k)\, dV_{cr} &= \iint_{s_{cr}} (\hat{\mathbf{n}}\cdot\ \mathbf{v}_k)\ (\epsilon_k \mathbf{v}_k)\, ds_{cr} \\ &= A_{cr} \epsilon_k \mathbf{v}_{zk} \mathbf{v}_{zk}\big|_{z+\Delta z}\ -\ A_{cr} \epsilon_k \mathbf{v}_{zk} \mathbf{v}_{zk}\big|_z\ . \end{aligned} \tag{D.62}$$

Note that as the mean flow is only in the vertical direction, the general momentum balance simplifies to an axial z-momentum balance. By the same method as employed for the mass balance derivation, the r.h.s. of eq. (D.62) is first substituted for the l.h.s. of eq. (D.61), and the resulting equation divided by Δz. Then, assuming $\Delta z \to 0$, the integrated momentum balance for phase k flow in the core is derived:

$$\rho_k \frac{d\,(A_{cr} \epsilon_k \mathbf{v}_{zk} |\mathbf{v}_{zk}|)}{dz} = A_{cr} \left[-\ \epsilon_k \frac{dp_g}{dz}\, \boldsymbol{\delta}_z\ +\ \epsilon_k \rho_k \mathbf{g} + \mathbf{M}_k^d\right] +\ \mathcal{P}_{ca}\,[\boldsymbol{\tau}_k\ + Q_k \mathbf{v}_k]\ . \tag{D.63}$$

To further simplify this momentum balance, the mass balance for phase k is multiplied by $\mathbf{v}_{zk}$:

$$\mathbf{v}_{zk} \rho_k \frac{d\,|\epsilon_k \mathbf{v}_{zk}|}{dz} = \mathcal{P}_{ca} Q_k \mathbf{v}_{zk}\ . \tag{D.64}$$

Equation (D.64) is then subtracted from eq. (D.63) to give a simpler form of the momentum balance for phase k:

$$A_{cr} \rho_k \epsilon_k \mathbf{v}_{zk} \frac{d|\mathbf{v}_{zk}|}{dz} = A_{cr} \left[-\ \epsilon_k \frac{dp_g}{dz}\, \boldsymbol{\delta}_z\ +\ \epsilon_k \rho_k \mathbf{g} + \mathbf{M}_k^d\right] +\ \mathcal{P}_{ca} \boldsymbol{\tau}_k\ . \tag{D.65}$$

Thus, for the gas phase, the integrated axial z-momentum balance for steady flow in the riser core is

$$A_{cr}\rho_g\epsilon_g\mathbf{u}_z\frac{d|\mathbf{u}_z|}{dz} = A_{cr}\left[-\epsilon_g\frac{dp_g}{dz}\boldsymbol{\delta}_z + \epsilon_g\rho_g\mathbf{g} + \mathbf{M}_g^d\right] + \mathcal{P}_{ca}\boldsymbol{\tau}_g \ , \tag{D.66}$$

where $\boldsymbol{\tau}_g$ is the shear force exerted on the core gas flow due to gas friction in the wall region. Similarly, the axial z-momentum balance for particle fraction i is

$$A_{cr}\rho_{pi}\epsilon_{pi}\mathbf{v}_{zi}\frac{d|\mathbf{v}_{zi}|}{dz} = A_{cr}\left[-\epsilon_{pi}\frac{dp_g}{dz}\boldsymbol{\delta}_z + \epsilon_{pi}\rho_{pi}\mathbf{g} + \mathbf{M}_{pi}^d\right] + \mathcal{P}_{ca}\left[\boldsymbol{\tau}_{ri} + \boldsymbol{\tau}_{si}\right] , \tag{D.67}$$

where $\boldsymbol{\tau}_{ri}$ and $\boldsymbol{\tau}_{si}$ are the shear forces on the core particle fraction i due to rebound and wall streamer particles entering the riser core. Expressions for $\boldsymbol{\tau}_{ri}$ and $\boldsymbol{\tau}_{si}$ are given in Chapter 8.

D.7.3 Particle Fluctuating Kinetic Energy Balance

The particle fluctuating energy differential balance (eq. (8.84)) may be integrated by the same method as that used for the momentum equation, and it is therefore not necessary to include the details. The resulting particle fluctuating energy balance for core fraction i is

$$A_{cr}\rho_{pi}\epsilon_{pi}|\mathbf{v}_{zi}|\frac{dK_i}{dz} = A_{cr}\left[P_{kt_i} - D_{kt_i} + \sum_{j=1}^{n}\left(P_{kk_{ij}} + S_{k_{ij}}\right)\right] + \mathcal{P}_{ca}\left[P_{kr_i} + P_{ks_i} + -D_{kr_i} - D_{ks_i}\right] , \tag{D.68}$$

where n is the total number of particle fractions. Expressions for all the r.h.s. terms in eq. (D.68) are given in Chapter 8.

D.8 Simultaneous Solution of the Particle and Gas Turbulent Energy Equations by Newton's Method

The riser core model differential equations developed in Chapter 8 are functions of $(3n + 2)$ independent variables, ϵ_g, ϵ_{pi}, $\mathbf{u}_z$, $\mathbf{v}_{zi}$ and K_i, and the $(n + 1)$ gas eddy and particle drift velocities, $\mathbf{u}_1'$ and $\mathbf{c}_{ti}$. The drift velocities are also functions of the independent variables. To advance the numerical solution of the differential equations, it is therefore necessary to also calculate the drift velocities at each numerical integration step. This requires simultaneous

solution of the $(n+1)$ non-linear algebraic equations describing the particle response to the turbulence, and the modulation of the gas turbulence by particles.

Newton's method, a general numerical technique that is described in numerical methods texts (e.g. Carnahan *et al.*, 1969), is used to solve the simultaneous equations. It is an iterative method that requires a Jacobian square matrix that contains the partial derivatives of all the equations in terms of all variables. The derivations of the expressions in this Jacobian matrix are outlined here so that the large number of otherwise undecipherable equations in the model code may be followed.

Define the number of equations to be simultaneously solved to be $nn = n+1$, where n is the total number of particle fractions. Let x_i be the ith independent variable, where $i = 1, nn$. More specifically, for $i = nn$, assume $x_{nn} = \mathbf{u}_1'$, and for $i \leq n$, let $x_i = \mathbf{c}_{tj}$, where $j = 1, n$. Similarly, let the function f_{nn} be defined by a form of the gas energy modulation equation (eq. (8.69)), and function f_i to correspond to the ith particle eddy drift equation (eq. (8.59)). For Newton's method, the functions, f, are written with all terms on one side, and thus equal zero.

First, consider the particle drift equation, eq. (8.59). By substituting eq. (8.60) into eq. (8.59), and re-arranging, we obtain

$$f_i = \frac{\epsilon_{pi}\rho_{pi}\mathbf{c}_{ti}}{\tau_{ri}(1-\lambda_{ei})} - \mathbf{F}_{Dt_i} - \sum_{j=1}^{n} \mathbf{F}_{kt_{ij}} = 0 \,, \tag{D.69}$$

which is applicable for $i = 1, n$. Before taking derivatives of f_i, f_i must be expressed in fundamental form, as a function of all x_i dependent variables. Note that we are solving the turbulent energy equations for a given set of *constants* for ϵ_g, ϵ_{pi}, $\mathbf{u}_z$, $\mathbf{v}_{zi}$ and K_i, i.e these parameters are constant in the ensuing analysis. Recall, also, that $K_i = \mathbf{c}_{ki}^2/2$ (eq. (8.1)). For drag on particle fraction i, eqs. (8.65) and (8.126) give

$$\mathbf{F}_{D_{ti}} = \frac{\epsilon_{pi}\rho_{pi}(\mathbf{u}_1' - \mathbf{c}_{ti})}{\epsilon_g^{1.8}\tau_p} \,. \tag{D.70}$$

Similarly, from eqs. (8.49) and (8.57), $\mathbf{F}_{kt_{ij}}$ may be written as

$$\mathbf{F}_{kt_{ij}} = H_{ij}C_{ij}(\mathbf{c}_{tj} - \mathbf{c}_{ti})\left(1 + \frac{1}{3\xi_{ij}^2}\right) \operatorname{erf}\left(\sqrt{\frac{3}{2}}\xi_{ij}\right) \,, \tag{D.71}$$

with H_{ij} given by

$$H_{ij} = \frac{\pi \epsilon_{pi} \epsilon_{pj} \rho_{pi} \rho_{pj} \eta_{ij} \, \sigma_{ij}^2 \, (1+e)}{m_{pi} \, (2-\lambda_j) + m_{pj} \, (2-\lambda_i) - e \, (m_{pi} \lambda_j + m_{pj} \lambda_i)} \, . \tag{D.72}$$

C_{ij} is the magnitude of the difference between the mean ith and jth particle fraction velocities, i.e.

$$\begin{aligned} C_{ij} &= |\mathbf{v}_j - \mathbf{v}_i| \\ &= \left[(\mathbf{v}_{zi} - \mathbf{v}_{zj})^2 + (\mathbf{c}_{ti} - \mathbf{c}_{tj})^2 \right]^{\frac{1}{2}} \, . \end{aligned} \tag{D.73}$$

The error function term, $(1 + 1/(3\xi_{ij}^2)) \, \mathrm{erf}(\sqrt{3/2}\, \xi_{ij})$, in eq. (D.71) corrects the type (i) collision frequency for the effects of fluctuating particle velocities. This may be approximated as a constant, 1.0, based on the discussion earlier in this appendix and a comparison of the $\mathcal{Z}'_{AB}$ curve and the aymptote (equivalent to $\mathcal{Z}'_{AB}$ without type (ii) collision effects) given in Figure D.1. This approximation is only unreasonable when the fluctuating velocities of particles due to collisions are significantly greater than the particle drift velocity. In this case the accuracy of the calculation of $\mathbf{c}_{ti}$ is not critical, as turbulence has negligible effect on the particles. Also, over the range of eddy gas velocities encountered by the particles, the collision and eddy velocity weighting factors, λ_i and λ_{ei}, the particle response time, τ_{pi}, and the eddy interaction period, τ_{ri}, may be shown to vary slowly in comparison to $\mathbf{c}_{ti}$ and $\mathbf{u}'_1$. Thus these four parameters are assumed to be constants in the derivation of the Jacobian. This assumption does not affect the accuracy of the final calculated $\mathbf{c}_{ti}$ and $\mathbf{u}'_1$ values, providing that the iterative Newton's method converges. However, it does increase the possibility of non-convergence. With these assumptions, H_{ij} in eq.(D.72) is also treated as a constant when derivatives are taken.

From the above discussion, the function f_i for the particle drift equation, eq.(D.69), may be written in terms of the independent variables, $x_i, i = 1, n$:

$$\begin{aligned} f_i &= \frac{\epsilon_{pi} \rho_{pi} x_i}{\tau_{ri} \, (1 - \lambda_{ei})} - \frac{\epsilon_{pi} \rho_{pi} \, (x_{nn} - x_i)}{\epsilon_g^{1.8} \tau_p} - \sum_{j=1}^{n} H_{ij} C_{ij} \, (x_j - x_i) \\ &= 0 \, , \end{aligned} \tag{D.74}$$

where, clearly,

$$C_{ij} = \left[(\mathbf{v}_{zi} - \mathbf{v}_{zj})^2 + (x_i - x_j)^2 \right]^{\frac{1}{2}} . \tag{D.75}$$

Recall from Chapter 3 that $(\mathbf{u}')^2 = 3u_e^2$, and $\tau_e = 1.6 l_e / u_e$. Using these relations to replace the terms u_{e1} and τ_{e1} by $\mathbf{u}_1'$ in the gas turbulent energy modulation equation, eq. (8.69), and re-arranging the result, gives the function f_{nn}, i.e

$$\begin{aligned} f_{nn} &= \frac{(\mathbf{u}_1')^3}{1.6\sqrt{3}l_e} + \frac{1}{\rho_g} \sum_{j=1}^{n} \frac{\epsilon_{pj}\rho_{pj}(\mathbf{u}_1' - \mathbf{c}_{tj})\,\mathbf{c}_{tj}}{2(1-\lambda_{ej})\,\tau_{pj}} - \frac{(\mathbf{u}_0')^3}{1.6\sqrt{3}l_e} \\ &= \frac{x_{nn}^3}{1.6\sqrt{3}l_e} + \frac{1}{\rho_g} \sum_{j=1}^{n} \frac{\epsilon_{pj}\rho_{pj}(x_{nn} - x_j)\,x_j}{2(1-\lambda_{ej})\,\tau_{pj}} - \frac{(\mathbf{u}_0')^3}{1.6\sqrt{3}l_e} \\ &= 0 . \end{aligned} \tag{D.76}$$

Equations for estimating the constant particle-free turbulent gas velocity, $\mathbf{u}_0'$ and energetic eddy size, l_e, are given in Chapters 3 and 8.

Newton's method requires repeated solution of the matrix:

$$\begin{bmatrix} \partial f_1/\partial x_1 & \cdots & \cdots & \cdots & \partial f_1/\partial x_n & \partial f_1/\partial x_{nn} \\ \vdots & & & & \vdots & \vdots \\ \vdots & & & & \vdots & \vdots \\ \partial f_n/\partial x_1 & \cdots & \cdots & \cdots & \partial f_n/\partial x_n & \partial f_n/\partial x_{nn} \\ \partial f_{nn}/\partial x_1 & \cdots & \cdots & \cdots & \partial f_{nn}/\partial x_n & \partial f_{nn}/\partial x_{nn} \end{bmatrix} \begin{bmatrix} \Delta x_1 \\ \vdots \\ \vdots \\ \Delta x_n \\ \Delta x_{nn} \end{bmatrix} = \begin{bmatrix} -f_1 \\ \vdots \\ \vdots \\ f_n \\ -f_{nn} \end{bmatrix}$$

Unlike the original non-linear equations, this system of linear equations may be solved by standard non-iterative numerical methods. This model uses Gauss elimination with partial pivot selection (routine DGAUSS in Appendix E). The updated solution values, x_i', after each iteration are given by $x_i' = x_i + \alpha\,\Delta x_i$, where α is a relaxation factor, typically of order 0.8.

Differentiation of eqs. (D.74) and (D.76) and algebraic manipulation of the results gives the partial derivatives in the Jacobian matrix. For $1 \le i \le n$, $1 \le j \le n$ and $i \ne j$:

$$\frac{\partial f_i}{\partial x_j} = -H_{ij} C_{ij} \left(1 + \frac{(x_i - x_j)^2}{C_{ij}^2} \right) . \tag{D.77}$$

For $1 \leq i \leq n$:

$$\frac{\partial f_i}{\partial x_i} = \sum_{j=1}^{n} H_{ij} C_{ij} \left(1 + \frac{(x_i - x_j)^2}{C_{ij}^2}\right) + \epsilon_{pi}\rho_{pi} \left(\frac{1}{\tau_{ri}(1-\lambda_{ei})} + \frac{1}{\tau_{pi}\epsilon_g^{1.8}}\right) , \tag{D.78}$$

$$\frac{\partial f_i}{\partial x_{nn}} = -\frac{\epsilon_{pi}\rho_{pi}}{\tau_{pi}\epsilon_g^{1.8}} , \tag{D.79}$$

and,

$$\frac{\partial f_{nn}}{\partial x_i} = \frac{\epsilon_{pi}\rho_{pi}(x_{nn} - 2x_i)}{2\tau_{pi}\epsilon_g(1-\lambda_{ei})} . \tag{D.80}$$

Finally,

$$\frac{\partial f_{nn}}{\partial x_{nn}} == \frac{\sqrt{3}x_{nn}^2}{1.6 l_e} + \frac{1}{\rho_g}\sum_{j=1}^{n} \frac{\epsilon_{pj}\rho_{pj}x_j}{2(1-\lambda_{ej})\tau_{pj}} . \tag{D.81}$$

In the CFB core model code (Appendix E), C_{ij}, H_{ij} and $\mathbf{F}_{kt_{ij}}$ are evaluated in the routine DYNCOL. Drag force is calculated in routine DRAGON, and the functions and function derivatives in the above matrices are assembled in routine PARTUR. Convergence of Newton's method is also tested for in PARTUR. Convergence is attained when all $|\Delta x_i / x_i| < \epsilon$. The accuracy parameter, ϵ, that was used for the core model simulations reported in this study was 10^{-2}. Several other constraints on the magnitude of $|\alpha\, \Delta x_i|$ are imposed in PARTUR to stop physically impossible values of x_i in the initial iteration steps. These are explained in the code. Although, in general, convergence of Newton's method is not guaranteed, no convergence problems have been encountered in this application. Originally, the non-linear turbulent energy equations were solved by a Gauss-Seidel method. Frequent convergence problems were encountered with this original method. Consequently, computation times for the CIRCOR model were significantly greater using the Gauss-Seidel method.

Appendix E

Core Collision and Wall Particle Trajectory Models: Program Listing and Documentation

The FORTRAN code listings given in this Appendix are for (i) "CIRCOR," the riser core collision and turbulent diffusion model described in Chapter 8, and (ii) "WALSTF," the particle trajectory model outlined in Chapter 9. The two models share many common general subroutines and input files. Consequently, the model listings have been divided into three sections. These sections contain, respectively, the main program code for CIRCOR, the main program code for WALSTF, and listings of all subroutines used in either model. Throughout the listings reference is made to "Level 3" modelling. This denotes that the routines are used in dynamic (mass, momenta, energy) models. Variables in common blocks and parameter statements have the same definition in any level 3 subroutine, and these routines may be incorporated in any level 3 model. (The semi-empirical "mass balanced" model described in Chapter 10 is designated as a "Level 2" model, and many of its routines, listed in Appendix G, are incompatible with the level 3 models).

Typical input and diagnostic message files and a program documentation file are also listed. The documentation file defines all common and parameter variables. All programs and subroutines are well documented, and definitions of key variables specific to each routine are given in the preamble to that routine. In a final section, listings of numerical routine codes developed specifically for this study are given. Execution of WALSTF also requires the non-proprietary stiff differential equation solver, LSODE (Hindmarsh, 1983). All code is in standard FORTRAN77. All routines were developed and debugged using "test driver" programs. The accuracies of the numerical routines have been tested for a number of problems with known

analytical solutions.

The execution time of the program CIRCOR is not excessive (generally less than 20 s CPU time on an IBM 3090, with vector processing), providing that the number of particle fractions is less than about 40.

E.1 Program Documentation

```
************ file: CIRBED3.DOC ****************************************
-----------------------------------------------------------------------
Program documentation for circulating fluidised bed level 3 models
Rev 1 Sept. 30  1991; Rev 5   Oct. 15  1991; Rev 6 Feb 05 1992

Code developed by Richard C. Senior, Univ. British Columbia, Canada
LEVEL 3 MODELLING: MASS AND MOMENTUM BALANCE HYDRODYNAMIC MODELLING

PROGRAMS: CIRCOR3.FOR - CFB core dynamic model
          WALIFT3.FOR - Discrete particle motion in riser wall region
          WALSTF3.FOR - Discrete particle motion in riser wall region
          CIRWAL3.FOR - Wall dynamics model at low suspension density
                        (under development)

SUBROUTINES:                    in CIRBED3.FOR
TEST PROGRAMS FOR SUBROUTINES: in CIRBED3.PRG
All code written in FORTRAN (double precision)
Executable code in CFB3.EXE

-----------------------------------------------------------------------
1. MODEL SUBROUTINES:
---------------------
Routine Cur. Test     Common Blocks   Sect. Program/s
        Vers Program
AIRPRO    1  DPDRAG   G               A     CIRCOR3
DATIN     1  DPDATI   E,G,H,I,J,O,P   A     CIRCOR3
DIFEQS    1  --       SUBB,SUBC,G     C     WALSTF3
DIFSTF    1  --       SUBB,SUBC,G     C     WALIFF3
DRAGON    1  DPDRAG   G,O,P           A     CIRCOR3
DRAGOP    1  --       G               C     WALIFT3, WALSTF3
DYNCOL    1  DPSYST   G,O,P,K,T       A     CIRCOR3
ERCHEK    1  --       E               A     CIRCOR3
ERINIT    1  --       E               A     CIRCOR3
FEDSIZ    1  DPFEDS   I,J,O,P         A     CIRCOR3
FLUCEN    1  DPSYST   O,P             B     CIRCOR3
GASTUR    1  DPSYST   G,H,I           A     CIRCOR3
ICONDS    1  DPSYST   E,G,H,I,O,P     B     CIRCOR3
PARTUR    1  DPSYST   G,H,I,O,P       B     CIRCOR3
PROFIL    1  --       SUBC            C     WALIFT3, WALSTF3
SAUTER    1  --       J,P             A     CIRCOR3
SYSTEQ    1  --       E,G,H,I,K,O,P,Y B     CIRCOR3
TERVEL    1  DPDRAG   G,O,P           A     CIRCOR3
WALCON    1  DPSYST   I,O,P           B     CIRCOR3

NOTE:
(i)   version X is labelled as routine version no 3.X level 3 code
(ii)  routine version listed is the routine current in the level 3
      models. Old or alternative versions are in CIRBED3.OLD
(iii) all test driver programs for debugging individual routines are
      in file CIRBED.PRG

Subroutines in CIRBED3.FOR are divided into three sections (i.e.
'sect.' above):
SECTION A: General routines common to more than one level 3 model
SECTION B: Routines specific to program CIRCOR (core model)
SECTION C: Routines specific to programs WALIFT, WALSTF and CIRWAL
           (wall dynamics modelling)
```

2. GENERAL NUMERICAL SUBROUTINES:

To run level 3 programs and test programs numerical routines DGAUSS, LENSTR, ODERKF and FHLBRG are required. These routines are in ZUB.FOR See this file for documentation. Executable versions in ZUB.EXE Widely available ODE solver LSODE from ODEPACK (or LSODE.FOR for older version) also required.

ROUTINE	DESCRIPTION
DGAUSS	Simultaneous linear equations - Gauss elimination with scaled partial pivotting
LSODE	Solution of a stiff system of initial value O.D.E.'s by Gears method.
LENSTR	Number of characters in a string excluding trailing blanks
ODERKF	Simultaneous O.D.E. solution by Runge-Kutta Fehlberg method, RKF computation in routine FHLBRG

3. LOGICAL UNIT ASSIGNMENTS

Unit	File	Ref. Version	File Type
11	{user input}	CBUSE3	Sequential
12	{user input}	CBWAL3	Sequential
14	{diagnostic messages}	CBERR3	Direct Access

Program Requirements:
CIRCOR3 : Units 11, 14
CIRWAL3 : Units 11, 14
WALIFT3, WALSTF3: Units 11, 12, 14

UNIX or DOS : All data files in sub-directory CIIRBED3/INPUT/
Mainframe MTS: All data files in composite file CIRBED3.DAT

4. PROGRAM UNITS

Input data file units are as defined in ref. version input file CBUSE3
All program working units are SI (kg, m, s, Kelvin, Newton, Joules, etc.), except: (i) particle diameters, mm
(ii) particle mean free paths, mm

5. COMMON BLOCKS AND PARAMETER STATEMENTS - VARIABLE DEFINITIONS

Variable definitions here are for parameter statements and common blocks only. Variables for each routine are defined in the preamble to that routine.

```
PARAMETER (NXP1=x1,NXP2=x2,NXP=x1+x2)
PARAMETER (NZB=zz,NZ=zz+1)
PARAMETER (NER1=e1,NERR=ee)

BLKE/IERROR(NERR),IERR1,IERR2
BLKG/AIR(20),TG,PG
BLKH/BED(10),IBED
BLKI/HYDG(20)
BLKJ/SIV(4,25),NSIV
BLKK/Z1T(NXP),Z2T(NXP),VWK(NXP)
BLKO/XP(NXP),WP(NXP),IXP(NXP)
BLKP/PP(2,10)
BLKT/CCOR,VCOR,FPCOR,ICOR
BLKY/ZS,ZF
SUBB/FDZ,FDY,FLFT,TAUP,UZY
SUBC/DPP,WTP,PSIP,RHOP,USTR,VISK,SX
```

6;PARAMETERS

```
------------
(A) PARAMETER (NXP1=xx,NXP2=yy):
NXP1 = no. particle fractions with particle density PP(1,1).
NXP2 = no. particle fractions with particle density PP(2,1).
NXP  = NXP1+NXP2, total no. particle fractions.
I    = particle fraction counter (i.e. I=1,NXP). First (NXP1)th
       fractions have particle density PP(1,1).

(B) PARAMETER (NZB=zz,NZ=zz+1):
NZB  = no. of increments of total riser height for computations.
L    = height counter, ZB(L) = height of bottom of Lth increment
       (i.e. L=1,NZ where NZ=NZB+1).

(C) PARAMETER (NER1=e1,NERR=e):
NERR      = no. diagnostic messages.
NER1      = no. warning messages.
NER2      = no. error messages (NER2=NERR-NERR1).
IERROR(J) = Jth error flag, J=1,NERR
```

6;E. ERROR FLAGS AND DIAGNOSTIC MESSAGES

```
BLKE/IERROR(NERR),IERR1,IERR2

Convention:
 IERR1,IERR2 = 0  ;Successful run, no warnings or error messages
 IERR1       = 1  ;Warning messages generated, but successful run
                   completion
 IERR2       = 2  ;Error, unsuccessful run, run terminated

 IERROR(J)   = 0  ;Warning/error no. J not incurred
 IERROR(J)   = 1  ;Jth warning incurred, output Jth diagnostic,
                   continue execution (J = 1 <-> NER1)
 IERROR(J)   = 2  ;Jth error incurred, output Jth diagnostic,
                   halt execution (J = NER1+1 <-> NERR)
```

6;G. GAS FLOWS AND PROPERTIES

```
BLKG/AIR(20),TG,PG

VARIABLE  DESCRIPTION                                    DEFINING
                                                         FILE/ROUTINE
--------  ----------------------------------------       ------------
AIR(1)    Air flowrate, m**3/s @ 273K, 101.325 kPa       CBUSE3
AIR(2)-AIR(5) (not assigned)
AIR(6)    Air/gas density at operating temp., kg/m**3    AIRPRO
AIR(7)    Air/gas viscosity at operating temp., kg/m.s   AIRPRO
AIR(8)-AIR(20) (not assigned)

TG        Mean combustor gas temperature,Kelvin          CBUSE3
PG        Mean combustor gas pressure, kPa(input),       CBUSE3
          Pa(in program computations)

Note:
(i)  AIR(1) is entered as standard cubic metres  per sec. (ie.@ 273K,
     101325 Pa).This flowrate is converted to m**3/s @ (TG, PG) in
     routine DATIN3.1.
```

6;H. REACTOR/RISER

```
COMMON/BLKH/BED(10),IBED

Convention: Heights are given relative to the gas distributor, unless
otherwise stipulated.
```

VARIABLE	DESCRIPTION	DEFINING FILE/ROUTINE
BED(1)	Reactor/riser wall roughness, mm (input):	CBUSE3
	m (prog)	DATIN
BED(2)-BED(3) (not assigned)		
BED(4)	Riser reactor cross sectional area, m**2	CBUSE3
BED(5)-BED(7) (not assigned)		
BED(8)	Riser hydraulic diameter, m	DATIN
BED(9)	(not assigned)	
BED(10)	Riser csa shape factor(Pi=circular, 4=square)	DATIN
IBED	Riser csa flag; 0=square, 1=circular	CBUSE3

6;I. SOLIDS HYDRODYNAMICS

COMMON/BLKI/HYDG(20)

VARIABLE	DESCRIPTION	DEFINING FILE/ROUTINE
HYDG(1)	Net solids mass upflux, kg/m**2.s	CBUSE3
HYDG(2)	Initial cond. - mass frac. type 1 particles	CBUSE3
HYDG(3)	Wall region thickness, mm (input); m (prog)	CBUSE3,DATIN
HYDG(4)	Average wall streamer voidage	CBUSE3
HYDG(5)	Core cross-sectional area, m2	DATIN
HYDG(6)	Gas superficial velocity, m/s	DATIN
HYDG(7)	Wall streamer velocity, m/s	CBUSE3
HYDG(8)	Wall-core interfacial area per unit height, m	DATIN
HYDG(9)	Fractional wall coverage by streamers	CBUSE3
HYDG(10-20) (not assigned)		

6;J. PARTICLE SIZE DISTRIBUTION

COMMON/BLKJ/SIV(4,25),NSIV

VARIABLE	DESCRIPTION	DEFINING FILE/ROUTINE
SIV(I,J)	Jth sieve aperture, Ith particle type, mm	CBUSE3
NSIV	Number of sieve sizings	CBUSE3

6;K. PARTICLE FRACTION COLLISION CHARACTERISTICS

COMMON/BLKK/Z1T(NXP),Z2T(NXP),VWK(NXP)

VARIABLE	DESCRIPTION	DEFINING FILE/ROUTINE
Z1T(I)	Ith fraction type (i) collision freq., 1/s	DYNCOL
Z2T(I)	Ith fraction type (ii) collision freq., 1/s	DYNCOL
VWK(I)	Ith fraction velocity weighting factor based on collision period.	DYNCOL

6;O. PARTICLE FRACTION SIZES

COMMON/BLKO/XP(NXP),WP(NXP),IXP(NXP)

VARIABLE	DESCRIPTION	DEFINING FILE/ROUTINE

XP(I)	Particle size of Ith fraction	FEDSIZ
WP(I)	Particle mass fraction (%) - initial cond.	FEDSIZ
IXP(I)	Particle density identifier, IXP(I)=1 for particles of density PP(1,1) IXP(I)=2 for particles of density PP(2,1)	FEDSIZ

6;P. PARTICLE PHYSICAL PROPERTIES

COMMON/BLKP/PP(2,10)

CONVENTION:PP(IP,J); IP=Particle type (i.e. 1 or 2)
(e.g. type 1 particle = inert bed particle; type 2 particle = fuel particle)

VARIABLE	DESCRIPTION	DEFINING FILE/ROUTINE
PP(IP,1)	Particle density,kg/m**3	CBUSE3
PP(IP,2)	Particle sphericity	CBUSE3
PP(IP,3)	Coefficient of restitution (particle-particle)	CBUSE3
PP(IP,4)	Coefficient of sliding friction (particle-wall)	CBUSE3
PP(IP,5)	Coefficient of restitution (particle-wall)	CBUSE3
PP(IP,6)-PP(IP,10) (unassigned)		

6;T. PARTICLE FLUCTUATING KINETIC ENERGY

COMMON/BLKT/CCOR,VCOR,FPCOR,ICOR
CONVENTION: I = particle size fraction no.

VARIABLE	DESCRIPTION	DEFINING FILE/ROUTINE
CCOR(I)	(not assigned)	
VCOR(I)	(not assigned)	
FPCOR(I)	(not assigned)	
ICOR	Number (I) of mid-size particle fraction with minimum axial collision force	DYNCOL

6;Y. RISER HEIGHTS

COMMON/BLKY/ZS,ZF

VARIABLE	DESCRIPTION	DEFINING FILE/ROUTINE
ZS	Height of start of current intergration, m	CIRCOR
ZF	Height of end of current intergration, m	CIRCOR

6;SUBB.

COMMON/SUBB/FDZ,FDY,FLFT,TAUP,UZY

VARIABLE	DESCRIPTION	DEFINING FILE/ROUTINE
FDZ	Axial (vertical) drag on single particle, N	DRAGOP
FDY	Lateral drag on single particle, N	DRAGOP
FLFT	Lateral lift on single particle, N	WALIFT,DIFEQS WALSTF,DIFSTF
TAUP	Particle respone time, s	DIFEQS,DIFSTF
UZY	Gas velocity at distance Y from wall, m/s	PROFIL

```
6;SUBC.
-------
COMMON/SUBC/DPP,WTP,PSIP,RHOP,USTR,VISK,SX
```

VARIABLE	DESCRIPTION	DEFINING FILE/ROUTINE
DPP	Particle diameter, mm	CBWAL3
WTP	Particle mas, kg	WALIFT,WALSTF
PSIP	Particle sphericity	CBWAL3
RHOP	Particle density, kg/m3	CBWAL3
USTR	Gas friction velocity, m/s	WALIFT,WALSTF
VISK	Gas kinematic viscosity, m2/s	WALIFT,WALSTF
SX	Gas flow correction factor	CIRWAL,GASVEL

E.2 Input and Diagnostic Message Files

Sample user input file for CIRCOR and WALSTF (logical unit 11):

```
***************CBUSE3*************************************************
CIRCULATING FLUIDISED BED LEVEL 3 DYNAMIC MODELLING:   USER INPUT FILE
REVISION 4     OCT.     29  1991                     REFERENCE VERSION
RISER    :
TEST     :
CONDITION:

BED GEOMETRY                     |IBED,BED(1),BED(4)
12345678901234567890123456789 0  |
     0                           |RISER CSA FLAG,0=SQUARE,1=CIRCLE
   0.5                           |RISER WALL ROUGHNESS, MM
   0.0232                        |RISER CROSS SECTIONAL AREA,M**2

GAS FLOWS AND PROPERTIES         |AIR(1),TG,PG
12345678901234567890123456789 0  |
   0.0253                        |AIR FLOWRATE, M**3/S @273K, 101KPA
1143.0                           |MEAN BED GAS TEMPERATURE,K
 101.325                         |MEAN BED GAS PRESSURE,KPA.

SOLIDS HYDRODYNAMICS             |HYDG(1-4),HYDG(7),HYDG(9)
12345678901234567890123456789 0  |
  35.0                           |NET SOLIDS MASS UPFLUX, KG/M*M.S
   0.98                          |I.C.: MASS FRACTION TYPE 1 PARTICLES
   5.0                           |WALL REGION THICKNESS, MM
   0.45                          |STREAMER VOIDAGE
  -1.1                           |WALL STREAMER VELOCITY, M/S
   0.3                           |FRACTION WALL COVERAGE BY STREAMERS

PARTICLE SIEVE SIZING ,WT%       |NSIV,SIV(1-3,NSIV-1)
18                               |NO. SIEVE SIZINGS
12345678901234567890123456789 0  |
  MM       TYPE1  TYPE2          |TYLER MESH    U.S. ALTERNATE
 7.925     0.0    0.00           |+2.5          +5/16 INCH
 5.613     0.0    0.44           |+3.5          +3.5
 3.962     0.59   3.50           |+5            +5
 2.794     0.97   9.25           |+7            +7
 1.981     0.85  10.92           |+9            +10
 1.397     1.17  13.18           |+12           +14
 0.991     1.05  12.11           |+16           +18
 0.701     0.98  11.09           |+24           +25
 0.495     0.94   8.73           |+32           +35
 0.351     8.72   7.75           |+42           +45
 0.246    37.09   5.48           |+60           +60
 0.175    33.59   4.75           |+80           +80
 0.124    11.01   3.74           |+115          +120
 0.088     2.52   3.41           |+170          +170
 0.053     0.42   3.99           |+270          +270
 0.045     0.05   1.29           |+325          +325
```

```
 0.038    0.05   0.00          |+400          +400
 0.000    0.0    0.0           |-400          -400

PARTICLE PHYSICAL PROPERTIES AND COMPOSITION
12345678901234567890123456789 0 |
TYPE 1 PARTICLES                |PP(1,1-5)
2700.0                          |PARTICLE DENSITY,KG/M**3
   0.95                         |SPHERICITY
   0.90                         |COEFFICIENT OF RESTITUTION (1-1)
   0.80                         |COEFFICIENT SLIDING FRICTION (1-WALL)
   0.70                         |COEFFICIENT OF RESTITUTION (1-WALL)
TYPE 2 PARTICLES                |PP(2,1-5)
1400.0                          |PARTICLE DENSITY,KG/M**3
   0.75                         |SPHERICITY
   0.70                         |COEFFICIENT OF RESTITUTION (2-2)
   0.80                         |COEFFICIENT SLIDING FRICTION (2-WALL)
   0.70                         |COEFFICIENT OF RESTITUTION (2-WALL)
```

Sample user input file for WALSTF (logical unit 12):

```
***************CBWAL3*****************************************************
INPUT FILE FOR STUDY OF THE BEHAVIOUR OF A DISCRETE PARTICLE NEAR A
VERTICAL WALL IN GAS FLOW
REVISION 0     NOV.   22 1991
 DP (MM)     | VYI (M/S)  | YWI (MM)    |
    0.040    |   -0.2     |  1.4        |

DP = PARTICLE DIAMETER
VYI= INITIAL LATERAL VELOCITY TOWARDS WALL
YWI= INITIAL DISTANCE FROM THE WALL
```

Diagnostic message file (direct access) for CIRCOR and WALSTF (logical unit 14):

```
**************CBERR3*****************************************************|
REVISION 0  MARCH 18 1991    REVISION 2  OCT   08 1991                  |
Contains warning and error messages for circulating fluidised bed        |
combustor program model at level no. 3  (CIRBED3.FOR) for all            |
versions.                                                                |
Routine ERCHEK controls error message output according to flags          |
IERROR(J) generated during program execution.                            |
*************************************************************************|
#1 WARNING IN ROUTINE       :                                            |
                                                                         |
                                                                         |
#2  WARNING IN ROUTINE PARTUR (V3.1) (CALLED FROM SYSTEQ V3.1):          |
GAS AND PARTICLE DRIFT VELOCITIES FAILED TO CONVERGE WITHIN THE          |
LIMITED NUMBER OF ITERATIONS. RESULTS MAY NOT BE REASONABLE.             |
#3 WARNING IN ROUTINE                                                    |
                                                                         |
                                                                         |
#1  ERROR IN ROUTINE FEDSIZ (V 3.1):                                     |
INPUT ERROR -- SIEVE MASSES DO NOT SUM TO 100%.  CHECK USER INPUT FILE|
                                                                         |
#2  ERROR IN ROUTINE PARTUR (V3.1) (CALLED FROM SYSTEQ V3.1):            |
GAS AND PARTICLE DRIFT VELOCITIES REPEATEDLY FAILED TO CONVERGE          |
WITHIN THE LIMITED NUMBER OF ITERATIONS.                                 |
#3  ERROR IN ROUTINE                                                     |
                                                                         |
                                                                         |
#4  ERROR IN ROUTINE DGAUSS:                                             |
GAUSS ELIMINATION FAILURE - ABNORMAL RETURN BECAUSE OF ZERO ENTRY ON     |
DIAGONAL                                                                 |
```

E.3 CIRCOR Program Listing

```
C*********CIRCOR3.1********CFB LEVEL 3 MODEL: MAIN PROGRAM************
      PROGRAM CIRCOR
```

```
C     CFB RISER CORE PARTICLE COLLISION AND TURBULENT DIFFUSION MODEL
C     REV 0 NOV   01 1991                AUTHOR:      RICHARD C. SENIOR
C     REV 1 NOV   06 1991.               UNIVERSITY OF BRITISH COLUMBIA
C     REV 5 JAN  19 1992.
C     REV 6 FEB  04 1992 (documentation only)
C
C     Routines required:
C     (i)   routines general to level 3 modelling;
C     AIRPRO3.1, DATIN3.1, DRAGON3.1, ERCHEK3.1, ERINIT3.1, FEDSIZ3.1,
C     GASTUR3.1, SAUTER3.1 (optional)
C
C     (ii)  routines specific to CIRCOR;
C     DYNCOL3.1, FLUCEN3.1, ICONDS3.1, PARTUR3.2, SYSTEQ3.2, WALCON3.1
C
C     (iii) general numerical routines
C     FHLBRG, ODERKF (ODE solvers)
C
C     Riser core collision model consisting of a system of o.d.e.s
C     that are assembled in routine SYSTEQ. NXP = number of particle
C     size fractions. There are (3*NXP+2) d.e.'s in the system:
C
C     F(1) =  gas mass balance;
C     F(2) =  gas momentum balance;
C     F(2+1) to F(2+NXP) = particle fraction mass balances;
C     F(2+NXP+1) to F(2+NXP+NXP) = part. fraction momentum balances;
C     F(2+2*NXP+1) to F(2+2*NXP+NXP) = particle fraction fluctuating
C     kinetic energy balances.
C
C     Independent variable:
C     Z = height, m
C
C     Dependent variables:
C     Y(1) = EG*UZC = (core voidage * core interstitial gas vel.)
C     Y(2) = PR     = (gas pressure)
C     Y(3),... = EP(I)*VZC(I) = (fraction vol.* fraction velocity)
C     Y(3+NXP), ... = VZC(I) = (particle fraction velocity)
C     Y(3+2*NXP), ... = FKE(I) = (particle fraction fluctuating
C     kinetic energy)
C
C     Model Level 3 Assumptions:
C     This model is designed to specifically investigate the
C     properties of a dilute suspension flowing within the core of a
C     CFB riser. Some aspects of riser wall dynamics are not
C     considered in detail, and constraints and assumptions are
C     included to handle specific cases of wall solids
C     distribution/motion.
C*********************************************************************
      IMPLICIT DOUBLE PRECISION(A-H,O-Z)
      PARAMETER (NXP1=9,NXP2=0,NXP=NXP1+NXP2)
      PARAMETER (NZB=20,NZ=NZB+1)
      PARAMETER (NER1=10,NERR=15)
      PARAMETER (IEV=2,IV=NXP+2,IK=2*NXP+2)
      COMMON/BLKE/IERROR(NERR),IERR1,IERR2
      COMMON/BLKG/AIR(20),TG,PG
      COMMON/BLKH/BED(10),IBED
      COMMON/BLKI/HYDG(10)
      COMMON/BLKO/XP(NXP),WP(NXP),IXP(NXP)
      COMMON/BLKP/PP(2,10)
      COMMON/BLKY/ZS,ZF
      DIMENSION FKE(NXP),VZC(NXP),EP(NXP)
      DIMENSION F(3*NXP+2),YA(3*NXP+2),LGT(3*NXP+2),LLT(3*NXP+2)
      DIMENSION YNEW(3*NXP+2),YB(3*NXP+2),YOLD(3*NXP+2)
      DIMENSION VTP(2)
      INTEGER FLAG
      EXTERNAL SYSTEQ
      DATA EPS/5.D-3/
      CALL ERINIT
      CALL DATIN
      CALL AIRPRO(0)
      CALL FEDSIZ
```

```
C-----------------------------------------------------------------
C     Optional input   (must be consistent with no. fractions, NXP)
C     Re-assign particle sizes, overwrite sizes and/or mass fractions
C-----------------------------------------------------------------
C     Option A: 3 type 2 particles: NXP2=3, wt. split of 0.25:0.5:0.25
C      XP(NXP-2)=40.D-3
C      XP(NXP-1)=250.D-3
C      XP(NXP)=2.D0
C      SUM=0.D0
C      DO 4 I=NXP-2,NXP
C      SUM=SUM+WP(I)
C      CONTINUE
C      WP(NXP-2)=SUM*.25D0
C      WP(NXP-1)=SUM*.5D0
C      WP(NXP)=SUM*.25D0
C-----------------------------------------------------------------
C     Option B: Nakamura and Capes Set-up - Binary particle expts.
C      XP(1)=535.D-3
C      XP(1)=1.08D0
C      XP(2)=2.34D0
C      XP(2)=2.90D0
C      WP(1)=.491D2
C      WP(1)=.321D2
C      WP(2)=1.D2-WP(1)
C      CALL TERVEL(VTP)
C      WRITE(6,42)VTP(1),VTP(2)
C42    FORMAT(1X,'PARTICLE TERMINAL VELOCITIES:  ',2F8.3,'  M/S')
C-----------------------------------------------------------------
C
C     Initial conditions routine ICONDS
C
       CALL ICONDS(VZC,FKE,EP,UZC,EG,PRS)
       ZS=0.D0
       YA(1)=EG*UZC
       YA(2)=PRS
       DO 80 I=1,NXP
       YA(I+IEV)=EP(I)*VZC(I)
       YA(I+IV)=VZC(I)
       YA(I+IK)=FKE(I)
 80    CONTINUE
C
C    Final conditions, step-size and desired accuracy
C
C      DZ=.02D0
       DZ=.2D0
C      HSTART=DZ/100.D0
       HSTART=DZ/10.D0
       HMIN=DZ/1.D4
       HMAX=DZ/10.D0
CI     HMAX=DZ
       M=2+3*NXP
       NGT=0
       NLT=0
       LB=1
C
       DO 300 J=1,NZ
       ZF=ZS+DZ
       CALL ODERKF(SYSTEQ,ZS,ZF,YA,F,EPS,HSTART,HMIN,HMAX,YB,
     1 NFUN,FLAG,M,NGT,NLT,LGT,LLT,LB,YNEW,YOLD)
C
       ZS=ZF
       YA(1)=YB(1)
       YA(2)=YB(2)
       DO 180 I=1,NXP
       YA(I+IEV)=YB(I+IEV)
       YA(I+IV)=YB(I+IV)
       YA(I+IK)=YB(I+IK)
 180   CONTINUE
 300   CONTINUE
       IF(IERR1.EQ.1.OR.IERR2.EQ.2) THEN
         CALL ERCHEK
```

```
      ENDIF
      STOP
      END
```

E.4 WALSTF Program Listing

```
C*************WALSTF3.1 ************* PROGRAM ************************
      PROGRAM WALSTF
C     REV 0 NOV   26 1991                    AUTHOR: RICHARD C. SENIOR
C     REV 1 NOV   29 1991  REV 2 DEC  31  1991
C     Routines required:
C     General level 3 model routines: AIRPRO3.1, DATIN3.1, ERINIT3.1,
c     ERCHEK3.1, GASTUR3.1, PROFIL3.1, TERVEL3.1
C     Routines specific to WALSTF/WALIFT: DIFSTF3.1, DRAGOP3.1
C     Numerical routines:  LSODE (and associated routines)
C
C     Calculates the trajectory of a discrete particle crossing a
C     vertical gas boundary layer in riser flow.
C     Assume:
C      1. Initial particle displacement YWI = input
C      2. Initial particle slip velocity is terminal velocity
C      3. Gas velocities at all distances from the wall given by 'Law
C         of the Wall' relations.
C
C     WALSTF also serves as test program for:
C     1. Routine PROFIL3.1 gas velocity profile
C     2. Routine DIFSTF3.1 gives velocity derivatives as a function of
C        position
C
C     WALSTF:  D.E.'s solved by Gears method for stiff systems
C     (WALIFT:  D.E.'s solved by Runge Kutta-Fehlberg method)
C*********************************************************************
      IMPLICIT DOUBLE PRECISION(A-H,O-Z)
      INTEGER FLAG
      PARAMETER (NXP1=1,NXP2=0,NXP=NXP1+NXP2)
      PARAMETER (NER1=10,NERR=15)
      PARAMETER (MF=22,IOPT=0,ITOL=1,ITASK=1)
      PARAMETER (NEQ=4,LRW=NEQ*(123+NEQ)+2,LIW=20+NEQ)
      COMMON/SUBC/DPP,WTP,PSIP,RHOP,USTR,VISK,SX
      COMMON/SUBB/FDZ,FDY,FLFT,TAUP,UZY
      COMMON/BLKE/IERROR(NERR),IERR1,IERR2
      COMMON/BLKG/AIR(20),TG,PG
      COMMON/BLKH/BED(10),IBED
      COMMON/BLKI/HYDG(10)
      COMMON/BLKO/XP(NXP),WP(NXP),IXP(NXP)
      COMMON/BLKP/PP(2,10)
      DIMENSION YA(NEQ),F(NEQ),YNEW(NEQ),YOLD(NEQ)
      DIMENSION YMAX(4),YMIN(4),VT(NXP)
      DIMENSION T(189),Z(189),Y(189),VZ(189),VY(189)
      DIMENSION FLW(189),FDZW(189),FDYW(189),TAUW(189),UZW(189)
      DIMENSION IWORK(LIW),RWORK(LRW)
      EXTERNAL DIFSTF
      DATA GA/-9.81D0/,EPS/1.D-2/,SX/1.D0/,EG/1.D0/
      PI=4.D0*DATAN(1.D0)
      CALL ERINIT
      CALL DATIN
      CALL AIRPRO(0)
      RHOP=PP(1,1)
      PSIP=PP(1,2)
      READ(12,10)DPP,VYI,YWI
 10   FORMAT(/////F12.6,1X,F12.6,1X,F12.6)
      YWI=YWI/1.D3
      XP(1)=DPP
      WTP=RHOP*PI*DPP**3/6.D9
      VISK=AIR(7)/AIR(6)
      U0=HYDG(6)
      RUFF=BED(1)
      CALL GASTUR(U0,RUFF,UPF,TAUGF,SFG)
      USTR=DSQRT(SFG/AIR(6))
```

```
C
C     Initial particle vertical velocity
C
      XP(1)=230.D-3
      CALL TERVEL(VT)
      XP(1)=DPP
      ZWI=0.D0
      CALL PROFIL(YWI,UZI,DUZ)
      VZI=UZI-VT(1)
      C1=(6.46D-6*DPP**2/4.D0)*DSQRT(AIR(6)*AIR(7))
      FLFT=C1*DSQRT(DUZ)*VT(1)
C
C     Report Writer
C
      WRITE(6,710)
 710  FORMAT('DISCRETE PARTICLE BEHAVIOUR IN A VERTICAL GAS',1X,
     1 'BOUNDARY LAYER'/'MODEL SIMULATION (LEVEL 3)',
     2 20X,'RICHARD C. SENIOR'//)
      WRITE(6,720)DPP,WTP,RHOP,PSIP,TG,VISK,BED(8),U0,PP(1,5),PP(1,4)
 720  FORMAT('PARTICLE DIAMETER (MM)                ',F10.5/
     1 'PARTICLE MASS (KG)                  ',E13.5/
     2 'PARTICLE DENSITY (KG/M3)            ',F10.5/
     3 'PARTICLE SPHERICITY                 ',F10.5/
     4 'GAS TEMPERATURE (K)                 ',F10.5/
     5 'GAS VISCOSITY (KG/MS)               ',E13.5/
     6 'RISER DIAMETER (M)                  ',F10.5/
     7 'SUPERFICIAL GAS VELOCITY (M/S)      ',F10.5/
     8 'PARTICLE-WALL COEFF. OF RESTITUTION ',F10.5/
     9 'WALL COEFF. SLIDING FRICTION        ',F10.5//)
C
C     Initialize for integration
C
      YLOW=DPP/2.D3
      DY=(YWI-YLOW)/10.D0
      TMAX=-DY/VYI
      DT=TMAX*5.D-2
      TA=0.D0
      TB=TA+DT
      YA(1)=VZI
      YA(2)=ZWI
      YA(3)=VYI
      YA(4)=YWI
      DO 30 I=1,4
      YOLD(I)=YA(I)
 30   CONTINUE
      YMIN(4)=YWI-DY
      YMAX(4)=YWI
      UR=0.D0
      VOID=1.D0
      CALL DRAGOP(DPP,PSIP,UZI,UR,VZI,VYI,VOID,REP,FDZ,FDY,CD)
      TAUW(1)=4.D-6*DPP**2*RHOP/(3.D0*AIR(7)*REP*CD)
      T(1)=TA
      Z(1)=ZWI
      VZ(1)=VZI
      Y(1)=YWI
      VY(1)=VYI
      FLW(1)=FLFT/WTP
      FDZW(1)=FDZ/WTP
      FDYW(1)=FDY/WTP
      UZW(1)=UZI
C
      ISTATE=1
      RTOL=1.D-4
      ATOL=1.D-8
      IB=1
 70   CALL LSODE (DIFSTF,NEQ,YA,TA,TB,ITOL,RTOL,ATOL,ITASK,
     1 ISTATE,IOPT,RWORK,LRW,IWORK,LIW,JAC,MF)
C
C     Particle hits wall?
C
      IF(YA(4).LT.YLOW) THEN
        YTEST=DABS(1.D0-YA(4)/YLOW)
```

```
          IF(YTEST.LT.5.D-2) GOTO 140
          ISTATE=1
          DO 80 J=1,4
          YA(J)=YOLD(J)
 80       CONTINUE
          TA=TAOLD
          TB=TA+.95D0*(TB-TA)
          GO TO 70
        ENDIF
 130    IF(YA(4).GT.YMIN(4).AND.YA(4).LT.YMAX(4)) GO TO 320
 140    IB=IB+1
        T(IB)=TB
        VZ(IB)=YA(1)
        Z(IB)=YA(2)
        VY(IB)=YA(3)
        Y(IB)=YA(4)
        FLW(IB)=FLFT/WTP
        FDZW(IB)=FDZ/WTP
        FDYW(IB)=FDY/WTP
        TAUW(IB)=TAUP
        UZW(IB)=UZY
C
C     Assign next starting values
C
C       TB=TA+DT
        YMAX(4)=YA(4)+DY
        IF(YMAX(4).GT.YWI) YMAX(4)=YWI
        YMIN(4)=YA(4)-DY
C
C     Particle rebounds from wall?
C
        IF(YA(4).GT.YLOW) GOTO 320
 90     YA(4)=YLOW
        YIN=YA(1)
        DVW=PP(1,4)*DABS((1.D0+PP(1,5))*YA(3))
        IF(YA(1).GE.0.D0) THEN
          YA(1)=YA(1)-DVW
        ELSE
         YA(1)=YA(1)+DVW
        ENDIF
        YCOM=YIN*YA(1)
        IF(YCOM.LE.0.D0) YA(1)=0.D0
        YA(3)=-PP(1,5)*YA(3)
        YMIN(4)=YA(4)
        ISTATE=1
        IB=IB+1
        YH=YA(4)
        VZH=YA(1)
        VYH=YA(3)
        CALL PROFIL(YH,UZY,DUZ)
        FLFT=C1*DSQRT(DUZ)*(UZY-VZH)
        CALL DRAGOP(DPP,PSIP,UZY,UR,VZH,VYH,VOID,REP,FDZ,FDY,CD)
        TAUW(IB)=4.D-6*DPP**2*RHOP/(3.D0*AIR(7)*REP*CD)
        T(IB)=TA
        VZ(IB)=YA(1)
        Z(IB)=YA(2)
        VY(IB)=YA(3)
        Y(IB)=YA(4)
        FLW(IB)=FLFT/WTP
        FDZW(IB)=FDZ/WTP
        FDYW(IB)=FDY/WTP
        TAUW(IB)=TAUP
        UZW(IB)=UZY
C
C     Test for return of particle out of b.l. or excessive time
C
 320    IF(YA(4).GE.YWI) GO TO 500
        IF(TB.GT.1.0D0) GO TO 500
        DO 110 J=1,4
        YOLD(J)=YA(J)
 110    CONTINUE
        TAOLD=TA
```

```
      TB=TA+DT
      GO TO 70
 500  IFIN=IB
C
C     Report writer
C
      WRITE(6,600)
 600  FORMAT(2X,'I',3X,'T (S)',5X,'Z (M)',5X,'Y (M)',5X,'VZ (M/S)',
     1 2X,'VY (M/S)',2X,'UZW (M/S)')
      DO 520 IB=1,IFIN
      WRITE(6,610) IB,T(IB),Z(IB),Y(IB),VZ(IB),VY(IB),UZW(IB)
 610  FORMAT(1X,I3,F9.5,5F10.5)
 520  CONTINUE
      WRITE(6,620)
 620  FORMAT(//2X,'I',3X,'T',9X,'LIFT/WP',3X,'FDZ/WP',4X,'FDY/WP',4X,
     1 'GA',8X,'TAUP'/7X,'(S)',7X,'(M2/S)',4X,'(M2/S)',4X,'(M2/S)',
     2 2X,'(M2/S)',4X,'(S)')
      DO 540 IB=1,IFIN
      WRITE(6,630) IB,T(IB),FLW(IB),FDZW(IB),FDYW(IB),GA,TAUW(IB)
 630  FORMAT(1X,I3,F9.5,5F10.5)
 540  CONTINUE
C
      IF(IERR1.EQ.1.OR.IERR2.EQ.2) THEN
        CALL ERCHEK
      ENDIF
      STOP
      END
```

E.5 CIRCOR and WALSTF Subroutine Listings

```
C*file:***CIRBED3.FOR*************************************************
C     REVISION 0   OCT. 01 1991,        AUTHOR:      RICHARD C. SENIOR
C     REV 3  NOV. 10 1991               UNIVERSITY OF BRITISH COLUMBIA
C     REV 4  DEC. 31 1991  REV 5  JAN. 03 1992
C
C     This file contains current routines required for
C     circulating fluidised bed modelling at level 3. Level 3
C     modelling entails mass and momentum balance hydrodynamic
C     modelling. Comprehensive descriptions of the program and routine
C     functions are given within the code. Alternative and outdated
C     routines are contained in CIRBED3.OLD.
C
C     Note that some of the routines have separate testing/development
C     programs. These are flagged below. The test driver programs are
C     contained in FORTRAN file CIRBED.PRG
C
C     Routine Current Author Test     Sect. Program/s
C             Version        Program
C     AIRPRO    1      RCS   DPDRAG   A     CIRCOR3, WALIFT3, WALSTF3
C     DATIN     1      RCS   DPDATI   A     CIRCOR3, WALIFT3, WALSTF3
C     DIFEQS    1      RCS   --       C     WALIFT3
C     DIFSTF    1      RCS   --       C     WALSTF3
C     DRAGON    1      RCS   DPDRAG   A     CIRCOR3
C     DRAGOP    1      RCS   --       C     WALIFT3, WALSTF3
C     DYNCOL    1      RCS   DPSYST   B     CIRCOR3
C     ERCHEK    1      RCS   --       A     CIRCOR3, WALIFT3, WALSTF3
C     ERINIT    1      RCS   --       A     CIRCOR3, WALIFT3, WALSTF3
C     FEDSIZ    1      RCS   DPFEDS   A     CIRCOR3
C     FLUCEN    1      RCS   DPSYST   B     CIRCOR3
C     GASTUR    1      RCS   DPSYST   A     CIRCOR3, WALIFT3, WALSTF3
C     ICONDS    1      RCS   DPSYST   B     CIRCOR3
C     PARTUR    2      RCS   DPSYST   B     CIRCOR3
C     PROFIL    1      RCS   --       A     WALIFT3, WALSTF3
C     SAUTER    1      RCS   --       A     CIRCOR3
C     SYSTEQ    1      RCS   --       A     CIRCOR3
C     TERVEL    1      RCS   DPDRAG   A     CIRCOR3, WALIFT3, WALSTF3
C     WALCON    1      RCS   DPSYST   B     CIRCOR3
C
C     This file is divided into three sections:
```

```
C     SECTION A;
C     General routines that may be common to more than one level 3
C     model
C     SECTION B;
C     Routines specific to program CIRCOR (core dynamics modelling)
C     SECTION C;
C     Routines specific to programs WALIFT, WALSTF and CIRWAL (wall
C     dynamics modelling) (CIRWAL under development documentation
C     incomplete)
C
C     Note: To run the the model and test programs, numerical routines
C     DGAUSS, LENSTR, ODERKF and FHLBRG are required.
C     FORTRAN versions in ZUB.FOR; Executable in ZUB.EXE
C     LSODE - Widely available stiff ODE solver also used.
C
C     Logical unit assignments:
C     Unit    File                Ref. Version      File Type
C     ----    ----                ------------      ---------
C     11   {user input}           CBUSE3            Sequential
C     12   {user input}           CBWAL3            Sequential
C     14   {diagnostic messages} CBERR3            Direct Access
C     UNIX or DOS  : All data files in sub-directory CIIRBED3/INPUT/
C     Mainframe MTS: All data files in composite file CIRBED3.DAT
C
C     All routines double precision FORTRAN code
C     For more documentation see file CIRBED3.DOC
C
C#################################################################
C  SECTION A: GENERAL LEVEL 3 MODELLING SUBROUTINES
C#################################################################
C*****************AIRPRO3.1*********************************************
      SUBROUTINE AIRPRO(IFLG)
C     REV 0 MARCH 18 1991  COMPATIBLE WITH MODEL LEVEL 3 VERSIONS
C     REV 1 OCT.  03 1991
C     INPUT:  TG      Isothermal gas/bed particle temperature,K
C             PG      Mean combustor gas pressure ,Pa(abs.)
C     OUTPUT: AIR(6)  Air density at temp. TG ,kg/m**3
C             AIR(7)  Air viscosity at temp. TG ,kg/m.s
C             AIR(8)  Thermal conductivity of air at TG ,W/m.K
C             AIR(9)  Air viscosity at temp. (TG+298K)/2 ,kg/m.s
C             AIR(10) Air heat capacity at TG ,J/kg.K
C     If IFLG=0, only AIR(6) and AIR(7) are calculated
C     (copy of CANMET/PRETO fits to thermophysical data)
C*****************************************************************
      IMPLICIT DOUBLE PRECISION(A-H,O-Z)
      COMMON/BLKG/AIR(20),TG,PG
      DIMENSION CP(3,4)
      DATA CP/6.1261D0,7.0155D0,7.7246D0,.31446D0,-.10279D0,
     1 .015807D0,-.0093772D0,.029194D0,.029945D0,-.37879D-5,
     2 -.11061D-2,-.10291D-2/
      AIR(6)=1.29425D0*273.3D0*PG/(TG*101325.D0)
      AIR(7)=6.31D-6+(TG*4.18D-8)-((TG**2)*6.70D-12)
      IF(IFLG.EQ.0) RETURN
      AIR(8)=.001D0*(19.178D0+.047567D0*TG)
      TAV=(TG+298.D0)/2.D0
      AIR(9)=6.31D-6+(TAV*4.18D-8)-((TAV**2)*6.70D-12)
      AIR(10)=0.D0
      TV=TG/1.D2
      DO 20 J=1,3
      CPAIR=CP(J,1)
      DO 10 I=1,3
      CPAIR=CPAIR+CP(J,I+1)*(TV**I)
 10   CONTINUE
      AIR(10)=AIR(10)+CPAIR*AIR(J+2)/100.D0
 20   CONTINUE
      AIR(10)=4.184D5*AIR(10)/(AIR(3)*32.D0+AIR(4)*28.D0+AIR(5)
     1 *18.D0)
      RETURN
      END
C*************DATIN3.1***********************************************
```

```
      SUBROUTINE DATIN
C     REV 7  NOV. 01 91
C     (REV 0 = copy of DATIN2.1, REV 43  JAN. 10 90)
C     Inputs user data, converts to program variables
C     Reference input data file - see CBUSE3
C*********************************************************************
      IMPLICIT DOUBLE PRECISION(A-H,O-Z)
      PARAMETER (NXP1=9,NXP2=0,NXP=NXP1+NXP2)
      PARAMETER (NZB=20,NZ=NZB+1)
      PARAMETER (NER1=10,NERR=15)
      COMMON/BLKE/IERROR(NERR),IERR1,IERR2
      COMMON/BLKG/AIR(20),TG,PG
      COMMON/BLKH/BED(10),IBED
      COMMON/BLKI/HYDG(20)
      COMMON/BLKJ/SIV(4,25),NSIV
      COMMON/BLKO/XP(NXP),WP(NXP),IXP(NXP)
      COMMON/BLKP/PP(2,10)
      PI=4.D0*DATAN(1.D0)
C     Insert following for UNIX systems (lower/uppercase important for
C     filename)
CI    OPEN(UNIT=11,FILE='{infile}',STATUS='OLD')
CI    OPEN(UNIT=14,FILE='{errfile}',STATUS='OLD')
CI    OPEN(UNIT=6,FILE='{outfile}',STATUS='OLD')
CI    OPEN(UNIT=6,FILE='{outfile}',STATUS='NEW')
C
C     Bed geometry
C
      READ(11,10) IBED
 10   FORMAT(/////////I6)
      READ(11,20) BED(1),BED(4)
 20   FORMAT(F12.7/F12.7)
      BED(1)=BED(1)/1.D3
C
C     Gas flows and properties
C
      READ(11,100) AIR(1),TG,PG
 100  FORMAT(///F12.7,2(/F12.7))
      AIR(1)=AIR(1)*TG/273.D0*101.325D0/PG
      PG=PG*1.D3
C
C     Solids hydrodynamics - Level 3 model assumes constant core and
C     total riser cross-sections. (Wall streamer thickness HYDG(3)
C     should be set to zero for wall dynamic model CIRWAL3).
C
      READ(11,150)(HYDG(I),I=1,4),HYDG(7),HYDG(9)
 150  FORMAT(//6(/F12.7))
      HYDG(3)=HYDG(3)/1.D3
      IF(IBED.EQ.1) THEN
        BED(10)=PI
      ELSE
        BED(10)=4.D0
      ENDIF
      BED(8)=2.D0*DSQRT(BED(4)/BED(10))
      DH=BED(8)-2.D0*HYDG(3)
      HYDG(5)=BED(10)*DH**2/4.D0
      HYDG(6)=AIR(1)/BED(4)
      HYDG(8)=BED(10)*DH
C
C     Particle sieve sizing
C
      READ(11,160) NSIV
 160  FORMAT(//I2//)
      DO 180 I=NSIV,1,-1
      READ(11,170)(SIV(J,I),J=1,3)
 170  FORMAT(F8.5,3F7.3)
 180  CONTINUE
C
C     Particle physical properties
C
      READ(11,190)(PP(1,I),I=1,5)
 190  FORMAT(///5(/F8.3))
```

```
      READ(11,200)(PP(2,I),I=1,5)
 200  FORMAT(5(/F8.3))
C
      RETURN
      END
C**************DRAGON3.1*********************************************
      SUBROUTINE DRAGON(VZC,CT,EP,FDZ,FDT,TAUP,UZC,UPL,EG)
C     REV 0, OCT    03   1991                AUTHOR: RICHARD C. SENIOR
C     Calculates the axial and transverse components of drag force for
C     spherical or non-spherical particles in a gas stream assuming
C     steady drag. Assumes radial velocities UZC AND VZC(I) are
C     in the same angular direction.
C
C     Available drag relationships:
C     (i)  spherical particle: "Bubbles, drops and particles", Clift,
C     Grace, Weber,  p.111-112.
C     (ii) spherical particle: Haider and Levenspiel, Powder Tech.,
C     58, 63-70 (1989) (eq.6).
C     (iii) non-spherical particle: Haider and Levenspiel, Powder
C     Tech., 58, 63-70 (1989) (eq.12).
C     Drag voidage dependency: Gibilaro, DiFelice, Weldram, Foscolo;
C     Chem. Eng. Sci. 40, pp1817, (1985).
C
C     Note: The Haider and Levenspiel correlation for non-spherical
C     particles uses the 'volume particle diameter' dv, rather than
C     the 'surface/volume' dsv. If the particle diameter DP in the
C     calling routine is defined as 'dsv', and the particle is not
C     spherical, then the conversion is: 'dv' = 'dsv'/ psi, where psi
C     is the particle sphericity. This conversion should be made
C     before calling this routine. Projected particle area for
C     non-spherical particles is calculated based on the volume
C     diameter.
C
C     Input:    XP(I)    Particle dia. ,mm
C               UZC      Gas interstitial axial velocity ,m/s
C               UPL      Gas interstitial transverse velocity,m/s
C               VZC(I)   Particle axial velocity ,m/s
C               CT(I)    Particle transverse velocity,m/s
C               EP(I)    Particle vol. fraction in suspension, m3/m3
C               EG       Gas vol. fraction (voidage), m3/m3
C               AIR(6)   Gas density kg/m**3 (common block)
C               AIR(7)   Gas viscosity kg/m.s(common block)
C               PSIP     Particle sphericity (=PP(IP,2))
C               RHOP     particle density, k/m3 (=PP(IP,1))
C     Variables REP      Particle Reynolds number (based on DP)
C               CD       Drag coefficient
C     Output    FDZ(I)   Axial component of drag force, kg/m2s2
C               FDT(I)   Transverse component of drag force, kg/m2s2
C               TAUP(I)  Particle characteristic response time, s
C*******************************************************************
      IMPLICIT DOUBLE PRECISION(A-H,O-Z)
      PARAMETER (NXP1=9,NXP2=0,NXP=NXP1+NXP2)
      COMMON/BLKG/AIR(20),TG,PG
      COMMON/BLKO/XP(NXP),WP(NXP),IXP(NXP)
      COMMON/BLKP/PP(2,10)
      DIMENSION VZC(NXP),CT(NXP),EP(NXP),TAUP(NXP)
      DIMENSION FDZ(NXP),FDT(NXP)
      GDWF=1.D0/EG**1.8D0
      DO 300 I=1,NXP
      RHOP=PP(IXP(I),1)
      PSIP=PP(IXP(I),2)
C
C     Particle Reynolds number
C
      DUV=DSQRT((UZC-VZC(I))**2+(UPL-CT(I))**2)
      REP=DUV*AIR(6)*XP(I)*1.D-3/AIR(7)
C
C     Drag coefficient - spherical particle
C
```

```
      IF(PSIP.LT.0.95D0) GO TO 100
C     Clift and Gauvin correlation
      CD=24.D0/REP*(1.D0+.15D0*REP**.687D0)+.42D0/(1.D0+4.25D4/
     1 REP**1.16D0)
C     Haider and Levenspiel
C      CD=24.D0/REP*(1.D0+.1806D0*REP**.6459D0)+.4251D0/(1.D0+
C    1 6880.95D0/REP)
      GO TO 200
C
C     Non-spherical particle
C     Haider and Levenspiel (eq.12)
C100  CD=24.D0/REP*(1.D0+8.1716D0*DEXP(-4.0655D0*PSIP)*
C    1 REP**(0.0964D0+0.5565D0*PSIP))+73.69D0*REP*
C    2 DEXP(-5.0748D0*PSIP)/(REP+5.378D0*DEXP(6.2122D0*PSIP))
C     Haider and Levenspiel (eq.11)
 100  C1=DEXP(2.3288D0-6.4581D0*PSIP+2.4486D0*PSIP*PSIP)
      C2=0.0964D0+.5565D0*PSIP
      C3=DEXP(4.905D0-13.8944D0*PSIP+18.4222D0*PSIP**2-10.2599D0*
     1 PSIP**3.D0)
      C4=DEXP(1.4681D0+12.2584D0*PSIP-20.7322D0*PSIP**2+15.8855D0*
     1 PSIP**3.D0)
      CD=24.D0/REP*(1.D0+C1*REP**C2)+C3/(1.D0+C4/REP)
C
C     Single particle drag force
C
 200  TAUP(I)=4.D0*XP(I)*1.D-3*RHOP/(3.D0*CD*AIR(6)*DUV)
      FDZ(I)=EP(I)*RHOP*(UZC-VZC(I))*GDWF/TAUP(I)
      FDT(I)=EP(I)*RHOP*(UPL-CT(I))*GDWF/TAUP(I)
 300  CONTINUE
      RETURN
      END
C*************ERCHEK3.1*************************************************
       SUBROUTINE ERCHEK
C     REV 0 MARCH 18 91 (= copy of vers 2.1 REV 8  JULY  27  1989)
C     REV 1 OCT.  01 91
C     COMPATIBLE WITH LEVEL 3 VERSIONS
C     Outputs diagnostic warning and error messages
C     INPUT:IERROR(J) ;Flag for Jth diagnostic warning/error message
C           IERR1     ;Flag to idicate a warning message is required
C           IERR2     ;Flag to idicate an error message is required
C           Flag=0    ;No error
C           Flag=1or2 ;Warning/error message is generated - a program
C                      a program variable is  outside the expected
C                      range,or an iterative loop has exceeded maximum
C                      iterations limit or a subruotine has failed
C           Flag=1    ;execution continues
C           Flag=2    ;execution terminates
C     Error messages contained in direct access file 'CBERR3'
C*******************************************************************
      IMPLICIT DOUBLE PRECISION(A-H,O-Z)
      PARAMETER (NER1=10,NERR=15)
      COMMON/BLKE/IERROR(NERR),IERR1,IERR2
      CHARACTER*71 WORD(3)
      CHARACTER*70 WORDM
      OPEN(UNIT=14,FILE='CBERR3',FORM='FORMATTED',ACCESS='DIRECT',
     1 RECL=71,STATUS='OLD')
C
C     Warning messages
C
      IF(IERR1.EQ.0) GO TO 410
      WRITE(6,20)
 20   FORMAT(//1X,'WARNING MESSAGES - RUN CONTINUES'/1X,
     1 '-------------------------------')
      DO 400 I=1,NER1
      IF(IERROR(I).EQ.1) THEN
        K=3*I+5
        DO 100 J=1,3
C     Mainframe direct access file
        LREC=(J+K)*1000
C     PC/Watfor77 direct access file
CI      LREC=J+K
```

```
          READ(14,50,REC=LREC) WORD(J)
 50       FORMAT(A71)
          WORDM=WORD(J)(1:70)
          WRITE(6,60) WORDM
 60       FORMAT(A70)
 100      CONTINUE
        ENDIF
 400    CONTINUE
 410    CONTINUE
        IF(IERR2.EQ.0) RETURN
        WRITE(6,420)
 420    FORMAT(//1X,'ERROR MESSAGES - RUN TERMINATES'/1X,
      1 '-----------------------------')
        NER2=NER1+1
        DO 500 I=NER2,NERR
        IF(IERROR(I).EQ.2) THEN
          K=3*I+5
          DO 450 J=1,3
C     Mainframe direct access file
CI        LREC=(J+K)*1000
C     PC/Watfor77 direct access file
          LREC=(J+K)
          READ(14,50,REC=LREC) WORD(J)
          WORDM=WORD(J)(1:70)
          WRITE(6,60) WORDM
 450      CONTINUE
        ENDIF
 500    CONTINUE
        RETURN
        END
C***************ERINIT3.1*********************************************
        SUBROUTINE ERINIT
C     REV 0 MARCH 18 91 (= copy of vers. 2.1 REV 0   APRIL 06 89)
C     REV 1 OCT.  01 91
C     Initializes error flags to 'no error' status
C     Must be called prior at start of all level 3 models and test
C     programs
C*******************************************************************
        IMPLICIT DOUBLE PRECISION(A-H,O-Z)
        PARAMETER (NER1=10,NERR=15)
        COMMON/BLKE/IERROR(NERR),IERR1,IERR2
        IERR1=0
        IERR2=0
        DO 10 I=1,NERR
        IERROR(I)=0
 10     CONTINUE
        RETURN
        END
C***************FEDSIZ3.1*********************************************
        SUBROUTINE FEDSIZ
C     REV 0  OCT. 02  1991                    AUTHOR: RICHARD C. SENIOR
C     REV 3  OCT. 29  1991
C     Generates mass fraction
C     versus size data. The total mass of each particle fraction (type
C     1 or 2) is evenly divided according to the number of respective
C     particle size fractions (i.e. NXP1 or NXP2).
C
C     Cumulative distribution obtained from seive data. Linear
C     interpolation between distribution points to obtain cum. weight
C     vrs particle diameter data.
C
C     Input:     NSIV*SIV(IP+1,J) Seive data for particle type
C                IP+1=2  Type 1 particles (e.g. bed)
C                IP+1=3  Type 2 particles (e.g. fuel)
C
C     Variables: X  Sieve sizes (adjusted for end points), single type
C                Y  Cumulative mass fraction
C
C     Output: WT(I)     weight fractions of Ith particle fractions
C             XP(I)     diameter of Ith particle fraction
C             IXP(I)    particle type identifier (1=type, 2=type 2)
```

```
C             WT(I) based on all NXP particle fractions (both types)
C     Note: If NXP2=0 then only one type of particle (type 1) will be
C     considered. An error will occur if NXP1<1.
C
C*********************************************************************
      IMPLICIT DOUBLE PRECISION(A-H,O-Z)
      PARAMETER (NXP1=9,NXP2=0,NXP=NXP1+NXP2)
      PARAMETER (NER1=10,NERR=15)
      COMMON/BLKE/IERROR(NERR),IERR1,IERR2
      COMMON/BLKI/HYDG(20)
      COMMON/BLKJ/SIV(4,25),NSIV
      COMMON/BLKO/XP(NXP),WP(NXP),IXP(NXP)
      COMMON/BLKP/PP(2,10)
      DIMENSION NX(2),Y(25),X(25)
      NX(1)=NXP1
      NX(2)=NXP2
C
C     Perform calculation for type 1 (IP=1) and 2 (IP=2) particles
C
      DO 70 IP=1,2
      IF(IP.EQ.2.AND.NXP2.EQ.0) GO TO 150
      II=0
      JJ=0
C
C     Sum weight %'s
C
      ALPHA=0.D0
      DO 10 I=1,NSIV
      ALPHA=ALPHA+SIV(IP+1,I)
 10   CONTINUE
      IF(ALPHA.LT.0.95D2.OR.ALPHA.GT.1.05D2) THEN
        IERR2=2
        IERROR(NER1+1)=2
        RETURN
      ENDIF
C
C     Identify zero sieve mass values
C
 15   IF(SIV(IP+1,II+1).EQ.0.D0) THEN
        II=II+1
        GO TO 15
      ENDIF
 20   IF(SIV(IP+1,NSIV-JJ).EQ.0.D0) THEN
        JJ=JJ+1
        GO TO 20
      ENDIF
C
C     Generate cumulative mass vrs size data
C
      NF=NSIV+1-II-JJ
      NI=1
C     IF(SIV(IP+1,1).EQ.0.D0) SIV(IP+1,1)=SIV(IP+1,2)/2.D0
      IF(SIV(IP+1,1).EQ.0.D0) SIV(1,1)=SIV(1,2)/2.D0
      IF(JJ.EQ.0) THEN
        Y(NF)=100.D0
C       X(NF)=2.D0*SIV(IP+1,NSIV)-SIV(IP+1,NSIV-1)
        X(NF)=2.D0*SIV(1,NSIV)-SIV(1,NSIV-1)
        NF=NF-1
      ENDIF
      SUM=0.D0
      DO 30 I=NI,NF
      X(I)=SIV(1,I+II)
      Y(I)=SUM
      SUM=SUM+SIV(IP+1,I+II)*100.D0/ALPHA
 30   CONTINUE
C
C     Calculate mass fraction per particle fraction, and corresonding
C     particle diameters.
C
      DWT=50.D0/NX(IP)
      IF(IP.EQ.2) THEN
        WTOT=(1.D0-HYDG(2))
```

```
          IT=NX(1)
        ELSE
          IT=0
          WTOT=HYDG(2)
        ENDIF
        IC=1
        DO 60 I=1,NX(IP)
        YT=DWT*(2*I-1)
 40     CONTINUE
        BETA=(X(IC+1)-X(IC))/(Y(IC+1)-Y(IC))
        IF(Y(IC+1).GT.YT) GO TO 50
        IC=IC+1
        GO TO 40
 50     XP(I+IT)=X(IC)+(YT-Y(IC))*BETA
        IXP(I+IT)=IP
        WP(I+IT)=DWT*2.D0*WTOT
 60     CONTINUE
 70     CONTINUE
 150    RETURN
        END
C***********GASTUR3.1*************************************************
        SUBROUTINE GASTUR(U0,RUFF,UPF,TAUGF,SFG)
C       REVISION  0          OCTOBER 05    1991   AUTHOR:R.C.SENIOR
C       REV 3  NOV. 1 1991
C       Calculates the turbulence velocity in a pipe or the core of a
C       riser for particle-free gas flow.
C
C       INPUT:      U0      Mean gas flow (in pipe or riser core)
C                   RUFF    Pipe (or riser core) relative roughness (e/D)
C                           (minimum of wall roughness and roughness due
C                           to particles resident at the wall)
C                   AIR(6)  Gas density (common block BLKG)
C                   AIR(7)  Gas viscosity (common block BLKG)
C                   HYDG(3) Wall region thickness (common block BLKI)
C                           (HYDG(3)=0.D0 for level 3 wall modelling)
C
C       VARIABLES:  FG      Fanning friction factor
C                   USTR    Particle-free mean pipe (or riser core) gas
C                           velocity
C                   RED     Pipe (or riser core) Reynolds Number
C       OUTPUT:     UPF     Particle-free turbulence velocity
C                   TAUGF   Energetic eddy decay time - particle-free eddy
C                   SFG     Core-wall interfacial gas shear force
C*********************************************************************
        IMPLICIT DOUBLE PRECISION(A-H,O-Z)
        COMMON/BLKG/AIR(20),TG,PG
        COMMON/BLKH/BED(10),IBED
        COMMON/BLKI/HYDG(20)
        DATA ICALL/0/
        ICALL=ICALL+1
C
C       Is pipe rough or smooth?
C
        RED=AIR(6)*U0*(BED(8)-HYDG(3))/AIR(7)
        PARM=RED*RUFF
        IF(PARM.GT.250.D0) GO TO 100
C
C       Smooth pipe - Blasius equation
C
        FG=0.0791/RED**0.25D0
        GO TO 200
C
C       Rough pipe - correlation given by Davies, 'Turbulence
C       Phenomena', Academic Press (1972), pp.33
C
 100    FG=0.03864D0*RUFF**0.3D0
C
C       Friction velocity and turbulence velocity (note turbulence
C       velocity is the r.m.s. fluctuating gas velocity accounting for
C       three dimensions.
```

```
C
 200    USTR=U0*DSQRT(FG/2.D0)
        SFG=AIR(6)*USTR**2
        UE=0.8D0*USTR
        UPF=DSQRT(3.D0)*UE
        TAUGF=1.6D0*0.11D0*(BED(8)-HYDG(3))/UE
        RETURN
        END
C***************SAUTER3.1*****************************************
        SUBROUTINE SAUTER(IP)
C     REV 0 OCT 30  1991
C     Calculates Sauter mean diameter from sieve data.
C     INPUT : IP              ;Particle type flag, (1 or 2)
C             SIV(I,J),NSIV ;Sieve data (common block)
C     OUTPUT: PP(IP,10)       ;Sauter mean diameter,mm
C*****************************************************************
        IMPLICIT DOUBLE PRECISION(A-H,O-Z)
        COMMON/BLKJ/SIV(4,25),NSIV
        COMMON/BLKP/PP(2,10)
        IPP=IP+1
        XPF=1.5D0*SIV(1,NSIV)-.5D0*SIV(1,NSIV-1)
        SUM=SIV(IPP,NSIV)/XPF
        DO 10 I=1,NSIV-1
        IF(SIV(1,1).LE.0.D0) THEN
          XP=(SIV(1,2))/2.D0
        ELSE
          XP=SIV(1,I)+SIV(1,I+1)
        ENDIF
        SUM=SUM+2.D0*SIV(IPP,I)/(SIV(1,I+1)+SIV(1,I))
 10     CONTINUE
        PP(IP,10)=100.D0/SUM
        RETURN
        END
C******************TERVEL3.1*****************************************
        SUBROUTINE TERVEL(VT)
C     REV 1 MARCH 18     1991
C     TERVEL3.1 REV 0 (= TERVEL2.1, REV 7, MAY 12  89)
C     REV 2 JUL 24 91 REV 5  NOV. 25 1991
C
C     Calculates terminal velocity of spherical or non-spherical
C     particles of given diameter XP(I).
C
C     For non-spherical particles this diameter is assumed to be the
C     particle volume diameter 'dv'. If the calling routine uses the
C     Sauter diameter  'dsv', then it must first be converted to the
C     volume diameter by dv = dsv / psi, where 'psi' is the particle
C     sphericity defined as PP(IP,2) in the code.
C
C     INPUT:    NXP       No. of particles
C               AIR(6)    Gas density
C               AIR(7)    Gas viscosity
C               XP(I)     Particle diameters ,mm
C               PP(IP,1)  Particle density, kg/m3
C               PP(IP,2)  Particle sphericity
C     OUTPUT:   VT(I)     Particle terminal velocities, m/s
C     VARIABLE: DPDM      Dim'less diameter (Archimedes No.)
C               VTDM      Dim'less particle terminal velocity
C               IP        Particle type flag (type 1 or 2)
C*****************************************************************
        IMPLICIT DOUBLE PRECISION(A-H,O-Z)
        PARAMETER (NXP1=9,NXP2=0,NXP=NXP1+NXP2)
        PARAMETER (MX=2+3*NXP)
        COMMON/BLKG/AIR(20),TG,PG
        COMMON/BLKO/XP(NXP),WP(NXP),IXP(NXP)
        COMMON/BLKP/PP(2,10)
        DIMENSION VT(NXP),B1(2),B2(2)
        DO 10 IP=1,2
        IF(NXP2.LE.0.AND.IP.EQ.2) GO TO 10
        B1(IP)=(AIR(6)*(PP(IP,1)-AIR(6))*9.81D0/
     1  (AIR(7)**2))**(1.D0/3.D0)*1.D-3
```

```
      B2(IP)=(AIR(7)*9.81D0*(PP(IP,1)-AIR(6))/
     1 AIR(6)**2)**(1.D0/3.D0)
 10   CONTINUE
C
C     Spherical particle - Grace, J.R., Can J. Chem. Eng., 64,
C     353-363 (1983).
C
      IP=1
      DO 120 I=1,NXP
      IF(I.GT.NXP1) IP=2
      DPDM=B1(IP)*XP(I)
      IF(PP(IP,2).LT.0.95D0) GO TO 100
      IF(DPDM.LE.3.8D0) THEN
        VTDM=DPDM**2/18.D0-3.1234D-4*DPDM**5+1.6415D-6*DPDM**8-
     1  7.278D-10*DPDM**11
      ELSE
        W=DLOG10(DPDM)
        IF(DPDM.LT.7.58D0) THEN
          VTDM=10.D0**(-1.5446D0+2.9162D0*W-1.0432D0*W*W)
        ELSE
          VTDM=10.D0**(-1.64758D0+2.94786D0*W-1.09703D0*W*W+.17129D0*
     1    W**3)
        ENDIF
      ENDIF
      GO TO 110
C
C     Non-spherical 'isometric' particle - correlation of Haider and
C     Levenspiel, Powder Tech., 58, 63-70 (1989).
C     Note dp used here is volume dia.. (dv = DP(Sauter)/sphericity)
C

 100  CONTINUE
      VTDM=1.D0/(18.D0/DPDM**2+(2.3348D0-1.7439*PP(IP,2))/
     1 DSQRT(DPDM))
 110  VT(I)=VTDM*B2(IP)
 120  CONTINUE
      RETURN
      END
C#################################################################
C  SECTION B: CORE DYNAMICS MODELLING SUBROUTINES
C#################################################################
C***********DYNCOL3.1*************************************************
      SUBROUTINE DYNCOL(DV,HK,VZC,CT,CK,EP,TAUP,TAUK,FKZ,FKT,UZC,DKT,
     1 PKK,SK,IMIN,ICONV)
C     REVISION  0          OCT.    04    1991   AUTHOR:R.C.SENIOR
C     REV  6    NOV. 04 1991
C     REV  7    DEC. 27 1991 (Addition of Z1T, Z2T for report writing)
C     REV  8    JAN. 07 1991 (Addition of ICOR)
C
C     INPUT:
C       VZC(I)   Axial particle fraction velocity
C       TAUP(I)  Particle response time
C       CT(I)    Particle eddy drift velocity
C       CK(I)    Particle collisional fluctuating velocity
C       EP(I)    Particle volume fraction
C       UZC      Gas interstitial velocity
C       ICONV    Convergence flag for iterative turbulence computation
C
C     VARIABLES:
C       SIGMA2(I,J) Collision area (radius**2), fractions I&J
C       PN(I)       Number of type I particles per unit volume
C       PVOL(I)     Discrete particle volume, fraction I
C       CKSQ(I)     CK(I)*CK(I)
C       VWK(I)      Velocity weighting factor based on TAUK(I)
C       Z1(I)       Type (i) collision frequency
C       Z2(I)       Type (ii) collision frequency
C       Z1T(I)      Type (i) collision freq., single type I particle
C       Z2T(I)      Type (ii) collision freq., single type I particle
C
C     OUTPUT:
```

```
C        DV(I,J)   Average velocity difference, fractions I&J
C         TAUK(I)  Mean period between type(i) collisions
C         FKZ(I)   Mean collision force between fractions
C         FKT(I)   Collisional force component within model eddy due
C                  to particle fraction drifts
C         HK(I,J)  Coefficient for Newton's method iterative solution
C                  in routine PARTUR (v3.2).
C         IMIN     Particle fraction closest to zero net collisional
C                  force -- eddy collisional component
C         ICOR     Particle fraction closest to zero net collisional
C                  force -- axial collisional component
C      Computes the collisional forces between the various particle
C      fractions arising from differences in mean fraction velocity
C      (type (i) collisions), and collisions due to the fluctuating
C      components of velocity (type (ii) collisions). This routine is
C      firstly repeatedly called as part of an iterative solution of
C      the gas-particle turbulence properties. When this computation
C      converges, FLUCEN is called from DYNCOL, where the particle
C      fraction fluctuating energy balance terms are evaluated.
C      Convergence is flagged by ICONV=2.
C
C*********************************************************************
       IMPLICIT DOUBLE PRECISION(A-H,O-Z)
       PARAMETER (NXP1=9,NXP2=0,NXP=NXP1+NXP2)
       COMMON/BLKG/AIR(20),TG,PG
       COMMON/BLKO/XP(NXP),WP(NXP),IXP(NXP)
       COMMON/BLKP/PP(2,10)
       COMMON/BLKK/Z1T(NXP),Z2T(NXP),VWK(NXP)
       COMMON/BLKT/CCOR,VCOR,FPCOR,ICOR
       DIMENSION VZC(NXP),CT(NXP),EP(NXP),CK(NXP),TAUP(NXP),TAUK(NXP)
       DIMENSION DV(NXP,NXP),SIGMA2(NXP,NXP),Z1(NXP,NXP),Z2(NXP,NXP)
       DIMENSION CKSQ(NXP),PVOL(NXP),PWT(NXP)
       DIMENSION FKZ(NXP),FKT(NXP)
       DIMENSION CONST(10),PN(NXP)
       DIMENSION HK(NXP,NXP),DKT(NXP),PKK(NXP),SK(NXP)
       SAVE SIGMA2,PVOL,PWT,CONST,PI,ICALL
       DATA ICALL/0/
       ICALL=ICALL+1
       IF(ICALL.GT.1) GO TO 60
C
C      Particle volumes, masses and collision radii
C
       PI=4.D0*DATAN(1.D0)
       CONST(1)=DSQRT(8.D0*PI/3.D0)
       CONST(2)=-1.4D0*DSQRT(1.5D0)
       CONST(3)=2.D0*DSQRT(PI/3.D0)
       DO 50 I=1,NXP
       PVOL(I)=PI*XP(I)**3/6.D9
       PWT(I)=PP(IXP(I),1)*PVOL(I)
       DO 40 J=1,NXP
       SIGMA2(I,J)=(XP(I)+XP(J))**2/4.D6
 40    CONTINUE
 50    CONTINUE
C
C      Mean velocity differences; collision efficiencies, frequencies
C      and periods
C
 60    DO 70 I=1,NXP
       PN(I)=EP(I)/PVOL(I)
       CKSQ(I)=CK(I)**2
       DV(I,I)=0.D0
       Z1(I,I)=0.D0
       Z2(I,I)=PN(I)**2*SIGMA2(I,I)*CONST(3)*CK(I)
 70    CONTINUE
       IF(NXP.EQ.1) GO TO 110
       DO 100 I=2,NXP
       DO 90 J=1,I-1
       DV(I,J)=DSQRT((VZC(I)-VZC(J))**2+(CT(I)-CT(J))**2)
       COEFF1=DSQRT(CKSQ(I)+CKSQ(J))
       COEFF2=PN(I)*PN(J)*SIGMA2(I,J)
       IF(COEFF1.LT.1.D-8) THEN
```

```
          Z1(I,J)=COEFF2*PI*DV(I,J)
          Z2(I,J)=0.D0
          GO TO 75
        ENDIF
        IF(DV(I,J).LT.1.D-8) THEN
          Z1(I,J)=0.D0
          Z2(I,J)=COEFF2*CONST(1)*COEFF1
          GO TO 75
        ENDIF
        DIMDV=DV(I,J)/COEFF1
        Z1(I,J)=COEFF2*PI*DV(I,J)*(1.D0+1.D0/(3.D0*DIMDV**2))*
     1  (1.D0-DEXP(CONST(2)*DIMDV))
        Z2(I,J)=COEFF2*CONST(1)*COEFF1*DEXP(-1.5D0*DIMDV**2)
 75     K=I
        M=J
        IF(TAUP(J).LT.TAUP(I)) THEN
          K=J
          M=I
        ENDIF
        PARM=PP(IXP(K),1)*(UZC-VZC(M))*XP(K)**2/(18.D3*AIR(7)*XP(M))
        IF(PARM.GE.4.D0) THEN
          ETA=1.D0
          GO TO 80
        ENDIF
        IF(PARM.LE.4.D-2) THEN
          ETA=0.D0
        ELSE
          ETA=DLOG10(5.D0*SQRT(PARM))
        ENDIF
        Z1(I,J)=ETA*Z1(I,J)
 80     DV(J,I)=DV(I,J)
        Z1(J,I)=Z1(I,J)
        Z2(J,I)=Z2(I,J)
 90     CONTINUE
 100    CONTINUE
 110    CONTINUE
        DO 150 I=1,NXP
        Z1T(I)=0.D0
        Z2T(I)=0.D0
        DO 130 J=1,NXP
        Z1T(I)=Z1T(I)+Z1(I,J)
        Z2T(I)=Z2T(I)+Z2(I,J)
 130    CONTINUE
        IF(Z1T(I).GT.1.D-2) THEN
          TAUK(I)=PN(I)/Z1T(I)
        ELSE
          TAUK(I)=1.D2*PN(I)
        ENDIF
        Z1T(I)=Z1T(I)/PN(I)
        Z2T(I)=Z2T(I)/PN(I)
 150    CONTINUE
C
C     Collision velocity weighting factor, VWK(I)
C
        DO 180 I=1,NXP
        RAT=TAUK(I)/TAUP(I)
        IF(RAT.LT.0.2D0) THEN
          VWK(I)=0.5D0
        ELSE
          IF(RAT.GT.5.D0) THEN
            VWK(I)=1.D0/RAT
          ELSE
            THETA=DEXP(-RAT)
            VWK(I)=1.D0/RAT-THETA/(1.D0-THETA)
          ENDIF
        ENDIF

 180    CONTINUE
C
C     Axial and eddy collision forces between fractions
C
        DO 220 I=1,NXP
```

```
      FKZ(I)=0.D0
      FKT(I)=0.D0
      DO 210 J=1,NXP
      CRST=(PP(IXP(I),3)+PP(IXP(J),3))/2.D0
      PARM1=PWT(I)*PWT(J)*Z1(I,J)*(1.D0+CRST)
      PARM2=(PWT(I)*(2.D0-VWK(J))+PWT(J)*(2.D0-VWK(I))-CRST*(PWT(I)
     2 *VWK(J)+PWT(J)*VWK(I)))
      PARM3=PARM1/PARM2
      HK(I,J)=PARM3
      FKZ(I)=FKZ(I)+PARM3*(VZC(J)-VZC(I))
      FKT(I)=FKT(I)+PARM3*(CT(J)-CT(I))
C************SENSITIVITY TEST ONLY
COUT  FKZ(I)=FKZ(I)+2.D0*PARM3*(VZC(J)-VZC(I))
COUT  FKT(I)=FKT(I)+2.D0*PARM3*(CT(J)-CT(I))
C*************
 210  CONTINUE
 220  CONTINUE
C
C     Fraction IMIN with the minimum net eddy collision force (i.e
C     mid-size fraction whose eddy interaction velocity weighting
C     factor equals the mean value considering all fractions.
C     Fraction ICOR with min. axial collision force (i.e. collisions
C     from larger and smaller particles partially cancel).
C
      FCOMP1=DABS(FKT(1))
      FCOMP2=DABS(FKZ(1))
      IMIN=1
      ICOR=1
      IF(NXP.EQ.1) GO TO 290
      DO 280 I=2,NXP
      IF(DABS(FKT(I)).LT.FCOMP1) THEN
        FCOMP1=DABS(FKT(I))
        IMIN=I
      ENDIF
      IF(DABS(FKZ(I)).LT.FCOMP2) THEN
        FCOMP2=DABS(FKZ(I))
        ICOR=I
      ENDIF
 280  CONTINUE
 290  IF(ICONV.NE.2) RETURN
C
C     Compute particle fraction fluctuating kinetic energy production,
C     transfer and dissipation
C
      CALL FLUCEN(DV,Z1,Z2,VWK,PWT,CKSQ,EP,TAUP,DKT,PKK,SK)
      RETURN
      END
C***********FLUCEN3.1*************************************************
      SUBROUTINE FLUCEN(DV,Z1,Z2,VWK,PWT,CKSQ,EP,TAUP,DKT,PKK,SK)
C     REVISION  0          OCTOBER 14    1991   AUTHOR:R.C.SENIOR
C
C     INPUT:
C       DV(I,J) Average velocity difference, fractions I&J
C       Z1(I)   Type (i) collision frequency
C       Z2(I)   Type (ii) collision frequency
C       VWK(I)  Velocity weighting factor based on TAUK(I)
C       PWT(I)  Discrete particle mass, fraction I
C       CKSQ(I) Particle collisional fluctuating velocity squared
C       EP(I)   Particle volume fraction
C       TAUP(I) Particle response time
C
C     VARIABLES:
C
C     OUTPUT:
C       DKT(I) Dissipation of fluctuating energy due to drag
C       SK(I)  Transfer of fluctuating energy by type (ii) collisions
C       PKK(I) Production of fluctuating energy due to type (i)
C              collisions
C
C     Computes the production, transfer and dissipation terms of the
```

```
C     particle fluctuating kinetic energy balance.
C*********************************************************************
      IMPLICIT DOUBLE PRECISION(A-H,O-Z)
      PARAMETER (NXP1=9,NXP2=0,NXP=NXP1+NXP2)
      COMMON/BLKO/XP(NXP),WP(NXP),IXP(NXP)
      COMMON/BLKP/PP(2,10)
      DIMENSION DV(NXP,NXP),Z1(NXP,NXP),Z2(NXP,NXP),CONST(2)
      DIMENSION VWK(NXP),PWT(NXP),CKSQ(NXP),EP(NXP),TAUP(NXP)
      DIMENSION DKT(NXP),PKK(NXP),SK(NXP)
      SAVE CONST
      DATA ICALL/0/
      ICALL=ICALL+1
      IF(ICALL.GT.1) GO TO 40
C
C     First call constants
C
      PI=4.D0*DATAN(1.D0)
      CONST(1)=PI**2/32.D0
      CONST(2)=0.9213D0**2
C
C     DKT -- Dissipation of fluctuating energy due to drag
C     PKK -- The production of fluctuating kinetic energy due to
C     collisions arising from differences in axial velocity of unlike
C     particle fractions (type (i) collisions).
C     SK  -- Fluctuating energy transfer between fractions due to the
C     fluctuating component of velocity (type (ii) collisions).
C
 40   DO 60 I=1,NXP
      PKK(I)=0.D0
      SK(I)=0.D0
      RHOS=EP(I)*PP(IXP(I),1)
      DKT(I)=-RHOS*CKSQ(I)/TAUP(I)
      DO 50 J=1,NXP
      CRST=(PP(IXP(I),3)+PP(IXP(J),3))/2.D0
      PARM1=PWT(J)*(1.D0+CRST)
      PARM2=(PWT(I)*(2.D0-VWK(J))+PWT(J)*(2.D0-VWK(I))-CRST*(PWT(I)
     1 *VWK(J)+PWT(J)*VWK(I)))
      PKK(I)=PKK(I)+CONST(1)*PWT(I)*Z1(I,J)*(PARM1*DV(I,J)/PARM2)**2
      PARM3=2.D0*(PWT(I)+PWT(J))
      SK(I)=SK(I)+CONST(2)*PWT(I)*Z2(I,J)*(PARM1/PARM3)*(PARM1*
     1 (CKSQ(I)+CKSQ(J))/PARM3-CKSQ(I))
 50   CONTINUE
 60   CONTINUE
      RETURN
      END
C***********ICONDS3.1*************************************************
      SUBROUTINE ICONDS(VZC,FKE,EP,UZC,EG,PRS)
C     REVISION  2          OCTOBER 11   1991   AUTHOR:R.C.SENIOR
C
C     Initial conditions for CFB core riser model (Level 3)
C*********************************************************************
      IMPLICIT DOUBLE PRECISION(A-H,O-Z)
      PARAMETER (NXP1=9,NXP2=0,NXP=NXP1+NXP2)
      PARAMETER (NZB=20,NZ=NZB+1)
      PARAMETER (NER1=10,NERR=15)
      COMMON/BLKE/IERROR(NERR),IERR1,IERR2
      COMMON/BLKG/AIR(20),TG,PG
      COMMON/BLKH/BED(10),IBED
      COMMON/BLKI/HYDG(20)
      COMMON/BLKO/XP(NXP),WP(NXP),IXP(NXP)
      COMMON/BLKP/PP(2,10)
      DIMENSION FKE(NXP),VZC(NXP),EP(NXP)
C
C     Initial gas volume fraction (voidage)
C     HYDG(4) = loose-packed voidage (input) (if used)
C
C     EG=0.9D0
      EG=.98D0
C     EG=1.D0-0.005D0
C
C     Particle volume fractions (routine FEDSIZ ver.3.1 must first be
```

```
C     called).
C
      VOLSUM=0.D0
      DO 10 I=1,NXP
      VOLSUM=VOLSUM+WP(I)/PP(IXP(I),1)
 10   CONTINUE
      RHOPAV=1.D2/VOLSUM
      VOLCRT=(1.D0-EG)/VOLSUM
      DO 40 I=1,NXP
      EP(I)=WP(I)*VOLCRT/PP(IXP(I),1)
 40   CONTINUE
C
C     Initial particle velocities and fluctuating k.e.
C
      DO 90 I=1,NXP
      GSUP=HYDG(1)-HYDG(7)*(1.D0-HYDG(4))*(1.D0-HYDG(5)/BED(4))
     1 *RHOPAV*HYDG(9)
      VZC(I)=GSUP*BED(4)/((1-EG)*HYDG(5)*RHOPAV)
C     FKE(I)=0.D0
      FKE(I)=0.01D0
 90   CONTINUE
C
C     Gas superficial velocity based on full riser c.s.a. = HYDG(6)
C     Assumed constant core c.s.a. = HYDG(5)
C
      UZC=HYDG(6)*(BED(4)/HYDG(5))/EG
C
C     Initial gas pressure (note choice is arbitrary, only dp of
C     interest)
C
      PRS=PG
      RETURN
      END
C***********PARTUR3.2*************************************************
      SUBROUTINE PARTUR(DV,HK,VZC,CT,EP,TAUP,TAUK,TAUR,FDT,FKT,PKT,
     1 UZC,UPL,UPF,TAUGL,TAUGF,EG,ICONV,IMIN)
C     REVISION  0          NOVEMBER 01   1991   AUTHOR:R.C.SENIOR
C     REVISION  1  NOVEMBER 07   1991
C
C     INPUT:
C       TAUP(I) Particle response time
C       TAUK(I) Mean period between type(i) collisions
C       FDT(I)  Transverse or eddy component of drag force
C       FKT(I)  Eddy collisional force component
C       UPF     Particle-free gas turbulence velocity
C       EP(I)   Particle vol. fractions
C       EG      Gas vol. fraction
C       IMIN    Particle fraction closest to zero net collision force
C       TAUGF   Particle-free eddy decay time
C       VZC(I)  Ith fraction axial velocity
C       UZC     Gas interstitial velocity - axial component
C       DV(I,J) Average velocity difference, fractions I&J
C       HK(I,J) Coefficient for Newton's method iterative solution
C
C     INPUT/OUTPUT (Iterative solution update):
C       TAUGL   Particle-free eddy decay time
C       CT(I)   Particle drift velocity
C       UPL     Particle-laden gas turbulence velocity
C
C     VARIABLES:
C       VWR(I)  Eddy interaction velocity weighting factor based on
C               TAUR(I) (no collisions)
C       VWE(I)  Vel. weighting factor with collisions
C
C     OUTPUT:
C        TAUR(I) Eddy interaction period
C        PKT(I)  Production of particle fraction fluctuating k.e. due
C                to gas turbulence (only called if ICONV=2)
C        ICONV   Convergence flag:
C                ICONV=0 for first call of new iteration
```

```
C                ICONV=1 for non-convergence
C                ICONV=2 for convergence
C
C     Iterative solution by Newton's method. Variable relaxation to
C     maintain gas turbulence and particle fluctuating velocity
C     estimates within limits 0.0 to UPF.
C
C     Note the turbulence may be "turned off"by setting ITURB equal
C     to 0 in the data initialisation statement of this routine.
C*********************************************************************
      IMPLICIT DOUBLE PRECISION(A-H,O-Z)
      DOUBLE PRECISION LE
      PARAMETER (NXP1=9,NXP2=0,NXP=NXP1+NXP2)
      COMMON/BLKG/AIR(20),TG,PG
      COMMON/BLKH/BED(10),IBED
      COMMON/BLKI/HYDG(20)
      COMMON/BLKO/XP(NXP),WP(NXP),IXP(NXP)
      COMMON/BLKP/PP(2,10)
      DIMENSION CT(NXP),EP(NXP),VZC(NXP),RHOS(NXP)
      DIMENSION CTO(NXP),CTN(NXP)
      DIMENSION TAUP(NXP),TAUK(NXP),TAUR(NXP),VWR(NXP),VWE(NXP)
      DIMENSION FDT(NXP),FKT(NXP),PKT(NXP)
      DIMENSION DV(NXP,NXP),HK(NXP,NXP),AG(NXP+1,NXP+2),XG(NXP+1)
      DIMENSION COEF(2),XGO(NXP+1)
      SAVE COEF,EPS1,UDT,UPLO,TAUGLO,NXF,NXU,ICOUNT,ITURB,ICALL
      SAVE CTO,RELAXO,IBAD,CONVO
      DATA EPS1/1.D-2/,ICALL/0/,ICOUNT/0/,ITURB/1/
      DATA RXMAX/0.8D0/
      ICALL=ICALL+1
C
C     ITURB=0? :PARTUR computation not required. Hence set turbulence
C     fluctuating velocities to zero
C
      IF(ITURB.EQ.0) THEN
        UPL=0.D0
        DO 10 I=1,NXP
        CT(I)=0.D0
        TAUR(I)=1.D4
        PKT(I)=0.D0
 10     CONTINUE
        ICONV=2
        TAUGL=1.D4
        RETURN
      ENDIF
C
      IF(ICALL.EQ.1) RELAXO=RXMAX
      ICOUNT=ICOUNT+1
C
C     First iteration (ICONV=0): define constants for ensuing
C     iteration process
C
      IF(ICONV.GT.0) GO TO 120
C     CONVO=1.D2
      ICOUNT=1
      IBAD=0
      NXF=NXP+2
      NXU=NXP+1
      LE=0.11D0*(BED(8)-HYDG(3))
      COEF(1)=DSQRT(3.D0)*1.6D0*LE
      COEF(2)=1.D0/EG**1.8D0
      UDT=UPF**2/TAUGF
      DO 20 I=1,NXP
      RHOS(I)=EP(I)*PP(IXP(I),1)
 20   CONTINUE

C
C     Particle interaction time TAUR(I) and eddy velocity weighting
C     factor VWR(I)
C
 120  TAUGL=1.6D0*DSQRT(3.D0)*LE/UPL
      DO 160 I=1,NXP
      TAUD=LE/(UZC-VZC(I))
```

```
      TAUR(I)=DMIN1(TAUD,TAUGL)
      RAT=TAUR(I)/TAUP(I)
      IF(RAT.LT.0.2D0) THEN
        VWR(I)=0.5D0
      ELSE
        IF(RAT.GT.5.D0) THEN
          VWR(I)=1.D0/RAT
        ELSE
          THETA=DEXP(-RAT)
          VWR(I)=1.D0/RAT-THETA/(1.D0-THETA)
        ENDIF
      ENDIF
 160  CONTINUE
C
C     Assemble augmented coefficient matrix for eqs 1 to NXP
C    (correspoding to particle drift eqs of motion.) and eq. NXU
C    (gas turbulence energy equation).
C

      SUM2=0.D0
      SUM3=0.D0
      DO 180 I=1,NXP
      SUM1=0.D0
      RAPT=4.D0*TAUK(I)/TAUR(I)
      IF(RAPT.GT.20.D0) THEN
        VWE(I)=VWR(I)
      ELSE
        PARM=DEXP(-RAPT)
        VWE(I)=PARM*VWR(IMIN)+(1.D0-PARM)*VWR(I)
      ENDIF
      PARM1=TAUR(I)*(1.D0-VWE(I))
      PARM2=2.D0*(1.D0-VWE(I))*TAUP(I)
      AG(I,NXF)=FDT(I)+FKT(I)-RHOS(I)*CT(I)/PARM1
      AG(I,NXU)=-RHOS(I)*COEF(2)/TAUP(I)
      DO 170 J=1,NXP
      IF(I.EQ.J) GO TO 170
      IF(DV(I,J).LE.1.D-6) THEN
        AG(I,J)=0.D0
        GO TO 170
      ENDIF
      AG(I,J)=-HK(I,J)*(1.D0+((CT(I)-CT(J))/DV(I,J))**2)
      SUM1=SUM1-AG(I,J)
 170  CONTINUE
      AG(I,I)=SUM1+RHOS(I)/PARM1-AG(I,NXU)
      AG(NXU,I)=RHOS(I)*(UPL-2.D0*CT(I))/(AIR(6)*PARM2)
      SUM2=SUM2-RHOS(I)*(UPL-CT(I))*CT(I)/PARM2
      SUM3=SUM3+RHOS(I)*CT(I)/PARM2
 180  CONTINUE
      AG(NXU,NXU)=3.D0*UPL**2/COEF(1)+SUM3/AIR(6)
      AG(NXU,NXF)=SUM2/AIR(6)+UDT-UPL**3/COEF(1)
C
C     Solve augmented matrix by Gauss elimination with scaled partial
C     pivot selection
C
      CALL DGAUSS(AG,NXU,NXU,NXF,XG,RNORM,IEROR)
      IF(IEROR.EQ.2) WRITE(6,174)
 174  FORMAT(1X,'GAUSS ELIMINATION FAILED')
C
C     Test for convergence
C
      IPC=1
      CONV=DABS(XG(NXU)/UPL)
      DO 200 I=1,NXP
      CONVP=DABS(XG(I)/CT(I))
      IF(CONVP.GT.CONV) THEN
        CONV=CONVP
        IPC=I
      ENDIF
 200  CONTINUE
      IF(CONV.LE.EPS1) THEN
        ICONV=2
```

```
          GO TO 500
        ENDIF
        IF(ICONV.EQ.0) GO TO 400
C
C     Update estimates of UPL, CT(I)
C
 400    IF(ICALL.EQ.1) RELAX=RXMAX
        RELAX=RELAXO*1.1D0
        IF(RELAX.GT.RXMAX) RELAX=RXMAX
 430    UPLN=UPL+RELAX*XG(NXU)
        DO 440 I=1,NXP
        CTN(I)=CT(I)+RELAX*XG(I)
 440    CONTINUE
C
C     Set constraints on step-size to keep CT's, UPL within physically
C     possible limits
C
        IF(UPLN.LE.0.D0) THEN
          RELAX=-UPL/(2.D0*XG(NXU))
          GO TO 430
        ENDIF
        IF(UPLN.GT.UPF) THEN
          RELAX=(UPF-UPL)/(2.D0*XG(NXU))
          GO TO 430
        ENDIF
        IF(CTN(IPC).LT.0.D0) THEN
          RELAX=-0.1D0*CT(IPC)/XG(IPC)
          GO TO 430
        ENDIF
        DO 450 I=1,NXP
        IF(CTN(I).GE.UPL) THEN
          RELAX=RELAX/2.D0
          GO TO 430
        ENDIF
 450    CONTINUE
C
C     Update old estimates
C
        RELAXO=RELAX
        DO 460 I=1,NXP
        CTO(I)=CT(I)
        CT(I)=CTN(I)
 460    CONTINUE
        UPLO=UPL
        UPL=UPLN
        DO 470 I=1,NXU
        XGO(I)=XG(I)
 470    CONTINUE
        TAUGLO=TAUGL
 500    TAUGL=1.6D0*DSQRT(3.D0)*LE/UPL
        IF(ICONV.EQ.0) ICONV=1
        IF(ICONV.EQ.1) GO TO 900
C
C     PKT -- Production of particle fluctuating kinetic energy due to
C     turbulence (Only calculate if convergence attained, ICONV=2)
C
        DO 800 I=1,NXP
        PKT(I)=RHOS(I)*CT(I)**2/(2.D0*TAUR(I)*(1.D0-VWE(I))**2)
 800    CONTINUE
 900    RETURN
        END
C*********SYSTEQ3.1******(EXTERNAL ODESYS)***************************
        SUBROUTINE SYSTEQ(Z,Y,F,LIMIT)
C     REV 6   NOV.  01  1991    REV 7   JAN   03  1992
C     System of o.d.e.'s for riser core collision model. Routine is
C     called by by generalized ODE solver FHLBRG. FHLBRG calls SYSTEQ
C     under the guise of the general name ODESYS. Thus SYSTEQ must be
C     equivocated with ODESYS by EXTERNAL declarator.
C
C     SYSTEQ:
C     NXP = number of particle size fractions. Thus there are
```

```
C     (3*NXP+2) d.e.'s in the system:
C
C     F(1) =  gas mass balance;
C     F(2) =  gas momentum balance;
C     F(3)--F(NXP+2) = particle fraction mass balances;
C     F(NXP+3)--F(2*NXP+2) = particle fraction momentum balances;
C     F(2*NXP+3)--F(3*NXP+2) = particle fraction fluctuating kinetic
C     energy balances.
C
C     Independent variable:
C     Z = height, m
C
C     Dependent variables:
C     Y(1) = EG*UZC = (core voidage * core interstitial gas vel.)
C     Y(2) = PR     = (gas pressure)
C     Y(3),... = EP(I)*VZC(I) = (fraction vol.* fraction velocity)
C     Y(3+NXP), ... = VZC(I) = (particle fraction velocity)
C     Y(3+2*NXP), ... = FKE(I) = (particle fraction fluctuating
C     kinetic energy)
C
C     Error flags:
C     LIMIT=0; Successful return
C     LIMIT=1; An attempt has been made to evaluate one or more
C     derivatives outside the [X,Y(1),Y(2),.....,Y(M)] space in
C     which the derivative is defined. ODE solver is flagged to
C     reduce step size in Z.
C     LIMIT=2; Warning in SYSTEQ or routines called by SYSTEQ,
C     probably due to failure of iterative calculation of turbulence
C     properties to converge. Continue Execution.
C
C     Model Level 3 Assumptions:
C     This model is designed to specifically investigate the
C     properties of a dilute suspension flowing within the core of a
C     CFB riser. Some aspects of riser wall dynamics are not
C     considered in detail, and constraints and assumptions are
C     included to handle specific cases of wall solids
C     distribution/motion. The principal model assumptions are:
C     (i)    Steady-state
C     (ii)   Riser and core cross-sections constant
C     (iii)  Particles entering from wall region into core are from
C            two sources: (A) rebounds from a bare wall;
C                         (B) entrainment from streamers.
C     (iv)   Gas viscous and inertial terms in gas momentum eqn.
C            negligible.
C     (v)    Net wall-core particle transfer rate is zero
C
C*********************************************************************
      IMPLICIT DOUBLE PRECISION(A-H,O-Z)
      PARAMETER (NXP1=9,NXP2=0,NXP=NXP1+NXP2)
      PARAMETER (NZB=20,NZ=NZB+1)
      PARAMETER (NER1=10,NERR=15)
      COMMON/BLKE/IERROR(NERR),IERR1,IERR2
      COMMON/BLKG/AIR(20),TG,PG
      COMMON/BLKH/BED(10),IBED
      COMMON/BLKI/HYDG(10)
      COMMON/BLKK/Z1T(NXP),Z2T(NXP),VWK(NXP)
      COMMON/BLKO/XP(NXP),WP(NXP),IXP(NXP)
      COMMON/BLKP/PP(2,10)
      COMMON/BLKY/ZS,ZF
      DIMENSION VZC(NXP),CT(NXP),CK(NXP),EP(NXP),TAUP(NXP),TAUR(NXP)
      DIMENSION FDZ(NXP),FDT(NXP),TAUK(NXP),FKZ(NXP),FKT(NXP)
      DIMENSION F(3*NXP+2),Y(3*NXP+2)
      DIMENSION DKT(NXP),PKK(NXP),SK(NXP),PKT(NXP),SFS(NXP),SFR(NXP)
      DIMENSION DKR(NXP),PKR(NXP),DKS(NXP),PKS(NXP),QC(NXP),CKT(NXP)
      DIMENSION DV(NXP,NXP),HK(NXP,NXP)
      CHARACTER*8 SHAPE
      SAVE CT,UOC,UPF,TAUGF,SFG,UPL,TAUGL,GA,ZFO,IEV,IV,IK,ICALL
      SAVE IPART
      DATA GA/-9.81D0/,ICALL/0/
      ICALL=ICALL+1
```

```
      IF(ICALL.GT.1) GO TO 100
      IEV=2
      IV=NXP+2
      IK=2*NXP+2
C
C     Particle-free gas flow properties
C
      UOC=HYDG(6)*(BED(4)/HYDG(5))
      RUFF=DMAX1(BED(1),HYDG(3))/(BED(8)-2.D0*HYDG(3))
      CALL GASTUR(UOC,RUFF,UPF,TAUGF,SFG)
C
C     First call guess - particle and gas drift velocities.
C     (For all future calls use SAVEd CT's, UPL, TAUGL as first guess)
C
      IPART=1
      DO 30 I=1,NXP
      CT(I)=0.1D0*UPF
 30   CONTINUE
      UPL=UPF
      TAUGL=TAUGF
C
C     Volume fractions EG, EP(I) and gas interstitial velocity, UZC
C
 100  SUM=0.D0
      DO 160 I=1,NXP
      IF(Y(I+IK).LT.0.D0.OR.Y(I+IV).LT.0.D0) THEN
        LIMIT=1
        RETURN
      ENDIF
      EP(I)=Y(I+IEV)/Y(I+IV)
      VZC(I)=Y(I+IV)
 150  SUM=SUM+EP(I)
 160  CONTINUE
      EG=1.D0-SUM
      UZC=UOC/EG
C
C     Collisional fluctuating particle velocities, CK(I)
C
      DO 180 I=1,NXP
      CK(I)=DSQRT(2.D0*Y(I+IK))
 180  CONTINUE
C
C     Gas and particle mass balances
C
      F(1)=0.D0
      DO 200 I=1,NXP
      F(I+IEV)=0.D0
 200  CONTINUE

C
C     Iterative solution of the particle-laden gas and particle
C     fraction drift velocities.
C
      ICONV=0
      LIMIT=0
      DO 300 ITER=1,110
      CALL DRAGON(VZC,CT,EP,FDZ,FDT,TAUP,UZC,UPL,EG)
      CALL DYNCOL(DV,HK,VZC,CT,CK,EP,TAUP,TAUK,FKZ,FKT,UZC,DKT,PKK,
     1 SK,IMIN,ICONV)
      CALL PARTUR(DV,HK,VZC,CT,EP,TAUP,TAUK,TAUR,FDT,FKT,PKT,UZC,
     1 UPL,UPF,TAUGL,TAUGF,EG,ICONV,IMIN)
      IPART=IPART+1
      IF(ICONV.EQ.2) GO TO 320
 300  CONTINUE
      IERR1=1
      IERROR(2)=1
      LIMIT=2
C
C     Fluctuating kinetic energy balance terms -- PKK, SK, DKT, PKT
C
 320  CALL DYNCOL(DV,HK,VZC,CT,CK,EP,TAUP,TAUK,FKZ,FKT,UZC,DKT,PKK,
     1 SK,IMIN,2)
```

```
      IF(ICONV.NE.2) THEN
        ICONV=2
        CALL PARTUR(DV,HK,VZC,CT,EP,TAUP,TAUK,TAUR,FDT,FKT,PKT,UZC,
     1 UPL,UPF,TAUGL,TAUGF,EG,ICONV,IMIN)
      IPART=IPART+1
      ENDIF
C
C     Wall boundary conditions:
C     Shear force terms -- SFS, SFR
C     Fluctuating kinetic energy balance terms -- DKS, PKS, DKR, PKR
C
      CALL WALCON(VZC,CK,CT,EP,SFS,SFR,PKS,PKR,DKR,DKS,QC,CKT)
C
C     1.Gas and particle momentum balances
C     2. Core particle fraction fluctuating kinetic energy balance
C
      FDGAS=0.D0
      PARM1=HYDG(8)/HYDG(5)
      DO 340 I=1,NXP
      FDGAS=FDGAS-FDZ(I)
      PARM2=PP(IXP(I),1)*EP(I)*Y(I+IV)
      F(I+IV)=GA/Y(I+IV)+(FDZ(I)+FKZ(I))/PARM2+PARM1*(SFS(I)+
     1 SFR(I))/PARM2
      F(I+IK)=(PKK(I)+SK(I)+PKT(I)+DKT(I))/PARM2+(PKS(I)+DKR(I)+
     1 PKR(I)+DKS(I))*PARM1/PARM2
 340  CONTINUE
      F(2)=FDGAS-SFG*PARM1
C
C     Report Writer: Gas and Particle Turbulence Characteristics
C
      IF(ICALL.EQ.1) THEN
        WRITE(6,350)
        ROUGH=BED(1)*1.D3
        IF(IBED.EQ.0) THEN
          SHAPE='SQUARE  '
        ELSE
          SHAPE='CIRCULAR'
        ENDIF
        WRITE(6,360)BED(8),SHAPE,ROUGH,HYDG(1),TG,PG,AIR(7),AIR(6),
     1  HYDG(9)
        IF(NXP2.GT.0) THEN
          WRITE(6,370)PP(1,1),PP(1,2),PP(1,3),PP(2,3),PP(1,5),
     1  PP(2,5),PP(1,2),PP(2,2),PP(1,4),PP(2,4)
        ELSE
          WRITE(6,365)PP(1,1),PP(1,3),PP(1,5),PP(1,2),PP(1,4)
        ENDIF
        GO TO 380
      ENDIF
 350  FORMAT('CIRCULATING FLUIDISED BED RISER CORE MODEL - CIRCOR'/
     1 '-----------------------------------------------------'//
     2 'SECTION A: INPUT; OPERATING CONDITIONS'/
     3 '-------------------------------------'/)
 360  FORMAT('RISER DIAMETER                    ',F8.3,2X,'M'/
     1 'RISER CROSS SECTION                ',A8/
     2 'WALL ROUGHNESS                     ',F8.1,2X,'MM'/
     3 'NET SOLIDS CIRCULATION RATE        ',F8.0,2X,'KG/M2.S'/
     4 'GAS TEMPERATURE                    ',F8.0,2X,'K'/
     5 'GAS PRESSURE                       ',F8.0,2X,'PA'/
     6 'GAS VISCOSITY                      ',E8.2,2X,'KG/M.S'/
     7 'GAS DENSITY                        ',F8.3,2X,'KG/M3'/
     8 'STREAMER FRACTIONAL WALL COVERAGE',F8.2//)
 365  FORMAT('PARTICLE PROPERTY                    TYPE 1'/
     1 'DENSITY (KG/M3)                  ',F8.0/
     2 'PARTICLE COEFF. RESTITUTION      ',F8.2/
     3 'PARTICLE-WALL COEFF. RESTITUTION',F8.2/
     4 'SPHERICITY                       ',F8.2/
     4 'WALL COEFF. SLIDING FRICTION     ',F8.2/)
 370  FORMAT('PARTICLE PROPERTY                    TYPE 1  TYPE 2'/
     1 'DENSITY (KG/M3)                  ',2F8.0/
     2 'PARTICLE COEFF. RESTITUTION      ',2F8.2/
     3 'PARTICLE-WALL COEFF. RESTITUTION',2F8.2/
     4 'SPHERICITY                       ',2F8.2/
```

```
    4 'WALL COEFF. SLIDING FRICTION    ',2F8.2/)
      IF(ZF.EQ.ZFO) GO TO 650
      IF(Z.NE.ZF) GO TO 650
      IF(ZF.GT.4.0D0) STOP
380   WRITE(6,390) ICALL,Z
390   FORMAT(/1X,'########SYSTEQ CALL NO.  ',I4,3X,'#########'/
    1 1X,'Z = ',F8.4//'SECTION B: RESULTS'/'------------------'//)
      WRITE(6,400)
400   FORMAT('GAS FLOW AND TURBULENCE'
    1 /4X,'U0C',4X,'UZC',4X,'UPF',4X,'UPL',3X,'TAUGF',2X,
    2 'TAUGL',3X,'EG',4X,'PG'/4X,'M/S',4X,'M/S',4X,'M/S',4X,'M/S',
    3 5X,'S',6X,'S',5X,'--',4X,'PA')
      WRITE(6,410)U0C,UZC,UPF,UPL,TAUGF,TAUGL,EG,PG
410   FORMAT(1X,7F7.3,F9.0/)
      WRITE(6,420)
420   FORMAT('PARTICLE-TURBULENCE INTERACTION'/
    1 2X,'XP',3X,'RHOP',4X,'VZC',3X,'TAUP',3X,'TAUR',4X,'EP',
    2 7X,'CT',8X,'FDT',7X,'FKT'/2X,'UM',3X,'KG/M3',3X,'M/S',3X,'S',
    3 7X,'S',7X,'--',6X,'M/S',7X,'N/M3',6X,'N/M3')
      DO 450 I=1,NXP
      XP(I)=XP(I)*1.D3
      WRITE(6,440)XP(I),PP(IXP(I),1),VZC(I),TAUP(I),TAUR(I),EP(I),
    1 CT(I),FDT(I),FKT(I)
440   FORMAT(1X,F5.0,F6.0,F7.3,2F7.3,F9.5,F8.4,2F10.4)
      XP(I)=XP(I)/1.D3
450   CONTINUE
      WRITE(6,460)
460   FORMAT(/'PARTICLE FLUCTUATING ENERGY BALANCE'/
    1 2X,'(i)  PKK',3X,'(ii) SK',4X,'(iii)PKT',3X,
    2 '(iv) DKT'/5X,'KG/MS3',5X,'KG/MS3',5X,'KG/MS3',5X,'KG/MS3')
      DO 480 I=1,NXP
      WRITE(6,470)PKK(I),SK(I),PKT(I),DKT(I)
470   FORMAT(1X,4E11.2)
480   CONTINUE
      WRITE(6,485)
485   FORMAT(/2X,'(v) PKS',3X,'(vi) PKR',3X,'(vii) DKR',3X,
    1 '(viii)DKS',3X,'SUM (i to viii)'/4X,'*PW/AC',5X,'*PW/AC',5X,
    2 '*PW/AC',5X,'*PW/AC'/5X,'KG/MS3',5X,'KG/MS3',5X,'KG/MS3',5X,
    3 'KG/MS3',5X,'KG/MS3')
      DO 495 I=1,NXP
      PKSC=PKS(I)*PARM1
      DKSC=DKS(I)*PARM1
      PKRC=PKR(I)*PARM1
      DKRC=DKR(I)*PARM1
      SUM=PKK(I)+SK(I)+PKT(I)+DKT(I)+PKSC+PKRC+DKRC+DKSC
      WRITE(6,490)PKSC,PKRC,DKRC,DKSC,SUM
490   FORMAT(1X,5E11.2)
495   CONTINUE
      WRITE(6,500)
500   FORMAT(/'PARTICLE AXIAL MOMENTUM BALANCE'/
    1 2X,'VZC',4X,'CK',9X,'FKZ',6X,'FDZ',
    2 7X,'SFS',7X,'SFR',5X,'GRF',6X,'SUM'/38X,'*PW/AC',4X,'*PW/AC'
    3 /2X,'M/S',4X,'M/S',8X,'N/M3',5X,
    4 'N/M3',6X,'N/M3',6X,'N/M3',4X,'N/M3',5X,'N/M3')
      RHOPT=0.D0
      SFSCT=0.D0
      SFRCT=0.D0
      DO 530 I=1,NXP
      RHOPT=RHOPT+EP(I)*PP(IXP(I),1)
      GRF=GA*EP(I)*PP(IXP(I),1)
      SFSC=SFS(I)*PARM1
      SFRC=SFR(I)*PARM1
      SFSCT=SFSCT+SFSC
      SFRCT=SFRCT+SFRC
      SUM=FKZ(I)+FDZ(I)+SFSC+SFRC+GRF
      WRITE(6,510)VZC(I),CK(I),FKZ(I),FDZ(I),SFSC,SFRC,GRF,SUM
510   FORMAT(1X,2F7.4,F10.3,F9.3,2F10.3,F8.3,F8.3)
530   CONTINUE
      SFGC=-SFG*PARM1
      RHOPA=F(2)/GA
      WRITE(6,540)FDGAS,SFGC,SFSCT,SFRCT,RHOPA,RHOPT
540   FORMAT(/'GAS FORCE BALANCE, PARTICLE AND GAS WALL SHEAR,',1X,
```

```
     1 'SUSPENSION DENSITY'/6X,'FDGAS',5X,'SFGC',5X,'SFSCT',4X,'SFRCT'
     2 ,4X,'RHOPA',5X,'RHOPT'/6X,'N/M3',6X,'N/M3',5X,'N/M3',5X,'N/M3',
     3 5X,'KG/M3',5X,'KG/M3'/1X,F12.3,3F9.3,2F10.4/)
       WRITE(6,550)
 550   FORMAT('PARTICLE COLLISION FREQUENCY AND MEAN FREE PATH'/
     1 2X,'XP',6X,'CKT',6X,'Z1T',6X,'Z2T',6X,'FPATH',4X,'VWK'/
     2 2X,'UM',6X,'M/S',6X,'1/S',6X,'1/S',7X,'MM',6X,'--')
       DO 590 I=1,NXP
       XP(I)=XP(I)*1.D3
       FPATH=1.D3*CKT(I)/(Z1T(I)+Z2T(I))
       WRITE(6,580)XP(I),CKT(I),Z1T(I),Z2T(I),FPATH,VWK(I)
 580   FORMAT(1X,F5.0,F9.4,2F9.3,2F9.4)
       XP(I)=XP(I)/1.D3
 590   CONTINUE
C
       IF(ICALL.NE.1) ZFO=ZF
 650   IF(LIMIT.EQ.2) GO TO 880
       GO TO 890
 880   CONTINUE
       WRITE(6,881)IPART
 881   FORMAT(1X,'PARTUR FAILED TO CONVERGE -- CALL NO. ',I6)
       LIMIT=0
 890   IF(ICALL.GE.7000) STOP
       RETURN
       END
C***********WALCON3.1*************************************************
       SUBROUTINE WALCON(VZC,CK,CT,EP,SFS,SFR,PKS,PKR,DKR,DKS,QC,CKT)
C     REVISION  0          OCTOBER 14    1991   AUTHOR:R.C.SENIOR
C     REV 4    OCTOBER 29  1991   REV 6 JAN 05   1992
C
C     INPUT:
C       HYDG(9)  Fractional coverage of the wall by wall streamers.
C                (assumed proportionalto the fraction of particles
C                leaving the core that are captured by streamers.)
C       VZC(I)   Axial particle fraction velocity
C       CT(I)    Particle eddy drift velocity
C       CK(I)    Particle collisional fluctuating velocity
C       EP(I)    Particle volume fraction
C
C     VARIABLES:
C       CKT(I)   Combined particle fluctuating velocity
C       MCOL(I)  Number of collision with core fraction I required to
C                accelerate a mean-sized wall particle.
C
C     OUTPUT:
C       SFS(I)  Shear force on the Ith core fraction due to entraining
C               streamer particles
C       SFR(I)  Shear force due particles rebounding from the wall
C       PKS(I)  Fluctuating k.e. production in core Ith fraction due
C               to interactions with entrained streamer particles
C       DKS(I)  Fluctuating k.e. loss due to wall streamer capture
C       PKR(I)  Fluctuating k.e. production due to wall rebounds
C       DKR(I)  Fluctuating k.e. dissipation due to wall collisions
C       QC(I)   Core-wall mass flowrate for fraction I per unit
C               interfacial area.
C
C     Computes the shear forces and fluctuating kinetic energy
C     production in the core suspension flow due to wall effects.
C     Level 3 model assumption: rate of transfer of particles from
C     wall to core equals the rate of transfer from core to wall.
C*****************************************************************
       IMPLICIT DOUBLE PRECISION(A-H,O-Z)
       PARAMETER (NXP1=9,NXP2=0,NXP=NXP1+NXP2)
       DOUBLE PRECISION MCOL(NXP)
       COMMON/BLKI/HYDG(10)
       COMMON/BLKO/XP(NXP),WP(NXP),IXP(NXP)
       COMMON/BLKP/PP(2,10)
       DIMENSION DKS(NXP),PKS(NXP),DKR(NXP),PKR(NXP),SFS(NXP),SFR(NXP)
       DIMENSION CT(NXP),CK(NXP),VZC(NXP),CKT(NXP),PWT(NXP),PVOL(NXP)
       DIMENSION SIGNUM(NXP),CHIW(NXP),CHIR(NXP),CRWC(NXP),RW(NXP)
```

```
      DIMENSION DVZ(NXP),EP(NXP),DVI(NXP),QC(NXP)
      SAVE PVOL,PWT,PI,CONST,ICALL
      DATA ICALL/0/
      ICALL=ICALL+1
      IF(ICALL.GT.1) GO TO 60
C
C     First call -- evaluate constants
C
      PI=4.D0*DATAN(1.D0)
      CONST=PI**2/64.D0
      DO 40 I=1,NXP
      PVOL(I)=PI*XP(I)**3/6.D9
      PWT(I)=PP(IXP(I),1)*PVOL(I)
 40   CONTINUE

C
C     Mass flux of particles from core to wall, QC(I)
C
 60   QWTOT=0.D0
      DO 80 I=1,NXP
      RHOS=EP(I)*PP(IXP(I),1)
      CKT(I)=DSQRT(CT(I)**2+CK(I)**2)
      QC(I)=RHOS*CKT(I)/4.D0
      QWTOT=QWTOT+QC(I)
 80   CONTINUE
C
C     Mean wall particle properties:
C     1.Sauter mean diameter of core particles, DPW = Sauter mean of
C     streamer particles entering the core (Level 3 model assumption).
C     2. Average coefficient of restitution of the mean returning wall
C     particle, CRW.
C     3. Average density of the mean returning particle, RHOPW
C     4. Wall particle mass, PWW
C
 100  SUM=0.D0
      CRW=0.D0
      VOLSUM=0.D0
      DO 120 I=1,NXP
      VOLSUM=VOLSUM+QC(I)/PP(IXP(I),1)
      SUM=SUM+QC(I)/XP(I)
      CRW=CRW+QC(I)*PP(IXP(I),3)
 120  CONTINUE
      CRW=CRW/QWTOT
      DPW=QWTOT/SUM
      RHOPW=QWTOT/VOLSUM
      PWW=PI*DPW**3*RHOPW/6.D9
C
C     Collision diameters (squared) between mean sized wall particle
C     (DPW) and each core particle fraction times their respective
C     number abundance.
C
      DO 140 I=1,NXP
      SIGMA2=(DPW+XP(I))**2/4.D6
      PN=EP(I)/PVOL(I)
      SIGNUM(I)=SIGMA2*PN
      CRWC(I)=(CRW+PP(IXP(I),3))/2.D0
      RW(I)=PWT(I)*(1.D0+CRWC(I))/(2.D0*(PWW+PWT(I)))
 140  CONTINUE
C
C     Level 3 CFB modelling option A:
C     Particles entering from the wall region come from wall
C     streamers (i.e. wall fully covered by streamers).
C
      SUM=0.D0
      DO 160 I=1,NXP
      MCOL(I)=-3.D0/DLOG10(1.D0-RW(I))
C     MCOL(I)=-2.D0/DLOG10(1.D0-RW(I))
      SUM=SUM+SIGNUM(I)*DABS(VZC(I))/MCOL(I)
 160  CONTINUE
      DO 180 I=1,NXP
      CHIW(I)=SIGNUM(I)*DABS(VZC(I))/(SUM*MCOL(I))
```

```
      SFS(I)=-CHIW(I)*QWTOT*HYDG(9)*VZC(I)
      PKS(I)=HYDG(9)*QWTOT*CHIW(I)*CONST*(1.D0+CRWC(I))*VZC(I)**2/
     1 (2.D0-RW(I))
      DKS(I)=-.5D0*HYDG(9)*QC(I)*CK(I)**2
 180  CONTINUE
C
C     Level 3 CFB modelling option B:
C     Particles entering from the wall region are particles that
C     are rebounding from the bare wall.
C
      SUM=0.D0
      DO 220 I=1,NXP
      DVZ(I)=-PP(IXP(I),4)*(1.D0+PP(IXP(I),5))*CKT(I)/2.D0
      SUM=SUM+(VZC(I)+DVZ(I))*QC(I)
 220  CONTINUE
      VZR=SUM/QWTOT
      SUM=0.D0
      DO 240 I=1,NXP
      DVI(I)=DABS(1.D0-VZR/VZC(I))
      IF(DVI(I).LT.1.D-3) GO TO 240
C     IF(DVI(I).LT.1.D-2) GO TO 240
      MCOL(I)=-(3.D0+DLOG10(DVI(I)))/DLOG10(1.D0-RW(I))
C     MCOL(I)=-(2.D0+DLOG10(DVI(I)))/DLOG10(1.D0-RW(I))
      SUM=SUM+SIGNUM(I)*DABS(VZC(I)-VZR)/MCOL(I)
 240  CONTINUE
      DO 260 I=1,NXP
      IF(DVI(I).LT.2.D-3) THEN
C     IF(DVI(I).LT.2.D-2) THEN
        CHIR(I)=0.D0
      ELSE
        CHIR(I)=SIGNUM(I)*DABS(VZC(I)-VZR)/(SUM*MCOL(I))
      ENDIF
      SFR(I)=-CHIR(I)*QWTOT*(1.D0-HYDG(9))*(VZC(I)-VZR)
      DKR(I)=-QC(I)*(1.D0-HYDG(9))*(1.D0+PP(IXP(I),5))*CKT(I)**2*
     1 (1.D0-PP(IXP(I),5)+2.D0*PP(IXP(I),4)*DABS(CKT(I)/VZC(I)))/8.D0
      PKR(I)=QWTOT*(1.D0-HYDG(9))*CHIR(I)*CONST*(1.D0+CRWC(I))*
     1 (VZC(I)-VZR)**2/(2.D0-RW(I))
 260  CONTINUE
      RETURN
      END
C#################################################################
C  SECTION C: WALL DYNAMICS MODELLING SUBROUTINES
C#################################################################
C*********DIFSTF3.1**(ZUB-ODESYS)*********************************
      SUBROUTINE DIFSTF(NEQ,X,Y,F)
C    REV 0   NOVEMBER 22   1991          AUTHOR: RICHARD C. SENIOR
C     Computes the lateral and vertical particle accelerations for a
C     discrete particle in a gas boundary layer. Routine is
C     called by stiff ODE solver LSODE
C     DIFSTF must be declared EXTERNAL in the main program and
C     subroutines calling LSODE
C
C     Four (=NEQ) first order d.e.'s describing the particle motion.
C     X     time, T
C     Y(1)  vertical velocity, VZ
C     Y(2)  vertical position, ZW
C     Y(3)  lateral velocity, VY
C     Y(4)  lateral position, YW
C*******************************************************************
      IMPLICIT DOUBLE PRECISION(A-H,O-Z)
      COMMON/BLKG/AIR(20),TG,PG
      COMMON/SUBC/DPP,WTP,PSIP,RHOP,USTR,VISK,SX
      COMMON/SUBB/FDZ,FDY,FLFT,TAUP,UZY
      DIMENSION Y(NEQ),F(NEQ)
      SAVE GA,C1,YLOW,ICALL
      DATA GA/-9.81D0/,ICALL/0/,EPS/2.5D-2/
      ICALL=ICALL+1
      IF(ICALL.GT.1) GO TO 100
      PI=4.D0*DATAN(1.D0)
      YLOW=DPP/2.D3*(1.D0-EPS)
      C1=(6.46D-6*DPP**2/4.D0)*DSQRT(AIR(6)*AIR(7))
```

```
 100    IF(Y(4).LT.YLOW) GO TO 50
        TIME=X
        VZ=Y(1)
        ZW=Y(2)
        VY=Y(3)
        YW=Y(4)
        UR=0.D0
        VOID=1.D0
        CALL PROFIL(YW,UZ,DUZ)
        UZY=UZ
        CALL DRAGOP(DPP,PSIP,UZ,UR,VZ,VY,VOID,REP,FDZ,FDY,CD)
        TAUP=4.D-6*DPP**2*RHOP/(3.D0*AIR(7)*REP*CD)
        F(1)=FDZ/WTP+GA
        F(2)=Y(1)
        FLFT=C1*DSQRT(DUZ)*(UZ-VZ)
        F(3)=(FLFT+FDY)/WTP
        F(4)=Y(3)
        LIMIT=0
        RETURN
 50     LIMIT=1
        RETURN
        END
C*************DRAGOP3.1*********************************************
        SUBROUTINE DRAGOP(DP,PSIP,UZ,UR,VZ,VR,VOID,REP,FDZ,FDR,CD)
C     REV 1, MAR    14   1991                AUTHOR: RICHARD C. SENIOR
C     REV 2, MAR    19   1991
C     REV 3, JUN    28   1991
C     REV 4, JUL    24   1991
C     Calculates the axial and transverse components of drag force
C     for a spherical or non-spherical particle in a gas stream under
C     steady flow (i.e no fluctuation in vel. of particle or fluid).
C     Assumes radial velocities UR,VR are in the same angular
C     direction
C     Available drag relationships:
C     (i)  spherical particle: "Bubbles, drops and particles",
C     Clift, Grace, Weber,  p.111-112.
C     (ii) spherical particle: Haider and Levenspiel, Powder Tech.,
C     58, 63-70 (1989) (eq.6).
C     (iii) non-spherical particle: Haider and Levenspiel,
C     Powder Tech., 58, 63-70 (1989) (eq.12).
C     Drag voidage dependency: Gibilaro, DiFelice, Weldram, Foscolo;
C     Chem. Eng. Sci. 40, pp1817, (1985).
C
C     Note: The Haider and Levenspiel correlation for non-spherical
C     particles uses the 'volume particle diameter' dv, rather than
C     the 'surface/volume' dsv. If the particle diameter DP in the
C     calling routine is defined as the Sauter diameter, and the
C     particle is not spherical, then the conversion:
C     DP (vol, i.e. 'dv') = DP ('dsv' or Sauter) / PSIP,
C     where PSIP is the particle sphericity, should be made before
C     calling this routine DRAGOP.
C     Projected particle area for non-spherical particles is
C     calculated based on the volume diameter.
C
C     Input:   DP      Particle dia. ,mm
C              UZ      Gas interstitial axial velocity ,m/s
C              UR      Gas interstitial transverse velocity,m/s
C              VZ      Particle axial velocity ,m/s
C              VR      Particle transverse velocity,m/s
C              VOID    Voidage,m**3/m**3
C              AIR(6)  Gas density kg/m**3 (common block)
C              AIR(7)  Gas viscosity kg/m.s(common block)
C              PSIP    Particle sphericity
C     Output   REP   Particle Reynolds number (based on DP)
C              FDZ   Axial component of drag force,kg.m/s**2
C              FDR   Transverse component of drag force,kg.m/s**2
C              CD    Drag coefficient
C*****************************************************************
       IMPLICIT DOUBLE PRECISION(A-H,O-Z)
```

```
      COMMON/BLKG/AIR(20),TG,PG
      PI=4.D0*DATAN(1.D0)
C
C     Particle Reynolds number
C
      DUV=DSQRT((UZ-VZ)**2+(UR-VR)**2)
      REP=DUV*AIR(6)*DP*1.D-3/AIR(7)
C
C     Drag coefficient - spherical particle
C
      IF(PSIP.LT.0.98D0) GO TO 100
C     Clift and Gauvin correlation
      CD=24.D0/REP*(1.D0+.15D0*REP**.687D0)+.42D0/(1.D0+4.25D4/
     1 REP**1.16D0)
C     Haider and Levenspiel
C     CD=24.D0/REP*(1.D0+.1806D0*REP**.6459D0)+.4251D0/(1.D0+
C    1 6880.95D0/REP)
      GO TO 200
C
C     Non-spherical particle
C     Haider and Levenspiel (eq.12)
C100  CD=24.D0/REP*(1.D0+8.1716D0*DEXP(-4.0655D0*PSIP)*
C    1 REP**(0.0964D0+0.5565D0*PSIP))+73.69D0*REP*
C    2 DEXP(-5.0748D0*PSIP)/(REP+5.378D0*DEXP(6.2122D0*PSIP))
C     Haider and Levenspiel (eq.11)
 100  C1=DEXP(2.3288D0-6.4581D0*PSIP+2.4486D0*PSIP*PSIP)
      C2=0.0964D0+.5565D0*PSIP
      C3=DEXP(4.905D0-13.8944D0*PSIP+18.4222D0*PSIP**2-10.2599D0*
     1 PSIP**3.D0)
      C4=DEXP(1.4681D0+12.2584D0*PSIP-20.7322D0*PSIP**2+15.8855D0*
     1 PSIP**3.D0)
      CD=24.D0/REP*(1.D0+C1*REP**C2)+C3/(1.D0+C4/REP)
C
C     Single particle drag force
C
 200  DPC=DP
      FDZ=CD*DUV*(UZ-VZ)*AIR(6)*PI*DPC**2*1.D-6/(8.D0*VOID**1.8D0)
      FDR=CD*DUV*(UR-VR)*AIR(6)*PI*DPC**2*1.D-6/(8.D0*VOID**1.8D0)
      RETURN
      END
C***********PROFIL3.1*************************************************
      SUBROUTINE PROFIL(YW,UZ,DUZ)
C     REVISION  0          NOVEMBER 22   1991   AUTHOR:R.C.SENIOR
C     REV 2   DEC 31  1991
C     Calculates the vertical gas velocity UZ and velocity gradient
C     DUZ at a given distance YW from a vertical flat wall using Law
C     of the Wall relationships.
C
C     INPUT:      USTR   Gas friction velocity, m/s
C                 VISK   Kimeatic gas viscosity, m2/s
C                 YW     Distance from the wall in 'y' lateral
C                        direction, mm
C
C     VARIABLES: YPLS    Dimensionless distance from the wall
C
C     OUTPUT:     UZ     Gas velocity, m/s
C                 DUZ    Gas velocity dradient (d UZ/ d Y), m/s2
C*********************************************************************
      IMPLICIT DOUBLE PRECISION(A-H,O-Z)
      COMMON/SUBC/DPP,WTP,PSIP,RHOP,USTR,VISK,SX
      YPLS=YW*USTR/VISK
      IF(YPLS.LE.5.D0) THEN
        UZ=SX*USTR*YPLS
        DUZ=SX*USTR**2/VISK
        RETURN
      ENDIF
      IF(YPLS.GT.30.D0) THEN
        UZ=SX*USTR*(5.5D0+2.5D0*DLOG(YPLS))
        DUZ=SX*2.5D0*USTR/YW
        RETURN
      ENDIF
```

```
      UZ=SX*USTR*(-3.05D0+5.D0*DLOG(YPLS))
      DUZ=SX*5.D0*USTR/YW
      RETURN
      END
```

E.6 Numerical Methods Routine Listings

```
C*******ZUB.FOR*****************************************************
C
C     Composite file of general numerical routines.
C     Compiled version: ZUB.EXE
C
C     Rev. 0  May 16, 1991.
C     Rev. 1  Nov 16, 1991. Rev. 2  Nov 26, 1991.
C*********************************************************************
C     ROUTINE REV     OTHER REQUIRED ROUTINES          REAL*8? TEST
C                      NUMERICAL         SPECIFIC               PROG?
C                                                               (MAIN)
C     ------- ---     ---------         --------       -------------
C     DLSODE                              --            YES     NO
C     DGAUSS   0          --              --            YES     NO
C     LENSTR   0          --              --            NO      NO
C     ODERKF   3     FHLBRG, ODESYS       --            YES     NO
C
C     ROUTINE DESCRIPTION:
C
C     DLSODE       Solution of a stiff system of initial value O.D.E.'s
C                  by Gears method.
C     ZUB-DGAUSS   Simultaneous linear equations - Gauss elimination
C                  with scaled partial pivotting
C     ZUB-LENSTR   Number of characters in a string excluding trailing
C                  blanks
C     ZUB-ODERKF   Simultaneous O.D.E.solution by Runge-Kutta Fehlberg
C                  method.
C*********************************************************************
C     ************ZUB-DGAUSS*****************************************
C     REVISION 0                                AUTHOR:R.C.SENIOR
C
      SUBROUTINE DGAUSS(A,N,NDR,NDC,X,RNORM,IERROR)
C
C     Purpose:
C          Uses Gauss elimination with scaled partial pivot
C          selection to solve simultaneous linear equations of
C          the form (A)*(X)=(C)
C     Arguments:
C          A  Augmented coefficient matrix containing all coefficients
C             and R.H.S. constants of equations to be solved.
C          N  Number of equations to be solved.
C        NDR  First (row) dimension of A in calling program.
C        NDC  Second (column) dimension of A in calling program.
C          X  Solution vector.
C      RNORM  Measure of size of residual vector (c)-(a)*(x)
C     IERROR  Error flag.
C             =1 Successful Gauss elimination.
C             =2 Zero diagonal entry after pivot selection.
C
      IMPLICIT DOUBLE PRECISION(A-H,O-Z)
      DIMENSION A(NDR,NDC),X(N),B(50,51),DELTA(50)
      NM=N-1
      NP=N+1
C
C     Set up working matrix B
C
      DO 20 I=1,N
      DO 10 J=1,NP
      B(I,J)=A(I,J)
 10   CONTINUE
 20   CONTINUE
```

```
C
C     Carry out elimination process N-1 times
C
      DO 80 K=1,NM
      KP=K+1
C
C     Search for largest coefficient in each row,for rows K
C     through N,and columns K through N.Then scale column K.
C
      DO 32 I=K,N
      BIG=DABS(B(I,K))
      DO 30 J=KP,N
      AB=DABS(B(I,J))
      IF(AB.LE.BIG) GO TO 30
      BIG=AB
 30   CONTINUE
      DELTA(I)=B(I,K)/BIG
 32   CONTINUE
C
C     Determine largest scaled coefficient in column K,for rows
C     K through N
C     IPIVOT is the row index of the largest scaled  coefficient
C
      BIG=DABS(DELTA(K))
      IPIVOT=K
      DO 34 I=KP,N
      AB=DABS(DELTA(I))
      IF(AB.LE.BIG) GO TO 34
      BIG=AB
      IPIVOT=I
 34   CONTINUE
C
C     Interchange rows K and IPIVOT if IPIVOT.NE.K
C
      IF(IPIVOT.EQ.K) GO TO 50
      DO 40 J=K,NP
      TEMP=B(IPIVOT,J)
      B(IPIVOT,J)=B(K,J)
      B(K,J)=TEMP
 40   CONTINUE
 50   IF(B(K,K).EQ.0.) GO TO 130
C
C     Eliminate B(I,K) from rows K+1 through N
C
      DO 70 I=KP,N
      QUOT=B(I,K)/B(K,K)
      B(I,K)=0.
      DO 60 J=KP,NP
      B(I,J)=B(I,J)-QUOT*B(K,J)
 60   CONTINUE
 70   CONTINUE
 80   CONTINUE
C
      IF(B(N,N).EQ.0.) GO TO 130
C
C     Back substitute to find solution vector
C
      X(N)=B(N,NP)/B(N,N)
      DO 100 II=1,NM
      SUM=0.
      I=N-II
      IP=I+1
      DO 90 J=IP,N
      SUM=SUM+B(I,J)*X(J)
 90   CONTINUE
      X(I)=(B(I,NP)-SUM)/B(I,I)
 100  CONTINUE
C
C     Calculate norm of residual vector, C-A*X
C     Normal return with IERROR=1
C
      RSQ=0.
```

```
      DO 120 I=1,N
      SUM=0.
      DO 110 J=1,N
      SUM=SUM+A(I,J)*X(J)
 110  CONTINUE
      RSQ=RSQ+(A(I,NP)-SUM)**2
 120  CONTINUE
      RNORM=DSQRT(RSQ)
      IERROR=1
      RETURN
C
C     Abnormal return because of zero entry on diagonal, IERROR=2
C
 130  IERROR=2
      RETURN
      END
C**********ODERKF.FOR******(contained in composite file ZUB.FOR*******
      SUBROUTINE ODERKF(ODESYS,A,B,YA,F,EPS,HSTART,HMIN,HMAX,YB,
     1 NFUN,FLAG,M,NGT,NLT,LGT,LLT,LB,YNEW,YOLD,YMAX,YMIN)
C     REV 3   MAY    25  1989            AUTHOR:R.C.SENIOR
C     REV 4   OCT 18 1991 (corrected error in LIMIT=1 return handling)
C     REV 5   NOV 22  1991
C
C     Genral routine which supervises numerical solution of M
C     simultaneous inital value ordinary differential equations by a
C     Runge-Kutta Fehlberg (RKF) method.The RKF method advances the DE
C     solution by a fifth order Runge-Kutta (RK) formula,and compares
C     fourth and fifth order RK computations to estimate the error.
C     ODERKF iteratively adjusts the independent variable (X)
C     increment for each RK computation to maintain the solution
C     within error tolerance,set by EPS
C
C     The ODE derivatives,specific to the user's sytem,must be
C     supplied by the user in a routine recognised by ODERKF as
C     ODESYS (use EXTERNAL declarator)
C     The ODE solution may be terminated when either B is reached or
C     one of the Y(I) values exceeds preset limits.
C
C     INPUTS  ODESYS R.h.s. routine - evaluates system derivatives
C             A      Initial independent variable
C             YA(I)  Array of dependent variable initial conditions
C             EPS    Accuracy parameter,ABS(YB(I)-YB(I)exact).LT.EPS
C             HSTART Starting step size (typically 1/10 (A:B))
C             HMIN   Minimum step size  (typically 1.D-4*(A:B))
C             HMAX   Maximum step size  (typically (A:B))
C             M      Number of variables (=eqautions)
C             LB  =1 Solution ceases at B if constraint not reached
C                    first
C             LB  =0 Solution continues until constraint reached
C             NGT    No. of dependent variable upper limit contraints
C             NLT    No. of dependent variable lower limit contraints
C             LGT(I) Variable no. to which upper constraint/s apply
C             LLT(I) Variable no. to which lower constraint/s apply
C             YMAX(I)Dependent variable upper limit constraint.
C             YMIN(I)Dependent variable lower limit constraint.
C
C     INPUT/OUTPUT (as defined in constraints):
C             B      Final indepebdent variable value
C
C     OUTPUT: NFUN   Number of calls to ODESYS*M
C             YB(I)  Array of final dependent variable values.
C             FLAG=0 Unable to satisfy accuracy requirement with
C                    given step size,HMIN ; error return
C                 =1 Solution terminates at B ; successful return
C                 =2 Constraint set beyond limit for which a r.h.s.
C                    is defined in ODESYS ; error return
C                 =3 Solution terminates at an independent variable
C                    constraint ; successful return
C*********************************************************************
      IMPLICIT DOUBLE PRECISION(A-H,O-Z)
```

```
      INTEGER FLAG
      DIMENSION YA(M),YB(M),YOLD(M),YNEW(M),F(M),LGT(M),LLT(M)
      DIMENSION YMAX(M),YMIN(M)
      EXTERNAL ODESYS
C
C     Initialize
C
      HOLD=HSTART
      X=A
      DO 20 I=1,M
      YOLD(I)=YA(I)
 20   CONTINUE
      NFUN=0
C
C     Check limiting variable flags
C
      NT=NGT+NLT
      IF(LB.NE.0.AND.LB.NE.1) GO TO 25
      IF(NGT.EQ.0.AND.NLT.EQ.0) GO TO 27
      IF(NT.GT.M) GO TO 25
      GO TO 30
 25   NLT=0
      NGT=0
 27   LB=1
C
 30   NFUN=NFUN+6*M
      CALL FHLBRG(ODESYS,F,X,YOLD,HOLD,YNEW,YDIFF,M,LIMIT)
 40   IF(LIMIT.EQ.1) THEN
        HNEW=HOLD/10.D0
        IF(HNEW.LT.HMIN) GO TO 120
        HOLD=HNEW
        GO TO 30
      ENDIF
      IF(YDIFF.EQ.0.D0) THEN
        HNEW=5.D0*HOLD
        GO TO 42
      ENDIF
      GAMMA=(EPS*HOLD/(YDIFF*(B-A)))**.25D0
      HNEW=.8D0*GAMMA*HOLD
      IF(GAMMA.GE.1.D0) GO TO 41
      IF(HNEW.LT.HOLD/10.D0) HNEW=HOLD/10.D0
      IF(HNEW.LT.HMIN) GO TO 80
      HOLD=HNEW
      GO TO 30
 41   IF(HNEW.GT.5.D0*HOLD) HNEW=5.D0*HOLD
 42   IF(HNEW.GT.HMAX) HNEW=HMAX
      BETA=0.D0
      KL=0
      IF(NGT.EQ.0) GO TO 50
      DO 45 I=1,NGT
      IF(YNEW(LGT(I)).GT.YMAX(LGT(I))) THEN
        ALPHA=DABS(.5D0*(YNEW(LGT(I))-YMAX(LGT(I)))/(YNEW(LGT(I))+
     1  YMAX(LGT(I))))
        IF(ALPHA.GT.BETA) THEN
          BETA=ALPHA
          KL=LGT(I)
          YB(KL)=YMAX(KL)
        ENDIF
      ENDIF
 45   CONTINUE
 50   IF(NLT.EQ.0) GO TO 58
      DO 55 I=1,NLT
      IF(YNEW(LLT(I)).LT.YMIN(LLT(I))) THEN
        ALPHA=DABS(.5D0*(YNEW(LLT(I))-YMIN(LLT(I)))/(YNEW(LLT(I))+
     1  YMIN(LLT(I))))
        IF(ALPHA.GT.BETA) THEN
          BETA=ALPHA
          KL=LLT(I)
          YB(KL)=YMIN(KL)
        ENDIF
      ENDIF
 55   CONTINUE
```

```
 58     IF(KL.EQ.0) GO TO 60
        FEPS=EPS/10.D0
        IF(BETA.LT.FEPS) GO TO 130
        HOLD=HOLD*(YOLD(KL)-YB(KL))/(YOLD(KL)-YNEW(KL))*(1.D0+EPS*.1D0)
        GO TO 30
 60     IF(LB.EQ.1.AND.X+HOLD.GE.B) GO TO 100
        X=X+HOLD
        HOLD=HNEW
        DO 70 I=1,M
        YOLD(I)=YNEW(I)
 70     CONTINUE
        GO TO 30
C
 80     FLAG=0
        B=X
        DO 90 I=1,M
        YB(I)=YOLD(I)
 90     CONTINUE
        RETURN
C
 100    FLAG=1
        HSTART=HNEW
        HOLD=B-X
        NFUN=NFUN+6*M
        CALL FHLBRG(ODESYS,F,X,YOLD,HOLD,YNEW,YDIFF,M,LIMIT)
        GO TO 150
 120    FLAG=2
        B=X
        GO TO 150
 130    FLAG=3
        B=X+HOLD
C
 150    DO 180 I=1,M
        YB(I)=YNEW(I)
 180    CONTINUE
        RETURN
        END
C*********************************************************************
        SUBROUTINE FHLBRG(ODESYS,F,X,Y,H,Y1,YDIFF,M,LIMIT)
C     REV 0   MAY    25  1989          AUTHOR:R.C.SENIOR
C     REV 1   OCT  18  1991 (LIMIT=1 test to reduce uneccessary calls)
C*********************************************************************
        IMPLICIT DOUBLE PRECISION(A-H,K,O-Z)
        PARAMETER (NXP1=9,NXP2=0,NXP=NXP1+NXP2,MX=2+3*NXP)
        DIMENSION Y(M),Y1(M),F(M),K(6,MX),C(6,6)
        EXTERNAL ODESYS
        DATA C(2,1),C(2,2)/.25D0,.25D0/
        DATA C(3,1),C(3,2),C(3,3)/.375D0,.09375D0,.28125D0/
        DATA C(4,1),C(4,2)/.92307692307692307 3D0,.87938097405553025 7D0/
        DATA C(4,3)/-3.27719617660446061D0/
        DATA C(4,4)/3.32089212562585323D0/
        DATA C(5,1)/1.D0/
        DATA C(5,2),C(5,3)/2.03240740740740722D0,-8.D0/
        DATA C(5,4),C(5,5)/7.17348927875243647D0,-.20589668615984405D0/
        DATA C(6,1),C(6,2)/.5D0,-.29629629629629629 4D0/
        DATA C(6,3),C(6,4)/2.D0,-1.38167641325536 05D0/
        DATA C(6,5),C(6,6)/.45297270955165691 6D0,-.275D0/
        DATA C71,C72/.11851851851851850 9D0,.51898635477582845 4D0/
        DATA C73,C74/.50613149034201665 4D0,-.18D0/
        DATA C75,C81/.03636363636363636 36D0,.00277777777777777778D0/
        DATA C82,C83/-.02994152046783625 68D0,-.02919989367357788 38D0/
        DATA C84,C85/.02D0,.03636363636363636 36D0/
        YDIFF=0.D0
        CALL ODESYS(X,Y,F,LIMIT)
        DO 10 J=1,M
        K(1,J)=H*F(J)
 10     CONTINUE
        DO 100 I=2,6
        XF=X+C(I,1)*H
        DO 30 J=1,M
        Y1(J)=Y(J)
        DO 20 II=2,I
```

```
      L=II-1
      Y1(J)=Y1(J)+C(I,II)*K(L,J)
 20   CONTINUE
 30   CONTINUE
      CALL ODESYS(XF,Y1,F,LIMIT)
      IF(LIMIT.EQ.1) RETURN
      DO 40 J=1,M
      K(I,J)=H*F(J)
 40   CONTINUE
 100  CONTINUE
      DO 110 J=1,M
      Y1(J)=Y(J)+C71*K(1,J)+C72*K(3,J)+C73*K(4,J)+C74*K(5,J)+
     1 C75*K(6,J)
      YD=DABS(C81*K(1,J)+C82*K(3,J)+C83*K(4,J)+C84*K(5,J)+C85*K(6,J))
      IF(YD.GT.YDIFF) YDIFF=YD
 110  CONTINUE
      RETURN
      END
C************ZUB-LENSTR*********************************************
      INTEGER FUNCTION LENSTR(STRING)
C     Determines length of a character string excluding end blanks
C     Input:  STRING   String whose length is to be determined
C     REV 0   DEC 1988
C*******************************************************************
      CHARACTER*(*) STRING
      CHARACTER*1 BLANK
      PARAMETER(BLANK=' ')
      INTEGER NEXT
C
C     Start with the last character and find the first non-blank
C
      NC=LEN(STRING)
      DO 10 NEXT=NC,1,-1
      IF(STRING(NEXT:NEXT).NE.BLANK) THEN
        LENSTR=NEXT
        RETURN
      ENDIF
 10   CONTINUE
      GETLEN=0
      RETURN
      END
```

Appendix F

Riser Core Model CIRCOR Output: Interpretation and Results

The discussion of the riser core model output in Chapter 8 contains selected results drawn from a large number of model simulations. This appendix contains complete model outputs for the following cases:

(a) A variation of parametric test base case (i) (G_s = 20 kg/m^{2}s, U_g = 7 m/s), with 5 wt% type 2 particles (see also corresponding G_s = 60 kg/m^{2}s, case (ii), discussed in Section 8.15.1);

(b) A simulation of the Nakamura and Capes (1976) glass bead test for U_g = 16.2 m/s and G_s = 24 kg/m^{2}s;

(c) The condition 3C cold unit test simulation for bimodal PSD particles;

(d) Simulations of an FCC riser operation with and without allowance for gas turbulence.

Outputs for cases (a)–(d) are representative of the different simulations performed in this study. The parametric study base cases for G_s = 20 and G_s = 60 kg/m^{2}s, described as cases "(i)" and "(ii)" in Chapter 8, were the same as case (a) above and the G_s = 60 kg/m^{2}s case discussed in the Chapter 8 section on model interpretation, respectively, except that the PSD was discretised in the parametric study into 9 fractions, rather than 5, and only type (i) particles were assumed.

In addition to sample model outputs, several tables of data are presented below, upon which some of the general discussion in section 8.15.4 is based. A list of definitions for the symbols in the model output is given in Table 8.3.

F.1 CIRCOR Riser Core Model Sample Outputs

F.1.1 Output (a): Fully-developed Flow for Typical Conditions in a Pilot-Scale Cold Unit Riser, $G_s = 20$ kg/m^{2}s

```
CIRCULATING FLUIDISED BED RISER CORE MODEL - CIRCOR
---------------------------------------------------
SECTION A: INPUT; OPERATING CONDITIONS
--------------------------------------
RISER DIAMETER                      0.152  M       PARTICLE PROPERTY                TYPE 1  TYPE 2
RISER CROSS SECTION              CIRCULAR          DENSITY (KG/M3)                  2700.   1400.
WALL ROUGHNESS                       2.5  MM      PARTICLE COEFF. RESTITUTION       0.90    0.70
NET SOLIDS CIRCULATION RATE          20.  KG/M2.S PARTICLE-WALL COEFF. RESTITUTION  0.80    0.75
GAS TEMPERATURE                     298.  K       SPHERICITY                        0.95    0.75
GAS PRESSURE                     101325.  PA      WALL COEFF. SLIDING FRICTION      0.58    0.58
GAS VISCOSITY                   0.18E-04  KG/M.S
GAS DENSITY                        1.187  KG/M3
STREAMER FRACTIONAL WALL COVERAGE 0.00
WALL REGION THICKNESS               0.00  MM

SECTION B: RESULTS
------------------
GAS FLOW AND TURBULENCE
    UOC    UZC    UPF    UPL   TAUGF  TAUGL   EG     PG
    M/S    M/S    M/S    M/S     S      S     --     PA
   6.998  7.008  0.728  0.708  0.064  0.065  0.999  101325.

PARTICLE-TURBULENCE INTERACTION
  XP    RHOP    VZC   TAUP   TAUR    EP       CT       FDT      FKT
  UM    KG/M3   M/S    S      S      --       M/S      N/M3     N/M3
  133.  2700.  5.775  0.080  0.014  0.00024  0.0539   5.4021  -0.1279
  188.  2700.  5.542  0.134  0.011  0.00025  0.0294   3.4734   0.0770
  219.  2700.  5.430  0.168  0.011  0.00026  0.0224   2.8539   0.1213
  259.  2700.  5.301  0.213  0.010  0.00027  0.0169   2.3258   0.1553
  343.  2700.  5.108  0.316  0.009  0.00028  0.0108   1.6424   0.1855
   40.  1400.  6.779  0.005  0.065  0.00003  0.5920   0.7877  -0.4130
  250.  1400.  5.672  0.096  0.013  0.00006  0.0427   0.6113  -0.0064
 2000.  1400.  4.300  0.789  0.006  0.00004  0.0032   0.0521   0.0082

PARTICLE FLUCTUATING ENERGY BALANCE
(i) PKK    (ii) SK    (iii)PKT   (iv) DKT  (v) PKS    (vi) PKR   (vii) DKR  (viii)DKS  SUM (i
   KG/MS3     KG/MS3     KG/MS3     KG/MS3   *PW/AC     *PW/AC     *PW/AC     *PW/AC    to viii)
                                            KG/MS3     KG/MS3     KG/MS3     KG/MS3     KG/MS3
  0.75E+00   0.23E-02  0.28E+00  -0.11E+01  0.00E+00  0.67E-01  -0.13E-01  0.00E+00  -0.18E-02
  0.21E+00  -0.73E-02  0.10E+00  -0.32E+00  0.00E+00  0.11E-01  -0.41E-02  0.00E+00  -0.96E-03
  0.11E+00  -0.29E-02  0.66E-01  -0.18E+00  0.00E+00  0.15E-02  -0.23E-02  0.00E+00  -0.74E-03
  0.79E-01  -0.25E-02  0.42E-01  -0.12E+00  0.00E+00  0.95E-04  -0.17E-02  0.00E+00  -0.77E-03
  0.84E-01  -0.84E-02  0.20E-01  -0.11E+00  0.00E+00  0.15E-01  -0.27E-02  0.00E+00  -0.16E-02
  0.46E+00  -0.14E-03  0.12E+00  -0.63E+00  0.00E+00  0.49E-01  -0.57E-02  0.00E+00  -0.78E-04
  0.56E-01  -0.94E-02  0.26E-01  -0.78E-01  0.00E+00  0.60E-02  -0.10E-02  0.00E+00  -0.14E-03
  0.44E-03  -0.62E-04  0.19E-03  -0.14E-01  0.00E+00  0.16E-01  -0.27E-02  0.00E+00   0.41E-04

PARTICLE AXIAL MOMENTUM BALANCE
 VZC     CK        FKZ      FDZ       SFS       SFR      GRF      SUM
                                     *PW/AC    *PW/AC
 M/S     M/S       N/M3     N/M3      N/M3      N/M3     N/M3     N/M3
 5.7746  0.3641   -2.832   10.196     0.000    -0.893   -6.456   0.016
 5.5421  0.2499   -0.499    7.509     0.000    -0.267   -6.726   0.017
 5.4295  0.2066    0.380    6.576     0.000    -0.072   -6.866   0.018
 5.3007  0.1873    1.289    5.750     0.000     0.013   -7.033   0.018
 5.1078  0.2152    2.574    4.479     0.000     0.264   -7.298   0.020
 6.7793  0.3038   -0.952    1.560     0.000    -0.246   -0.362   0.000
 5.6721  0.2912   -0.268    1.228     0.000    -0.094   -0.865   0.002
 4.3001  0.4412    0.308    0.200     0.000     0.064   -0.570   0.002

GAS FORCE BALANCE, PARTICLE AND GAS WALL SHEAR, SUSPENSION DENSITY
      FDGAS     SFGC     SFSCT    SFRCT    RHOPA    RHOPT
      N/M3      N/M3     N/M3     N/M3     KG/M3    KG/M3
```

```
      -37.499   -8.618    0.000   -1.231    4.7011    3.6876

PARTICLE COLLISION FREQUENCY, MEAN FREE PATH AND MASS FRACTIONS
  XP      CKT       Z1T       Z2T      FPATH     VWK    FEED    CORE    WALL
  UM      M/S       1/S       1/S       MM       --     WT%     WT%     WT%
  133.   0.3681    29.287     5.374  10.6194   0.4645  19.00   17.85   26.01
  188.   0.2516    53.555     8.046   4.0841   0.5000  19.00   18.59   18.52
  219.   0.2078    73.862     7.336   2.5588   0.5000  19.00   18.98   15.61
  259.   0.1881   107.395     5.439   1.6669   0.5000  19.00   19.44   14.48
  343.   0.2154   201.775     3.037   1.0519   0.5000  19.00   20.17   17.21
   40.   0.6654    20.105     0.782  31.8555   0.1092   1.25    1.00    2.63
  250.   0.2944    81.419    14.330   3.0742   0.5000   2.50    2.39    2.79
 2000.   0.4413  8502.825     0.610   0.0519   0.5000   1.25    1.58    2.75
```

F.1.2 Output (b): Simulation of Nakamura and Capes (1976) Pneumatic Conveying Glass Bead Experiment; $G_s = 20$ kg/m^{2}s, $U_g = 16$ m/s.

```
CIRCULATING FLUIDISED BED RISER CORE MODEL - CIRCOR
---------------------------------------------------
SECTION A: INPUT; OPERATING CONDITIONS
--------------------------------------

RISER DIAMETER                    0.076  M       PARTICLE PROPERTY                TYPE 1
RISER CROSS SECTION            CIRCULAR          DENSITY (KG/M3)                  2900.
WALL ROUGHNESS                      0.5  MM      PARTICLE COEFF. RESTITUTION       0.90
NET SOLIDS CIRCULATION RATE         24.  KG/M2.S PARTICLE-WALL COEFF. RESTITUTION  0.80
GAS TEMPERATURE                    298.  K       SPHERICITY                        0.95
GAS PRESSURE                    101325.  PA      WALL COEFF. SLIDING FRICTION      0.58
GAS VISCOSITY                  0.18E-04  KG/M.S
GAS DENSITY                       1.187  KG/M3
STREAMER FRACTIONAL WALL COVERAGE 0.00

SECTION B: RESULTS
------------------
GAS FLOW AND TURBULENCE
    UOC    UZC    UPF    UPL   TAUGF  TAUGL   EG    PG
    M/S    M/S    M/S    M/S     S      S     --    PA
  16.201 16.252  1.468  1.468  0.016  0.016  0.997  101325.

PARTICLE-TURBULENCE INTERACTION
  XP   RHOP    VZC   TAUP   TAUR    EP       CT       FDT      FKT
  UM   KG/M3   M/S   S      S       --       M/S      N/M3     N/M3
 1080. 2900.  3.413  0.570  0.001  0.00079  0.0008   5.9211  -0.0049
 2900. 2900.  2.454  1.744  0.001  0.00232  0.0003   5.6912   0.0049

PARTICLE FLUCTUATING ENERGY BALANCE
(i)  PKK    (ii) SK    (iii)PKT    (iv) DKT  (v) PKS    (vi) PKR   (vii) DKR  (viii)DKS   SUM (i
                                              *PW/AC     *PW/AC     *PW/AC     *PW/AC     to viii)
   KG/MS3     KG/MS3     KG/MS3     KG/MS3    KG/MS3     KG/MS3     KG/MS3     KG/MS3      KG/MS3
  0.37E+01  -0.12E+00  0.49E-02  -0.35E+01  0.00E+00   0.27E+01  -0.28E+01  0.00E+00  -0.32E-02
  0.19E+00  -0.29E-01  0.15E-02  -0.27E+00  0.00E+00   0.22E+00  -0.12E+00  0.00E+00   0.15E-02

PARTICLE AXIAL MOMENTUM BALANCE
  VZC     CK        FKZ       FDZ       SFS       SFR      GRF      SUM
                                        *PW/AC    *PW/AC
  M/S     M/S       N/M3      N/M3      N/M3      N/M3     N/M3     N/M3
  3.4127 0.9327    -8.083    51.812     0.000   -21.207  -22.42   0.099
  2.4542 0.2639     8.083    53.497     0.000     4.577  -65.95   0.203

GAS FORCE BALANCE, PARTICLE AND GAS WALL SHEAR, SUSPENSION DENSITY
      FDGAS     SFGC     SFSCT    SFRCT    RHOPA    RHOPT
      N/M3      N/M3     N/M3     N/M3     KG/M3    KG/M3
    -105.309  -69.949    0.000  -16.631   17.8652   9.0088

PARTICLE COLLISION FREQUENCY AND MEAN FREE PATH
  XP      CKT       Z1T       Z2T      FPATH     VWK
  UM      M/S       1/S       1/S       MM       --
 1080.   0.9327    2.370     3.126  169.7039   0.4388
```

2900.	0.2639	15.600	3.888	13.5420	0.5000

F.1.3 Output (c): Condition 3*C* Cold Unit Test Simulation for Bimodal PSD Particles; $G_s = 60$ kg/m^{2}s, $U_g = 6.5$ m/s.

```
CIRCULATING FLUIDISED BED RISER CORE MODEL - CIRCOR
---------------------------------------------------
SECTION A: INPUT; OPERATING CONDITIONS
--------------------------------------

RISER DIAMETER                    0.152  M       PARTICLE PROPERTY                TYPE 1
RISER CROSS SECTION            CIRCULAR          DENSITY (KG/M3)                  2700.
WALL ROUGHNESS                     1.0  MM      PARTICLE COEFF. RESTITUTION       0.90
NET SOLIDS CIRCULATION RATE         60.  KG/M2.S PARTICLE-WALL COEFF. RESTITUTION 0.80
GAS TEMPERATURE                    298.  K       SPHERICITY                       0.95
GAS PRESSURE                    101325.  PA      WALL COEFF. SLIDING FRICTION      0.58
GAS VISCOSITY                  0.18E-04  KG/M.S
GAS DENSITY                       1.187  KG/M3
STREAMER FRACTIONAL WALL COVERAGE 0.30

SECTION B: RESULTS
------------------
GAS FLOW AND TURBULENCE
    UOC    UZC    UPF    UPL   TAUGF  TAUGL   EG    PG
    M/S    M/S    M/S    M/S     S      S     --    PA
   7.342  7.392  0.842  0.788  0.053  0.057  0.993  101325.

PARTICLE-TURBULENCE INTERACTION
  XP   RHOP    VZC   TAUP   TAUR    EP       CT       FDT      FKT
  UM   KG/M3   M/S    S      S      --       M/S      N/M3     N/M3
  114. 2700.  4.943  0.050  0.007  0.00070  0.0432   28.4531  -3.7611
  141. 2700.  4.837  0.070  0.006  0.00071  0.0323   21.2137  -1.4778
  160. 2700.  4.781  0.084  0.006  0.00072  0.0273   17.7888  -0.5295
  194. 2700.  4.697  0.113  0.006  0.00074  0.0211   13.6414   0.3897
  365. 2700.  4.451  0.286  0.006  0.00078  0.0091    5.7876   1.1378
  403. 2700.  4.419  0.329  0.005  0.00078  0.0080    5.0725   1.1207
  440. 2700.  4.390  0.373  0.005  0.00079  0.0071    4.5005   1.0924
  478. 2700.  4.364  0.419  0.005  0.00079  0.0063    4.0347   1.0584
  570. 2700.  4.308  0.537  0.005  0.00080  0.0050    3.1972   0.9694

PARTICLE FLUCTUATING ENERGY BALANCE
(i) PKK    (ii) SK    (iii)PKT   (iv) DKT  (v) PKS    (vi) PKR   (vii) DKR  (viii)DKS   SUM (i
   KG/MS3     KG/MS3     KG/MS3     KG/MS3   *PW/AC     *PW/AC     *PW/AC     *PW/AC     to viii)
                                            KG/MS3     KG/MS3     KG/MS3     KG/MS3      KG/MS3
  0.10E+02   0.27E+02  0.11E+01  -0.48E+02  0.13E+02   0.11E+01  -0.14E+01  -0.29E+01   0.43E-04
  0.65E+01   0.82E+01  0.63E+00  -0.27E+02  0.14E+02   0.89E+00  -0.92E+00  -0.20E+01   0.31E-04
  0.48E+01   0.87E+00  0.47E+00  -0.20E+02  0.15E+02   0.77E+00  -0.71E+00  -0.16E+01   0.26E-04
  0.30E+01  -0.63E+01  0.30E+00  -0.12E+02  0.16E+02   0.59E+00  -0.53E+00  -0.12E+01   0.20E-04
  0.38E+00  -0.13E+02  0.62E-01  -0.40E+01  0.18E+02   0.13E+00  -0.37E+00  -0.89E+00   0.13E-04
  0.26E+00  -0.13E+02  0.49E-01  -0.33E+01  0.17E+02   0.92E-01  -0.34E+00  -0.83E+00   0.13E-04
  0.20E+00  -0.13E+02  0.39E-01  -0.28E+01  0.16E+02   0.64E-01  -0.31E+00  -0.77E+00   0.12E-04
  0.16E+00  -0.12E+02  0.32E-01  -0.24E+01  0.15E+02   0.44E-01  -0.29E+00  -0.72E+00   0.12E-04
  0.14E+00  -0.11E+02  0.21E-01  -0.17E+01  0.13E+02   0.16E-01  -0.24E+00  -0.60E+00   0.11E-04

PARTICLE AXIAL MOMENTUM BALANCE
  VZC    CK        FKZ       FDZ       SFS       SFR      GRF      SUM
                                      *PW/AC    *PW/AC
  M/S    M/S       N/M3      N/M3      N/M3      N/M3     N/M3     N/M3
  4.9433 1.1294   -49.207   93.597   -16.408   -9.464  -18.518   0.000
  4.8369 0.9936   -26.972   71.769   -17.720   -8.151  -18.925   0.000
  4.7810 0.9205   -16.119   61.097   -18.431   -7.400  -19.147   0.000
  4.6975 0.8387    -3.184   47.959   -19.175   -6.113  -19.487   0.000
  4.4507 0.7395    17.247   21.867   -16.630   -1.916  -20.568   0.000
  4.4186 0.7213    18.461   19.346   -15.614   -1.475  -20.717   0.000
  4.3902 0.7022    19.289   17.309   -14.615   -1.132  -20.851   0.000
  4.3645 0.6835    19.858   15.636   -13.658   -0.862  -20.974   0.000
  4.3079 0.6432    20.627   12.601   -11.563   -0.416  -21.250   0.000
```

GAS FORCE BALANCE, PARTICLE AND GAS WALL SHEAR, SUSPENSION DENSITY

FDGAS	SFGC	SFSCT	SFRCT	RHOPA	RHOPT
N/M3	N/M3	N/M3	N/M3	KG/M3	KG/M3
-361.180	-12.249	-143.813	-36.928	38.0661	18.3933

PARTICLE COLLISION FREQUENCY AND MEAN FREE PATH

XP	CKT	Z1T	Z2T	FPATH	VWK
UM	M/S	1/S	1/S	MM	--
114.	1.1302	64.614	125.645	5.9403	0.4742
141.	0.9941	84.959	154.771	4.1469	0.5000
160.	0.9210	97.899	174.112	3.3857	0.5000
194.	0.8389	121.277	209.701	2.5347	0.5000
365.	0.7396	296.694	416.090	1.0376	0.5000
403.	0.7214	347.069	463.719	0.8897	0.5000
440.	0.7023	401.348	511.500	0.7693	0.5000
478.	0.6835	459.877	559.448	0.6706	0.5000
570.	0.6432	623.922	677.706	0.4942	0.5000

F.1.4 Output (d): FCC Riser Simulation; $G_s = 200$ kg/m^{2}s, $U_g = 9.0$ m/s.

Simulation including gas turbulence effects:

CIRCULATING FLUIDISED BED RISER CORE MODEL - CIRCOR

SECTION A: INPUT; OPERATING CONDITIONS

RISER DIAMETER	1.000	M	PARTICLE PROPERTY	TYPE 1
RISER CROSS SECTION	CIRCULAR		DENSITY (KG/M3)	1070.
WALL ROUGHNESS	2.0	MM	PARTICLE COEFF. RESTITUTION	0.80
NET SOLIDS CIRCULATION RATE	200.	KG/M2.S	PARTICLE-WALL COEFF. RESTITUTION	0.70
GAS TEMPERATURE	723.	K	SPHERICITY	0.95
GAS PRESSURE	101325.	PA	WALL COEFF. SLIDING FRICTION	0.58
GAS VISCOSITY	0.33E-04	KG/M.S		
GAS DENSITY	0.489	KG/M3		
STREAMER FRACTIONAL WALL COVERAGE	0.70			
WALL REGION THICKNESS	50.00	MM		

SECTION B: RESULTS

GAS FLOW AND TURBULENCE

UOC	UZC	UPF	UPL	TAUGF	TAUGL	EG	PG
M/S	M/S	M/S	M/S	S	S	--	PA
11.111	11.380	1.387	0.467	0.209	0.620	0.976	101325.

PARTICLE-TURBULENCE INTERACTION

XP	RHOP	VZC	TAUP	TAUR	EP	CT	FDT	FKT
UM	KG/M3	M/S	S	S	--	M/S	N/M3	N/M3
29.	1070.	11.351	0.002	0.620	0.00261	0.4658	3.1626	-0.8530
37.	1070.	11.333	0.002	0.620	0.00262	0.4650	2.8850	-0.7232
43.	1070.	11.323	0.003	0.620	0.00262	0.4645	2.5813	-0.4945
49.	1070.	11.315	0.004	0.620	0.00262	0.4641	2.3118	-0.2423
54.	1070.	11.308	0.005	0.620	0.00262	0.4638	2.0731	-0.0135
60.	1070.	11.302	0.006	0.620	0.00262	0.4635	1.8681	0.1867
66.	1070.	11.296	0.008	0.620	0.00263	0.4631	1.6721	0.3855
75.	1070.	11.288	0.010	0.620	0.00263	0.4626	1.4335	0.6574
93.	1070.	11.273	0.015	0.620	0.00263	0.4615	1.1520	1.0968

PARTICLE FLUCTUATING ENERGY BALANCE

(i) PKK	(ii) SK	(iii)PKT	(iv) DKT	(v) PKS *PW/AC	(vi) PKR *PW/AC	(vii) DKR *PW/AC	(viii)DKS *PW/AC	SUM (i to viii)
KG/MS3	KG/MS3	KG/MS3	KG/MS3	KG/MS3	KG/MS3	KG/MS3	KG/MS3	KG/MS3
0.26E+00	0.15E+02	0.50E+00	-0.35E+02	0.19E+02	0.60E-02	-0.79E-02	-0.99E-02	0.34E-14
0.21E+00	0.10E+02	0.50E+00	-0.34E+02	0.23E+02	0.60E-02	-0.85E-02	-0.16E-01	0.14E-14
0.14E+00	0.52E+01	0.50E+00	-0.31E+02	0.25E+02	0.60E-02	-0.88E-02	-0.20E-01	0.78E-14
0.96E-01	0.40E+00	0.50E+00	-0.28E+02	0.27E+02	0.59E-02	-0.91E-02	-0.23E-01	0.25E-14
0.67E-01	-0.39E+01	0.50E+00	-0.24E+02	0.28E+02	0.58E-02	-0.93E-02	-0.25E-01	0.68E-14

0.51E-01	-0.75E+01	0.49E+00	-0.22E+02	0.29E+02	0.56E-02	-0.95E-02	-0.27E-01	-0.34E-14
0.41E-01	-0.11E+02	0.49E+00	-0.19E+02	0.29E+02	0.53E-02	-0.96E-02	-0.29E-01	0.10E-13
0.37E-01	-0.14E+02	0.49E+00	-0.15E+02	0.29E+02	0.49E-02	-0.98E-02	-0.31E-01	0.48E-14
0.39E-01	-0.17E+02	0.49E+00	-0.11E+02	0.27E+02	0.38E-02	-0.10E-01	-0.33E-01	0.42E-14

PARTICLE AXIAL MOMENTUM BALANCE

VZC	CK	FKZ	FDZ	SFS *PW/AC	SFR *PW/AC	GRF	SUM
M/S	M/S	N/M3	N/M3	N/M3	N/M3	N/M3	N/M3
11.3507	0.1373	-17.222	56.098	-11.316	-0.138	-27.423	0.000
11.3333	0.1729	-14.139	54.282	-12.540	-0.138	-27.465	0.000
11.3229	0.1912	-8.953	49.646	-13.068	-0.135	-27.490	0.000
11.3151	0.2036	-3.775	44.722	-13.308	-0.131	-27.509	0.000
11.3084	0.2128	0.799	40.197	-13.345	-0.126	-27.525	0.000
11.3025	0.2199	4.669	36.212	-13.222	-0.120	-27.540	0.000
11.2964	0.2260	8.301	32.301	-12.935	-0.112	-27.555	0.000
11.2877	0.2329	12.648	27.301	-12.273	-0.100	-27.576	0.000
11.2729	0.2411	17.672	20.750	-10.732	-0.079	-27.612	0.000

GAS FORCE BALANCE, PARTICLE AND GAS WALL SHEAR, SUSPENSION DENSITY

FDGAS	SFGC	SFSCT	SFRCT	RHOPA	RHOPT
N/M3	N/M3	N/M3	N/M3	KG/M3	KG/M3
-361.510	-2.179	-112.739	-1.077	37.0733	25.2491

PARTICLE COLLISION FREQUENCY, MEAN FREE PATH AND PARTICLE MASS FRACTIONS

XP	CKT	Z1T	Z2T	FPATH	VWK	FEED	CORE	WALL
UM	M/S	1/S	1/S	MM	--	WT%	WT%	WT%
29.	0.4856	156.853	352.424	0.9535	0.2213	11.11	11.07	10.59
37.	0.4961	255.253	510.741	0.6476	0.3741	11.11	11.09	10.84
43.	0.5023	333.425	632.349	0.5201	0.4262	11.11	11.10	10.98
49.	0.5068	401.914	747.245	0.4410	0.4512	11.11	11.11	11.09
54.	0.5103	470.985	863.837	0.3823	0.4660	11.11	11.11	11.17
60.	0.5130	541.007	982.532	0.3367	0.4754	11.11	11.12	11.24
66.	0.5153	622.926	1121.544	0.2954	0.4823	11.11	11.12	11.29
75.	0.5179	758.737	1349.998	0.2456	0.5000	11.11	11.13	11.36
93.	0.5207	1043.965	1812.629	0.1823	0.5000	11.11	11.15	11.44

Simulation excluding gas turbulence effects:

CIRCULATING FLUIDISED BED RISER CORE MODEL - CIRCOR

SECTION A: INPUT; OPERATING CONDITIONS

RISER DIAMETER	1.000	M	PARTICLE PROPERTY	TYPE 1
RISER CROSS SECTION	CIRCULAR		DENSITY (KG/M3)	1070.
WALL ROUGHNESS	2.0	MM	PARTICLE COEFF. RESTITUTION	0.80
NET SOLIDS CIRCULATION RATE	200.	KG/M2.S	PARTICLE-WALL COEFF. RESTITUTION	0.70
GAS TEMPERATURE	723.	K	SPHERICITY	0.95
GAS PRESSURE	101325.	PA	WALL COEFF. SLIDING FRICTION	0.58
GAS VISCOSITY	0.33E-04	KG/M.S		
GAS DENSITY	0.489	KG/M3		
STREAMER FRACTIONAL WALL COVERAGE	0.70			
WALL REGION THICKNESS	50.00	MM		

SECTION B: RESULTS

GAS FLOW AND TURBULENCE

UOC	UZC	UPF	UPL	TAUGF	TAUGL	EG	PG
M/S	M/S	M/S	M/S	S	S	--	PA
11.111	11.379	1.387	0.000	0.209*******		0.976	101325.

PARTICLE-TURBULENCE INTERACTION

XP	RHOP	VZC	TAUP	TAUR	EP	CT	FDT	FKT
UM	KG/M3	M/S	S	S	--	M/S	N/M3	N/M3
29.	1070.	11.361	0.002*******		0.00261	0.0000	0.0000	0.0000
37.	1070.	11.349	0.002*******		0.00261	0.0000	0.0000	0.0000
43.	1070.	11.340	0.003*******		0.00262	0.0000	0.0000	0.0000

49.	1070.	11.332	0.004*******	0.00262	0.0000	0.0000	0.0000
54.	1070.	11.324	0.005*******	0.00262	0.0000	0.0000	0.0000
60.	1070.	11.318	0.006*******	0.00262	0.0000	0.0000	0.0000
66.	1070.	11.310	0.008*******	0.00262	0.0000	0.0000	0.0000
75.	1070.	11.299	0.010*******	0.00262	0.0000	0.0000	0.0000
93.	1070.	11.280	0.015*******	0.00263	0.0000	0.0000	0.0000

PARTICLE FLUCTUATING ENERGY BALANCE

(i) PKK	(ii) SK	(iii)PKT	(iv) DKT	(v) PKS *PW/AC	(vi) PKR *PW/AC	(vii) DKR *PW/AC	(viii)DKS *PW/AC	SUM (i to viii)
KG/MS3	KG/MS3	KG/MS3	KG/MS3	KG/MS3	KG/MS3	KG/MS3	KG/MS3	KG/MS3
0.92E-01	0.12E+01	0.00E+00	-0.46E+01	0.33E+01	0.12E-03	-0.74E-05	-0.13E-03	0.16E-14
0.83E-01	0.10E+01	0.00E+00	-0.50E+01	0.39E+01	0.10E-03	-0.18E-04	-0.32E-03	-0.50E-15
0.70E-01	0.72E+00	0.00E+00	-0.51E+01	0.43E+01	0.83E-04	-0.29E-04	-0.51E-03	-0.57E-15
0.54E-01	0.32E+00	0.00E+00	-0.50E+01	0.46E+01	0.67E-04	-0.40E-04	-0.71E-03	0.52E-15
0.40E-01	-0.11E+00	0.00E+00	-0.48E+01	0.49E+01	0.53E-04	-0.52E-04	-0.92E-03	0.25E-14
0.30E-01	-0.53E+00	0.00E+00	-0.46E+01	0.51E+01	0.40E-04	-0.63E-04	-0.11E-02	0.48E-14
0.23E-01	-0.97E+00	0.00E+00	-0.43E+01	0.52E+01	0.29E-04	-0.77E-04	-0.14E-02	0.30E-14
0.21E-01	-0.15E+01	0.00E+00	-0.38E+01	0.53E+01	0.15E-04	-0.97E-04	-0.17E-02	0.53E-14
0.27E-01	-0.21E+01	0.00E+00	-0.30E+01	0.51E+01	0.00E+00	-0.13E-03	-0.23E-02	0.35E-14

PARTICLE AXIAL MOMENTUM BALANCE

VZC	CK	FKZ	FDZ	SFS *PW/AC	SFR *PW/AC	GRF	SUM
M/S	M/S	N/M3	N/M3	N/M3	N/M3	N/M3	N/M3
11.3608	0.0497	-6.361	35.738	-1.970	-0.009	-27.398	0.000
11.3488	0.0669	-5.939	35.577	-2.202	-0.008	-27.427	0.000
11.3397	0.0779	-4.728	34.500	-2.316	-0.007	-27.449	0.000
11.3317	0.0868	-2.943	32.799	-2.381	-0.006	-27.469	0.000
11.3244	0.0944	-0.912	30.815	-2.412	-0.005	-27.486	0.000
11.3176	0.1010	1.084	28.837	-2.413	-0.005	-27.503	0.000
11.3102	0.1075	3.213	26.698	-2.387	-0.004	-27.521	0.000
11.2992	0.1159	6.158	23.692	-2.299	-0.002	-27.548	0.000
11.2802	0.1278	10.428	19.224	-2.057	0.000	-27.594	0.000

GAS FORCE BALANCE, PARTICLE AND GAS WALL SHEAR, SUSPENSION DENSITY

FDGAS	SFGC	SFSCT	SFRCT	RHOPA	RHOPT
N/M3	N/M3	N/M3	N/M3	KG/M3	KG/M3
-267.879	-2.179	-20.437	-0.047	27.5289	25.2187

PARTICLE COLLISION FREQUENCY, MEAN FREE PATH AND PARTICLE MASS FRACTIONS

XP	CKT	Z1T	Z2T	FPATH	VWK	FEED	CORE	WALL
UM	M/S	1/S	1/S	MM	--	WT%	WT%	WT%
29.	0.0497	66.095	128.459	0.2554	0.0996	11.11	11.07	5.98
37.	0.0669	99.943	197.363	0.2249	0.2312	11.11	11.09	8.06
43.	0.0779	132.055	252.103	0.2028	0.3261	11.11	11.10	9.39
49.	0.0868	164.981	303.623	0.1852	0.3847	11.11	11.10	10.47
54.	0.0944	200.454	355.217	0.1699	0.4214	11.11	11.11	11.40
60.	0.1010	239.450	406.611	0.1563	0.4448	11.11	11.12	12.20
66.	0.1075	288.476	464.926	0.1426	0.4620	11.11	11.12	12.99
75.	0.1159	377.071	555.528	0.1243	0.4777	11.11	11.14	14.02
93.	0.1278	588.162	718.186	0.0978	0.5000	11.11	11.15	15.49

F.2 Parametric Test Results

Table F.1: Predicted effects of particle coefficient of restitution, e, and particle-wall coefficient of sliding friction, μ_w on riser core apparent and true suspension density and average particle fluctuating velocities.

		Case (i), $G_s = 20$ kg/m^{2}s			Case (ii), $G_s = 60$ kg/m^{2}s		
e (–)	μ_w (–)	ρ_{sa} (kg/m^3)	ρ_s (kg/m^3)	$\mathbf{c}_k$ (m/s)	ρ_{sa} (kg/m^3)	ρ_s (kg/m^3)	$\mathbf{c}_k$ (m/s)
0.40	0.58	4.7	3.7	0.23	38	17	0.64
0.55	0.58	4.7	3.7	0.24	40	18	0.70
0.70	0.58	4.7	3.7	0.25	43	18	0.78
0.85	0.58	4.7	3.7	0.26	47	18	0.90
1.00	0.58	4.7	3.7	0.28	55	19	1.12
0.85	0.10	4.7	3.7	0.26	46	18	0.89
0.85	0.90	4.8	3.7	0.26	49	19	0.91

Case (i): $\mathbf{u}_z = 7.0$ m/s, Case (ii): $\mathbf{u}_z = 8.0$ m/s.
Cases (i) and (ii): $U_g = 7.0$ m/s, $D = 0.15$ m, $\rho_p = 2700$ kg/m^3, $T = 25$ °C, $\overline{d_p} = 205$ μm, PSD given in Table 8.4.

Table F.2: Predicted effects of riser diameter, D, on particle and gas flow properties in the riser core.

	Case (i), $G_s = 20$ kg/m^{2}s					Case (ii), $G_s = 60$ kg/m^{2}s				
D (m)	$(\mathbf{u}_1'/\mathbf{u}_0')^2$ (–)	ρ_{sa} (kg/m^3)	ρ_s	$\mathbf{v}_z$ (m/s)	$\mathbf{c}_k$	$(\mathbf{u}_1'/\mathbf{u}_0')^2$ (–)	ρ_{sa} (kg/m^3)	ρ_s	$\mathbf{v}_z$ (m/s)	$\mathbf{c}_k$
Test series 1: $T_g = 25$ °C.										
0.15	96	4.7	3.7	5.4	0.26	88	47	18	5.2	0.90
0.5	70	4.0	3.7	5.4	0.29	46	21	15	6.1	0.62
1.0	41	3.8	3.7	5.3	0.28	21	17	15	6.3	0.45
4.0	9	3.8	3.7	5.4	0.26	5	15	15	6.5	0.30
Test series 2: $T_g = 850$ °C.										
0.15	66	3.8	3.5	5.7	0.256	50	46	17	5.5	0.931
0.5	20	3.6	3.5	5.7	0.247	30	19	14	6.5	0.607
1.0	9	3.5	3.5	5.7	0.239	4	16	14	6.7	0.438
4.0	3	3.5	3.5	5.7	0.232	2	14	14	6.9	0.270
Test series 3: $T_g = 850$ °C, no gas turbulence effects ($\mathbf{u}_1' = 0$).										
0.15	0	3.8	3.5	5.7	0.220	0	46	17	5.5	0.926
0.5	0	3.6	3.5	5.7	0.224	0	19	14	6.5	0.598
1.0	0	3.5	3.5	5.7	0.225	0	16	14	6.7	0.426
4.0	0	3.5	3.5	5.7	0.225	0	14	14	6.9	0.252

Case (i): $\mathbf{u}_z = 7.0$ m/s.
Case (ii):$\mathbf{u}_z = 8.0$ m/s.
Cases (i) and (ii): $U_g = 7.0$ m/s, $\rho_p = 2700$ kg/m^3, $\overline{d_p} = 205$ μm, $e = 0.85$, $e_w = 0.8$, $\mu_w = 0.58$, PSD given in Table 8.4.

Appendix G

Semi-Empirical Predictive CFB Hydrodynamic Model RHOQUE: Description and Program Listing

This appendix contains the source code for the CFB riser model RHOQUE. All code is in standard FORTRAN77. In addition to the program and ancillary routines listed, RHOQUE requires the routines FHLBRG, ODERKF, DGAUSS, and LENSTR for execution. Code listings for these routines are given in Appendix E. A program documentation file that defines all key variables and logical unit assignments is also listed below. Results showing the accuracy of fit of a proposed correlation for the solids volume fraction at the CFB combustor riser solids return location are also presented.

G.1 Correlations for Solids Volume Fraction near Base of Riser

To develop the CFB combustor model RHOQUE (Chapter 10) a method for prediction of the solids volume fraction near the base of the riser was required. Experimental values for the solids volume fraction, ϵ_{pr}, at the solids return location were estimated from apparent suspension densities measured in the UBC pilot-scale combustor (Figure 7.3). All relevant operating conditions for these tests are given in Chapter 7. These experimental data were compared to values predicted by the "dense phase" region correlation proposed by Li and Kwauk (1980) (eq. (9.17)). This correlation gave poor predictions, and an alternative correlation, eq. (9.19), was proposed. To determine the coefficients in the new correlation, a least squares non-linear multi-parameter regression was performed (Bowen, 1987). The predicted values for ϵ_{pr} obtained from both the Kwauk correlation and eq. (9.19) are compared with experimental data in Figure G.1. The proposed equation reasonably correlates the data. The Kwauk correlation does

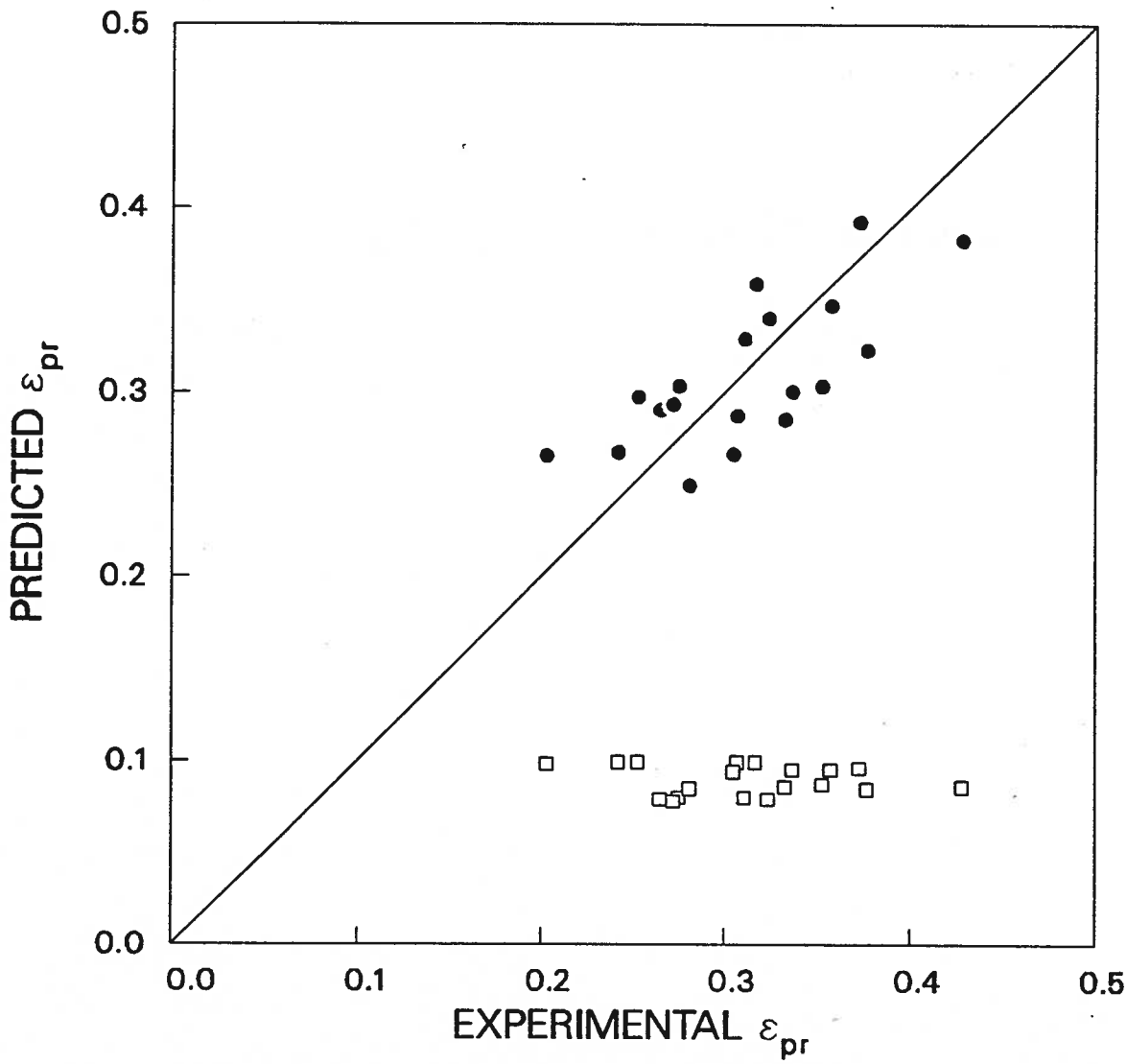

Figure G.1: Comparison of experimental and predicted solids volume fractions, ϵ_{pr}, at the UBC combustor solids return height. Solid circles: proposed correlation, eq. (9.19). Open squares: Li and Kwauk (1980) "dense phase" correlation, eq. (9.17).

not reproduce the observed trends.

G.2 Sample User Input File Listing

```
***************USERIN2.1*********************************************
CFB COMBUSTOR MODEL VERSION 2.1 - USER INPUT FILE:REFERENCE VERSION
REVISION 21     JANUARY  03  1990
COMBUSTOR:
TEST     :
CONDITION:

BED GEOMETRY                      |LBED(1),IBED,KBED,BED(1-6),BED(11-20)
12345678901234567890123456789 0   |
     0                            |EXIT GEOMETRY,0=SHARP 90DEG.,1=SMOOTH
     0                            |RISER CSA FLAG,0=SQUARE,1=CIRCLE
     0                            |PRIMARY ZONE CSA,0=TAPERED,1=FULL CSA
   0.01415                        |PRIMARY ZONE VOLUME,M**3
   0.914                          |PRIMARY ZONE HEIGHT,M
   6.299                          |SECONDARY ZONE HEIGHT,M
   0.0232                         |RISER CSA (ABOVE SEC. ZONE),M**2
   0.00817                        |STANDPIPE DIAMETER,M**2
   4.72                           |STANDPIPE LENGTH,M
   0.152                          |SOLIDS RECIRC. HEIGHT ABOVE DIST.,M
   0.527                          |FUEL FEED HEIGHT ABOVE GAS DIST.,M
   0.914                          |HEIGHT OF TAPERED SECTION,M
   0.00774                        |RISER CSA AT GAS DISTRIBUTOR,M**2
   0.01032                        |RISER CSA AT RECIRC. SOLIDS INLET,M**2
   0.01660                        |RISER CSA AT FUEL FEED HEIGHT,M**2
   0.1016                         |RISER EXIT DIMENSION - WIDTH,M
   0.2032                         |RISER EXIT DIMENSION - HEIGHT,M
   3.0                            |HEIGHT OF TOP OF MEMBRANE WALL, M
   0.0                            |
GAS FLOWS AND PROPERTIES          |AIR(1-5),AIR(11-12),TG,PG,GAST(5),
                                  |GAST(11)
12345678901234567890123456789 0   |
   0.0253                         |PRIMARY AIR FLOWRATE,M**3/S,@273K
   0.0158                         |SECONDARY AIR FLOWRATE,M**3/S,@273K
  20.8                            |COMBUSTION AIR MOL% O2
  78.2                            |COMBUSTION AIR MOL% N2
   1.0                            |COMBUSTION AIR MOL% H2O
   0.000236                       |STANDPIPE/L-VALVE AERATION,M**3/S@273K
   0.0080                         |PNUEMATIC FUEL FEED AIR,M**3/S@273K
1143.0                            |MEAN BED GAS TEMPERATURE,K
 101.325                          |MEAN BED GAS PRESSURE,KPA.
  20.0                            |% EXCESS AIR (FOR FUEL COMBUST. ONLY)
   3.5                            |% O2 IN PRODUCT GAS (DRY)
                                  |
SOLIDS HYDRODYNAMICS              |HYDG(1-2),HYDG(10),HYDZ(5)
12345678901234567890123456789 0   |
  35.0                            |CYCLONE SOLIDS RETURN FLUX,KG/M*M.S
   0.00583                        |FUEL FEEDRATE (DRY EQUIV.), KG/S
   0.0                            |MASS SOLIDS IN COMBUSTOR,KG
   0.70                           |REACTOR TOP REFLECTION COEFFICIENT

PARTICLE SIEVE SIZING ,WT%        |NSIV,SIV(1-4,1-NSIV)
18                                |NO. SIEVE SIZINGS
12345678901234567890123456789 0   |
  MM       FUEL    LIME    BED    |TYLER MESH    U.S. ALTERNATE
 7.925     0.00    0.0     0.0    |+2.5          +5/16 INCH
 5.613     0.44    0.0     0.0    |+3.5          +3.5
 3.962     3.50    0.0     0.59   |+5           +5
 2.794     9.25    0.34    0.97   |+7           +7
 1.981    10.92    0.61    0.85   |+9           +10
 1.397    13.18    1.36    1.17   |+12          +14
 0.991    12.11    0.95    1.05   |+16          +18
 0.701    11.09    4.33    0.98   |+24          +25
 0.495     8.73   14.06    0.94   |+32          +35
 0.351     7.75   13.33    8.72   |+42          +45
 0.246     5.48   13.19   37.09   |+60          +60
```

```
 0.175    4.75  20.54  33.59   |+80          +80
 0.124    3.74  19.76  11.01   |+115         +120
 0.088    3.41   7.02   2.52   |+170         +170
 0.053    3.99   2.91   0.42   |+270         +270
 0.045    1.29   1.51   0.05   |+325         +325
 0.038    0.00   0.0    0.05   |+400         +400
 0.000    0.0    0.0    0.0    |-400         -400

PARTICLE PHYSICAL PROPERTIES AND COMPOSITION
12345678901234567890123456789 0 |
FUEL:                           |PP(1,1-10)
1400.0                          |PARTICLE DENSITY,KG/M**3
  18.0                          |WT% ASH
  61.0                          |WT% CARBON
   9.0                          |WT% HYDROGEN
   4.0                          |WT% OXYGEN
   8.0                          |WT% SULPHUR
  40.0                          |ULTIMATE VOLATILES YIELD,WT%
   1.05                         |SWELLING FACTOR,DIA.CHAR/DIA.FUEL
   0.0                          |WT% NITROGEN
   0.0                          |FUEL MOISTURE (KG/KG WET FUEL)
LIMESTONE:                      |PP(2,1-3)
1500.0                          |PARTICLE DENSITY,KG/M**3
  98.0                          |WT% CALCIUM CARBONATE
   4.5                          |CA:S MOLAR RATIO
   0.0                          |
   0.0                          |
BED:                            |PP(3,1-9)
2500.0                          |MEAN PARTICLE DENSITY,KG/M**3
   0.61                         |WALL STREAMER VOIDAGE
   0.47                         |STANDPIPE LOOSE-PACKED VOIDAGE
   0.67                         |PARTICLE RADIATION EMISSIVITY
   0.0                          |THERMAL CONDUCTIVITY,W/M.K
 900.0                          |PARTICLE HEAT CAPACITY,J/KG K
   50.0D-6                      |PARTICLE ROUGHNESS, M
   0.0                          |
   0.9                          |COEFFICIENT OF RESTITUTION
PARTIALLY DEVOLATILIZED FUEL:   |PP(4,2-4)
   0.251                        |THERMAL CONDUCTIVITY,W/M.K
   2.00D-7                      |THERMAL DIFFUSIVITY,M**2/K
   0.85                         |PARTICLE RADIATION EMISSIVITY
   0.0                          |
   0.0                          |

MASS TRANSFER AND  KINETIC DATA
12345678901234567890 |
DEVOLAT. KINETICS    |VOLK(1-3)
 220.0               |MEAN OF ACTIVATION ENERGY DISTRIBUTION,KJ/MOL
   1.67D13           |APPARENT FREQUENCY FACTOR,1/S
  20.0               |S.D.OF ACTIVATION ENERGY DISTRIBUTION,KJ/MOL

CYCLONE GEOMETRY
12345678901234567890123456789 0 |ICYC,CYC(1-2,1-8)
 2                              |FLAG,1=PRIMARY ONLY,2=PRIMARY AND SEC.
  PRIMARY   SECONDARY           |
   0.152     0.140              |INLET HEIGHT,M
   0.064     0.044              |INLET WIDTH,M
   0.305     0.203              |CYCLONE DIAMETER,M
   0.152     0.076              |SOLIDS OUTLET DIAMETER,M
   0.152     0.194              |VORTEX FINDER LENGTH,M
   0.464     0.305              |HEIGHT OF CONSTANT DIAMETER SECTION,M
   1.226     0.660              |TOTAL CYCLONE HEIGHT,M
   0.152     0.102              |GAS OUTLET DIAMETER,M

BED TO WALL HEAT TRANSFER
12345678901234567890123456789 0 |HEAT(1-3)
 380.0                          |MEAN MEMBRANE WALL TEMPERATURE,K
   0.67                         |PARTICLE-WALL RADIATION EMISSIVITY
   0.85                         |ACCOMODATION COEFFICIENT
```

G.3 Program Input File Listings

```
*************PROGIN2.1*************************************************
CFB COMBUSTOR MODEL VERSION 2.1 - PROGRAM INPUT FILE
REVISION 19  DEC.  22  89       - REFERENCE FOR LATEST VERSION

GAS FORMULA MATRIX AND                          |GASNAM(1-20),A(1-20,J)
KINETIC/EQUILIBRIUM FLAGS                       |KA(1-20)
10                                              |NO. OF SPECIES IN GAS,NS
 5                                              |NO. ELEMENTS IN GAS,NE
12345678901234567890123456789012345678 90
 CO  CO2 O2  H2O NO  NO2 N2  H2  SO2 CH4 |GAS SPECIES NAME
   1   1   1   1   0   0   0   1   0   1 |1=AT EQUILIBRIUM CONC.
                                         |0=KINETICALLY CONTROLLED
  1.  1.  0.  0.  0.  0.  0.  0.  0.  1. |C CARBON
  0.  0.  0.  2.  0.  0.  0.  2.  0.  4. |H HYDROGEN
  1.  2.  2.  1.  1.  2.  0.  0.  2.  0. |O OXYGEN
  0.  0.  0.  0.  1.  1.  2.  0.  0.  0. |N NITROGEN
  0.  0.  0.  0.  0.  0.  0.  0.  1.  0. |S SULPHUR
                                         |
 NH3 SO3                                 |GAS SPECIES NAME
   0   0   0   0   0   0   0   0   0   0 |1=ACTIVE AT EQUILIBRIUM
                                         |0=KINETICALLY CONTROLLED
  0.  0.  0.  0.  0.  0.  0.  0.  0.  0. |C CARBON
  3.  0.  0.  0.  0.  0.  0.  0.  0.  0. |H HYDROGEN
  0.  3.  0.  0.  0.  0.  0.  0.  0.  0. |O OXYGEN
  1.  0.  0.  0.  0.  0.  0.  0.  0.  0. |N NITROGEN
  0.  1.  0.  0.  0.  0.  0.  0.  0.  0. |S SULPHUR

SOLIDS HYDRODYNAMICS            |HYDZ(3),HYDV(2-3),HYDQ(2),HYDZ(7-9),
                                |HYDQ(1)
12345678901234567890123456789 0 |
     0.008                    *|100% COVERAGE STREAMER THICKNESS,M
    -1.1                      *|MEAN STREAMER SOLIDS VELOCITY,M/S
     1.0                       |VELOCITY DEVIATION FACTOR(RANGE:0-1)
     0.01                      |ANNULUS TO CORE FLUX COEFF.,M/S
   310.0                      *|WALL SOLIDS LAYER DISTURBANCE FACTOR
     2.0                      *|WALL STREAMER ELLIPTIC SHAPE FACTOR
     0.9                       |FRACTION CAPTURE INTO STREAMERS (0:1)
     0.20                     *|CORE TO WALL FLUX COEFF.,M/S

FINITE DIFFERENCE GRID SIZING   |NXP(1-3),NZB * NXC(1-3),NXBC
12345678901234567890123456789 0 |
 FINE     * COARSE              |NO. PARTICLE SIZE INCREMENTS
 10       *  4                  |0-100 MICRON      (MAXIMUM:      )
 20       * 10                  |100-1000MICRON    (NXP(1+2+3)=84)
 10       *  4                  |1-10 MM           (NXC(1+2+3)=30)
 20       * 10                  |NO. BED HEIGHT INCREMENTS (SEC ZONE)
NUMERICAL INTEGRATION GRIDS     |NVOL(3)
12345678901234567890123456789 0 |
 10                             |DEVOLAT. TIME INCREMENT(MAX=10)
  5                             |DEVOLAT. ACT.ENERGY INCREMENT(MAX=10)
  4                             |PARTICLE TEMP. PROFILE(MAX=8)
```

G.4 Definition of Program Variables

MODEL ROUTINES:

ROUTINE	VERSION/S	TEST PROGRAM	COMMON BLOCKS	OUTDATED VERSIONS
AIRPRO	2.1	DENBED2.3	G	
ANFLUX	2.1	DENBED2.7	G,H,I	
DATIN	2.1	DATIN2.1	A-Z(block ref.)	
DENBED	2.10,7,8,9	DENBED2.X	E,H,I,G,P,U,Z	2.1,2.2
DENVAR	2.8	DENBED2.7	H,I	
ERCHEK	2.1	ERCHEK2.1	E	
ERINIT	2.1	ERCHEK2.1	E	
MASBAL	2.2	MASBAL2.X	G,P	2.1

```
NETFLX   2.1            DENBED2.7     H,I
SAUTER   2.1            DENBED2.3     J,P
SOLAIR   2.10           DENBED2.10    E,G,H,I,P,Z
SULPHA   2.1            DENBED2.7     G
TERVEL   2.1            TERVEL2.1     G,O,P
UGCORE   2.2            DENBED2.3     G,H,I
WALCON   2.1            DENBED2.7     H,I,Z

NOTE:(i)  version 2.X is routine version no.X of CFB level model 2
     (ii) routine version first listed is the routine current in
          CFB level 2 model RHOQUE

COMMON BLOCKS - SUMMARY:          REFERENCE: DATIN2.1, REVISION 41
------------------------          -------------------------------

BLKA/KS(20),NSQ
BLKB/A(5,20),KE(5),NS,NE,NEQ
BLKC/CYC(2,8),EFFCYC(89),ICYC
BLKE/IERROR(100),IERR1,IERR2
BLKG/AIR(20),GAST(40),UG(5),TG,PG
BLKH/BED(20),LBED(5),IBED,KBED
BLKI/HYDK(3,100),HYDZ(20),HYDQ(10),HYDG(30),HYDV(10)
BLKJ/SIV(4,25),NSIV
BLKO/XP(85),NXP(20),XC(30),NXC(20)
BLKP/PP(5,10)
BLKQ/HEAT(20)
BLKU/HYDA(4,101)
BLKV/VOLC(88,6),VOLT(88,2),VOLK(3),NVOL(3)
BLKW/VC(2,30,101),UI(2,101),CSA(2,101),VA(101),PRS(101)
BLKX/FMB(3,30,101),FLUX(2,30,100),EFC(29,29)
BLKY/Q(100),R(101),S(100)
BLKZ/DB(3,101),DBAV(10),DBEX(10),ZB(101),NZB,NXBC

E. ERROR FLAGS AND DIAGNOSTIC MESSAGES
---------------------------------------
BLKE/IERROR(100),IERR1,IERR2
Convention:
 IERR1,IERR2 = 0  ;Successful run,no warnings or error messages
 IERR1       = 1  ;Warning messages generated,but successful run
                   completion
 IERR2       = 2  ;Error,unsuccessful run,run terminated

 IERROR(J)   = 0  ;Warning/error no. J not incurred
 IERROR(J)   = 1  ;Jth warning incurred,output Jth diagnostic
                   (J = 1 <-> 49)
 IERROR(J)   = 2  ;Jth error incurred,output Jth diagnostic
                   (J = 50 <-> 100)

6;G. COMBUSTION GAS FLOWS AND PROPERTIES
----------------------------------------
BLKG/AIR(20),GAST(40),UG(5),TG,PG

VARIABLE  DESCRIPTION                                  DEFINING FILE/ROUTINE
--------  ---------------------------------------      ---------------------
AIR(1)    Primary zone air flowrate,m**3/s               USERIN
AIR(2)    Secondary air flowrate,m**3/s                  USERIN
AIR(3)    Mole % O2 in feed air                          USERIN
AIR(4)    Mole % N2 in feed air                          USERIN
AIR(5)    Mole % H2O in feed air                         USERIN
AIR(6)    Air/gas density at combustor temp.,kg/m**3     AIRPRO2.1
AIR(7)    Air/gas viscosity at combustor temp.,kg/m.s    AIRPRO2.1
AIR(8)    Air/gas thermal conductivity at combustor
          temp.,kg/m.s                                   AIRPRO2.1
AIR(9)    Air/gas viscosity at mean surface temp. of
          devolatilizing particle,kg/m.s                 AIRPRO2.1
AIR(10)   Air/gas specific heat at comb. temp.,J/kg.K    AIRPRO2.1
AIR(11)   Aeration gas to non-mechanical solids return
          valve,m**3/s                                   USERIN
AIR(12)   Pnuematic fuel feed air,m**3/s                 USERIN
AIR(13)
GAST(1)   Product gas flowrate (wet) @ TG, PG (m3/s)     MASBAL2.2
```

GAST(2)	Product gas flowrate (dry) @ TG, PG (m3/s)	MASBAL2.2
GAST(5)	% excess air (based on 100% fuel combustion)	USERIN/MASBAL2.2
GAST(6)	Mean molecular weight of product gas (wet)	MASBAL2.2
GAST(7)	% SO2 capture efficiency	
GAST(11)	Product gas (dry) - O2 (vol. %)	USERIN/MASBAL2.2
GAST(12)	Product gas (dry) - CO2 (vol. %)	MASBAL2.2
GAST(13)	Product gas (dry) - SO2 (ppm)	MASBAL2.2
GAST(16)	Product gas (wet) - O2 (vol. %)	MASBAL2.2
GAST(17)	Product gas (wet) - CO2 (vol. %)	MASBAL2.2
UG(1)	Secondary zone core interstitial gas velocity,m/s	UGCORE2.1
UG(2)	Sec. zone mean wall layer int. gas vel.,m/s	SOLAIR2.8
UG(3)	Sec. zone csa mean interstitial gas vel.,m/s	SOLAIR2.8
UG(4)	Primary zone mean interstit. gas velocity,m/s	SOLAIR2.8
UG(5)	Secodary zone superficial gas velocity,m/s	SOLAIR2.8
TG	Mean combustor gas temperature,Kelvin	USERIN
PG	Mean combustor gas pressure, kPa(input)/Pa(in program computations)	USERIN

Note:
(i) AIR(1),AIR(2),AIR(11),AIR(12) are entered as standard cubic metres per sec. (ie.@ 273K,101325 Pa).These flowrates are converted to m**3/s @ (TG,PG) in routine DATIN2.1. Furthermore,in routine DATIN2.1,AIR(1) and AIR(2) are redefined as follows:

```
AIR(1)=AIR(1)+AIR(11)
AIR(2)=AIR(2)+AIR(12)
```

(ii) An alternative routine to SOLAIR2.8 is SOLGAS2.2

6;H. REACTOR RISER AND STANDPIPE GEOMETRY

COMMON/BLKH/BED(20),LBED(5),IBED,KBED

Convention: Heights are given relative to the gas distributor,unless otherwise stipulated.

VARIABLE	DESCRIPTION	DEFINING FILE/ROUTINE
BED(1)	Primary zone volume,m**3	USERIN
BED(2)	Primary zone height,m	USERIN
BED(3)	Secondary zone height (to bottom of exit),m	USERIN
BED(4)	Full reactor csa (above sec.air),m**2	USERIN
BED(5)	Standpipe diameter,m	USERIN
BED(6)	Standpipe vertical length (exclude cyclone),m	USERIN
BED(7)	Standpipe horizontal length,m	USERIN
BED(8)	Riser hydraulic diameter(above sec.air),m	DATIN2.1
BED(9)	Riser mean hydraulic dia. in primary zone,m	DATIN2.1
BED(10)	Riser csa shape factor(Pi=circular,4.=square)	DATIN2.1
BED(11)	Solids recirculation entry height,m	USERIN
BED(12)	Fuel feed entry height,m	USERIN
BED(13)	Height of tapered section,m	USERIN
BED(14)	Riser c.s.a. at gas distributor,m**2	USERIN
BED(15)	Riser csa at solids recirc. entry point,m**2	USERIN
BED(16)	Riser csa at fuel feed height,m**2	USERIN
BED(17)	Riser exit dimension - width,m	USERIN
BED(18)	Riser exit dimension - height,m	USERIN
BED(19)	Height of top of membrane wall, m	USERIN
LBED(1)	Exit geometry;0=sharp 90 degree,1=top take-off	USERIN
IBED	Riser csa flag;0=square,1=circular	USERIN
KBED	Primary zone shape flag;0=tapered,1=constant for full riser length.	USERIN

6;I. SOLIDS HYDRODYNAMICS

COMMON/BLKI/HYDK(3,100),HYDZ(20),HYDQ(10),HYDG(30),HYDV(10)

CONVENTION:HYDK(1,L) ;L=Bed level counter

VARIABLE	DESCRIPTION	DEFINING FILE/ROUTINE
HYDZ(1)	Mean core csa above sec. air,m**2	WALCON
HYDZ(2)	Mean wall streamer csa above sec. air,m**2	WALCON
HYDZ(3)	Min. wall layer streamer thickness for 100% wall coverage by streamers,m	PROGIN
HYDZ(4)	Mean perimeter of core region,m	WALCON
HYDZ(5)	Reactor top reflection coefficient	USERIN
HYDZ(6)	Mean hydraulic diameter of core region,m	WALCON
HYDZ(7)	Wall solids layer disturbance factor	PROGIN
HYDZ(8)	Wall streamer semi-elliptic shape factor	PROGIN
HYDZ(9)	Fraction capture of particles into streamer	PROGIN
HYDZ(10)	Wall solids viscous shear entrainment factor	DENBED
HYDZ(11)		
HYDQ(1)	Core to wall flux coefficient - constant velocity zone (m/s)	PROGIN
HYDQ(2)	Streamer to core mass flux coefficient,m/s	PROGIN/DENBED2.X
HYDQ(3)	Streamer to core mass flux coefficient at zero wall layer thickness,m/s	DENBED2.X
HYDK(1,L)	Core to wall mass flux coefficient,m/s	DENBED
HYDK(2,L)	Streamer to core mass flux coefficient,m/s	DENBED2.X
HYDK(3,L)		
HYDG(1)	Solids recirculation flux,kg/m**2.s	USERIN
HYDG(2)	Fuel feedrate,kg/s	USERIN/MASBAL2.2
HYDG(3)	Limestone feedrate,kg/s	MASBAL2.2
HYDG(4)		
HYG(10)	Mass of solids in the CFB system	USERIN
HYDV(1)	Solids velocity in core (based on total gas flow at 50% fuel combustion level) (m/s)	SOLGAS
HYDV(2)	Mean wall streamer velocity	PROGIN
HYDV(3)	Core velocity deviation factor(range 0:1)	PROGIN
HYDV(4)	Solids velocity in core (based on primary air rate) (m/s)	SOLGAS
HYDV(5)	Terminal velocity of mean bed particle,m/s	SOLAIR

Note: (i) HYDQ(2) may be input via PROGIN or calculated in routine DENBED. Versions DENBED2.8,DENBED2.9 compute HYDQ(2).

(ii) Variables HYDZ(3),HYDZ(7-9) may or may not be required by a particular version of DENBED.The documentation of the routine version in use should be consulted.

6;P. PARTICLE PHYSICAL PROPERTIES AND COMPOSITION

COMMON/BLKP/PP(5,10)

CONVENTION:PP(IP,J);IP=Particle type
;J =Property

PP(IP,J) IP=1,COAL PARTICLE

VARIABLE	DESCRIPTION	DEFINING FILE/ROUTINE
PP(1,1)	Particle density,kg/m**3	USERIN
PP(1,2)	wt% ash in coal,%	USERIN
PP(1,3)	wt% carbon in coal,%	USERIN
PP(1,4)	wt% hydrogen in coal,%	USERIN
PP(1,5)	wt% oxygen in coal,%	USERIN
PP(1,6)	wt% sulphur in coal,%	USERIN
PP(1,7)	Ultimate volatiles yield,wt%	USERIN
PP(1,8)	Swelling factor,dia. char/dia. coal	USERIN

PP(1,9)		
PP(1,10)	Particle Sauter mean diameter,mm	SAUTER

PP(IP,J) IP=2,LIMESTONE PARTICLE

VARIABLE	DESCRIPTION	DEFINING FILE/ROUTINE
PP(2,1)	Particle density,kg/m**3	USERIN
PP(2,2)	wt% calcium carbonate,%	USERIN
PP(2,3)	Ca:S moalr ratio	USERIN
PP(2,10)	Particle Sauter mean diameter,mm	

PP(IP,J) IP=3,BED PARTICLE

VARIABLE	DESCRIPTION	DEFINING FILE/ROUTINE
PP(3,1)	Particle density,kg/m**3	USERIN
PP(3,2)	Wall streamer voidage	USERIN
PP(3,3)	Standpipe loose-packed voidage	USERIN
PP(3,4)	Particle radiation emissivity	USERIN
PP(3,5)	Particle thermal conductivity (W/mK)	USERIN
PP(3,6)	Particle heat capacity (J/kgK)	USERIN
PP(3,7)	Particle roughness,m	USERIN
PP(3,9)	Coefficient of restitution	USERIN
PP(3,10)	Particle Sauter mean diameter,mm	SAUTER2.1

PP(IP,J) IP=4,DEVOLATILIZING PARTICLE

VARIABLE	DESCRIPTION	DEFINING FILE/ROUTINE
PP(4,1)	Particle density,kg/m**3	VOLATE2.1
PP(4,2)	Thermal conductivity,W/mK	USERIN
PP(4,3)	Thermal diffusivity,m**2/K	USERIN
PP(4,4)	Particle radiation emissivity	USERIN

PP(IP,J) IP=5,CHAR PARTICLE

VARIABLE	DESCRIPTION	DEFINING FILE/ROUTINE
PP(5,1)		

6;Q. BED TO WALL HEAT TRANSFER

COMMON/BLKQ/HEAT(20)

VARIABLE	DESCRIPTION	DEFINING FILE/ROUTINE
HEAT(1)	Wall temperature (K)	USERIN
HEAT(2)	Particle wall radiation emissivity	USERIN
HEAT(3)	Accomodation coefficient	USERIN

6;U. HYDRODYNAMIC VARIABLES

COMMON/BLKU/HYDA(4,101)

Convention:HYDA(1,L),L=Bed level counter relative to sec. air entry point.

VARIABLE	DESCRIPTION	DEFINING FILE/ROUTINE
HYDA(1,L)	Core area ,m**2	DENBED (7)
HYDA(2,L)	Wall streamer area,m**2	DENBED (7)
HYDA(3,L)	Wall layer thickness,m	DENBED (7)
HYDA(4,L)	Fraction of wall coverage	DENBED (7)

6;Z. RISER SUSPENSION DENSITIES

COMMON/BLKZ/DB(3,101),DBAV(10),DBEX(10),ZB(101),NZB,NXBC

All densities are in kg/m3

VARIABLE	DESCRIPTION	DEFINING FILE/ROUTINE
DB(1,J)	Core suspension density @ Jth height	DENBED
DB(3,J)	Cross-sectional averaged riser suspension density @ Jth height	DENBED
DBAV(1)	Ave. primary zone density	DENBED
DBAV(2)	Ave. density for sec. air to riser exit	DENBED
DBAV(3)	Ave. density for riser (excl. exit region)	DENBED
DBAV(5)	Ave. bulk density in core (above sec. air)	DENBED
DBAV(6)	Ave. density in wall region (above sec. air)	DENBED
DBAV(7)	Density @ fuel feed location	DENBED
DBAV(8)	Streamer (wall solids layer) density	DENBED
DBAV(9)	Density @ solids recirculation entry point	DENBED
DBEX(1-3)	Densities in the riser exit region	DENBED
ZB(J)	Height above sec. air of Jth point	DENBED
NZB | NZBC |	No. of subdivisions of riser for computational purposes (NZB for fine grid, NZBC for coarse)	DENBED

G.5 Model Output for UBC Combustor, $U_g = 7.3$ m/s, $G_s = 44$ kg/m^{2}s

```
          CIRCULATING FLUIDIZED BED RISER MODEL
          -------------------------------------

     RUN RESULTS OF HYDRODYNAMIC ROUTINE DENBED,VERSION 2.10

 COMBUSTOR: UBC COMBUSTOR
 CASE:      RUN NO. 21, APRIL 21 1988

          RISER GEOMETRY
          --------------
 RISER CROSS SECTIONAL AREA              0.02320    M2
 SECONDARY AIR HEIGHT                    0.91400    M
 HEIGHT TO START OF RISER EXIT           7.31500    M

          COMBUSTION CONDITIONS
          ---------------------
 SOLIDS RECIRCULATION                   43.7        KG/M2.S
 NOMINAL SUPERFICIAL GAS VELOCITY        7.3        M/S
 MEAN COMBUSTOR GAS TEMPERATURE        863.0        DEG.C
 MEAN COMBUSTOR GAS PRESSURE           101.3        KPA
 GAS DENSITY AT COMBUSTOR TEMP           0.311      KG/M3
 GAS VISC. AT COMBUSTOR TEMP             0.451E-04  KG/M.S
 BED PARTICLE DENSITY                 2650.0        KG/M3
 SAUTER MEAN PARTICLE SIZE               0.191      MM

          HYDRODYNAMIC PARAMETERS
          -----------------------
 WALL SOLIDS LAYER DISTURBANCE FACTOR  310.00
 RISER TOP REFLECTION COEFFICIENT        0.86
 WALL STREAMER VELOCITY                 -1.100      M/S
 MIN. WALL STREAMER THICKNESS FOR 100% WALL COVERAGE
                                         0.008      M

          BULK DENSITIES, KG/M3
          ---------------------
 PRIMARY ZONE AT SOLIDS RECIRCULATION ENTRY POINT   923.0
 PRIMARY ZONE AT FUEL FEED LOCATION                 464.2
 MEAN PRIMARY ZONE BULK DENSITY                     456.2
 MEAN CORE ZONE                                      20.8
 WALL STREAMER ZONE                                1113.0
 MEAN SECONDARY ZONE                                102.1
 MEAN FOR ENTIRE RISER                              132.9

HEIGHT ABOVE  CORE  STREAMERS FULL CSA | HEIGHT ABOVE  CORE   STREAMERS FULL CSA
SEC.AIR                                | SEC.AIR
   M        KG/M3   KG/M3     KG/M3    |    M        KG/M3    KG/M3     KG/M3
```

0.00	47.0	1113.0	242.8	3.52	14.1	1113.0	59.6
0.32	29.6	1113.0	153.3	3.84	15.0	1113.0	65.5
0.64	21.4	1113.0	106.1	4.16	16.2	1113.0	73.3
0.96	17.4	1113.0	81.2	4.48	17.8	1113.0	83.8
1.28	15.4	1113.0	68.1	4.80	20.1	1113.0	97.8
1.60	14.3	1113.0	61.1	5.12	23.2	1113.0	116.9
1.92	13.7	1113.0	57.5	5.44	27.7	1113.0	142.8
2.24	13.4	1113.0	55.6	5.76	34.1	1113.0	178.3
2.56	13.3	1113.0	54.6	6.08	43.7	1113.0	226.9
2.88	13.2	1113.0	54.0	6.40	57.0	1113.0	288.6
3.20	13.4	1113.0	55.1				

MASS FLUX COEFFICIENTS,M/S

HEIGHT ABOVE SEC. AIR M	CORE TO STREAMERS M/S	STREAMERS TO CORE M/S	HEIGHT ABOVE SEC. AIR M	CORE TO STREAMERS M/S	STREAMERS TO CORE M/S
0.16	0.6440	0.0094	3.36	0.2000	0.0044
0.48	0.5508	0.0072	3.68	0.2000	0.0047
0.80	0.4477	0.0059	4.00	0.2000	0.0050
1.12	0.3646	0.0052	4.32	0.2000	0.0053
1.44	0.3083	0.0048	4.64	0.2000	0.0058
1.76	0.2739	0.0045	4.96	0.2000	0.0064
2.08	0.2543	0.0044	5.28	0.2000	0.0072
2.40	0.2435	0.0043	5.60	0.2000	0.0082
2.72	0.2377	0.0043	5.92	0.2000	0.0095
3.04	0.2346	0.0043	6.24	0.2000	0.0115

SOLIDS MASS FLUXES, KG/M2.S

HEIGHT ABOVE SEC. AIR M	CORE TO STREAMER KG/M2.S	STREAMER TO CORE KG/M2.S	UP CORE KG/M2.S	DOWN STREAMER KG/M2.S	HEIGHT ABOVE SEC. AIR M	CORE TO STREAMER KG/M2.S	STREAMER TO CORE KG/M2.S	UP CORE KG/M2.S	DOWN STREAMER KG/M2.S
0.16	22.07	11.94	268.16	-1224.3	3.36	2.60	3.11	96.13	-1224.3
0.48	12.91	7.57	178.73	-1224.3	3.68	2.75	3.41	101.69	-1224.3
0.80	8.11	5.29	136.17	-1224.3	4.00	2.94	3.82	109.13	-1224.3
1.12	5.62	4.13	114.85	-1224.3	4.32	3.19	4.38	119.18	-1224.3
1.44	4.32	3.54	103.91	-1224.3	4.64	3.54	5.13	132.88	-1224.3
1.76	3.64	3.22	98.22	-1224.3	4.96	4.02	6.17	151.84	-1224.3
2.08	3.28	3.06	95.24	-1224.3	5.28	4.68	7.62	178.50	-1224.3
2.40	3.09	2.98	93.67	-1224.3	5.60	5.63	9.65	216.72	-1224.3
2.72	2.99	2.93	92.85	-1224.3	5.92	6.98	12.43	272.63	-1224.3
3.04	2.96	2.93	93.15	-1224.3	6.24	8.83	15.82	352.88	-1224.3

STREAMER CROSS SECTIONAL AREA AND WALL COVERAGE

HEIGHT ABOVE SEC. AIR M	STREAMER AREA M2	STREAMER AREA % OF TOTAL	STREAMER WALL COVERAGE %	HEIGHT ABOVE SEC. AIR M	STREAMER AREA M2	STREAMER AREA % OF TOTAL	STREAMER WALL COVERAGE %
0.00	0.0043	18.3747	100.00	3.52	0.0010	4.1438	50.11
0.32	0.0026	11.4202	83.19	3.84	0.0011	4.6022	52.81
0.64	0.0018	7.7535	68.55	4.16	0.0012	5.2103	56.19
0.96	0.0014	5.8203	59.39	4.48	0.0014	6.0221	60.41
1.28	0.0011	4.8010	53.94	4.80	0.0017	7.1135	65.66
1.60	0.0010	4.2636	50.83	5.12	0.0020	8.5912	72.16
1.92	0.0009	3.9803	49.11	5.44	0.0025	10.6057	80.17
2.24	0.0009	3.8309	48.18	5.76	0.0031	13.3648	90.00
2.56	0.0009	3.7521	47.69	6.08	0.0040	17.1381	100.00
2.88	0.0009	3.7106	47.42	6.40	0.0051	21.9262	100.00
3.20	0.0009	3.7965	47.97				

GAS VELOCITIES,M/S

SEC. ZONE SUPERFICIAL VELOCITY	7.54
MEAN CORE REGION INTERSTITIAL VELOCITY	8.02
MEAN STREAMER REGION INTERSTITIAL VELOCITY	3.98
SEC ZONE MEAN INTERSTITIAL VELOCITY	7.84
PRIMARY ZONE MEAN INTERSTITIAL VELOCITY	6.72

G.6 Model FORTRAN Code Listing

```
C****************RHOQUE*************************************************
      PROGRAM RHOQUE
C     REVISION 3    JANUARY  05   1989          AUTHOR: R.C.SENIOR
C     MAIN PROGRAM FOR :DENSITY PROFILE ROUTINE,DENBED2.10
C                      :ASSOCIATED ROUTINE DENVAR2.8
C                      :CORE/STREAMER SIZE ROUTINE,WALCON2.1
C                      :WALL TO CORE FLUX COEFFICIENT ROUTINE,
C                       ANFLUX2.1
C                      :SUPERVISORY ROUTINE,SOLAIR2.10
C                      :GAS VELOCITY ROUTINE,UGCORE2.2
C                      :NET WALL TO CORE SOLIDS FLOW ROUTINE,NETFLX2.1
C                      :HEAT TRANSFER ROUTINES SUPERVISED BY ROUITNE
C                       STUD6 (AUTHOR:C.M.H.BRERETON)
C                      :HEAT TRANSFER REPORT WRITER, -------
C     ROUTINES RUN WITH COMBUSTOR MODEL NO.2:VERSION NO.1:'CFB2.1'
C     DATIN2.1,TERVEL2.1,ERCHEK2.1,ERINIT2.1,SAUTER2.1,AIRPRO2.1,
C     ZUB-ODERKF ALSO REQUIRED
C*********************************************************************
      IMPLICIT DOUBLE PRECISION(A-H,O-Z)
      PARAMETER(NPR=100)
      COMMON/BLKE/IERROR(100),IERR1,IERR2
      COMMON/BLKH/BED(20),LBED(5),IBED,KBED
      COMMON/BLKI/HYDK(3,100),HYDZ(20),HYDQ(10),HYDG(30),HYDV(10)
      COMMON/BLKG/AIR(20),GAST(40),UG(5),TG,PG
      COMMON/BLKP/PP(5,10)
      COMMON/BLKU/HYDA(4,101)
      COMMON/BLKZ/DB(3,101),DBAV(10),DBEX(10),ZB(101),NZB,NXBC
      COMMON/SUBE/PC(101),PA(101),PF(101),Z0
C     DIMENSION DP(88),VT(88)
      DIMENSION X(NPR),Y(NPR)
      CHARACTER*65 NAMCOM
      CHARACTER*55 NAMCAS,NAMCON
      CHARACTER*1 FSET,AST,DOL
      CHARACTER*4 ASET
      CHARACTER*5 UPL,GSPL
      CHARACTER*7 ARSPL
      PARAMETER(AST='*',DOL='$')
C
C     Assign UNIT=12 as file for output of axial density profile
C     data for later plotting if desired.
C     If data is to be written to to this file set IPLOT=1, otherwise
C     set IPLOT=0. If data write is flagged, ensure correct data file
C     name and appropriate OLD/NEW is stipulated in the
C     OPEN statement.
C
      IPLOT=1
      IF(IPLOT.NE.1) GO TO 35
      OPEN(UNIT=12,FILE='DENP02')
C
 35   CALL ERINIT
C
C     USER INPUT OPTIONS:
C     Set ISET < 1 : only one data set contained in user input file
C                    (see USERIN for sample file).
C     Set ISET = SET NO., e.g. 2 (see multiple cases userin sample
C                file, USES01) : search required for required data
C                set.
      ISET=0
      IF(ISET.LT.1) GO TO 45
 510  READ(11,520,END=590) FSET
 520  FORMAT(A1)
      IF(FSET.EQ.AST) THEN
        READ(11,530)FSET,ITEST
 530    FORMAT(A1,I3)
        IF(ITEST.EQ.ISET) THEN
          BACKSPACE(UNIT=11)
          READ(11,540)ASET
 540      FORMAT(A4)
          GO TO 45
```

```
          ENDIF
        ENDIF
        GO TO 510
 590    IERROR(75)=2
        IERR2=2
        GO TO 300
C
C     Write report heading and case run
C
 45     WRITE(6,10)
 10     FORMAT(10X,'CIRCULATING FLUIDIZED BED RISER MODEL'/
      1 10X,'-------------------------------------'//,5X,
      2 'RUN RESULTS OF HYDRODYNAMIC ROUTINE DENBED,VERSION 2.10'/
      3 5X,'AND BED-WALL HEAT TRANSFER  ROUTINE STUD6'//)
        READ(11,5)NAMCOM,NAMCAS,NAMCON
 5      FORMAT(///A65/10X,A55/10X,A55)
        WRITE(6,15)NAMCOM,NAMCAS
 15     FORMAT(/1X,A65/1X,'CASE:      ',A55/)
        DO 55 I=1,6
        BACKSPACE(UNIT=11)
 55     CONTINUE
C
C     Input user data (UNIT=11) and program control data (UNIT=10)
C
        CALL DATIN
C
C     Initial estimate of mean core and wall region sizes
C
        CALL WALCON(0)
        NZ=NZB+1
C
C     Gas and particle properties
C
        CALL AIRPRO
        CALL SAUTER(3)
C
C     Overall mass balances
C
        CALL MASBAL(1)
C
C     Output riser geometry, hydrodynamic parameters, and combustion
C     conditions to output report file UNIT=6
C
        WRITE(6,400)
 400    FORMAT(//10X,'RISER GEOMETRY'/10X,'--------------')
        HEXIT=BED(2)+BED(3)
        WRITE(6,410) BED(4),BED(2),HEXIT
 410    FORMAT(1X,'RISER CROSS SECTIONAL AREA ',8X,F12.5,4X,'M2'/
      1 1X,'SECONDARY AIR HEIGHT        ',8X,F12.5,4X,'M'/
      2 1X,'HEIGHT TO START OF RISER EXIT',6X,F12.5,4X,'M')
        WRITE(6,420)
 420    FORMAT(//10X,'COMBUSTION CONDITIONS'/10X,
      1 '---------------------')
        PGK=PG/1.D3
        TGC=TG-273.D0
        USUP=(AIR(1)+AIR(2))/BED(4)
        WRITE(6,430)HYDG(1),USUP,TGC,PGK,(AIR(I),I=6,7),
      1 PP(3,1),PP(3,10)
 430    FORMAT(1X,'SOLIDS RECIRCULATION         ',5X,F10.1,8X,'KG/M2.S'
      1 /1X,'NOMINAL SUPERFICIAL GAS VELOCITY',1X,F10.1,8X,'M/S'
      1 /1X,'MEAN COMBUSTOR GAS TEMPERATURE ',2X,F10.1,8X,'DEG.C'
      1 /1X,'MEAN COMBUSTOR GAS PRESSURE   ',F13.1,8X,'KPA'
      2 /1X,'GAS DENSITY AT COMBUSTOR TEMP ',8X,F7.3,6X,'KG/M3'
      3 /1X,'GAS VISC. AT COMBUSTOR TEMP ',11X,E10.3,2X,'KG/M.S'
      4 /1X,'BED PARTICLE DENSITY ',12X,F10.1,8X,'KG/M3'
      5 /1X,'SAUTER MEAN PARTICLE SIZE ',12X,F7.3,6X,'MM')
        WRITE(6,440)
 440    FORMAT(//10X,'HYDRODYNAMIC PARAMETERS'/10X,
      1 '-----------------------')
        WRITE(6,450)HYDZ(7),HYDZ(5),HYDV(2),HYDZ(3)
 450    FORMAT(1X,'WALL SOLIDS LAYER DISTURBANCE FACTOR',F8.2
      1 /1X,'RISER TOP REFLECTION COEFFICIENT   ',2X,F7.2
```

```
     2 /1X,'WALL STREAMER VELOCITY            ',5X,F7.3,6X,'M/S'
     7 /1X,'MIN. WALL STREAMER THICKNESS FOR 100% WALL COVERAGE',
     8  /37X,F9.3,6X,'M')
C
C     Solve riser hydrodynamics
C
      CALL SOLAIR
      IF(IERR2.EQ.2) GO TO 300
C
C     Output hydrodynamic results to output report file UNIT=6
C
      X(1)=DBAV(9)
      Y(1)=BED(11)
      X(2)=DBAV(7)
      Y(2)=BED(12)
      WRITE(6,30)
 30   FORMAT(//10X,'BULK DENSITIES, KG/M3 '/10X,
     1 '---------------------')
      WRITE(6,40)DBAV(9),DBAV(7),DBAV(1),DBAV(5),DBAV(6),DBAV(2),
     1 DBAV(3)
 40   FORMAT(1X,'PRIMARY ZONE AT SOLIDS RECIRCULATION ENTRY POINT',
     1 1X,F7.1/
     2 1X,'PRIMARY ZONE AT FUEL FEED LOCATION',12X,F10.1/
     3 1X,'MEAN PRIMARY ZONE BULK DENSITY',7X,F19.1/
     4 1X,'MEAN CORE ZONE',30X,F12.1/
     5 1X,'WALL STREAMER ZONE',26X,F12.1/
     6 1X,'MEAN SECONDARY ZONE',25X,F12.1/
     7 1X,'MEAN FOR ENTIRE RISER',23X,F12.1)
      WRITE(6,50)
 50   FORMAT(/8X,'HEIGHT ABOVE ',4X,'CORE',7X,
     1 'STREAMERS ',5X,'FULL CSA '/8X,'SEC.AIR'/12X,'M',11X,
     2 'KG/M3',8X,'KG/M3',10X,'KG/M3')
      DZ=BED(3)/NZB
      DO 70 I=1,NZ
      ZHI=(I-1)*DZ
      WRITE(6,60)ZHI,DB(1,I),DBAV(6),DB(3,I)
 60   FORMAT(1X,F14.2,3F14.1)
      Y(I+2)=BED(2)+(I-1)*(BED(3)/NZB)
      X(I+2)=DB(3,I)
 70   CONTINUE
      WRITE(6,80)
 80   FORMAT(//10X,'MASS FLUX COEFFICIENTS,M/S'/10X,
     1 '--------------------------')
      WRITE(6,90)
 90   FORMAT(8X,'HEIGHT ABOVE',4X,'CORE TO STREAMERS',3X,
     1 'STREAMERS TO CORE'/8X,'SEC. AIR'/12X,'M',17X,'M/S',17X,'M/S')
      DO 110 I=1,NZB
      ZHI=(I-1)*DZ+DZ/2.D0
      WRITE(6,100)ZHI,HYDK(1,I),HYDK(2,I)
 100  FORMAT(1X,F14.2,2F20.4)
 110  CONTINUE
      WRITE(6,470)
 470  FORMAT(///10X,'SOLIDS MASS FLUXES, KG/M2.S'/10X,
     1 '---------------------------')
      WRITE(6,480)
 480  FORMAT(2X,'HEIGHT ABOVE      CORE TO       STREAMER     ',1X,
     1 'UP CORE          DOWN'/1X,
     2 ' SEC. AIR          STREAMER      TO CORE   ',2X,
     3 '                 STREAMER'/
     4 5X,'M',14X,'KG/M2.S',7X,'KG/M2.S',8X,'KG/M2.S',7X,'KG/M2.S')
      DO 500 I=1,NZB
      ZHI=(I-1)*DZ+DZ/2.D0
      FSC=((PA(I)+PA(I+1))*HYDK(2,I)+(PC(I)+PC(I+1))*HYDQ(3))*DBAV(6)
     1 /(2.D0*BED(8)*BED(10))
      FCS=(PF(I)*DB(1,I)+PF(I+1)*DB(1,I+1))*HYDK(1,I)/(2.D0*BED(8)*
     1 BED(10))
      FUP=(DB(1,I)+DB(1,I+1))*HYDV(1)/2.D0
      FDN=DBAV(6)*HYDV(2)
      WRITE(6,490)ZHI,FCS,FSC,FUP,FDN
 490  FORMAT(1X,F7.2,F19.2,F13.2,F15.2,F15.2)
 500  CONTINUE
      WRITE(6,160)
```

```
 160   FORMAT(///10X,'STREAMER CROSS SECTIONAL AREA AND WALL',1X
     1 ,'COVERAGE'/10X,'-------------------------------------',
     2 '---------')
       WRITE(6,170)
 170   FORMAT(2X,'HEIGHT ABOVE',10X,'STREAMER AREA',13X,
     1 'STREAMER WALL'
     1 /2X,'SEC. AIR',11X,'--------------------',10X,'COVERAGE'
     2 /5X,'M',16X,'M2        % OF TOTAL',13X,'%')
       DO 190 I=1,NZ
       ZHI=(I-1)*DZ
       FRCOV=HYDA(4,I)*100.D0
       FRAR=HYDA(2,I)/BED(4)*100.D0
       WRITE(6,180)ZHI,HYDA(2,I),FRAR,FRCOV
 180   FORMAT(1X,F8.2,F18.4,F13.4,F18.2)
 190   CONTINUE
       WRITE(6,210)
 210   FORMAT(/////1X,'GAS VELOCITIES,M/S'/1X,'------------------')
       UOS=(AIR(1)+AIR(2)+GAST(1))/(2.D0*BED(4))
       WRITE(6,220)UOS,(UG(K),K=1,4)
 220   FORMAT(1X,'SEC. ZONE SUPERFICIAL VELOCITY',11X,F10.2/
     1 1X,'MEAN CORE REGION INTERSTITIAL VELOCITY',3X,F10.2/
     2 1X,'MEAN STREAMER REGION INTERSTITIAL VELOCITY',4X,F5.2/
     3 1X,'SEC ZONE MEAN INTERSTITIAL VELOCITY',F16.2/
     4 1X,'PRIMARY ZONE MEAN INTERSTITIAL VELOCITY',4X,F8.2/)
C
C     Solve bed-wall heat transfer
C
       CALL STUD6
C
C     Output heat transfer results to output report file UNIT=6
C
C      CALL YYYYY
C
C     Output axial density profile data and key hydrodynamic
C     parameters to UNIT=12 for later plotting. (Optional - see
C     flag IPLOT setting instructions above)
C
       IF(IPLOT.NE.1) GO TO 290
       N=NZ+2
 600   READ(12,620,END=630,ERR=630) FSET
 620   FORMAT(A1)
       GO TO 600
 630   IF(ISET.LT.1) ASET='    '
       BACKSPACE(UNIT=12)
       WRITE(12,640)AST,ASET,NAMCAS
 640   FORMAT(A1/A4/A55)
       UPL=NAMCON(1:5)
       GSPL=NAMCON(9:13)
       ARSPL=NAMCON(17:23)
       WRITE(12,650)UPL,GSPL,ARSPL
 650   FORMAT(5X,A5,8X,A5,6X,A7)
       WRITE(12,120)N
 120   FORMAT(I6)
       DO 140 I=1,N
       WRITE(12,130)X(I),Y(I)
 130   FORMAT(F9.1,10X,F8.3)
 140   CONTINUE
       WRITE(12,150)BED(11),BED(2),HYDZ(5),HYDZ(7),HYDZ(3),HYDV(2),
     1 HYDQ(1)
 150   FORMAT(7(/F8.3))
       WRITE(12,660)DOL
 660   FORMAT(A1)
C
C     Errors or warning messages
C
 290   IF(IERR1.EQ.0) GO TO 320
 300   CALL ERCHEK
 320   STOP
       END
C*****************AIRPRO2.1*******************************************
       SUBROUTINE AIRPRO
```

```
C     REVISION 2     AUG. 23  88  COMPATIBLE WITH MODEL VERSION 2.1
C     INPUT:  TG      Isothermal gas/bed particle temperature,K
C             PG      Mean combustor gas pressure ,Pa(abs.)
C     OUTPUT: AIR(6)  Air density at temp. TG ,kg/m**3
C             AIR(7)  Air viscosity at temp. TG ,kg/m.s
C             AIR(8)  Thermal conductivity of air at TG ,W/m.K
C             AIR(9)  Air viscosity at temp. (TG+298K)/2 ,kg/m.s
C             AIR(10) Air heat capacity at TG ,J/kg.K
C     (copy of CANMET/PRETO fits to thermophysical data)
C*****************************************************************
      IMPLICIT DOUBLE PRECISION(A-H,O-Z)
      COMMON/BLKG/AIR(20),GAST(40),UG(5),TG,PG
      DIMENSION CP(3,4)
      DATA CP/6.1261D0,7.0155D0,7.7246D0,.31446D0,-.10279D0,
     1 .015807D0,-.0093772D0,.029194D0,.029945D0,-.37879D-5,
     2 -.11061D-2,-.10291D-2/
      AIR(6)=1.29425D0*273.3D0*PG/(TG*101325.D0)
      AIR(7)=6.31D-6+(TG*4.18D-8)-((TG**2)*6.70D-12)
      AIR(8)=.001D0*(19.178D0+.047567D0*TG)
      TAV=(TG+298.D0)/2.D0
      AIR(9)=6.31D-6+(TAV*4.18D-8)-((TAV**2)*6.70D-12)
      AIR(10)=0.D0
      TV=TG/1.D2
      DO 20 J=1,3
      CPAIR=CP(J,1)
      DO 10 I=1,3
      CPAIR=CPAIR+CP(J,I+1)*(TV**I)
 10   CONTINUE
      AIR(10)=AIR(10)+CPAIR*AIR(J+2)/100.D0
 20   CONTINUE
      AIR(10)=4.184D5*AIR(10)/(AIR(3)*32.D0+AIR(4)*28.D0+AIR(5)
     1 *18.D0)
      RETURN
      END
C************ANFLUX2.1*************************************************
      SUBROUTINE ANFLUX(IEQN,VOID,AC,RW,FCTR,HYDK2W)
C     REVISION 1                    JULY 17 1989   AUTHOR: R.C.SENIOR
C     Returns  (i)  HYDK2W       for IEQN =  0
C              (ii) UC,RHOC,FSGC for IEQN <> 0
C     HYDK2W Wall streamer to core solids flux coefficient,m/s.
C     UC     Superficial core homogeneous velocity
C     RHOC   Core homogeneous density
C     FSGC   Pipe friction factor for smooth wall case and
C            homogeneous gas/solid core flow assumption
C     (UC=VAL(12),RHOC=VAL(13),FSGC=VAL(14) returned by common bl.)
C
C     FCTR    Wall solids viscous shear entrainment factor(HYDZ(10)
C     VOID    Core voidage
C     AC      Core csa,m**2
C     RW      Mean wall streamer thickness,m.
C     VAL(15)|
C     VAL(16)|Defined in routine DENBED
C*****************************************************************
      IMPLICIT DOUBLE PRECISION (A-H,O-Z)
      COMMON/BLKG/AIR(20),GAST(40),UG(5),TG,PG
      COMMON/BLKH/BED(20),LBED(5),IBED,KBED
      COMMON/BLKI/HYDK(3,100),HYDZ(20),HYDQ(10),HYDG(30),HYDV(10)
      COMMON/SUBD/VAL(20),IVAL(10)
      UC=AC*(UG(1)*VOID+HYDV(1)*(1.D0-VOID))/BED(4)
      RHOC=(UG(1)*VOID*AIR(6)+HYDV(1)*(1.D0-VOID)*VAL(2))/
     1 (UG(1)*VOID+HYDV(1)*(1.D0-VOID))
      RESGC=UC*RHOC*BED(8)/AIR(7)
C
C     Blasius equation for smooth wall friction factor,FSGC
C
      FSGC=0.0791D0/RESGC**.25D0
      IF(IEQN.NE.0) THEN
        VAL(12)=UC
        VAL(13)=RHOC
        VAL(14)=FSGC
```

```
          RETURN
        ENDIF
        ALPHA=VAL(16)*RHOC*UC**2*FSGC*(1.D0+VAL(15)*RW)
        HYDK2W=FCTR*ALPHA
        RETURN
        END
C*************DATIN2.1*************************************************
        SUBROUTINE DATIN
C     REVISION 43  JAN. 10 90  - CFB MODEL VERSION 2.1
C     Inputs user and program data,converts to program variables
C     Version 2.1: 10 gas species,5 constituent elements-see PROGIN2.1
C     DEFAULT VALUES:
C       IBED   1   Square reactor cross section
C       KBED   1   No tapering of riser primary zone
C*********************************************************************
C
C     Maximum gas species allowed =20
C
        IMPLICIT DOUBLE PRECISION(A-H,O-Z)
        CHARACTER SPACE
        DIMENSION KA(20),GASNAM(20)
        COMMON/BLKA/KS(20),NSQ
        COMMON/BLKB/A(5,20),KE(5),NS,NE,NEQ
        COMMON/BLKC/CYC(2,8),EFFCYC(89),ICYC
        COMMON/BLKE/IERROR(100),IERR1,IERR2
        COMMON/BLKG/AIR(20),GAST(40),UG(5),TG,PG
        COMMON/BLKH/BED(20),LBED(5),IBED,KBED
        COMMON/BLKI/HYDK(3,100),HYDZ(20),HYDQ(10),HYDG(30),HYDV(10)
        COMMON/BLKJ/SIV(4,25),NSIV
        COMMON/BLKO/XP(85),NXP(20),XC(30),NXC(20)
        COMMON/BLKP/PP(5,10)
        COMMON/BLKQ/HEAT(20)
        COMMON/BLKU/HYDA(4,101)
        COMMON/BLKV/VOLC(88,6),VOLT(88,2),VOLK(3),NVOL(3)
        COMMON/BLKW/VC(2,30,101),UI(2,101),CSA(2,101),VA(101),PRS(101)
        COMMON/BLKX/FMB(3,30,101),FLUX(2,30,100),EFC(29,29)
        COMMON/BLKY/Q(100),R(101),S(100)
        COMMON/BLKZ/DB(3,101),DBAV(10),DBEX(10),ZB(101),NZB,NXBC
        PI=4.D0*DATAN(1.D0)
CI      OPEN(UNIT=10,FILE='PROGIN',STATUS='OLD')
CI      OPEN(UNIT=11,FILE='USERIN',STATUS='OLD')
C
C     Bed geometry
C
        READ(11,10) LBED(1),IBED,KBED
 10     FORMAT(////////3(/I6))
        READ(11,20)(BED(I),I=1,6),(BED(I),I=11,20)
 20     FORMAT(F12.7,15(/F12.7))
C
C     Gas flows and properties
C
        READ(10,30)NS,NE
 30     FORMAT(//////,I2/I2)
        READ(10,40)(GASNAM(I),I=1,10)
 40     FORMAT(/10A4)
        READ(10,50)(KA(I),I=1,10)
 50     FORMAT(10I4)
        READ(10,60)SPACE
 60     FORMAT(A1)
        DO 80 I=1,NE
        READ(10,70)(A(I,J),J=1,10)
 70     FORMAT(10F4.1)
 80     CONTINUE
        READ(10,40)(GASNAM(I),I=11,20)
        READ(10,50)(KA(I),I=11,20)
        READ(10,60)SPACE
        DO 90 I=1,NE
        READ(10,70)(A(I,J),J=11,20)
 90     CONTINUE
        READ(11,100)(AIR(I),I=1,5),AIR(11),AIR(12),TG,PG,GAST(5),
     1 GAST(11)
 100    FORMAT(////F12.7,10(/F12.7)//)
```

```
      AIR(1)=AIR(1)*TG/273.D0*101.325D0/PG
      AIR(2)=AIR(2)*TG/273.D0*101.325D0/PG
      AIR(11)=AIR(11)*TG/273.D0*101.325D0/PG
      AIR(12)=AIR(12)*TG/273.D0*101.325D0/PG
      AIR(1)=AIR(1)+AIR(11)
      AIR(2)=AIR(2)+AIR(12)
      PG=PG*1.D3
C
C     Index gas elements and species as active/inactive in
C     equilibrium calculations.
C
      NSM=NS
      NSQ=0
      DO 110 I=1,NS
      IF(KA(I).EQ.1) THEN
        NSQ=NSQ+1
        KS(NSQ)=I
      ELSE
        KS(NSM)=I
        NSM=NSM-1
      ENDIF
 110  CONTINUE
      NEQ=0
      NEM=NE
      DO 130 I=1,NE
      DO 120 J=1,NSQ
      IF(A(I,KS(J)).GT.0.) THEN
        NEQ=NEQ+1
        KE(NEQ)=I
        GO TO 130
      ENDIF
 120  CONTINUE
      KE(NEM)=I
      NEM=NEM-1
 130  CONTINUE
C
C     Solids hydrodynamics
C
      READ(10,140)HYDZ(3),HYDV(2),HYDV(3),HYDQ(2),(HYDZ(I),I=7,9),
     1 HYDQ(1)
 140  FORMAT(////F12.7,7(/F12.7))
      READ(11,150)HYDG(1),HYDG(2),HYDG(10)
 150  FORMAT(///F12.7,/F14.9/F12.7)
      IF(IBED.EQ.1) THEN
        BED(10)=PI
      ELSE
        BED(10)=4.D0
      ENDIF
      BED(8)=2.D0*DSQRT(BED(4)/BED(10))
      BED(9)=2.D0*DSQRT(BED(1)/(BED(10)*BED(2)))
      IF(KBED.NE.0.AND.KBED.NE.1) KBED=1
      READ(11,155)HYDZ(5)
 155  FORMAT(F12.7)
C
C     Particle sieve sizing
C
      READ(11,160) NSIV
 160  FORMAT(//I2//)
      DO 180 I=1,NSIV
      READ(11,170)(SIV(J,I),J=1,4)
 170  FORMAT(F8.5,3F7.3)
 180  CONTINUE
C
C     Particle physical properties
C
      READ(11,190)(PP(1,I),I=1,10)
 190  FORMAT(////F8.3,9(/F8.3))
      READ(11,200)(PP(2,I),I=1,3)
 200  FORMAT(3(/F8.3))
      READ(11,210)(PP(3,I),I=1,9)
 210  FORMAT(//6(/F8.3)/D10.3/F8.3/F8.3)
      READ(11,215)(PP(4,I),I=2,4)
```

```
 215   FORMAT(/F8.3/D10.3/F8.3//)
C
C     Mass transfer and kinetic data
C
       READ(11,220)(VOLK(I),I=1,3)
 220   FORMAT(////,F8.3/D10.3/F8.3)
       VOLK(1)=VOLK(1)*1.D3
       VOLK(3)=VOLK(3)*1.D3
C
C     Cyclone geometrie/s
C
       READ(11,230)ICYC
 230   FORMAT(///I2/)
       DO 250 I=1,8
       READ(11,240)(CYC(J,I),J=1,ICYC)
 240   FORMAT(2F10.5)
 250   CONTINUE
C
C     Program finite difference grid sizings
C
       READ(10,260)SPACE
 260   FORMAT(///A1)
       DO 280 I=1,3
       READ(10,270)NXP(I),SPACE,NXC(I)
 270   FORMAT(I3,A7,I3)
 280   CONTINUE
       READ(10,290)NZB,SPACE,NXBC
 290   FORMAT(I3,A7,I3)
C
C     Program numerical integration grid sizings
C
       READ(10,300)(NVOL(I),I=1,3)
 300   FORMAT(/3(/I3))
C
C     Bed to wall heat transfer
C
       READ(11,320)(HEAT(I),I=1,3)
 320   FORMAT(//3(/F13.8))
       RETURN
       END
C**********DENBED2.10*************************************************
       SUBROUTINE DENBED
C     REVISION 3   DEC. 30 1989   COMPATIBLE WITH CFB2.1
C     AUTHOR:  R.C.SENIOR
C        CFB Riser hydrodynamic routine based on core annulus zone
C     model. Solids flow up the core and downwards in the annular wall
C     region of the riser. Lateral interchange of solids between the
C     two regions may occur, resulting in a variation in axial mean
C     suspension density with riser height.
C        The riser section below secondary air (primary zone) and the
C     first one to two metres of the riser above secondary air is
C     termed the developing flow region. In this region the relatively
C     rapid decay in bulk suspension density (gamma) with height is
C     determined from an empirical equation. Core-wall solids inter-
C     change above the secondary air is inferred from the density
C     profile in this region.
C        Above the developing flow region is the steady flow region.
C     Here the core to wall flux coefficient (see below for
C     definition) is assumed constant. Changes in suspension density
C     with riser height in this region are typically smaller than
C     in the developing flow region.
C
C     (A) Lateral exchange of solids between wall and core regions:
C     ------------------------------------------------------------
C     (i)  Solids lateral mass  transfer expression
C          E = Exchange (kg/unit height/s)
C            = (Pa*ka + Pc*kao)*(beta) - Pf*kc*(alpha)
C
C          where beta  = wall streamer suspension density (kg/m3)
C                alpha = core suspension density (kg/m3)
C                Pa    = streamer interfacial area/unit height (m)
```

```
C               Pf     = core perimeter (m)
C               Pc     = Pw*Pw/Pt
C               Pt     = riser perimeter (m)
C               Pw     = riser perimeter not covered by streamers (m)
C               ka     = wall to core flux coefficient (m/s)
C               kao    = wall to core flux coefficient at zero wall
C                        layer thickness (m/s)
C               kc     = core to wall flux coefficient (m/s)
C
C     (ii) Wall to core solids exchange coefficient
C          Based on analogy with gas-liquid annular flow
C          ka = flux coefficient (m/s)
C             = C1/(2.*beta*Vc) * (rhoc*Uc**2) * fsg * (1 + C2*RW/Dh)
C
C          where C1     = wall solids viscous shear entrainment factor
C                         (s/m)
C                Vc     = core solids velocity (m/s)
C                rhoc   = combined core gas/solids bulk density (kg/m3)
C                Uc     = combined core gas/solids velocity (m/s)
C                fsg    = smooth pipe single phase friction factor
C                C2     = wall solids layer disturbance factor
C                RW     = wall layer thickness (m)
C                Dh     = hydraulic diameter (m)
C
C     (iii)Core to wall solids exchange coefficient
C          kc = flux coefficient (m/s)
C             = constant (steady flow region)
C             = a function of the density profile such that mass
C               balance constraints are satisfied (developing flow
C               region)
C
C     (B) Axial supension bulk density profiles:
C     ------------------------------------------
C     (i)  At solids return location - correlation of UBC combustor
C          data.
C          gamma(i) = bulk density @ solids return point (kg/m3)
C                   = C3*(UST**C4) * (Gs/(rhop*(Vc-Vt)))**C5
C
C          where: C3,C4,C5 = correlation coefficients
C                 UST      = dimensionless gas velocity
C                 Gs       = solids recirculation (kg/m2.s)
C                 rhop     = bed particle density (kg/m3)
C                 Vt       = bed particle terminal velocity (m/s)
C
C     (ii) Developing flow region density variation
C          gamma(z) = bulk density @ 'z' metres above solids return
C                     (kg/m3)
C          (gamma(z)-gamma(e))/(gamma(0)-gamma(e)) = exp(-zeta*(z-z0))
C
C          where:gamma(0) = constant reference density (kg/m3)
C                gamma(e) = final limiting density - found by iter-
C                atively comparing the densities and flux coefficients
C                at the developing flow/steady flow region boundaries
C                zeta     = decay contsant
C                z0       = decay distance from gamma(0) to gamma(i)
C
C     (iii)Steady flow region suspension density
C          Found by solving the differential equation for the core
C          density as a function of height:
C          Ac * d(alpha)/dz = (1/Vc - alpha/(Va*beta))  * E
C          then:
C          Aa + Ac = At
C          At * gamma = (Ac * alpha) + (Aa * beta)
C          where:A   = horizontal area (m2)
C                a     denotes  annulus (or streamer)
C                c     denotes  core
C                t     denotes total riser cross-section
C                Va  = velocity of annular streamers (-ve) (m/s)
```

```
C                z   = height up the riser (m)
C          Note: beta is the streamer voidage - assumed constant
C          Boundary condition: Fraction of solids travelling up the
C          core which return down the walls rather than exiting at the
C          top of the riser- termed the reflection coefficient.
C
C
C     INPUT:
C     common block variables (see common block definitions):
C     /BLKG/ gas flow & properties AIR(1),AIR(6),AIR(7),UG(1)
C     /BLKH/ bed geometry BED(1-20)
C     /BLKI/ hydrodynamics HYDZ(1-8),HYDQ(1),HYDG(1),HYDV(1-2),HYDV(5)
C     /BLKP/ particles properties PP(3,1),PP(3,2),PP(3,10)
C     /BLKZ/ no. divisions of riser length for computations ,NZB
C
C     VARIABLES:
C      AA          Annulus cross sectional area (m2)
C      AAMAX       Min. annulus area at which streamers fully cover the
C                  riser wall (m2)
C      AC          Core cross sectional area (m2)
C      EDEV        Voidage at top of dev. flow region
C      EDIL        Core suspension voidage below which a downward
C                  moving wall solids region no longer exists.
C      EGSL        Lowest possible voidage at given solids circulation.
C      EPRI        Voidage at solids recirculation point
C      ESTE        Voidage at bottom of steady flow region
C      ICALL       Call counter-number of calls to this routine
C      (IZS-1)*DZ Height above sec. air of developing flow region (m)
C      RW          Wall layer (streamer) thickness (m)
C      U0          Ave. gas superficial velocity in primary zone, (m/s)
C      ZETA        Developing flow correlation - decay constant (1/m)
C      Z0          Developing flow correlation - see B(ii) above
C
C     OUTPUT (contained in common blocks BLKI,BLKZ,SUBE):
C      DBAV(1)    Mean primary zone bulk density,kg/m**3
C      DBAV(2)    Mean secondary zone bulk density,kg/m**3
C      DBAV(3)    Mean bed bulk density,kg/m**3
C      DBAV(5)    Mean core bulk density,kg/m**3
C      DBAV(6)    Wall streamer bulk density (=DBMAX),kg/m**3
C      DBAV(7)    Approx. pri. zone bulk density @ fuel feed,kg/m**3
C      DBAV(8)    Pnuematic conveying density at which a
C                 downwardly moving wall layer first appears,kg/m**3
C      DBAV(9)    Bulk density at primary zone solids recirc.
C                 entry point,kg/m**3
C      DB(I,J)    Solids bulk density in Ith zone,at Jth height
C                  I=1,Core zone
C                  I=3,Area average of core and wall densities
C      HYDK(1,J)  Core to annulus solids flux coeff. at Jth height,m/s
C      HYDK(2,J)  Wall streamer to core flux coeff. at Jth height,m/s
C      HYDA(1,J)  Core area @ Jth height,m**2
C      HYDA(2,J)  Wall streamer area @ Jth height,m**2
C      HYDA(3,J)  Mean streamer thickness @ Jth height,m
C      HYDA(4,J)  Fraction wall coverage @ Jth height
C      HYDZ(1)    Mean core csa above secondary air,m**2
C      HYDZ(2)    Mean wall streamer area above secondary air,m**2
C      HYDZ(4)    Mean perimeter of core region,m
C      HYDZ(6)    Mean hydraulic diameter of core region,m
C      DZ         Differential height of sec. zone bed used in finite
C                 difference computations
C      PC(J)      Area/unit height across which core to annulus
C                 particles flux,m
C      PA(J)      Surface area/unit height of wall streamers,m
C      PF(J)      Effective area/unit height for re-entrainment (or
C                 rebound) from wall void of streamers,m
C*********************************************************************
      IMPLICIT DOUBLE PRECISION(A-H,O-Z)
      PARAMETER(DBREF=8.D2,ZETA=2.0D0)
```

```
      PARAMETER(EPS2=1.D-2,EPS3=1.D-3,EPS4=1.D-4,EPS5=1.D-5,
     1 EPS6=1.D-6)
      PARAMETER(M=1,NGT=0,NLT=0,LB=1)
      PARAMETER(RELAX=.5D0)
      COMMON/BLKE/IERROR(100),IERR1,IERR2
      COMMON/BLKG/AIR(20),GAST(40),UG(5),TG,PG
      COMMON/BLKH/BED(20),LBED(5),IBED,KBED
      COMMON/BLKI/HYDK(3,100),HYDZ(20),HYDQ(10),HYDG(30),HYDV(10)
      COMMON/BLKP/PP(5,10)
      COMMON/BLKU/HYDA(4,101)
      COMMON/BLKZ/DB(3,101),DBAV(10),DBEX(10),ZB(101),NZB,NXBC
      COMMON/SUBD/VAL(20),IVAL(10)
      COMMON/SUBE/PC(101),PA(101),PF(101),Z0
C     DIMENSION HYDAS(4)
      DIMENSION DBS(101)
      DIMENSION YA(2),YB(2),YOLD(2),YNEW(2),DF(2),LGT(2),LLT(2)
      DIMENSION BFIT(5)
      DIMENSION AP(11),DBP(11)
      INTEGER FLAG
      EXTERNAL DENVAR
      SAVE BFIT,DZ,NZ,DBMAX,PI,PERIMF,AAMAX,RDF1,RDF2,ICALL
      DATA ICALL/0/
      DATA BFIT/2.1062698D0,.2920853D0,.3661963D0,0.D0,0.D0/
C
C     First call to DENBED only:
C     Generate repeatedly used constants and assign them to working
C     common block SUBD. SUBD is used in routines DENBED, NETFLX,
C     DENVAR and ANFLUX.
C
CI    IF(ICALL.GT.0) GO TO 30
      PI=4.D0*DATAN(1.D0)
      PERIMF=BED(10)*BED(8)*PI*DSQRT(.5D0+.5D0/HYDZ(8)**2)/
     1 (HYDZ(3)*2.D0)
      AAMAX=PI*BED(10)*BED(8)*HYDZ(3)/4.D0
      RDF1=BED(8)-PI*HYDZ(3)/2.D0
      RDF2=RDF1**2+PI*HYDZ(3)*BED(8)
      DZ=BED(3)/NZB
      NZ=NZB+1
      DBMAX=(1.D0-PP(3,2))*PP(3,1)
      DBAV(6)=DBMAX
C
      IVAL(1)=-1
      VAL(2)=PP(3,1)
      VAL(5)=DBMAX
      VAL(6)=AAMAX
      VAL(7)=BED(10)*BED(8)
      VAL(8)=PERIMF
      VAL(9)=PI
      VAL(10)=DBAV(8)
      VAL(15)=HYDZ(7)/BED(8)
      VAL(17)=RDF1
      VAL(18)=RDF2
C
C     Check for column choking - Punwani correlation [39]
C
      J=0
      ALPHA=8.72D-3*AIR(6)**.77D0/(2.D0*9.81D0*BED(8))
      VT=UG(1)-HYDV(1)
      ECH=.97D0
 10   VCH=HYDG(1)/(PP(3,1)*(1.D0-ECH))+VT
      BETA=ALPHA*(VCH-VT)**2+1.D0
      ECHN=1.D0/(BETA**4.7D0)
      IF(ECHN.GT.1.D0) ECHN=1.D0
      J=J+1
      EPS=DABS(1.D0-ECHN/ECH)
      IF(EPS.LT.1.D-4) GO TO 20
      IF(J.GT.20) THEN
        IERROR(12)=1
        IERR1=1
        GO TO 20
      ENDIF
      ECH=(ECHN+ECH)/2.D0
```

```
      GO TO 10
 20   UCH=VCH*ECH
      IF(UCH.GT.UG(5)) THEN
        IERROR(64)=2
        IERR2=2
        RETURN
      ENDIF
C
C     Check reasonableness of hydrodynamic inputs
C
      IF(HYDV(2).GE.0.D0) IERROR(69)=2
      IF(HYDV(1).LE.0.D0) IERROR(70)=2
      IF(HYDG(1).LE.0.D0) IERROR(71)=2
      IF(PP(3,2).GT.1.D0.OR.PP(3,2).LT..2D0) IERROR(72)=2
      TEST=HYDV(2)*(HYDV(1)*DBMAX-HYDG(1))/(HYDV(1)*(HYDV(2)*DBMAX-
     1 HYDG(1)))
      IF(HYDZ(5).GE.TEST.OR.HYDZ(5).GE.1.D0) IERROR(73)=2
      IF(HYDZ(5).LT.0.D0) IERROR(73)=2
      IF(HYDZ(7).LE.0.D0) IERROR(74)=2
      IERR2=MAX0(IERROR(69),IERROR(70),IERROR(71),IERROR(72),
     1 IERROR(73),IERROR(74))
      IF(IERR2.EQ.2) RETURN
C
C     Lower riser density limit at which downward moving wall layer
C     disappears
C     -Kono and Saito correlation modified by Knowlton [39](version 9)
C     -constant pending satisfactory correlation (version 10)
C
 30   CONTINUE
C     VT=UG(1)-HYDV(1)
C     VP=UG(5)-VT
C     REG = AIR(6)*BED(8)*UG(5)/AIR(7)
C     DBAV(8)=.27685D0*(AIR(6)*UG(5)*VP/(BED(8)*9.81D0))/REG**.25D0
      DBAV(8)=2.0D0
      EDIL=1.D0-DBAV(8)/PP(3,1)
      EGSL=1.D0-HYDG(1)/(PP(3,1)*HYDV(1))
      EMIN=DMIN1(EDIL,EGSL)
C
C     Primary zone bulk density at solids recirc.
C
      APRI=BED(1)/BED(2)
      U0=AIR(1)/APRI
      UST=U0*(AIR(6)**2/(AIR(7)*9.81D0*(PP(3,1)-AIR(6))))**
     1 (1.D0/3.D0)
      VELRAT=HYDG(1)/(PP(3,1)*(U0-HYDV(5)))
C     CDRAG=4.D0*AR**(1.D0/3.D0)/(3.D0*UST*UST)
C     GRAT=HYDG(1)/(AIR(6)*U0)
C     AR=PP(3,10)**3*AIR(6)*(PP(3,1)-AIR(6))*9.81D-9/(AIR(7)**2)
      EPRI=1.D0-BFIT(1)*UST**BFIT(2)*VELRAT**BFIT(3)
C-----------------------------------------------------------------------
C
C     Estimate wall solids viscous shear entrainment factor HYDZ(10)
C
CO    VAL(16)=-1.D0/(2.D0*DBMAX*HYDV(2))
      VAL(16)=1.D0/(2.D0*DBMAX*HYDV(1))
      V2=1.D0-DBAV(8)/PP(3,1)
      AC2=BED(4)
      RW2=0.D0
      CALL ANFLUX(1,V2,AC2,RW2,FCTR,HYDK20)
CI    B3=(VAL(13)*VAL(12)**2*VAL(14))/(2.D0*DBMAX*HYDV(1))
      B3=(VAL(13)*VAL(12)**2*VAL(14))**.25D0/(2.D0*DBMAX*HYDV(1))
      B4=DBAV(8)/DBMAX
      HYDZ(10)=HYDQ(1)*B4/B3
      FCTR=HYDZ(10)
      IF(FCTR.LE.0.D0) THEN
        IERR2=2
        IERROR(65)=2
        RETURN
      ENDIF
      CALL ANFLUX(0,V2,AC2,RW2,FCTR,HYDK20)
      VAL(4)=HYDK20
```

```
      HYDQ(3)=HYDK20
C
C     Find zero flux condition (Root finding - Muller's method)
C
C     XF=EPRI
      XF=PP(3,2)
      XS=EMIN
      X1=EMIN*(1.D0-EPS3)
      CALL NETFLX(X1,Y1)
      DX=(XF-XS)/2.D1
 100  X3=X1+DX
      IF(X3.LT.XF) GO TO 190
      CALL NETFLX(X3,Y3)
      IF(Y3*Y1)120,170,110
 110  X1=X3
      Y1=Y3
      GO TO 100
 120  ITER=0
 130  X2=(X1*Y3-X3*Y1)/(Y3-Y1)
      CALL NETFLX(X2,Y2)
      ITER=ITER+1
      IF(ITER.GT.66) THEN
        IERR2=2
        IERROR(66)=2
        RETURN
      ENDIF
      IF(ITER.EQ.0) GO TO 145
      IF(DABS((X2-X20)/(X2+X20)).LE.EPS6) GOTO 180
 145  IF(Y1*Y2)150,180,160
 160  X1=X2
      Y1=Y2
      X20=X2
      GO TO 130
 150  X3=X2
      Y3=Y2
      X20=X2
      GO TO 130
 170  X2=X3
 180  NR=1
      EQFLX=X2
      ZERFLX=X2
      GO TO 200
 190  NR=0
      IERROR(76)=2
      IERR2=2
      RETURN
 200  CONTINUE
C-----------------------------------------------------------------------
C
C     Riser top densities (incl. test for negligible wall layer)
C
      ALPHA=HYDV(1)*(HYDZ(5)/(HYDV(2)*DBMAX)+(1.D0-HYDZ(5))/HYDG(1))
      BETA=1.D0/(DBMAX*.8D0)
      IF(ALPHA.LT.BETA) THEN
        IERROR(67)=2
        IERR2=2
        RETURN
      ENDIF
      IERROR(13)=0
      DB(1,NZ)=1.D0/ALPHA
      IF(DB(1,NZ).GT.DBAV(8)) THEN
        HYDA(1,NZ)=BED(4)*(1.D0+HYDZ(5)*HYDG(1)/((1.D0-HYDZ(5))*
     1  HYDV(2)*DBMAX))
        HYDA(2,NZ)=BED(4)-HYDA(1,NZ)
        IF(HYDA(2,NZ).GT.AAMAX) THEN
          RD=.5D0*(RDF1-DSQRT(RDF2-4.D0*HYDA(2,NZ)/BED(10)))
          HYDA(3,NZ)=HYDZ(3)+RD
          HYDA(4,NZ)=1.D0
          PA(NZ)=PERIMF*HYDZ(3)*(1.D0-RD/BED(8))
        ELSE
          HYDA(3,NZ)=2.D0*DSQRT(HYDA(2,NZ)*HYDZ(3)/
     1     (PI*BED(10)*BED(8)))
```

```
          HYDA(4,NZ)=HYDA(3,NZ)/HYDZ(3)
          PA(NZ)=HYDA(3,NZ)*PERIMF
        ENDIF
      ELSE
        IERROR(13)=1
        IERR1=1
        DB(1,NZ)=HYDG(1)/HYDV(1)
        HYDA(1,NZ)=BED(4)
        HYDA(2,NZ)=0.D0
        HYDA(3,NZ)=0.D0
        HYDA(4,NZ)=0.D0
      ENDIF
      PC(NZ)=BED(10)*BED(8)*(1.D0-HYDA(4,NZ))**2
      PF(NZ)=BED(10)*(BED(8)-2.D0*HYDA(3,NZ))
      DB(3,NZ)=DBMAX-(DBMAX-DB(1,NZ))*HYDA(1,NZ)/BED(4)
C-----------------------------------------------------------------------
C
C     Primary zone bulk density at:(i)fuel feed point,and (ii)
C     sec. air.
C
      IF(DB(1,NZ).LE.DBAV(8)) EQFLX=EMIN
      ITRP=0
      DBAV(9)=PP(3,1)*(1.D0-EPRI)
 300  DBFLX=PP(3,1)*(1.D0-EQFLX)
      Z0=DLOG((DBAV(9)-DBFLX)/(DBREF-DBFLX))/ZETA
      Z=BED(12)-BED(11)
      IF(Z.LT.0.D0) THEN
        DBAV(7)=DBAV(9)*BED(12)/BED(11)
      ELSE
        BETA=DEXP(-ZETA*(Z-Z0))
        DBAV(7)=DBFLX+(DBREF-DBFLX)*BETA
      ENDIF
      Z=BED(2)-BED(11)
      BETA=DEXP(-ZETA*(Z-Z0))
      DBS(1)=DBFLX+(DBREF-DBFLX)*BETA
      Z1=BED(2)-BED(11)-Z0
C
C     Region of developing solids flow above the secondary air:
C     Task (i)   CSA mean suspension bulk densities DBS(I) vrs height
C                 - decaying exponential relationship
C          (ii)  Core densities and annulus areas  DB(1,I),HYDA(2,I)
C          (iii) Core to annulus flux coefficients HYDK(1,I)
C          (iv)  Define height of end of developing flow zone as the
C                location where the core to ann. flux coefficient
C                computed from finite difference representation
C                of decaying suspension curve matches the value
C                assumed constant in the fully developed flow regime
C                ( (IZS-1)*DZ) )
C
      I=0
 330  CONTINUE
      I=I+1
      Z=(I-1)*DZ+Z1
      BETA=DEXP(-ZETA*Z)
      DBS(I)=DBFLX+(DBREF-DBFLX)*BETA
      DB(3,I)=DBS(I)
C
      IF(DBS(I).GE.DBMAX) THEN
        IERROR(64)=2
        IERR2=2
        RETURN
      ENDIF
      DB(1,I)=DBMAX*(HYDG(1)-HYDV(2)*DBS(I))/(DBMAX*
     1 (HYDV(1)-HYDV(2))+HYDG(1)-HYDV(1)*DBS(I))
      HYDA(1,I)=BED(4)*(DBMAX-DBS(I))/(DBMAX-DB(1,I))
      HYDA(2,I)=BED(4)-HYDA(1,I)
      IF(HYDA(2,I).GT.AAMAX) THEN
        RD=.5D0*(RDF1-DSQRT(RDF2-4.D0*HYDA(2,I)/BED(10)))
        HYDA(3,I)=HYDZ(3)+RD
        HYDA(4,I)=1.D0
        PA(I)=PERIMF*HYDZ(3)*(1.D0-RD/BED(8))
```

```
        ELSE
          HYDA(3,I)=2.D0*DSQRT(HYDA(2,I)*HYDZ(3)/
     1    (PI*BED(10)*BED(8)))
          HYDA(4,I)=HYDA(3,I)/HYDZ(3)
          PA(I)=HYDA(3,I)*PERIMF
        ENDIF
        PC(I)=BED(10)*BED(8)*(1.D0-HYDA(4,I))**2
        PF(I)=BED(10)*(BED(8)-2.D0*HYDA(3,I))
        IF(I.EQ.1) GO TO 330
C
        IP=I-1
        VOID=1.D0-(DB(1,I)+DB(1,IP))/(2.D0*PP(3,1))
        AC=(HYDA(1,I)+HYDA(1,IP))/2.D0
        RW=(HYDA(3,I)+HYDA(3,IP))/2.D0
        CALL ANFLUX(0,VOID,AC,RW,FCTR,HYDK2W)
        HYDK(2,IP)=HYDK2W
        HYDK(1,IP)=DBMAX*(2.D0*HYDV(2)*(HYDA(2,I)-HYDA(2,IP))/DZ+
     1 HYDK2W*(PA(I)+PA(IP))+HYDK20*(PC(I)+PC(IP)))/
     2 (PF(I)*DB(1,I)+PF(IP)*DB(1,IP))
        HTEST=HYDK(1,IP)/HYDQ(1)-1.D0
        DBMIN=(1.D0-EMIN)*PP(3,1)
        IF(ITRP.GT.1.AND.ESTE.LT.ZERFLX) THEN
          IF(I.LT.IZS) GO TO 330
          GO TO 345
        ENDIF
        HEND=DBS(I)/DBFLX-1.D0
        IF(HEND.LT.EPS2) GO TO 340
        IF(HTEST.GT.5.D-2) GO TO 330
 340    IZS=I
 345    IF(DB(1,NZ).LE.DBAV(8)) GO TO 500
C-----------------------------------------------------------------
C
C     Solve core bulk denity d.e.;d(DB(1,I))/dZ, in the steady flow
C     region from riser top down to top of developing flow region.
C
        HMAX=DZ
        HSTART=1.D-2*HMAX
        DO 360 I=NZB,IZS,-1
        YA(1)=DB(1,I+1)
        Z1=(NZB-I)*DZ
        Z2=Z1+DZ
        HMIN=1.D-7*HMAX
        CALL ODERKF(DENVAR,Z1,Z2,YA,DF,EPS4,HSTART,HMIN,HMAX,YB,
     1 NFUN,FLAG,M,NGT,NLT,LGT,LLT,LB,YNEW,YOLD)
        IF(FLAG.EQ.0) THEN
          IERROR(60)=2
          IERR2=2
          RETURN
        ENDIF
        IF(FLAG.EQ.3) THEN
          IERROR(62)=2
          IERR2=2
          RETURN
        ENDIF
        DB(1,I)=YB(1)
        HYDA(1,I)=BED(4)*(HYDG(1)-HYDV(2)*DBMAX)/(HYDV(1)*DB(1,I)
     1 -HYDV(2)*DBMAX)
        HYDA(2,I)=BED(4)-HYDA(1,I)
        IF(HYDA(2,I).GT.AAMAX) THEN
          RD=.5D0*(RDF1-DSQRT(RDF2-4.D0*HYDA(2,I)/BED(10)))
          HYDA(3,I)=HYDZ(3)+RD
          HYDA(4,I)=1.D0
          PA(I)=PERIMF*HYDZ(3)*(1.D0-RD/BED(8))
        ELSE
          HYDA(3,I)=2.D0*DSQRT(HYDA(2,I)*HYDZ(3)/
     1    (PI*BED(10)*BED(8)))
          HYDA(4,I)=HYDA(3,I)/HYDZ(3)
          PA(I)=HYDA(3,I)*PERIMF
        ENDIF
        DB(3,I)=DBMAX-(DBMAX-DB(1,I))*HYDA(1,I)/BED(4)
        PC(I)=BED(10)*BED(8)*(1.D0-HYDA(4,I))**2
        PF(I)=BED(10)*(BED(8)-2.D0*HYDA(3,I))
```

```
      IP=I+1
      VOID=1.D0-(DB(1,I)+DB(1,IP))/(2.D0*PP(3,1))
      AC=(HYDA(1,I)+HYDA(1,IP))/2.D0
      RW=(HYDA(3,I)+HYDA(3,IP))/2.D0
      CALL ANFLUX(0,VOID,AC,RW,FCTR,HYDK2W)
      HYDK(2,I)=HYDK2W
      HYDK(1,I)=HYDQ(1)
 360  CONTINUE
C-----------------------------------------------------------------------
C
C     Match top of developing solids flow region to bottom of constant
C     flow region.
      EDEV=1.D0-DBS(IZS)/PP(3,1)
      ESTE=1.D0-DB(3,IZS)/PP(3,1)
      EQTST=DABS((EDEV-ESTE)/(1.D0-ESTE))
      IF(EQTST.LE.5.D-2) GO TO 740
      IF(ITRP.EQ.0) THEN
        IF(ESTE.LT.ZERFLX) THEN
          EQFLX=ESTE
          E1=ESTE
          GO TO 410
        ELSE
          EQL=ZERFLX
          EQFLX=EMIN
          GO TO 410
        ENDIF
      ENDIF
      IF(ITRP.EQ.1) THEN
        IF(EQFLX.EQ.EMIN.AND.EDEV.LT.ESTE) GO TO 620
        IF(ESTE.GT.ZERFLX) THEN
          EQH=EMIN
        ELSE
          EQL=DMIN1(ESTE,E1)
          EQH=DMAX1(ESTE,E1)
        ENDIF
        GO TO 400
      ENDIF
      IF(EDEV.LT.ESTE) THEN
        EQL=EQFLX
      ELSE
        EQH=EQFLX
      ENDIF
 400  CONTINUE
      IF(ITRP.GT.10) THEN
        EQFLX=(1.D0-RELAX)*EQFLX+RELAX*(EQL+EQH)/2.D0
      ELSE
        EQFLX=(EQL+EQH)/2.D0
      ENDIF
 410  ITRP=ITRP+1
      IF(ITRP.GT.15) THEN
        IERROR(15)=1
        IERR1=1
C        IERROR(68)=2
C        IERR2=2
C        RETURN
      ENDIF
      DBFLX=(1.D0-EQFLX)*PP(3,1)
      GO TO 300
C-----------------------------------------------------------------------
C
C     Dilute pnuematic conveyor
C
 500  DO 540 I=IZS+1,NZ
      DB(1,I)=DB(1,NZ)
      DB(3,I)=DB(3,NZ)
      HYDA(1,I)=BED(4)
      HYDA(2,I)=0.D0
      HYDA(3,I)=0.D0
      HYDA(4,I)=0.D0
      PA(I)=0.D0
      PC(I)=BED(10)*BED(8)
      PF(I)=PC(I)
```

```
 540   CONTINUE
       DO 550 I=IZS,NZB
       HYDK(2,I)=HYDK20
 550   CONTINUE
 620   CONTINUE
C-----------------------------------------------------------------
C     Core to annulus flux coefficients in riser steady flow region
C
 740   DO 750 I=IZS,NZB
       HYDK(1,I)=HYDQ(1)
 750   CONTINUE
C-----------------------------------------------------------------
C
C     Zone mean areas and bulk densities-Simpson's rule integration
C
 840   DBAV(5)=0.D0
       CALL WALCON(1)
       NP=2*((NZ-1)/2)-1
       DO 850 I=1,NP,2
       DBAV(5)=DBAV(5)+DB(1,I)*HYDA(1,I)+4.D0*DB(1,I+1)*HYDA(1,I+1)
     1 +DB(1,I+2)*HYDA(1,I+2)
 850   CONTINUE
       IF(NP+2.EQ.NZ) GO TO 860
       DBAV(5)=DBAV(5)+2.D0*DB(1,NZB)*HYDA(1,NZB)+1.25D0*DB(1,NZ)*
     1 HYDA(1,NZ)+.25D0*DB(1,NZ-2)*HYDA(1,NZ-2)
 860   DBAV(5)=DBAV(5)*DZ/(3.D0*BED(3)*HYDZ(1))
       DBAV(2)=(DBAV(5)*HYDZ(1)+DBAV(6)*HYDZ(2))/BED(4)
       MASSP=0.D0
       DZP=(BED(2)-BED(11))/10.D0
       DO 820 I=1,11
       Z=(I-1)*DZP
       BETA=DEXP(-ZETA*(Z-Z0))
       DBP(I)=DBFLX+(DBREF-DBFLX)*BETA
       AP(I)=BED(15)+(BED(4)-BED(15))*Z/(BED(2)-BED(11))
 820   CONTINUE
       DO 830 I=1,9,2
       MASSP=MASSP+AP(I)*DBP(I)+4.D0*AP(I+1)*DBP(I+1)+AP(I+2)*DBP(I+2)
 830   CONTINUE
       DBAV(1)=(MASSP*DZP/3.D0+DBAV(9)*BED(11)*(2.D0*BED(15)+BED(14))
     1 /6.D0)/BED(1)
       DBAV(3)=(DBAV(1)*BED(1)+DBAV(2)*BED(3)*BED(4))/(BED(1)+
     1 BED(3)*BED(4))
C
       ICALL=ICALL+1
       RETURN
       END
C**************DENVAR2.8*****************************************
       SUBROUTINE DENVAR(Z,Y,DY,LIMIT)
C     REVISION 1      JULY   21   1989
C     Computes the derivative DY(1) of the core density vrs riser
C     height function at height Z and core suspension density Y(1).
C     IVAL(1)=1  :Solution advances in direction sec. air to top .
C     IVAL(1)=-1 :Solution advances in direction top to sec. air.
C     Differential equation constants:
C     VAL(1)                 VAL(2)=PP(3,1)     VAL(3)
C     VAL(4)=HYDK20          VAL(5)=DBMAX       VAL(6)=AAMAX
C     VAL(7)=BED(10)*BED(8) VAL(8)=PERIMF      VAL(9)=PI
C     VAL(10)=DBAV(8)        VAL(11)
C     VAL(12-16) see routine ANFLUX
C     VAL(17)=RDF1           VAL(18)=RDF2
C*****************************************************************
       IMPLICIT DOUBLE PRECISION(A-H,O-Z)
       COMMON/BLKH/BED(20),LBED(5),IBED,KBED
       COMMON/BLKI/HYDK(3,100),HYDZ(20),HYDQ(10),HYDG(30),HYDV(10)
       COMMON/SUBD/VAL(20),IVAL(10)
       DIMENSION Y(1),DY(1)
       Z=Z
       IF(Y(1).GT.VAL(5)) THEN
         LIMIT=1
         RETURN
       ENDIF
```

```
      LIMIT=0
      AC=BED(4)*(HYDG(1)-HYDV(2)*VAL(5))/(HYDV(1)*Y(1)-HYDV(2)
     1 *VAL(5))
      AA=BED(4)-AC
      IF(AA.GT.VAL(6)) THEN
        RD=.5D0*(VAL(17)-DSQRT(VAL(18)-4.D0*AA/BED(10)))
        RW=HYDZ(3)+RD
        PA=VAL(8)*HYDZ(3)*(1.D0-RD/BED(8))
      ELSE
        RW=2.D0*DSQRT(AA*HYDZ(3)/(VAL(9)*VAL(7)))
        PA=VAL(8)*RW
      ENDIF
      PC=VAL(7)*(1.D0-RW/HYDZ(3))**2
      PF=VAL(7)*(1.D0-2.D0*RW/BED(8))
      VOID=1.D0-Y(1)/VAL(2)
      FCTR=HYDZ(10)
      CALL ANFLUX(0,VOID,AC,RW,FCTR,HYDK2W)
      FLX=(PA*HYDK2W+PC*VAL(4))*VAL(5)-HYDQ(1)*Y(1)*PF
      DY(1)=(1.D0/HYDV(1)-Y(1)/(HYDV(2)*VAL(5)))*FLX/AC
      IF(IVAL(1).EQ.-1) DY(1)=-DY(1)
      RETURN
      END
C*************ERCHEK2.1*********************************************
       SUBROUTINE ERCHEK
C     REVISION 8  JULY    27  1989
C     COMPATIBLE WITH VERSION CFB2.1
C     Outputs diagnostic warning and error messages
C     INPUT:IERROR(J) ;Flag for Jth diagnostic warning/error message
C           IERR1     ;Flag to idicate a warning message is required
C           IERR2     ;Flag to idicate an error message is required
C           Flag=0    ;No error
C           Flag=1or2 ;Warning/error message is generated - a program
C                      a program variable is  outside the expected
C                      range,or an iterative loop has exceeded maximum
C                      iterations limit or a subruotine has failed
C           Flag=1    ;Run continues
C           Flag=2    ;Run terminates
C     Error messages contained in direct access file 'ERMSSG'
C*******************************************************************
      IMPLICIT DOUBLE PRECISION(A-H,O-Z)
      COMMON/BLKE/IERROR(100),IERR1,IERR2
      CHARACTER*74 WORD(3)
      OPEN(UNIT=14,FILE='ERMSSG',FORM='FORMATTED',ACCESS='DIRECT',
     1 RECL=74,STATUS='OLD')
      WRITE(6,10)
 10   FORMAT(1X/)
C
C     Warning messages
C
      IF(IERR1.EQ.0) GO TO 410
      DO 400 I=1,15
      IF(IERROR(I).EQ.1) THEN
        K=3*I+5
        DO 100 J=1,3
C       LREC=(J+K)*1000
        LREC=(J+K)
        READ(14,50,REC=LREC)WORD(J)
 50     FORMAT(A75)
        WRITE(6,60)WORD(J)
 60     FORMAT(1X,A75)
 100    CONTINUE
      ENDIF
 400  CONTINUE
 410  CONTINUE
      IF(IERR2.EQ.0) RETURN
      WRITE(6,10)
      DO 500 I=50,76
      IF(IERROR(I).EQ.2) THEN
        K=3*I+5
        DO 450 J=1,3
C       LREC=(J+K)*1000
```

```
          LREC=(J+K)
          READ(14,50,REC=LREC)WORD(J)
          WRITE(6,60)WORD(J)
 450      CONTINUE
        ENDIF
 500    CONTINUE
        WRITE(6,10)
        RETURN
        END
C***************ERINIT2.1*********************************************
        SUBROUTINE ERINIT
C     REVISION 0   APRIL 06 89
C     Initializes error flags to 'no error' status
C     Must be called prior to calling any CFB model version 2.1
C     routines ,or running the complete CFB 2.1 model.
C*******************************************************************
        IMPLICIT DOUBLE PRECISION(A-H,O-Z)
   9            COMMON/BLKE/IERROR(100),IERR1,IERR2
        IERR1=0
        IERR2=0
        DO 10 I=1,100
        IERROR(I)=0
 10     CONTINUE
        RETURN
        END
C**************MASBAL2.2**********************************************
        SUBROUTINE MASBAL(MFLAG)
C     REVISION 0      DEC.  15  1989                AUTHOR: R.C.Senior
C     Performs overall mass balance computations for the CFB combustor
C     based on 100% combustion efficiency.
C
C     INPUT: Ultimate analysis of fuel (wt% ash,C,H,O,S,N), (variables
C            PP(1,2-6),PP(1,9) in common block BLKP
C            Gas species molecular weights (defined below - PARAMETER)
C            Limestone Ca:S ratio and %CaCO3 in limestone (PP(2,2-3))
C            Capture efficiency of SO2 (GAST(7))
C
C     INPUT/OUTPUT:
C            (i)  Fuel feedrate, kg/s                          HYDG(2)
C            (ii) Mole % O2 in the product gas (dry basis)     GAST(11)
C            (iii)Excess air, %                                GAST(5)
C
C     OPTIONS:
C            (a)  MFLAG=-1 , input (i) and compute (ii),(iii)
C            (b)  MFLAG= 0 , input (iii) and compute (i),(ii)
C            (c)  MFLAG= 1 , input (ii) and compute (i),(iii)
C
C     OUTPUT:(iv)  Product wet gas flowrate, m3/s @ TG,PG     GAST(1)
C            (v)   Product dry gas flowrate, m3/s @ TG,PG     GAST(2)
C            (vi)  Mean molecular weight of product gas       GAST(6)
C            (vii) Mole % CO2 in the product gas (dry basis) GAST(12)
C            (viii)PPM SO2 in the product gas (dry basis)     GAST(13)
C            (ix)  Mole % O2 in the product gas (wet basis)  GAST(16)
C            (x)   Mole % CO2 in the product gas (wet basis) GAST(17)
C            (xi)  Limestone feedrate, kg/s                   HYDG(3)
C
C*******************************************************************
        IMPLICIT DOUBLE PRECISION(A-H,O-Z)
        COMMON/BLKE/IERROR(100),IERR1,IERR2
        COMMON/BLKG/AIR(20),GAST(40),UG(5),TG,PG
        COMMON/BLKI/HYDZ(10),HYDK2,HYDK(3,100),HYDG(4),HYDM,HYDV(3)
        COMMON/BLKP/PP(5,10)
        PARAMETER(WCO2=44.D0,WH2O=18.D0,WSO2=64.D0,WO2=32.D0,WN2=28.D0)
        PARAMETER(WCACO3=100.D0)
        PARAMETER(AC=12.D0,AO=16.D0,AN=14.D0,AS=32.D0,AH=1.D0)
        PARAMETER(RG=8.314D0)
C
        AIRSUP=PG*(AIR(1)+AIR(2))/(RG*TG)*1.D-3
        O2SUP=AIR(3)*AIRSUP*1.D-2
        ALPHA=PP(1,6)/AS*(PP(2,3)-1.5D-2*GAST(7))+PP(1,4)*.25D0/AH+
```

```
     1 PP(1,9)/WN2+PP(1,5)/WO2+1.D2*PP(1,10)/((1.D0-PP(1,10))*WH2O)
       GAMMA=PP(1,6)/AS*(PP(2,3)-1.5D-2*GAST(7))-PP(1,4)*.25D0/AH+
     1 PP(1,9)/WN2+PP(1,5)/WO2
       BETA=PP(1,3)/AC+PP(1,4)*.25D0/AH+PP(1,6)*(1.D0+.5D-2*GAST(7))/
     1 AS-PP(1,5)/WO2
C********
C      WRITE(6,1)AIRSUP,O2SUP,ALPHA,BETA,MFLAG
C1     FORMAT(1X,'AIRSUP,O2SUP,ALPHA,BETA,MFLAG'/1X,4F14.6,I4)
C*************
       IF(MFLAG) 100,200,300
C
C     Fuel feedrate known  (HYDG(2))
C
 100   CONTINUE
       O2REQT=1.D-2*HYDG(2)*(PP(1,3)/AC+.25D0*PP(1,4)/AH+PP(1,6)/AS)
       O2FUEL=1.D-2*HYDG(2)*PP(1,5)/WO2
       O2REQS=O2REQT-O2FUEL
       O2XS=O2SUP-O2REQS
       GAST(5)=1.D2*O2XS/O2REQS
       GAST(11)=1.D2*(O2SUP-1.D-2*HYDG(2)*BETA)/(AIRSUP*(1.D0-AIR(5)/
     1 1.D2)+1.D-2*HYDG(2)*GAMMA)
       GO TO 400
C
C     Excess air known (GAST(5))
C
 200   CONTINUE
       O2REQS=O2SUP/(GAST(5)/1.D2+1.D0)
       HYDG(2)=1.D2*(O2REQS/(PP(1,3)/AC+.25D0*PP(1,4)/AH+
     1 PP(1,6)/AS-PP(1,5)/WO2))
       GAST(11)=1.D2*(O2SUP-1.D-2*HYDG(2)*BETA)/(AIRSUP*(1.D0-AIR(5)/
     1 1.D2)+1.D-2*HYDG(2)*GAMMA)
       GO TO 400
C
C     Volume (mole) % of oxygen in dry product gas known (GAST(11))
C
 300   CONTINUE
       O2FR=GAST(11)/1.D2
       HYDG(2)=1.D2*(O2SUP-AIRSUP*(1.D0-AIR(5)/1.D2)*O2FR)/
     1 (BETA+O2FR*GAMMA)
       O2REQT=1.D-2*HYDG(2)*(PP(1,3)/AC+.25D0*PP(1,4)/AH+PP(1,6)/AS)
       O2FUEL=1.D-2*HYDG(2)*PP(1,5)/WO2
       O2REQS=O2REQT-O2FUEL
       O2XS=O2SUP-O2REQS
       GAST(5)=1.D2*O2XS/O2REQS
 400   CONTINUE
       WVOUT=1.D-2*HYDG(2)*ALPHA+AIRSUP
C*********
C      WRITE(6,2)WVOUT,HYDG(2),GAST(5),GAST(11)
C2     FORMAT(1X,'WVOUT,HYDG(2),GAST(5),GAST(11)'/1X,4F11.3)
C**********
C      DVOUT=1.D-2*HYDG(2)*GAMMA+AIRSUP*(1.D0-AIR(5)/1.D2)
       H2O=1.D-2*HYDG(2)*(PP(1,4)*.5D0/AH+1.D2*PP(1,10)/
     1 ((1.D0-PP(1,10))*WH2O))+AIRSUP*1.D-2*AIR(5)
       CO2=HYDG(2)*1.D-2*(PP(1,3)/AC+PP(2,3)*PP(1,6)/AS)
       O2=O2SUP-1.D-2*HYDG(2)*BETA
       SO2=HYDG(2)*(1.D-2-1.D-4*GAST(7))*PP(1,6)/AS
       GAST(1)=WVOUT*TG*RG/(1.D-3*PG)
       GAST(2)=(WVOUT-H2O)*TG*RG/(1.D-3*PG)
       GAST(11)=1.D2*O2/(WVOUT-H2O)
       GAST(12)=1.D2*CO2/(WVOUT-H2O)
       GAST(13)=1.D6*SO2/(WVOUT-H2O)
       GAST(16)=1.D2*O2/WVOUT
       GAST(17)=1.D2*CO2/WVOUT
       WGOUT=1.D-2*HYDG(2)*(WCO2*(PP(1,3)/AC+PP(2,3)*PP(1,6)/AS)+
     1 WH2O*PP(1,4)*.5D0/AH+WSO2*(1.D0-GAST(7)/1.D2)*PP(1,6)/AS+
     2 PP(1,9)-BETA*WO2)+O2SUP*WO2+AIRSUP*(AIR(5)*WH2O+AIR(4)*WN2)/
     3 1.D2
       GAST(6)=WGOUT/WVOUT
       IF(PP(2,2).LE..2D0) THEN
         IERR1=1
         IERROR(14)=1
         PP(2,2)=1.D2
```

```
      ENDIF
      HYDG(3)=HYDG(2)*PP(1,6)/AS*PP(2,3)*WCACO3/PP(2,2)
      END
C**************NETFLX2.1*********************************************
      SUBROUTINE NETFLX(ERV,FLX)
C     Computes the net mass flow FLX (kg/s per metre of riser height)
C     away from  the riser wall for a given lateral mean riser
C     voidage, ERV.
C
C     Variables:HYDG(1),HYDV(2),HYDV(1),BED(4),BED(10),HYDZ(3),BED(8),
C               VAL(2)=PP(3,1),VAL(5)=DBMAX,VAL(6)=AAMAX,VAL(17)=RDF1,
C               VAL(18)=RDF2,VAL(8)=PERIMF,
C               VAL(4)=HYDK20,VAL(9)=PI.
C               (see common block definitions)
C               DB3    Riser horizontal mean bulk density
C               DB1    Core bulk density
C
C*****************************************************************
      IMPLICIT DOUBLE PRECISION(A-H,O-Z)
      COMMON/BLKH/BED(20),LBED(5),IBED,KBED
      COMMON/BLKI/HYDK(3,100),HYDZ(20),HYDQ(10),HYDG(30),HYDV(10)
      COMMON/SUBD/VAL(20),IVAL(10)
        DB3=(1.D0-ERV)*VAL(2)
        DB1=VAL(5)*(HYDG(1)-HYDV(2)*DB3)/(VAL(5)*
      1 (HYDV(1)-HYDV(2))+HYDG(1)-HYDV(1)*DB3)
        AC=BED(4)*(VAL(5)-DB3)/(VAL(5)-DB1)
        AA=BED(4)-AC
        IF(AA.GT.VAL(6)) THEN
        RD=.5D0*(VAL(17)-DSQRT(VAL(18)-4.D0*AA/BED(10)))
        RW=HYDZ(3)+RD
        FRCV=1.D0
        PAT=VAL(8)*HYDZ(3)*(1.D0-RD/BED(8))
      ELSE
        RW=2.D0*DSQRT(AA*HYDZ(3)/
     1  (VAL(9)*BED(10)*BED(8)))
        FRCV=RW/HYDZ(3)
        PAT=RW*VAL(8)
      ENDIF
      PCT=BED(10)*BED(8)*(1.D0-FRCV)**2
      PFT=BED(10)*(BED(8)-2.D0*RW)
      VOID=1.D0-DB1/VAL(2)
      FCTR=HYDZ(10)
      CALL ANFLUX(0,VOID,AC,RW,FCTR,HYDK2W)
      FLX=(PAT*HYDK2W+PCT*VAL(4))*VAL(5)-PFT*DB1*HYDQ(1)
      RETURN
      END
C***************SAUTER2.1*********************************************
      SUBROUTINE SAUTER(IP)
C     Calculates Sauter mean diameter from sieve data.
C     INPUT : IP              ;Particle type flag,1=coal,2=lime,3=bed,
C                              4=devolat. particle,5=char
C             SIV(I,J),NSIV ;Sieve data (common block)
C     OUTPUT: PP(IP,10)       ;Sauter mean diameter,mm
C*****************************************************************
      IMPLICIT DOUBLE PRECISION(A-H,O-Z)
      COMMON/BLKJ/SIV(4,25),NSIV
      COMMON/BLKP/PP(5,10)
      IPP=IP+1
      SUM=2.D0*SIV(IPP,1)/(10.D0+SIV(1,1))
      DO 10 I=2,NSIV
      SUM=SUM+2.D0*SIV(IPP,I)/(SIV(1,I-1)+SIV(1,I))
 10   CONTINUE
      PP(IP,10)=100.D0/SUM
      RETURN
      END
C**********SOLAIR2.10*********************************************
      SUBROUTINE SOLAIR
C     REVISION 0   DEC 27  89  COMPATIBLE WITH CFB2.1,DENBED2.10
C     (adapted from SOLGAS2.2:
C     VOID(1),VOID(2) adjusted to match DENBED2.10
C                                                AUTHOR: R.C.SENIOR
```

```
C     Supervises calculation of reactor solids bulk density profile
C     and gas velocities
C     OUTPUT:  UG(2)    Mean secondary zone interstitial gas velocity
C                       through wall streamers,m/s
C              UG(3)    Mean secondary zone interstitial gas vel.,m/s
C              UG(4)    Mean primary zone interstitial gas vel.,m/s
C              UG(5)    Sec. zone superficial gas velocity,m/s
C              HYDV(1)  Mean solids velocity in solids core,m/s
C*********************************************************************
      IMPLICIT DOUBLE PRECISION(A-H,O-Z)
      COMMON/BLKE/IERROR(100),IERR1,IERR2
      COMMON/BLKH/BED(20),LBED(5),IBED,KBED
      COMMON/BLKI/HYDK(3,100),HYDZ(20),HYDQ(10),HYDG(30),HYDV(10)
      COMMON/BLKP/PP(5,10)
      COMMON/BLKZ/DB(3,101),DBAV(10),DBEX(10),ZB(101),NZB,NXBC
      COMMON/BLKG/AIR(20),GAST(40),UG(5),TG,PG
      DIMENSION VOID(2),DP(88),VT(88)
      EXTERNAL DENVAR
      ITER=1
      CALL SULPHA
      UG(5)=(AIR(1)+AIR(2)+GAST(1))/(2.D0*BED(4))
      CALL SAUTER(3)
      DP(1)=PP(3,10)
      VOID(1)=.97D0
      VOID(2)=PP(3,2)
      CALL TERVEL(1,3,DP,VT)
      HYDV(5)=VT(1)
 10   CALL UGCORE(VOID)
      HYDV(1)=UG(1)-VT(1)
      IF(ITER.EQ.1) GO TO 20
      BETA=DABS(1.D0-UG(1)/UGOLD)
      IF(BETA.LT..01D0) GO TO 60
 20   CALL DENBED
      IF(IERR2.EQ.2) GO TO 70
      VOID(1)=1.D0-DBAV(5)/PP(3,1)
      VOID(2)=PP(3,2)
      UGOLD=UG(1)
      ITER=ITER+1
      IF(ITER.GT.20) THEN
        IERROR(1)=1
        IERR1=1
        GO TO 60
      ENDIF
      GO TO 10
 60   CALL DENBED
      IF(IERR2.EQ.2) GO TO 70
      GASFLW=.5D0*(AIR(1)+AIR(2)+GAST(1))
      UG(2)=(GASFLW*PP(3,1)-UG(1)*HYDZ(1)*(PP(3,1)-DBAV(5)))
     1 /(HYDZ(2)*(PP(3,1)-DBAV(6)))
      UG(3)=GASFLW*PP(3,1)/(BED(4)*(PP(3,1)-DBAV(2)))
      UG(4)=AIR(1)*PP(3,1)*BED(2)/(BED(1)*(PP(3,1)-DBAV(1)))
 70   RETURN
      END
C**********************SULPHA2.1*************************************
      SUBROUTINE SULPHA
C     REVISION 0      DECEMBER  27   1989      AUTHOR: R.C.SENIOR
C     Computes the sulphur capture efficiency of the limestone in a
C     CFB
C*********************************************************************
      IMPLICIT DOUBLE PRECISION(A-H,O-Z)
      COMMON/BLKG/AIR(20),GAST(40),UG(5),TG,PG
      GAST(7)=.75D2
      RETURN
      END
C**********UGCORE2.2*****************************************************
      SUBROUTINE UGCORE(VOID)
C     REVISION 0  dec.  27  89  COMPATIBLE WITH CFB2.1
C     Calculates the core gas velocity assuming:
C       (i)  zero gas velocity at combustor wall
C       (ii) constant gas velocity across 'core'
```

```
C       (iii)linear velocity profile across 'annulus'
C       (iv) a mean annulus/streamer csa
C     Hydraulic radius is used for square reator c.s.a's
C     INPUT:  VOID(1)   Core mean voidage
C             VOID(2)   Annulus mean voidage
C             AIR(11),BED(10),HYDZ(6)  (common blocks)
C     OUTPUT: UG(1)     Mean sec. zone core interstitial velocity
C                       assuming 50% of fuel has combusted (m/s)
C*********************************************************************
      IMPLICIT DOUBLE PRECISION(A-H,O-Z)
      COMMON/BLKG/AIR(20),GAST(40),UG(5),TG,PG
      COMMON/BLKH/BED(20),LBED(5),IBED,KBED
      COMMON/BLKI/HYDK(3,100),HYDZ(20),HYDQ(10),HYDG(30),HYDV(10)
      DIMENSION VOID(2)
      PI4=DATAN(1.D0)
      DX=(BED(8)-HYDZ(6))/2.D0
      IF(IBED.EQ.1) THEN
        ALPHA=PI4*(VOID(1)*HYDZ(6)**2+2.D0*VOID(2)*(BED(8)**3/6.D0-
     1  HYDZ(6)**2*BED(8)/2.D0+HYDZ(6)**3/3.D0)/(BED(8)-HYDZ(6)))
      ELSE
        ALPHA=VOID(1)*HYDZ(6)**2+VOID(2)*(2.D0*DX*HYDZ(6)
     1  +8.D0/3.D0*DX**2)
      ENDIF
      UG(1)=(AIR(1)+AIR(2)+GAST(1))/(2.D0*ALPHA)
      RETURN
      END
C******************TERVEL*************************************************
      SUBROUTINE TERVEL(NP,IP,DP,VT)
C     COMPATIBLE WITH CFB2.1   ,REVISION 7     ,MAY   12  89
C
C     Calculates terminal velocity of spherical particles of given
C     diameters
C     INPUT:  IP        Particle type flag (1=coal,2=lime,3=bed,
C                         4=devolat. particle,5=char particle)
C             NP        No. of particles
C             AIR(1-11) Gas properties (common block)
C             DP        Particle diameters ,mm
C     OUTPUT: VT        Particle terminal velocities,m/s
C*********************************************************************
      IMPLICIT DOUBLE PRECISION(A-H,O-Z)
      COMMON/BLKG/AIR(20),GAST(40),UG(5),TG,PG
      COMMON/BLKO/XP(85),NXP(20),XC(30),NXC(20)
      COMMON/BLKP/PP(5,10)
      DIMENSION DP(88),VT(88)
      B1=(AIR(6)*(PP(IP,1)-AIR(6))*9.81D0/(AIR(7)**2))**(1.D0/3.D0)
     1 *1.D-3
      B2=(AIR(7)*9.81D0*(PP(IP,1)-AIR(6))/AIR(6)**2)**(1.D0/3.D0)
      DO 20 I=1,NP
      DPDM=B1*DP(I)
      IF(DPDM.LE.3.8D0) THEN
        VTDM=DPDM**2/18.D0-3.1234D-4*DPDM**5+1.6415D-6*DPDM**8-
     1  7.278D-10*DPDM**11
      ELSE
        W=DLOG10(DPDM)
        IF(DPDM.LT.7.58D0) THEN
          VTDM=10.D0**(-1.5446D0+2.9162D0*W-1.0432D0*W*W)
        ELSE
          VTDM=10.D0**(-1.64758D0+2.94786D0*W-1.09703D0*W*W+.17129D0*
     1    W**3)
        ENDIF
      ENDIF
      VT(I)=VTDM*B2
 20   CONTINUE
      RETURN
      END
C*************WALCON2.1*********************************************
      SUBROUTINE WALCON(IWALL)
C     REVISION 0          JUNE 25  1989            AUTHOR:R.C.SENIOR
C     Input  :IWALL =0 Evoked version of CFB routine DENBED assumes
C                      constant wall layer thickness
C             IWALL =1 Evoked version has a variable wall layer
```

```
C                       thickness
C              IBED,NZB,BED(3),HYDA(1,I),BED(4) (common blocks)
C
C     Output :HYDZ(1)  Mean sec. zone core cross sectional area,m**2
C             HYDZ(2)  Mean sec. zone streamer csa,m**2
C             HYDZ(4)  Mean sec. zone core perimeter,m
C             HYDZ(6)  Mean sec. zone hydraulic diameter,m
C*********************************************************************
      IMPLICIT DOUBLE PRECISION (A-H,O-Z)
      COMMON/BLKH/BED(20),LBED(5),IBED,KBED
      COMMON/BLKI/HYDK(3,100),HYDZ(20),HYDQ(10),HYDG(30),HYDV(10)
      COMMON/BLKU/HYDA(4,101)
      COMMON/BLKZ/DB(3,101),DBAV(10),DBEX(10),ZB(101),NZB,NXBC
      IF(IWALL.EQ.1) GO TO 100
C
C     Constant wall layer thickness case
C
      HYDZ(6)=2.D0*(DSQRT(BED(4)/BED(10))-HYDZ(3))
      HYDZ(1)=BED(10)*HYDZ(6)**2/4.D0
      HYDZ(4)=BED(10)*HYDZ(6)
      HYDZ(2)=BED(4)-HYDZ(1)
      RETURN
C
C     Variable wall layer thickness case (Simpson's Rule Integration)
C
 100  CONTINUE
      NZ=NZB+1
      DZ=BED(3)/NZB
      NP=2*(NZB/2)-1
      SUM=0.D0
      DO 120 I=1,NP,2
      SUM=SUM+HYDA(1,I)+4.D0*HYDA(1,I+1)+HYDA(1,I+2)
 120  CONTINUE
      IF(NP+2.EQ.NZ) GO TO 130
      SUM=SUM+2.D0*HYDA(1,NZB)+1.25D0*HYDA(1,NZ)+.25D0*HYDA(1,NZ-2)
 130  HYDZ(1)=SUM*DZ/(3.D0*BED(3))
      HYDZ(2)=BED(4)-HYDZ(1)
      HYDZ(6)=2.D0*DSQRT(HYDZ(1)/BED(10))
      HYDZ(4)=BED(10)*HYDZ(6)
      RETURN
      END
```